Soil-Foundation-Structure Interaction

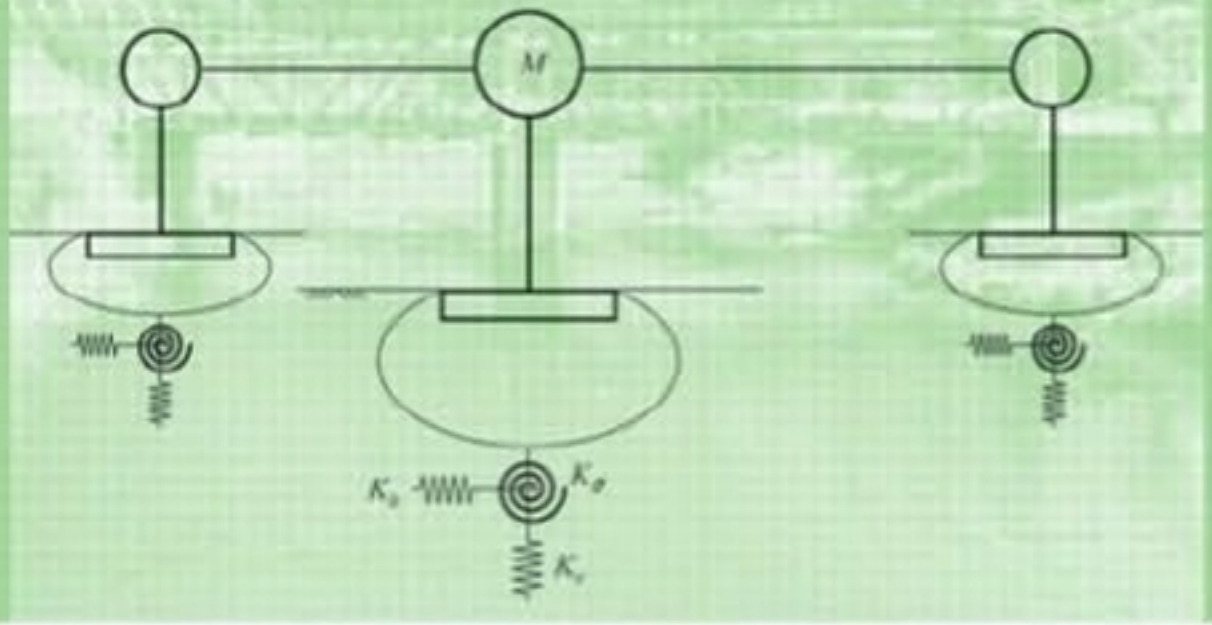

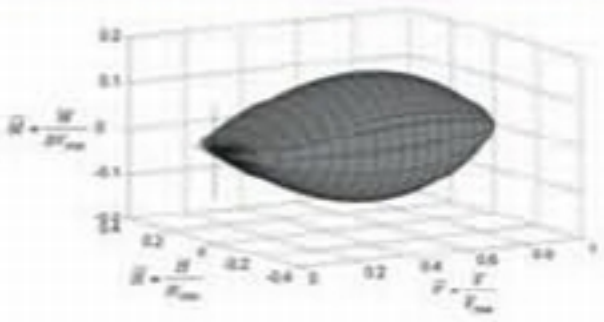

Editors: Rolando P. Orense
Nawawi Chouw
Michael J. Pender

CRC Press
Taylor & Francis Group
A BALKEMA BOOK

SOIL-FOUNDATION-STRUCTURE INTERACTION

SELECTED PAPERS FROM THE INTERNATIONAL WORKSHOP ON SOIL-FOUNDATION-STRUCTURE INTERACTION (SFSI 09), AUCKLAND, NEW ZEALAND, 26–27 NOVEMBER 2009

Soil-Foundation-Structure Interaction

Editors

Rolando P. Orense, Nawawi Chouw & Michael J. Pender
Department of Civil & Environmental Engineering,
University of Auckland, New Zealand

CRC Press
Taylor & Francis Group
Boca Raton London New York Leiden

CRC Press is an imprint of the
Taylor & Francis Group, an **informa** business

A BALKEMA BOOK

CRC Press/Balkema is an imprint of the Taylor & Francis Group, an informa business

Typeset by MPS Ltd. (A Macmillan Company), Chennai, India

Printed and bound in Great Britain by Antony Rowe (a CPI group company),
Chippenham, Wiltshire

Published by: CRC Press/Balkema
P.O. Box 447, 2300 AK Leiden, The Netherlands
e-mail: Pub.NL@taylorandfrancis.com
www.crcpress.com – www.taylorandfrancis.co.uk – www.balkema.nl

ISBN: 978-0-415-60040-8 (Hbk)
ISBN: 978-0-203-83820-4 (eBook)

Soil-Foundation-Structure Interaction – Orense, Chouw & Pender (eds)
© 2010 Taylor & Francis Group, London, ISBN 978-0-415-60040-8

Table of Contents

Towards improved SFSI design procedures

Soil-Foundation-Structure Interaction – Orense, Chouw & Pender (eds)
© 2010 Taylor & Francis Group, London, ISBN 978-0-415-60040-8

Some participants of the SFSI Workshop 09

Soil-Foundation-Structure Interaction – Orense, Chouw & Pender (eds)
© 2010 Taylor & Francis Group, London, ISBN 978-0-415-60040-8

Preface

A topic of long standing interest to both structural and geotechnical engineers is traditionally known as soil-structure interaction. For a long period this has involved linear elastic interaction between the foundation and the underlying soil. The appropriate analysis for this case is well developed for both static and dynamic interaction. In recent years there has been a growing interest in including the effects of nonlinear soil behavior in this modeling. Probably the earliest application of these ideas in practice was to the representation of pile head lateral load response using an array of nonlinear Winkler springs to model the interaction – an approach which continues to be developed to the present time. In recent years there has been interest in considering nonlinear soil foundation interaction in the design of shallow foundations, both for static and dynamic loading. To distinguish this approach from the classical linear elastic soil-structure interaction the term *soil-foundation-structure-interaction* (SFSI) has been coined recently. Another interesting aspect of this has been the development of shallow foundation macro-elements as an alternative to using finite elements, at least for design studies. These are single computational entities that embrace, in a simplified way, the interaction between the soil and structure. Related SFSI work involves retaining structures, particularly the representation of the passive resistance of bridge abutment walls.

Currently, the development of these approaches is occurring rapidly with many groups active in various parts of the world. The *Soil-Foundation-Structure Interaction Workshop (SFSI 09)* held at the University of Auckland, New Zealand from 26–27 November 2009 brought together representatives from several of these groups to review the current state of development, discuss the potential for application in performance based design, and consider how work in this area might develop in the next few years. The emphasis in the workshop was on application of these ideas to the foundation design process.

The participation was by invitation. Our intention was to gather a good representation of those involved in experimental investigation and physical modeling as well as those who have been involved in numerical modelling. Given that the application of these ideas to foundation design will require interaction between the structural and geotechnical communities, some structural engineers attended the workshop. In addition to paper presentations, two discussion sessions aimed at eliciting important comments about the current state of our understanding and to indicate which developments are likely to be most beneficial, were also conducted.

All participants were asked to prepare a paper describing their work. These preprints were circulated in pdf form to those who planned to attend at least a month before the workshop to encourage thinking about the topics to be addressed in the discussion sessions. After the event, the authors were then requested to revise their papers to include some of the comments made during the workshop presentation.

The proceedings consist of 28 high quality papers from geotechnical and structural engineers and researchers which have been individually refereed to check for relevance to the theme of the workshop as well as for quality of technical content and presentation. In addition, full accounts of the two discussion sessions are also included in this volume. The editors therefore hope that the papers presented in this workshop will further advance our understanding of soil-foundation-structure interaction.

Soil-Foundation-Structure Interaction – Orense, Chouw & Pender (eds)
© 2010 Taylor & Francis Group, London, ISBN 978-0-415-60040-8

Acknowledgements

The SFSI 09 Organising Committee would like to acknowledge the financial support provided by the New Zealand Earthquake Commission (EQC) through the University of Auckland's Institute for Earth Science and Engineering (IESE). The committee would also like to thank Ms. Anu Singhal for setting-up the workshop website, Ms. Andrea Ross for transcribing the minutes of the summary sessions and the staff and students of the Department of Civil and Environmental Engineering, University of Auckland, for making the workshop a success. Finally, a sincere thanks to all colleagues and friends who supported this endeavour, especially to those who contributed papers to the workshop and actively participated in the discussion sessions and to the panel of reviewers who donated their precious time, for making this volume possible.

Soil-Foundation-Structure Interaction – Orense, Chouw & Pender (eds)
© 2010 Taylor & Francis Group, London, ISBN 978-0-415-60040-8

Organising Committee

Soil-Foundation-Structure Interaction – Orense, Chouw & Pender (eds)
© 2010 Taylor & Francis Group, London, ISBN 978-0-415-60040-8

Panel of Reviewers

Each paper included in this volume has been carefully reviewed for relevance to the workshop theme as well as for quality of technical content and presentation by at least two members of a panel consisting of the following experts:

Ioannis Anastasopoulos
Mohamed Ashour
Brendon Bradley
CY Chin
Nawawi Chouw
Misko Cubrinovski
W.D. Liam Finn
Michio Iguchi
Graeme Jamieson
Boris Jeremic
Naotaka Kikkawa
Yoshiake Kikuchi
Mark Kiryakos
Takaji Kokusho
Junichi Koseki
Bruce Kutter
Carlo Lai
Ignatius (Po) Lam
Tam Larkin
Geoff Martin
Michele Maugeri
David Muir-Wood
George Mylonakis
Masayuki Nagano
Rolando Orense
Jack Pappin
Alain Pecker
Michael Pender
Harry Poulos
Shamsher Prakash
Satyawan Pranjoto
Jean-Francois Semblat
Sri Sritharan
Timothy Sullivan
Ertugrul Taciroglu
Claudo Tamagnini
Takashi Tazoh
Jeremy Toh
Carlo Viggiani
John Wood
Liam Wotherspoon

Understanding SFSI through experiments and case studies

Soil-Foundation-Structure Interaction – Orense, Chouw & Pender (eds)
© 2010 Taylor & Francis Group, London, ISBN 978-0-415-60040-8

Assessment of varying dynamic characteristics of a SFSI system based on earthquake observation

M. Iguchi
Tokyo University of Science, Noda, Chiba, Japan

M. Kawashima
Sumitomo Mitsui Construction Co. Ltd., Nagareyama, Chiba, Japan

T. Kashima
Building Research Institute, Tsukuba, Ibaraki, Japan

ABSTRACT: Variation in dynamic characteristics of a SFSI system for about ten years is investigated based on 67 earthquake records observed in and around a densely instrumented structure. The results show about 30% reduction of the base-fixed and sway-fixed frequencies in ten years. On the other hand, the extracted rigid-body rocking mode frequency is unchanged over the years. It is shown that the change of the structural frequency is attributed to the deterioration of stiffness of the superstructure. The variation in frequency during some specific earthquakes is also studied, whose result exhibits strong amplitude dependence during the shaking and the frequency recovers almost to the initial state as the shaking is terminated.

1 INTRODUCTION

In recent years, change in dynamic characteristics of soil-structure systems over years has been discussed based on the continuous observation of the system vibrations. Several reasons have been brought out for the causes of the change, but there still remains some unknowns to be investigated. At the same time, since there has been a growing interest in establishing a structural health monitoring technique (Ghanem & Sture 2000, Todorovska & Trifunac 2008), it has become important to capture the actual state of variation and to elucidate the cause of the change based on long-term observations.

A few studies have been presented dealing with the change in system frequencies (or periods) which reflect the global structural stiffness of the system including a soil. Luco et al. (1987) and Clinton et al. (2006) discussed the change in system frequencies over years for a common building, the Millican Library Building (CIT, USA). In the paper by Luco et al. (1987), the cause of the change in system frequency was attributed to the stiffness degradation of the superstructure, in other words, the change was interpreted as being caused by the structural damage. On the other hand, Clinton et al. (2006) suggested that the reduction in system frequency could be attributed to non-linear soil-structure-interaction, and at the same time mentioned other possible causes. In spite of these detailed researches, the cause of the change of the system frequency has not been revealed. In establishing health monitoring procedure, it becomes essential to elucidate the causes of the frequency change of structures.

Recently, Todorovska (2009a, b) has thrown new light on the problem by analyzing a soil-structure interaction (SSI) system by using a system identification method. The system frequency was evaluated taking into account the effects of rigid-body rotational (rocking) motions of the foundation, thus it made possible to ascertain that the shifts of resonant frequencies could have been caused by the stiffness degradations of rocking motions of the structure. Especially, it was shown that the rocking stiffness could degrade significantly during intense earthquakes because of large nonlinearity in the supporting soil (Trifunac et al. 2001a, b). The causes of the change in dynamic characteristics of structures could differ from one building to another. It is desired, therefore, to study the change in as many types of structure as possible.

In this paper, the variation in dynamic characteristics of a soil-structure system is investigated based on earthquake records observed in a densely instrumented building for about ten years. In a previous paper, the aging of the same building has been investigated by Kashima & Kitagawa (2006) using the data before the middle of 2005. Some additional analyses are performed in this study including new data and from different viewpoints. The base-fixed and sway-fixed frequencies and damping factors of the system are extracted from the observed records by means of the subspace identification method (Van Overschee & De Moor 1993) focusing on how the dynamic characteristics of the building vary with the passage of

Figure 1. Front view of BRI annex building (left) and main building (right). These two buildings are connected by passage ways as seen in the picture.

time over years. Focus of the paper is also placed on discussing the cause of the variation.

2 OUTLINE OF OBSERVATORY BUILDING AND OBSERVATION SYSTEM

2.1 *BRI annex building*

Continuous earthquake observation has been conducted in Building Research Institute (BRI) of Japan since 1950s. The BRI annex building is one of the stations of the BRI strong motion network, and a large number of earthquake records have been observed with accelerometers densely installed within the building as well as in the surrounding soil (Kashima & Kitagawa 2006).

The annex building is a steel-reinforced concrete framed structure with eight stories above ground and one story basement, and was completed in 1998. The external view of this building is shown in Figure 1. The building is supported by a flat mat foundation embedded 8.2 m deep in the soil and has no pile. The annex building is connected to the main building with passage ways, but the two buildings are separated by expansion joint and are structurally independent.

2.2 *Seismic observation system*

The seismic observation system at BRI site is composed of 22 accelerometers installed in the annex building, surrounding soil and the main building, and these are deployed so as to enable to extract the dynamic characteristics of soil-structure interaction effects. The configuration of the seismic observation system is shown in Figure 2. Eleven accelerometers are installed in the annex building, and seven in the surrounding soil.

Three accelerometers are installed on both sides of the basement and top floors, which enables us to evaluate not only translational but also rotational (rocking and torsional) motions of the system.

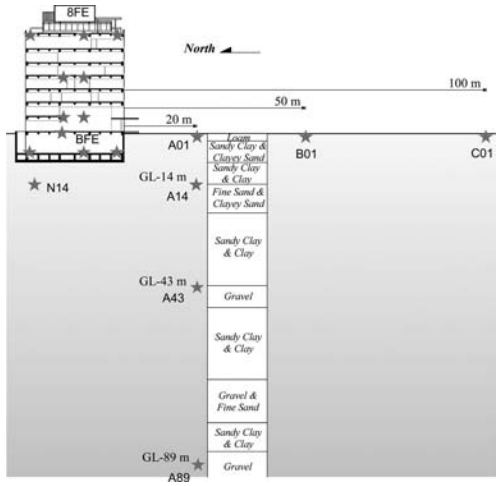

Figure 2. Layout of the seismic observation system in BRI annex building and in surrounding soil.

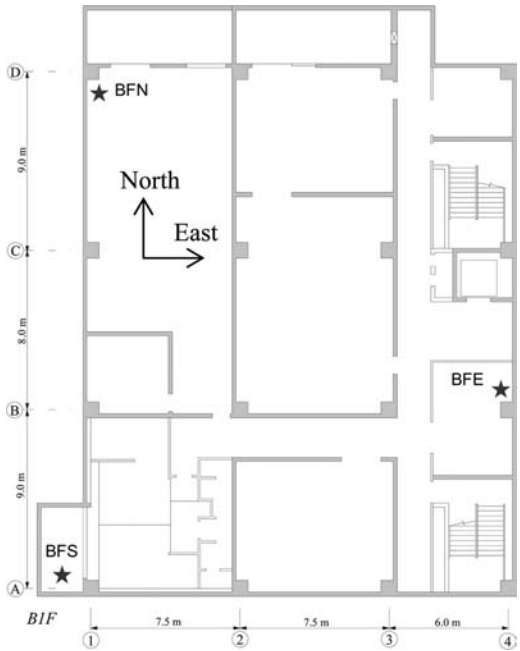

Figure 3. Plan of basement floor and location of three accelerometers installed.

Figure 3 shows the plan of the basement floor and locations of the seismographs. In addition, two accelerometers are deployed in the east and west sides of the fifth and second floors. In computing translational motions, floor responses are evaluated by averaging over the whole records observed on the floor. Rigid-body rocking motions are evaluated by dividing the difference of vertical motions at both sides of foundation by the separation distance between the sensors. In this paper, the effects of torsional motions are not taken into account.

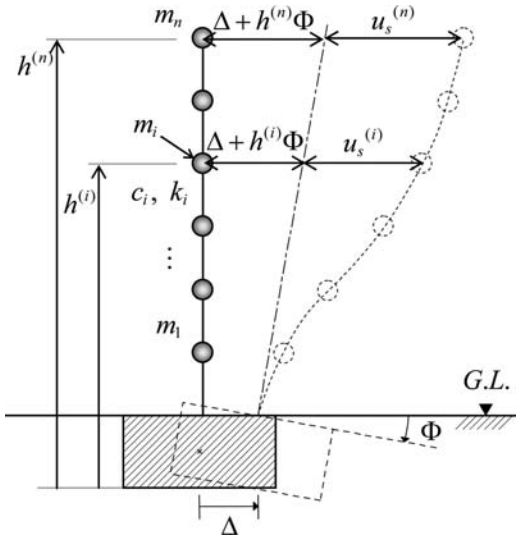

Figure 4. Multi-mass model of a soil-structure system.

2.3 *Observed records*

More than 560 sets of earthquake records have been observed in the BRI annex building since the start of observation in 1998. Among them, the records with peak ground acceleration (PGA) larger than 10 cm/s^2 are selected for analyses. But, somewhat smaller (PGA > 8 cm/s^2) records are included when data satisfying the above criteria were not available for more than a year. As a result, 67 sets of records were analyzed in this paper.

The peak ground accelerations (PGA) of the recorded motions are small in general. The largest PGA of the records is 74 cm/s^2 and the largest inter-story drift angle was 4.7×10^{-5} rad on the average. The BRI annex building can be considered not to have experienced serious structural damage during the earthquakes.

3 METHODOLOGY

3.1 *Equation of motion for SSI system*

In what follows, a formulation of the equation of motion for a SSI system is developed on the assumption that the superstructure is modeled as n degrees-of-freedom shear building supported by a rigid foundation. Figure 4 shows the analysis model and the coordinates of the soil-structure system. The equation of motion for the superstructure may be expressed as

$$[M]\{\ddot{u}_s\} + [C]\{\dot{u}_s\} + [K]\{u_s\} = -[M][R]\{\ddot{u}_F\} \tag{1}$$

where $[M]$, $[C]$, and $[K]$ denote mass, damping, and stiffness matrices of the superstructure, respectively, and $\{u_s\} = \{u_s^{(n)}, u_s^{(n-1)}, \cdots, u_s^{(1)}\}^T$ denotes the relative displacement vector of the superstructure measured removing the rigid body motion from the total displacement. In addition, the vector $\{u_F\} = \{\Delta, L\Phi\}^T$ represents the response of the rigid foundation, in which the components Δ and Φ represent the translational displacement and rocking angle of the foundation, respectively. L denotes a reference length and superscript T denotes the transpose of a vector. The matrix $[R] = [\{1\}L^{-1}\{h\}]$ represents a matrix which relates $\{u_F\}$ to the nodes at which accelerations of the effective input motions apply, where $\{1\}$ is a vector of ones, and $\{h\} = \{h^{(n)}, h^{(n-1)}, \cdots, h^{(1)}\}^T$ represents the height of a floor from the bottom of the basement. The vector $\{u_F\}$, which represents the response of a foundation during earthquakes and may be interpreted as actual input motions for the superstructure, is referred to as an effective input motion (Iguchi et al. 2007). The effective input motion differs from the free-field motions because of both kinematic and inertial interactions.

3.2 *Modal decomposition in state-space*

The objective of this section is to review briefly the fundamental identification procedure for the continuous-time state-space model including the SSI effects for preparation for the next section.

The second order differential equation (Equation 1) may be reduced to the following continuous-time state-space model:

$$\{\dot{x}_c\} = [A_c]\{x_c\} + [B_c]\{u_c\} \tag{2a}$$

$$\{y_c\} = [C_c]\{x_c\} + [D_c]\{u_c\} \tag{2b}$$

where

$$\{x_c\} = \{\{u_s\}^T,\ \{\dot{u}_s\}^T\}^T \tag{3}$$

$$\{u_c\} = \{\ddot{u}_F\} \tag{4}$$

are state and input vectors having $2n$ elements. And,

$$\{y_c\} = \{\ddot{u}_s\} + [R]\{\ddot{u}_F\} = \{\ddot{u}_s\} + \{1\}\ddot{\Delta} + \{h\}\ddot{\Phi} \tag{5}$$

is the output vector whose elements represent absolute accelerations of masses. The matrices $[A_c]$, $[B_c]$, $[C_c]$ and $[D_c]$ are composed of $[M]$, $[C]$, $[K]$ and $[R]$. Subscript c indicates the continuous-time model.

After solving the eigenvalue problem for the system matrix $[A_c]$, modal decomposition of Equations 2a and 2b can be achieved as shown by:

$$[A_c][\Psi] = [\Psi][\Lambda_c]. \tag{6}$$

Thus, we have

$$[A_c] = [\Psi][\Lambda_c][\Psi]^{-1} \tag{7}$$

where $[\Lambda_c]$ is the diagonal matrix composed of eigenvalues λ_j $(j = 1, 2, \ldots, 2n)$, and $[\Psi]$ is a matrix consisting of the corresponding eigenvector, $\{\psi_j\}$. The eigenvalues and eigenvectors are given in the form of n pairs of complex conjugate.

The input-output relations of the system will be given in the image space of the Laplace transform as shown by:

$$\{Y_c(s)\} = [H_c(s)]\{U_c(s)\} \tag{8}$$

where $\{Y_c(s)\}$ and $\{X_c(s)\}$ are the Laplace transform of $\{y_c\}$ and $\{x_c\}$, respectively, $[H_c(s)]$ is a transfer function matrix defined by

$$[H_c(s)] = [V_c](s[I] - [\Lambda_c])^{-1}[L_c]^T + [D_c] \tag{9}$$

where $[V_c] = [C_c][\Psi]$ and $[L_c]^T = [\Psi]^{-1}[B_c]$ represent the mode shape matrix and participation matrix, respectively. It will be found that the poles of Equation 9 correspond to the eigenvalues of system matrix $[A_c]$, and the eigenvalues λ_j may be expressed as follows:

$$\lambda_j,\ \lambda_j^* = -\xi_j\omega_j \pm \mathrm{i}\,\omega_j\sqrt{1-\xi_j^2},\quad j = 1,\ 2,\ \cdots,\ n \tag{10}$$

where ω_j and ξ_j are the system circular frequency and damping factor of j-th mode, respectively.

It should be noted that above formulation is valid not only for the base-fixed system but for the soil-structure system. If we set as $\{u_F\} = \{\Delta,\ L\Phi\}^T$, then the corresponding results will be those of the base-fixed system. In case of evaluating the sway-fixed mode, the effective input motion to the superstructure should be chosen as $\{u_F\} = \Delta$. The sway-fixed mode may be interpreted as the soil-structure system which allows only the rigid-body rocking motion of the foundation (Stewart & Fenves 1998, Todorovska 2009a, b).

3.3 *System identification and parameter estimation*

Since some advanced system identification methods are available at present, one can chose an appropriate method applicable to the problem. In this study, subspace identification method (Conte et al. 2008) is adopted for identifying dynamic characteristics of soil-structure system. The subspace method has several advantages; the noticeable one is the capability for applying to multi-input multi-output system without difficulties. Several algorisms for the subspace identification have been proposed, and, among those, the N4SID algorism (Van Overschee et al. 1993) are applied in this study. It is beyond the scope of this paper to go deep into the subspace identification methodology. The detail may be found elsewhere (Van Overschee & De Moor 1993, Katayama 2005). The essentials of the subspace identification formulation will be summarized in what follows.

The discrete-time state-space equations corresponding to Equations 2(a) and (b) can be expressed as follows.

$$\{x_d\}_{k+1} = [A_d]\{x_d\}_k + [B_d]\{u_d\}_k \tag{11a}$$

$$\{y_d\}_k = [C_d]\{x_d\}_k + [D_d]\{u_d\}_k \tag{11b}$$

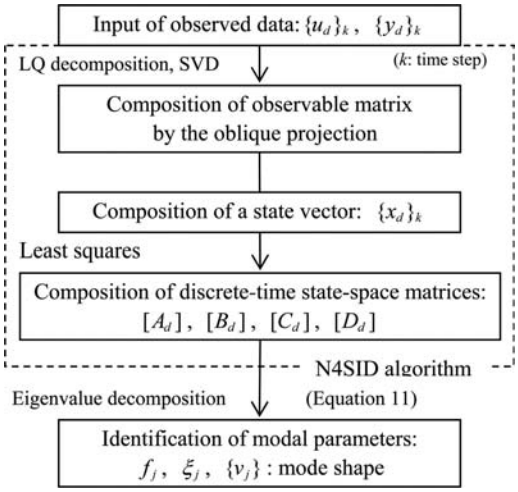

Figure 5. Flowchart of the subspace system identification method for evaluating structural modal parameters. SVD means singular value decomposition.

where $\{x_d\}_k = \{x_c(k\Delta t)\}$ is the observed discrete-time state vector, $[A_d]$, $[B_d]$, $[C_d]$ and $[D_d]$ are system matrices (subscript d denotes discrete-time), and the subscript k denotes discrete-time step. The system matrices $[A_d]$ and $[B_d]$ for the discrete-time series will be distinct by comparing with those of the continuous-time, but these two models are convertible with each other by using appropriate technique such as the zero-order-fold assumption. Taking into account the relation $[A_d] = e^{[A_c]\Delta t}$ (Δt denotes time interval), the eigenvalue decomposition of the matrix $[A_d]$ may be performed in the same manner as Equation 7, resulting in:

$$[A_d] = [\Psi]\mathrm{e}^{[\Lambda_c]\Delta t}[\Psi]^{-1} = [\Psi][\Lambda_d][\Psi]^{-1} \tag{12}$$

where $[\Lambda_d]$ is a diagonal matrix which consists of the eigenvalues of $[A_d]$, μ_j. From the definition, the relations between the eigenvalues of continuous-time and discrete-time models may be shown as:

$$\mu_j = \mathrm{e}^{\lambda_j\Delta t}. \tag{13}$$

From above equation,

$$\lambda_j = \frac{\ln(\mu_j)}{\Delta t}. \tag{14}$$

Eigenfrequencies and damping factors of the continuous-time model can be evaluated by substituting the results obtained by Equation 14 into Equation 10.

The flowchart of the system identification method is shown in Figure 5.

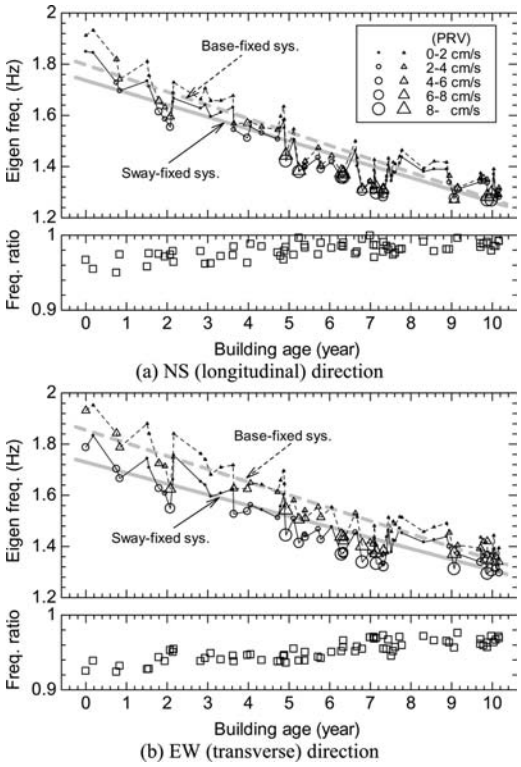

Figure 6. Variation in base-fixed (f_1) and sway-fixed ($\tilde{f}_1$) frequencies. (a) Top: base-fixed ($^{\Delta}$; connected by dashed line) and sway-fixed (°; connected by light solid line) frequencies for NS (longitudinal) direction. The plotted size implies the magnitude of peak relative velocities (*PRV*) of superstructure. Dashed (base-fixed) and solid (sway-fixed) straight lines represent the regression lines for all plots by the least squares method. Bottom: ratios of sway-fixed and base-fixed frequencies $\tilde{f}_1/f_1$. (b) Base-fixed and sway-fixed frequencies for EW (transverse) direction in the same manner as in (a).

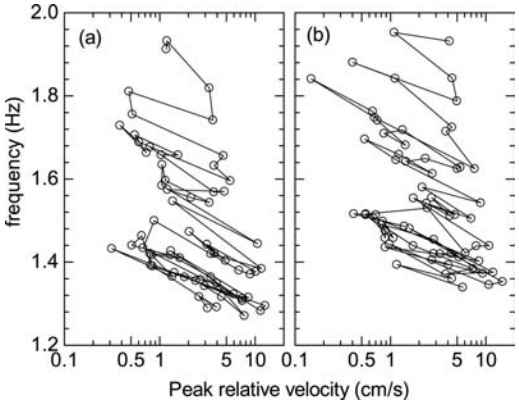

Figure 7. The relationship between base-fixed frequency and peak relative velocity (*PRV*). (a) NS (longitudinal) direction; (b) EW (transverse) direction. The plots are connected by light lines in chronological order.

4 RESULTS AND DISCUSSION

4.1 *Variation in base-fixed and sway-fixed frequencies*

The variation in fundamental frequencies for the base-fixed mode (f_1) and the sway-fixed mode ($\tilde{f}_1$) of the structure for about ten years is shown in Figure 6. The transverse axis is the elapsed years from the start of observation. The plotted results are categorized into five groups according to the amplitudes of peak relative velocities (*PRV*) defined by

$$PRV = |\ddot{u}_s^{(7)} - \ddot{\Delta} - h^{(7)}\ddot{\Phi}|_{\max}. \tag{15}$$

We will notice from Figure 6 that base-fixed frequencies f_1 have dropped from 1.9 Hz to 1.3 Hz in about ten years for both longitudinal and transverse directions. Since there have been no changes in building usage, these results may be attributed mainly to the degradation of the global stiffness of the structure, which corresponds to about a 50% reduction in the rigidity.

The ratio of sway-fixed to base-fixed frequencies, $\tilde{f}_1/f_1$, are also shown in Figure 6. These results show that the sway-fixed frequency $\tilde{f}_1$ tends to approach to the base-fixed frequency f_1 with a lapse of years in both directions of the structure. This implies that the effect of SSI on the fundamental structural frequency has been relatively decreasing, but does not mean that the rigidity of soil has changed. The average of the ratio $\tilde{f}_1/f_1$ for all records are 0.98 for NS (longitudinal) and 0.95 for EW (transverse) directions, respectively.

The sway-fixed mode can be decomposed into base-fixed and rigid-body-rocking modes, and the sway-fixed frequency ($\tilde{f}_1$) and rocking frequency (f_R) may be expressed by (Stewart & Fenves 1998, Todorovska 2009a, b):

$$\frac{1}{\tilde{f}_1^2} \approx \frac{1}{f_1^2} + \frac{1}{f_R^2} \Leftrightarrow f_R \approx \tilde{f}_1 \left(1 - \left(\tilde{f}_1 / f_1\right)^2\right)^{-1/2}. \tag{16}$$

It should be noted that Equation 16 was derived for a structure with a flat foundation supported on a soil surface. Though approximate, the equation may be used for an evaluation of the rigid-body rocking frequency of a structure with a basement (Todorovska 2009a). As anticipated from Equation 16, for the case of $\tilde{f}_1/f_1$ which is nearly 1, the estimated frequency f_R tends to result in an unstable solution.

As the rocking frequency f_R is subjected to the rigidity of the soil, the results will reflect the variation in soil properties. Though not shown here, the estimated result for f_R was found to be almost constant throughout the observation. The computed rocking frequencies for NS (longitudinal) and EW (transverse) directions are 7∼8 Hz and 5 Hz, respectively.

Inspecting the results shown in Figure 6, it may be observed that the fundamental frequency tends to drop suddenly for relatively large *PRV*s and to increase in the next small shaking. The relationship between the

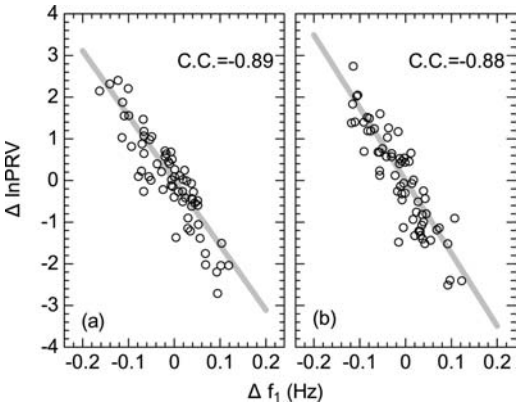

Figure 8. The relationship between differences of base-fixed frequency Δf_1 and the logarithm of peak relative velocity (*PRV*). (a) NS (longitudinal) direction; (b) EW (transverse) direction. Gray thick line represents the regression line and C.C. indicates the correlation coefficient.

base-fixed frequency f_1 and *PRV* connected in chronological order is shown in Figure 7. The results are suggesting that there is an obvious relation between the logarithm of *PRV* and change in structural frequency f_1 within a short time span. The relationship between differences in the logarithm of *PRV*,

$$\Delta \ln PRV = \ln PRV^{(n+1)} - \ln PRV^{(n)} \tag{17}$$

and the difference of the structural frequencies,

$$\Delta f_1 = f_1^{(n+1)} - f_1^{(n)} \tag{18}$$

is shown in Figure 8, where superscript (n) indicates the n-th event. There is almost linear relations between $\Delta \ln PRV$ and Δf_1. Thus, introducing a proportionality constant Ω, we have a following empirical expression:

$$f_1^{(n+1)} = f_1^{(n)} + \Omega^{-1} \ln R_{PV} \tag{19}$$

where $R_{PV} = \dfrac{PRV^{(n+1)}}{PRV^{(n)}}$. The values $\Omega^{-1} \ln R_{PV}$ can be a measure for estimating the amplitude dependence of structural frequencies. The estimated proportionality constants Ω are $\Omega \approx -15.6$ for NS direction and $\Omega \approx -17.5$ for EW direction. The Equation 19 can be used to estimate the base-fixed frequency using the value of R_{PV}.

4.2 *Variation in damping factor*

The computed results of damping factors for base-fixed (ξ_1) and sway-fixed systems ($\tilde{\xi}_1$) are shown in Figure 9. The results of damping factors tend to fluctuate from one earthquake to another, and are showing somewhat outliers for the events with relatively small *PRV*s. This is perhaps the result of lack of resolution accuracy in the numerical computation. The tendencies about aging and amplitude dependence of the damping factors can not be detected so clearly as in

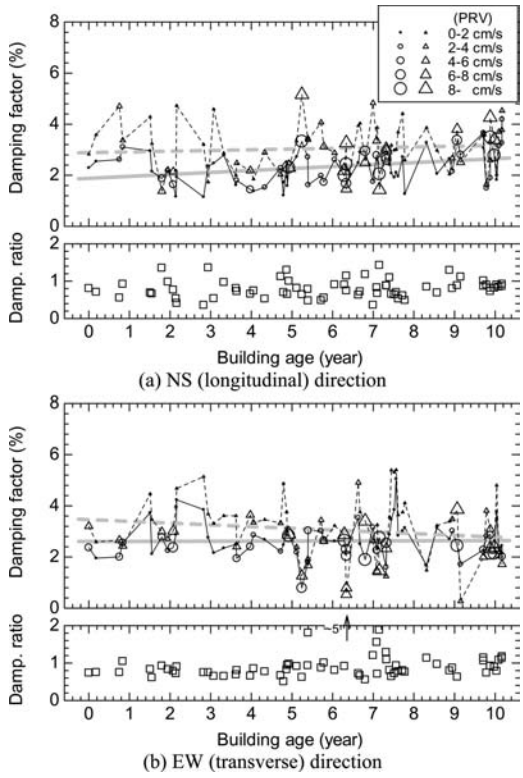

Figure 9. Variation in base-fixed and sway-fixed damping factors. (a) Top: base-fixed ($^{\Delta}$; connected by dashed line) and sway-fixed ($^{\circ}$; connected by light line) damping factors for NS (longitudinal) direction. The plotted sizes implies magnitudes of peak relative velocities (*PRV*) of superstructure. Dashed (base-fixed) and solid (sway-fixed) straight lines represent regressed results for all plots by the least squares method. Bottom: ratio of base-fixed and sway-fixed damping factors $\tilde{\xi}_1/\xi_1$. (b) Base-fixed and sway-fixed damping factors for EW (transverse) direction in the same manner as in (a).

the fundamental mode frequencies shown in the previous section. On the average, the damping factor for the base-fixed system is 3.1% for both directions, and for the sway-fixed system the damping factors are 2.3% for NS and 2.6% for EW directions. The ratio of damping factors for these two systems, $\tilde{\xi}_1/\xi_1$, is also shown in Figure 9.

It should be noted that the damping factors of the sway-fixed mode ($\tilde{\xi}_1$) are smaller than the base-fixed mode (ξ_1). This tendency may be understood by recalling the relations between ξ_1 and $\tilde{\xi}_1$. Damping factors of sway-fixed system may be approximated by (Stewart & Fenves 1998):

$$\tilde{\xi}_1 \approx \left(\frac{\tilde{f}_1}{f_1}\right)^3 \xi_1 + \left(\frac{\tilde{f}_1}{f_R}\right)^3 \xi_R \tag{20}$$

where ξ_R represents the damping factor of the rigid-body rocking mode, which is generally small comparing with ξ_1. In addition, as the ratio $\tilde{f}_1/f_R$ is smaller than

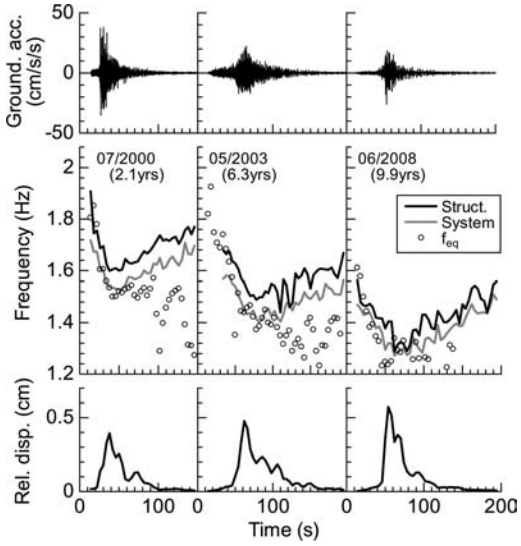

Figure 10. Variation in the fundamental frequencies during earthquake motions (EW (transverse) direction). Top: Time histories of the earthquake ground motions; Middle: Time histories of base-fixed (structural) frequency (black line) and sway-fixed (system) frequency (gray line); Bottom: Time histories of root mean square value of the relative displacement of the superstructure.

$\tilde{f}_1/f_1$ the second term of the equation can be omitted. Eliminating the second term from Equation 20, then we have:

$$\tilde{\xi}_1 \approx \left(\frac{\tilde{f}_1}{f_1}\right)^3 \xi_1. \tag{21}$$

Since $\tilde{f}_1/f_1 < 1$ as indicated in the previous section, we have $\tilde{\xi}_1 < \xi_1$.

4.3 *Variation in frequency during earthquake*

It is interesting to study the variation in dynamic characteristics of soil-structure system not only over a long period of time but during an earthquake. Especially the short term change in the frequency is evidently attributed to strong nonlinearity of structure that might be associated with damage in the structure. Thus, it becomes important to observe the frequency change during an earthquake in evaluation of the seismic-resistance performance of structures. In this section, we will investigate the change in base-fixed and sway-fixed frequencies during specific earthquake motions which have exhibited relatively large structural responses.

Figure 10 shows the change in frequencies during three selected earthquakes. The results are numerically evaluated by means of the subspace identification method introducing a box-type moving window onto wave forms. In the figure, the frequency change evaluated by the zero crossing method is also plotted for

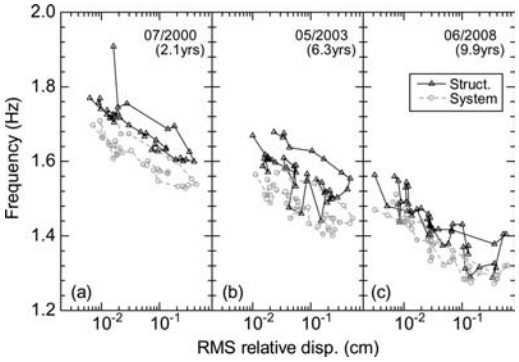

Figure 11. Variation in the fundamental frequencies versus RMS of relative displacement amplitude of superstructure. Black solid and gray broken lines are the results of base-fixed (structural) and sway-fixed (system) frequencies, respectively.

reference (open circles). In the method, the predominant frequency is determined by zero crossing with positive slope (Clough & Penzien 1993). As the number of zero crossing can be expressed by the spectral moments in the frequency domain, it may be rewritten in the form of Equation 22 for the time domain by use of the Parseval's theorem. Thus, we have

$$f_{eq}(\tau) = \frac{1}{2\pi} \cdot \sqrt{\frac{\int_{\tau-\Delta T}^{\tau+\Delta T} |\dot{u}_s(t)|^2 \, \mathrm{d}t}{\int_{\tau-\Delta T}^{\tau+\Delta T} |u_s(t)|^2 \, \mathrm{d}t}} \tag{22}$$

where ΔT denotes the half width of window, which was chosen as $\Delta T = 4$ sec . The computation was performed every 4 sec by shifting the time τ along the time axis. In Figure 10, waveforms of free-field surface accelerations and root mean squares (RMS) of relative displacements of the superstructure are shown simultaneously.

Inspection of the results shown in Figure 10 reveals that both the base-fixed and sway-fixed frequencies tend to decrease with increase in the structural response. The minimal values of frequencies correspond to the time when the largest structural response occurred. After that, the frequencies tend to resume gradually as the structural response becomes smaller, and the frequencies recover almost to pre-earthquake values at the end of shaking. Furthermore, the above mentioned tendencies may be observed in common for both base-fixed and sway-fixed frequencies. On the other hand, the results obtained by zero crossing method correspond approximately to the results obtained by the sophisticated method for large response amplitudes. However, results by the method tend to be unreliable for small response amplitudes.

The change in frequency versus structural response (RMS of relative displacements of superstructure) is shown in Figure 11. One of the distinct features detected from the results is that the frequencies are very much amplitude dependent. It is also interesting to notice that the variation in frequencies is almost linear with respect to the logarithm of amplitudes of

structural displacement responses. The slopes of the results shown in Figure 11 have special meaning in estimating the variation in natural frequency based on the displacement response of the structure.

5 CONCLUSIONS

The variation in dynamic characteristics of the eight-story steel-reinforced concrete building with the passage of time was investigated based on the earthquake records observed in the building for about ten years. In order to evaluate the SSI effects, the dynamic characteristics of the base-fixed and sway-fixed modes were isolated from the records.

It was revealed that the base-fixed frequency has decreased from 1.9 Hz to 1.3 Hz in about ten years both in the longitudinal and transverse directions, which corresponds to about a 50% reduction in the global stiffness of the superstructure. On the other hand, the sway-fixed frequencies were less than the base-fixed frequencies by 5% in the transverse direction and 2% in the longitudinal direction, respectively.

With use of the results of the sway-fixed and base-fixed frequencies, the frequency of rigid-body rocking mode was estimated, which showed almost constant value throughout the observation. These results indicate that the observed variation in frequencies of the building could be attributed to the stiffness degradation of the superstructure.

Finally, it was shown that the subspace identification method developed by Van Overschee & De Moor (1993) could be successfully applied to the SSI system.

ACKNOWLEDGEMENT

This research was partially supported by the Ministry of Education, Culture, Sports, Science and Technology, Grants-in-Aid for Scientific Research (C), Grant Number 19560580, 2007–2008.

REFERENCES

Clinton, J. F., Bradford, S. C., Heaton, T. H. & Favela, J. 2006. The observed wander of the natural frequencies in a structure, *Bull. Seism. Soc. Am.* 96(1), 237–257.

Clough, R. W. & Penzien, J. 1993. *Dynamics of structures*, 2nd ed., McGraw-Hill.

Conte, J. P., He, X., Moaveni, B., Masri, S. F., Caffrey, J. P., Wahbeh, M., Tasbihgoo, F., Whang, D. H. & Elgamal, A. 2008. Dynamic testing of Alfred Zampa memorial bridge, *J. Struct. Eng*., ASCE, 134(6), 1006–1016.

Ghanem, R. & Sture, S. (ed.) 2000. Special issue: structural health monitoring, *J. Engrg. Mech*., ASCE, 126(7), 665–777.

Iguchi, M., Kawashima, M. & Minowa, C. 2007. A measure to evaluate effective input motions to superstructure, *The 4th U.S.-Japan Workshop on Soil-Structure-Interaction*, Tsukuba, Japan.

Kashima, T. & Kitagawa, Y. 2006. Dynamic characteristics of an 8-storey building estimated from strong motion records, *Proc. of 1st European Conference on Earthquake Engineering and Seismology*, Geneva, Switzerland.

Katayama, T. 2005. *Subspace Methods for System Identification*, Springer-Verlag, London.

Luco, J. E., Trifunac, M. D. & Wong, H. L. 1987. On the apparent change in dynamic behavior of nine-story reinforced concrete building, *Bull. Seism. Soc. Am*. 77(6), 1961–1983.

Stewart, J. P. & Fenves, G. L. 1998. System identification for evaluating soil-structure interaction effects in buildings from strong motion recordings, *Earthquake Engng. Struct. Dyn*. 27, 869–885.

Todorovska, M. I. & Trifunac, M. D. 2008. Impulse response analysis of the Van Nuys 7-story hotel during 11 earthquakes and earthquake damage detection, *Strut. Control Health Monit.*, 15, 90–116.

Todorovska, M. I. 2009a. Seismic interferometry of a soil-structure interaction model with coupled horizontal and rocking response, *Bull. Seism. Soc. Am*., 99(2A), 611–625.

Todorovska, M. I. 2009b. Soil-structure system identification of Millikan Library North-South response during four earthquakes (1970–2002): what caused the observed wandering of the system frequencies?, *Bull. Seism. Soc. Am*. 99(2A), 626–635.

Trifunac, M. D., Ivanović, S. S. & Todorovska, M. I. 2001a. Apparent periods of a building. I: Fourier analysis, *J. Struct. Eng*., ASCE, 127(5), 517–526.

Trifunac, M. D., Ivanović, S. S. & Todorovska, M. I. 2001b. Apparent periods of a building. II: Time-frequency analysis, *J. Struct. Eng*., ASCE, 127(5), 527–537.

Van Overschee, P. & De Moor, B. 1993. N4SID: subspace algorithms for the identification of combined deterministic and stochastic systems, *Automatica*, 30(1), 75–93.

Soil-Foundation-Structure Interaction – Orense, Chouw & Pender (eds)
© 2010 Taylor & Francis Group, London, ISBN 978-0-415-60040-8

Site amplification of ground motion during the 1995 Kobe earthquake and unsolved issue on SFSI problem

M. Nagano
Tokyo University of Science, Chiba, Japan

ABSTRACT: The deep basin-edge structure beneath Kobe City is a plausible cause for ground motion amplification in the damage belt during the 1995 Kobe earthquake. Strong motions were recorded at two neighboring sites, Takatori and Shin-Nagata, located in the western part of the damage belt. The latter site, which was the basement of a high-rise building, was less than half the amplitude observed at the former site. This difference has raised an issue related to the soil-foundation-structure interaction problem. The deep subsurface structures were not a direct cause of the spatial variation between the two sites. It appears that the strong, site-specific nonlinearity associated with the surrounding soil partially contributed to a large reduction of the foundation input motion.

1 INTRODUCTION

More than 6,000 people were killed as a result of the 1995 Hyogo-ken Nanbu, Japan earthquake (hereafter, the 1995 Kobe earthquake). In addition, strong ground shaking during the earthquake caused devastating damage to a large number of structures including old wooden houses. Most of the structural damage was spatially concentrated in the "heavily damaged belt zone," which corresponds to a Japanese seismic intensity scale of 7 (Japan Meteorological Agency (JMA) scale). This zone is illustrated in Figure 1, and it is a 1–2 km wide area between Rokko Mountain and Osaka Bay. Ground velocity waveforms obtained from the records of the event have large amplitude pulses with a predominant period of about 1 second, which is nourished in the rupture process of a seismic fault beneath Kobe City.

One of the plausible explanations for the peculiar damage pattern that was observed is the existence of a basin-edge structure in the deep subsurface soil beneath Kobe City (e.g., Motosaka & Nagano 1997). Kobe City is located at the edge of the Osaka Plain where the level of the seismic bedrock surface abruptly drops off at the foot of Rokko Mountain.

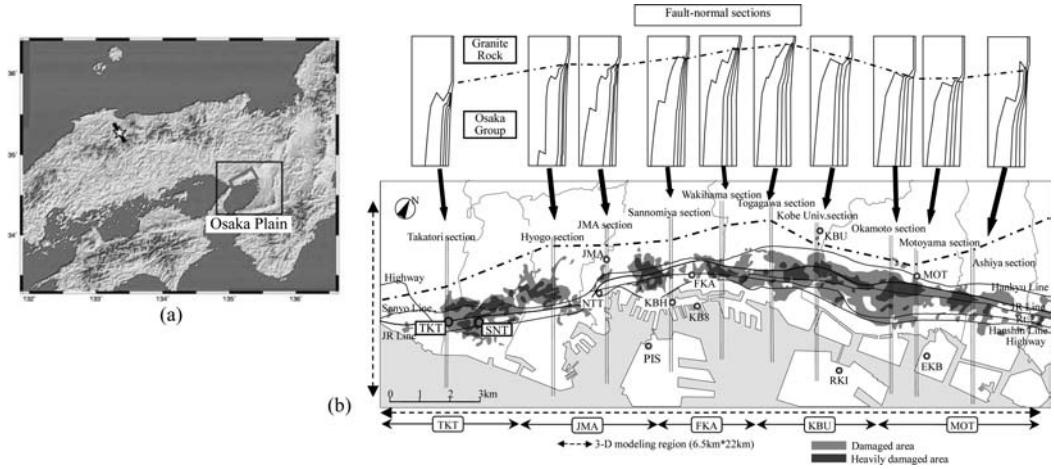

Figure 1. Location of Kobe City, Japan, and the damage belt during the 1995 Kobe earthquake. (a) Kobe City located in the western part of Honshu Island, Japan. A thick inclined rectangle corresponds to area in (b). (b) The heavily damaged belt zone during the 1995 Kobe earthquake. A dash-dotted line indicates structural boundary between rock and sediments along Rokko Mt. Fault-normal sections of deep underground structure for 2-D analyses are illustrated. Takatori (TKT) and Shin-Nagata (SNT) are about 1 km apart and they are both located in the western part of the damage belt.

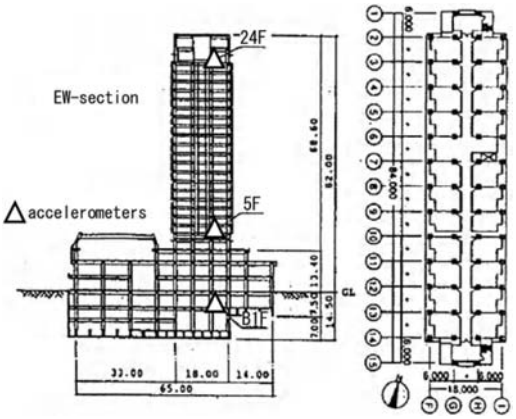

Figure 2. High-rise SRC building constructed at SNT and location of accelerometers. Seismograms in Figure 3 were obtained at the first basement floor level. A section plan is illustrated in EW direction. (after Yasui et al. 1998).

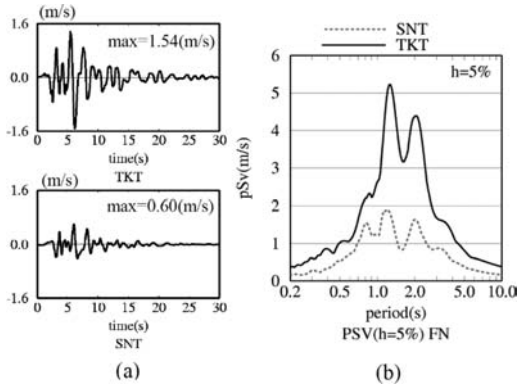

Figure 3. Strong ground motions at TKT and SNT during the 1995 Kobe earthquake. (a) Velocity seismograms and (b) Pseudo velocity response spectra.

Although more than 14 years have passed, damages during the Kobe earthquake has been the icon of natural disaster prevention with regard to seismology, earthquake engineering, and civil/structural engineering. Nevertheless, some issues have gone unresolved from the standpoint of the relationship between observed ground motion and actual damage. Some researchers suggest that the loss of foundation input motion might be much larger than expected from analytical studies or observations of small earthquakes or micro tremor measurements. This paper addresses a particular issue related to the soil-foundation-structure interaction (SFSI) problem, and it focuses on the strong motion records at two sites in the western part of Kobe City, Takatori and Shin-Nagata (see Figure 1). The amplitudes of the ground motion at the two sites are quite different, even though both sites, which are separated by about 1 km, are within the damage belt.

2 RECORDS AT TAKATORI AND SHIN-NAGATA

Several records of ground motion in and around the "heavily damaged belt zone" in Kobe City during the main shock were obtained. In the western part of the damage belt, two strong ground motion records were obtained for Takatori (TKT) and Shin-Nagata (SNT). The former is a record of ground surface motion, and the latter is from the first basement level of the 25-story SRC building shown in Figure 2 (Yasui et al. 1998). The SNT record consequently includes effects of SFSI.

Figure 3 shows the velocity waveforms and pseudo velocity spectra at the two sites. They are rotated to the fault-normal direction as a principal axis, N150E and N140E, for TKT and SNT, respectively.

The ground motion record from the TKT site is one of the most important records in the Kobe earthquake because the peak ground velocity (PGV) exceeded 1.5 m/s, which was the largest ground velocity reported in Japan at that time. Its waveform is pulse-like with a predominant period of about 1 s. In contrast, the PGV at SNT is approximately 0.6 m/s, which is less than half of that at TKT. This difference applies not only to the PGV, but also to the response spectra. Accelerometer data at SNT were slightly saturated during the main shock. However, this problem introduced only a minor error in the velocity waveforms because the duration of the saturation was limited. Indeed, the peak ground acceleration (PGA) loss is estimated to be about 10% of the restored accelerometer data (Yasui et al. 1998).

These observations suggest that several different questions need to be addressed. Namely: why did large discrepancy occur between the two records; is there any difference in the characteristics of the ground motion amplification due to the deep or shallow geological condition; and is there any great loss of foundation input motion due to the embedded basement of the building?

3 GROUND MOTION AMPLIFICATION IN THE "HEAVILY DAMAGED BELT ZONE"

3.1 *Underground structure beneath Kobe City*

Several authors (e.g., Nagano et al. 1998, Koyamada et al. 1998) have investigated the relationship between ground motion amplification and the geological condition beneath Kobe City. Based on the results of geophysical explorations (e.g., Huzita & Sano 1996, Sano 1998), long-term movement of the Rokko faults generated a structural boundary that essentially represents a vertical discontinuity between the rock and sedimentary regions along the faults. This process formed a deep, irregular underground structure similar to the edge of a sedimentary basin.

Deep subsurface structures in several fault-normal sections in Kobe City are illustrated in Figure 1. In general, the underground structure along the Rokko Faults can be regarded as approximately two-dimensional. In

Table 1. List of soil properties. These values are used in both 2-D & 3-D analyses of main shock.

Soil type	V_S(m/s)	V_P(m/s)	ρ(t/m^3)	damping factor
Osaka Group-1	500	1800	1.8	0.03
Osaka Group-2	600	1900	1.9	0.03
Osaka Group-3	800	2200	2.0	0.02
Osaka Group-4	1000	2500	2.1	0.02
Weathered rock	1350	3100	2.2	0.02
Granite rock	3200	5400	2.7	0.01

Table 2. Peak velocities (m/s) and accelerations (m/s^2) of records, deconvolved motions on Osaka group and seismic bedrock. All motions are low-pass filtered at 5 Hz. Values in parentheses are peak accelerations. (Nagano et al. 1998).

Site name	Records	On Osaka Group	On granite bedrock
MOT	0.70(4.58)	–	0.53(3.70)
KBU	0.54(3.11)	–	0.59(3.71)
FKA	1.31(8.54)	1.29(7.52)	0.49(3.72)
PIS(GL-83m)	0.72(4.86)	0.96(6.93)	0.53(3.85)
JMA	1.04(8.35)	0.82(5.87)	0.51(2.91)
TKT	1.51(7.13)	1.37(6.17)	0.55(2.23)

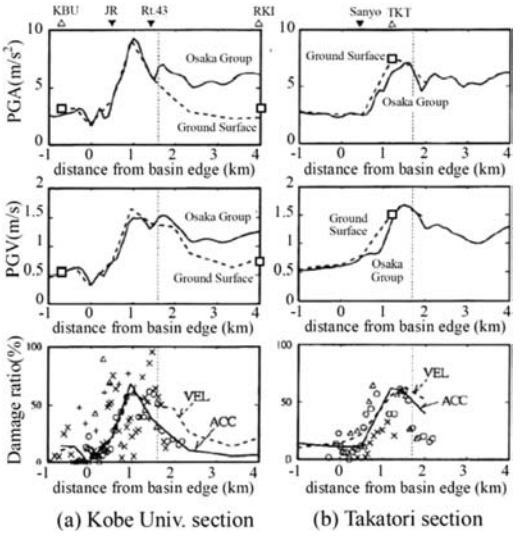

Figure 4. Distributions of peak ground motions in (a) Kobe Univ. section and (b) Takatori section. Origin of distance is basin-edge between rock and sediments. Broken line indicates coastal line of Osaka Bay. The top and middle figures correspond to accelerations and velocities. OG stands for ground motions on Osaka Group, GS for ground surface. Values of records are plotted by □. The bottom includes distributions of ratios of collapsed wooden houses (× ◯ △) by several research groups. (Koyamada et al. 1998).

the area of the bay, 1–2 km thick sedimentary layers (the Osaka Group) overlay granite rock. A soft surface layer with a thickness of 10–100 m can also exist on top of the Osaka Group.

3.2 *Evaluation of bedrock motions*

As a first step, outcrop motions were evaluated on the Osaka Group layers ($V_S = 500$ m/s)—regarded as "engineering bedrock" in Japan—and on seismic bedrock ($V_S = 3200$ m/s) using observed ground motions at 6 sites (including TKT) that were relatively un-affected by liquefaction. The site effect of the soft surface soil overlying the Osaka Group ($V_S < 500$ m/s, with a thickness of 10–100 m) was eliminated by using an iterative method for a 1-D, nonlinear time-domain analysis. The seismic bedrock motions were then deconvolved by using a 2-D Finite Element Method (FEM) analysis, shown in Figure 1. The Osaka Group layer is outcropped as ground surface, assuming that the 1-D amplification in soft surface soil can be evaluated separately. Soil properties used in the 2-D models are listed in Table 1. Soil responses were obtained by frequency-domain analyses in 0–5 Hz.

Table 2 is a comparison of peak velocities and accelerations for the observed and deconvolved motions on the Osaka Group and on seismic bedrock. The PGVs of observed motions vary from 0.54–1.51 m/s and those on the Osaka Group layers vary from 0.82–1.37 m/s although some deviation from site-to-site can be noted. However, the PGVs of bedrock motions converge to approximately 0.55 m/s. These results imply that a deep, irregular underground structure affects the amplification of ground motions at both the ground surface and at the Osaka Group layers.

3.3 *Distribution of ground motion*

Ground motion distributions on the Osaka Group layers were evaluated using 2-D models of fault-normal sections using the motion of the seismic bedrock as input. Amplification in soft surface soil was evaluated using a nonlinear analysis of a 1-D soil column. In Figure 4, PGA and PGV distributions are plotted for the ground surface and the Osaka Group layers at the Takatori and Kobe Univ. sections. Solid black squares are the maximum values of the observed motion on ground surface.

Seismic motion was amplified significantly at about 1 km from the basin edge corresponding to $x = 0$ km. The PGVs are amplified from 0.55 m/s on seismic bedrock to more than 1.5 m/s on the ground surface or on the Osaka Group layers. The damage ratios, defined as a ratio of collapsed wooden houses to total number in specific local area (Nagano et al. 1998), are also illustrated in Figure 4 comparing with PGAs and PGVs distributions by adjusting absolute amplitudes to match with damage ratio (Hayashi et al. 1997). The distribution pattern estimated from both the PGA and PGV data show good agreement with the observed damage, especially in the heavily damaged belt zone where the damage ratio exceeded 50%.

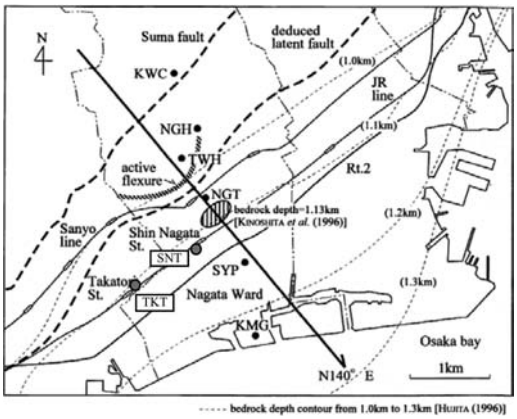

Figure 5. Map of western part of Kobe City including Nagata Ward. Six stations for aftershock observation are located along the thick solid line in the fault-normal direction. (Nagano et al. 1999).

In the reclaimed area, the damage ratios are drastically reduced corresponding to the reduction of PGA due to liquefaction.

Ground motion was locally—and significantly—amplified in a very narrow zone in the sedimentary site adjacent to the structural boundary between rock and sediments. This can be interpreted as constructive interference of multi-pathing motions, i.e., one vertically passing through the sedimentary layer, and one induced at the vertical discontinuity and then travelling into the sedimentary site horizontally (Nagano 1998).

4 SIMULATION OF RECORDS DURING AFTERSHOCKS IN THE WESTERN PART OF KOBE CITY

4.1 *Linear array observation in Nagata ward*

Simulated waveforms designed to replicate data obtained from temporal aftershock observations in the Nagata Ward region (see Figure 5) were used in an effort to validate the effects of the deep subsurface structure on ground motion amplification in the western part of Kobe City. These simulations included the subsurface basin-edge structure (Nagano et al. 1998). Strong motion during the aftershocks that followed the 1995 Kobe earthquake was observed using a six-station linear array from the Rokko Mountain to the coast of Osaka Bay. The SNT site is located approximately between NGT and SYP.

The subsurface structure under these stations was determined from the results of geophysical surveys (e.g., Huzita & Sano 1996), the spectral ratio of the observed horizontal components at the sediment stations to those at KWC on granite, and the difference between the travel times of the SP-converted waves and the direct S-waves at the sediment stations. In addition to the Suma Fault at the edge of sedimentary layers, there appears to be a latent fault, which

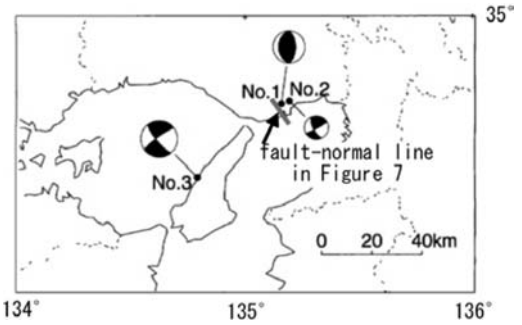

Figure 6. Locations of epicenters and focal mechanisms of three aftershocks of the 1995 Kobe earthquake. A thick solid line corresponds to that in Figure 7. (Nagano et al. 1999).

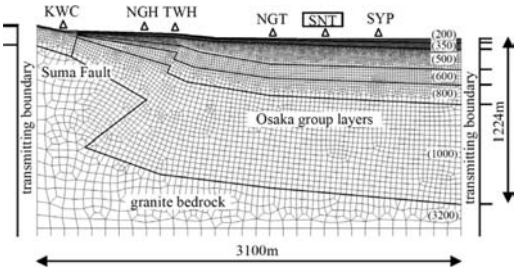

Figure 7. Two-dimensional modeling of the underground structure at the cross section along the thick solid line in Figure 6. Soft surface layers on Osaka Group layers are included in this model. Values in parentheses correspond to initial S-wave velocities (m/s). Energy transmitting boundaries (Lysmer & Drake 1972) are used at both sides of the FE region. (Nagano et al. 1999).

produces a wedge-like configuration in the deep part of the subsurface structure.

4.2 *Simulation analysis using 2-D model*

The velocity seismograms at the five stations on sediment were synthesized from the observed records at the KWC station on granite for the three aftershocks in Figure 6. The FE grid shown in Figure 7 was used for 2-D in-plane and anti-plane analyses. Soft surface strata, with $V_S = 200$ m/s and $V_S = 350$ m/s overlying the Osaka Group layers, are also included in the 2-D modeling. Element size is set to guarantee S-wave propagation up to 5 Hz (approximately 6 elements per S-wavelength) for frequency response calculations.

Figure 8 shows a comparison of PGV distributions for the three aftershocks. Local amplification, corresponding to the damage belt, can also be seen in both the recorded data and the simulated motions. Site effects due to the basin-edge structure were also presented in the aftershocks.

The observed and computed velocity seismograms at the six array stations during the No. 3 earthquake are compared in Figure 9. The solid triangles indicate the distinctive later phases on the seismograms during the No. 3 earthquake. The computed waveforms

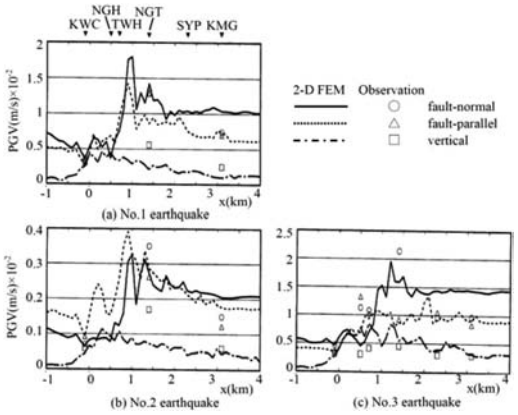

Figure 8. Distributions of peak ground velocities of synthesized ground motions in the fault-normal, fault-parallel and vertical directions from the three aftershocks. The open data points indicate the peak ground velocities of the observed records. (Nagano et al. 1999).

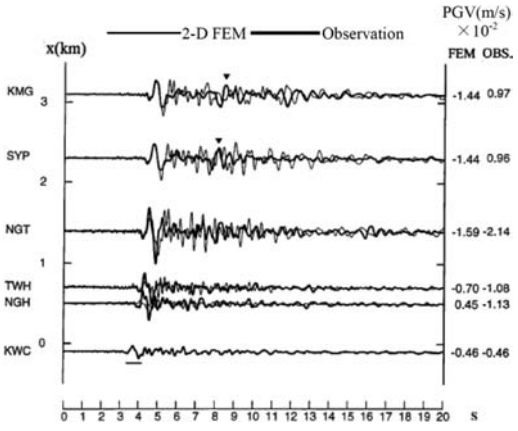

Figure 9. Comparison between the observed and synthesized velocity seismograms at the six array stations during the No.3 earthquake. The thick solid lines indicate the observed seismograms. The thin solid lines indicate the synthesized seismograms, which are calculated by the 2-D FEM using the observed records at the KWC station as the control motions. The solid triangles indicate the distinctive later phases on the seismograms during the No. 3 earthquake. (Nagano et al. 1999).

explain not only the direct S-wave response, but also the conspicuous later phase that was found in the data records at the SYP and KMG stations near the coast of Osaka Bay. Later phases in SYP and KMG are generated by interference of reflected S-wave upward and diffracted surface waves induced at the basin-edge boundary. (Nagano et al. 1998) These results suggest that the basin-edge structure near by TKT and SNT, as well as ground motion amplification, can be validated by simulation analyses of aftershock records.

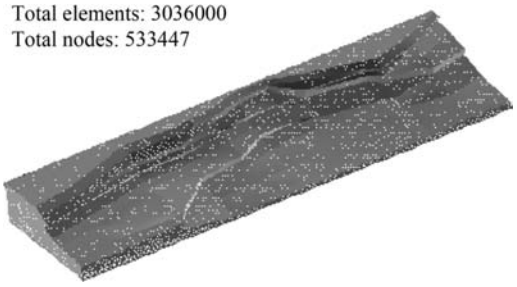

Figure 10. Surface configuration of seismic bedrock in the 3-D finite element model. (Nagano & Yamada 2002).

5 THE 3-D GEOLOGICAL EFFECT ON GROUND MOTIONS IN KOBE CITY

Ground motion amplification can be examined by considering the 3-D basin-edge configuration of the deep subsurface structure. As previously stated, the deep underground structure along the Rokko Faults can be regarded as approximately two-dimensional, even though the planar and sectional subsurface structure varies slightly along the Rokko Mountain and coastal line. An FEM analysis was used to evaluate effects related to the 3-D geological structure. Such effects could be another reason for the existence of a large discrepancy between the results observed at TKT and SNT.

The region in Figure 1(b) is modeled in this 3-D analysis, where the 3-D bedrock configuration is illustrated in Figure 10. Previously evaluated seismic bedrock motions were used as input motions at the bottom of the 3-D FEM region, where the incident wave field is assumed to be the same as that observed for the region adjacent to the site where the bedrock motion is deconvolved. In Takatori area, the bedrock motion from TKT is used. Soil responses are calculated in a time-domain analysis based on an explicit scheme. The effective frequency range is up to 2 Hz for the mesh size used in this modeling. All the motions evaluated on the Osaka Group were low-pass filtered at 2 Hz, as were the recorded motions.

Figure 11 shows a comparison of velocity seismograms between observed and simulated data at TKT and SNT. Naturally, velocity seismograms at TKT were well reproduced, whose difference is due to that of 2-D and 3-D effect. The amplitude of the calculated motion at SNT is the same as observed for TKT or even larger. The calculation apparently overestimates recorded motions at SNT. The 3-D effects of the deep underground structure seem to be small within 1 km. This is expected, however, considering that TKT and SNT are both located roughly the same distance from the basin-edge boundary.

Even in simulation analyses that include both a 3-D geology and the rupture of an extended seismic fault, the computed ground motions at SNT tend to be overestimated (e.g., Matsushima & Kawase 2009). The spatial variation of ground motion is also small, considering the complexity of the incident wave field due

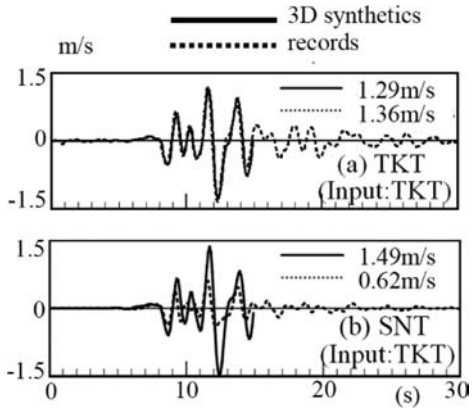

Figure 11. Comparison of fault-normal velocity seismograms between 3-D synthetic motions and deconvolved records on the Osaka Group. These are filtered from 0 to 2 Hz. Synthetic motion in SNT overestimates observed motion. (Nagano & Yamada 2002).

to the variation of fault rupture. It therefore appears that 3-D geological effects did not directly cause the large discrepancy of ground motion levels between TKT and SNT.

6 FOUNDATION INPUT MOTIONS CONSIDERING SITE NONLINEARITY OF SURROUNDING SOIL DURING MAINSHOCK

Yasui et al. (1998) carried out a detailed analysis of the dynamic SFSI problem at the SNT site. They simulated nonlinear structural response using records at 3 floors (B1F, 5F, 24F) in the building, along with ground motions on the free-field surface that were based on an iterative scheme that included nonlinearity of the surrounding soil. The peak structural response at the first floor was estimated to be 23% less than the free-field motion for peak acceleration, and 10% less for peak velocity. The estimated PGV for the free field at SNT is 0.65 m/s, which is still less than one half of the PGV at TKT. Note that any errors related to instrumentation are likely to be small since the observed and calculated damage pattern for the upper floors were in reasonable agreement.

In Yasui et al. (1998), equivalent soil properties were determined using an iterative calculation based on data records at SNT. This approach helps ensure that the site nonlinearity associated with the surrounding soil is taken into account in the SFSI analysis. The average ratio of the equivalent S-wave velocity, V_{Se}, to the initial S-wave velocity, V_{S0}, is 0.84 in the soft surface layers on engineering bedrock. This ratio appears to be small considering that the PGV at TKT exceeded 1.5 m/s in the principal direction (e.g., Tokimatsu et al. 1989). Equivalent soil properties of surface layers were evaluated using outcropped motions on the Osaka Group layers at TKT (shown in Table 1)

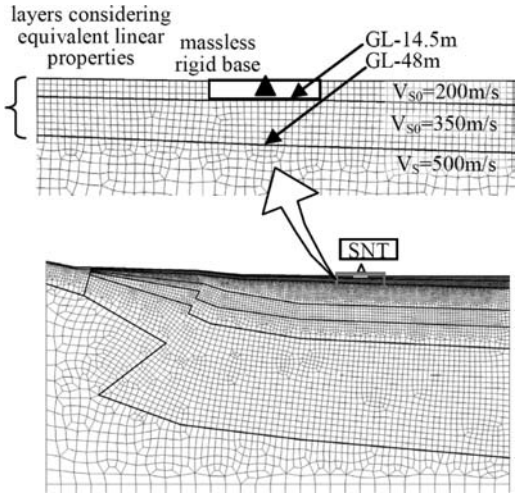

Figure 12. Finite element model for evaluation of foundation input motion at SNT. Rigid massless solid elements are buried between NGT and SYP.

Table 3. List of equivalent linear properties of top surface layers used in 2D-FEM.

CASE	Equivalent shear wave velocity V_{Seq}/V_{S0}	Equivalent damping factor h_{eq}
CASE-1	1.0	0.03
CASE-2	0.84	0.05
CASE-3	0.5	0.10

as an input motion to the 1-D soil column at SNT. In a time-domain nonlinear analysis, averaged curves of G/G_0-γ, h-γ for sand and clay (Koyamada 2005) are used for soil nonlinearities. It should also be noted that the average maximum shear strain was 8×10^{-3}. This shear strain value corresponds to a V_{Se}/V_{S0} ratio of about 0.5, which is much smaller than the value given by Yasui et al. (1998).

The large reduction of the ground motion at SNT is then examined in terms of the loss of input motion of a rigid foundation embedded in soft soil with low S-wave velocity, by using the subsurface structure passing through SNT in Figure 7. This was calibrated by the aftershock simulations in the previous section. Rigid, massless solid elements were embedded between NGT and SYP in the 2-D model, as shown in Figure 12. The basement was 84 m long in the NS direction and 14.5 m deep. Initial S-wave velocities of the top layers are 200 m/s and 350 m/s. Responses of the massless rigid base are evaluated by frequency domain 2-D analysis.

The three cases listed in Table 3 were examined. Original linear properties were used in CASE-1. CASE-2 employed the average coefficient for the reduction of V_S from Yasui et al. (1998), i.e., 0.84. A smaller V_S evaluated using bedrock motions at TKT was used in CASE-3. The same coefficients and damping ratio were applied for each layer in both CASE-1

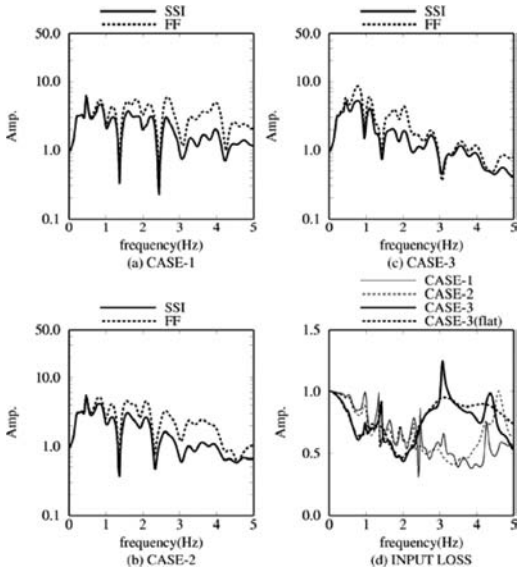

Figure 13. Comparison of foundation input motions(SSI) and free surface ground motions(FF) for (a) CASE-1, (b) CASE-2, (c) CASE-3 in Table 3. Transfer functions of foundation input motions to free surface motions are presented in (d). Result by flatly layered model for CASE-3 (thick broken line) is also compared to elucidate effects of the deep basin-edge structure.

and CASE-2. In CASE-3, mesh size is rather coarse for S-wave propagation in the frequency range over 3Hz. Considering that predominant period of ground motion at TKT and SNT is less than 0.5s. (see Figure 3(b)), however, effects of numerical dispersion would be small in evaluation of input motions.

Transfer functions of the input motion at the basement and free-field motion on the ground surface for a vertically incident SV-wave are plotted in Figure 13, parts (a)–(c). Foundation input motion (i.e., the ratio of input motion to free surface motion) for the three cases are also compared in Figure 13, part (d). Foundation input motion, using a horizontally flat, layered soil beneath the SNT site, were also evaluated to clarify the effects of the deep basin-edge structure on rigid base responses.

In CASE-1 and CASE-2, a decrease of foundation input motion is small for frequencies below 1 Hz, where it is not possible to account for a large reduction of ground motion amplitude at SNT.

In CASE-3, free surface motion amplifies because of the nonlinear effect of soft surface soil for frequencies below 1 Hz. This leads to a small trough seen at around 0.8 Hz in the foundation input motions, resulting in nearly 2/3 of the ground surface. It appears that the foundation response is reduced as a result of the constraint of the waves in the soft surface layers by a rigid base, especially due to the constraint effect at sides of the rigid base.

Results for a flatly layered soil almost coincide with CASE-3, implying that the influence of an irregularity of the deep underground structure on foundation input motion is quite small.

Responses of a rigid foundation at SNT were evaluated using the ground motions determined at TKT and then multiplying by the transfer function in Figure 13. Figure 14 shows calculated velocity seismograms and the response spectra.

In CASE-1, the peak velocities almost remain the same as TKT, implying that large reduction at SNT can not be explained only by a kinematic effect of a rigid foundation. In CASE-2, where site nonlinearity in Yasui et al.(1998) is referred, both a velocity waveform and a response spectrum are almost the same level as CASE-1.

The peak velocity in CASE-3 is reduced to 1.06 m/s, which is about 2/3 of TKT. The CASE-3 still overestimates the actual motion at SNT, however, the loss of foundation input motion due to the strong site nonlinearity of the surrounding soil partially accounts for a significant reduction of the foundation input motion. Use of an elastic base instead of a rigid one will underestimate a reduction of the foundation input motion, resulting in overestimation of the observed motion.

7 FINAL REMARKS

Although we have not provided a definite answer that can account for the large reduction of recorded motion at the basement of the high-rise building during the 1995 Kobe earthquake, it appears that the strong site nonlinearity of the surrounding soil partially contributed to a large reduction of the foundation input motion. Other factors related to local nonlinearities in SFSI (e.g., uplift and slippage between the basement and the surrounding soil), in addition to the inertial effect of the upper structure, should be incorporated in this analysis to help identify the mechanism that reduced the effective input motion to the building during the Kobe earthquake.

A lack of correspondence between recorded motion and actual structural damage was also observed in recent inland earthquakes in Japan. During the 2004 Niigata-ken Chuetsu earthquake, northern central part of Honshu Island, a strong motions record with a pulse-like waveform was obtained at Kawaguchi site, adjacent to the epicenter. Level of the ground motions are comparable with TKT in terms of PGV(1.5 m/s) and response spectra, though, the structural damage of the adjacent RC building is much smaller than inferred from records. It is evident that solving these problems will not only strengthen physical accountability related to observed failures, but it will also lead to a better understanding of SFSI phenomena during large earthquakes.

ACKNOWLEDGMENTS

Seismology records were provided by Railway Technical Research Institute, Urban Renaissance Agency,

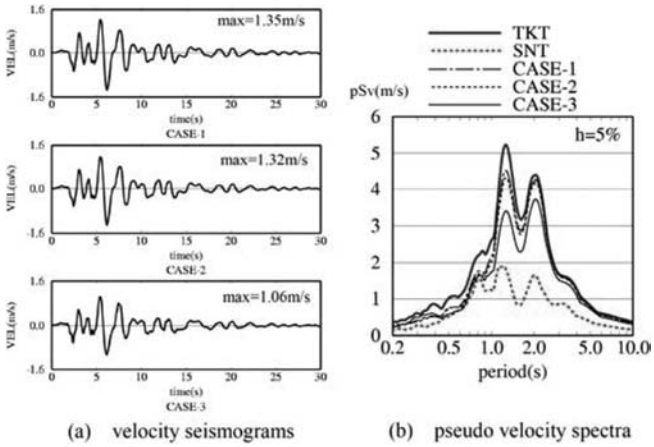

Figure 14. Foundation input motion at SNT using TKT as free surface motion and transfer function of CASE-3. (a) velocity seismogram, (b) pseudo velocity spectra compared with records at TKT and SNT.

Earthquake Research Institute, and so many other organizations. We would like to thank all those who were engaged in observations and disclosure of these records for their efforts.

REFERENCES

Hayashi, Y., J. Miyakoshi, K. Tamura & Kawase, H. 1997. Peak ground velocity evaluated from damage ratio of low-rise buildings during the Hyogo-ken Nambu earthquake of 1995 (in Japanese). *J. Struct. Constr. Eng., AIJ.* 494: 59–66

Huzita, K. & Sano, M. 1996. Hanshin-Awaji earthquake disaster and the Rokko Movements (in Japanese). *Kagaku*, 66:793–805

Koyamada, K., Nagano, M., Kato, K. & Ohno,S. 1998. Simulation of strong ground motions during the 1995 Hyogo-ken Nanbu earthquake using 2-D seismic profiles at six sections in Kobe City, *Proc of 2nd International Symposium on the Effects of Surface Geology on Seismic Motion*: 1457–1464.

Koyamada, K. 2005. Effects of soil nonlinearity on evaluation of site response (in Japanese). *Proceedings of the 32nd Symposium of Earthquake Ground Motion*, 97–104.

Lysmer, J. & Drake, L. A., 1972, A Finite Element Method for Seismology, *Methods in Computational Physics*, 11, 181–216.

Matsushima, S. & Kawase, H. 2009. Re-evaluation of strong motion and damage of wooden houses in Kobe City during the 1995 Kobe earthquake (in Japanese). *Journal of Structural Engineering, AIJ.* 537–543.

Motosaka, M. & Nagano, M. 1997. Analysis of amplification characteristics of ground motions in the heavily damaged belt zone during the 1995 Hyogo-ken Nanbu earthquake, *Earthquake Engineering and Structural Dynamics*, 26: 377–393.

Nagano, M., Ohno, S., Koyamada, K. & Kato, K. 1998. Bedrock motions and site amplifications in Kobe City during the 1995 Hyogo-Ken Nanbu earthquake (in Japanese), *J. Struct. Constr. Eng., AIJ*, 511: 77–84.

Nagano, M. 1998. Amplification characteristics of ground motions in deep irregular underground structure with vertical discontinuity, *Proc of 2nd International Symposium on the Effects of Surface Geology on Seismic Motion*: 859–866.

Nagano, M., Kudo, K. & Takemura, M. 1999. Simulation analyses of the array strong motion records from the aftershocks of the 1995 Hyogo-ken Nanbu earthquake ($MJ = 7.2$) regarding the irregularity of the underground structure in Nagata Ward, Kobe (in Japanese), *Zisin 2*, 52: 25–41.

Nagano, M. 2002. Ground motion amplification and interference of surface waves in 2D basin edge structure (in Japanese), *J. Struct. Constr. Eng., AIJ*, 552: 85–92.

Nagano, M., Yamada, A., Tsuji, K. & Oda, S. 2002. Earthquake response simulation analysis of high-rise RC building and effect of deep subsurface structure (in Japanese), *J. Struct. Constr. Eng., AIJ*, 560: 75–82.

Nagano, M. & Yamada, A. 2002 Amplification characteristics of ground motions adjacent to boundary of 3D basin-edge structure (in Japanese), *J. Struct. Constr. Eng., AIJ*, 560: 51–58.

Sano, M. 1998. Underground structures and active hidden faults in Osaka Basin (in Japanese). *11th Seminar of Fault Research & Information Center.* :6–23

Tokimatsu, K., Midorikawa, S & Yoshimi, Y. 1989. Dynamic soil properties obtained from strong motion records, *Proc. 12th Int. Conf. on Soil Mechamics and Foundation Engineering*, 3: 2015–2018.

Yasui, Y., Iguchi, M., Akagi, H., Hayashi, Y. & Nakamura, M. 1998. Examination of effective input motion to structures in heavily damaged zone in the 1995 Hyogo-Ken Nanbu earthquake (in Japanese), *J. Struct. Constr. Eng., AIJ*, 512: 111–118.

Soil-Foundation-Structure Interaction – Orense, Chouw & Pender (eds)
© 2010 Taylor & Francis Group, London, ISBN 978-0-415-60040-8

Settlement of footings in sand using dynamic soil properties

K. Park, K.H. Stokoe II & R.E. Olson
Department of Civil, Architectural, and Environmental Engineering, University of Texas, Austin, Texas, USA

W. Seo
GS Engineering and Construction Co. Ltd., Seoul, Korea

ABSTRACT: Most existing methods of estimating the settlement of footings in cohesionless soils under working stresses are empirical and based on correlations with field measurements of settlement. The result is considerable scatter and a lack of a basis for long term improvements. In this paper we propose a method of analysis based on equivalent-linear elasticity that involves measurement of real soil properties and uses simple analytical methods. We also propose methods to determine and/or estimate the needed soil properties. We report here on load tests of two footings and one plate with diameters ranging from 0.25 m to 0.91 m, in silty sand, in which measured settlement is compared with settlement predicted using the theory and soil properties determined in the field from seismic tests. We also compare measured settlements with values calculated with Schmertmann's widely used method based on penetration testing.

1 INTRODUCTION

The traditional way to estimate settlement of footings in cohesionless soils, under working stresses, has been to utilize correlations between measured settlements and some parameter from reasonably simple field tests, in particular with N-values from standard penetration tests (SPT) or q_c values from cone penetration tests (CPT). Such correlations are convenient in the short term but provide little possibility of providing rational analyses in the long term. Further, most current correlations overpredict settlements.

The goal of the writers is to begin the analysis using a theoretically correct model and associated equations, and then to find ways of measuring the needed soil properties that are economical and provide more complete information about overall site conditions than measurements taken only at selected points.

We use the classical theories of elasticity for the analyses, measure the small-strain moduli using seismic methods in the field, and match measured load-settlement curves by multiplying the small-strain moduli by modulus reduction factors (MRF) to obtain secant moduli that vary with the stress level, an approach that is termed the *equivalent-linear elastic* method (Kramer 1996). The method is likely to be most accurate when the strains in the soil are small, as is the case when predicting settlements under working stresses (Menzies 2001). This approach is rational, simple to apply, and allows the effects of interactions between adjacent footings to be included. A major problem involves measurement of the critical parameter, Young's modulus, economically. The typical approach is to use laboratory triaxial compression tests with reconstituted samples at the field density, e.g., Briaud and Gibbens (1994) and Lehane et al. (2008). Such tests allow for determination of the effects of stress state and stress level on soil properties. However, over the past 20 years, nonintrusive seismic methods based on surface wave measurements have been developed (Stokoe et al. 2004; Stokoe & Santamarina 2000) which make it possible to obtain profiles of shear modulus in the field, both rapidly and cost effectively. Further, these measurements allow determination of properties spatially rather then just where soil borings are made.

The general approach we are using was presented by Mayne and Poulos (1999) although our analytical approach is somewhat different from theirs. They presented analyses to account for Poisson's ratio, finite layer thicknesses, foundation geometry, foundation rigidity, Gibson profiles, and footing embedment and presented design charts.

Progress in predicting settlement of footings in sand has been hampered from the beginning by a series of problems. For example, there are only a few tests where load-settlement curves are available for footings of the sizes typically used in engineering practice. For those, data on soil properties have tended to be indirect, e.g., parameters from SPT and CPT tests. Properties of cohesionless soils often vary in short distances and detailed information on soil conditions is sparse, e.g., there might be a single boring with SPT data in the vicinity. In 1994, in recognition of this situation, researchers at Texas A&M University performed field tests to obtain load-settlement curves for five footings in a silty sand at the National Geotechnical Experimentation Site (Briaud & Gibbens 1994). These

load-settlement tests were then used in blind predictions presented in a 1994 ASCE conference (Briaud & Gibbens 1994). Three contributors considered seismic data along with other soil data and two of them overpredicted settlements less than most of the other contributors.

More recently, a study of case histories was performed by Smith (2005) in which predicted and measured movements in soil were compared. Smith (2005) found 41 case histories that involved predictions based on both penetration and seismic measurements. Predictions based on seismic measurements were generally closer to measured settlements in the working stress range.

2 FIELD TEST SITE

2.1 *National Geotechnical Experimentation Site at Texas A&M University*

Static load-settlement tests were performed with two concrete footings and one steel plate at the National Geotechnical Experimentation Site (NGES) on the Riverside Campus at Texas A&M University (Briaud 1997). Our load-settlement tests were performed in the vicinity of the footing tests reported by Briaud and Gibbens (1994).

2.2 *Site conditions*

Soil at the site is generally cohesionless. Four layers were indicated by Briaud and Gibbens (1994). The top layer is medium dense, tan silty fine sand with a thickness of 3.5 m. That layer extends to a depth of about four times the width of our largest footing and thus the deeper layers of sandy soil that extend to a depth of 7 m, and deeper hard clay, had a negligible effect on settlements and are thus not considered further. The surface of the site was leveled by removing 0.5 to 1.5 m of overburden for the earlier studies presented by Briaud and Gibbens (1994). For our study, an additional 0.2 m of surficial soil was locally excavated to provide the surface upon which the concrete footings (discussed below) were cast.

The ground water table is at a depth of about 4.9 m. The water content of the sand near the surface, at the time of our tests, ranged from about 12–14% and the total unit weight was about 19.8 kN/m^3.

Briaud and Gibbens (1994) presented results from SPT and CPT tests that were performed close to our footing locations (Fig. 1). They also presented crosshole tests results in this area that showed tolerably uniform shear wave velocities (V_S) (Fig. 2a). As part of our investigation, seismic spectral-analysis-of-surface-waves (SASW) tests were performed along three lines near the footing locations and small-scale downhole measurements were performed beneath our concrete footings. The shear wave velocities from the SASW and downhole tests were combined to develop a best-estimate V_S profile for use in our analyses (Fig. 2).

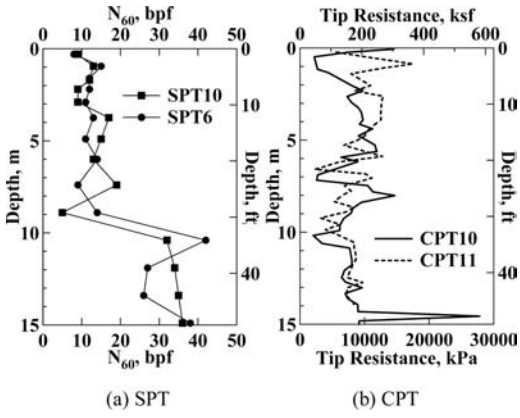

Figure 1. SPT and CPT profiles at the NGES sand site (from Briaud & Gibbens 1994; Briaud 1997).

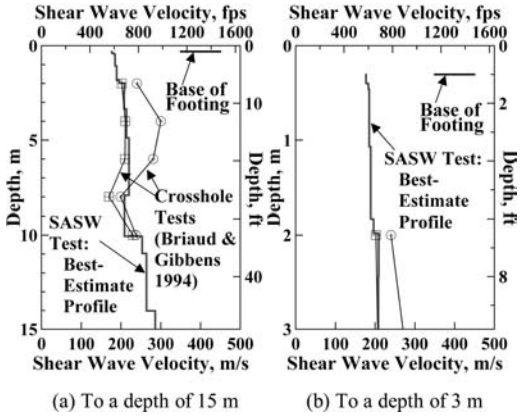

Figure 2. Shear wave velocity profiles at the NGES sand site.

The best-estimate profile within 2 m of the base of the two footings has an average V_S equal to 189 m/s (Fig. 2b).

The equivalent-linear elastic analysis uses Young's modulus (E_{max}), which was determined from $E_{max} = 2(1+\nu)G_{max}$, where G_{max} is the shear modulus and ν is Poisson's ratio. In turn, $G_{max} = \rho V_S^2$, where ρ is mass density and V_S is taken from the seismic measurements (Fig. 2b). Values of Poisson's ratio were determined from the shear and compression wave velocities in the field by:

$$\nu = \frac{\left(0.5 \times V_P^{\,2} - V_S^{\,2}\right)}{\left(V_P^{\,2} - V_S^{\,2}\right)} \qquad (1)$$

where V_P is compression wave velocity. The range in ν was from 0.23 to 0.44. A value of $\nu = 0.3$ was adopted for our analyses. Note that these values correspond to small strains and to in situ stress conditions. During a load test, the stress levels and stress states will vary spatially and thus local values of ν will also vary.

3 FIELD LOAD-SETTLEMENT TESTS

3.1 *Field test set-up*

Two circular concrete footings with diameters of 0.91 m (36 in.) and 0.46 m (18 in.) and one, 0.25-m (10-in.) diameter steel plate were loaded. Each concrete footing was 0.30 m (1 ft) thick, reinforced, and cast in place. The steel plate was 25 mm (1 in.) thick. Before constructing the concrete footings, vertical arrays of 3-dimensional geophones were embedded in the ground (Fig. 3), one beneath the 0.46-m footing and three beneath the 0.91-m footing. These geophones were used to evaluate initial stiffness of the soil in the critical zone directly beneath the footings.

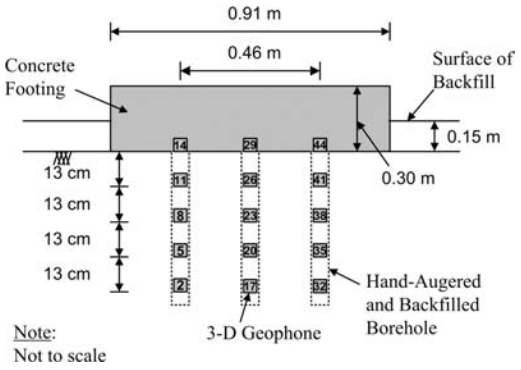

Figure 3. Cross-sectional view of the 0.91-m diameter footing.

3.2 *Field testing*

The footing testing procedure involved application of load by jacking against a large truck (a vibroseis called T-Rex) and measuring settlements (Fig. 4). Settlements were measured at three locations on each of the two concrete footings and at two locations on the steel plate. T-Rex was first positioned at the testing location over the footing. Two reference frames were placed near the footing to support displacement potentiometers which were arranged in an equilateral triangle on each concrete footing. Loads were applied in stages. Each stage consisted of building up the load during a period of 10–20 seconds, followed by a "resting period" of about four minutes where the loading process stopped. In the resting period, there was a slight reduction in load and continued settlements at a decreasing rate. Then the next loading stage began. For the steel plate, the loading stages were applied until there was a large settlement (Fig. 5c) and the footing was essentially in a state of bearing capacity failure. For the concrete footings, staged loading was again used but the load was decreased to zero two or three times (Figs. 5a and 5b) and other dynamic testing was performed. These additional tests generally involved small strains. It was necessary to remove the extensometers during these dynamic tests but the applied strains were so small that we assumed there was no settlement during the dynamic testing and the load-settlement curves, for loads in excess of the maximum previous value, had not been affected.

The peak load on the 0.91-m diameter footing was limited by the weight of T-Rex. There was an interest in non-dimensionalizing the applied pressures by dividing by the bearing capacity, but the bearing capacity could not be reached for the concrete footings. Accordingly, the test on the 0.25-m diameter steel plate was added so its bearing capacity could be determined (Fig. 5c) and scaled up to the size of the other two footings using the N_γ term of classical bearing capacity theory. That scaling is approximate because of the difficulty in including the effects of partial saturation and negative pore water pressures but the extrapolation should be more accurate than the bearing capacity calculated using the existing range in bearing capacity theories.

(a) Testing the 0.91-m diameter footing

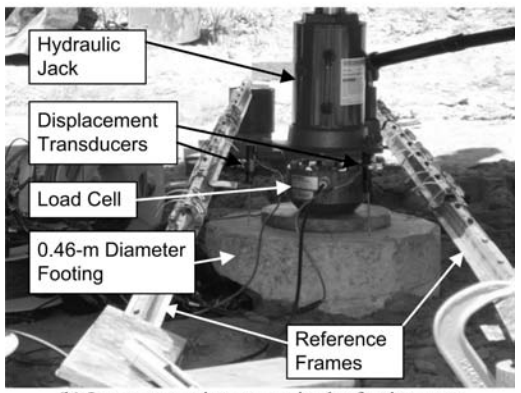

(b) Instrumentation set-up in the footing tests

Figure 4. Pictures of static load-settlement tests at the NGES sand site.

3.3 *Field load-settlement results*

For the 0.46-m and 0.91-m diameter footings with staged load-unload cycles, backbone curves were fit to approximate a continuous loading response for each footing (Figs. 5a and 5b, respectively). The backbone curves were used to calculate modulus reduction factors (MRF) as discussed in Section 4.2.3.

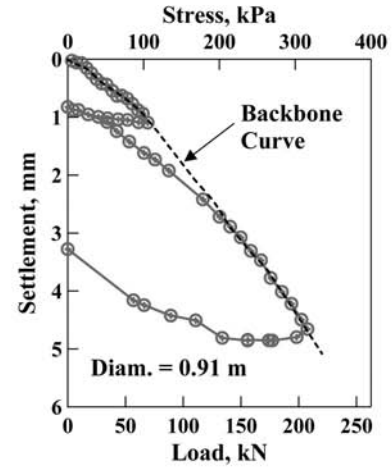

(a) 0.91-m diameter footing

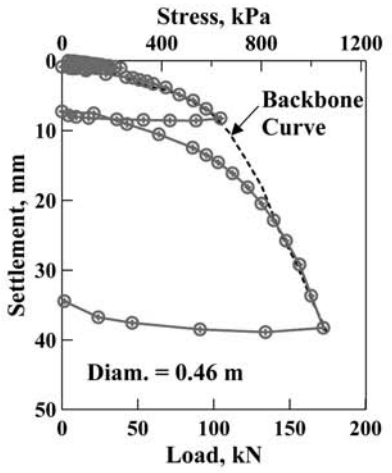

(b) 0.46-m diameter footing

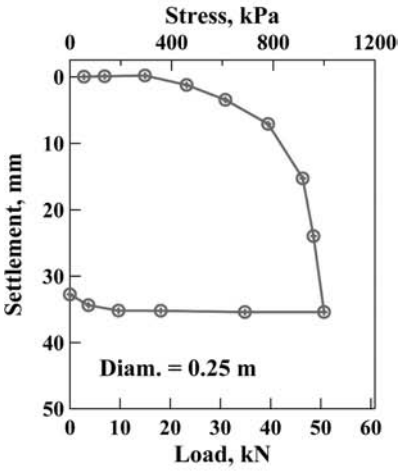

(c) 0.25-m diameter plate

Figure 5. Original load-settlement curves and backbone curves used to evaluate the MRFs.

4 ANALYSIS

4.1 *Schmertmann's method using SPT, CPT and SASW measurements*

Schmertmann's method (Schmertmann 1970) uses Young's modulus (E) to predict settlements. Schmertmann originally obtained values of E from load-displacement tests of screw anchors. He correlated his values of E with cone tip resistances (q_c). In this study, the correlation expressed by $E = (1.5)q_c$ is used for silty sand. When SPT data are used, the correlation between E and N_{60} is used as suggested by Coduto (2001) for silty sand:

$$E = 50000\sqrt{OCR} + 12000N_{60} \quad (2)$$

where E is in psf, OCR is the overconsolidation ratio, and N_{60} is the standard penetration resistance in blows/30 cm corrected to a hammer efficiency of 60%. In the analysis, the subsoil was divided into three to five layers to depths of two times the footing widths (B).

Values of N_{60}, q_c and V_S were selected based on SPT10 (Fig. 1a), CPT10 and CPT11 (Fig. 1b), and the best-estimate V_S profile (Fig. 2), respectively. In the absence of data on the OCR, it was simply set equal to one.

Settlements predicted from Schmertmann's method with moduli from the SPT and CPT tests for the 0.91-m and 0.46-m diameter footings are generally in excess of the measured values (Fig. 6).

The working stress employed in common practice for this silty fine sand is often in the range of 200 to 400 kPa. At the average stress in this range, the predicted settlements are about 5 to 7 times the measured value for both concrete footings when the CPT and SPT correlations were used. Use of E_{max} values obtained from field seismic measurements (Fig. 2) led to underpredictions of the settlements in the working stress range. For the 0.91-m and 0.46-m diameter footings, the predicted settlements were both about 0.34 times the measured settlements (Fig. 6) but the measured settlements are so small that this error seems irrelevant.

These results show that moduli from small-strain seismic tests yield better settlement predictions with Schmertsmann's method than moduli estimated from SPT and CPT correlations for our two footings in the range of design pressures typically used for footings in similar soils. Schmertmann's method was not intended for prediction of small movements and he may have followed the lead of Terzaghi and Peck (1948) and others by providing a method that was conservative (overpredicted settlements).

4.2 *Analytical method based on the theory of elasticity*

Use of the theory of elasticity to predict settlements is quick and easy once simple equations have been inserted into a spreadsheet or incorporated in a computer code. The subsoil is usually approximated as a

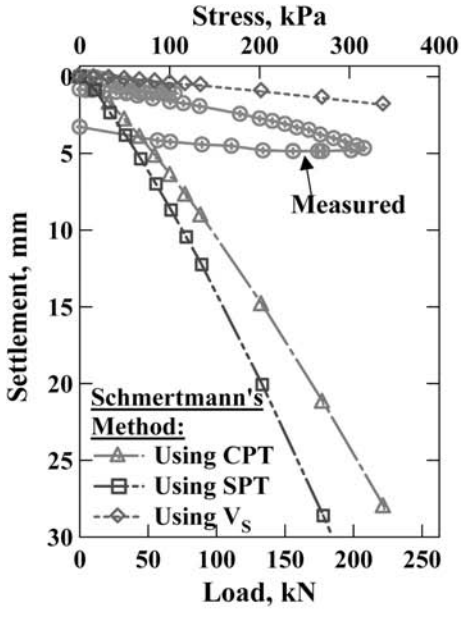

(a) 0.91-m diameter footing

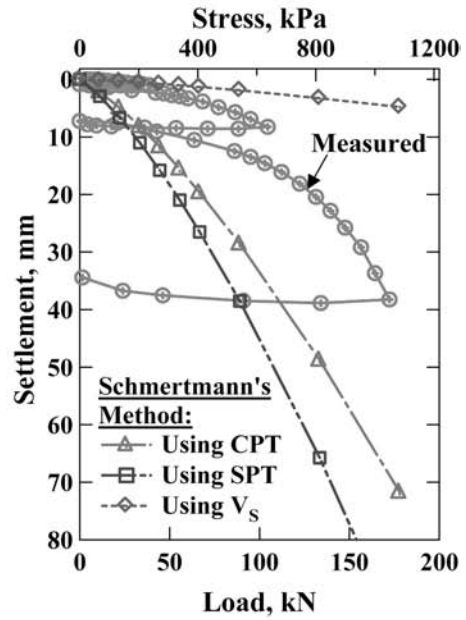

(b) 0.46-m diameter footing

Figure 6. Comparison of measured settlements with settlements predicted using Schmertmann's method.

half space of homogeneous, isotropic, linearly elastic material. The analysis automatically accounts for movements due to both volume change and lateral displacement of the soil under the footing and can be used with multiple footings, in which case the interaction of the footings is taken into account. Layered systems can be approximated by using the properties of each layer separately, as if that layer occupied the entire half space, calculating displacements at the top and bottom of each layer, and taking the difference as the contribution of that layer to overall footing settlement. Those contributions are added for the different layers to obtain an estimate of footing movement.

The analyses typically involve the assumption that the footing applies a uniform pressure to the half space. Our test footings were essentially rigid. As a result, we calculated displacements at various points on the base of the footing and used a weighted average to obtain an estimate of settlement for a rigid footing. The easier approach is to calculate the settlement of the center of a flexible footing and then multiply by a factor. Mayne and Poulos (1999) indicate that for an infinitely deep elastic body this factor is 0.785. For depths we have encountered for real soils, the factor backed out of our weighted average settlement was about 0.82, which practically duplicates the value from Mayne and Poulos (1999).

The two solutions we have used are for rectangular footings (Harr 1966; Poulos & Davis 1974) and for circular footings (Ahlvin & Ulery 1962).

4.2.1 *Rectangular footings*

For rectangular footings, the settlement under one corner is given by:

$$S = \frac{pB}{E}\left(1-\nu^2\right)\left(F_1 - \frac{1-2\nu}{1-\nu}F_2\right) \tag{3}$$

where p is the mean footing pressure, B is footing width (the smaller dimension for rectangular footings), E is Young's modulus, ν is Poisson's ratio, and F_1 and F_2 are:

$$F_1 = \frac{1}{2\pi}\left[\ln\left(\frac{\sqrt{1+\lambda^2+\zeta^2}+\lambda}{\sqrt{1+\lambda^2+\zeta^2}-\lambda}\right)\right] + \lambda\ln\left(\frac{\sqrt{1+\lambda^2+\zeta^2}+1}{\sqrt{1+\lambda^2+\zeta^2}-1}\right)$$

and

$$F_2 = \frac{\zeta}{2\pi}\tan^{-1}\left(\frac{\lambda}{\zeta\sqrt{1+\lambda^2+\zeta^2}}\right) \tag{4}$$

where λ is the ratio of footing length to footing width, and ζ is the ratio of depth where movement is to be predicted to footing width. Note that for points under a footing, the settlement is calculated using four sub-footings so the point of interest is under a corner of each sub-footing. The result is that the length and width are defined for each sub-footing separately.

4.2.2 *Circular footings*

Ahlvin and Ulery (1962) presented an equation for calculating vertical strain (ε_v) in an elastic body subject to a uniform pressure on a circular area on the surface. Their equation is:

$$\varepsilon_v = p\frac{1+\nu}{E}\left[(1-2\nu)A + B\right] \tag{5}$$

where E is Young's modulus, ν is Poisson's ratio, and A and B are space dependent coefficients, values of which were tabulated by Ahlvin and Ulery (1962). We applied this equation by dividing the subsoil into a number of layers and calculating the strain at the middle of each layer. The strains were averaged over the radius of the footing to obtain the estimated compression for a rigid footing. The weighted mean strains were multiplied by the thicknesses of the layers to obtain compressions, and the compressions were added to obtain the estimate of footing settlement.

We have used the appropriate equation depending on footing shape but comparative analyses for square and circular footings of the same base area indicate that the solutions are interchangeable and the calculated settlements differ by less than about 0.1%.

4.2.3 *Modulus reduction factor*

Actual load-settlement relationships are nonlinear and vary widely depending on such factors as relative density of sands and the effects of cementation. The easiest way to model such load-settlement curves may be to begin with a measureable field property, viz., Young's modulus at strains less than about 0.001% (E_{max}) and multiply E_{max} by an empirical parameter, termed the *modulus reduction factor* (MRF), to obtain a secant modulus that defines the settlement at a particular footing pressure. That approach seemed impractical decades ago because sample disturbance meant that values of E measured in the laboratory were too small. Currently, values of E_{max} can be evaluated using seismic techniques so the empiricism appears in trying to model the load-settlement curve for finite strains. In our case, we have fit theoretical settlements to our measured values using the theories discussed previously and empirical values of MRF. In the absence of detailed measurements of strain in soil layers beneath our footings, we have chosen to use the same values of MRF for all layers. That approach also ignores the fact that E_{max} increases as the confining pressure increases, and such increases occur in the field due to the footing load itself. All such refinements will appear here in the empirical values of the MRF.

Ideally, the initial slope of the field load-settlement curves would correspond to values predicted using MRF = 1.0. In reality, multiple problems exist at small loads. For example, the soil at shallow depth may have been affected by construction of the footing and that effect should diminish as load increases. In one test, under very small loads the settlement readings indicated the footing rose a tiny amount (possibly wind loading of the beam supporting extensometers, or someone bumped a supporting stake, etc.). Experience showed that the fractional scatter diminished as the load increased, in agreement with similar findings by Lehane et al. (2008).

To be useful, the MRF needs to be expressed as a function of some convenient parameter. The first settlement charts in wide use (Terzaghi & Peck 1948) were based on the assumption that settlements up to 25 mm could be tolerated so those authors began with a limiting settlement and provided the applied stress as a function of footing dimensions and relative density for sands. In the case of our footings, the settlement of 25 mm corresponds to values of MRF slightly less than 0.1 (Fig. 7a). This relatively low value of MRF means that the 25-mm settlement results in use of elevated footing pressures (Fig. 7c) and reduced factor of safety against a bearing capacity failure (Fig. 7b), but a smaller, more economical footing.

Some engineers prefer to design for a given factor of safety. Such an approach seems problematic considering the lack of accuracy in bearing capacity equations when the soil is unsaturated and/or fully drained. In such cases, clear bearing capacity failures do not occur. Furthermore, the actual failure mode does not conform to the assumptions embodied in the theory, e.g. log spiral failure surfaces do not form (Vesic 1967). However, in our case we have a fair idea of the bearing capacity based on the load-settlement tests of the 0.25-m diameter steel plate and we scale that bearing pressure up to larger footings assuming the stress at failure is a linear function of footing size. The values of MRF for factors of safety (FS) between 2 and 3 (Fig. 7b) are again around 0.1.

Some designers apply the local building code or local rules of practice. Building codes set conservative design footing pressures, often termed, *presumptive pressures*, but these pressures vary widely among various jurisdictions in the United States. For a typical range of presumptive pressures between say 200 and 400 kPa, the MRF is around 0.2 to 0.5 (Fig. 7c). These elevated values of MRF are the result of the reduced footing pressure.

Finally, laboratory tests typically present ratios of G/G_{max} versus shear strain. We do not have something similar for the present analysis but we can plot MRF versus settlement expressed as a fraction of footing width (Fig. 7d). Again, for the typical range of presumptive pressures and associated small settlements, the values of MRF are around 0.1 to 0.3.

Designers can begin with the parameters of their choice, e.g. limiting settlement, presumptive bearing pressures, or limiting factors of safety, and use data such as in Fig. 7 to obtain reasonable values of MRF and use those values of MRF together with the equations presented previously, to obtain estimates of other parameters used to check the design.

Our plots (Fig. 7) suggest a significant range in values of MRF even for footings on the same site and in close proximity. However, values of MRF at negligible applied pressures seem generally irrelevant, as are values where the footing is close to a bearing capacity failure. Therefore, values of MRF could be based on criteria such as a common limiting settlement (say 25 mm), a typical range in factors of safety (FS = 2 to 3) or a presumptive bearing pressure (200–400 kPa) as shown in Figs. 7a, 7b and 7c, respectively. The choice of criterion and MRF values to use is left to the judgment and experience of the designer.

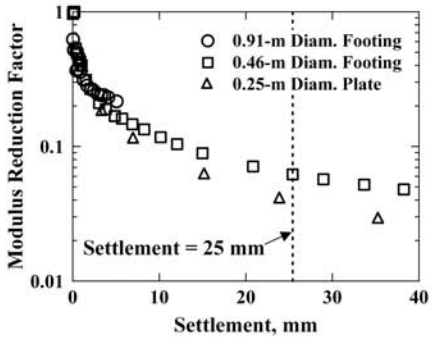

(a) MRF vs. settlement

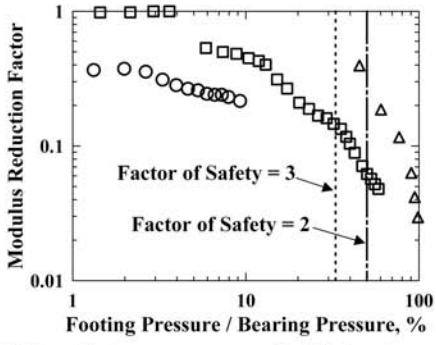

(b) MRF vs. footing pressure normalized by bearing capacity

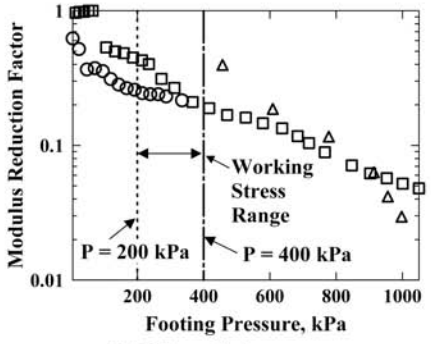

(c) MRF vs. footing pressure

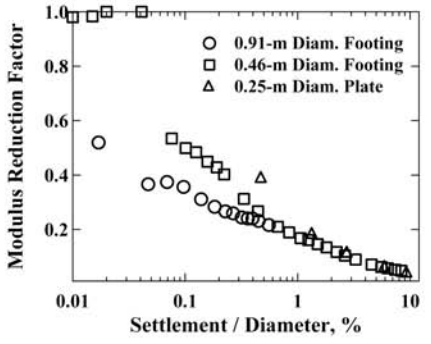

(d) MRF vs. settlement over footing diameter

Figure 7. Variation of MRF with various representations of footing pressure and settlement.

Finally, the approach here is perhaps more to provide a methodology than to provide detailed values of MRF. Documented experience with a range of soil types and footing sizes will clarify the accuracy of this approach.

5 SUMMARY AND CONCLUSIONS

Most existing methods used to predict settlement of footings in cohesionless soils are empirical and involve correlating measured settlements with parameters from tests that are convenient and widely used (SPT and CPT) but which do not measure, directly, a relevant soil property. These empirical methods resulted in major improvements in design when they were introduced but advances in technology in recent decades suggest that it would be preferable to use a real soil property, the velocity of propagation of a shear wave (V_S), which can then be converted to the shear modulus at small strains (G_{max}), and finally to Young's modulus at small strains (E_{max}). For actual footings, a secant value of E is needed and it is obtained by multiplying E_{max} by a modulus reduction factor (MRF). The MRF is backed out of case histories and is thus also empirical, but it begins with a real soil property which can be measured in the field. The value of MRF that should be used depends on the chosen independent variable. Thus, if a settlement of 25 mm (one inch) is selected, the MRF is small but the applied load is large and the cost of the footing is reduced. Other values of MRF result if the designer chooses to use a certain factor of safety or some presumptive footing pressure.

The importance of seismically determined moduli in settlement predictions is also demonstrated using Schmertmann's method. In this case, settlements measured in our two load tests on concrete footings are compared with settlements predicted using SPT and CPT correlations with Young's modulus and with E_{max} evaluated from small-strain seismic tests. In the working stress range, use of seismically determined values of Young's modulus, with Schmertmann's method, led to underprediction of settlements by a factor of about three, but settlements were so small that the actual error in settlement was inconsequential. However, use of SPT and CPT values led to overprediction of settlements that increased as the load increased and were significant for purposes of design.

In addition to the advantage of using a real soil property (such as E_{max}) in settlement predictions/analyses, field seismic measurements make it possible to provide information about a whole site much more accurately than can be obtained with point measurements in soil borings or soundings.

As usual, this approach to design needs refinement from case histories on a range of sites with different soil properties. The shear modulus is an effective stress property so it seems possible that this approach could be useful for clays but case histories will be more difficult to find or develop.

ACKNOWLEDGEMENTS

Financial support for this study was provided through the National Science Foundation under grant CMS-0421275. Financial support for the development of the nees@utexas Equipment Site was provided by the George E. Brown, Jr. Network for Earthquake Engineering Simulation (NEES) under grant CMS-0086605. The writers wish to thank to Dr. Giovanna Biscontin, Dr. Jose Roesset, Dr. Luciana Barroso, Dr. Farn-Yuh Menq, Mr. Cecil Hoffpauir, Mr. Andrew Valentine, and Mr. Christopher Stanton for the help that they provided throughout this work.

REFERENCES

Ahlvin, R.G. & Ulery, H.H. 1962. Tabulated values for determining the complete pattern of stresses, strains, and deflection beneath a uniform circular load on a homogeneous half space, *Highway Research Board Bulletin 342, Stress Distribution in Earth Masses*: 1–13.

Briaud, J.-L. 1997. *The National Geotechnical Experimentation Sites at Texas A&M University: Clay and Sand*, Report No. NGES-TAMU-007, Texas A&M University

Briaud, J.-L. & Gibbens, R.M. 1994. *Predicted and measured behavior of five spread footings*, ASCE, Geotechnical Special Publication, No. 41.

Coduto, D.P. 2001. *Foundation Design, Principles and Practices*, New Jersey: Prentice-Hall.

Harr, M.E. 1966. *Foundations of Theoretical Soil Mechanics*, New York City: McGraw-Hill.

Kramer, S.L. 1996. *Geotechnical Earthquake Engineering*, New Jersey: Prentice-Hall.

Lehane, B.M., Doherty, J.P. & Schneider, J.A. 2008. Settlement Prediction for Footings in Sand, *Deformational Characteristics of Geomaterials*, Burns, Mayne, and Santamarina (eds): 133–150.

Mayne P.W. & Poulos, H.G. 1999. Approximate displacement influence factors for elastic shallow foundations. *Journal of Geotechnical and Geoenvironmental Engineering, ASCE*, 125(6): 453–460.

Menzies, B. 2001. Near-surface site characterization by ground stiffness profiling using surface wave geophysics. In Saxena & Sharma (eds.), *Instrumentation in Geotechnical Engineering, H. C. Varma Commemorative Volume*, New Delhi, India: Oxford & IBH Publishing Co. Pvt. Ltd.

Peck, R.B., Hansen, W.E., & Thornburn, T.H. 1974. *Foundation Engineering*, New York City: John Wiley & Sons.

Poulos, H.G. & Davis, E.H. 1974. *Elastic Solutions for Soil and Rock Mechanics*, New York City: John Wiley & Sons.

Schmertmann, J.H. 1970. Static cone to compute static settlement over sand. *Journal of Soil Mechanics and Foundation Division*, ASCE, 96(SM3): 1011–1043.

Smith, R.T. 2005. *Prediction of Static Deformations with Dynamic Soil Properties: A Review of Case Histories*. M.S. Thesis: University of Texas at Austin.

Stokoe, K.H., S-H Joh & Woods, R.D. 2004. Some contributions of in-situ geophysical measurements in solving geotechnical engineering problems. *Proc., 2nd International Conf. on Site Characterization*, ISC'2, Porto, Portugal.

Stokoe, K.H. & Santamarina, J.C. 2000. Seismic-wave-based testing in geotechnical engineering. *GeoEng 2000*, Melbourne, Australia: 1490–1536.

Terzaghi, K. & Peck, R.B. 1948. *Soil Mechanics in Engineering Practice*, New York City: John Wiley & Sons.

Soil-Foundation-Structure Interaction – Orense, Chouw & Pender (eds)
© 2010 Taylor & Francis Group, London, ISBN 978-0-415-60040-8

Plugging mechanism of open-ended piles

Y. Kikuchi, T. Mizutani & Y. Morikawa
Port & Airport Research Institute, Yokosuka, Japan

T. Sato
Kumamoto University, Kumamoto, Japan

ABSTRACT: The mechanism of plugging phenomenon at the toe of vertically loaded open-ended piles was observed in this study. The behavior of the surrounding ground at the pile toe is discussed based on the observation of the movement of iron particles, which were mixed with sand to form layers in the model ground, extracted from visualized X-ray CT data. In addition, the movement of sand particles was extracted using PIV (Particle Image Velocimetry) method. The CT images of the experimental results showed that the condition of wedge formation below the open-ended pile was clearly different from that below the closed-ended pile. Although the penetration resistance of the open-ended pile and closed-ended pile was similar, the movement of soil inside the open-ended pile was not stopped but was restricted, as shown by intermittent increase and decrease in penetration resistance during pile penetration.

1 INTRODUCTION

For more than 50 years, steel pipe piles were used for port facilities, because of its flexural capacity and ease of pile driving. During these decades, diameters and embedded lengths of steel pipe piles were dramatically changed. Such changes may affect the plugging behavior of the pile.

The mechanism of plugging phenomenon at the toe of vertically loaded open-ended piles was observed in this study. Three series of static penetration experiments with model piles were conducted by using a micro-focus X-ray CT scanner (Kikuchi et al. 2006). And a series of large scale model pile penetration experiments was conducted in a model sandy ground to investigate the bearing capacity of open-ended piles. The model piles used in this study were open-ended piles and closed-ended piles.

The behavior of the surrounding ground at the pile toe is discussed based on the observation of the movement of iron particles, which were mixed with sand to form layers in the model ground, extracted from visualized X-ray CT data. In addition, the movement of sand particles was extracted using PIV (Particle Image Velocimetry) method. From large scale pile penetration experiments, the periodic behavior of bearing resistance of open-ended piles after plug formation was discussed. Finally we concluded an expected plugging mechanism of open-ended piles.

2 VISUALIZATION OF THE PLUGGING PHENOMENON

The first series of experiments was conducted to grasp the plugging phenomenon. The piles used in this series were open-ended stainless steel piles with 16 mm in outer diameter and 80 mm in length and the thickness of the pile wall was 0.3 mm. The container used was made of acrylic resin with 85 mm in inner diameter and 160 mm in height. The model ground was prepared with dry Toyoura sand ($D_{50} = 0.2$ mm, $U_c = 1.6$). The thickness of the ground was 150 mm. Relative densities of the ground were set to 5, 70, and 98%. The pile was penetrated into the ground at a rate of 1 mm/min. The pile penetration experiment was conducted outside the X-ray CT scanner room. The penetration resistance and depth were measured at the pile top. When the pile had penetrated to about 30 and 60 mm, the load was released and the container was moved into the CT room, and X-ray CT scanning was performed.

The relation between penetration resistance and depth is shown in Figure 1. Penetration resistance increases as the relative density of the model ground increases.

Figure 2 shows vertical sections from selected CT images to obtain views through the central axis of the pile at each depth. The white lines are the pile, the gray area is sandy ground, and the black part in the pile is air. The top of the CT images is the ground surface. It was observed that the ground surface, where the inner pipe pile was located, slid down with the pile in the test case involving low density ground (Case 1, $D_r = 5\%$). Although it is guessed that the plug occurred at the pile toe, penetration resistance did not increase. In the test case involving high density ground (Case 3, $D_r = 98\%$), penetration resistance was relatively high although the ground surface did not slide down with the pile. From these results, it is realized that the occurrence of ground invasion phenomenon into the pipe pile toe depends on the balance of ground reaction and

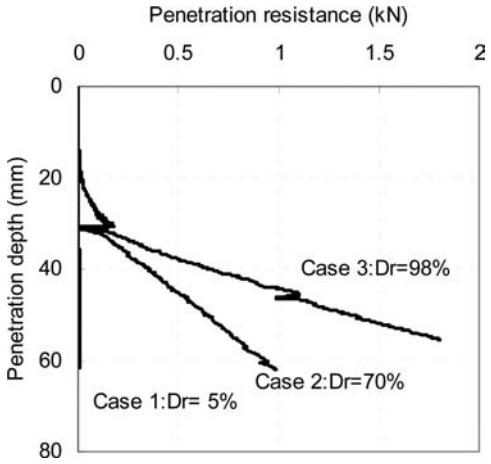

Figure 1. Relationship between penetration resistance and depth.

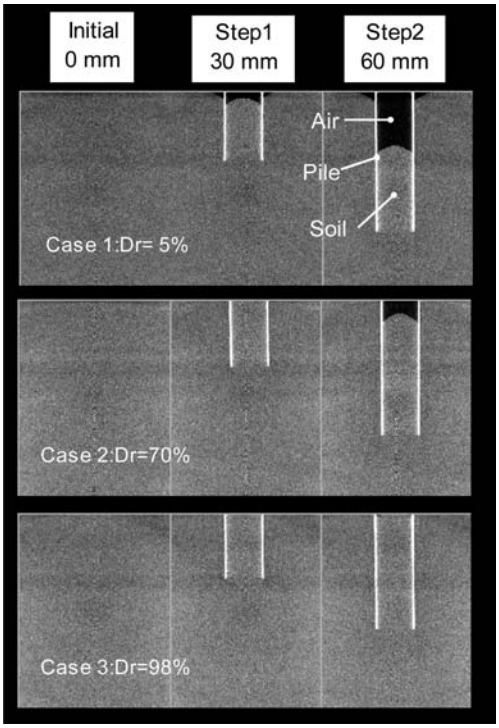

Figure 2. Vertical section of CT images.

frictional resistance of the pile inside and the weight of the soil. Therefore, the increment of resistance and appearance of the plugging phenomenon do not have a one-to-one correspondence. In other words, there are cases in which resistance occurred without the appearance of plugging phenomenon.

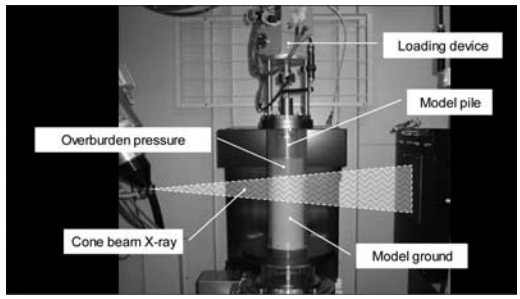

Figure 3. Penetration test in CT chamber.

3 GROUND BEHAVIOR AROUND THE PILE TOE

Referring to the previous test results, a series of detailed pile penetration experiments were conducted. New penetration apparatus was made to improve test accuracy. The dimensions of the model piles were 15 mm in diameter, 40 mm in length, and 1 mm in thickness for open-ended piles. The pile was made of aluminum. The container was made of acrylic resin, with 100 mm in inner diameter, and 440 mm in height. The sand used for the ground was Toyoura sand ($D_{50} = 0.2$ mm, $U_c = 1.6$). The model ground was 270 mm high with 65% relative density and prepared by air pluviation method. An overburden pressure of 2.5 kPa was applied by stainless steel balls (diameter: 2 mm).

In order to investigate the movement of the ground from X-ray CT results, a layer of iron particles (diameter: 0.3 mm) was used. The pile was penetrated into the ground from the ground surface at a rate of 1 mm/min. The entire pile penetration experiment was conducted in the micro-focus X-ray CT scanner chamber, as shown in Figure 3. When the piles had penetrated to about 35 mm and 70 mm, pile penetration was stopped, the load was released, and extension rods were added. To obtain test data, pile penetration was stopped at penetration intervals of 3 mm, and X-ray CT scanning was performed.

The relationship between penetration resistance and depth is shown in Figure 4. Small drops of resistance in each 3 mm intervals were observed in each relationship, because penetration was stopped to perform CT scanning. As a distinctive feature of the bearing capacity of open-ended pile, penetration resistance does not occur at the beginning of penetration, and penetration resistance decreases and increases in the middle of penetration. The increment of penetration resistance in both cases was almost equal after about 35 mm of penetration depth. This means that sufficient plugging of the open-ended pile may have developed. With the open-ended pile, resistance decreased and increased in the course of penetration at about 55 to 60 mm of penetration depth due to corresponding changes in the plugging effect. In other words, these results suggest that full plugging is not continuous but a plug is formed and broken repeatedly during pile penetration.

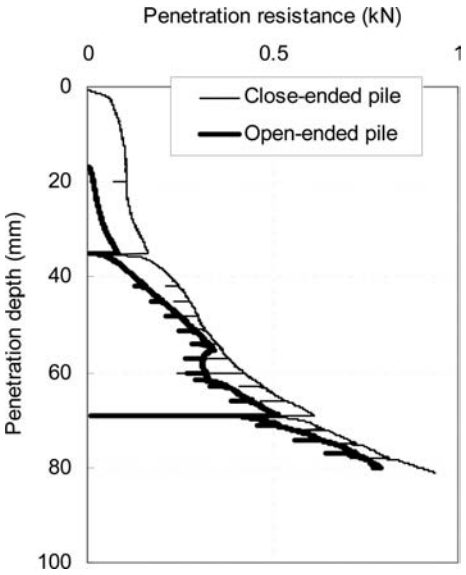

Figure 4. Relationship between penetration resistance and depth.

Figure 5 shows the movement of the particles during the pile penetration, depth of which was from 42 mm to 81 mm, with points and lines as extracted from the CT images. The points are the relative positions of the particles for pile at each 3-mm step of penetration, and the lines are the particle routes. In the case of closed-ended pile, the particles below the pile showed a tendency to be pushed out to the outside of the pile toe. A clear wedge was constructed at this area, and the soil was unable to intrude there. Some of the particles below the pile were caught at the surface of the wedge, and some were discharged to the side of the pile at the edge and then moved along the pile. Because the wedge unified with the penetrating pile, the relative movement of soil at the surface of the wedge was greatly different. This implies that a shear zone may develop at the wedge surface. On the other hand, the particles below the pile toe were able to move upward and penetrate into the pile. The particles outside the pile were pushed out to the outside of the pile toe.

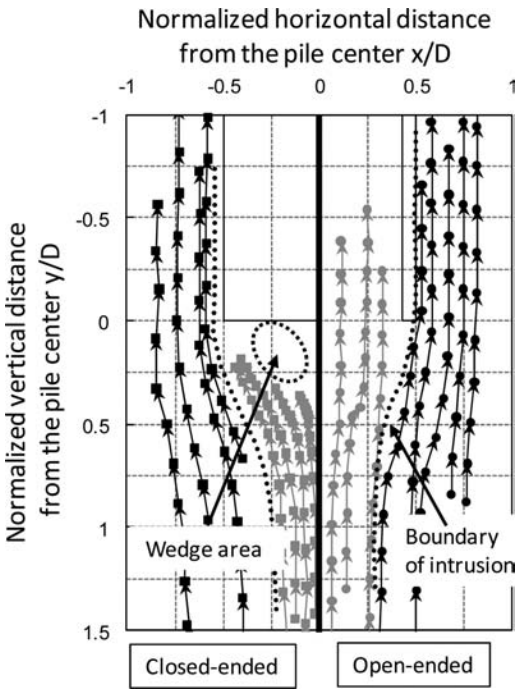

Figure 5. Relative movement of particular particles with respect to the pile at each 3 mm penetration. Traces of the particles started from 42 mm of pile penetration. Particles presented were located from one to two times the diameter beneath the pile tip in the beginning of the trace and they moved upward with penetration of the pile. Plots were observed positions and connecting lines showed the movement of each particle.

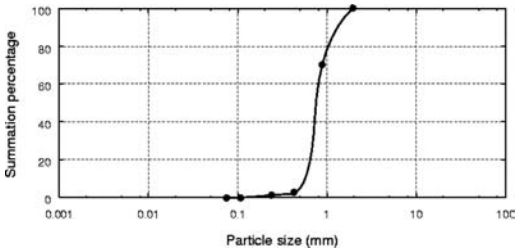

Figure 6. Grain size distribution curve of Souma sand #4.

4 DEFORMATION ANALYSIS USING PIV

In order to examine in detail the ground behavior, PIV method was applied to the CT images. This series of experiments was conducted so as to focus on the evolution process of the plugging phenomenon.

In this series, the model pile was set up in the model ground at the initial penetration depth of 50 mm. The container and the loading device in this series of experiment were the same as the previous case. The pile used in this series was open-ended with 32 mm in diameter, 140 mm in length, and 1.5 mm in thickness. The pile was made of aluminum.

The sand used was Souma sand #4 ($D_{50} = 0.7$ mm, $U_c = 1.6$). The density of the soil particles of Souma sand #4 is equal to 2.644 g/cm^3, maximum and minimum void ratios are 0.634 and 0.970 respectively. Figure 6 shows the grain size distribution of Souma sand #4.

A larger-diameter model pile and larger-diameter sand were used to observe the ground behavior of the inner pipe pile by PIV in this series of experiments. The model ground was 270 mm high with 65% relative density and prepared by air pluviation method. An overburden pressure of 2.5 kPa was applied by stainless steel balls (diameter: 2 mm). The pile was penetrated into the ground at a rate of 1 mm/min from

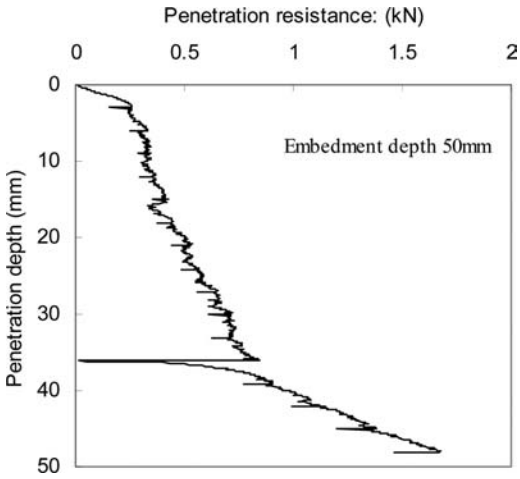

Figure 7. Relationship between penetration resistance and depth.

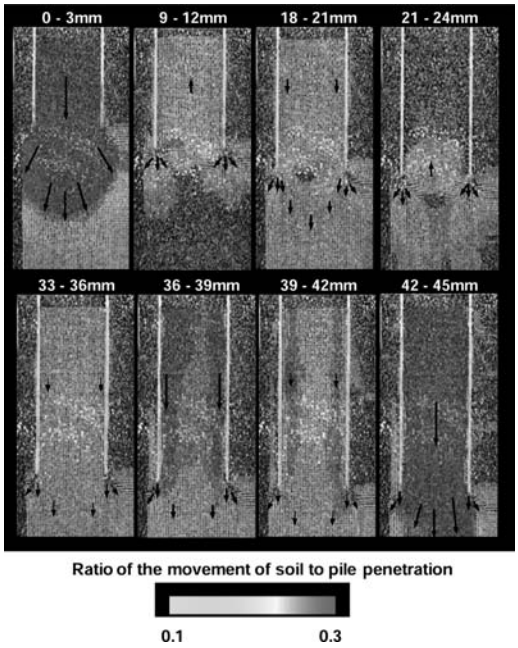

Figure 8. Images of ground displacements from CT images using PIV method. Black arrows show major direction and the amount of displacement of the ground during the 3 mm penetration. The penetration depth is shown above each picture.

50 mm to 98 mm in depth. The entire pile penetration experiment was conducted in the micro-focus X-ray CT scanner chamber.

The relationship between penetration resistance and depth is shown in Figure 7. Resistance occurred in the early stages of penetration in this experiment, because soil had been packed in the pile at the start of penetration.

In the PIV analysis, one pixel of the CT image was 0.1 mm square. The size of one element for the PIV analysis was 1.5 mm square, and the reference frame size was 4.5 mm.

The vectors of ground displacement that were measured by the PIV method are shown in Figure 8. The displacement vectors presented were measured between each 3 mm of penetration. The numbers shown at the top of each figure are penetration depths for each figure. The pile is shown as two white lines and gradations show the displacement of the ground. As it is difficult to recognize the deformation of the ground in this figure in detail, major displacements were presented by arrows in the figure.

The soil inside and below the pile moved downward when the penetration depth was from 0 to 3 mm. This is because the soil inside the pile during in the initial state created frictional resistance and made a plug. When the penetration depth increased slightly, the rate of change of resistance went down immediately at the penetration depth from 3 to 6 mm. Low rates of resistance increment were observed at the penetration depth from 3 to 33 mm. Movements of the soil inside and below the pile were small at this penetration depth. The transient process of plugging effect occurred at this stage. Relatively large movement of the soil inside the pile was observed at the penetration depth from 18 to 21 mm. But little movement was observed in the next stage of penetration. It was confirmed that repeated production and destruction of plug occurred at these steps. The rate of resistance increment rose again after 33 mm of penetration. The displacement of the soil inside and below the pile got larger at penetration depth from 30 to 36 mm; in particular, a downward movement of the soil existed and maintained at the penetration depth from 36 to 42 mm. A sufficient plugging effect occurred at this step. In this way, the relationship between penetration resistance and ground deformation was observed by using PIV method.

5 PENETRATION EXPERIMENT OF OPEN-ENDED PILES IN MODEL GROUND

To examine the plugging effect, a series of penetration experiments of open-ended pile in model ground was performed (Mizutani et al. 2003).

The model ground was made of Souma sand #4. Physical properties of Souma are presented in the previous section. Dried Souma sand was pluviated into the container, which was 6 m in length, 3 m in width and 3 m in depth, through a pipe with diameter of 3 cm. The height of the sand fall was kept 1 m above the surface during sample preparation. The relative density of the model ground was about 40%.

After the sample preparation was completed, model piles were driven into the ground. The model pile, with 20 cm diameter and about 2 m long, was made of acrylic resin. The model pile could be used as both

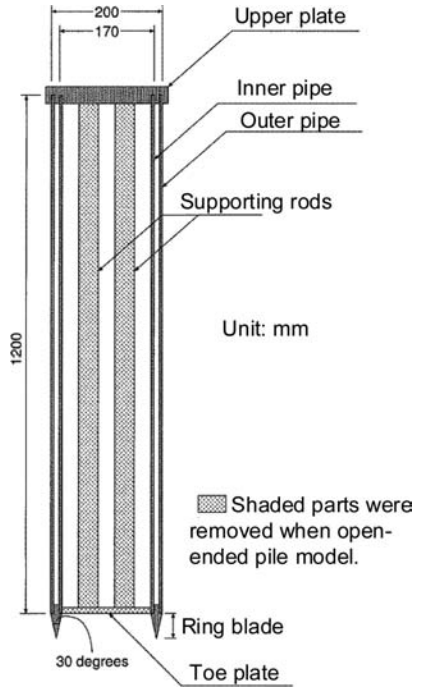

Figure 9. Vertical cross section of the model pile used in experiments.

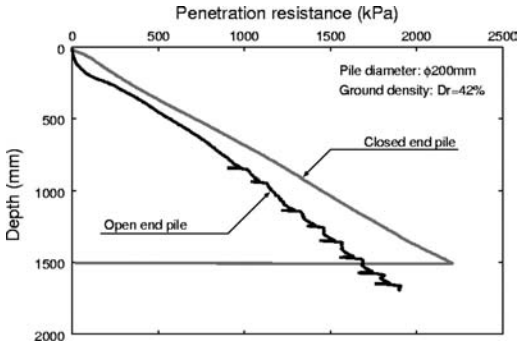

Figure 10. The relationship between the depth and the penetration resistance.

the closed-ended pile and the open-ended pile through a removable bottom plate, as shown in Figure 9.

The model piles were driven into the model ground statically at a speed of 20 mm/min. Penetration resistance at the head of piles and height change of the surface of the ground inside open-ended piles were measured continuously during the penetration of model piles.

Figure 10 shows the relationship between the depth and the penetration resistance of model piles. In case of the closed-ended pile, the penetration resistance increased immediately after the onset of the pile driving, while the penetration resistance of the open-ended

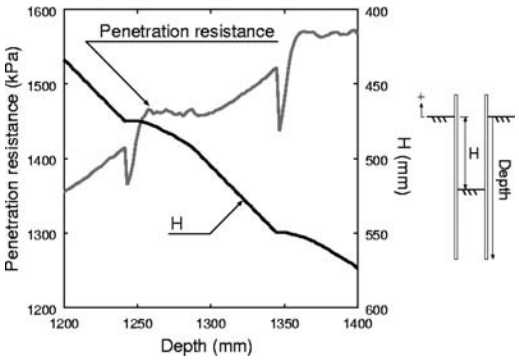

Figure 11. Cyclic changing of the penetration resistance of the open-ended pile compared with the height change of the inside ground.

pile increased gradually. After the penetration depth reached 800 mm, a remarkable change of the penetration resistance of the open-ended pile appeared, that is, the penetration resistance increased and decreased periodically.

One cycle of this periodically changing penetration resistance was enlarged and displayed in Figure 11, comparing with the height change of the inside ground surface of the open-ended pile. The cyclic behavior included four phases as follows:

1) A sudden reduction of the penetration resistance took place at about 1250 mm in depth. At that moment, the height change of the inside ground surface indicated as '*H*' in Figure 11, came to a standstill.
2) The penetration resistance increased rapidly, while the height of the inside ground surface was standing at about 475 mm.
3) From 1260 mm to 1300 mm in depth, the penetration resistance stopped to increase, and kept a constant value. In the meantime, *H* increased gradually, however, the increment of *H* was less than the increment of the pile penetration depth.
4) After the depth exceeded 1300 mm, the penetration resistance resumed increasing. At this stage, the increment of *H* was equal to the increment of the depth, that is, the inside soil and the open-ended pile itself penetrated into the model ground as one body.

Thus, open-ended pile could not continuously remain under a fully-plugged condition, and intermittent plugging was observed. This sort of phenomenon has been already reported by Hight et al. (1996) who conducted another type of model tests. In their investigation, submerged sand columns were pushed up from their base inside steel pipe piles using a rigid platen, and the load-displacement relationships for the sand plug were obtained by monitoring the load on the platen and its displacement. It is noteworthy that the identical behavior was observed in different types of model tests.

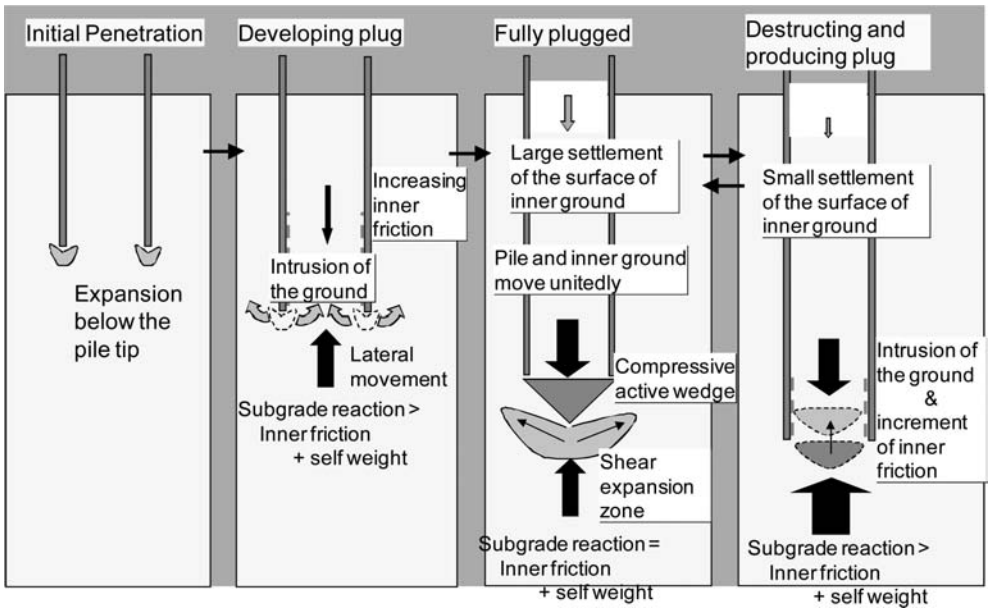

Figure 12. Plugging mechanism of open-ended pile.

6 PLUGGING MECHANISM OF OPEN-ENDED PILES

From these observations, expected plugging mechanism is presented in Figure 12 (Kikuchi et al. 2008). The ground below the pile toe is deformed by pile penetration. The deformed and dilated soil intrudes inside the pile and friction is produced between the pile and the intruding soil. If the inner friction resistance and self weight balance with the bearing resistance of the ground below the pile toe, a plug is produced. Then, the area below the pile is compacted to form a soil wedge. However, if the bearing resistance of the ground below the pile overcomes the resistance of the inner friction, the plug is destroyed and the wedge and the ground underneath intrude into the pile interior. This generation and destruction of the plug is repeated during the penetration of open-ended piles.

7 CONCLUSIONS

In this study, the behavior of surrounding ground around a pile toe was discussed based on static penetration test. During the penetration test, the movement of the ground was observed using a micro-focus X-ray CT scanner. The CT images of the experimental results showed that the condition of wedge formation below open-ended pile was clearly different from that below closed-ended pile. Although the penetration resistance of the open-ended pile and closed-ended pile was similar, the movement of soil inside the open-ended pile was not stopped but restricted, as shown by intermittent increase and decrease in penetration resistance during pile penetration. As a result, a plugging mechanism was proposed in Figure 12.

REFERENCES

Hight, D. W., Lawrence, D. M., Farquhar, G. B., Milligan, G. W. E., Gue, S. S. and Potts, D. M. 1996. "Evidence for scale effects in the end bearing capacity of open-ended piles in sand." *Proc. of the 28th Annual Offshore Tech. Conf.*, pp.181–192.

Kikuchi Y, Mizutani T, Nagatome T and Hata T. 2006. "Study on applicability of micro-focus X-ray CT scanner for geomaterials". *Technical Note of the Port and Airport Research Institute*, No.1125 (in Japanese).

Kikuchi Y, Sato T, and Morikawa Y. 2008. "Observation of the plugging phenomenon in a vertically loaded open-ended pile". *Technical Note of the Port and Airport Research Institute*, No.1177. (In Japanese)

Mizutani T, Kikuchi Y and Taguchi H. 2003. "Cone penetration tests for the examination of plugging effect of open-ended piles." *Proc. of IC on Foundations*, BGA, 655–664.

Soil-Foundation-Structure Interaction – Orense, Chouw & Pender (eds)
© 2010 Taylor & Francis Group, London, ISBN 978-0-415-60040-8

Pile head lateral forced vibration tests

N.M. Sa'don, M.J. Pender, R.P. Orense & A.R. Abdul Karim
Department of Civil & Environmental Engineering, University of Auckland, New Zealand

ABSTRACT: This paper presents the initial results of a full-scale field study of single free-head piles embedded in Auckland residual clay. Four hollow steel pipe piles, each with an outside diameter of 273 mm and wall thickness of 9.3 mm were installed at a site in Albany, Auckland (NZ). The piles were excited dynamically with an eccentric mass shaker mounted at the pile head. Dynamic tests ranging from low level excitation (a zero-mass loading) to high dynamically-induced force amplitudes were performed after a wet winter period, so that the soil was saturated to the ground surface. Prior to the large force amplitude excitation, the shaker was run with zero mass installed and the observed natural frequency of the system was found to be about 11.0 Hz. After the high-level shaking, the natural frequency had reduced to 8.2 Hz. The reduction in natural frequency demonstrated the non-linear response of the pile-soil system due to the degradation of soil stiffness and the formation of gaps between the pile shaft and the surrounding soil. After three weeks of rest and some more rain, the gap between the pile and soil had disappeared and a natural frequency of 10.2 Hz was measured.

1 INTRODUCTION

Piles are used to support structures in a variety of situations by transmitting actions applied at the pile head to material beneath the ground surface capable of providing the required resistance. The behaviour of single piles under lateral loading is important for foundations, which provide resistance against earthquake, wind and wave loading. In all three cases dynamic effects are significant, particularly with regard to the development of the damping component of the pile resistance. Earthquake loading differs from the other two in that the primary excitation comes from the ground below the pile.

However, it is possible to break the response of a pile to earthquake excitation into two parts, the so-called kinematic interaction and the inertial interaction. Kinematic interaction deals with the flexing of the pile shaft in the ground as the earthquake wave travels upwards. Inertial interaction models the response of the pile head to actions generated by the inertial response of the structural mass attached to the pile head. The analysis of this inertial pile response to earthquake excitation is essentially the same as that required for the pile response to wind loading and wave loading. The primary purpose of the pile testing discussed herein is to measure the inertial response of piles in Auckland soils and to investigate how the lateral stiffness decreases with increasing pile head excitation.

The main tool that used for analysis of the response of the pile was the elastic continuum model (ECM) for a long elastic pile in an elastic soil (Gazetas, 1991). This model has been extended to enable nonlinear behaviour of the soil around the pile to be represented (Davies and Budhu, 1986).

The field work involved measurement of the small strain stiffness of the soil using wave activated stiffness (WAK) tests (Briaud and Lepert, 1990), spectral analysis of surface waves (SASW) (Nazarian and Stokoe, 1984), seismic cone penetration tests (SCPT), and low level response of the pile generated by hammer blows and also by excitation from an eccentric mass shaker (Anco Engineers MK-140-10-50) with small or no mass attached. All of these indicate a consistent value for the small strain stiffness of the soil. The approach taken to interpret the field response is to estimate the factor by which the small strain stiffness of the soil needs to be reduced to give the operational stiffness for the cyclic loading loops. In other words, this approach evaluates the response of the pile using an approach similar to the design approach outlined in Table 4.1 of EC8 part 5 (BS EN 1998-5).

2 FIELD TESTING PROGRAM

2.1 *Site descriptions*

The test site was located at the Pine Hill subdivision in Albany, Auckland. The material at the site was classified as Auckland residual clay, a product of the in-situ weathering of Waitemata group sandstones and siltstones. The CPT recorded an average cone penetration resistance of about 1 MPa with a friction ratio of 1.5% to 6% indicating cohesive soil. The shear-wave velocity recorded from the SCPT was approximately 155 m/s and was fairly constant with depth. The soil

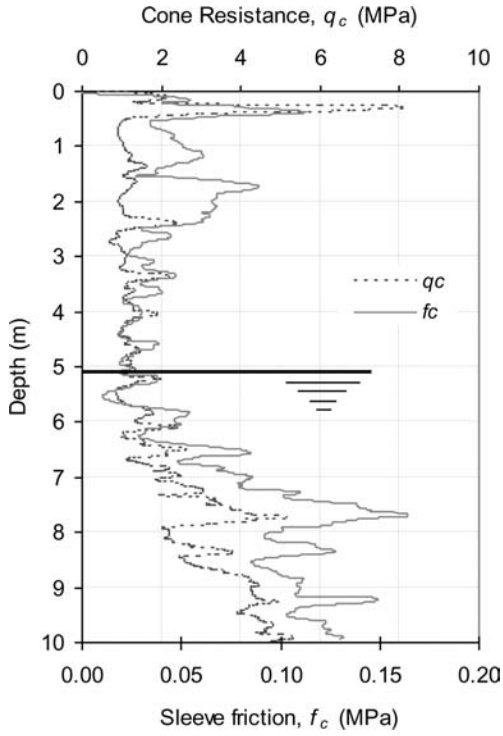

Figure 1. Results of field investigation from the CPT data.

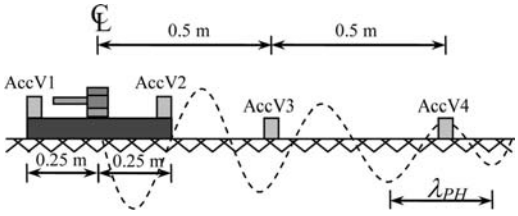

Figure 2. Experimental setup for WAK and SASW testing.

undrained shear strength (s_u) value of 100 kPa was estimated from CPT results. The CPT profile is illustrated in Figure 1.

In situ tests were done to determine the dynamic stiffness of the Auckland residual soils at the site using the WAK (wave-activated stiffness [K]) and spectral analysis of surface waves (SASW) methods. The dynamic tests were done by applying vertical impact loads to a circular steel plate of 50 cm diameter in a vertical direction with an instrumented hammer (Dytran model 5803A) equipped with a dynamic force transducer to record the impact load. Two vertical accelerometers (AccV1 & AccV2) were screwed on top of the circular steel plate as shown in Fig. 2.

The remaining two accelerometers, AccV3 and AccV4, were securely placed on the ground surface at 50 cm and 100 cm from the centre of the steel plate to measure the surface wave velocities for the SASW interpretation. By applying the experimental setup shown in Figure 2, the WAK and SASW tests were implemented one after the other. The dynamic stiffness of soil was obtained by considering the soil to be vibrating as a single degree of freedom (SDOF) system. The results of WAK and SASW tests performed to determine the shear wave velocity, V_s, and shear modulus, G_s, of the soils in the target sites were then calculated as shown in Table 1. CPT, SCPT and WAK tests were conducted at the intended pile locations.

Table 1. Average results for dynamic soil properties.

Test	Shear Modulus (G_s) MPa	Shear Wave Velocity V_s (m/s)
WAK	40	153
SASW	42	157
SCPT	41	155

* Note: $\rho_s = 17\ \text{kg/m}^3$; $G_s = \rho_s V_s^2$

Figure 3. Pile driving at Albany, Auckland.

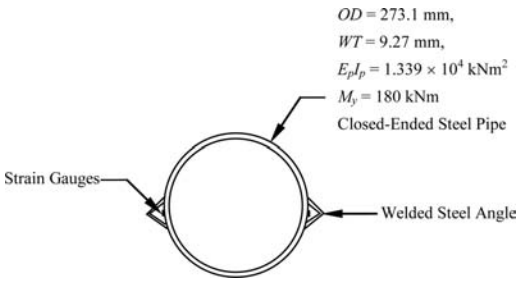

Figure 4. Details of pile properties.

2.2 *Pile details*

Four steel pipe piles (referred to as Piles 1–4) were driven closed-ended to a depth of 7.0 m using a 3000 kg drop hammer. The pile driving rig is shown in Figure 3. The piles have an outside diameter of 273 mm, wall thickness of 9.3 mm, and lengths of 7.5 m. The yield moment is approximately 180 kNm, allowing the piles to be loaded repeatedly to relatively large displacements without yielding. Further pile details are given in Figure 4.

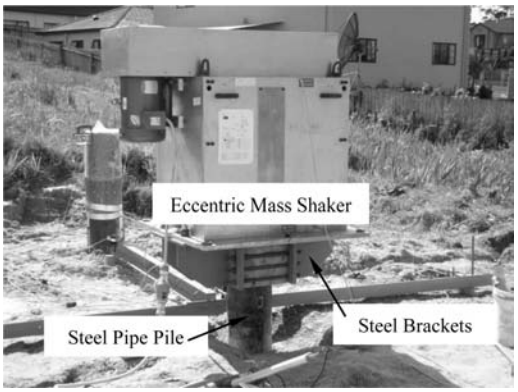

Figure 5. Experimental setup for single pile.

Piles 1 and 4 were instrumented with ten pairs of waterproof strain gauges along the length of the pile up to 7 m depth in order to measure flexural strains and moments during loading. Two of the strain gauges were located above the ground surface and were used to estimate the applied actions at the pile head. A steel angle was tack-welded to each side of the pile to protect the strain gauges and lead wires during driving. All piles were instrumented with 2 pairs of strain gauges attached at 0.4 m and 0.6 m above the ground. In this paper, only the results from Pile 3 are presented and discussed.

2.3 *Instrumentation and data acquisition*

A total of four accelerometers with a maximum range of ±10 g and two direct current displacement transducers (DCDTs) were used throughout the tests to measure accelerations and deflections at the pile head generated by the shaker. Two accelerometers were mounted on top of the shaker plate and the remaining two accelerometers were attached to the pile shaft to capture the mode of excitation.

Figure 5 shows custom-made steel brackets on which the eccentric mass shaker was mounted to provide harmonic lateral excitation at the pile head. The force amplitude was varied by changing the amount of masses in the shaking machine. The total above-ground mass was estimated to be approximately 600 kg, excluding any masses in the shaker. The centre of mass was estimated at 1.0 m above the ground surface. The forced-vibration tests were conducted after the wet winter season, so that the soil can be assumed to be saturated to the ground surface. Also, before the tests were started, a depth of 150 mm of top soil surrounding the pile was carefully removed by using a hand spade to provide a flat and clear surface for observing pile-soil gap opening.

All the response signals produced during the testing were simultaneously recorded using the NZNEES data acquisition system with a sampling rate of 200 readings per second. This system used LabVIEW 8.6 and is controlled using a laptop computer. All the test data was archived locally and uploaded onto the NZNEES data turbine server where it can be reviewed over the Kiwi Advanced Research & Education Network (KAREN). Additionally, video and numeric data were streamed back live to the NZNEES facilities via a satellite connection. Power to this recording system and to the eccentric mass shaker was provided by a 100 KVA (80 KW) diesel generator. From these vibration records, the frequency and the corresponding vibration amplitudes were calculated. Mathcad11® (PTC 2007) software was generally used for data presentation and the analysis of test data.

3 ELASTIC CONTINUUM MODEL (ECM) FOR PILE-SOIL SYSTEM

The elastic continuum solution for a point force in an elastic half space was obtained by Mindlin (1936). This was one of the starting points in the approach developed by Poulos (1971a, b) to investigate the response of a laterally loaded pile in an elastic soil. The Young's modulus, E_s, of the soil can be determined either by: (a) field test, (b) laboratory testing on undisturbed samples and (c) back calculation from pile load tests.

A first step in calculating the pile head displacements, assuming elastic behavior for both the pile shaft and the surrounding soil, is to find the groundline deflections, u_{gl}, and rotation, θ_{gl}, of the pile shaft:

$$u_{gl} = f_{uH}H + f_{uM}M \tag{1}$$

$$\theta_{gl} = f_{\theta H}H + f_{\theta M}M \tag{2}$$

where: H is the applied pile head horizontal load, M is the applied pile head moment, and f_{uH}, f_{uM}, $f_{\theta H}$, $f_{\theta M}$ are the flexibility coefficients of the pile shaft which are given as follows (Pender, 1993):

$$f_{uH} = \frac{1.3K^{-0.18}}{E_s D} \tag{3a}$$

$$f_{uM} = f_{\theta H} = \frac{2.2K^{-0.45}}{E_s D^2} \tag{3b}$$

$$f_{\theta M} = \frac{9.2K^{-0.73}}{E_s D^3} \tag{3c}$$

where: D = pile diameter, and K = ratio of Young's modulus of the pile to that of the soil, i.e. E_p/E_s.

Frequently, the actions are applied at some distance above the ground-line. By assuming the pile to be cantilevered from the ground-line to the point of application of applied actions, the lateral displacement (u_{pile}) and rotation (θ_{pile}) of the pile shaft at the point of application of the actions can be determined by adding cantilever displacements to the above ground-line displacements.

The components of the ground-line pile shaft stiffness are determined using the following equation:

$$\begin{pmatrix} K_{HH} & K_{HM} \\ K_{MH} & K_{MM} \end{pmatrix} = \frac{1}{\left(f_{uH}f_{\theta M} - f_{uM}^2\right)} \begin{pmatrix} f_{\theta M} & -f_{uM} \\ -f_{\theta H} & f_{uH} \end{pmatrix} \tag{4}$$

where: K_{HH}, K_{HH}, K_{HH}, K_{HH} are the components of the ground-line pile shaft stiffness matrix.

Then, the equivalent unrestrained pile shaft ground-line stiffnesses are obtained from:

$$K_h = \frac{K_{HH}K_{MM} - K_{HM}^2}{K_{MM} - eK_{HM}} \tag{5a}$$

$$K_\theta = \frac{K_{HH}K_{MM} - K_{HM}^2}{K_{HH} - K_{HM}/e} \tag{5b}$$

where: K_h is the unrestrained ground-line horizontal stiffness, K_θ is the unrestrained ground-line rotational stiffness of the pile shaft and e_1 gives the ratio of the ground-line moment to shear.

For the dynamic response, Wolf (1985) gives an equivalent SDOF model, which has three component stiffnesses: that of the extension of the pile shaft above the ground-line, and the ground-line horizontal and rotational stiffness of the pile shaft. The natural frequency of the equivalent SDOF (f_{SDOF}) model is determined as follows:

$$f_{SDOF} = \frac{f_s}{\left(1 + \frac{k_s}{K_h} + \frac{e_1^2 k_s}{K_\theta}\right)^{0.5}} \tag{6}$$

where: k_s is the stiffness of the projection of the pile shaft above the ground line ($=3E_pI_p/e_1^3$) and f_s is the natural frequency of the pile shaft mass system which is above the ground-line.

Further, there are a number of components damping values (for the structure, the horizontal and rotational deformation of the pile) and these are combined into a single equivalent value given as shown below (Pender, 1993):

$$\zeta = \frac{\zeta_s + \zeta_h \frac{k_s}{K_h} + \zeta_\theta \frac{k_s e_1^2}{K_h}}{1 + \frac{k_s}{K_h} + \frac{k_s e_1^2}{K_\theta}} \tag{7}$$

where: ζ is the damping value for the equivalent SDOF model, ζ_s is the damping for the structure, ζ_h is the damping for the horizontal motion of the foundation, and ζ_θ is the damping for the rotational motion of the foundation. The latter two of these damping values were estimated using the expressions given by Gazetas (1991). In this paper, the damping for the steel pipe pile and material damping for soil is taken as 5%.

4 DYNAMIC TESTING OF SINGLE PILE

4.1 *Free vibration tests*

Two free vibration tests were carried out on Pile 3 by simply giving the pile head mass a small displacement and then letting it vibrate freely. The pile head was also excited by a small tap by using an instrumented sledgehammer (Dytran model 5803A) before and after the forced vibration tests. In all cases, the operator attempted to apply a similar force for the tests.

Table 2. Measured and computed natural frequencies and damping ratios at low level excitation.

	Natural Frequency & Damping Ratio	
Approach	Series 1	Series 2
Elastic Continuum Model 1	13.9 (5.6%)	
Free Vibration – Initial	12.8 (4.4%)	10.7 (2.9%)
Zero-Mass Loading 1	11.0 (6.3%)	10.2 (4.9%)
	8-Mass Loading	1-Mass Loading
Zero-Mass Loading 2	8.2 (4.9%)	9.0 (3.7%)
Free Vibration – Final	8.1 (4.1%)	9.8 (1.9%)
Elastic Continuum Model 2	8.9 (6.3%)	

4.2 *Forced vibration tests*

An Anco Engineers MK-140-10-50 eccentric mass shaker was used to generate steady-state lateral forced excitation to the pile head. Two series of tests were performed for Pile 3. For Series 1, the maximum excitation was from 8-mass loading (256 kg of additional mass attached to the flywheels), over a frequency range of 0.5 Hz to 3.5 Hz. After three weeks of rest and some more rain, this was followed by Series 2 at 1-mass loading (32 kg) with frequency range from 0.5 Hz to 6 Hz. All the forced vibration tests were conducted with each frequency step lasting for 30 sec. The force amplitude was varied up to 40 kN at higher frequencies by changing the number of masses installed in the shaking machine.

A typical test sequence started by applying zero-mass force amplitude (without the addition of eccentric masses) by increasing the frequency up to the limit; usually well past the first natural frequency. Then the high amplitude excitation was applied. The test was completed by another zero-mass excitation.

5 RESULTS AND DISCUSSION

5.1 *Free vibration response*

The natural frequency and damping ratio of the pile-soil system determined from the free-vibration records are compared with the calculated values in Table 2. The average signals of three taps were employed in order to reduce the random noise which may be present during the tests. The damping ratio, ζ_{Free}, was computed from the time history of acceleration by using the logarithmic decrement method, as given in the following equation:

$$\zeta_{Free} = \frac{1}{2\pi} \ln \frac{a_j}{a_{j+1}} \tag{8}$$

where: a_j and a_{j+1} are the maximum amplitudes of vibration in two successive cycles.

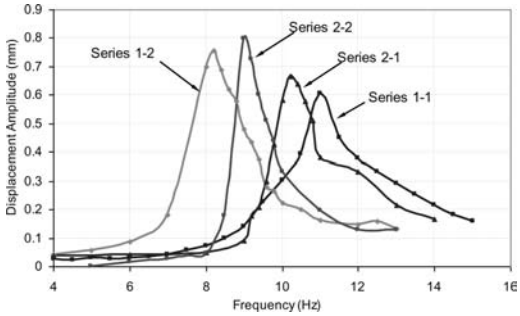

Figure 6. Single pile responses for low level excitation.

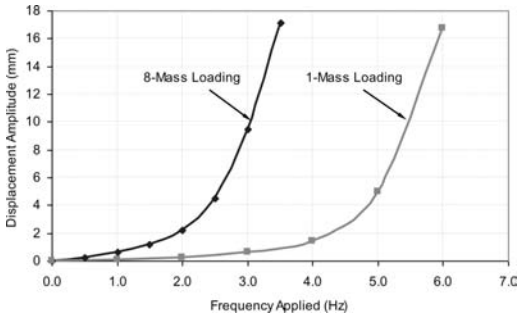

Figure 7. Single pile responses for high level excitation.

5.2 *Low level of forced vibration response*

The natural frequency and damping ratio determined for the single pile during low-level forced vibration are also tabulated in Table 2. The frequency response curve for displacement amplitudes plotted directly from the measured data is shown in Figure 6. From the figure, the natural frequencies of the pile are clearly identified and the damping ratios were calculated from the shape of the frequency response curve using the half-power bandwidth method. Also, the figure illustrates that, after the high level excitation, the natural frequency decreased because gaps had formed between the pile shaft and the surrounding soil.

5.3 *Natural frequency and damping ratio*

An ECM was initially used to predict the natural frequency of the pile-soil system. By assuming fully saturated soil conditions, a Poisson's ratio of 0.5 was used to determine the initial value of Young's modulus of the soil ($E_s = 3G_s$).

The natural frequency and damping ratio calculated using the ECM equations (6 and 7) are presented in Table 2. For ECM 1, the calculation of natural frequency and damping ratio was performed by assuming good contact between pile and surrounding soil (i.e. no pile-soil gap opening). After the high-level excitation the calculation of natural frequency and damping ratio for ECM 2 was done by allowing for a gap depth of 0.4 m. Therefore, the summation of the e_1 with the gap depth was used in determining the natural frequency and damping ratio for ECM 2. The gap depth of 0.4 m was taken from the maximum gap depth measured for Pile 3. In general, it can be seen that the computed natural frequency based on ECM was in good agreement with the natural frequency obtained from the free-vibration and low level of forced-vibration tests.

Figure 8. Gap opening after 8-mass loading.

Figure 9. Gap disappeared after three weeks of rest and rain.

Table 2 and Figure 6 summarize the natural frequencies and damping ratios for the single pile-soil system obtained from free vibration and low level (zero mass) forced vibration tests. The natural frequency of 11.0 Hz (Series 1–1) determined from the first low level of forced-vibration test decreased to 8.2 Hz (Series 1–2) after the higher level 8-mass force amplitude. Also, the reduction in the natural frequency from 10.8 Hz to 8.1 Hz was evident between the initial and final free vibration tests. The reduction in natural frequency is due to the opening of a gap of approximately 18 mm wide and 0.4 m deep at the pile-soil interface measured on the surface at the end of the test, as shown in Figure 8.

After three weeks of rest and some more rain, the gap had disappeared (Figure 9) and the natural frequency recorded for the next test (Series 2) was 10.2 Hz as shown in Table 2 and Figure 6.

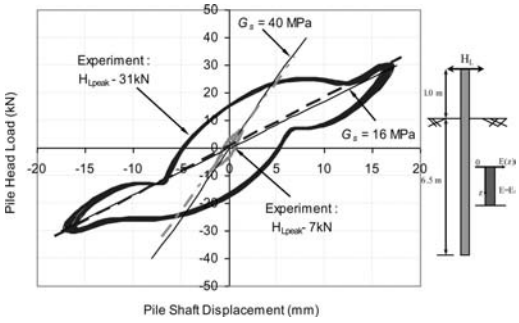

Figure 10. Dynamic pile head load-pile shaft displacement loop.

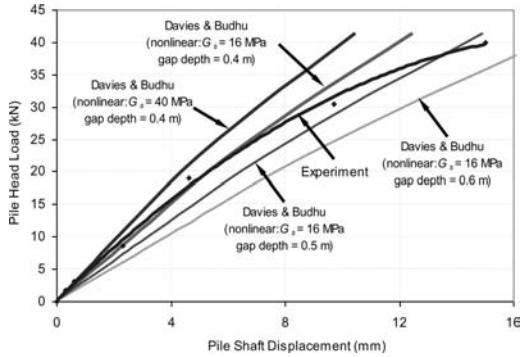

Figure 11. Dynamic pile head load-pile shaft displacement curve.

The pile was tested again with 1-mass loading to cover a wide range of frequency and the natural frequency recorded from the subsequent zero-mass loading was reduced to 9.0 Hz (Series 2–2). For Series 2, the high level of shaking applied not intense as Series 1, thus the decrease in natural frequency recorded was less. Both the initial and final free vibration tests show a decrement in the damping ratios from 4.40% to 4.10% and 2.9% to 1.9% for Series 1 and 2, respectively. The zero-mass loadings 1 and 2, also show a small decrease in the damping ratios.

5.4 *High level of forced vibration response*

Figure 7 illustrates the high level of forced vibration response for 1-mass loading and 8-mass loading, where the displacement amplitude was measured at 0.4 m below the pile head. Unfortunately, for these tests it was impossible to cover the full response curve as the shaking machine did not have sufficient power to provide the higher excitation forces at the large displacements involved. Once the cyclic displacement amplitude reached about 18 mm the controller command for higher frequency produced no change in the response. Thus Figure 7 gives only part of the rising branch of the response curve. It was also noted that at higher frequencies and force amplitudes the way the shaking machine was attached to the pile shaft allowed some rotational motion.

5.5 *Pile head response of high level of excitation*

Figure 10 illustrates the pile head response of high level of forced vibration tests (1-mass loading) at two force amplitudes. The calculated cyclic stiffness using the small strain stiffness of the soil is labelled '$G_s = 40$ MPa'. This is seen to model the cyclic stiffness of the pile when subject to cyclic force amplitude is 7 kN. A reduction factor of 0.4 applied to the small strain soil stiffness and a gap depth of 0.6 m were found to be necessary to arrive at the operational stiffness of the soil which describes the cyclic pile stiffness when the force amplitude is 31 kN.

Figure 10 shows that the hysteresis loops for the 31 kN force amplitude excitation has a "beak-end" shape. This is thought to be a consequence of the gapping between the pile shaft and the soil. When the pile reaches an extreme in one direction, there is a gap on one side between the pile and the soil (Figure 8 shows the residual gap at the ground surface once the shaking is completed). Then when the direction of motion is reversed the unsupported part of the pile shaft is lengthened by the depth of the gap.

This means that the lateral stiffness of the pile is reduced until the pile shaft comes into contact with the soil at the side of the gap at which point, there is an increase in stiffness of the pile and hence the bump along the hysteresis loop. Further along the loading curve a gap opens on the other side, so there is then another reduction in stiffness. Consequently, opening and closing of gaps during the cyclic loading leads to a quite complex shape for the hysteresis loops.

Figure 11 attempts to relate the decrease in stiffness to degradation in the soil stiffness adjacent to the pile shaft and increasing gap depth. The analyses are based on an extension of the ECM model proposed by Davies and Budhu (1986) which introduces nonlinear behaviour of the soil adjacent to the pile shaft. This is known to give reasonable modelling of nonlinear pile-soil lateral load response, M.Sa'don et al., (2009). In Figure 11 a number of load deformation curves are plotted with various initial stiffness's for the soil and gap depths. The diagram shows that the measured load deformation curve is more curved than the calculated using the Davies and Budhu method. This suggests that there is a progressive deepening of the pile-soil gap during the lateral loading.

6 CONCLUSIONS

This paper briefly described the initial stages of an experimental study on the behavior of full-scale single piles in Auckland residual clay subjected to dynamic lateral loading. Based on the results, the following conclusions were obtained.

- The ECM provided good estimation of natural frequencies and damping ratios when compared to

the low-level forced vibration and free vibrations results.

- After experiencing several cycles of higher force amplitude, a considerable strain softening of the load-deflection curve and a large pile-soil gap formation were observed.
- The gap almost disappeared after three weeks of rest and rain. This was evident from the frequency response recorded during the zero mass loading.
- The results of the full-scale tests suggest that the elastic continuum model has potential useful application to the laterally loaded pile design. First the elastic continuum model gives the correct small displacement lateral stiffness of the pile. If a model can be developed that gives the depth of gap formation, then the nonlinear lateral stiffness with gap formation should be obtainable. From there the challenge is to predict cyclic response.

ACKNOWLEDGEMENTS

The authors would like to express gratitude to the Kiwi Advanced Research & Education Network (KAREN) for providing funding for this project, the New Zealand Network for Earthquake Engineering Simulation, NZNEES@Auckland, for supplying the mobile laboratory equipment for the field testing, CDL Investments for permission to use the land for the tests, Perry Drilling for carrying out the CPT and SCPT testing, and the Ministry of Higher Education (MOHE) Malaysia and the Universiti Malaysia Sarawak (UNIMAS) for financial support for the doctoral studies of the first and last named authors.

REFERENCES

Briaud, J.-L., and Lepert, P. 1990. “WAK test to find spread footing stiffness.” *Journal of Geotechnical Engineering*, 116(3), 415–431.

Davies, T. G. and Budhu, M. 1986. “Non-linear analysis of laterally loaded piles in heavily overconsolidated clays.” *Geotechnique*, 36(4), 527–538.

EN 1998. *Eurocode 8 Design of Structures for Earthquake Resistance*. Comité Européen de Normalisation (CEN).

Gazetas, G. 1991. “Foundation Vibration.” *Foundation Engineering Handbook, Chap. 15*, 2nd Edition - Hsai-Yan Fang Eds, Van Nostrand Reinhold, New York, 553–593.

Mindlin R. D. 1936, “Force at a point in the interior of a semi-infinite solid.” *Physics 7*, 195–202.

M.Sa’don, N., Pender, M. J., Orense, R. P. and Abdul Karim, A. R. 2009. “A macro-element for pile head response to cyclic lateral loading.” *New Zealand Society for Earthquake Engineering Conference (NZSEE 2009)*, Christchurch, New Zealand, April 03–05.

Nazarian, S. and Stokoe, K. H. II. 1984. “In situ shear wave velocities from spectral analysis of surface waves.” *Proc. of the Eighth World Conference on Earthquake Engineering*, San Francisco, California, Vol. III, July 21–28, 31–38.

Parametric Technology Corporation 2007. *Mathcad 11*, Massachusetts.

Pender, M. J. 1993. “Aseismic pile foundation design analysis.” *Bulletin of New Zealand National Society for Earthquake Engineering*, 26(1), Wellington, New Zealand, 49–161.

Poulos, H. G. 1971a. “Behaviour of laterally loaded piles. I: Single piles.” *J. Soil Mech. Found. Div.*, ASCE, 97 (5), 711–731.

Poulos, H. G. 1971b. “Behaviour of laterally loaded piles. II: Pile groups.” *J. Soil Mech. Found. Div.*, ASCE, 97 (5), 733–751.

Wolf, J. P. 1985. *Dynamic soil-structure interaction*. Prentice Hall, Eaglewood Cliffs, N.J.

Soil-Foundation-Structure Interaction – Orense, Chouw & Pender (eds)
© 2010 Taylor & Francis Group, London, ISBN 978-0-415-60040-8

Kinematic response of batter pile foundation: Centrifuge tests

T. Tazoh
Institute of Technology, Shimizu Corporation, Japan

M. Sato
National Research Institute for Earth Science & Disaster Prevention, Japan

J. Jang & Y. Taji
Institute of Technology, Shimizu Corporation, Japan

G. Gazetas & I. Anastasopoulos
National Technical University of Athens, Greece

ABSTRACT: We carried out centrifuge tests to clarify the seismic behavior of batter-pile foundations. A vertical-pile foundation and a batter-pile foundation without the presence of a superstructure were installed parallel to each other in a soil container filled with dry sand, and were excited simultaneously. Through a comparison of the acceleration and displacement response of the footing, as well as the axial and bending strains of the piles for the two pile foundations, the kinematic response of the seismic behavior of the batter-pile foundation was experimentally investigated.

1 INTRODUCTION

The lateral stiffness of a pile foundation can be increased by adopting batter piles, which is why they are commonly used in landing piers that are subject to large lateral forces. However, batter piles are seldom used for buildings or civil engineering structures even in the case of large lateral forces. The reasons are as follows:

1) When soil settlement occurs, not only the safety of the pile foundation but also that of the structure as a whole system may be threatened by settlement-induced vertical loads acting on the batter piles.
2) During an earthquake, the piles in a batter-pile foundation may be subject to excessive axial compression and pullout forces, which are not generated in a vertical-pile foundation.
3) The strength of concrete piles is reduced by decreasing the compressive force acting on the piles due to rocking motions induced by the adopted batter piles.
4) Since infinite lateral ground planes cannot be assumed for batter piles, they cannot be expected to have the same horizontal subgrade reaction as that of vertical piles.
5) In urban areas, the use of batter piles is constrained by the boundary lines of adjacent land.

The 1995 Great Hanshin Earthquake in Japan has increased the demand for pile foundations with high seismic performance, as well as lower cost and easier construction. Batter piles can be used with little additional expense, no special design, and hardly any difficulty in construction. Therefore, the seismic behavior of batter piles has recently attracted much research interest, such as in research and development related to easy and accurate methods of installing batter piles (Gerolymos et. al. 2008, Giannakou et. al. 2007, Poulos 2006).

In this study, we carried out centrifuge shaking table tests to clarify the seismic behavior of batter-pile foundations. A vertical-pile foundation and a batter-pile foundation were installed parallel to each other in a soil container filled with dry sand, and were excited simultaneously (Tazoh et. al. 2005, 2007). As our objective was to investigate the fundamental characteristics of the seismic behavior of batter piles, none of the pile-foundation models had a superstructure. This study focused on the kinematic interaction of batter piles (Fan et. al. 1991, Mylonakis et. al. 1997, Mylonakis 2001, Nikolaou et. al. 2001, Sica et. al. 2007, Tazoh et. al. 1987). Through a comparison of the acceleration and displacement response of the footing, as well as the axial and bending strains of the piles for the two pile foundations, the kinematic nature of the seismic behavior of the batter-pile foundation was experimentally studied.

2 CENTRIFUGE TESTS

The most direct and effective way to quantitatively and qualitatively investigate the seismic behavior of batter piles is to compare the seismic behavior between

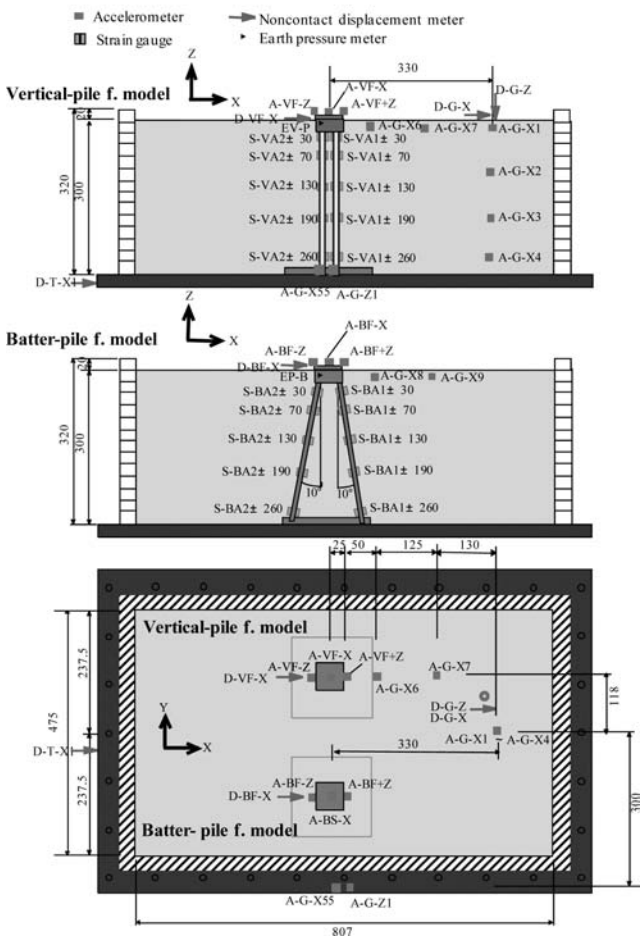

Figure 1. Longitudinal sections and plan of the 1/30-scale centrifuge model (scale unit: mm, for the prototype dimensions: multiply by 30. A vertical-pile foundation and a batter-pile foundation without the presence of a superstructure were set parallel to each other in a soil container which was filled with dry sand, and were excited simultaneously.).

a vertical-pile foundation and a batter-pile foundation under the same input motions. Each test for each model must be carried out under nearly identical conditions with respect to input motions, soil conditions, and soil behavior. Note, however, that it is impossible to achieve complete similarity between shaking table tests due to the difficulty of reproducing the input motion and nonlinear behavior of the soil.

Therefore, a vertical-pile foundation and a batter-pile foundation without the presence of a superstructure were installed parallel to each other in a soil container, as shown in Figure 1, and were excited simultaneously.

A laminar box was used as the soil container to allow shear deformation of the soil deposit as in the free field. Actually, installing two models that behave differently in a laminar box is not an appropriate testing method because the behavior of the models might influence each other. However, considering the inconsistency of the input motion and the difficulty of reproducing the soil conditions and nonlinearity, we believe that this method is more reasonable than individually testing the vertical-pile foundation and batter-pile foundation separately (Tazoh et. al. 2005, 2007).

The interior of the soil container is 805 mm in length, 474 mm in width, and 324 mm in height. All tests were conducted at centrifugal acceleration of 30 g on a 1/30-scale model. The vertical-pile foundation and the batter-pile foundation each have four piles, and the pile heads and pile tips are rigidly connected to the footing and the base of the soil container, respectively. The batter piles are identically inclined at a 10° angle. The soil deposit is a uniform layer consisting of dry silica sand No. 7 (Mean particle diameter $D_{50} = 0.15$ mm; Soil density $\rho_s = 2.635\,\mathrm{g/cm^3}$; Maximum dry density $\rho_{max} = 1.539\,\mathrm{g/cm^3}$; Minimum dry

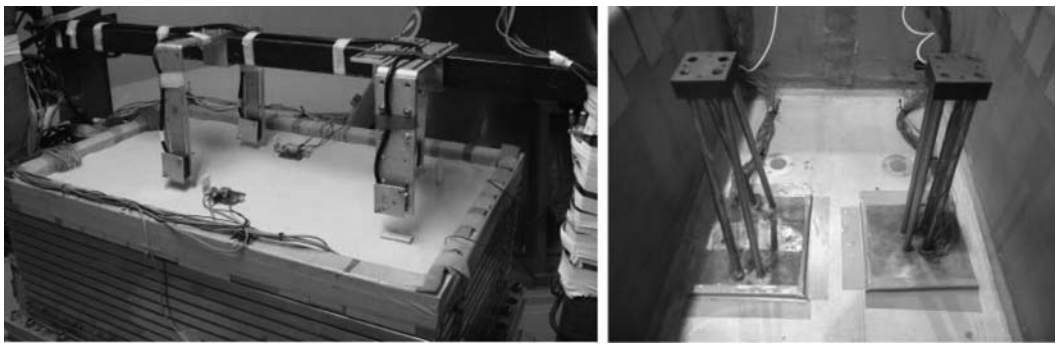

Figure 2. Testing Model (The pile foundations have four piles).

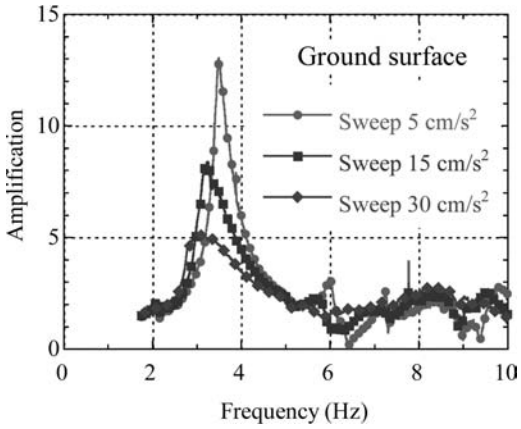

Figure 3. Frequency transfer function of the ground surface obtained from sweep test (5 cm/s^2, 15 cm/s^2, 30 cm/s^{2}l).

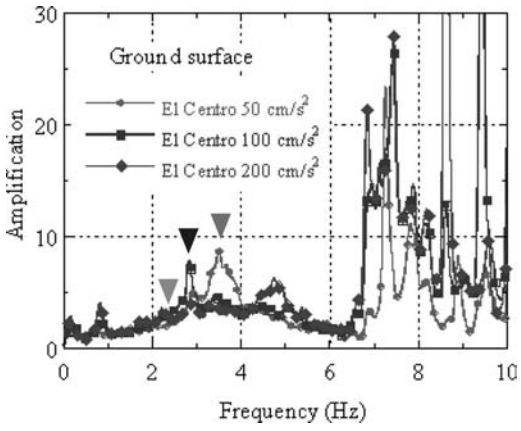

Figure 4. Frequency transfer function of the ground surface obtained from the El Centro record excitations (50 cm/s^2, 100 cm/s^2, 200 cm/s^2).

density $\rho_{\min} = 1.206\,\mathrm{g/cm^3}$). Thickness and relative density of the soil deposit is 300 mm (prototype: 9 m) and $D_r = 60\%$, respectively.

Figure 2 shows the test model. Sixty-two monitoring channels in total were installed, with the sensors

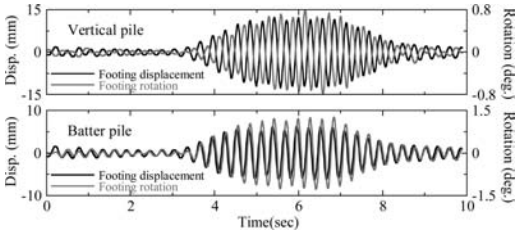

Figure 5. Comparisons of horizontal displacement and rotational angle of the footings between the vertical-pile foundation and the batter-pile foundation (Sinusoidal excitation: 3.5 Hz, 200 cm/s^2).

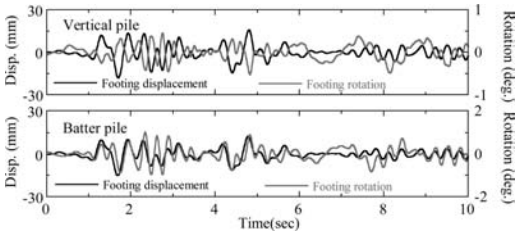

Figure 6. Comparisons of horizontal displacement and rotational angle of the footings between the vertical-pile foundation and the batter-pile foundation (El Centro record: 200 cm/s^2).

comprising seventeen accelerometers, five non-contact displacement meters, and forty strain gauges. The test was conducted a total of nine times, by varying the input motion and maximum acceleration.

While the purpose of this study was to clarify the kinematic interaction of the batter piles, consideration must also be given to the effects from the mass of the footing (made of steel, size: $3 \times 5 \times 5$ cm). The inertial interaction caused by the inertial force of the footing might be included in the results, which consequently may not represent the perfect kinematic interaction.

3 KINEMATIC NATURE OF SEISMIC BEHAVIOR OF BATTER PILE

Figure 3 shows the frequency transfer function calculated from the acceleration records between the soil

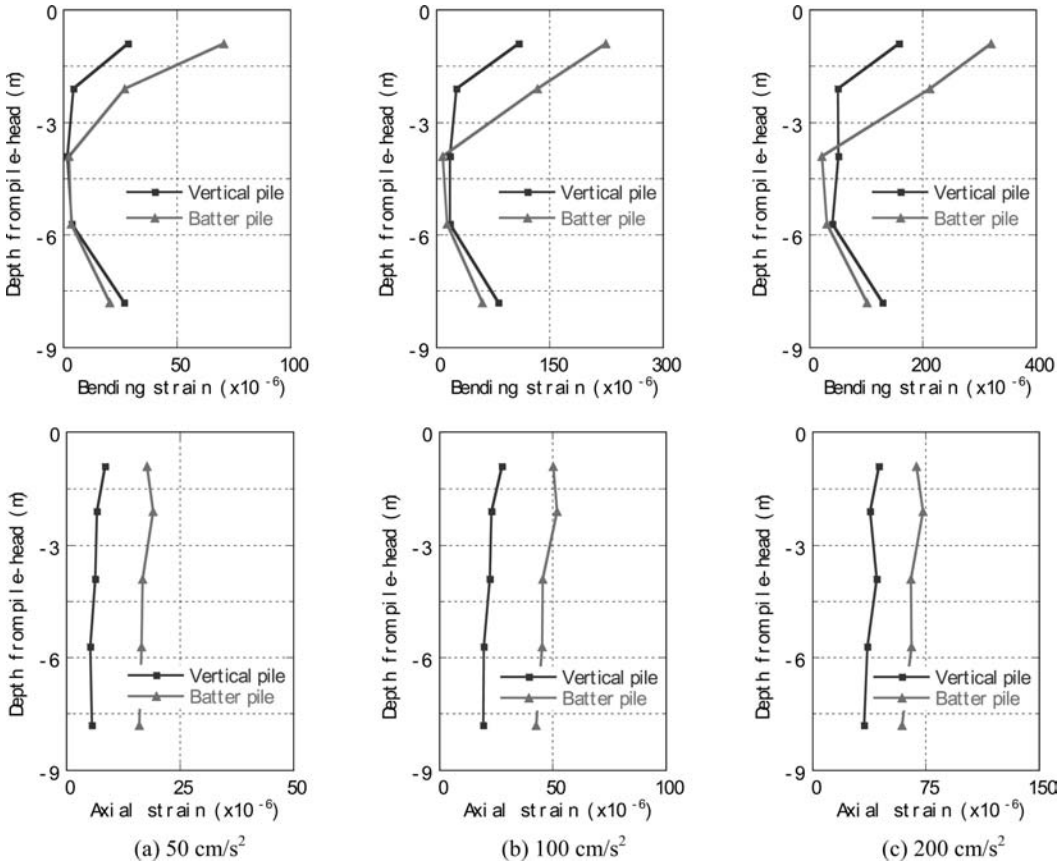

Figure 7. Bending and Axial strains distributions of the vertical-pile foundation (pile-VA1) and the batter-pile foundation (pile-BA1) obtained from El Centro record (50 cm/s^2, 100 cm/s^2, 200 cm/s^2).

surface and the input motion of the sweep test. The predominant frequency of the ground is 3.5 Hz in the case of maximum acceleration of input motion at 5 cm/s^2. The predominant frequencies are 3.2–3.3 Hz and 3.0–3.1 Hz, and also the peak acceleration amplification factors decrease corresponding to the increase in maximum acceleration of the input motion to 15 cm/s^2 and 30 cm/s^2.

Figure 4 shows the frequency transfer function between the ground surface and input motion obtained from El Centro record excitation. The predominant frequency of the ground is 3.4 Hz in the case of maximum acceleration of input motion at 50 cm/s^2. The predominant frequencies are 2.8–2.9 Hz and 2.4–2.5 Hz, and also the peak acceleration amplification factors decrease according to the increase in maximum acceleration of the input motion to 100 cm/s^2 and 200 cm/s^2. These phenomena were obviously produced by the nonlinearity of the soil.

Figure 5 shows the relationship between horizontal displacement and rotational angle of the footing based on the data from sinusoidal excitation of 3.5 Hz, in order to investigate the rotational characteristics of the footing of the vertical-pile foundation and the batter-pile foundation. The rotational angle is calculated by dividing the difference in the vertical displacement based on the data of the accelerometers installed at both sides of the footing by the distance between the two accelerometers.

The fact that there is no phase difference between the sway and the rocking motion indicates that the response of the footing to motion to the right is counterclockwise rotation. There is no phase difference between the sway and the rocking motion of the vertical-pile foundation; on the other hand, anti-phase behavior can be seen in the data for the batter-pile foundation.

Figure 6 shows the data obtained from El Centro record excitation at the maximum acceleration of 200 cm/s^2. The same trend as seen in the case of sinusoidal excitation can also be found in Figure 6. The phenomena of the opposite phase between the sway and the rocking motions of the vertical-pile foundation and the batter-pile foundation can be found in all of the other test data. From Figures 5 and 6, it can also be seen that the rotation angles of the batter-pile foundation are almost two times larger than those of the vertical-pile foundation.

Figure 7 shows the maximum-value distribution of the bending and axial strains of the piles in the

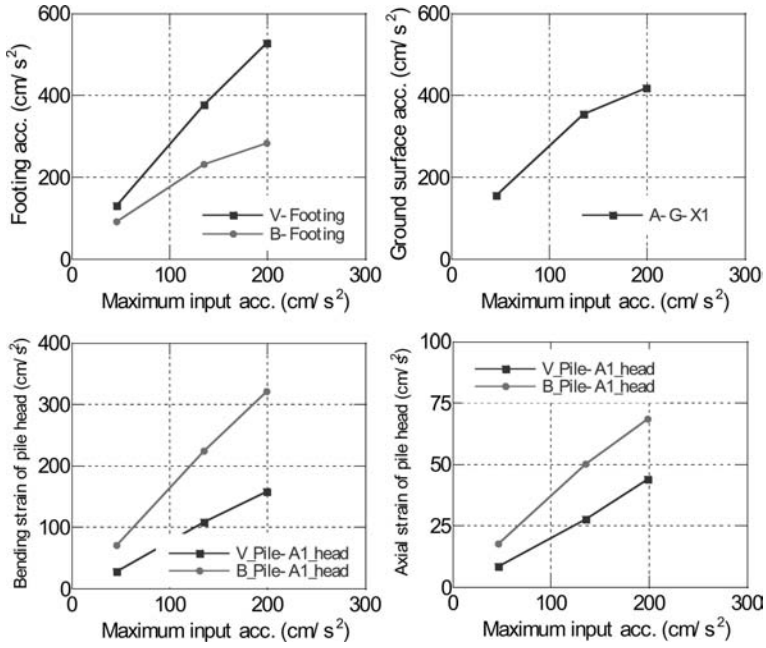

Figure 8. Maximum values of the accelerations of the footings and the ground surfaces, and the bending and axial strains at the pile-heads (El Centro record).

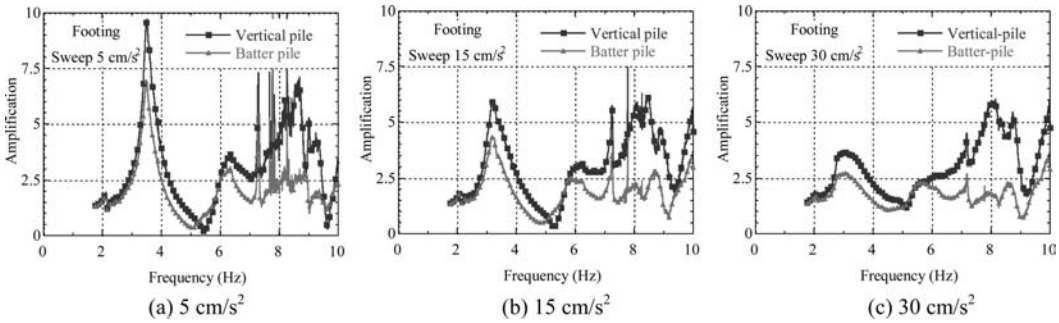

Figure 9. Aseismicity of the batter-pile foundation: Comparison of the frequency transfer function between the horizontal acceleration of the footing and input motion in the vertical-pile foundation and the batter-pile foundation obtained from sweep tests (5 cm/s^2, 15 cm/s^2, 30 cm/s^2).

vertical-pile foundation (pile-VA1) and the batter-pile foundation (pile-BA1) obtained from El Centro record excitation. The largest values were obtained at the pile heads, and the bending and axial strains of the batter-pile foundation are larger than those of the vertical-pile foundation in all cases.

Figure 8 shows the maximum values for acceleration of the footings and the ground surface, and the bending and axial strains at the pile heads corresponding to the increments in maximum acceleration of the input motion. From the figure, it can be seen that the maximum acceleration of the footing of the vertical-pile foundation is larger than that of the batter-pile foundation and that both the bending and axial pile strains of the batter-pile foundation are larger than those of the vertical-pile foundation.

4 ASEISMICITY OF BATTER PILE

Figures 9 and 10 compare the frequency transfer functions of the horizontal acceleration of the footing and input motion between the vertical-pile foundation and the batter-pile foundation obtained from sweep test and El Centro record excitation. The difference between the frequency transfer functions of the two pile foundations represents the aseismicity of the batter-pile foundation. From these figures, it can be elucidated that the batter-pile foundation has a certain level of aseismicity in all of the frequency ranges.

Figures 11 and 12 compare the frequency transfer functions of the bending and axial strains of the piles and input motion between the vertical-pile foundation and the batter-pile foundation calculated using

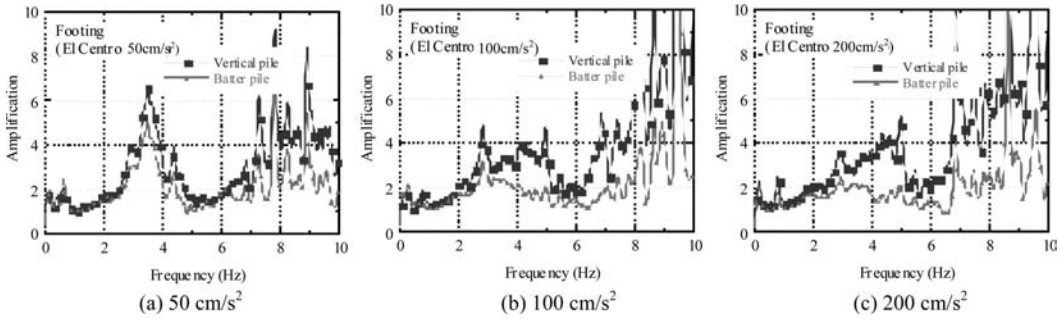

Figure 10. Aseismicity of the batter-pile foundation: Comparison of the frequency transfer function between the horizontal acceleration of the footing and input motion in the vertical-pile foundation and the batter-pile foundation obtained from El Centro record (50 cm/s^2, 100 cm/s^2, 200 cm/s^2).

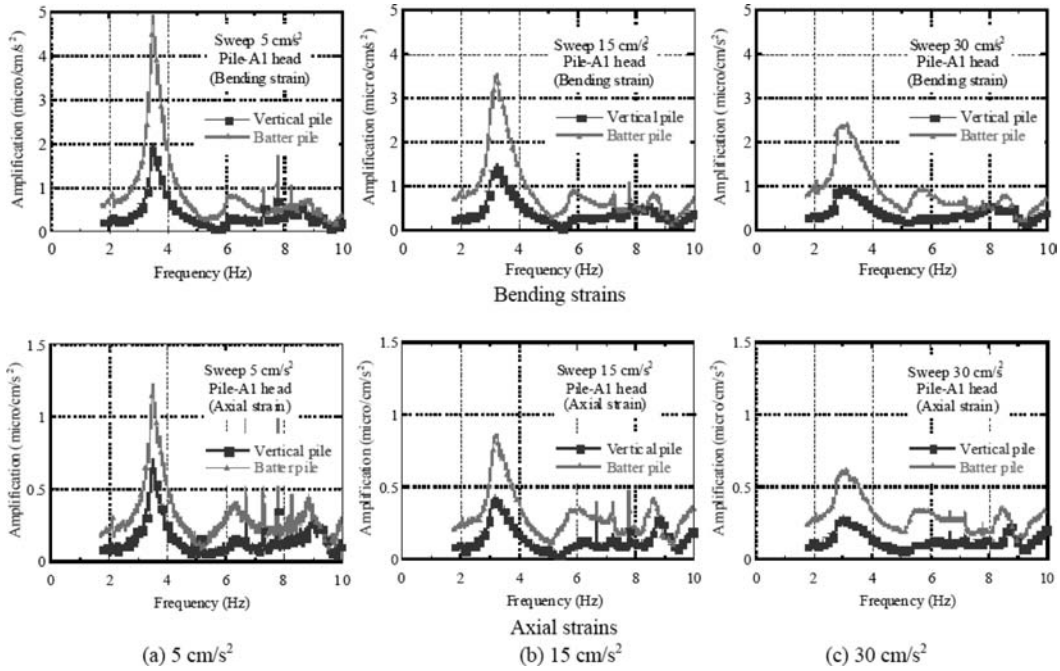

Figure 11. Comparisons of the frequency transfer functions of the bending and axial strains of the piles and input motion between the vertical-pile foundation and the batter-pile foundation (Sweep tests).

the data from the sweep test and El Centro record excitation. From these figures, it can be seen that the strain of the batter piles is larger than that of the vertical piles. Therefore, it is considered that the compensation for the aseismicity of batter piles seeks large cross-sectional efficiency for the batter piles.

5 CONCLUSIONS

The main conclusions of the study are as follows:

1) The response of the footing of the vertical-pile foundation to motion to the right is counterclockwise rotation. On the other hand, that of the batter-pile foundation is rotation in the opposite direction to that of the vertical-pile foundation.
2) Bending and axial strains attain the largest values at the pile heads in both the vertical-pile foundation and batter-pile foundation.
3) Improved aseismicity by adopting batter piles can be gained in almost all frequency ranges.
4) Bending and axial strains of the batter-pile foundation are larger than those of the vertical-pile foundation. In other words, the compensation for the aseismicity of batter piles seeks large cross-sectional efficiency for the batter piles.

ACKNOWLEDGEMENT

We would like to express our sincerest gratitude to Mr. Katsumi Yoshinari for his invaluable help to carry out the centrifuge tests.

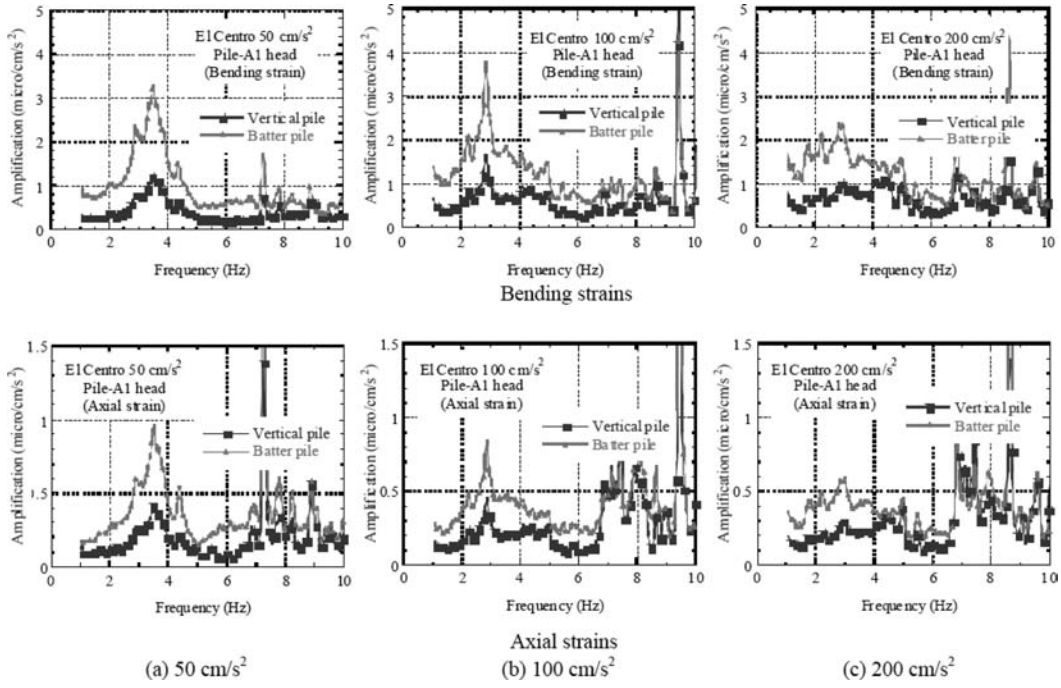

Figure 12. Comparisons of the frequency transfer functions of the bending and axial strains of the piles and input motion between the vertical-pile foundation and the batter-pile foundation.

REFERENCES

Fan, K., Gazetas, G., Kaynia, A., Kausel, E., & Ahmad, S. 1991. Kinematic seismic response of single piles and pile groups, *Journal of Geotechnical Engineering*, 117, 1860–1879.

Gerolymos, N., Giannakou, A., Anastasopoulos, I. & Gazetas, G. 2008. Evidence of beneficial role of inclined piles: observations and summary of numerical analyses, *Bulletin of Earthquake Engineering*: Vol. 6, No. 4, 705–722: Springer.

Giannakou, A., Gerolymos, N., & Gazetas, G. 2007. Kinematic response of groups with inclined piles, *Proceedings of the 4th International Conference on Earthquake and Geotechnical Engineering (ICEGE)*, Thessaloniki, Greece, on CD-Rom.

Mylonakis, G., Nikolau, S., & Gazetas, G. 1997. Soil-pile bridge seismic interaction: kinematic and inertial effects. Part I: Soft soil, *Earthquake Engineering and Structural Dynamics*, 26, 337–359.

Mylonakis, G. 2001. Simplified model for seismic pile bending at soil layer interfaces, *Soils and Foundations*, 41, 4, 47–58.

Nikolaou, S., Mylonakis, G., Gazetas, G., & Tazoh, T. 2001. Kinematic pile bending during earthquakes: analysis and field measurements, *Geotechnique*, 51, 5, 425–440.

Poulos, N. 2006. Raked piles—virtues and drawbacks, *Journal of Geotech Geoenviron Engineering*, 132(6), 795–803. Doi:10.1061/ (ASCE) 1090–0241(2006)132:6(795).

Sica, S., Mylonakis, G., & Simonelli, A. L., 2007. Kinematic bending of piles: Analysis vs. code provisions, *Proceedings of the 4th International Conference on Earthquake and Geotechnical Engineering (ICEGE)*, Thessaloniki, Greece, on CD-Rom.

Tazoh, T., Shimizu, K., & Wakahara, T. 1987. Seismic observations and analysis of grouped piles. *Geotechnical Special Publication No. 11, Dynamic Response of Pile Foundations, ASCE*, 1–20.

Tazoh, T., Sato, M., & Gazetas, G. 2005. Centrifuge tests on pile-foundation structure systems affected by liquefaction-induced flow due to quay-wall collapse, *Proceedings of the 1st Greece-Japan Workshop on Seismic Design, Observation and Retrofit of Foundations*, Athens, Greece, 79–106.

Tazoh, T., Sato, M., Jang, J., & Gazetas, G. 2007. Centrifuge tests on remedial measure using batter piles against liquefaction-induced soil flow after quay wall failure, *Proceedings of the 2nd Greece-Japan Workshop on Seismic Design, Observation and Retrofit of Foundations*, Tokyo, Japan, 431–439.

Soil-Foundation-Structure Interaction – Orense, Chouw & Pender (eds)
© 2010 Taylor & Francis Group, London, ISBN 978-0-415-60040-8

Performance of bridge systems with nonlinear soil-footing-structure interactions

L. Deng, B.L. Kutter & S. Kunnath
University of California, Davis, CA, USA

T.B. Algie
University of Auckland, New Zealand

ABSTRACT: The performance of ordinary highway bridges with rocking/ fixed-base footings and inelastic columns was investigated by centrifuge modeling tests and numerical simulations. This paper discusses the mechanism of controlling a nonlinear part of a bridge by changing the moment capacity ratio of the footing to the associated column. It briefly presents two series of tests modeling single-degree-of-freedom bridges and whole bridge systems. Some models were designed specifically so that rocking footings could be mobilized and the performance of these models was compared with the non-rocking models. Two-dimensional numerical models are built using finite elements and compared to the experimental results of the SDOF models. The footings are simulated by 2-D beam-on-nonlinear-Winkler-foundation (BNWF) approach. The nonlinear behavior of columns was simulated by an elastic beam with a pre-determined plastic hinge. Numerical modeling is shown to be able to capture the crucial characteristics of a rocking footing.

1 INTRODUCTION

Soil-structure interaction has been the focus of researchers for the past decades. Crucial characteristics of a rocking footing (i.e., rocking moment capacity, stiffness, cyclic backbones) under various foundations and loading conditions have been experimentally or mathematically quantified to enable the full application of the rocking foundation concept (e.g., Gajan & Kutter 2008). Despite this fact, regarding ordinary bridges with potential rocking footings, the interaction between the nonlinear rocking footing and the nonlinearly flexible column bent is still not well understood. The adoption of rocking footings has not been widely accepted by engineering practioners.

This paper presents two centrifuge test series (named LJD01 and LJD02 by convention) performed at the University of California, Davis. The first series tested isolated single-degree-of-freedom bridge models considering nonlinear footings and nonlinear flexible columns with an intentional plastic hinge at the bottom. The second series tested two footing-column-deck-abutment bridge systems. Brief results from the two experiments are presented in this paper.

Numerical models in OpenSEES (Open System for Earthquake Engineering Simulation) were built to calibrate the behaviors of these physical models. Preliminary results from the first series LJD01 were calibrated. The models integrated beam-on-nonlinear-Winkler-foundation (BNWF) concepts to model the rocking mechanism and included elastic columns with plastic hinges.

It is worth defining the rocking moment capacity of a footing:

$$M_{c\_foot} = \frac{V \cdot L_f}{2} \cdot \left(1 - \frac{A_c}{A}\right) \quad (1)$$

where $V =$ vertical load on footing; $L_f =$ footing length in shaking direction; $A =$ footing base area; and $A_c =$ the critical contact area required to support the vertical load. The ratio of A_c to A is typically much less than 1. So the rocking moment capacity is approximately equal to $V^*L_f/2$ and is insensitive to the ratio A_c/A.

2 MODEL TESTS

Two model test series were performed on the centrifuge facility of UC Davis. Bridge models fabricated out of steel and aluminum were prototyped from two real reinforced concrete bridges (one with a single-column bent and the other with a two-column bent) in Central and Southern California. Both bridges are in zones of medium-to-strong seismicity. The two series involved many spins and tens of shaking events to the bridge models. Both tests were built upon uniform Nevada sand with varying relative density. Table 1 summarizes the information of each spin, including structure model names and types, soil conditions, and event types.

2.1 *Model design details*

Crucial properties of the prototype bridges (e.g., deck mass, column stiffness and height, and bending

Table 1. Summary of test conditions and chronology.

Tests	Model name	Structure type	Footing length (m)[1]	Dr. [2]	Events
LJD01_04	SC	shear wall	6.70	0.44	cyclic
LJD01_08	SD-2	SDOF	6.70	0.73	Dynamic
	MD-2	SDOF	9.76	0.73	Dynamic
LJD02	SD	3-D	5.04	0.77	Dynamic
	LD	3-D	7.56	0.77	Dynamic

Note: 1. The footing length in the shaking direction is presented in prototype scale; 2. Dr = the relative density of the sand.

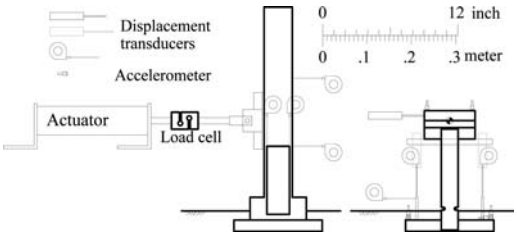

Figure 1. Models in LJD01: (L) a rigid shear wall for slow cyclic tests; (R) a lollipop SDOF model with a nonlinearly flexible column for dynamic tests.

moment capacity of columns) were carefully matched in the model design. The column stiffness of the models, except the rigid shear wall model as shown in Figure 1, were designed to match the prototype stiffness in terms of conventional $3*E*I/L^3$ according to the scaling law of centrifuge modeling as the metal model columns were selected and manufactured with special stiffness. Model columns made with aluminum tubes were designed to be nonlinear at the plastic hinge section. The columns were notched through at the bottom adjacent to the footings to control the ultimate strength, i.e., the bending moment capacity, of the columns.

Two types of loading mechanisms were adopted in LJD01. Slow cyclic tests on rigid shear walls (loaded by a displacement-control actuator) were performed to seek the moment vs. rotation characteristics of the rocking footings on various sand conditions; while dynamic tests were designed to explore the interaction between nonlinear columns and rocking/elastic footings. Figure 1 shows the setup of slow cyclic and dynamic shaking tests.

Two models (SD and LD as in Table 1) were built to be identical except for their footing dimensions. The model LD was designed according to conventional procedure which utilizes columns as the main nonlinear part of a bridge system, and the footing with larger rocking moment capacity was supposed to remain essentially elastic during dynamic events. The other model SD was designed with smaller footings which had a rocking moment capacity that was less than the bending moment capacity of the column; therefore the footing would rock before the column yielded.

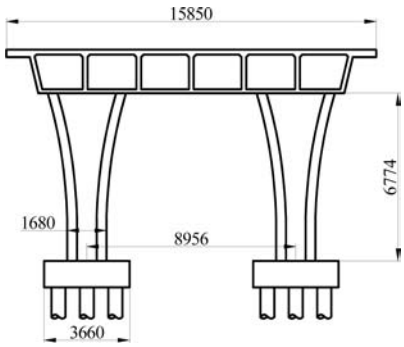

Figure 2. Elevation view of the prototype bridge in LJD02 (unit: mm).

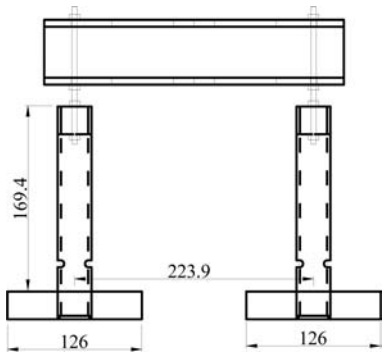

Figure 3. Elevation view of model SD in LJD02 (unit: mm).

Figure 2 shows the prototype two-column-bent bridge with pile foundations. The model bridge deck rested on seat-type abutments. Figure 3 displays the elevation view of the model SD, wherein notches could be seen to simulate potential plastic hinges close to the footings. While normal prototype connections are fixed, it is notable in Figure 3 that the columns were pinned to the deck. Probably not matching the prototype connection, the model pin is to protect the column from damages in the head. If the column head were fixed, plastic hinges would still develop in the column, even if the footing is allowed to rock. The 3-D setup of the models in LJD02 is show in Figure 4. The shaking was input in N-S direction.

2.2 *Natural period of bridges*

The assembled SDOF models in the LJD01 test were fixed to a heavy table at the base, struck at the deck mass, and the free vibration history of the deck was recorded. From the free vibration graph in Figure 5, the prototype scale period of the fixed-base bridge model was 1.19 sec. The damping ratio, ξ, of the model was 0.4% assessed using Equation (2).

$$\xi = \ln\left(\frac{u_1}{u_{k+1}}\right) \Big/ \left(2 \cdot \pi \cdot k\right) \tag{2}$$

where u = amplitude of the displacement; and k = number of cycles counted for degradation. The

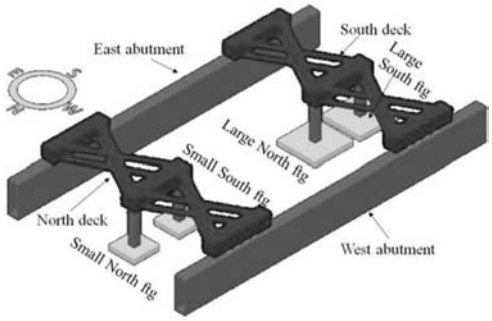

Figure 4. 3-D setup of bridge models in LJD02.

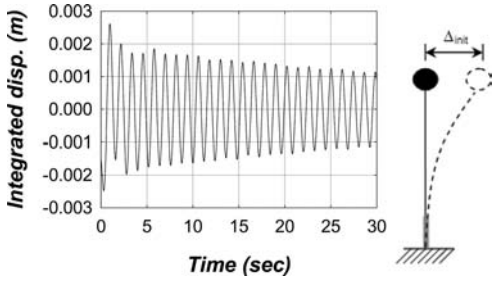

Figure 5. Integrated displacement in the free vibration test.

finite element model with fixed support shows a period of 1.21 sec, consistent with the measured period; this fact is encouraging for subsequent simulations.)

3 EXPERIMENT RESULTS

Selected results from the past two centrifuge tests are presented in this section. Note that all results presented in this paper have been converted to prototype scale using the conventional centrifuge scaling laws with a scale factor of 49 for LJD01 and 40 for LJD02 test.

3.1 *Slow cyclic tests*

Rocking moment vs. rotation curve of the footing in LJD01_04 slow cyclic tests are presented in Figure 6. The moment was calculated by the load cell force multiplied by the distance from horizontal loading point to the footing bottom. The upper and lower straight lines depict the theoretical rocking moment capacity of the footing.

The actual capacity is a bit smaller than the theoretical value, maybe due to the contribution of P-Δ effect. The banana-shape curve is very typical; several other cyclic tests display the same pattern. The initial rocking stiffness of the footing, shown as the sloping line in Figure 6, is approximately 2.1E6 kN*m/rad. FEMA 2000 provides a set of equations to describe the rocking and translation behavior spread footings. The rocking stiffness is defined in Equation (3).

$$K_{rock} = \frac{G_0 \cdot B_f^{\,3}}{1-\nu} \cdot \left[0.4 \cdot \left(\frac{L_f}{B_f} \right) + 0.1 \right] \cdot \beta_{rock} \qquad (3)$$

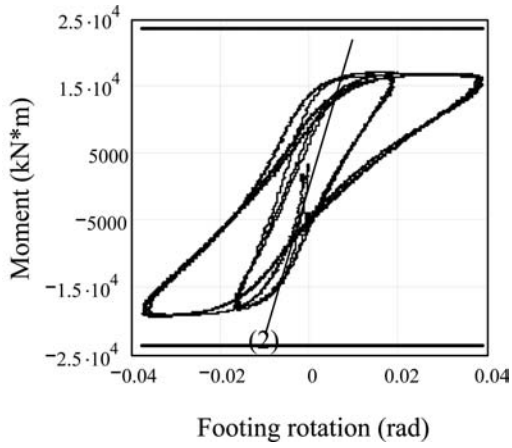

Figure 6. Moment vs. rotation for SC model in LJD01_04.

where,

$$B_{rock} = 1 + 1.4 \cdot \left(\frac{d}{L_f} \right)^{0.6} \cdot \left[1.5 + 3.7 \cdot \left(\frac{d}{L_f} \right)^{1.9} \cdot \left(\frac{d}{D} \right)^{-0.6} \right] \qquad (4)$$

where d = footing thickness, D = footing embedment depth, L_f and B_f = the footing dimensions, and G_0 = representative shear modulus of the soil under the footing, and ν = Poisson's ratio. Equation (5) (Hardin 1978) is used to calculate the shear modulus and Equation (6) (Perkins & Madson 2000) is to calculate the representative mean confining stress.

$$G_0 = \frac{625 \cdot \sqrt{100kPa \cdot \sigma_m}}{0.3 + 0.7 \cdot e^2} \qquad (5)$$

$$\sigma_m = \left(0.52 - 0.04 \cdot \frac{L_f}{B_f} \right) \cdot \frac{\sigma_v}{6} \qquad (6)$$

where e = the void ratio of the soil, σ_m = the mean confining stress of the soil underneath the footing, σ_v = the vertical stress of the soil.

The calculated initial K_{rock} is 1.13E7 kN*m/rad which is 530% of the experimental stiffness, which means either Equation (3) or (5) is overestimated. Reduced stiffness parameters will be used in the numerical models described in subsequent sections.

Figure 7 shows the footing settlement vs. rotation curve. Some features can be obtained from the curves in Figures 6 and 7. First, the definition of the rocking moment capacity of a footing is verified by the slow cyclic tests. Most of the experiments observed the maximum acting moment on the footing that was enveloped by the rocking moment capacity. Second, big loops of the non-degrading moment vs. rotation curves indicate that rocking provides a good mechanism for energy absorption. Thirdly, footing settlement due to rocking can be significant as in this case. In this experiment, the prototype settlement was about 7.5 cm after 6 cycles. The vertical bearing capacity factor of safety for this was about 9.6 leading to significant soil yielding and compression.

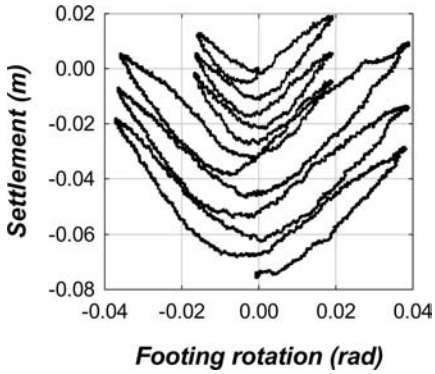

Figure 7. Settlement vs. rotation correlations for the SC model in LJD01_04.

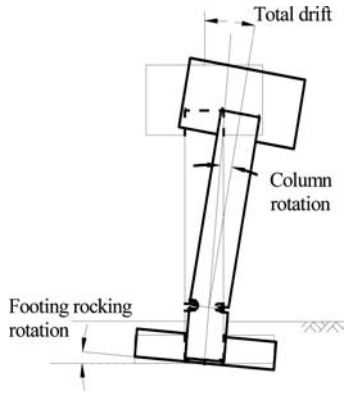

Figure 8. Illustration of footing rocking and column rotation.

3.2 *Dynamic tests on SDOF models*

This section presents the brief results of the dynamic shaking tests on SD-2 and MD-2 in LJD01_08 subject to an input motion recorded in 1971 San Fernando earthquake which has 0.62 g PGA and a predominant period of 0.39 sec. The diagram in Figure 8 shows the concept of a rocking foundation with nonlinear plastic columns and labels rotations of different parts of the SDOF models. Note that the column rotation hereafter is the rotation relative to the footing.

The bending moment vs. rotation curves for the columns on the two models in LJD01_08 test are shown in Figure 9. The maximum column rotations on the two footings were 2.7% and 7.8%, respectively. The ductility ($\mu = \Delta u/\Delta u_y$) demand on the column with small footing was less than 4.0, but the demand increased dramatically to about 11 for the columns on large footings. If rocking does not occur, the structure relies on the plastic columns to absorb energy; the ductility demand for the columns on small footings is significantly less. Permanent rotations of columns with small and medium footings were 1.7% and 7.2% respectively. The P-Δ effects tended to accumulate plastic and irreversible deformation in the columns.

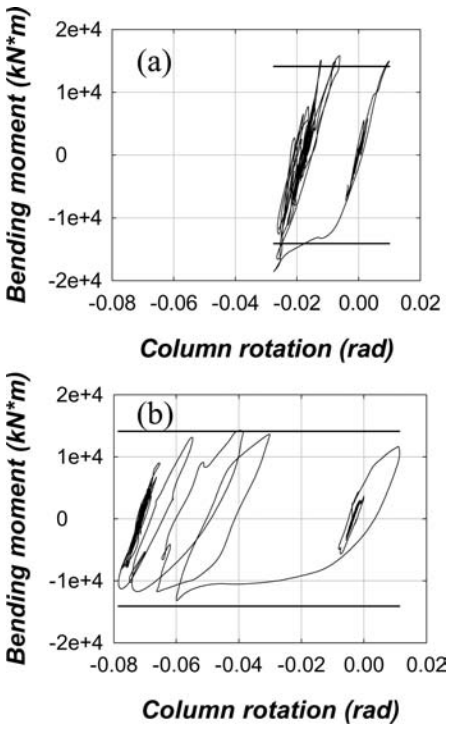

Figure 9. Bending moment at the plastic hinge position vs. rotation of the column tip of the models (a) SD-2 and (b) MD-2 in LJD01_08.

It is also true for a prototype concrete SDOF column. When a plastic hinge forms in an actual column, cover concrete crushes and spalls off, making the column longitudinal reinforcing bars susceptible to buckling.

Figure 10 shows the time histories of total deck drift, column rotation and footing rocking rotation for the SD-2 and MD-2 model in LJD01_08 experiment. Note that each vertical grid represents 0.04 rad. The rocking rotation of the small footing reached up to 2%, but the medium footing reached only up to 0.5% which is almost negligible. It is obvious that, as the soil beneath the footing yielded back and forth, the rocking hysteresis of the small footing was able to consume much more seismic energy than the medium footing. Another finding is that rocking footings tend to re-center themselves. The mechanism is simply due to the gap formation, which tends to pull the footing back to the opposite direction, when the footing rocks to one side. Soil beneath the footing may yield as the footing rocks but can still regain the strength after many cycles to bring the footing back to the initial level. In this dynamic test, permanent rotation of the small footing was 0.8%, meaning it almost re-centered itself to the initial position.

3.3 *Test results from LJD02*

Figure 11 plots the correlations between the rocking moment and rotation of small (rocking) and large

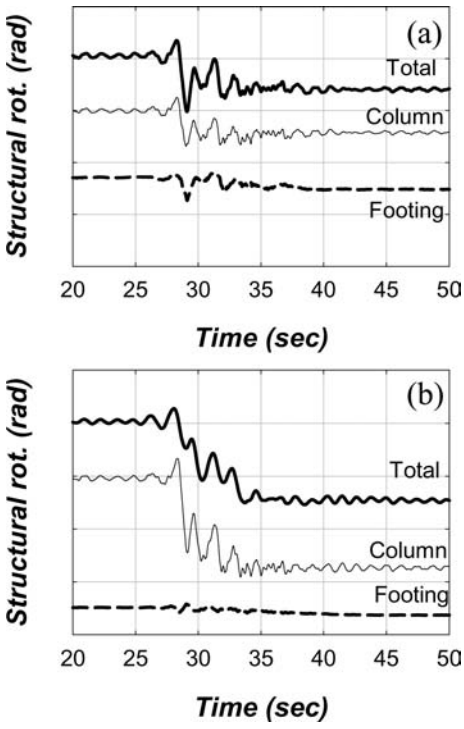

Figure 10. Time histories of total deck drift, column rotation and footing rotation for (a) SD-2 and (b) MD-2 in LJD01_08.

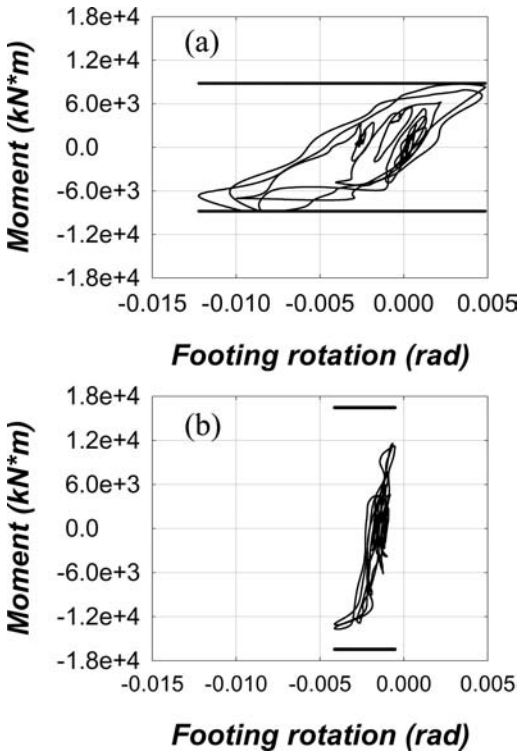

Figure 11. Moment vs. rotation curves of footings in the models: (a) SD (b) LD.

(elastic) footings subject to an input motion recorded in 1976 Gazli (Uzbekistan) earthquake, which has 0.62 g PGA and a predominant period of 0.67 sec. Notice that residual rotation of the footings due to previous shakes are indicated in Figure 11. The theoretical rocking moment capacities of the footings defined in Equation (1) are also plotted in the figure for comparison.

The small rocking footing displayed banana-shaped moment-rotation correlation. The moment capacity of the footing did not show any degradation even after at least two full cycles. The large hysteretic loops dissipated a great amount of kinematic energy. The maximum moment that the footings could take did not overpass the theoretical rocking capacity, confirming the validity of the moment capacity equation. The peak rotation of the small footing was 1.25% while the permanent rotation was 0.34%. The double-column frame could also help to prevent the deck from accumulating permanent rotation. The foundation started to yield when the rotation was larger than approximately 0.002 rad.

Figure 12 delineates the bending moment on the column at the plastic hinge location vs. the rotation of the columns relative to the footings. The moment vs. rotation curve of the notched column subjected to laterally static loading is also shown in Figure 12 as dash-dot lines for comparing the shapes. It is

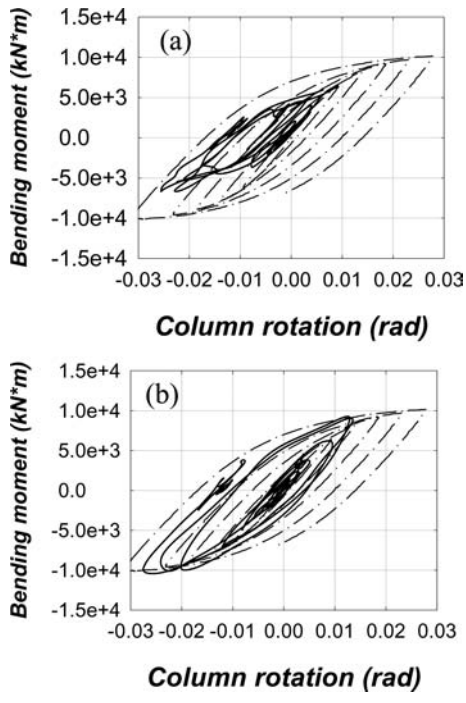

Figure 12. Moment vs. rotation curves of columns of model (a) SD; (b) LD.

observed that dynamic loops matched the static loading loops accurately. The peak rotation of the column with the large footing was 2.75% while its permanent rotation was 1.3%. The large hysteretic loops of the column absorbed most of the earthquake energy, which is expected to occur when an elastic foundation is designed. The peak rotation of the column with the small footing was 2.55% and the permanent rotation was 1.1%. Adoption of small rocking footings could reduce the ductility demand of the columns as well as reduce the permanent drift of columns.

4 NUMERICAL MODELING

In this study, foundations were simulated by a series of decoupled nonlinear spring models. Following the provision of FEMA 2000, the footing base is divided into the end and central zones with end-zones (B_f/6 width) springs mainly providing rocking stiffness while the central zone (L_f–B_f/3 wide) providing mainly vertical loading stiffness.

The BNWF approach is capable to model the shallow foundation response in lieu of more rigorous analysis; however, the accuracy of the model is highly dependent of the spring parameters obtained from soil stiffness and strength. For instance, Harden & Hutchinson (2009) provided a recipe for parameter selections based on the calibration modeling of prior centrifuge and large-scale shallow foundation tests. There is no universal parameter set useful for all cases. This section will describe the attributes of the numerical model determined by the calibration using results of the static loading tests in LJD01.

4.1 *Attributes of footing springs*

The zoned footing base is shown in Figure 13. Generally the unit length stiffness of individual springs is defined in Equation (7) following FEMA 2000.

$$k_{end} = \frac{6.83 \cdot G_0}{1-\nu} \qquad k_{mid} = \frac{0.73 \cdot G_0}{1-\nu} \tag{7}$$

The stiffness per unit length multiplying the length assigned to each spring yields the stiffness of the spring in the dimension of force/length.

$$K_{end} = k_{end} \cdot \Delta L \qquad K_{mid} = k_{mid} \cdot \Delta L \tag{8}$$

Clearly, the accuracy of spring stiffness, K_{end} and K_{mid}, is linearly affected by the shear modulus of the soil underneath the footing and the tributary length of each spring.

"QzSimple1" springs available in OpenSEES (Boulanger 2000), were used to model gapping and yielding behavior of the soil. As the spring is unloaded to zero strength, a gap will form and continue to grow with assigned tensile strength (usually very small); when the spring is loaded back again, it will not gain significant stiffness until the gap closure has be fully

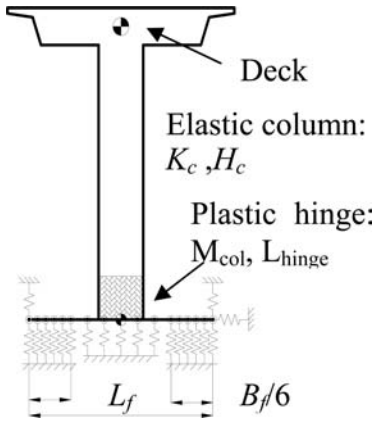

Figure 13. Springs configuration and numerical model.

reached. Input attributes to QzSimple1 springs include Q_{ult} (the ultimate strength in the dimension of force), tensile strength ratio, z50 (the displacement associated with mobilization of 50% of the ultimate strength), and viscous damping on the far-field (elastic) component of the displacement rate (velocity). More details about this spring model can be found in Harden & Hutchinson (2009).

The backbone responses of the foundation in terms of rocking and vertical loading are sensitive to the initial stiffness of the QzSimple1 springs. As mentioned in the prior section, the stiffness parameters overestimated the initial stiffness obtained from experiments. Therefore it is reasonable to apply a reduction factor to each spring stiffness (or strength) in order to capture the backbone footing stiffness as well as the experimental curves. For the static loading test, a uniform reduction factor of 20% was applied to the theoretical values listed in Equations 7–8.

The conventional equation of the limit bearing pressure for spread footings (such as Salgado 2008) was adopted to estimate the ultimate capacity of QzSimple1 springs. The capacity of each spring (in the dimension of the force) is the product of limit bearing pressure and the area represented by individual springs.

4.2 *Modeling of pier columns*

The single-column bent in the numerical model uses the experimental column material (aluminum). The stiffness of 6063 Al material is 68.9 GPa, and the yielding strength is 230 MPa with strain hardening ratio of 0.005, observed from the lateral loading tests on the columns.

The mathematical column adopts the Steel02 material which is good at predicting hysteretic behavior of metals with isotropic strain hardening. As illustrated in Figure 13, the column was simulated by simply a beamWithHinges element (Scott & Fenves 2006). This element divides the column into three parts: hinges at the both/ either ends and a linear-elastic region in the

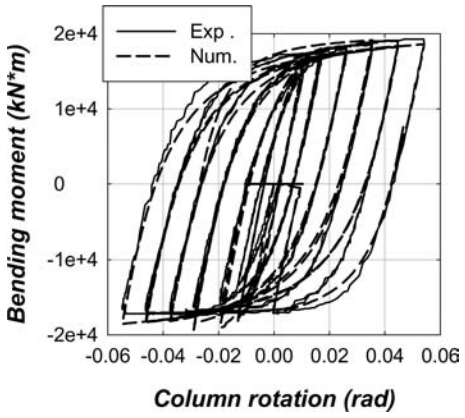

Figure 14. Bending moment at plastic hinge location vs. column rotation.

middle of the element. It considers plasticity to be concentrated in the customary hinge section. The length of the whole column element is 10.88 m which is from the footing to the center gravity of the model bridge deck. The length of the plastic hinge at bottom end of the column is 1.25 m. The column was connected to the deck lumped mass monolithically, and no hinge was assigned. Fixed at the base, the mathematical cantilever beam was subject to lateral loads monotonically or cyclically at the top node to calibrate material properties and compute the moment vs. curvature relationship of the mathematical column section at the localized hinge position. The algorithm of numerical loading exactly mimicked the experimental loading tests.

The hysteretic loops of the bending moment at the bottom hinge location vs. column rotation are plotted in Figure 14. Column rotation is simply the lateral drift of the column tip divided by the column length. The two curves agreed with each other very well. It shows that the column has an unlimited curvature, being able to deform to an extremely large ductility. The columns designed today can sustain ductility in the range of 6 to 10. Even with ductility 10, the column would probably not collapse as it can support the gravity loads. Hence the numeric column model with extremely large ductility should be appropriate for this study.

5 RESULTS OF SIMULATIONS

5.1 *Effects of rocking footings on structural period*

Mylonakis & Gazetas (2000) were concerned with the elongated fundamental period of a structure (especially a bridge) due to soil-structure interaction. The elongation may have a detrimental effect on the imposed seismic demand in a specific site and earthquake conditions, when long period contents dominate the seismic motion.

Eigenvalues of the global stiffness matrix were obtained to determine the first-mode natural period

Table 2. Periods of numerical SDOF models.

Footing conditions	Fixed-base	Medium footing	Small footing
T (sec)	1.21	1.61	2.14

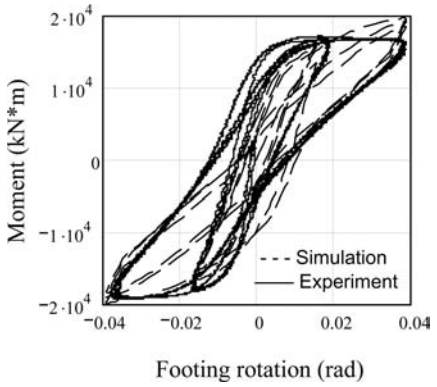

Figure 15. Moment vs. rotation curves of small-footing model.

of the SDOF numerical model. Listed in Table 2, the periods of some models in this research were evaluated after the composite models were built up.

The natural period of the fixed-base model is very close to the experimental value (1.19 sec aforementioned). It is obvious that the natural periods are elongated as the rocking behavior becomes more significant.

5.2 *Simulation of slow cyclic tests*

As a routine in OpenSEES simulations, the model with small footings was loaded progressively and vertically to the full gravity load. Then it is cyclically loaded with the same cyclic amplitudes as the physical tests. The column in this case was assumed to be rigid.

The moment vs. footing rotation curves are shown in Figure 15. The simulation models are proved to be able to capture the backbone shapes of the experimental curves as well as the rocking moment capacity. The initial rocking stiffness is matched pretty well. The settlement vs. rotation curves from simulation and centrifuge modeling are illustrated in Figure 16. The settlement in the simulation is 0.125 m, slightly larger than the experimental 0.075 m settlement. The simulation also appropriately captures the footing uplift during loading and net settlement during unloading in a half cycle. The settlement comes from the nonlinear behavior of footing springs, especially those in end zones.

5.3 *Earthquake input to SDOF models*

The model was subjected to the same ground motion as mentioned in Section 3.2. The bending moment on the column and the footing rotation are recorded through

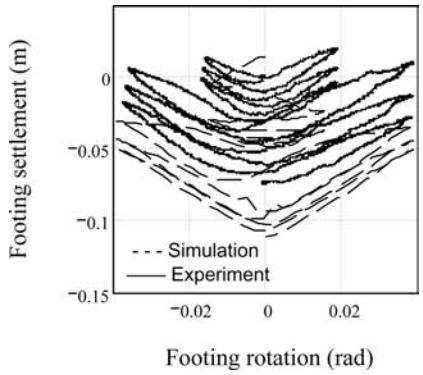

Figure 16. Settlement vs. rotation of small-footing model.

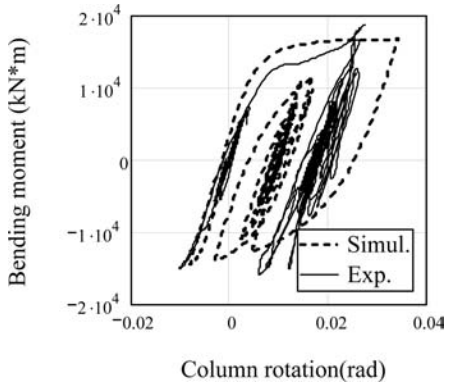

Figure 17. Bending moment vs. column rotation.

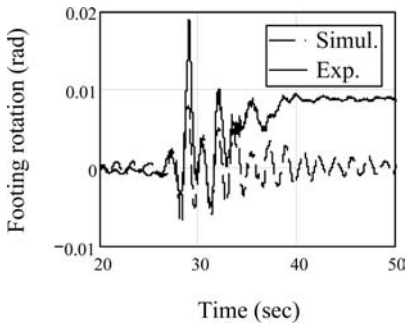

Figure 18. Time histories of footing rocking rotation.

simulation, and are plotted in Figures 17 and 18. It is observed that the overall shape of the curves is matched. Additionally the vibration period of the footing is also well captured. Nonetheless the problem with the simulation is that numerical results underestimate the permanent rotation of the footing and the column. This is to be addressed in future studies.

6 CONCLUSIONS

(1) An ordinary bridge designed with rocking footings may have better performance than a fixed-base bridge system in terms of ductility demand on columns, energy absorption, and self-centering mechanisms.
(2) The numerical models built with the BNWF approach in the OpenSEES platform were proved to be able to capture the crucial characteristics of the rocking footings and the nonlinear columns. The experimentally observed permanent deformations were larger than the numerically calculated permanent deformations.
(3) The natural periods of the SDOF models were elongated because of the rocking footings. It remains to be addressed whether the performance of the bridge with rocking footings subject to long-period motions is better.

ACKNOWLEDGMENTS

The project was awarded by the California Department of Transportation (Caltrans) under the contract 59A0575 and George E. Brown, Jr. Network for Earthquake Engineering Simulation (NEES). The former research work of Prof. S. Gajan of North Dakota State Univ. is highly appreciated. The authors also appreciate the assistance of the staff at the Center for Geotechnical Modeling of UC Davis.

REFERENCES

Boulanger, R. W. 2000. *The PySimple1, TzSimple1, and QzSimple1 Material Models*, documentation for the OpenSees platform, http://opensees.berkeley.edu.

California Department of Transportation. 2006. *Seismic Design Criteria*. Sacramento, CA, USA.

Federal Emergency Management Agency.2000. *Prestandard and Commentary for the Seismic Rehabilitation of Buildings*. D. C., USA.

Gajan, S., Kutter, B.L. 2008. Capacity, Settlement, and Energy Dissipation of Shallow Foundations Subjected to Rocking. *Journal of Geotechnical & Geoenvironmental Engineering* 134 (8): 1129–1141.

Harden, C. W., Hutchinson, T. 2009. Beam-on-Nonlinear-Winkler-Foundation Modeling of Shallow, Rocking-Dominated Footings. *Earthquake Spectra* 25(2): 277–300.

Hardin, B.O. 1978. The Nature of Stress-Strain Behavior of Soils. *Earthquake Engineering & Soil Dynamics*. ASCE vol. 1: 108–119.

Mylonakis, G., Gazetas, G. 2000. Seismic Soil-Structure Interaction: Beneficial or Detrimental? *Journal of Earthquake Engineering* 4(3): 277–301.

Perkins, S., Madson, C. 2000. Bearing Capacity of Shallow Foundations on Sand: A Relative Density Approach. *Journal of Geotechnical & Geoenvironmental Engineering* 126(6): 521–530.

Salgado, R. 2008. *The Engineering of Foundations*. The McGraw-Hill Companies Inc., NY, USA.

Scott, M.H., Fenves, G.L. 2006. Plastic Hinge Integration Methods for Force-Based Beam-Column Elements. *Journal of Structural Engineering* 132(2):244–252.

Soil-Foundation-Structure Interaction – Orense, Chouw & Pender (eds)
© 2010 Taylor & Francis Group, London, ISBN 978-0-415-60040-8

Large scale field tests of rocking foundations on an Auckland residual soil

T.B. Algie, M.J. Pender & R.P. Orense
University of Auckland, New Zealand

ABSTRACT: This paper details scaled field experiments conducted on rocking shallow foundations. First, a full geotechnical investigation was carried out to determine soil conditions. A test structure, made from structural steel, was designed and fabricated specifically for this testing. Road construction plates were attached to the structure to create realistic vertical loads, and achieve different factors of safety in bearing. Tests carried out so far have had estimated bearing strength factors of safety of 47 and 10. Non-linear behaviour of the foundations and underlying soil was evident and typical performance graphs, such as moment-rotation and settlement-rotation, were analysed. The foundations displayed good energy dissipation during the rocking cycles.

1 INTRODUCTION

This paper is concerned with the particular aspect of geotechnical performance-based design that deals with the response during earthquakes of shallow foundations on cohesive soils. It outlines experiments conducted on shallow foundations on an Auckland residual soil. A simple steel-framed structure was built and excited using an eccentric mass shaker capable of delivering a sinusoidal forcing function.

The experiment was focussed particularly on making the foundations rock. The rocking concept was first proposed by Housner with his study on the rocking of inverted pendulum structures (Housner 1963). Rocking foundations have advantages in earthquake design, utilising hysteretic damping characteristics of soil, to mitigate earthquake energy.

Numerous experimental studies on rocking foundations have been carried out in the past. Taylor et al. (1981) conducted slow cyclic tests on shallow foundations sitting on both clay and sand and suggested that spread footings may be intentionally designed to yield during high intensity earthquakes. Gajan et al. (2008) carried out centrifuge tests on rocking shear walls sitting on moderately dense sand. Ugalde et al. (2007) conducted similar centrifuge experiments, however testing single degree of freedom structures; modelling bridge columns with square footings. Algie et al. (2008) expanded on the rocking bridge foundation concept to include yielding columns coupled with yielding foundations and this was carried out on both single degree of freedom structures and holistic bridge systems.

Numerically there has also been substantial research undertaken. A numerical model is being developed in parallel with the experimental program to predict shallow foundation behaviour. Several different types of numerical models are currently available. A spring bed model, which uses springs to represent soil behaviour, is perhaps the most common approach to modelling the soil-structure interaction (Sivapalan Gajan et al. 2008, Mergos & Kawashima 2005, Raychowdhury & Hutchinson 2009, Toh & Pender 2008, Wotherspoon 2007). Pender at al. (2009) compare three such models (a spring bed model, a bearing strength surface macro-element model and a contact interface model) with data obtained from centrifuge tests conducted on San Francisco Bay Mud. The results indicated that all three modelling approaches give reasonable representations of the observed responses.

The motivation for this particular research stems from the current earthquake loadings standard in New Zealand, NZS 1170.5 (Standards New Zealand 2004). The previous earthquake standard, NZS 4203, (Standards New Zealand 1992) had, in principle, an allowance for rocking structures that stated:

> *"Where dissipation of energy is primarily through rocking of foundations, the structure shall be subject to a special study, provided that this need not apply if the structural ductility factor is equal to or less than 2.0."*

The understanding of this was that engineers could design a foundation for the reduced forces from a ductility factor (μ) of 2 without any extra analysis. Thus the foundation could be sized such that at design forces for $\mu = 2$, the overturning moment equals the restoring moment and rocking occurs. Consequently foundations could be made smaller because of the reduced forces associated with the rocking mechanism.

The current standard, NZS 1170.5, removed this $\mu = 2$ provision for rocking structures. This was partly because there were no guidelines as to the design philosophy of these foundations, giving no specific soil conditions or limitations. Another reason was that although there had been considerable research done on rocking foundations, not enough experimental evidence existed for New Zealand conditions

to develop a design guideline. Hence NZS 1170.5 specified:

> *"Where energy dissipation is through rocking… the actions on the structures and parts being supported by the structures shall be determined by special study."*

In New Zealand, a special study is defined as a detailed analysis of structural actions and responses. Non-linear time history analysis of a soil-foundation-structure system would need to be calculated for several different earthquake motions (Kelly 2009). This analysis is frequently beyond design office capabilities, and when feasible, much time and effort is expended.

2 EXPERIMENTAL DESIGN

2.1 *Concept*

The concept of the experiments was to test shallow foundations that, in practice, could be implemented in a design solution. The majority of rocking foundations that have been designed in New Zealand using the older NZS 4203 standard were foundations beneath shear walls, predominately concrete shear walls. There were however, some problems with testing reinforced concrete shear walls. These issues included: testing dynamically may damage the concrete, making a wall usable for one test only; loading the wall vertically with enough mass to be realistic and at the same time maintain stability; mounting the shaking machine which has a footprint of around 1 m square.

The idea of this research was to build a structure that would be versatile enough to conduct these experiments, yet realistic enough to be produce useful results.

First, it had to be demountable and reusable, making it possible to test this structure on different soils around New Zealand. The structure had to be built to allow rocking foundations but remain essentially elastic as a yielding structure would create difficulties for subsequent use. Lastly, it had to be large enough to accommodate sufficient mass to achieve realistic soil pressures, and to support the earthquake shaker. It was decided to design and construct a steel frame because this can accommodate all the above requirements. Figure 1 shows a 3D representation of the structure designed. Figure 2 shows a plan view of the top frame of the structure, the foundations are also included and the shaking direction given.

2.2 *Structural design*

A steel design was performed on the proposed structure and this design was fabricated by professional steel fabricators. Structurally it was designed for a 100 kN horizontal load as a fixed base system. The frame consisted of three parts which enabled the whole structure to be transported with relative ease. Two vertical end frames; these were connected to the foundations

Figure 1. 3D figure of the designed structure.

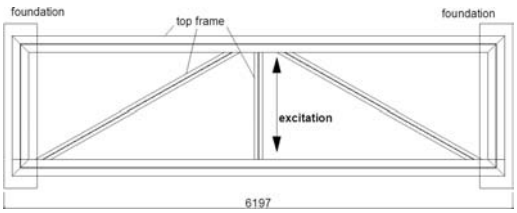

Figure 2. A plan view of the test, showing the foundations, top frame, and shaking direction.

by anchor bolts. The third component was the horizontal top frame, which bridged the two end frames and supported the shaker and additional mass.

A large steel plate was welded onto the middle of the top frame and the shaker was bolted to this using eight M24 8.8 structural bolts. Two universal column sections were used in the design; 200 UC 42.6 and 100 UC 14.8. The three components were bolted together using M20 8.8 structural bolts. Bracing was used to make the structure as stiff as possible. A 100 circular hollow section (CHS) ran horizontally between the two end frames close to the ground surface. In addition 20 mm diameter steel braces were fixed diagonally across the structure.

2.3 *The site*

The site for the testing was located east of the Auckland Northern motorway in the Pinehill subdivision of the suburb of Albany. The land owners along with their consultants facilitated access to the site. A total of 8 foundations were cast into the soil at relatively close spacing, but far enough apart not interact with each other. This made the tests possible at 4 different locations (2 foundations per test). However for this paper only tests conducted on one set of foundations are discussed and all of the data presented is from the West foundation. A thorough geotechnical investigation was undertaken prior to testing; the different geotechnical tests are detailed below. Table 1 summarises the geotechnical properties deduced from the

Table 1. Summary of soil conditions for the West foundation.

	North CPT	South CPT
ρ (kg/m^3)	1750	1750
$V_{s,2-3m}$ – SCPT (m/s)	144	150
$V_{s,surface}$ – WAK (m/s)	153	155
s_u - average (kPa)	200	155
$G_{max,2-3m}$ – SCPT (MPa)	36	39
$G_{max,surface}$ – WAK (MPa)	41	42

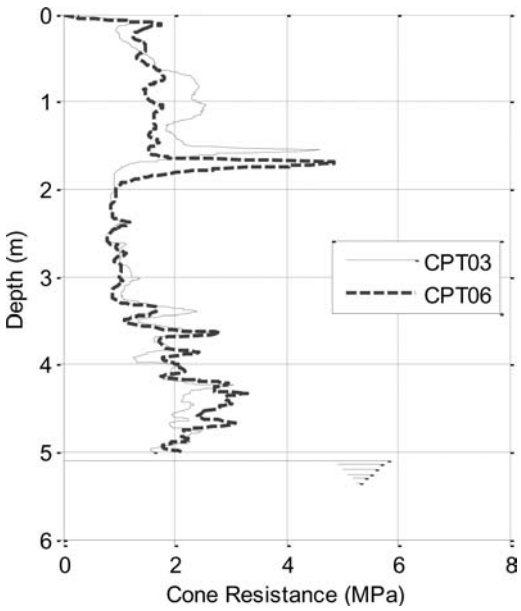

Figure 3. Cone resistance plots, taken from the CPT data.

investigation for the West foundation. In addition to the field tests, laboratory testing of the soil is underway.

2.3.1 *Cone penetration tests*

Standard and seismic cone penetration tests (CPT's and SCPT's) were performed extensively onsite. A CPT and a SCPT was performed at each end of every foundation. Every CPT was done with a target depth of 10 m and the seismic readings were taken between 2 and 3 m deep. The Cone Resistance plots, for CPT 3 and CPT 6 (the two CPT's that corresponded to the West foundation), are given in Figure 3.

Note that these two CPT's only reached a depth of 5 m. It is evident from the above Cone Resistance plots that the soil is comparatively similar from one end of the foundation to the other. The CPT data shows that the upper layers of soil consist of very stiff clayey sand down to a depth of around 1.6 m. There is a thin layer of very stiff fine grained material at around 1.6 m which could account for the spike in the plots. Below that the soil is mostly clay to silty clay or clayey silt to silty clay. This picture is consistent between the north (CPT 6) and the south (CPT 3) positions. The CPT pore pressure response puts the water table at 5.1 m below the ground surface, but the soil was considered saturated to near the surface because the tests were conducted near the end of the wet season.

The SCPT results, given in Table 1 show that the shear wave velocity, and consequently the shear modulus, remained relatively consistent.

2.3.2 *Wave activated stiffness tests*

Wave activated stiffness tests, WAK tests, were first described by Briaud and Lepert (Briaud & Lepert 1990). A WAK test is a simple test conducted to determine the small strain shear modulus near the ground surface. A 500 mm diameter plate was bedded onto the ground surface with accelerometers each side. An instrumented hammer strikes the middle of the plate and acceleration readings recorded. The modulus is obtained as explained by Briaud and Lepert. As Table 1 shows, there is good correlation between the small strain shear moduli (G_{max}) obtained from the SCPT and WAK tests.

2.3.3 *Hand shear vane tests*

Hand shear vane tests were conducted to determine the undrained shear strength of the soil. At each foundation location five shear vane tests were performed. The undrained shear strength values (s_u) given in Table 1 are an average of the opposite ends of the foundation. As the table shows the values can vary a large amount over the 2 m length of foundation. Laboratory tests are underway to supplement the field test data about the soil shear strength and stiffness. The s_u values were used in determining the bearing capacity of the soil. As the results show, the ground is very stiff to hard (which confirms the information gained from the CPT tests). The average undrained shear strengths recorded for each end of the West foundation were 155 and 200 kPa.

2.4 *Structural mass*

The structure by itself was relatively light; around 50 kN of vertical load, and thus putting minimal stresses in the soil beneath the foundations. It was desired to conduct tests with varying vertical load to achieve different static factors of safety in bearing. Traditionally a factor of safety (FoS) of 3 is typically used for the lower bound in shallow foundation design. Using the results from the hand shear vane tests, an approximate amount of mass was determined to be needed to achieve various factors of safety from the bearing capacity equation for cohesive undrained soils; shown in Equation 1:

$$q_u = N_c \cdot s_u \cdot \gamma_s \cdot \gamma_d \cdot \gamma_i + q \quad (1)$$

where q_u = ultimate bearing capacity; N_c = bearing capacity factor (5.14); s_u = undrained shear strength of the soil; γ_s = shape factor; γ_d = depth factor; γ_i = inclination factor; and q = surcharge pressure.

The undrained shear strength for the foundation positions ranged between 100 kPa to 200 kPa. Assuming the self weight is spread over both foundations,

25 kN is applied to each 2 m by 0.4 m footing. Based on this the factor of safety in bearing was 47. To achieve a factor of safety of around 10, 75 kN was added to each end frame, making the total load around 200 kN.

The additional mass came in the form of road construction plates. These were lifted on the structure and 'sandwiched' into place using channel sections.

2.5 *Excitation*

The dynamic excitation of the structure was from an eccentric mass shaker attached to the top middle of the structure. This shaker works by two counter-rotating fly wheels, with various numbers of masses attached to one half of each of them. As they rotate, the forces from the masses add in one direction but cancel in the perpendicular direction, delivering a sinusoidal forcing function. The force that the shaker delivers is dependent on the frequency, and how many masses are attached. At full capacity the shaker can deliver 98 kN dynamic force at a frequency of 7 Hz.

One main purpose of the tests was to find how the response of the foundations changed as the dynamic force increased. As explained above the magnitude of the dynamic force depends on the shaker frequency and the number of masses attached to the flywheels. The initial and final stages of a test run consisted of a frequency sweep with only small masses installed; this enabled the initial small excitation response of the system to be determined and then the change in this after the high level shaking to be determined.

Results from two test runs are presented in this paper. During test 1, no extra mass was on the structure, and the maximum frequency reached was 2.3 Hz, delivering around 10 kN of dynamic load. Test 2, with an additional 150 kN of vertical load, reached a frequency of 4.2 Hz (around 34 kN dynamic load).

3 INSTRUMENTATION

3.1 *Pressure sensors*

Pressure sensors are thin instruments that can record change of pressure acting on a defined bearing area. They were placed at intervals on the underside of the foundation. Under constant loads these sensors tend to drift, making calibration of them nearly impossible because they were sitting under the concrete foundations. However the main purpose of the sensors was to achieve a 'before and after' picture of what's happening to the soil underneath the footing. By recording before, during and after the excitation one would be able to achieve an idea of how much soil is still in contact with the foundation and what the length of any gap between the foundation and underlying soil is.

3.2 *Strain gauges*

It was decided that the best way to record the forces on the foundations was through strain gauges attached to the steel columns. Recording the axial and bending strain in the members, the axial force and bending moment can be obtained.

3.3 *Accelerometers*

Accelerometers were placed on the foundation and the structure, these measured the acceleration in all three directions; vertical, longitudinal and transverse. The accelerometers used had a range of $+/-2$ g.

3.4 *Linear variable differential transformers*

Linear variable differential transformers (LVDT's) were attached to the foundation to measure vertical and horizontal movement. The vertical movement was used to calculate settlement and rotation of the foundation and the horizontal movement was used to calculate sliding.

These LVDT's were in turn attached to a 6 m long 125 mm $\times$ 50 mm piece of timber that was anchored to the ground at each end and not in contact for the remainder of its length. This was done to ensure minimal vibrations from the foundation rocking were transferred into the LVDT recordings. It was determined the span of the beam (6 m) was far enough away from the foundations for the readings to be unimpaired.

4 CONSTRUCTION

4.1 *Foundations*

To reduce the impact of drying and cracking in hot sunny weather, or alternatively flooding due to heavy rain, the foundation excavation and construction was completed in one day. The foundation dimensions were 0.4 m by 0.4 m by 2 m in length. They acted as strip footings underneath each end of the frame and were embedded to 0.4 m, with the top of the concrete at the ground surface.

An excavator cut the foundation trenches to the required width; any parts needing extra work were done by hand with a spade. Following the holes being excavated, the pressure sensors were placed along the ground surface. A layer of geotextile was laid on top of the pressure sensors for protection from the concrete and the reinforcing steel cages were placed.

The anchor bolts for the structure were located within the reinforcing steel using templates made from plywood to make sure the bolt pattern was accurate with the frame base plates. The distance between the two foundations, specifically the foundation bolts, were carefully set-out to ensure there was no issue with the structure connecting to the foundations.

Once all the steel was placed and the anchor bolts carefully positioned, concrete was poured until it rose to the underside of the plywood templates; or the ground surface. Once all the foundations were cast, the concrete was left to cure for 28 days before the testing began.

Figure 4. Complete frame with shaker and road plates.

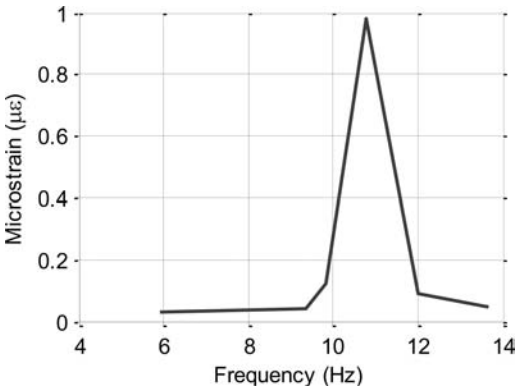

Figure 5. Frequency response curve of the low level shake, test 1-a.

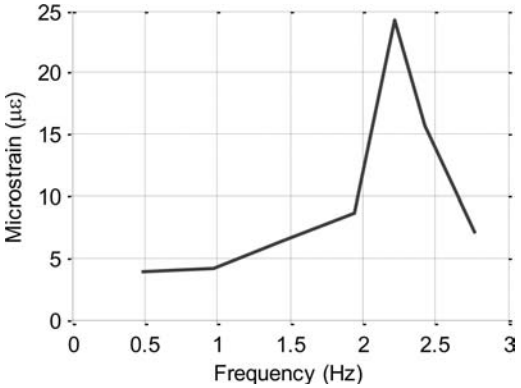

Figure 6. Frequency response curve of the high level shake, test 1-b.

4.2 *Structural frame*

The set up of the frame onsite was done piece by piece. Firstly, mortar was placed on the foundations to ensure the end pieces were level. Each end piece was carefully lowered using a crane and bolted into place.

The top frame was placed on top of the end frames and bolted down. Lastly, the tubes and braces were added which stiffened the frame and made the structure complete. Figure 4 shows the structure just before testing with the shaker and road plates attached.

5 RESULTS

Two sets of results are presented below. These were tests conducted with no road plates – test 1, and with 150 kN of road plates – test 2. The corresponding static factors of safety for these tests were 47 and 10 respectively. For each test there was up to three shakes with the eccentric mass shaker. An initial low level shake with no eccentric mass in the shaker, a high level shake with all the eccentric mass in the shaker, and another low level shake with no eccentric mass in the shaker. These are subsequently labelled a, b, c respectively.

All the frequency response curves have the strain gauge amplitudes plotted against the frequency. The particular gauge used was that on the outside of the North-West column. Strain gauge data, in microstrain ($1\ \mu\varepsilon = 10^{-6}$ mm/mm), was chosen because it had the best resolution at low amplitudes.

In the performance curves, not all the time history data are given, as this would clutter the graphs.

5.1 *Test 1 – factor of safety of 47*

5.1.1 *Frequency response*

The initial low level shake with no eccentric mass in the shaker, test 1-a, shows one dominant frequency at 10.8 Hz, evident in the response curve in Figure 5. The system was modelled initially in the structural analysis software SAP (CSI 2004) as a fixed base model. The calculated fundamental frequency in the SAP model was 11.4 Hz; close to the 10.8 Hz generated in the experiment. Thus soil-structure interaction has little effect at low levels of excitation.

The response in test 1 of the structure in the stronger shake with all the eccentric mass in the shaker (test 1-b) is plotted in Figure 6. Again the response shows one dominant frequency at 2.2 Hz, suggesting this is the fundamental rocking frequency of the soil-foundation-structure system.

5.1.2 *Performance curves*

Performance of a rocking foundation during earthquakes can be quantified by moment capacity and residual settlement and rotation. Thus good performance plots are moment-rotation and settlement-rotation plots. These are given in Figures 7 and 8 for the high level shake, with all the eccentric mass in the shaker, test 1-b.

A reduction of rotational stiffness, during the stronger excitation, is evident in the moment-rotation curves. This is illustrated by the increase in maximum rotation with each cycle while the moment remains relatively constant, depicting clear non-linear behaviour. However the sharp peaks give us an indication of the very high factor of safety. The sharp peaks are from

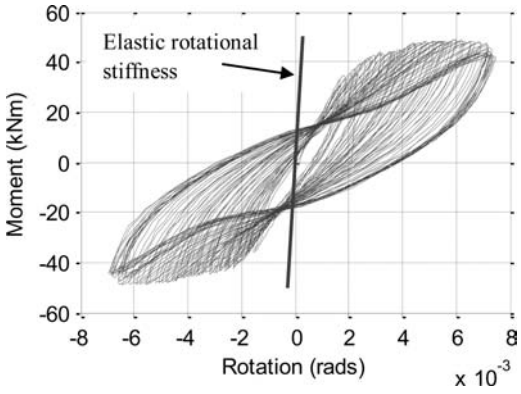

Figure 7. Moment-rotation of the high level shake, test 1-b, with the small strain, elastic rotational stiffness depicted.

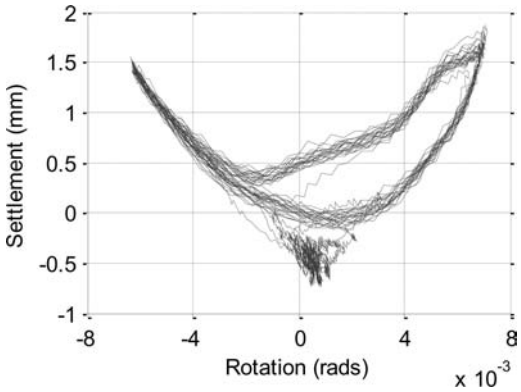

Figure 8. Settlement-rotation of the high level shake, test 1-b.

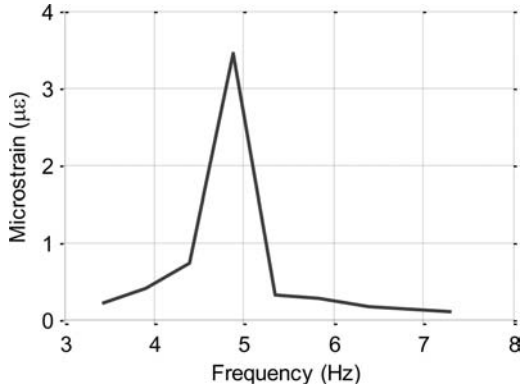

Figure 9. Frequency response curve of the initial low level shake, test 2-a.

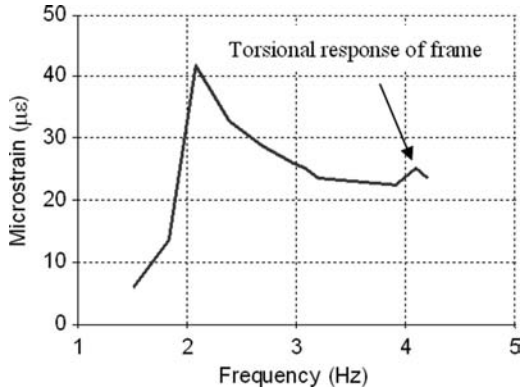

Figure 10. Frequency response curve of the high level shake, test 2-b.

a bearing capacity failure over only a very small part of the end of the foundation. If the factor of safety was lower, more of the soil would have yielded and the moment-rotation would be more flat rather than pointed. Despite this the hysteresis loops show good energy dissipation with each cycle.

The maximum moment reached was around 48 kNm, and the maximum rotation 0.007 radians. The straight line on the graph represents the small strain elastic rotational stiffness calculated by the Gazetas equation (Gazetas 1990). The G_{max} value used in the equations was an average of the geophysical tests, and taken as 40 MPa for all calculations.

The observed rotational stiffness is much less than the rotational stiffness determined using the small strain shear modulus, shown by the straight line. This elastic stiffness was calculated assuming full foundation contact. At the beginning of yielding, the experimental stiffness is around 20% of the elastic value. At the maximum yielding shown in Figure 7, the rotational stiffness had reduced to 6% of the elastic value. Thus it is clear from Figure 7 that the design stiffness of the foundations should be based on an equivalent soil modulus much less than G_{max}.

The settlement-rotation profile, Figure 8, indicates uplift of the edges of the foundation. Figure 8 shows the settlement during this test was small – 0.85 mm.

5.2 *Test 2 – factor of safety of 10*

5.2.1 *Frequency response*

The frequency response from tests 2-a, b and c are shown in Figures 9, 10 and 11 respectively. As mentioned above, the difference between test 1 and test 2 was the extra 150 kN of vertical load from the road plates. The response for the initial low level shake with no eccentric mass in the shaker, test 2-a, is shown in Figure 9. As is the case in test 1-a (the low level shake of test 1), there is one predominant frequency, at 4.9 Hz. A fixed base SAP model gave a frequency of 6.2 Hz. This difference suggests that soil-structure interaction is more significant for test 2.

Figure 10, test 2-b, the high level shake with all eccentric mass in the shaker, shows the rocking frequency of the structure to be 2.1 Hz. The frequency response does not fall away as sharply as the high level shake of test 1 (test 1-b – Fig. 6). In addition Figure 10 shows the response starting to increase again around

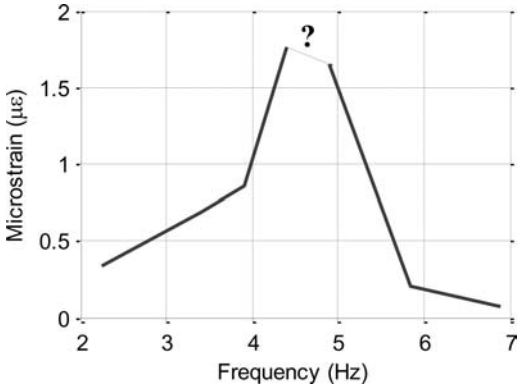

Figure 11. Frequency response of the second low level shake, test 2-c (that followed the high level shake test 2-b).

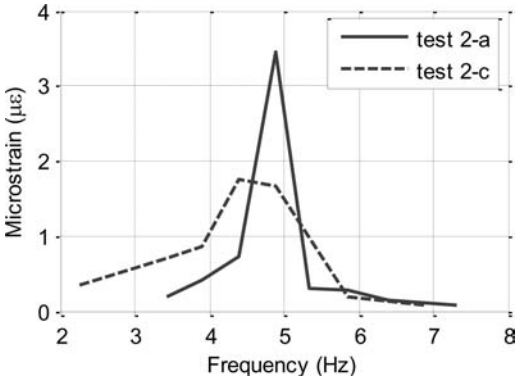

Figure 12. Frequency response of both of the low level shakes, test 2-a and 2-c.

3.8 Hz, this was due to the frame beginning to behave in a torsional mode.

Figure 11 depicts the frequency response from test 2-c, a repeat of the low level excitation. Here it shows that the response is a lot more rounded and not pointed as is the case in Figure 9. This may be because the frequency with the peak response was not exactly 'hit' by the shaker, and if we had 'hit' this frequency, the spike in Figure 11 would be a lot more pointed, as in Figure 9. The main frequency of test 2-c was 4.4 Hz, however as indicated by Figure 11 the peak response was likely in between 4.4 and 4.9 Hz.

Figure 12 shows the change in response between test 2-a and 2-c. The frequency of test 2-c has shifted slightly to the left, however as the values suggest and as Figure 12 suggests, the shift was very minimal.

5.2.2 *Performance curves*

The moment-rotation and settlement-rotation plots from test 2-b are shown in Figures 13 and 14, respectively. The maximum moment of test 2-b was around 110 kNm and the maximum rotation was 0.0028 radians. Again the loops indicate good energy dissipation during rocking. Similarly to high level shake, test 1-b, the observed rotational stiffness is considerably less than the elastic rotational stiffness. Figure 13 shows an initial stiffness of the system that is around 40% of the Gazetas value. The larger loops in Figure 13 are at approximately 10% of the elastic value. As is the case with test 1-b however, this elastic rotational stiffness value was calculated from G_{max} and full soil foundation contact.

Figure 14 shows that the uplift in test 2-b was not as prominent as test 1-b, because the settlement does not curve up as much at the edges. This is due from the extra energy required to lift the greater mass. Dynamically the test settled around 2.5 mm (2.0 mm more than shown). The static settlement in test 2-b was 20 mm, so in comparison the additional 2.5 mm settlement induced by the cyclic loading is negligible.

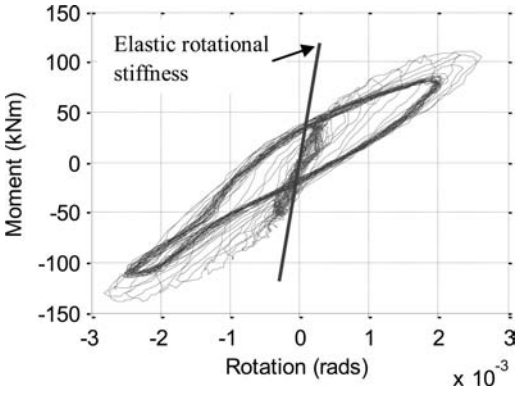

Figure 13. Moment-rotation of high level shake, test 2-b.

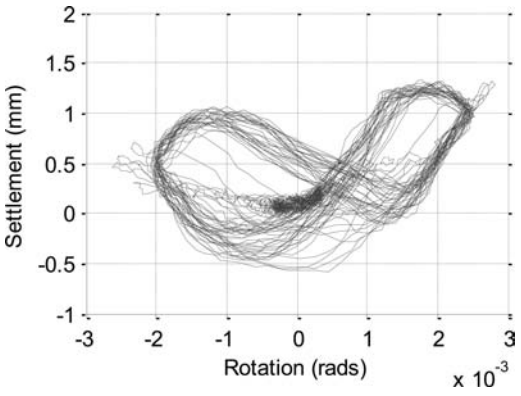

Figure 14. Settlement-rotation of high level shake, test 2-b.

6 DISCUSSION

The low capacity shakes give a good indication of the structural response of the system. The response to the initial shake was similar to that calculated with the SAP2000 fixed-based model for test 1-b. Test 2-b showed a slight difference between the SAP2000 and

calculated response. This could be due to some rounding of the contact between the soil and foundation induced in the previous test.

The stronger shakes (test 1-b and test 2-b) demonstrate a prominent rocking frequency. This was 2.2 Hz for test 1-b and 2.0 Hz for test 2-b. These values indicate that the shaking level is now sufficiently severe to induce nonlinear soil structure interaction. A question for the remaining part of this research programme will be to separate the contribution of irrecoverable deformation between the underside of the foundation and the soil beneath, what was referred to as rounding of the contact above, and nonlinear stress-strain behaviour of the soil under the foundation.

The maximum moments reached by the foundation increased from around 48 kNm for tests 1 to around 110,kNm for tests 2 after the extra mass of the road plates was included. A simple static equation for predicting the moment capacity (M_{ult}) of a rocking foundation at the ground surface was developed by Gajan et al. (2005), and is given by:

$$M_{ult} = \frac{V \cdot L}{2} \cdot \left[1 - \frac{L_c}{L}\right] \quad (2)$$

where V = vertical load; L = foundation length; and L_c = length of foundation where the bearing capacity factor of safety equals 1 – termed the critical length.

The tests conducted and presented in this paper all had embedded foundations. Therefore passive and active earth pressures, as well as sidewall effects must be taken into account in estimating the critical contact length (L_c).

The static moment capacity equated using Equation 2 for test 1, without road plates was calculated as 46 kNm – similar to the experimental results of around 48 kNm.

The calculated moment capacity for test 2 was 120 kNm, slightly greater than the recorded moments.

The moment-rotation of test 2-b (Figure 13) did not show as much non-linear behaviour as test 1-b. This is reinforced by the static moment capacity calculated using Equation 2 compared with the experimental results. Despite this, nonlinear behaviour was still observed as evident by the area of the loops in Figures 7 and 13 Consequently the moment-rotation plots of test 1-b and test 2-b both show good energy dissipation; promising when considering design applications.

From the extra mass loaded on the structure, the axial loads through the steel columns were far greater. As Figures 8 and 14 show, there is less uplift in test 2-b because of this extra vertical load.

Very small amounts of settlement occurred during the strong shaking events. Test 1-b settled 0.85 mm whilst test 2-b settled 2.5 mm. In past research, settlement has traditionally been a major issue for rocking foundations. Too much settlement or differential settlement results in poor performance. The amount of settlement during the tests is encouraging because it shows there is potential for good resistance to settlement during a strong seismic shaking on an Auckland residual soil. When comparing the settlement-rotation behaviour to a past centrifuge test done on clay (Rosebrook & Kutter 2001), the results are comparable. In that test, the factor of safety of the system was calculated at 2.8 – much less than in the tests presented herein. The residual settlement was measured at around 7 mm and the maximum rotation around 0.01 rad. Therefore the settlements recorded in tests 1-b and 2-b (0.85 mm and 2.5 mm) are adequate when considering the large factor of safety both of those tests had.

There are more tests still to be conducted in this experimental program. We would like to induce more material yielding in the foundations and produce flat top moment-rotation curves; potentially by reducing the static factor of safety. In addition, future tests are planned with the foundations having a 'recovery' period to judge how a rocking foundation will recover over time.

7 CONCLUSIONS

From the results, several conclusions were reached:

- The experiments achieved non-linear behaviour of the soil, as evident from the moment-rotation plots.
- The SAP2000 models of the structure predicted the fixed base frequency well when compared to the low capacity shakes, test 1-a and 2-a. However, test 2-a, with a heavier structure, showed a slight difference, indicating more soil-foundation-structure interaction.
- In the more vigorous tests, only yielding of a very small part of soil occurred due to the large factors of safety associated with these tests. To achieve more flat-topped moment-rotation plots, more vertical load must be included.
- The static equation for the moment capacity compared well with the experimental results. This equation took into account the passive and active earth pressures as well as side wall affects.
- The foundations showed good energy dissipation from the area of the moment-rotation loops.
- The settlement that occurred during the strong shaking was minimal, encouraging for future design aspects of rocking foundations. The settlement-rotation behaviour was comparable to a past centrifuge test done on clay when considering the difference in the factor of safety.

8 ACKNOWLEDGEMENTS

Due to the large scale nature of this experiment, several people and businesses gave time and resources to help the tests take place. The authors would like to thank CDL Investments for allowing the use of their land for this experiment, and also their engineering representative Coffey Geotechnics for their involvement; Associate Professor Charles Clifton and Mr. Craig Stevenson for their assistance and guidance in

designing the frame; Hicks Bros. for creating an access way onsite; Fletcher Reinforcing and Pacific Steel for supplying the concrete reinforcement and the diagonal bracing respectively; Firth for supplying the concrete for the foundations; Perry drilling for carrying out the extensive CPT testing; and finally BHP piling for providing a crane on site.

REFERENCES

Algie, T.B., Deng, L., Erduran, E., Kutter, B.L. & Kunnath, S. 2008. Centrifuge Modeling of Innovative Foundation Systems to Optimize Seismic Behavior of Bridge Structures. *14th World Conference on Earthquake Engineering (14 WCEE)*.

Briaud, J.-L. & Lepert, P. 1990. WAK Test to Find Spread Footing Stiffness. *Journal of geotechnical engineering, 116*(3), 415–431.

CSI. 2004. *SAP2000 Integrated Structural Analysis and Design Software*. Computers and Structures Inc. Berkeley, California.

Gajan, S., Hutchinson, T.C., Kutter, B.L., Raychowdhury, P., Ugalde, J.A. & Stewart, J.P. 2008. *Numerical models for analysis and performance-based design of shallow foundations subjected to seismic loading*, Pacific Earthquake Engineering Research Center, College of Engineering, University of California, Berkley, PEER Report 2007/04

Gajan, S., Kutter, B.L., Phalen, J.D., Hutchinson, T.C. & Martin, G.R. 2005. Centrifuge modeling of load-deformation behavior of rocking shallow foundations. *Soil Dynamics and Earthquake Engineering, 25*(7–10), 773–783.

Gazetas, G. 1990. Foundation vibration. In *Foundation Engineering Handbook 2nd Ed.*

Housner, G.W. 1963. Behavior of inverted pendulum structures during earthquakes. *Seismological Society of America – Bulletin, 53*(2), 403–417.

Kelly, T.E. 2009. Tentative Seismic Design Guidelines for Rocking Structures. *Bulletin of the New Zealand National Society for Earthquake Engineering, 42*(4), 239–274.

Mergos, P.E. & Kawashima, K. 2005. Rocking isolation of a typical bridge pier on spread foundation. *Journal of Earthquake Engineering, 9*(SPEC. ISS. 2), 395–411.

Pender, M.J., Toh, J.C.W., Wotherspoon, L.M., Algie, T.B. & Davies, M.C.R. 2009. Earthquake induced permanent displacements of shallow foundations – performance based design. *IS Tokyo*, Tokyo, Japan.

Raychowdhury, P. & Hutchinson, T.C. 2009. Performance evaluation of a nonlinear Winkler-based shallow foundation model using centrifuge test results. *Earthquake Engineering and Structural Dynamics, 38*(5), 679–698.

Rosebrook, K.R. & Kutter, B.L. 2001. *Soil-foundation-structure interaction: shallow foundations. Centrifuge Data Report for test series KRR03*, University of California, Davis, Report No. UCD/CGMDR-01/11

Standards New Zealand. 1992. *Code of practice for General Structural Design and Loadings for Buildings, NZS 4203:1992*: Standards, New Zealand.

Standards New Zealand. 2004. *Structural Design Actions Part 5 : Earthquake actions New Zealand, NZS 1170.5*: Standards, New Zealand.

Taylor, P.W., Bartlett, P.E. & Wiessing, P.R. 1981. Foundation Rocking Under Earthquake Loading. *Proceedings of the International Conference on Soil Mechanics and Foundation Engineering, 3*, 313–322.

Toh, J.C.W. & Pender, M.J. 2008. Earthquake performance and permanent displacements of shallow foundations. *New Zealand Society of Earthquake Engineering Conference*, Wairakei, New Zealand.

Ugalde, J.A., Kutter, B.L., Jeremic, B. & Gajan, S. 2007. Centrifuge Modeling of Rocking Behavior of Structures on Shallow Foundations. *Fourth International Conference on Earthquake Geotechnical Engineering*.

Wotherspoon, L.M. 2007. *Integrated modeling of Structure-Foundation systems.* Ph.D. thesis, University of Auckland, New Zealand.

Numerical analysis and modeling of SFSI

Soil-Foundation-Structure Interaction – Orense, Chouw & Pender (eds)
© 2010 Taylor & Francis Group, London, ISBN 978-0-415-60040-8

Aspects of soil structure interaction

W.D. Liam Finn
University of British Columbia, Vancouver, Canada

ABSTRACT: This paper offers a guided tour through the various ways of accounting for soil-structure interaction from analysis of the total soil-structure system to analysis of various approximate models of the system. The focus is on two types of structures, tall buildings with several levels of underground parking and bridges on pile foundations. The results of the analyses of approximate models are compared with "best model" solutions and recorded response data. The comparison provides insight on the more important features of soil-structure interaction and guidance on the selection of approximate models.

1 INTRODUCTION

This paper offers a guided tour through the various ways, used in practice, of accounting for soil-structure interaction in design and analysis, ranging from a complete analysis of the total combined system of foundation soil and structure to approximate models of the system. The focus is on two types of structures, tall buildings with several levels of underground parking and bridges on pile foundations.

When analysis of the total soil-structure system is carried out, the effects of soil-structure interaction (SSI) are implicitly included in the analysis and reflected in the results. No special consideration of SSI is required. However this type of analysis, while feasible, is rarely practical in practice because the structural analysis programs used usually by structural engineers cannot handle the nonlinear soil continuum directly. There are powerful commercial programs available that can do complete analyses but the learning curve is steep and long and the computational time too long for designers requirements except for special projects. Total system analysis is feasible but it is currently impractical in most cases. Therefore it is necessary to select simpler computational models of the system, uncoupled from the soil, and to include soil-structure interaction by approximate procedures for design.

2 MODELS FOR TALL BUILDINGS

2.1 *Most accurate model (MA)*

An embedded tall building is shown in Figure 1.

The process of exploring what may be effective models of this structure starts with the construction of the most accurate computational model (MA) compatible with current structural software. The response of this model to the Northridge earthquake is evaluated to provide baseline response data against which the performance of various simpler models can be checked. The MA model of the 54 storey building is shown in Figure 2. The models and findings presented in this section were all developed by Naeim et al, (2008).

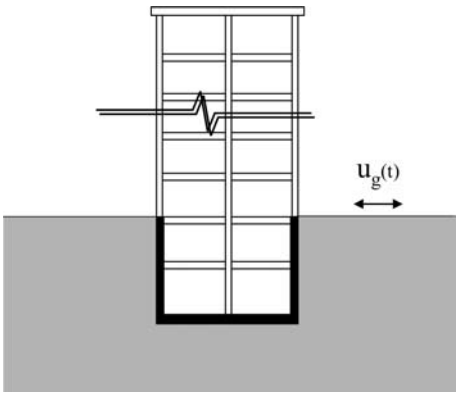

Figure 1. Schematic drawing of model of 54 storey building with several basement levels.

The action of the foundation soil against the basement walls is modeled by appropriate horizontal springs. The vertical and rocking stiffnesses of the base slab are modeled simultaneously by vertical springs with an appropriate distribution of stiffnesses.

Depth dependent free field ground motions are applied to the horizontal springs and the bottom of the base slab.

The response of the MA structural model to the Northridge earthquake was evaluated and the accelerations at different elevations in the building were compared with those recorded during the earthquake. The MA model was tuned to give good agreement with the recorded accelerations.

Many different simplified soil-structure models were tested but only 3 will be presented here to illustrate how simpler models tend to behave.

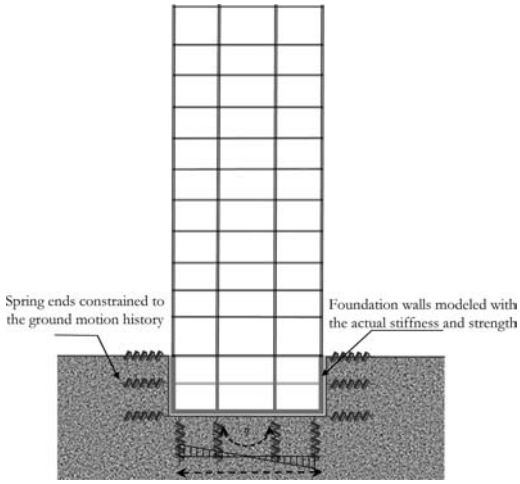

Figure 2. Most accurate model of 54 storey building.

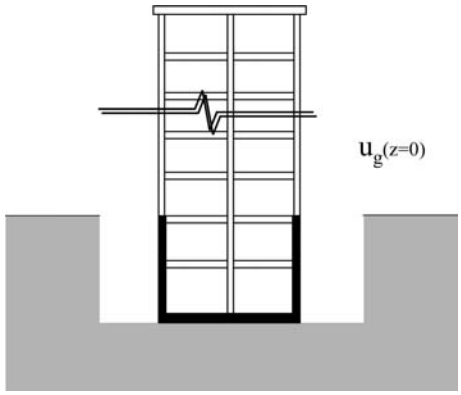

Figure 3. Model #3c with no foundation interaction.

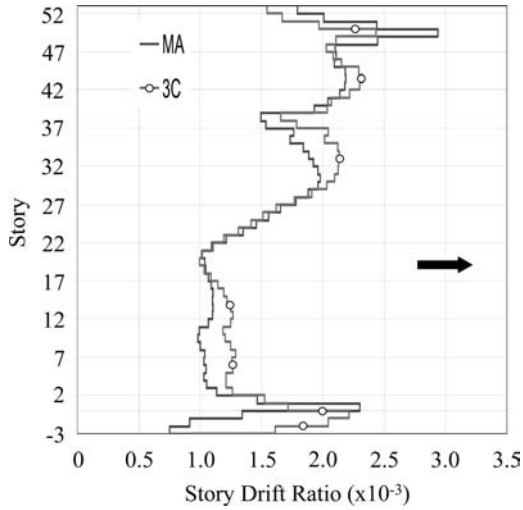

Figure 4. Drift ratios for models MA and #3c.

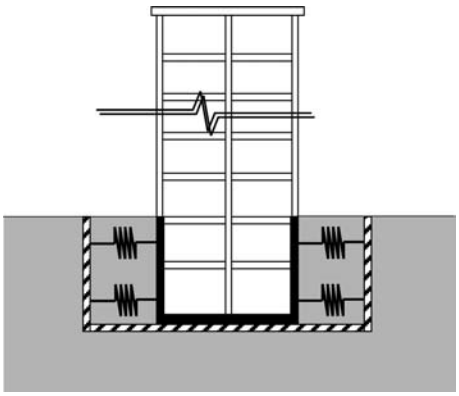

Figure 5. Model #3b.

2.2 *Approximate models*

The simplest model (#3c) is shown in Figure 3.

The building is assumed to rest on a rigid base and is subjected to the free field surface motions. There is no interaction with either the foundation soil or the basement walls. The motion at the ground surface is used as input motion at the rigid base.

The performance of this model is compared with that of the MA model in terms of several different response parameters but, owing to space limitations the comparison is limited here to the inter-storey drifts ratios shown in Figure 4. For such a crude model the results are surprisingly good except in the basement levels where the inter-storey drift ratios are overestimated and near the roof where the drift ratios are underestimated.

The next model #3b (Figure 5) rests on a rigid base but some passive lateral restraint is imposed on the basement walls by springs. The ends of these springs are fixed in rigid vertical walls. Surface motions are used as input at the base.

The drift ratios of this model are compared with those of the MA model in Figure 6. Despite the introduction of some restraint on the basement walls to model the effects of the soil the drift ratios predicted by this model compare very poorly with the ratios from the MA model.

The last model to be considered is model #3d shown in Figure 7. In this model the free field ground motion is applied at ground level in the structure. The response of this model to the Northridge earthquake compares surprisingly well with the MA model as shown in Figure 8. However the drift ratios are overestimated by model #3d in the basement levels and underestimated near the roof.

2.3 *Observations*

Arbitrary selection of simpler models can be risky because the reliability of their response is unknown.

Furthermore it seems that the effectiveness of a simpler model depends on building characteristics such

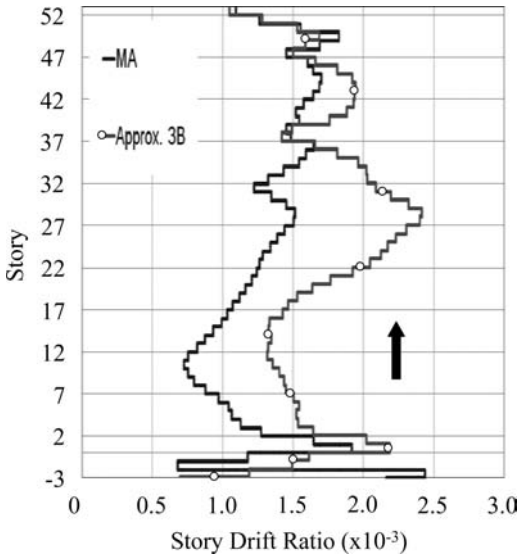

Figure 6. Drift ratios for models MA and #3b.

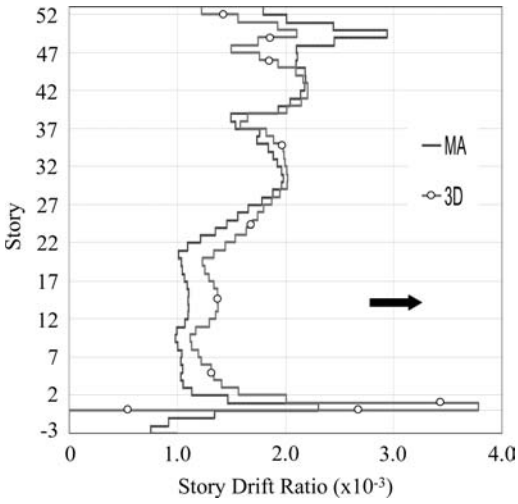

Figure 8. Drift ratios for models MA and #3d.

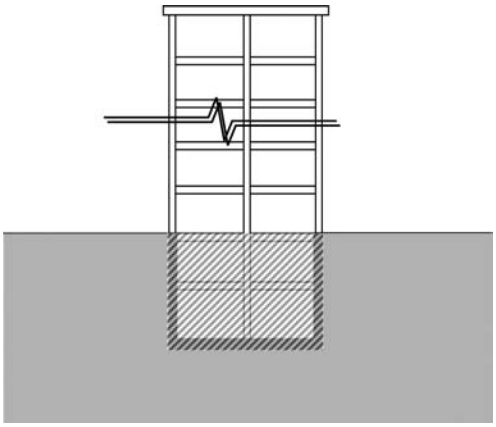

Figure 7. Model #3d.

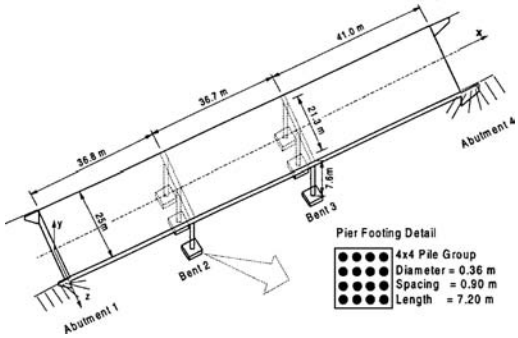

Figure 9. Three span bridge on pile foundations.

as the height of the building and so a model that works well for one building may not be appropriate for another. Behavior of simpler models has not been adequately checked for different building types to provide a data base to guide model development. The selection of the appropriate ground motions for input and the appropriate input location appears to be somewhat arbitrary also.

3 BRIDGE PIERS ON PILES

3.1 *Model bridge*

A three span continuous box girder bridge structure shown in Fig. 9 was chosen for a fundamental study of soil-structure interaction in pile foundations. A rigid base version of this bridge is used as an example in the guide to the seismic design of bridges published by the American Association of State Highway and Transportation Highway Officials, (AASHTO, 1983). The sectional and physical properties of the superstructure and piers were taken from the AASHTO guide.

Each pier is supported on a group of sixteen (4×4) concrete piles. The diameter and length of each pile are 0.36 m and 7.2 m respectively. The piles are spaced at 0.90 m, center to center. The Young's modulus and mass density of the piles are $E = 22{,}000$ MPa and $\rho = 2.6\,\mathrm{Mg\,m^{-3}}$ respectively.

The soil beneath the foundation is assumed to be a nonlinear hysteric continuum with unit weight, $\gamma = 18\,\mathrm{kNm^{-3}}$ and Poisson's ratio, $\nu = 0.35$. The low strain shear modulus of the soil varies as the square root of the depth with values of zero at the surface and 213 MPa at 10 m depth. The variations of shear moduli and damping ratios with shear strain are those recommended by Seed and Idriss (1970) for sand. The surface soil layer overlies a hard stratum at 10 m. For the PILE-3D (Wu & Finn, 1997) finite element mesh, it was divided into 10 sub-layers of varying thicknesses. Sublayer thicknesses decrease towards the surface where

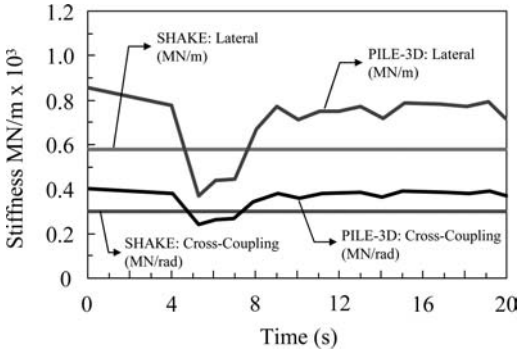

Figure 10. Time histories of kinematic lateral and cross-coupling stiffnesses.

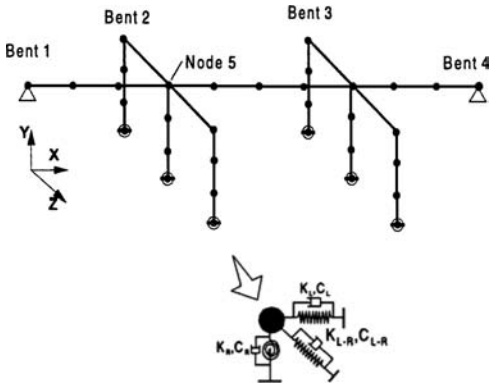

Figure 11. Computational model of the bridge.

soil-pile interaction effects are stronger. 900 brick elements were used to model the soil around the piles and 8 beam elements were used to model each pile. The input acceleration record used in the study was the first 20 seconds of the N-S component of the free field accelerations recorded at CSMIP Station No.89320 at Rio Dell, California during the April 25, 1992 Cape Mendocino Earthquake. The power spectral density of this acceleration record shows that the predominant frequency of the record is 2.2 Hz.

3.2 *Pile cap stiffnesses*

The pile cap stiffnesses of the pile foundation shown in Fig. 9 will be determined for two different ratios of the column/foundation stiffness ratio, 7% and 50%. A PILE 3-D analysis is conducted first and the spatially varying time histories of modulus and damping are stored. Then an associated program PILIMP calculates the time histories of dynamic pile head impedances using the stored data. The dynamic impedances are calculated at any desired frequency by applying a harmonic force of the same frequency to the pile head and calculating the generalized forces for unit displacements. In this paper the focus will be on the stiffnesses only as these are the parameters of primary interest for current practice. However the effects of damping are always included in the analyses.

The stiffnesses are calculated first without taking into account inertial interaction between the superstructure and the pile foundation. This is the usual condition in which stiffness is estimated either by static loading tests, static analysis or by elastic formulae. The stiffnesses are calculated also taking the inertial effects of the superstructure into account. In this latter case both kinematic and inertial interactions are taken into account. Since the entire pile group is being analyzed, pile-soil-pile interaction is automatically taken into account under both linear and non-linear conditions. Therefore the usual difficult problem of what interaction factors to use or what group factor to apply is avoided. Time histories of lateral and cross coupling stiffnesses are shown in Figure 10.

These stiffnesses, resulting from kinematic interaction only, were calculated for the predominant frequency of the input motions, f = 2.2 Hz. It is clearly not an easy matter to select a single representative stiffness to characterize the discrete single valued springs used in structural analysis programs to represent the effects of the foundation. In the absence of a complete analysis, probably a good approach to including the effects of soil nonlinearity on stiffness is to get the vertical distribution of effective moduli by a SHAKE (Schnabel et al, 1972) analysis of the free field and calculate the stiffnesses at the appropriate frequency using PILIMP with these moduli. The constant stiffnesses calculated in this way are shown also in Fig. 10. However these are kinematic stiffnesses. Later it is shown that inertial interaction by the superstructure may cause greater non-linear behavior leading to substantially reduced frequencies. The SHAKE analysis cannot capture this effect.

4 SEISMIC RESPONSE OF CODE BRIDGE TO TRANSVERSE EARTHQUAKE LOADING

4.1 *Model of the bridge*

A three dimensional space frame model of the bridge is shown in Fig. 11.

At the abutments, the deck is free to translate in the longitudinal direction but restrained in the transverse and vertical directions. Rotation of the deck is allowed about all three axes. The space frame members are modeled using two 8-noded 3-D beam elements with twelve degrees of freedom, six degrees at each end. The bridge deck was modeled using 13 beam elements and each pier was modeled by 3 beam elements. The cap beam that connects the tops of adjacent piers was modeled using a single beam element. The sectional and physical properties of the deck and the piers are those provided in the AASHTO Guide (1983). The pier foundation is modeled using a set of time-dependent nonlinear springs and dashpots that simulate exactly the time histories of stiffnesses and damping from the PILE-3D analyses.

The response of the bridge structure was analyzed for different foundation conditions to study the

influence of various approximations to foundation stiffnesses and damping, using the computer program BRIDGE-NL. The free field acceleration was used as the input acceleration and the peak acceleration was set to 0.5 g.

4.2 *Foundation conditions for analyses*

The seismic response of the bridge to transverse earthquake loading was analyzed for the four different foundation conditions listed below.

1. Rigid foundation and fixed base condition is assumed.
2. Flexible foundation with elastic stiffness and damping.
3. Flexible foundation with kinematic time dependent stiffness and damping.
4. Flexible foundation with stiffness and damping based on the 'SHAKE' effective moduli.

The fundamental transverse mode frequency of the computational model of the bridge structure with a fixed base was found to be 3.18 *Hz*. This is the frequency quoted in the AASHTO-83 guide. This agreement in fundamental frequencies indicates an acceptable structural model. In this analysis, the lateral stiffness of the bridge pier is only 7% of the foundation stiffness. For this extremely low stiffness ratio, the columns control the fundamental frequency of the bridge and the influence of the foundation is negligible. Results from analyses in which the column/foundation stiffness ratio is 50% will be presented here. The stiffness ratio was raised by increasing the stiffness of the piers only, with no changes to the super-structure. Normally much stiffer piers would imply a heavier superstructure and therefore higher inertial forces.

For a 50% stiffness ratio, the fixed base fundamental frequency of the bridge is 5.82 Hz. When the stiffnesses associated with low strain initial moduli are used, the fundamental frequency is 4.42 Hz, a 24% reduction from the fixed base frequency. With kinematic strain dependent stiffnesses, the frequency reached to a minimum value of 3.97 Hz during strong shaking, a 32% reduction from the fixed base frequency. When the foundation stiffnesses are based on effective shear moduli from a SHAKE analysis of the free field, the frequency was 4.18 Hz, a 28% change from the fixed base frequency. Fig. 12 shows the variation with time in fundamental transverse modal frequency for the different foundation conditions.

4.3 *Inertial interaction of structure and pile*

The time dependent stiffnesses used in the analyses described above were computed without taking the inertial interaction of superstructure and foundation into account. The primary effect of this interaction is to increase the lateral pile displacements and cause greater strains in the soil. This in turn leads to smaller moduli and increased damping. The preferred method of capturing the effect of superstructure interaction is

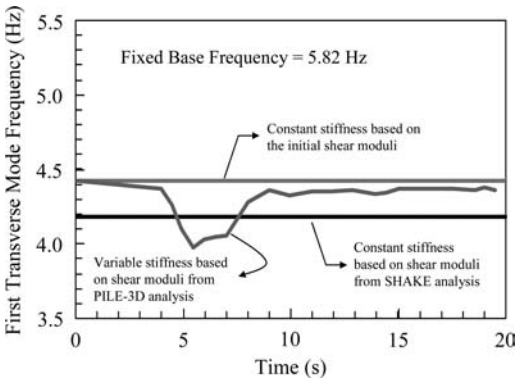

Figure 12. Time history of transverse modal frequencies for different foundation conditions.

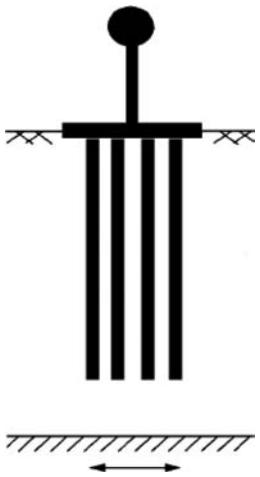

Figure 13. Pile foundation with superstructures.

to consider the bridge structure and the foundation as a fully coupled system in the finite element analysis. However, such a fully coupled analysis is not possible with current commercial structural software. Even if it were, it would not be feasible in practice because it would require enormous amounts of computational storage and time using the more sophisticated computer codes.

An approximate way of including the effect of superstructure interaction is to use the model shown in Fig. 13. In this model, the superstructure is represented by a single degree of freedom (SDOF) system. The mass of the SDOF system is assumed to be the portion of the superstructure mass carried by the foundation. The stiffness of the SDOF system is selected so that the system has the period of the mode of interest of the fixed base bridge structure.

This approximate approach will be demonstrated by the analysis of the center pier at Bent 2. The fundamental transverse mode frequency of the fixed base model was found earlier to be 5.82 Hz. The static portion of the mass carried by the center pier is 370 Mg.

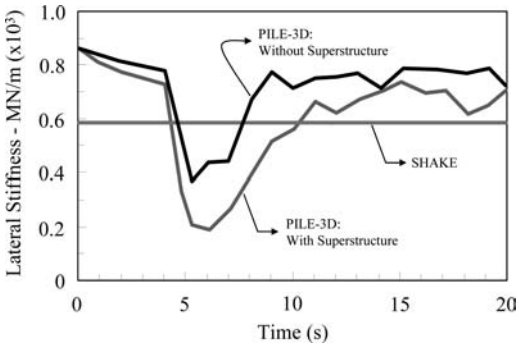

Figure 14. Effect of inertial interaction on lateral pile cap stiffness.

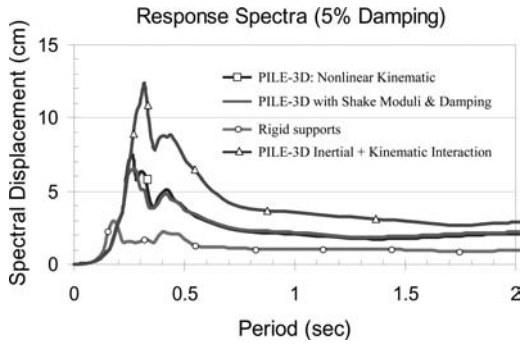

Figure 15. Spectral displacements of bridge for 4 different foundation conditions.

The superstructure can be represented by a SDOF system having a mass of 370 Mg at the same height as the pier top and frequency 5.82 Hz. The corresponding stiffness of the SDOF system is 495 MN/m.

A coupled soil-pile-structure interaction analysis can be carried out using PILE-3D by incorporating the SDOF model into the finite element model of the pile foundation. The pile foundation stiffnesses derived from this finite element model incorporate the effects of both inertial and kinematic interactions and are called total stiffnesses. The time histories of stiffnesses with and without the superstructure are shown in Figure 14.

The reduction in lateral stiffness is greater throughout the shaking, when the inertial interaction is included. There is a similar reduction in the rotational and cross-coupling stiffnesses. When inertial interaction is included, the lateral stiffness reached a minimum of 188 MN/m which is 22% of the initial value. When the inertial interaction was not included, the minimum was 400 MN/m. Clearly in this case, inertial interaction has a major effect on foundation stiffness.

The results of the analyses for four different foundation conditions are summarized in the displacement spectra for transverse vibrations of the bridge, shown in Figure 15. The displacement spectra clearly show the importance of including inertial interaction, when calculating foundation stiffnesses in this case. The fixed base model for estimating response is inadequate. As the ratio of super-structural stiffness to foundation stiffness is reduced, the effect of inertial interaction on system frequency is reduced and kinematic stiffnesses become adequate. Only for low stiffness ratios is the fixed base model adequate.

For the example bridge, when effective moduli from a SHAKE analysis of the free field are used in an elastic analysis to obtain a discrete, foundation stiffness for each degree of freedom, the corresponding system frequencies lead to acceleration and displacement responses very close to the responses from a PILE-3D nonlinear analysis. This is true when the complete pile foundation is included in the analysis. It may or may not be true, if the effective moduli are used to get the stiffness of a single pile and the stiffness of the pile group is developed from this with the help of empirical factors for group effects. This result suggests that kinematic stiffnesses may be obtained taking nonlinear soil effects into account, by an elastic structural program that can model the pile group foundation, if the effective moduli from a SHAKE analysis are used. This needs to be verified by a few more case histories.

A more detailed discussion of soil-structure interaction of pile foundation and a critical review of foundation springs used in practice may be found in Finn (2005).

5 AN EXAMPLE FROM PRACTICE

A description of the determination of the pile head stiffness matrix for a very important California bridge is presented to demonstrate the high level of geotechnical practice that can be applied to critical structures. One of the bridge bents is shown in Figure 16. The action of the soils on the pile foundation is represented by nonlinear springs, which were linearized for the calculation of the stiffness matrix. The pile foundation was analyzed without the superstructure and so the stiffness matrix is kinematic. The pile cap was replaced by rigid links witch were connected to a master node. The kinematic stiffness matrix and the kinematics motions calculated at the node are applied to base of the computational model of the superstructure shown in Figure 17.

Although the procedure followed in developing the computational model in Figure 16 follows the highest level of current practice, the effectiveness of the model is subject to considerable uncertainty. There are three major sources of uncertainty; the potential impact of inertial interaction which is not addressed in the modeling, the appropriateness of the kinematic input motions as input motions and the reliability of the interaction springs in representing the soil-pile interaction. The study of the seismic response of the AASHTO bridge, described above, has illustrated the potential impact of inertial effects and when kinematic ground motions may be appropriate. The reliability of the

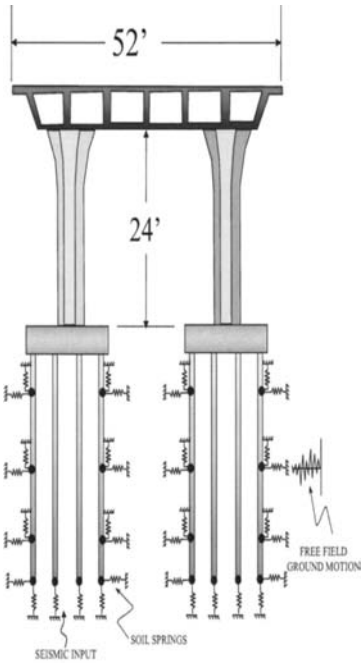

Figure 16. Computational model of bridge bent including pile foundation.

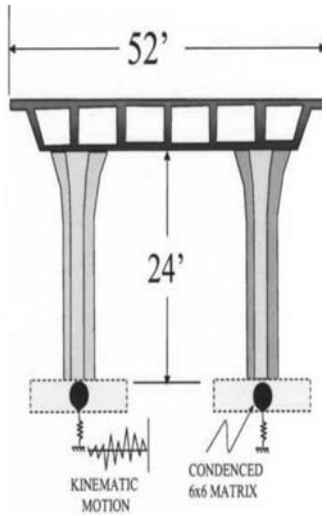

Figure 17. Computational model of bridge superstructure.

interaction springs could not be discussed here because of space limitations but is critically reviewed in some detail in Finn (2005), where the opinion is expressed that the reliability of the springs is not very high.

6 CONCLUDING REMARKS

The coupled analysis of structures and foundations is not a feasible option in engineering practice at present because of practical difficulties with the analysis. Therefore the analysis is conducted on a purely structural model with add-ons, usually linear or nonlinear springs, to simulate soil structure effects. The uncertainties inherent in these uncoupled systems needs to be more fully documented. The sensitivity of response to spring characteristics is especially important.

Naeim et al. (2008) have demonstrated that computational models that completely neglect soil-structure interaction may yield useful results for very tall buildings with several basement levels. Presumably in very tall buildings, the response is relatively insensitive to interaction effects near the base in a structural response version of St. Venant's principle. It would be interesting to explore the range in heights over which these crude models work satisfactorily.

ACKNOWLEDGEMENTS

The author is very grateful to 3 reviewers whose perceptive comments and suggestions did much to improve the presentation.

REFERENCES

AASHTO, 1983. *Guide specifications for seismic design of highway bridges*. American Association of State Highway and Transportation Officials, Washington, DC, USA.

Finn W. D. Liam, 2004. Characterizing pile foundations for evaluation of performance based seismic design of critical lifeline structures, I*nvited keynote lecture, 13th WCEE*, Vancouver, BC, Canada, August.

Finn, W. D. Liam 2005. A Study of Piles during Earthquakes: Issues of Design and Analysis, *Bulletin of Earthquake Engineering*, 3:141–234

Naeim F., Stewart J., Tileylioglu S & Amoradi A. 2008, Impact of Foundation Modeling on the accuracy of seismic response history analysis, Seminar on Time History Analysis, *University of British Columbia*, Vancouver, BC, 14–15 November.

Schnabel PB, Lysmer J, & Seed HB. 1972. "SHAKE: A computer program for earthquake response analysis of horizontally layered sites." *Report No. EERC72-12*, Earthquake Engineering Research Center, University of California, Berkeley, CA.

Seed HB, Idriss IM. 1970 "Soil moduli and damping factors for dynamic response analysis." *Report No. EERC70-10*, Earthquake Engineering Research Center, University of California, Berkeley, CA.

Wu G, Finn WD Liam. 1997. "Dynamic nonlinear analysis of pile foundations using the finite element method in the time domain." *Canadian Geotechnical Journal*, (34), 144–152.

Soil-Foundation-Structure Interaction – Orense, Chouw & Pender (eds)
© 2010 Taylor & Francis Group, London, ISBN 978-0-415-60040-8

A robust probabilistic evaluation of soil-foundation-structure interaction effects on structural response

M. Moghaddasi, M. Cubrinovski, S. Pampanin & A. Carr
Department of Civil and Natural Resources Engineering, University of Canterbury, New Zealand

J.G. Chase
Mechanical Engineering Department, University of Canterbury, New Zealand

ABSTRACT: Evaluation of soil-foundation-structure interaction (SFSI) effects on structural response is a challenging task because of the involved impact of uncertainties in system's parameters and randomness in the input earthquake motion. In this paper, a rational method is utilized to elucidate these effects through the use of a rheological soil-foundation-structure model in a robust probabilistic simulation. Realistic, but random models with varied soil and structural parameters within relevant range of values are generated out of a Monte Carlo simulation and subjected to an ensemble of earthquake motions. Both linear and nonlinear structural behavior due to earthquake motion is considered. The SFSI effects on linear structural response are quantified by the median response and the accompanied dispersion and are then used as a reference when evaluating the SFSI effects for superstructures with nonlinear behavior. In addition, for the structural systems with linear behavior detrimental SFSI scenarios are identified. The achieved quantification of SFSI effects can be used as a significant step towards a reliable seismic design framework incorporating SFSI. Note that in all analyses the nonlinearity in soil behavior has been accounted for through the equivalent linear approach.

1 INTRODUCTION

A robust evaluation of soil-foundation-structure interaction (SFSI) effects on structural response with a consistent outcome needs to consider the combined impact of the uncertainty in soil and structural parameters along with the inherent randomness of the input ground motion. Without respecting this fact and based on the traditional quantification of SFSI effects via period lengthening and damping increase (Jennings & Bielak 1973, Veletsos & Meek 1974, Veletsos & Nair 1975), it has been concluded and implemented in major design codes (ATC-3-06 1984, FEMA 440 2005) that SFSI consideration in the dynamics analysis is beneficial. However, it has been also recognized that soil-structure interaction effects may be detrimental (Gazetas & Mylonakis 1998, Mylonakis & Gazetas 2000, Dutta & Bhattacharya 2004) and increase the structural response as compared to a fixed base model. To overcome these controversies, probabilistic approaches have gained a growing attention to investigate SFSI effects on the structural response (Jin & Lutes 2000, Moghaddasi et al. 2009, Lutes et al. 2000).

In this study, the effects of soil and structural variability have been investigated in conjunction with the randomness of the input earthquake motion. An idealized, but commonly accepted soil-shallow foundation-structure (SFS) model was adopted for the analysis representing the superstructure as a SDOF system and the soil-foundation element as an equivalent linear cone model with frequency independent coefficients (Wolf 1994, Stewart 2003). Two series of analyses were conducted in which the superstructure was modeled as a linear or nonlinear system respectively in order to investigate the effect of structural nonlinearity in the SFSI problem. A Monte Carlo simulation was utilized to generate all the random parameters of the analytical model in such a way that all generated models represent realistic soil-foundation-structure systems. The generated SFS models were then subjected to a suite of 40 earthquake motions recorded on stiff/soft soils to account for variability in the input motion characteristics. Hence, soil, structural and earthquake motion variability were systematically covered in the analyses.

As a result of this numerical study, the effects of SFSI on the linear structural response were investigated by using the median response and associated dispersion to build up a conceptual understanding of the SFSI effects and evaluate the prevailing engineering view implemented in the seismic design codes. Following this quantification, cases with detrimental effects were scrutinized in order to identify a relation between characteristics of the SFSI system and earthquake that causes increased structural response when SFSI effects are incorporated. Finally, the influence of structural nonlinearity in the SFSI problem was evaluated by comparing the median structural responses in linear and nonlinear structural systems.

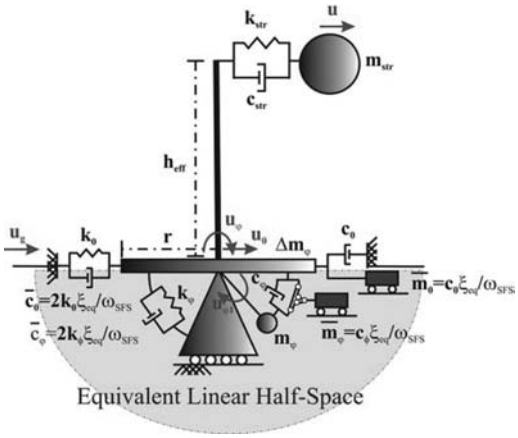

Figure 1. Dynamic soil-shallow foundation-structure model for horizontal and rocking foundation motions.

2 PROBABILISTIC SIMULATIONS

2.1 *Methodology*

To elucidate the effects of SFSI on the structural response, a probabilistic simulation using a wide range of SFS systems subjected to a range of earthquake motions with different characteristics were considered. A fairly simple rheological SFS model (defined in Sec. 2.2) was implemented in the analyses. Its parameters were systematically defined randomly through a Monte Carlo simulation by carefully ensuring to satisfy the requirements of realistic SFS models and nonlinear soil behavior (explained in Sec. 2.3). The generated SFS models were then imposed to an ensemble of 40 earthquake ground motions recorded on stiff/soft soils to account for variability in the input motion spectrum and type (introduced in Sec. 2.4). A closed-form solution programmed in MATLAB was used for the analyses with linear structures whereas the analyses with nonlinear superstructures were conducted using an FEM code (Ruaumoko 2D). Results from the analyses were illustrated through a comprehensive statistical presentation, described in Section 2.5.

2.2 *Soil-shallow foundation-structure model*

The adopted SFS model was constructed by a single-degree-of-freedom (SDOF) superstructure linked to a lumped-parameter soil-foundation element as shown in Figure 1. The superstructure is modeled by a mass-spring-dashpot system which is connected to a rigid link with the height of h_{eff}. This system is characterized by: structural mass participating in the structural fundamental mode of vibration, m_{str}, structural lateral stiffness, k_{str}, and 5% equivalent viscous damping at structural fundamental frequency.

Structural nonlinearity due to earthquake motion was considered through two types of hysteretic model: Takeda degrading stiffness (TKDS) and bilinear elasto-plastic (BLEP) representing the concrete-framed and steel-framed structures respectively.

The soil-foundation interface was modeled by a lumped-parameter element with frequency independent coefficients. It represents a rigid circular shallow foundation resting on an equivalent linear soil half-space. To define the parameters of this element, the parameters of the presented model by Wolf (1994), which are based on linear viscoelastic half-space, were modified consistent with the conventional equivalent linear method (Seed 1970). This approach is based on representing the soil nonlinearity by choosing the secant stiffness and the equivalent damping which are compatible with the free-field strains. The adopted coefficients of the soil-foundation element are:

1 Horizontal stiffness and damping:

$$k_0 = \frac{8G_{sec}r}{2-\nu},\ c_0 = \rho(V_s)_{sec}A \tag{1}$$

2 Rocking stiffness:

$$k_\varphi = \frac{8G_{sec}r^3}{3(1-\nu)} \tag{2}$$

3 Rocking damping:

$$\text{if } \nu \le 1/3:\ c_\varphi = \rho(V_p)_{sec}I_r \tag{3a}$$

$$\text{if } 1/3 \le \nu \le 1/2:\ c_\varphi = \rho[2(V_s)_{sec}]I_r \tag{3b}$$

4 Rocking added mass:

$$\text{if } 1/3 \le \nu \le 1/2:\ \Delta m_\varphi = 1.2(\nu - 1/3)\rho I_r r \tag{4}$$

5 Rocking internal mass moment of inertia:

$$\text{if } \nu \le 1/3:\ m_\varphi = \frac{9\pi}{32}\rho I_r r(1-\nu)[(\frac{V_p}{V_s})_{sec}]^2 \tag{5a}$$

$$\text{if } \nu \le 1/3:\ m_\varphi = \frac{9\pi}{32}\rho I_r r(1-\nu)[(\frac{V_p}{V_s})_{sec}]^2 \tag{5a}$$

where r is the equivalent radius of the foundation, A is the area of the foundation ($A=\pi r^2$), I_r is the mass moment of inertia for rocking motion ($I_r=\pi r^4/4$), and ρ, υ, $(V_s)_{sec}$, $(V_p)_{sec}$, G_{sec} are soil mass density, Poisson's ratio, soil shear wave velocity, soil longitudinal wave velocity and soil shear modulus, respectively.

Material damping due to soil nonlinearity was implemented in the adopted soil-foundation element by making use of classical Voigt model of viscoelasticity. It was assumed to augment each original spring (with stiffness of k_i) by an additional parallel connected dashpot of $\bar{c}_i$ where:

$$\bar{c}_i = 2k_i(\xi_{eq}/\omega_{SFS}) \tag{6}$$

and each original dashpot (with damping of c_i) by an additional parallel connected inertial mass of $\bar{m}_i$ where:

$$\bar{m}_i = c_i(\xi_{eq}/\omega_{SFS}) \tag{7}$$

Here, ξ_{eq} is an equivalent material damping and ω_{SFS} is the effective frequency of the SFS system

($\omega_{SFS} = 2\pi/T_{SFS}$). Index i can be either *0* or ϕ representing the modification in horizontal or rocking directions respectively.

2.3 *Generation of models with random parameters*

To investigate the SFSI effects on structural response, a design spectrum style was selected. In this spectrum, a period range of 0.2, 0.3… 1.8 sec was defined to: (*i*) represent the fixed-base (FB) superstructures with total height of 3–30 m and (*ii*) satisfy the period-height relationship introduced in New Zealand Standard (NZS1170.5). For each considered period (T_{FB}), 1000 SFS models were generated via assembling the randomly defined parameters for the soil-foundation-superstructure system. These parameters are defined either by random selection from a defined range or by using predefined parameters in a commonly accepted relationship. The number 1000 was chosen with the intention to: (*i*) give the best fit uniform distribution for the randomly selected parameters and (*ii*) increase the accuracy of the Monte-Carlo simulation compared to the exact expected solution (Fishman 1995). The procedure adopted in defining the parameters is elaborated below:

1. Initial soil shear wave velocity [$(V_s)_0$] was selected in the range between 80 and 360 m/sec representing soft to relatively stiff soils.
2. Shear wave velocity degradation ratio [$(V_s)_{sec}/(V_s)_0$] was selected from the variation range of 0.15-0.7. This degradation range is resulted from using a representative shear wave velocity reduction curve for sand and assuming the range of 0.1–1% for induced shear strain in the soil due to the earthquake motion. The shear strain range was selected as a representative ground response considering the fact that the employed earthquake motions have magnitudes between 6.2 and 7.6, and source-to-site distances of less than 40 km.
3. Soil mass density [ρ] was selected from the variation range of 1600–1900 kg/m^3.
4. Poisson's ratio [υ] was selected from the variation range of 0.3–0.45.
5. Degraded shear modulus [G_{sec}] was defined through the previously introduced degraded shear wave velocity, $(V_s)_{sec}$ as:

$$G_{sec} = \rho(V_s)_{sec}^2 \tag{8}$$

6. Soil material damping [ξ_{eq}] was defined as a constant value by implementing $(V_s)_{sec}/(V_s)_0$ ratio in the following expression:

$$\frac{25-\xi_{eq}}{25-10} = \frac{(V_s)_{sec}/(V_s)_0 - 0.15}{0.7-0.15} \tag{9}$$

   To define equation 9, a representative damping curve for sand corresponding to the utilized shear wave velocity reduction curve and increasing with shear strain has been used. A linear link was established between the level of degradation in shear wave velocity and hysteretic damping in the soil to represent 10–25% damping ratios for degradation ratios of 0.7–0.15 respectively.
7. Effective height of the superstructure [h_{eff}] was selected from the variation ranges defined in Table 2. These limitations are based on: (*i*) a typical period-height relationship adopted in NZS 1170.5 and (*ii*) the considered limitation for the structural total height, 3–30 m.
8. Foundation radius [r] was selected from variation range defined in Table 2. To define these limitations, the building aspect ratio (h_{eff}/r) was used. It was assumed that h_{eff}/r ratio for conventional building structures varies in between 1 and 4 and also r is limited to the range of 2–12 m, representing structures having 1–3 bays with length of 4–8 m each.
9. Structural mass [m_{str}] was defined based on relative mass index ($\bar{m}$), which is defined as:

$$\overline{m} = \frac{m_{str}}{\rho r^2 h_{eff}} \tag{8}$$

   A uniform distribution for $\overline{m}$ within the range of 0.4–0.6 representing conventional building structures (Stewart 1999) was considered and the predefined values for ρ, r and h were implemented in Equation 8 to define $\overline{m}$.
10. Initial structural stiffness [$(k_{str})_i$]: was defined by implementing the predefined values of m_{str} in:

$$(k_{str})_i = \frac{4\pi^2}{T_{FB}^2} m_{str} \tag{10}$$

11. Structural damping coefficient [c_{str}] was defined by implementing the predefined values for m_{str} and $(k_{str})_i$ in:

$$c_{str} = 2(0.05)\sqrt{(k_{str})_i m_{str}} \tag{11}$$

12. Predominant period of the SFS system [T_{SFS}] was defined as:

$$T_{SFS} = T_{FB}\sqrt{1 + \frac{(k_{str})_i}{k_0} + \frac{(k_{str})_i h^2}{k_\varphi}} \tag{12}$$

Table 1. Ranges of variation for h_{eff}.

T_{FB} (sec)	h_{eff} (m)
0.2… 0.32	2… $26.8T_{FB}^{1.33}$
0.32… 0.8	$9.1T_{FB}^{1.33}$… $26.8T_{FB}^{1.33}$
0.8… 1.8	$(9.1T_{FB}^{1.33})$… 20

Table 2. Ranges of variation for r.

h_{eff} (m)	r (m)
2… 8	2…h_{eff}
8… 12	$(h_{eff}/4)$… h_{eff}
12… 20	$(h_{eff}/4)$…12

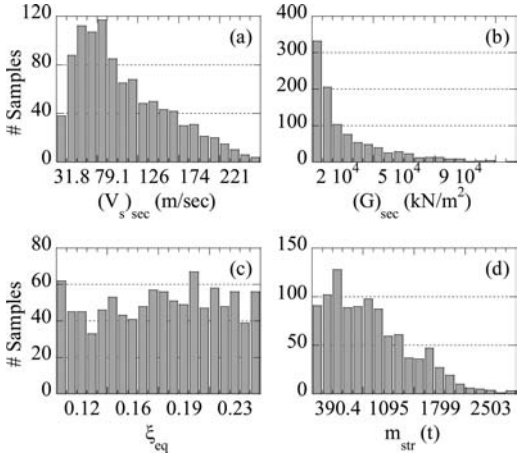

Figure 2. Distributions of randomly generated models for $T_{FB} = 1.0$ sec: (a) degraded shear wave velocity, (b) degraded shear modulus (c) soil material damping and (d) structural mass.

As an example of randomly generated distributions used in the analyses, Figure 2 illustrates the distribution of $(V_s)_{sec}$, G_{sec}, ξ_{eq} and m_{str} for a superstructure with a fixed base period of $T_{FB} = 1.0$ sec.

2.4 *Selection of input earthquake motions*

A suite of 40 earthquake motions recorded on stiff/soft soil (specifically, type C and D based on USGS classification) was used in the adopted time-history simulations. The number 40 was chosen to obtain an estimate of median response within a factor ± 0.1 with 95% confidence (Shome et al. 1998). The records were constrained as follows: (*i*) the magnitude in the range of 6.5–7.5, (*ii*) the closest source-to-site distance in the range of 15–40 km and (*iii*) the peak ground acceleration (PGA) greater than 0.1 g.

The selected records were then scaled to have reasonably distributed PGAs within the range of 0.3–0.8 g, assuming that a nonlinear behavior of the superstructure will be caused by those levels of intensity. Respecting rigorous scaling criteria and recommendations in NZS 1170.5, all scaling factors were chosen to be less than 3.0.

2.5 *Presentation of results from the analyses*

Two aspects of structural response were considered for this investigation: (*i*) structural distortion, u, and (*ii*) structural total displacement, u_{str}. Structural distortion is the horizontal displacement of the superstructure relative to the foundation that represents the transmitted displacement/force to the superstructure. The structural total displacement is defined as the summation of the horizontal foundation displacement, structural lateral displacement due to foundation rocking and structural distortion, and it represents the expected top floor displacement.

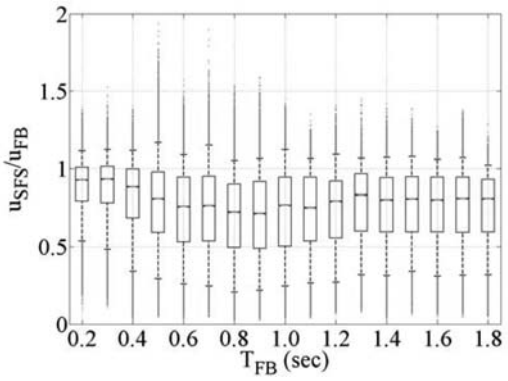

Figure 3. Structural distortion modification spectrum.

In order to simplify the presentation of the results from numerous time-history simulations, only the maximum values of the selected structural response parameters were considered. These values are presented in a normalized format as a ratio with respect to the results obtained from corresponding fixed base (FB) systems when subjected to the same earthquake excitation. Based on this type of presentation, SFSI is recognized to be detrimental when: (*i*) structural distortion modification factor, u_{SFS}/u_{FB}, is greater than unity; or (*ii*) structural total displacement modification factor, $(u_{str})_{SFS}/(u_{str})_{FB}$, is greater than unity.

The resulted normalized values are presented in a box and whisker plot format to characterize the central tendency (median) and the accompanied dispersion at different levels of probability. In a box and whisker plot, the box has lines at 25th percentile (bottom line), median (middle line), and 75th percentile (top line) values. Whiskers extend from each end of the box to the 5th percentile and 95th percentile respectively. Outliers are the data with values beyond those indicated by the whiskers.

3 RESULTS AND DISCUSSION

3.1 *SFSI effects on linear structures*

Figure 3 illustrates the results for u_{SFS}/u_{FB} (structural distortion modification factor) for all groups of SFS models categorized based on T_{FB}. Clearly, consideration of SFSI may cause structural distortion to be increased in some cases even up to 1.8 times; however, the median of the u_{SFS}/u_{FB} ratio is less than unity through all period ranges. The evaluated risk of having detrimental effects in terms of structural distortion is in the order of 20–30% for stiff structures ($T_{FB} < 0.5$ sec) and 10–15% for more flexible structures, as shown in Figure 3.

The impact of SFSI consideration on the structural total displacement is shown in Figure 4 by presenting $(u_{str})_{SFS}/(u_{str})_{FB}$ (structural total displacement modification factor). Noticeably, foundation flexibility may cause structural total displacement to increase as much

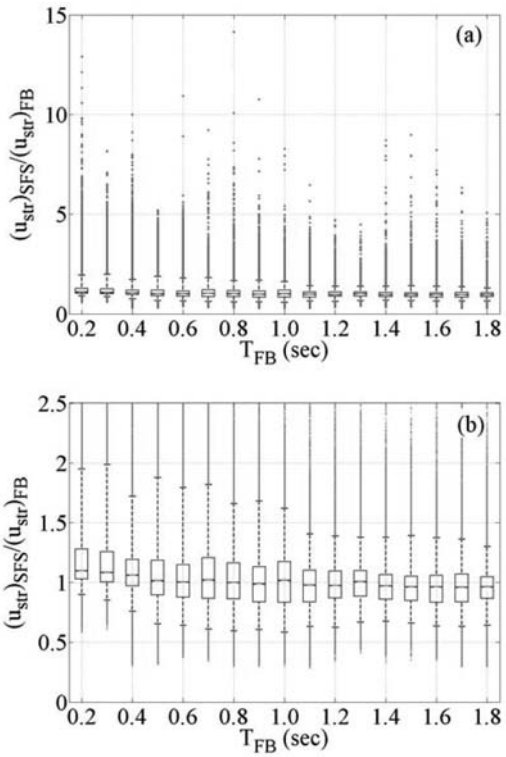

Figure 4. Structural total displacement modification spectrum in: (a) global view, (b) close view around unity.

as 15 times, however, in 50% or more of all cases, it does not cause a significant change in the response. The risk of detrimental effects in this case of structural total displacement is in the order of 50–80% for stiff structures ($T_{FB} < 0.5$ sec) and 40–50% for more flexible structures.

3.2 *Identification of detrimental SFSI scenarios in terms of structural strength demand*

Since it is recognized that SFSI consideration can cause an increase in the structural distortion (or strength demand in linear analysis), contradicting to the prevailing view in most conventional building design codes (ATC-3-06 1984, FEMA 440 2005), it is important to identify scenarios for which consideration of SFSI effects will cause an increase in the structural response. As already perceived, it is the combined effect of SFS system properties and the earthquake motion characteristics that may result in detrimental SFSI effects on structural responses. This fact is demonstrated in Figure 5, as an example, by the histogram of earthquake motions causing an amplification in structural distortion for the set of models with $T_{FB} = 1.0$ sec. Clearly, for some earthquake motions the SFSI effects increased the structural response for many soil-foundation-structure models while for other earthquakes the SFSI effects were either trivial or absent.

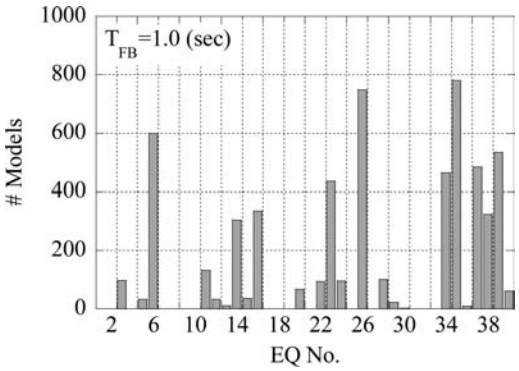

Figure 5. Histogram of the earthquake motions causing $u_{SFS}/u_{FB} > 1.0$ for group of models with $T_{FB} = 1.0$ sec.

In order to investigate what characteristic of the motion makes an earthquake to produce an amplification in the structural response, the maximum acceleration response of the SFS models are compared with the maximum acceleration response of the FB models (acceleration response spectrum) for two types of earthquakes: one with significant detrimental effects (increase in the structural response due to SFSI effects) and the other with no detrimental effects. Figure 6 shows this comparison for models with $T_{FB} = 1.0$ sec and for earthquakes number 23 and 2, where $(S_a)_{EQ}$, $(a_t)_{FB}$ and $(a_t)_{SFS}$ are the earthquake acceleration response spectrum, acceleration response for the FB model and the corresponding SFS models respectively. As illustrated in this figure, the response of SFS models (points represented by hollow circle) nearly follows the acceleration response spectrum of the earthquake (solid line), however, it could be either beyond or bellow the spectrum line. The key difference between the two spectra presented in Figures 6a and 6b is that for periods slightly greater than T_{FB} they show an ascending or descending branch in the spectrum respectively.

The observed behavior could be conceptually summarized as depicted in Figure 7. The figure indicates that in order to define whether SFSI consideration is beneficial or detrimental, the response of two systems: (*i*) the original FB system and (*ii*) the equivalent FB counterpart of the original SFS system needs to be compared using the acceleration spectrum of the earthquake input motion. Note that the equivalent FB system is defined as a FB system with the same mass and stiffness as the original SFS system but with a modification in the structural damping. This equivalent system is also subjected to a modified input earthquake motion. The period of the SFS system (which is also equals to the period of the equivalent fixed-base system) is always greater than the period of the original fixed-base system ($T_{SFS} > T_{FB}$); hence, due to this period shift, the response of the original FB system, $S_a(T_{FB})$, is shifted to $Sa(T_{SFS})$ on the earthquake spectrum. In addition, as a result of the modification in damping of the superstructure and the imposed input

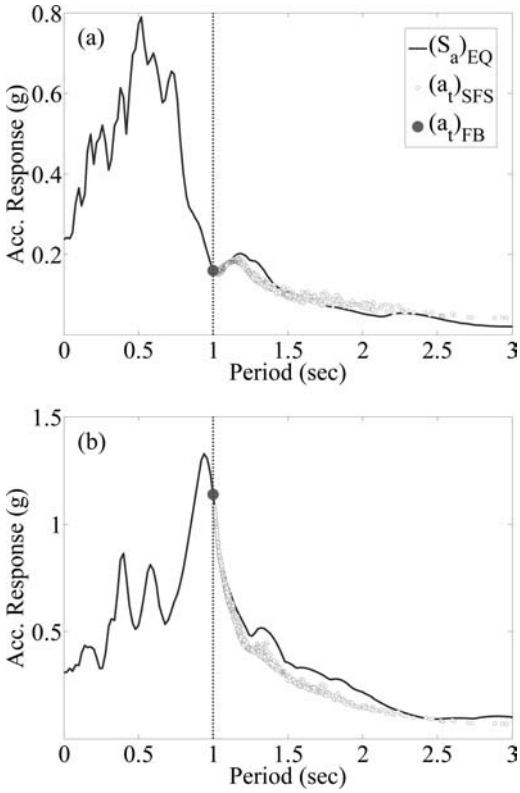

Figure 6. Comparison between the earthquake acceleration response spectrum and the acceleration response of the SFS systems for: (a) EQ 23 (PGA = 0.24 g) and (b) EQ 2 (PGA = 0.31 g) at $T_{FB} = 1.0$ sec.

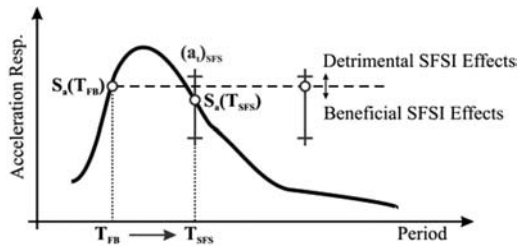

Figure 7. Conceptual presentation of SFSI detrimental/ beneficial effects.

earthquake, the actual response of the equivalent FB system, $(a_t)_{SFS}$, varies either beyond or bellow $S_a(T_{FB})$. Based on this reasoning, if the resulting $(a_t)_{SFS}$ is greater than $S_a(T_{FB})$, then detrimental SFS effects are expected. Clearly, depending on the earthquake spectrum characteristics in the region of the fundamental periods of the FB system and respective SFS system, SFSI may results either in detrimental or beneficial effects.

In order to quantify the variation of $(a_t)_{SFS}/S_a(T_{FB})$, its probability of occurrence through the related

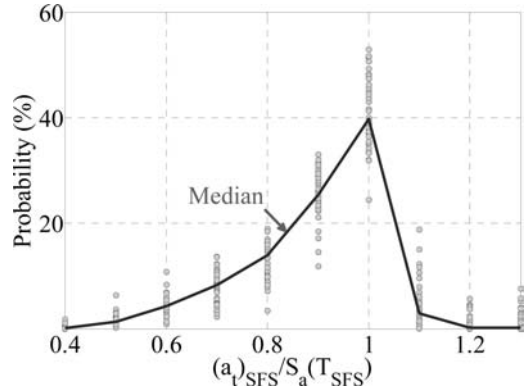

Figure 8. Probability of $(a_t)_{SFS}/S_a(T_{SFS})$ ratio for all EQs and models.

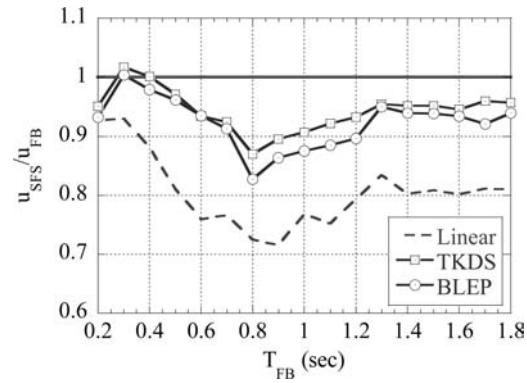

Figure 9. Comparison between median structural distortions for Linear, TKDS and BLEP structural systems.

variation range was evaluated. Figure 8 illustrates this quantification. In this figure, each circle represents the probability of a certain value of $(a_t)_{SFS}/S_a(T_{FB})$ among all the resulted values of $(a_t)_{SFS}/S_a(T_{FB})$ for an earthquake motion and all models. In addition, Figure 8 shows the median probability curve which is produced to represent the likelihood of $(a_t)_{SFS}/S_a(T_{FB})$ for 50% of the cases and more. Clearly, $(a_t)_{SFS}/S_a(T_{FB})$ ratio varies between 0.4–1.3 and it is more probable to vary in the range of 0.8–1.

3.3 *Effects of structural nonlinearity*

To investigate the influence of structural nonlinearity on the SFSI effects, Figures 9 and 10 compare the median values of the modification in structural distortion and structural total displacement between all three considered structural systems (Linear, TKDS and BLEP), respectively.

As illustrated in Figure 9, for 50% of the cases, consideration of SFSI in nonlinear structural systems causes a reduction in the expected deformation of the superstructure similar to what is observed in

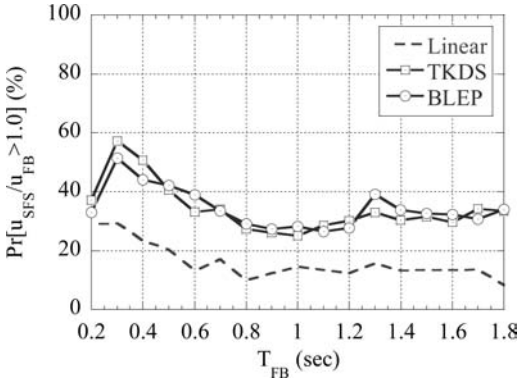

Figure 10. Probability of increase in structural distortion due to SFSI effects.

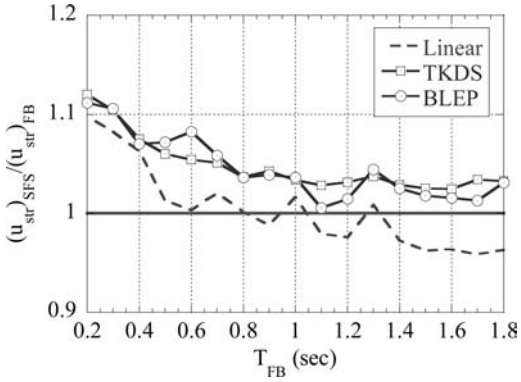

Figure 11. Comparison between median structural total displacements for Linear, TKDS, BLEP structural systems.

linear cases. However, the expected reduction factor decreases due to nonlinearity in structural behavior. In Figure 10, the probability of the cases in which SFSI increases structural distortion ($u_{SFS}/u_{FB} > 1.0$) is shown. The probability value is between 10–30% for linear structural systems while it increases to 30–60% due to structural nonlinear behavior. From the presented results in Figures 9 and 10, it can be concluded that SFSI effect on structural distortion is more pronounced when structures exhibiting nonlinear behavior.

In terms of structural total displacement, as shown in Figure 11, for the 50th percentile response, an amplification ratio up to 1.1 is observed for nonlinear structural systems. Noted that for linear structural systems, except for stiff structures ($T_{FB} < 0.5$ sec), consideration of SFSI does not cause a significant change in the response. For probability of increase in structural total displacement due to SFSI effects, Figure 12 compares the probability values for three structural systems. The probability is within the range of 40–80% and 60–90% for linear and nonlinear structural systems respectively. Thus, similar to what is observed for structural distortion, nonlinearity in structural

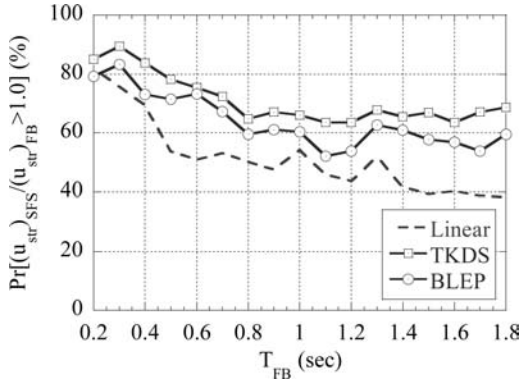

Figure 12. Probability of increase in structural total displacement due to SFSI effects.

behavior also amplifies SFSI effect on structural total displacement.

4 CONCLUSIONS

Soil-foundation-structure interaction (SFSI) effects on structural response have been investigated through a robust probabilistic study covering uncertainties in model parameters and input earthquake motion. In the numerical simulations, an established rheological soil-shallow foundation-structure (SFS) model representing: (*i*) a single-degree-of-freedom (SDOF) superstructure with linear and nonlinear hysteretic behavior and (*ii*) a shallow foundation resting on an equivalent linear half-space was utilized. The parameters of the model were randomly generated via a Monte Carlo simulation in a way to result in realistic SFS systems. All the adopted models were subjected to an ensemble of 40 earthquake motions. Key findings from the analyses can be summarized as follows:

1. Consideration of SFSI in dynamic analysis with linear structural behavior may increase the structural distortion up to 2 times, even though, in a median sense, a reduction is expected. The risk of having an increase in the structural distortion is on the order of 10–30% depending on the stiffness of the superstructure. For the total structural horizontal displacement this value is on the order of 40–80%.
2. Detrimental SFSI effects in terms of increase in the structural distortion occur for a specific earthquake spectrum characteristics relative to the fundamental periods of the fixed-base system and those of the respective SFS system. Increase in the response occurs when the period of the SFS system is located on an ascending branch of the spectrum.
3. Based on the median structural responses and probability of increase in the structural responses due to SFSI, detrimental effects of SFSI are more pronounced for nonlinear structural systems; this implies that the evaluation of SFSI effects based on linear systems is unconservative.

REFERENCES

Applied Technology Council 1984. *Tentative Provisions for the Development of Seismic Regulations for Buildings*; ATC-3-06: California.

Dutta, S.C. & Bhattacharya, K. & Roy, R. 2004. Response of low-rise buildings under seismic ground excitation incorporating soil-structure interaction. *Soil Dynamics and Earthquake Engineering* 24: 893–914.

FEMA 440 2005. *Recommended Improvements of Nonlinear Static Seismic Analysis Procedures*. Applied Technology Council: California.

Fishman, G.S. 1995. *Monte Carlo: Concepts, Algorithms, and Applications*. New York: Springer-Verlag.

Gazetas, G. & Mylonakis, G. 1998. Seismic soil-structure interaction: new evidence and emerging issues. *Geotechnical Earthquake Engineering and Soil Dynamics 3: proceedings of speciality conference (ASCE)*: 1119–74.

Jennings, P.C. & Bielak J. 1973. Dynamics of building-soil interaction. *Bulletin of the Seismological Society of America* 63(1): 9–48.

Jin, S. & Lutes, L.D. & Sarkani S. 2000. Response variability for a structure with soil-structure interactions and uncertain soil properties. *Probabilistic Engineering Mechanics* 15: 175–183.

Lutes, L.D. & Sarkani, S. & Jin, S. 2000. Response variability of an SSI system with uncertain structural and soil properties. *Engineering Structures* 22: 605–620.

Moghaddasi, M. & Cubrinovski, M. & Pampanin, S. & Carr, A. & Chase, J.G. 2009. Monte Carlo Simulation of SSI Effects Using Simple Rheological Soil Model. *2009 NZSEE Conference, 3–5 April 2009*. Christchurch: New Zealand.

Mylonakis, G. & Gazetas, G. 2000. Seismic soil-structure interaction: beneficial or detrimental. *Journal of Earthquake Engineering* 4(3): 227–301.

Seed, H.B. & Idriss, I.M. 1970. Soil moduli and damping factors for dynamic response analysis. *Report EERC 70–10*. Earthquake Engineering Research Centre.

Shome, N. & Cornell, C.A. & Bazzurro, P. & Carballo J.E. 1998. Earthquakes, records, and nonlinear responses. *Earthquake Spectra* 14(3): 469–500.

Stewart, J.P. & Kim S. & Bielak J. & Dobry R. & Power M.S. 2003. Revisions to soil-structure interaction procedures in NEHRP design provisions. *Earthquake Spectra* 19(3): 677–96.

Veletsos, A.S. & Meek, J.W. 1974. Dynamic behaviour of building-foundation systems. *Earthquake Engineering and Structural Dynamics* 3: 121–38.

Veletsos, A.S. & Nair V.D. 1975. Seismic interaction of structures on hysteresis foundations. *Journal of the structural division (ASCE)* 101: 109–129.

Wolf, J.P. 1994. *Foundation Vibration Analysis Using Simple Physical Model*. Englewood Cliffs, NJ: Prentice-Hall.

Soil-Foundation-Structure Interaction – Orense, Chouw & Pender (eds)
© 2010 Taylor & Francis Group, London, ISBN 978-0-415-60040-8

Soil-structure interaction in deep foundations

M.A. Ashour
University of Alabama, Huntsville, USA

G.M. Norris
University of Nevada, Reno, USA

J.P. Singh
JP Singh and Associates, Richmond, California, USA

ABSTRACT: The paper demonstrates the effect of soil-structure interaction on the response of laterally loaded piles and drilled shafts in layered soil (sand and/or clay) and weak rock deposits. The paper also presents the capabilities of the Strain Wedge (SW) model technique and how it accounts for soil and pile property influence on the pile/shaft lateral response. The SW model has been validated and verified through several comparison studies with model- and full-scale lateral load tests. Several factors and features related to the problem of a laterally loaded isolated pile and pile group are covered by the SW model. For example, the nonlinear behavior of both soil and pile material, soil-pile interaction (i.e. the assessment of the p-y curves rather than the adoption of empirical ones), the potential of soil to liquefy, the interference among neighboring piles in a pile group, the pile cap contribution and the consideration of the pile/shaft type (short/intermediate and long) are considered in SW model analysis. The SW model analyzes the response of laterally loaded piles based on pile properties (pile stiffness, cross-sectional shape, pile-head conditions, etc.) as well as soil properties.

1 INTRODUCTION

The problem of a laterally loaded pile is often solved as a beam on an elastic foundation (BEF) involving nonlinear modeling of the soil-pile interaction response (p-y curve). Currently employed p-y curve models were established/verified based on the results of field tests (Reese et al. 1974; Matlock 1970; and Reese & Welch 1975) and adjusted mathematically using empirical parameters to extrapolate beyond the soil's specific field test conditions. While most designers prefer the p-y curve method as compared to elastic continuum or finite element analysis of laterally loaded pile behavior, the profession has reached a state where it is time that closer scrutiny be given the traditional "Matlock-Reese" p-y curves used in the analysis. The traditional p-y curves were derived from a number of well-instrumented field tests that reflect a limited set of conditions. To consider these p-y curves as unique is questionable. The traditional p-y curve models are semi-empirical models in which soil response is characterized as independent nonlinear springs (Winkler springs) at discrete locations and do not account for a change in pile properties such as pile bending stiffness, pile cross-sectional shape, pile-head fixity and pile-head embedment below the ground surface. Soil-pile interaction or p-y curve behavior is not unique but a function of both soil and pile properties. Such influences can be considered using available theoretical means (SW model formulation) that allows transformation of envisioned three-dimensional soil-pile interaction response to one-dimensional BEF parameters. As Terzaghi (1955) and Vesic (1961) stated, the subgrade modulus, E_s (and, therefore, the p-y curve), is not just a soil but, rather, a soil-pile interaction (and, therefore, a pile property dependent) response (Figure 1). Kim et al. (2004) showed experimentally the significant effect of pile head fixity on the shape of the p-y curve in the same soil (Figure 2).

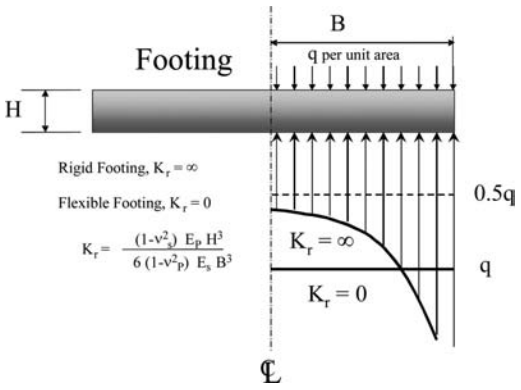

Figure 1. Subgrade reaction variation versus structure stiffness (Terzaghi 1955).

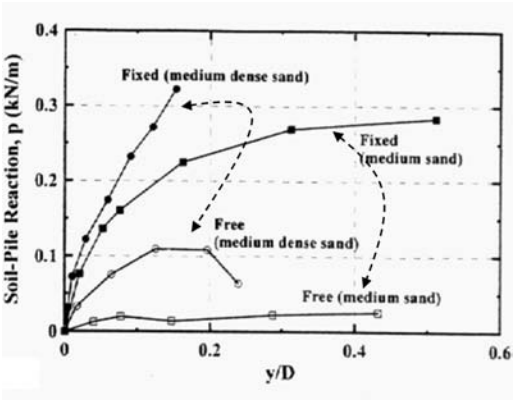

Figure 2. Effect of pile-head fixity on the p-y curve (Kim et al. 2004).

2 OVERVIEW OF THE STRAIN WEDGE MODEL BASIC CONCEPTS

The SW model parameters are related to an envisioned three-dimensional passive wedge of soil developing in front of the pile (Figure 3). The basic purpose of the SW model is to relate stress-strain-strength behavior of the layered soil in the wedge to one-dimensional BEF parameters. The SW model is, therefore, able to provide a theoretical link between the more complex three-dimensional soil-pile interaction and the simpler one-dimensional BEF characterization (Norris 1986). The previously noted correlation between the SW model response and BEF characterization reflects the following interdependence:

- the horizontal strain (ε) in the soil of the developing passive wedge in front of the pile to the deflection pattern (y versus depth, x) of the pile;
- the horizontal soil stress change ($\Delta\sigma_h$) in the developing passive wedge to the soil-pile reaction (p) associated with BEF analysis; and
- the nonlinear variation in the Young's modulus ($E = (\Delta\sigma_h/\varepsilon)$ of the soil to the nonlinear variation in the modulus of subgrade reaction ($E_s = p/y$) associated with BEF characterization as illustrated in detail by Norris (1986), Ashour et al. (1998) and Ashour & Norris (2000).

The reason for linking the SW model to BEF analysis is to allow the appropriate selection of BEF parameters to solve the following differential equation:

$$EI\left(\frac{d^4y}{d^4x}\right) + Q\left(\frac{d^2y}{d^2x}\right) + E_s(x)\,y = 0 \qquad (1)$$

EI indicates the pile bending stiffness, Q symbolizes the axial load, y represents the lateral deflection of the pile and E_s (x) is the modulus of subgrade reaction at depth x. It should be noted that axial load ($Q-y$) effect (i.e. induced moment) is part of the numerical analysis (Finite Difference Method) used to solve the

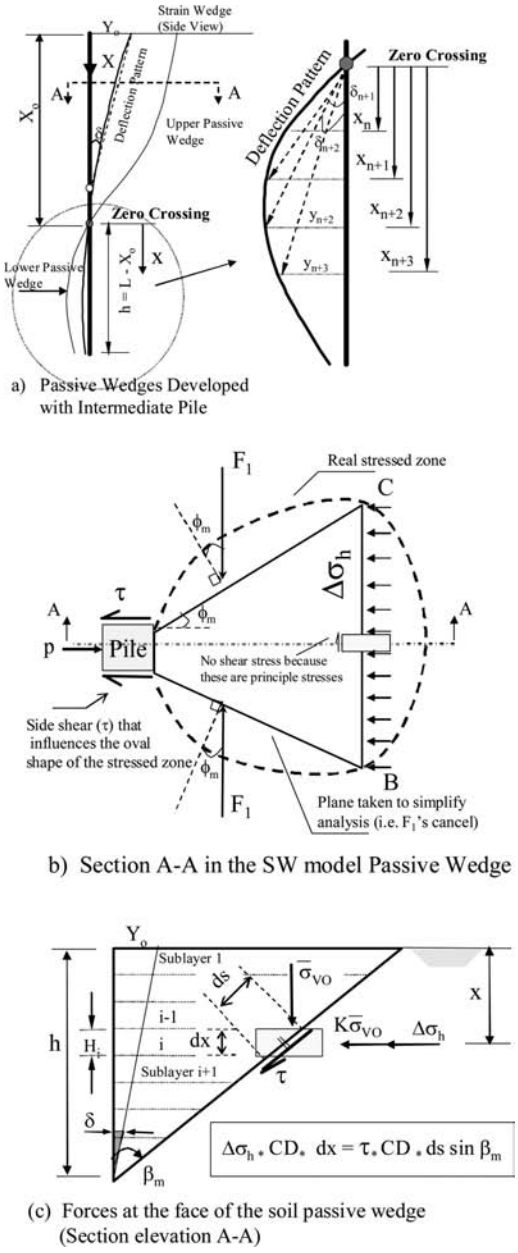

Figure 3. SW model force equilibrium, deflection and configuration.

BEF. Axial load along with bending moment are considered in the calculation of normal stresses at any pile cross section that, in return, affect the pile cross section neutral axis and EI of that section.

The SW model is also a semi-empirical approach (AASHTO 2007) because, while based on theoretical concepts, stress-strain characterization is formulated from triaxial test behavior. The SW model yields successive points on the p-y curves caused by a change in the modulus of subgrade reaction, $E_s(x)$, profile

with increasing soil strain, ε (considered constant with depth in the upper passive wedge). Such an assumption is also valid with the short pile deflection pattern (Figure 8) where the value of soil strain would be the same along the pile length for the upper and lower passive wedges. However, this is not the case with the deflected portion of the long and intermediate pile below the first zero-deflection point (lower passive wedge) shown in Figure 3a. At any increment of lateral loading, the lower passive soil wedge of the long and intermediate pile maintains different values of soil strain as shown in Figure 3a.

$$\delta_i = y_i/(h-x_i) \qquad \text{where } i < n \ (i.e.\ xi < Xo) \tag{2}$$

$$\delta_i = y_i/(x_i - X_o) \qquad \text{where } i \geq n \ (i.e.\ x_i > X_o) \tag{3}$$

$$\varepsilon_i = \Psi \delta_i \tag{4}$$

where Ψ is a parameter that relates the deflection angle (δ) to the soil strain ε in soil sublayer (i).

An effective stress (ES) analysis is also employed with clay as well as sand. The ES analysis for clay includes the development of excess porewater pressure with undrained loading based on Skempton's equation (1954). By using an ES analysis with clay, the three-dimensional strain wedge geometry (Figure 3b) can be defined based on the more appropriate mobilized effective stress and friction angle, $\overline{\varphi}_m$. The relationship between the normally consolidated clay undrained shear strength, S_u, φ, and $\Delta\sigma_h$ and the vertical effective stress, $\overline{\sigma}_{vo}$, is presented in Ashour et al. (1998).

The SW model can handle the problem of multiple soil layers of different type. The soil profile and the loaded pile are divided into sublayers and segments of constant thickness, as shown in Figure 3c. Each sublayer of soil is considered to behave as a uniform, isotropic, homogenous material and to have its own properties according to the sublayer location and soil type. The depth, h, of the passive wedge is controlled by the stability of the pile under the current pile head load. The effects of soil and pile properties are part of the soil-pile reaction along the pile length as reflected by the Young's modulus of the soil (E), the stress level in the soil (SL), the pile deflection pattern (y vs. x or δ), and the BEF modulus of subgrade reaction (E_s) between the pile segment and each soil sublayer (Figure 3c). To account for the interaction between soil layers and between the soil and pile, the deflected length of the pile is considered to be a continuous beam of different short segments each with a uniform load resulting from the nonlinear E_s supports from that sublayer (Figure 3c).

3 CHARACTERIZATION OF SOIL-PILE INTERACTION (p-y) OF A LATERALLY LOADED PILE

Corresponding to the horizontal equilibrium of a slice (a soil sublayer i) of the passive wedge at depth x (Figure 3b), the relationship between the soil-pile reaction (p) and the horizontal and shear stress changes $\Delta\sigma_h$ and τ at horizontal strain ε at a certain depth can be expressed as

$$p_i = (\Delta\sigma_h)_i \, \overline{BC}_i \, S_1 + 2\tau_i \, D \, S_2 \tag{5}$$

where the face width (BC) of the wedge at depth x is in relation to the pile width, D.

$$\left(\overline{BC}\right)_i = D + (h - x_i)\, 2 \left(\tan\beta_m\right)_i \left(\tan\varphi_m\right)_i \tag{6}$$

$$\left(\beta_m\right)_i = 45 + \frac{(\varphi_m)_i}{2} \tag{7}$$

As presented by Ashour and Norris (2000), the ultimate values of p in sand and clay soils are determined as

$$\left(p_{ult}\right)_i = \left(\Delta\sigma_{hf}\right)_i \overline{BC}_i \, S_1 + 2\left(\tau_f\right)_i D \, S_2 \quad \text{(sand)} \tag{8}$$

$$\left(p_{ult}\right)_i = 10\left(S_u\right)_i D \, S_1 + 2\left(S_u\right)_i D \, S_2 \quad \text{(clay)} \tag{9}$$

S_1 and S_2, on the other hand, are shape factors that are 0.75 and 0.5, respectively, for a circular pile cross section, and 1.0 for a square pile (Briaud et al. 1984). By combining the equations of the developing passive wedge geometry and the stress level with the above relationship, one finds that

$$A_i = S_1\left(1 + \frac{(h - x_i)\, 2\left(\tan\beta_m \tan\varphi_m\right)_i}{D}\right) + \frac{2\, S_2 \left(\overline{\sigma}_{vo}\right)_i \left(\tan\phi_s\right)_i}{\left(\Delta\sigma_h\right)_i} \quad \text{(sand)} \tag{10}$$

$$A_i = S_1\left(1 + \frac{(h - x_i)\, 2\left(\tan\beta_m \tan\overline{\varphi}_m\right)_i}{D}\right) + \frac{S_2\left(SL_t\right)_i}{SL_i} \quad \text{(clay)} \tag{11}$$

Here the parameter A is a function of pile and wedge dimensions, applied stresses, and soil properties.

A separate expression for the stress level (SL) vs. ε gives the shape of the associated triaxial test normalized stress (SL) versus axial strain curve (Ashour et al. 1998). S_u is the undrained shear strength of clay.

The level of mobilization of the passive wedge in a sublayer depends on SL of the soil in the wedge and the shear resistance, τ, along the pile sides. The values of $\overline{\sigma}_{vo}$, SL and τ vary according to drained sand or undrained clay conditions of that sublayer. The side shear stress in sand (Eqn 10) is a function of the mobilized side shear friction angle, φ_s, that reaches its ultimate value ($\varphi_s = \varphi$) prior to that of the mobilized friction angle, φ_m, of the sand in the wedge (i.e. SL_t and SL). The level of shear stress (SL_t) along the pile sides (as in a direct or simple shear test) differs from the stress level (SL) of the soil in the wedge in front of the pile (as in the triaxial compression test with the horizontal direction in the field representing the axial direction in the lab).

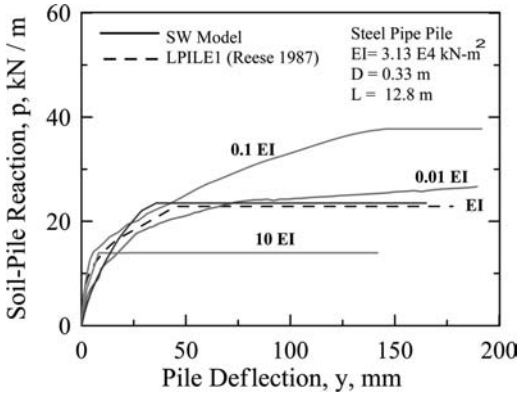

Figure 4a. Effect of pile bending stiffness on the p-y curve at 0.915-m depth (soft clay, Sabine River test).

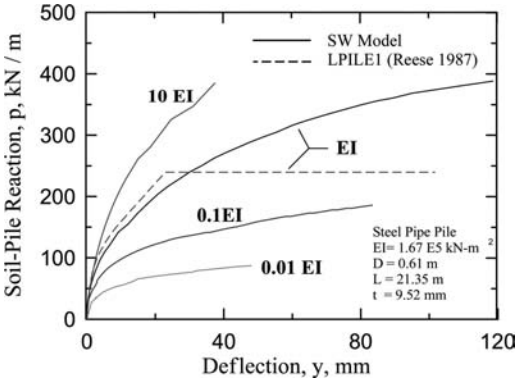

Figure 4b. Effect of pile bending stiffness on the p-y curve at 1.83-m depth (Mustang island test site).

Table 1. Properties of soils used in the comparisons.

Soil Type	Unit Wt, $\bar{\gamma}$ (kN/m^3)	E_{50} %	ϕ (degree)	*S_u (kN/m^2)
Loose Sand	16.5	0.005	30	
Dense Sand	19.6	0.0025	40	
Soft Clay	15.7	0.015		24
Stiff clay	19.6	0.005		86

4 EFFECT OF SOIL AND PILE PROPERTIES ON THE p-y CURVE

The influence of pile properties (such as pile bending stiffness, pile-head conditions, pile cross-sectional shape and pile-head embedment depth), and the effect of a change in the neighboring soil (above and/or below the given sublayer) on the nature of the resulting p-y curve can be demonstrated via the SW model approach.

Based on SW model analysis, pile properties have a significant effect on the shape and geometry of the developing passive wedge and, hence, the values of p_{ult} and A_{ult} in flow-around failure. In order to address this issue, consider two piles of the same diameter ($D = 0.33$ m, original $EI = 31300$ kN-m^2) driven in soft clay (Matlock 1970) but of different bending stiffnesses (different materials). Figure 4a presents the free-head SW model p-y curves at 0.915 m below the ground surface for different EI values. It is noted that the ultimate resistance of soil-pile reaction is controlled by the soil-pile combination (Eqns 9 and 11, $p_{ult} = 14.35$ kPa). A very stiff pile (10 EI) in this soft clay does not interact well with the soil, and a deep and large passive wedge at higher stress levels (SL and SL_t) quickly develops. Consequently, as A_i (given by Eqn 11) reaches its ultimate value, flow-around failure occurs at this depth and the soil-pile reaction, p, ceases at a value less than p_{ult} (Eqn 11) (Ashour and Norris 2000).

Reducing the bending stiffness of the pile to that of the original steel pipe pile (EI) yields an increase in A_i (compared to the first case) and an increase in the range of soil-pile interaction until flow around failure again occurs at $A = A_{ult}$ for $p < p_{ult}$. A greater reduction in pile stiffness (similar to a R/C pile of *0.1EI*) increases the ductility of the p-y curve resulting in approximately the same value of p at flow around failure ($A = A_{ult}$). However, for a very flexible pile (timber pile of *0.01EI*) in this soft clay, very large deflection is required before the soil-pile reaction reaches p_{ult} at $A = A_{ult}$. This is because of the very slow growth of the passive wedge and parameter A.

Figure 4b presents the interaction between pile and sand at a depth of 1.83 m for conditions similar to the Mustang Island test (Cox et al. 1974). Changing the pile stiffness results in very different p-y curves. Because the surrounding sand is dense, increasing the pile stiffness causes the p-y curve to become stiffer. The p-y curve in the sand would cease to grow due to the development of a plastic hinge (yield moment) well before any flow-around failure. Note that the effect of yield moment is shown only for the Mustang Island test and SW p-y curves. Linear and nonlinear pile material models are employed in the SW model analysis. This includes elastic-plastic steel model and stress-strain model for confined concrete (Ashour et al 2001).

5 THE NON-UNIQUENESS OF THE p-y CURVE

5.1 *Effect of pile bending stiffness on the p-y curve*

Two free-head piles (stiff and flexible), 0.305 m in diameter and 12 m long with different stiffnesses (31300 kN-m^2 and 4300 kN-m^2), are used to further demonstrate the effect of pile stiffness on the nature of the p-y curve. Both piles are assumed to be driven in loose and dense sand and soft and stiff clay (Table 1). The SW model is used to determine the values of the p-y curves at 1.22 m below the pile head.

Figure 5 shows the effect of pile stiffness on the SW model predicted p-y curves of a free-head pile in soft

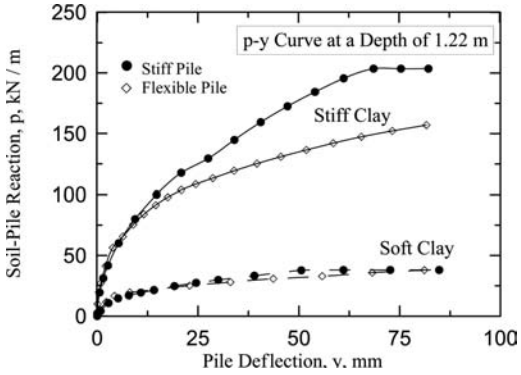

Figure 5. Effect of pile stiffness on the p-y curve.

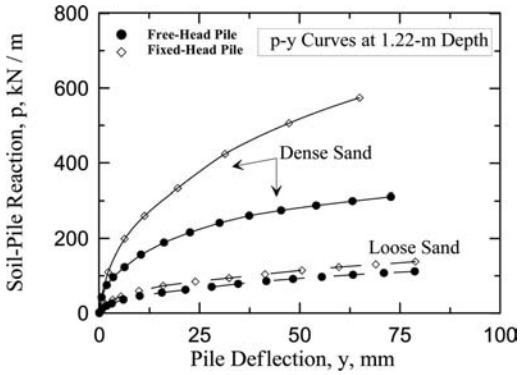

Figure 6. Effect of pile-head fixity on the p-y curve.

and stiff clay at 1.22 m depth. As expected, the stiff pile in stiff clay exhibits the highest soil resistance. Pile stiffness has a greater effect on the p-y response in stiff clay. Changing the value of pile stiffness in soft clay has only a slight influence on the characteristic of the p-y curve as long as the soil has not failed.

5.2 *Effect of pile-head conditions on the p-y curve*

Figure 6 shows the effect of pile-head conditions (free or fixed-head) as a significant factor in the SW model analysis that is affecting the shape of the developed p-y curve. Note that the fixed head p-y curve in stiff and soft clay (Figure 11) reaches p_{ult} at lower deflection (and pressure) than that of the free head p-y curve. This is the result of the development of a larger passive wedge for the fixed head case at the same value of soil strain, ε (Ashour and Norris 2000). This is also in agreement with the results obtained by Kim et al. 2004 and shown in Figure 2.

5.3 *Effect of pile cross-sectional shape on the p-y curve in sand*

The SW model was used to assess the p-y curves at a 1.22-m depth in sand and clay of two reinforced concrete piles which are assumed to have the same bending

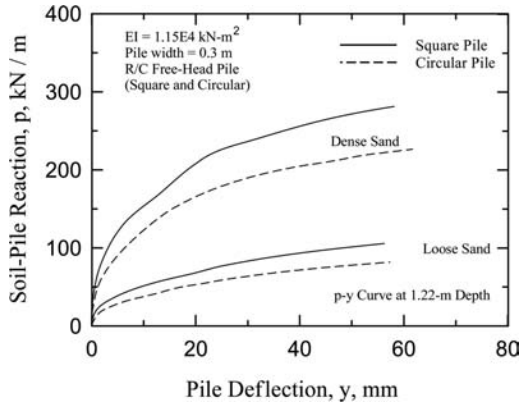

Figure 7. Effect of pile-cross sectional shape on the p-y curve in sand.

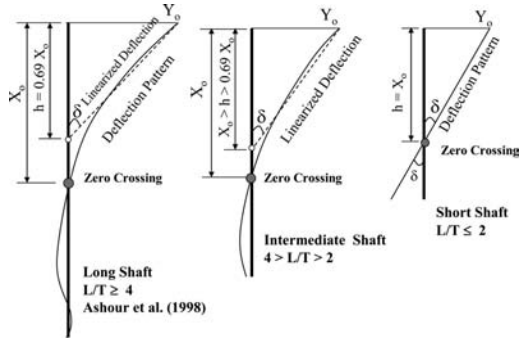

Figure 8. Deflection patterns of long, intermediate and short piles.

stiffness of 11500 kN-m^2. The first pile has a square cross-section of 0.305-m width, while the second pile has a circular cross-section of 0.305-m diameter. The only difference between the two piles is their cross-sectional shapes. As shown in Figure 7, the square pile in loose and dense sand exhibits a soil-pile resistance higher than that of the circular pile.

5.4 *Effect of pile length on the p-y curve*

Pile is defined as "a long pile" for $L/T >= 4$. L is the pile length and T is the soil-pile relative stiffness defined as $(EI/f)^{0.2}$ for sand and normally consolidated clay, where f is the coefficient of subgrade reaction (F/L^3). The value of relative stiffness, T, varies with EI and f. For a short pile, the bending stiffness (EI) in the analysis could have a constant value (linear elastic) as a result of small flexural deformations.

The coefficient of subgrade reaction, f, varies with level of deflection and decreases with increasing lateral load. The chart attributable to Terzaghi (DM 7.2, NAVFAC 1982) provides average (design) values of f as a function of the sand's relative density. The pile behaves as an "intermediate" pile when $[4 > (L/T) > 2]$. If an intermediate or short pile is analyzed as a long pile

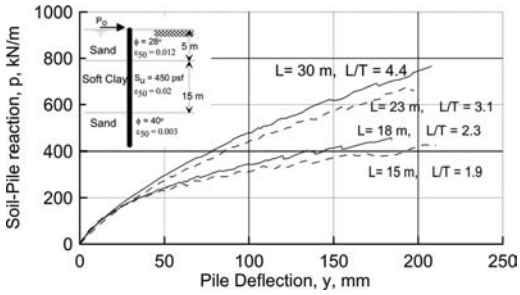

Figure 9. Effect of pile length on the shape of p-y curve at 3.3 m below ground.

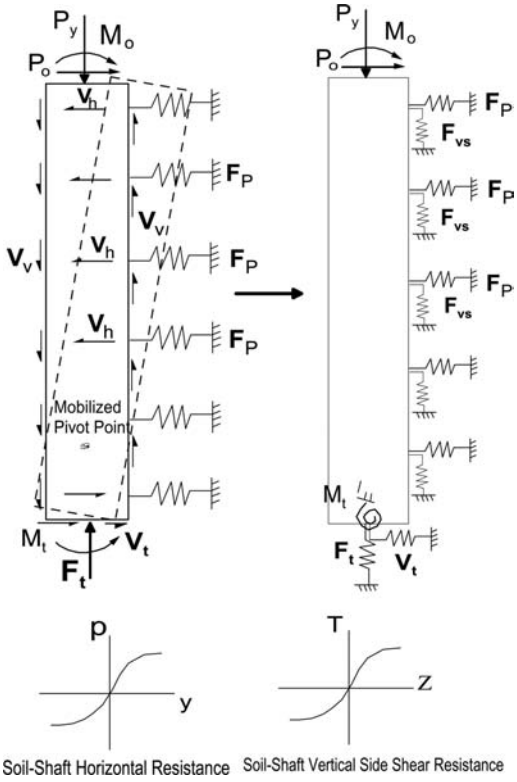

Figure 10. Modeling large diameter drilled shaft with vertical as well as horizontal soil-shaft resistance.

(e.g. using p-y curves of long piles), an overestimated (stiffer) lateral pile response could be obtained.

Short, intermediate and long pile classifications are based on pile properties (i.e. length, diameter and bending stiffness) and soil stiffness. The traditional (Matlock-Reese) p-y curves for sand and clay were developed from full scale long pile test data (Matlock 1970, and Reese et al. 1974). The development of the mobilized three-dimensional passive soil wedges along the deflected length of short, intermediate and long piles was experimentally observed by Hughes et al. (1978).

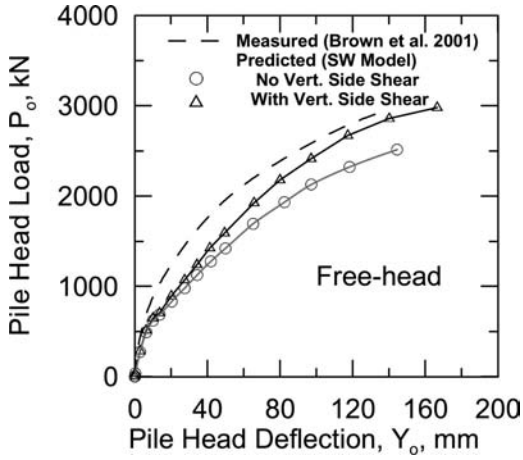

Figure 11. Lateral response of large diameter shaft at the Taiwan test (Brown et al. 2001).

Four different values for the pile length (15, 18, 23 and 30 m) are used with a 1.5-m-diameter shaft embedded in the soil profile shown in Figure 9. The p-y curve at 3.3-m depth below the pile head changes according to the pile characterization (short, intermediate or long). Such behavior reflects the influence of soil-pile interaction and pile type on the associated shape of the p-y curve.

5.5 *Effect of vertical side shear resistance (large diameter shafts)*

Since the traditional p-y curve have been developed using lateral load tests performed on long slender piles, the vertical shear resistance (V_v) acting along the pile or shaft perimeter has no significant influence on the lateral response of shafts and piles with diameters less than 0.91 m. However, V_v contributes significantly to the lateral capacity of large diameter shafts. The SW model accounts for the horizontal and vertical shear resistance (V_h and V_v) acting along the sides of the large diameter shafts in addition to base resistance (Ashour et al 2004a). Figure 11 shows the contribution of the vertical side shear resistance to the lateral resistance of the 1.5-m diameter shaft tested at the Taiwan test (Brown et al. 2001).

6 PILE/SHAFT GROUP INCLUDING THE CAP EFFECT

As presented by Ashour et al. (2004b), the SW model allows the assessment of the mobilized group action among the piles in a group with no need for P-multipliers to be assumed. The interference (overlapping) among neighboring passive soil wedges is determined along the piles at any kevel of loading. The evaluation of the group action of pile group in the SW model analysis accounts for front and transverse pile spacing, soil types, level of lateral loading,

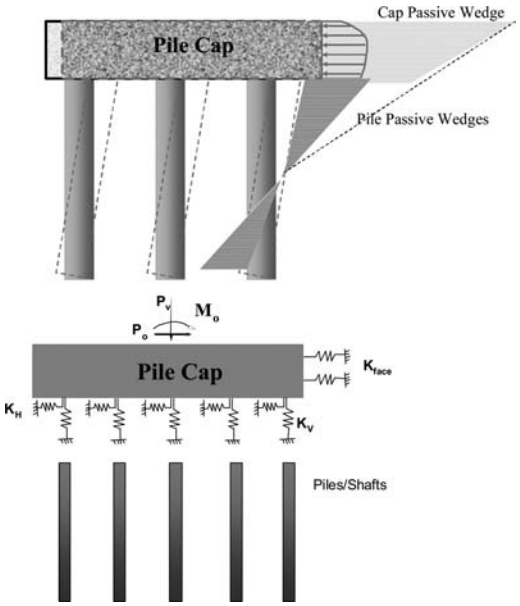

Figure 12. Simplified modeling of a pile group with a pile cap in the SW model.

and the depth of pile interference all of which are not considered in the p-multiplier technique. Several full- and model-scale case have been used to validate the laterally loaded pile group modeling in the SW model technique (WSDOT 2007, Ashour et al. 2004b, Rollins et al. 2005).

The SW model analyzes the pile cap as an element of the whole pile group foundation system (Figure 12) that is influenced by the pile head stiffness and the type of pile-head fixity. Front passive soil and side shear resistance for pile cap lateral movement is incorporated in the analysis. Figure 13 shows the varying contribution of the pile cap to the lateral resistance of the deep foundation system that is caused by free- and fixed-head shaft-cap connection at the same lateral displacement.

The lateral response of deep foundation shown in Figure 13 is obtained from 2-ft diameter 3×3 pile group (3*D* spacings) embedded in the soil profile shown in Table 2 and connected with a $19 \times 19 \times 7$ ft pile cap.

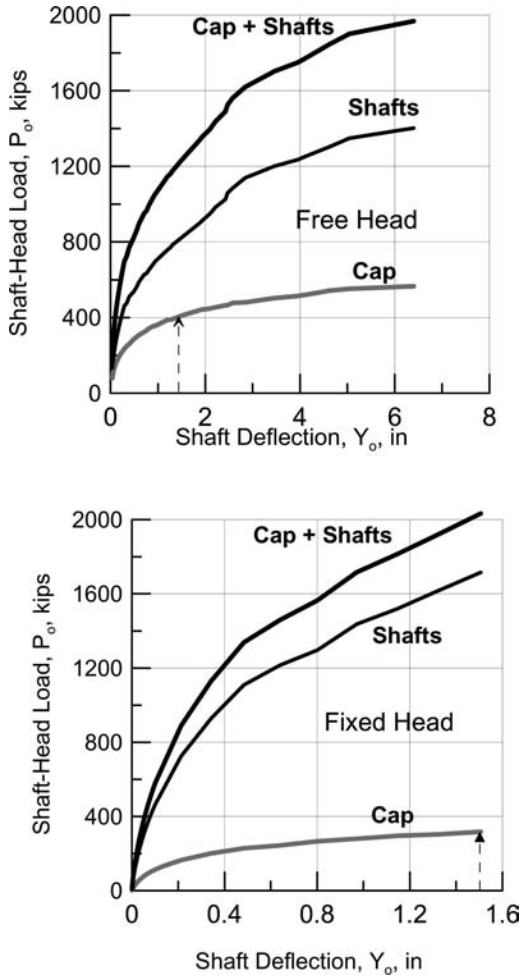

Figure 13. Lateral deflection of pile group with cap under free and fixed head pile conditions.

Table 2. Soil properties used in the pile group analysis.

Soil layer	Soil	Thick. (ft)	γ(pcf)	ϕ(deg.)	ε_{50}*
Layer 1	Sand	10	120	35	0.0
Layer 2	Sand	40	47.5	30	0.0
Layer 3	Sand	60	72	40	0.0

*SW model compute program default

7 SUMMARY AND CONCLUSIONS

The SW model provides p-y curves that are a good match with traditional p-y curves. However, the p-y curve for a given soil is not unique; it depends upon the neighboring soil and pile properties (bending stiffness, head condition, shape and embedment of the pile head). Such "soil" reaction, *p*, is really a soil-pile reaction. The SW model provides a means for evaluating such dependence and the accompanying effects which influence the nature of the p-y curve. It allows the designer to be more discerning in his choice of the pile to take full advantage of design variables he can influence (pile properties, e.g. shape, bending stiffness, head fixity).

REFERENCES

AASHTO 2007. LRFD Bridge Design Specifications. *AASHTO*. Section C.10.7.2.4.

Ashour, M., Norris, G. M., and Shamsabadi, A. 2001. Effect of the non-linear behavior of pile material on the response

of laterally loaded piles. *4th International Conf. on Recent Advances in Geotechnical Earthquake Engineering and Soil Dynamics.* San Diego, California, USA.

Ashour, M. & Norris, G. M. 2000. Modeling lateral soil-pile response based on soil-pile interaction. *Journal of Geotechnical and Geoenvironmental Engineering, (ASCE)* 126(5): 420–428.

Ashour, M., Norris, G. & Pilling, P. 1998. Lateral loading of a pile in layered soil using the strain wedge model. *Journal of Geotechnical and Geoenvironmental Engineering (ASCE).* 124(4): 303–315.

Ashour, M., Norris, G. M., and Elfass, S. 2004a. Analysis of laterally loaded intermediate or long drilled shafts of small or large diameter in layered soil. Report No. CCEER-06-04, *Civil Engineering Dept. University of Nevada, Reno*.

Ashour, M., Pilling, P. & Norris, G. M. 2004b. Lateral behavior of pile group in layered soils. *Journal of Geotechnical and Geoenvironmental Engineering (ASCE)* 130(6): 580–592.

Briaud, J. L., Smith, T. & Mayer, B. 1984. Laterally loaded piles and the pressuremeter comparison of existing methods. *ASTM*. STP 835: 97–111.

Brown, D. A., O'Neill, M. W., McVay, M., El Naggar, M. H., & Chakraborty, S. 2001. Static and dynamic lateral loading of pile groups. *National Cooperative Highway Research Program (NCHRP), National Academy Press*, Washington, D.C., USA

Cox, W. R., Reese, L. C. & Grubbs, B. R. 1974. Field testing of laterally loaded piles in sand. *6th Annual Offshore Technology Conference*. Houston. Texas. OTC 2079: 459–472.

Hughes, J., M., Goldsmith, P.R., and Fendall, H.D.W. 1978. The behavior of piles subjected to lateral loads. Report No. 178, *University of Auckland, School of Engineering*, Auckland, New Zealand.

Kim BT, Kim NK, Lee WJ & Kim YS. 2004. Experimental load-transfer curves for laterally loaded Piles in Nak-dong River sand. *Journal of Geotechnical and Geoenvironmental Engineering (ASCE)* 130(4): 416–425.

Matlock, H. 1970. Correlations for design of laterally loaded piles in soft clay. *The 2nd annual offshore technology conference*. Houston. Texas. OTC 1204: 577–607.

NAVFAC. 1982. Foundations and earth retaining structures design manual. *Dept. of Navy*, DM 7.2, Alexandria, VA.

Norris, G. M. 1986. Theoretically based bef laterally loaded pile analysis. *Proceedings, Third international conference on numerical methods in offshore piling*, Nantes. France: 361–386.

Reese, L. C. 1987. Documentation of The Computer Program LPILE1. *Ensoft Inc.*, Post Office Box 180348, Texas 78718.

Reese, L. C., Cox, W. R., & Koop, F. D. 1974. Analysis of Laterally Loaded Piles in Sand. *The Six Annual Offshore Technology Conference*, Houston, Texas, OTC 2080: 473–483.

Reese, L.C. & Welch, R. C. 1975. Lateral Loading of Deep Foundations in Stiff Clay. *Journal of geotechnical engineering division (ASCE)*. (101)7: 633–649.

Rollins, K. M, Lane, J. D. & Gerber, T. M. 2005. Measured and computer lateral response of a pile group in sand. *Journal of Geotechnical and Geoenvironmental Engineering (ASCE).* (131)1: 103–114.

Skempton, A. W. 1954. The Pore Pressure Coefficients A and B. *Geotechnique*, 4, pp. 148.

Terzaghi, K. 1955. Evaluation of Coefficients of Subgrade Reaction. *Geotechnique*, 5(4): 297–326.

Vesic, A. 1961. Bending of Beams Resting on Isotropic Elastic Solid. *Journal of Engineering Mechanics Div (ASCE)* 87(2): 35–53.

Washington State Department of Transportation (*WSDOT*). 2007. Bridge Design Manual M-22.

Soil-Foundation-Structure Interaction – Orense, Chouw & Pender (eds)
© 2010 Taylor & Francis Group, London, ISBN 978-0-415-60040-8

Soil-pile interaction in liquefying soils: Modelling issues

M. Cubrinovski
University of Canterbury, Christchurch, New Zealand

J.J.M. Haskell
Schofield Centre, University of Cambridge, Cambridge, UK

B.A. Bradley
Geological and Nuclear Sciences (GNS), Lower Hutt, New Zealand

ABSTRACT: This paper focuses on two established (and very different) methods for analysis of piles in liquefying soils: a simplified pseudo-static analysis, and an advanced seismic effective stress analysis. The paper highlights the need for a systematic approach in the use of the pseudo-static analysis allowing for identification of key parameters and uncertainties in the analysis. Numerical simulations of shake table tests are used to illustrate some important aspects in the modelling and application of the seismic effective stress analysis.

1 INTRODUCTION

Pile foundations are often used to support engineering structures in areas where surface soils are liquefiable. Hence the abundance of case histories from strong earthquakes on damaged piles and poor performance of pile foundations in liquefied and laterally spreading soils. In the 1995 Kobe earthquake, for example, a large number of bridges, buildings and storage tanks on pile foundations were severely affected by soil liquefaction and lateral spreading, which caused damage to the piles, loss of function or even collapse of the superstructure (JGS 1998).

Over the past 10–15 years, significant efforts have been made to improve our understanding of the behaviour of piles in liquefying soils during earthquakes. This included benchmark experiments on full-size piles using large scale shake table tests (e.g., Tamura & Tokimatsu 2005; Cubrinovski et al. 2006; Tokimatsu & Suzuki 2009), detailed analyses of well-documented case histories from strong earthquakes (e.g. JGS 1998; Tokimatsu & Asaka 1998) and development of new concepts and analysis procedures in an effort to explore design methodologies for piles in liquefying soils. On the analytical front, significant progress has been made across a broad range of analysis methods, from simple design-oriented approaches to the most advanced numerical procedures for dynamic analysis (e.g., O'Rourke et al. 1994; Tokimatsu & Asaka 1998; Yasuda & Berrill 2000; Finn & Thavaraj 2001; Cubrinovski & Ishihara 2004; Cubrinovski et al. 2008).

This paper focuses on the analysis of piles in liquefying or laterally spreading soils and issues around numerical modeling when using two representative methods for analysis: a simple design-oriented approach (pseudo-static analysis), and an advanced numerical analysis (seismic effective stress analysis). There are numerous variations in the details and development of these methods which are beyond the scope of this paper. Here, the aim is to provide an overview of important issues in the application of these methods to the analysis of piles in liquefying soils and to identify areas that require further development and improvement.

2 STATEMENT OF THE PROBLEM

2.1 *Response characteristics of liquefying soils*

Soil liquefaction involves very large changes in stiffness and strength of foundation soils over a very short period of time, typically during the strong ground shaking caused by an earthquake. This highly dynamic and extreme variation in stress-strain characteristics of the foundation soils is probably the first thing to acknowledge when analyzing liquefaction problems.

Strong ground shaking gives rise to a rapid build-up in excess pore water pressures and consequent reduction in stiffness and strength of liquefying soils. In a period of only few seconds (or several tens of seconds) the stiffness of the liquefying soil may change from its initial value to nearly zero (at least temporarily in the course of shaking). The significant reduction in stiffness and strength results in a large lateral ground deformation either of cyclic nature (with peak shear strains on the order of several percent) or in the form

of lateral spreads (permanent shear strains on the order of several tens of percent). Clearly, soil liquefaction involves an extreme level of material nonlinearity and quite often a significant geometric nonlinearity due to the very large lateral displacements and associated loss of stability of the ground or supported structure.

All of the above depicts the complexity of the response with regard to its dynamic nature (time-dependent component). The process is also highly variable in space. The progressive development of liquefaction throughout the depth of the deposit could be very non-uniform and uniquely affected by the complex cross interaction amongst soil layers, ground response and earthquake motion characteristics.

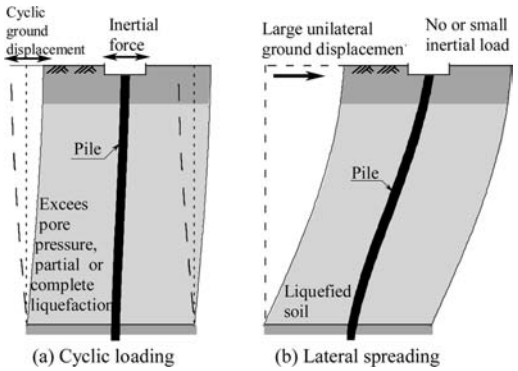

Figure 1. Schematic illustration of loads on pile (and characteristics of foundation soils) during strong ground shaking (cyclic phase) and post-liquefaction lateral spreading.

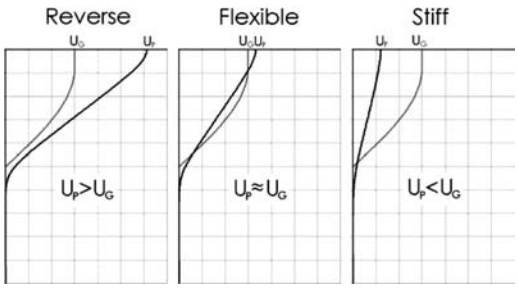

Figure 2. Schematic illustration of *reverse-pile-behaviour*, *flexible-pile-behaviour* and *stiff-pile-behaviour* based on the relative displacements between the pile and free field soil.

2.2 *Soil-pile interaction in liquefying soils*

In the course of rapid build-up of excess pore pressures and development of liquefaction (temporal and spatial), piles are generally subjected to two significant lateral loads arising from the ground movement (kinematic load) and vibration of the superstructure (inertial load). Both these loads are oscillatory in nature with magnitudes and spatial distribution dependent on the ground motion characteristics, soil density, presence of non-liquefied crust at the ground surface, predominant periods of the ground and superstructure, and the relative stiffness of the foundation soil and the pile, among others. In view of the significant variation of these loads and rapidly changing stiffness and strength characteristics of the foundation soils in the process of development of liquefaction, it is useful to distinguish between several different phases in the soil-pile interaction (e.g., Tokimatsu & Asaka 1998; Cubrinovski & Ishihara 2004). Such strategy has been adopted in many design codes where, for example, the cyclic phase and lateral spreading phase of the response are considered by two separate analysis procedures. As illustrated schematically in Figure 1, in the two separate analyses different combinations of kinematic and inertial loads, and also different characteristics (stiffness and strength) of the foundation soils are used in order to depict representative scenarios for the analysis of the pile during a specific phase of the evolving seismic response.

Putting aside for a moment the complex issues around the combined kinematic and inertial effects on the pile response, one may identify three general scenarios for the pile response in terms of the displacement of the pile relative to that of the free field ground. A schematic illustration of the three types of responses is shown in Figure 2 for the so-called *stiff-pile-behaviour*, *flexible-pile-behaviour* and *reverse-pile-behaviour* respectively. As implied by the size of the cyclic and permanent ground deformation described in Section 2.1, cyclic lateral ground displacements in liquefied soils and lateral spreading displacements in particular could be very large. Hence, cases where either flexible-pile-behaviour or reverse-pile-behaviour occurs, i.e. lateral pile displacement (U_P) is either similar to the ground displacement (U_G) or greater, imply serious damage to the pile and unacceptable performance in the case of strong ground motions. In other words, the stiff-pile-behaviour where the pile foundation has the capacity to resist the ground movement, and hence control the deformation and damage to the pile, is the preferred type of response, from a performance viewpoint.

2.3 *Analysis and design issues*

Undoubtedly, the analysis and design of piles in liquefiable soils are burdened by the extreme complexity of the phenomena considered and unknowns in the analysis. A rigorous analysis of the problem would need to address the following issues (not an exhaustive list though):

- Temporal and spatial characteristics of liquefaction
- Effects of excess pore water pressures and liquefaction on ground response and stress-strain characteristics of foundation soils
- Soil-pile interaction in liquefying soils including characteristic loads (kinematic and inertial loads) and deformation mechanism
- The need to estimate inelastic deformation and damage to piles
- Assessment of the response and performance of the soil-pile-foundation-structure system including all critical components and the system as a whole

– Uncertainties in the ground motion (earthquake load) and system characteristics

There is no universal analysis method that rigorously addresses all the above issues, but rather different methods focus on different aspects of the problem and provide a specific contribution in the assessment. Some issues in the application of two principal methods for analysis of piles in liquefying soils are discussed in the following sections.

3 SIMPLIFIED PSEUDO-STATIC ANALYSIS

3.1 *Characteristics and objectives*

The pseudo-static analysis is a conventional method for analysis of seismic problems that has its version for analysis of piles in liquefying soil. As a practical design-oriented approach based on conventional engineering concepts, this method is commonly adopted in the seismic design codes. Even though there are significant differences between different pseudo-static analysis approaches, in concept they are all similar, and hence share common features and problems in their application. In this context, the method used herein should be taken as a representative of the pseudo-static analysis that illustrates key features of this analysis approach.

The adopted pseudo-static method was designed to satisfy the following requirements in the analysis:

(a) To capture the relevant deformation mechanism for piles in liquefying soils (combined kinematic and inertial loads, and degradation of soil stiffness and strength due to liquefaction).
(b) To permit estimation of inelastic deformation and damage to piles (conventionally, foundations are designed to remain in the elastic range of deformations, but this may be very restrictive and expensive strategy for pile foundations in liquefying soils).
(c) To address the uncertainties (and unknowns) associated with liquefaction and soil-pile interaction in liquefying soils.

The method could be applied to a pile group including a superstructure, and hence it could address some aspects in the performance of the soil-pile-foundation-structure system. Here, a single-pile model is used for the sake of simplicity and clarity of argument.

3.2 *Soil-pile model*

A typical beam-spring model representing the soil-pile system in the pseudo-static analysis is shown in Figure 3 (Cubrinovski & Ishihara 2004; Cubrinovski et al. 2009a). The model can easily incorporate a stratified soil profile (multi-layer deposit) with liquefied layers of different thicknesses sandwiched between a crust of non-liquefiable soil at the ground surface and an underlying non-liquefiable base layer. As illustrated in the figure, the proposed model incorporates

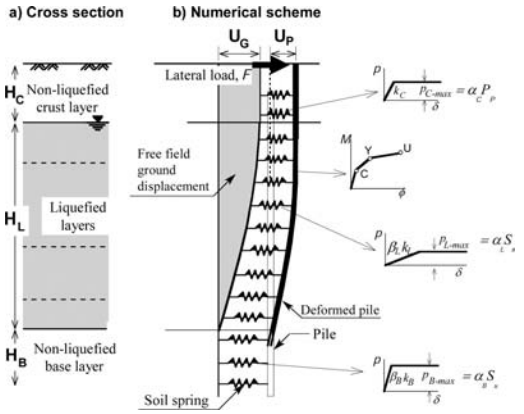

Figure 3. Beam-spring model for pseudo-static analysis of piles in liquefying soils (Cubrinovski and Ishihara, 2004; Cubrinovski et al. 2009a).

simple non-linear load-deformation relationships for the soil and the pile. The soil is represented by bilinear springs, the stiffness and strength of which can be degraded to account for effects of nonlinear behaviour and liquefaction. The pile is modelled using a series of beam elements with a tri-linear moment-curvature relationship. Parameters of the model are summarized in Figure 3b for a three-layer configuration in which a liquefied layer is sandwiched between a surface layer and a base layer of non-liquefiable soils.

In the model, two equivalent static loads are applied to the pile: a lateral force at the pile head (F), representing the inertial load on the pile due to vibration of the superstructure, and a horizontal ground displacement (U_G) applied at the free end of the soil springs (for the liquefied layer and overlying crust), representing the kinematic load on the pile due to lateral ground movement (cyclic or spreading) in the free field. As indicated in Figure 3, it has been assumed that the non-liquefied crust at the ground surface is carried along with the underlying liquefied soil and that it undergoes the same ground displacement as the top of the liquefied layer, U_G.

3.3 *Influence of soil stiffness and strength*

The application of the method to the analysis of piles in liquefying soils is burdened by the aforementioned uncertainties associated with soil liquefaction, soil-pile interaction in liquefying soils and the need to reduce a very complex dynamic problem to a simple equivalent static analogy. Questions posed to the user are ‘what stiffness and strength to adopt for the liquefied soil’, ‘how to combine dynamic kinematic and inertial loads in a static analysis’ and ‘what is the sensitivity of the pile response to a certain model parameter’, among others. A thorough discussion on these issues may be found in (Cubrinovski et al. 2009a, 2009b) whereas herein the focus is placed on only one albeit important aspect of the problem.

The load-deformation relationships for the soil springs shown in Figure 3b are characterized essentially by two groups of parameters: one related to the stiffness, and the other to the strength (ultimate pressure) of the soil. Before going into a detailed examination of the variation of these parameters, it is useful to consider the sensitivity of the pile response to the stiffness and strength of the soil. For this purpose, Haskell (2009) conducted a comprehensive sensitivity study in which a wide range of soil-pile systems, loading conditions and load-deformation characteristics for the soil and the pile were considered. One of the important outcomes from this study is summarized in Figure 4 where a conceptual illustration of the influence of stiffness and strength of the liquefied soil on the pile response is comparatively shown. The size of the horizontal bars on the left-side of the figure indicates the degree of sensitivity of the pile response to the soil stiffness or strength respectively; the solid symbol on the load-deformation relationships on the right-hand side indicates the particular deformation (load) level of the spring for which the respective sensitivities apply. For example, the plots at the top of the figure indicate a large influence of soil stiffness on the pile response and no influence of soil strength when the spring deformation is below the yield level. Conversely, the plots at the bottom of the figure indicate that soil strength strongly influences the pile response when yielding in the soil occurs. While this transition from soil stiffness to soil strength controlled pile response with increasing deformation is intuitive, the abovementioned study (Cubrinovski et al. 2009b) provides quantification of these effects.

It was argued in Section 2.2 that the stiff-pile-behaviour is the preferred type of pile response, because this type of behaviour (where the pile resists the ground movement) provides a controlling mechanism for the pile deformation (damage). Figure 2 clearly shows that the stiff-pile-behaviour results in a large relative displacement between the free field soil and the pile which implies yielding in the soil spring. With reference to the schematic plots shown in Figure 4, the stiff-pile-behaviour is represented by the bottom plots where effects of soil stiffness are negligible while the ultimate soil pressure (strength) strongly influences the pile response. Hence, the focus in the modelling should be placed on the ultimate soil pressure.

3.4 *Ultimate soil pressure on the pile*

In the adopted model, the ultimate soil pressure from the crust of non-liquefied soil at the ground surface per unit width of the pile is approximated as

$$p_{C-max} = \alpha_C \, p_p \qquad (1)$$

where $p_p(z)$ is the Rankine passive pressure while α_C is a scaling factor accounting for the difference in the lateral pressure between a single pile and an equivalent wall. Results from experimental studies indicate

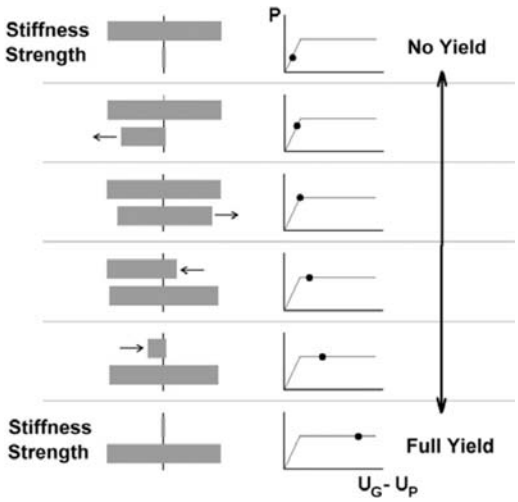

Figure 4. Conceptual illustration of sensitivity of the pile response (size of horizontal bars) to stiffness and strength of liquefied soil as a function of spring deformation (relative displacement $U_G - U_P$); Haskell 2009, Cubrinovski et al. 2009b.

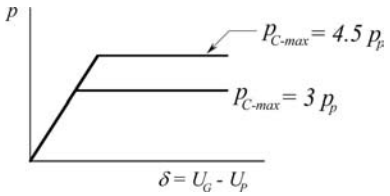

Figure 5. Uncertainties in the ultimate pressure from a crust of non-liquefied soil on the pile.

that α_C typically takes value in the range between 3 and 5; a value of 4.5 has been back-calculated from benchmark lateral spreading experiments on full-size piles (Cubrinovski et al. 2006). In many guidelines, however, a value of $\alpha_C = 3$ has been adopted based on the study of Broms (1964) which is based on active-pile-loading (in which the soil provides resisting force to the pile deformation), from a range of measured values between $\alpha_C = 3$ and 6. Hence, the uncertainty in the ultimate pressure form the crust layer on the pile illustrated in Figure 5.

The ultimate pressure from the liquefied soil is similarly estimated as

$$p_{L-\max} = \alpha_L \, S_r \qquad (2)$$

where S_r and α_L are the residual strength and the scaling factor respectively for the liquefied soil. Note that α_L is different from the corresponding parameter α_C for the crust, because the interaction and mobilization of soil pressure on the pile is different for liquefied and non-liquefied soils. The value of α_L is highly uncertain and could be approximated anywhere between 1 and 6 depending on the underlying assumptions in

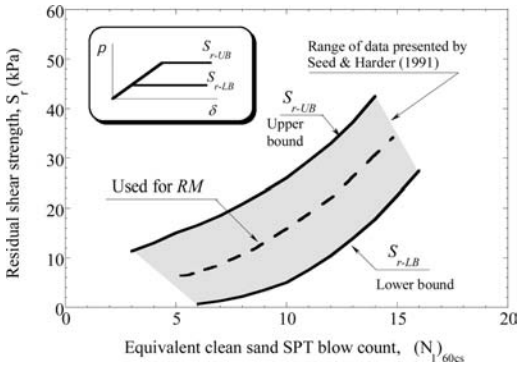

Figure 6. Empirical correlation for the residual strength of liquefied soils (after Seed and Harder, 1991).

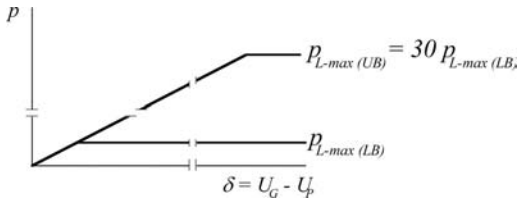

Figure 7. Uncertainties in the ultimate pressure from the liquefied soil on the pile.

the calculations. The residual strength could be estimated using empirical correlation, such as that based on the SPT blow count proposed by Seed and Harder (1991), shown in Figure 6. A large scatter exists in this correlation indicating significant uncertainty in the value of S_r for a given $(N_1)_{60cs}$ value. For example, for $(N_1)_{60cs} = 10$, the value of S_r can be anywhere between 5 kPa (lower bound value) and 25 kPa (upper bound value). By combining the uncertainties in α_L and S_r, the possible variation in the ultimate pressure from the liquefied soil could vary by a factor of 30 for this case, as illustrated schematically in Figure 7.

The relative contribution or influence of the ultimate soil pressure from the crust and liquefied soil could be very different depending on the thickness of the crust. This is illustrated in Figure 8 where the sensitivity of the pile response ($\Delta\phi/\phi_{ref}$) on the ultimate pressure parameters of the liquefied soil (S_r and α_L) is plotted for two different scenarios, one without crust ($H_C = 0$ m) and the other with a 1.5 m thick crust ($H_C = 1.5$ m). The effects of liquefied soil parameters on the pile response substantially decrease with an increasing thickness of the crust, as the crust load represents a greater proportion of the total load and hence becomes the dominant load component. Clearly, uncertainties in model parameters could be quite important and should not be evaluated in an isolated manner but rather by considering the 'system response'.

Clearly, there are significant uncertainties in the pseudo-static analysis associated with the ultimate

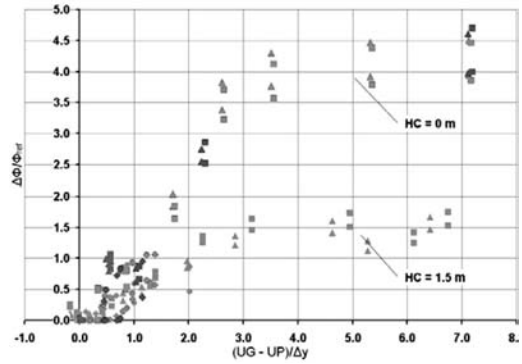

Figure 8. Sensitivity of the pile response ($\Delta\phi/\phi_{ref}$) on the ultimate pressure parameters of the liquefied soil (S_r and α_L) as a function of the crust thickness (H_C).

pressure from the crust and liquefied soil on the pile. In order to address these uncertainties, a systematic approach is needed including the development of a design strategy, selection of relevant deformation mechanism and identification of key parameters influencing the pile response. Then, by focussing on the critical uncertainties in the analysis, a range of relevant pile responses could be estimated. Needless to say, additional uncertainties, such as those related to the inertial load, need to be considered, however, the same systematic approach as above is generally applicable (Cubrinovski et al. 2009b). This approach provides means for more consistent use of the pseudo-static analysis and proper treatment of the uncertainties in the analysis, which is a key issue in the assessment of piles in liquefying soils.

4 SEISMIC EFFECTIVE STRESS ANALYSIS

4.1 *Characteristics and objectives*

The seismic effective stress analysis permits detailed simulation of the entire process of excess pore pressure build-up, development of liquefaction and associated ground deformation in a rigorous dynamic analysis. For this reason, it has been established as a premier tool for analysis of liquefaction problems. One of the key contributions of this analysis is that it allows us to examine the performance of the soil-pile-foundation-structure system during strong earthquakes using a realistic numerical simulation accounting for interaction effects, nonlinear behaviour and soil liquefaction. Needless to say, the method is quite complex and demanding on the user, hence requires a string of conditions to be satisfied in order to achieve the above objective. Details of the application of this method to the analysis of piles in liquefiable soils are beyond the scope of this paper, rather some modelling issues are discussed through the simulation of a series of shake table tests.

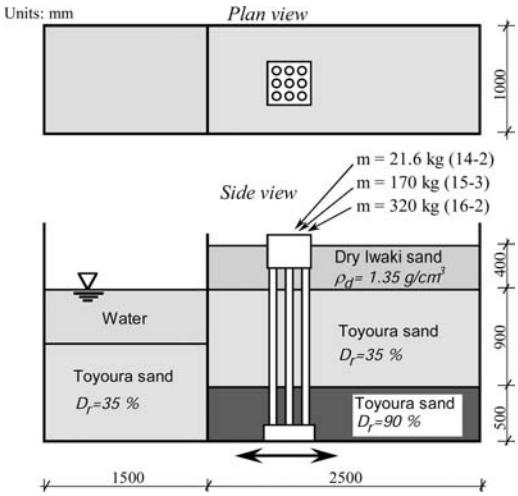

Figure 9. Soil-pile model(s) used in shake table tests.

4.2 *3-D simulation of shake table experiments*

A comprehensive study on pile foundations in liquefiable soils was carried out in Japan over the period 2002–2007 involving large-scale shake table tests and numerical simulations by advanced methods of analysis (e.g., NIED 2006). Within this project, a series of shake-table experiments on piles in liquefying soils undergoing lateral spreading was conducted at the Public Works Research Institute (PWRI), Tsukuba, Japan (Tanimoto et al., 2003). For all experiments, Class-B numerical predictions were made using two different constitutive models and numerical procedures utilizing 3-D effective stress analysis (Cubrinovski et al. 2008; Uzuoka et al. 2008). Here, some of the results are briefly discussed to highlight the outcomes from these simulations.

Various factors were varied in the aforementioned shake table experiments such as the amplitude and direction of shaking (transverse, longitudinal and vertical), mass of the superstructure and number and arrangement of piles. A typical physical model used in these tests is shown in Figure 9 consisting of a 3×3 pile foundation embedded in a liquefiable sand deposit, located in the vicinity of a sheet pile wall. The model ground consisted of three sand layers: a crust layer of coarse sand overlying loose liquefiable sand, and a dense sand layer at the base. The model was built in a rigid container and subjected to a sine-wave excitation.

4.3 *Results and discussion*

The ground response observed in the tests was characterized by a sudden pore pressure build-up and liquefaction of the loose sand within the first two cycles of shaking. In the course of the subsequent shaking following the initiation of liquefaction, large lateral movement of the sheet pile wall occurred towards the water which was accompanied by ground-flow and spreading of the liquefied backfills.

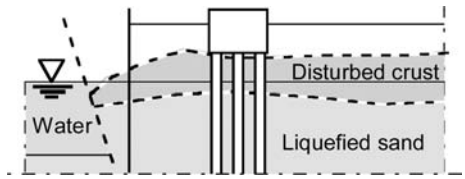

Figure 10. Deformed configuration of backfill soils and sheet pile wall in Test 14-2, after shaking.

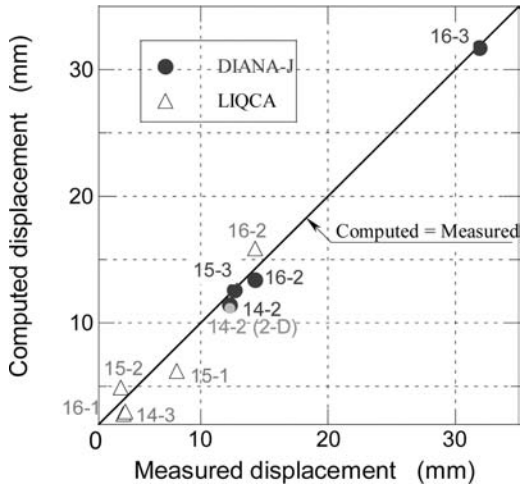

Figure 11. Comparison of computed and measured peak horizontal displacements of footing (pile top).

In Test 14-2, for example, the lateral displacement of the top of the sheet pile was approximately 380 mm at the end of the shaking (note that the height of the deposit was 1800 mm). Figure 10 schematically illustrates the deformed configuration of the sheet pile and backfill soils at the end of the shaking. In spite of the large lateral ground movement associated with the spreading of liquefied soils, in this test the peak lateral displacement of the foundation piles was only 12.3 mm and the residual displacement was less than 5 mm. Hence the pile foundation resisted the ground movement and exhibited *stiff-pile-behaviour*.

In general, the numerical predictions were in good agreement with the observations in the experiment capturing the rapid pore pressure build-up, development of liquefaction and consequent ground deformation. In fact, the response of the foundation piles was very well predicted by both analysis methods for all experiments, as indicated in Figure 11 where computed and measured peak horizontal displacements at the pile head are shown for nine different tests. Comparisons of measured and computed peak bending moments for Pile 1 (front row pile) in three tests are shown in Figure 12, again demonstrating very good agreement between the observed and predicted pile behaviour.

The analyses, however, underestimated the displacement of the sheet pile wall, as summarized in Figure 13. It was found that the prediction of the large

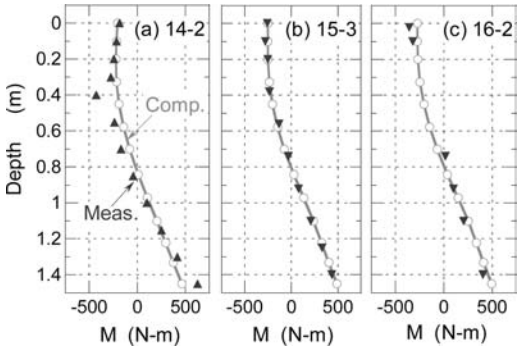

Figure 12. Comparison of computed and measured bending moments of Pile 1 (at peak horizontal displacement of footing).

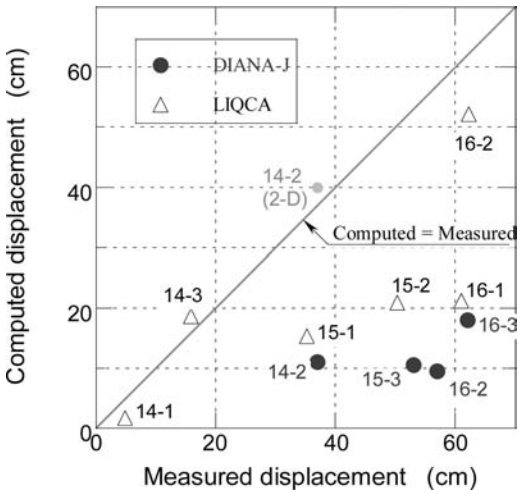

Figure 13. Comparison of computed and measured peak horizontal displacements at the top of the sheet pile.

lateral movement of the sheet pile wall including instability in the backfills and foundation soils was the most difficult to accurately predict with the advanced seismic analyses. A close scrutiny of the results indicates that the 'average shear strain' in the liquefied soil behind the sheet pile was on the order of 30–40% which is quite challenging to model with conventional soil-pile and soil-wall interfaces located only 600 mm apart (distance between the front-row of piles and sheet pile). In the tests, effects of geometric nonlinearity due to large ground deformation were also significant, as evident in Figure 10.

Figure 14 shows a comparison of computed and measured horizontal displacements of the footing (pile top) for Test 14-2. Notable is the very good agreement in the first few cycles and subsequent increase in the discrepancy between the computed and measured displacements. The amplitude reduction of footing displacements and elastic rebound of the pile observed in the test is related to the large lateral displacement and

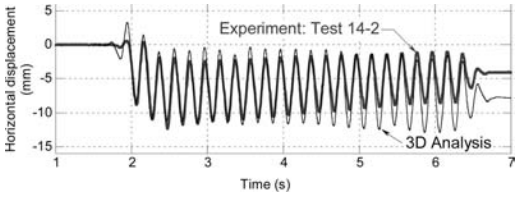

Figure 14. Comparison of computed and measured horizontal displacements of the footing (pile top), for Test 14-2.

settlement of the ground shown in Figure 10. The settlement resulted in a gradual reduction (and eventual loss) of contact between the crust and the back-side of the footing causing reduction in the lateral pressure from the crust on the footing. Since effects of geometric nonlinearity were not considered in the analysis, this deformation mechanism could not be captured in the analysis. The presented results clearly demonstrate the importance of geometric nonlinearity effects in cases involving large ground displacements associated with spreading.

4.4 *Modelling issues*

Various modelling issues need to be addressed when using the effective stress method for analysis of piles in liquefying soils. These can be generally summarized in three groups:

(i) The most critical of all is the performance of the constitutive soil model. It is essential that the constitutive model provides reasonably good accuracy in predicting the excess pore pressures and stress-strain behaviour of soils in order to allow proper evaluation of the soil-pile interaction effects.

(ii) Details of the numerical procedure, including mesh size, boundary conditions and interface behaviour may also influence the response of the soil-pile-structure system. In the abovementioned analyses, initial stresses in the soil were first computed, and specific boundary conditions and soil-pile interfaces were defined in order to allow a deformation pattern associated with lateral spreading to develop. In fact, the limitations of the model and numerical procedure (small-strain formulation ignoring geometric nonlinearity effects) in this regard were found to be the major reason for the deficiencies in the predicted response. Despite the anomalies in the prediction of the sheet pile displacements, however, the peak response of the piles was accurately predicted due to the exhibited stiff-pile-behaviour thus demonstrating the importance of the mode of deformation for the accuracy of the prediction.

(iii) A rigorous implementation of the analysis across all phases (e.g., determination of geotechnical model, constitutive parameters, numerical model and parameters, interpretation of results) is required.

One could argue that improvements across all abovementioned modelling issues are still needed in order to further increase the credibility and use of the seismic effective stress analysis.

5 SUMMARY AND CONCLUSIONS

A consistent use of the pseudo-static method for analysis of piles in liquefying soils requires a systematic approach in which the soil-pile deformation mechanism and uncertainties in the analysis are carefully considered. A significant reduction of the uncertainties in this analysis may not be possible, and hence the great importance of a clear strategy and methodical approach in the assessment.

The accuracy of the seismic effective stress analysis in predicting the pile response in liquefying soils relies heavily on the qualities of the constitutive soil model. Numerical details, however, may adversely influence the performance of the analysis and hence require due attention. The effects of modelling decisions need to be considered in conjunction with the anticipated mode of deformation for the soil-pile-foundation-structure system.

ACKNOWLEDGEMENTS

The authors would like to acknowledge the financial support provided by the Earthquake Commission (EQC), New Zealand.

REFERENCES

Broms B. (1964). Lateral resistance of piles in cohesionless soils. *ASCE Journal of Soil Mechanics and Foundation Engineering*, 90 (SM3): 123–156.

Cubrinovski, M. & Ishihara, K. 2004. Simplified method for analysis of piles undergoing lateral spreading in liquefied soils. *Soils and Foundations* 44(25): 119–133.

Cubrinovski, M., Kokusho, T. & Ishihara, K. 2006. Interpretation from large-scale shake table tests on piles undergoing lateral spreading in liquefied soils. *Soil Dynamics and Earthquake Engineering* 26: 275–286.

Cubrinovski, M., Uzuoka, R., Sugita, H., Tokimatsu, K., Sato, M., Ishihara, K., Tsukamoto, Y. & Kamata, T. 2008. Prediction of pile response to lateral spreading by 3-D soil-water coupled dynamic analysis: shaking in the direction of ground flow. *Soil Dynamics and Earthquake Engineering* 28, 421–435.

Cubrinovski, M., Ishihara, K. & Poulos, H. 2009a. Analysis of piles in liquefying soils by the pseudo-static approach. *Special Issue. Bulletin of NZ Society for Earthquake Engineering*, 42(1): 28–38.

Cubrinovski, M., Haskell, J.M. & Bradley, A.B. 2009b. Pseudo-static analysis of piles subjected to lateral spreading. *Earthquake Geotechnical Engineering Conf., XVIIth Int. Conf. of ISSMGE 2009, Alexandria, Egypt (in press)*.

Finn, W.D.L. & Thavaraj, T. 2001. Deep foundations in liquefied soils: case histories, centrifuge tests and methods of analysis. *Proc. 4th Int. Conf. on Recent Advances in Geotech. Earthq. Engrg. and Soil Dynamics*, San Diego, California, CD-ROM, Paper SOAP-1.

Haskell, J.J.M. 2009. Pseudo-static modelling of the response of piles in liquefying soils. *Research Report, University of Canterbury*.

Japanese Geotechnical Society 1998. Special Issue on Geotechnical Aspects of the January 17 1995 Hyogoken-Nambu Earthquake. *Soils and Foundations 1998*.

NIED 2006. Special project for earthquake disaster mitigation in urban areas. *NIED Technical Report* (in Japanese).

O'Rourke, T.D., Meyersohn, W.D., Shiba, Y. & Chaudhuri, D. 1994. Evaluation of pile response to liquefaction-induced lateral spread, *Proc. 5th US-Japan Workshop on Earthq. Resistant Design of Lifeline Facilities and Countermeasures Against Soil Liquefaction,Tech. Report NCEER-94-0026*, 457–479.

Seed, R.B. & Harder, L.F. 1991. SPT-based analysis of cyclic pore pressure generation and undrained residual strength. *H. Bolton Seed Memorial Symposium Proc.*, 2: 351–376.

Tamura, S. & Tokimatsu, K. 2005. Seismic earth pressure acting on embedded footing based on large-scale shaking table tests, *ASCE Geotechnical Special Publication 145*: 83–96.

Tanimoto, S., Tamura, K. & Okamura M 2003. Shaking table tests on earth pressures on a pile group due to liquefaction-induced ground flow. *Journal of Earthquake Engineering, JSCE*; 27: Paper No. 339 (in Japanese).

Tokimatsu K. & Asaka Y. 1998. Effects of liquefaction-induced ground displacements on pile performance in the 1995 Hyogoken-Nambu earthquake. *Special Issue of Soils and Foundations*, September 1998: 163–177.

Tokimatsu K. & Suzuki, H. 2009. Seismic soil-pile interaction based on large shake table tests. *Performance-Based Design in Earthquake Geotechnical Engineering*, Kokusho, Tsukamoto and Yoshimine (eds), Taylor and Francis, 77–104.

Uzuoka, R., Cubrinovski, M., Sugita, H., Sato, M., Tokimatsu, K., Sento, N., Kazama, M., Zhang, F., Yashima, A. & Oka, F. 2008. Prediction of pile response to lateral spreading by 3-D soil-water coupled dynamic analysis: shaking perpendicular to ground flow. *Soil Dynamics and Earthquake Engineering* 28, 436–452.

Yasuda, S. & Berrill, J.B. 2000. Observation of the earthquake response of foundations in soil profiles containing saturated sands, *GeoEng2000, Proc. Int. Conf. on Geotech. And Geological Engineering*, Melbourne, 1, 1441–1470.

Soil-Foundation-Structure Interaction – Orense, Chouw & Pender (eds)
© 2010 Taylor & Francis Group, London, ISBN 978-0-415-60040-8

Soil-pile interaction under lateral load

S. Iai, T. Tobita & M.N. Hussien
Disaster Prevention Research Institute, Kyoto University, Uji, Kyoto, Japan

K.M. Rollins
Brigham Young University, Provo, Utah, USA

O. Ozutsumi
Meisosha Co., Tokyo, Japan

ABSTRACT: The paper reviews (1) soil-pile interaction in horizontal plane, (2) a simplified approach for idealizing the soil-pile interaction in terms of a non-linear spring, and (3) effect of soil-pile separation. The review is based on the experimental (laboratory and full scale in-situ tests) and numerical studies performed by the authors over recent years.

1 INTRODUCTION

Performance of laterally loaded pile group has been under study for more than four decades. The results of these extensive studies have formed the basis for the current design practice of pile group under lateral loads. However, there are certain categories of mechanisms that are not fully studied in research and consequently not fully considered in design practice. Soil-pile interaction in horizontal plane and effect of soil-pile separation belong to those categories among others. This paper reviews these issues based on experimental and numerical studied performed by the authors over recent years.

2 SOIL-PILE INTERACTION IN HORIZONTAL PLANE

In order to study the local soil displacement field in the vicinity of the piles associated with a global displacement of soil around the pile foundation, two dimensional model tests were performed on a horizontal cross section of a soil-pile system in a pile foundation (Iai et al, 2006). Two dimensional effective stress analyses in horizontal plane were also performed to generalize the findings from the model tests. An effective stress model based on multiple shear mechanisms is used through a computer code FLIP (Iai et al, 1992).

Actual soil deformation is three dimensional and does not always follow the assumption made in this study that primary soil movement around the pile is in plane. This aspect of the problem is partially solved by incorporating the horizontal 2D behavior as soil-pile interaction spring in the vertical 2D analysis domain as discussed in Chapter 4.

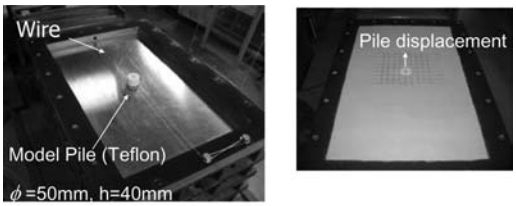

Figure 1. Apparatus for model tests for soil-pile interaction in horizontal plane.

In an aluminum container (inner dimensions: 800 mm long, 500 mm wide, 40 mm high), a cylindrical pile model made of Teflon, 40 mm high with a diameter of 50 mm, was embedded in a sand deposit formed in the container as shown in Figure 1. The sand deposit was formed by air pluviation for dry condition, and by pouring a slurry mixture of sand and viscous fluid (120cSt) for saturated condition. Silica No.7 sand was used. Relative densities of the sand deposits were about 70% for dry condition and about −150% (negative relative density) for saturated condition. After the sand deposit was formed, an acrylic plate was placed on the surface on the sand deposit. Displacement was induced to the pile model by pulling a wire attached to the mid portion of the pile model at the rate of 7.2 mm/min. Although the pile model was moved in the model tests, the primary interest of the model tests was to measure the displacement field of soil relative to the movement of the pile. Thus, the results of the model tests are readily applicable to the conditions when the global soil movement is induced around the pile foundation.

The local displacement field monitored through a video-camera was plotted in terms of displacement

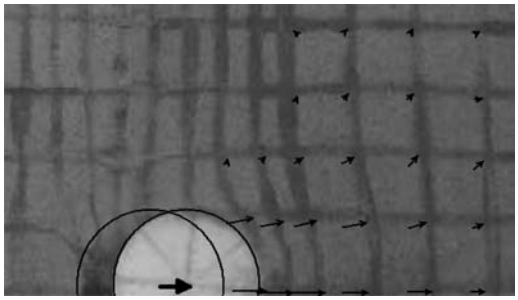

Figure 2. Measured displacement field (pile displacement 11mm, load = 20 N) (Case-1: dry).

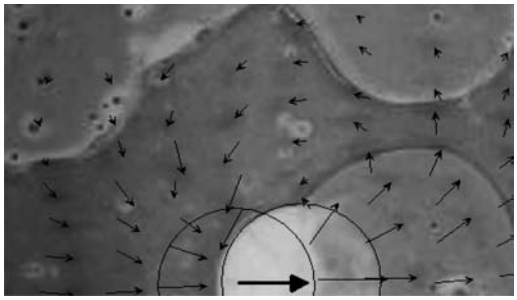

Figure 3. Measured displacement field (pile displacement 21mm, load = 6N) (Case-3: saturated).

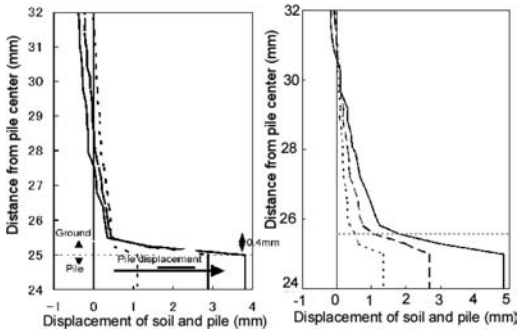

Figure 4. Displacement distributions in the vicinity of soil-pile interface for dry and saturated sand deposits (Cases-1 and 3).

vectors at nodes of the grid formed by colored sand markers. Under dry condition (Case-1), the displacement vectors were directed away from the front of the pile in a pattern of a fan as shown in Figure 2. The displacement vectors at pile side rapidly decreased with an increasing distance from soil-pile interface. A void was formed behind the pile following the movement of the pile. Under saturated condition (Case-3), vortices were formed at pile side as shown in Figure 3. Void formation was not observed behind the pile under saturated condition. Displacement distribution in the vicinity of soil-pile interface was obtained as shown in Figure 4.

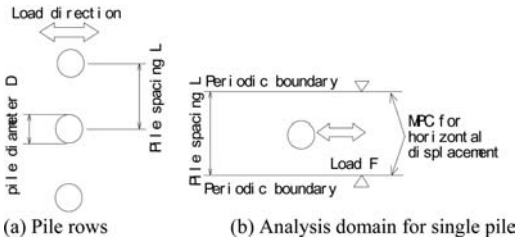

Figure 5. Two dimensional analysis of a soil-pile system in horizontal plane.

Two dimensional analysis of a horizontal cross section of the soil-pile system was performed under pseudo-static conditions. An effective stress model based on multiple shear mechanism was used through a computer code FLIP (Iai et al, 1992). In this analysis, a single row of equally spaced piles deployed perpendicular to the direction of load (Figure 5(a)) was idealized into an analysis domain defined by the boundaries that run parallel to the load direction and go through the centers of the pile spacing. These boundaries were periodic, sharing the same displacements at the boundary nodes with the same x-coordinate through the multiple constraint conditions (MPC) applied, where x-axis is directed towards right on the figure. At the right and left side boundaries on the figure, x-displacements were fixed.

Finite element mesh used for the analysis of a single row of piles with a spacing of $L = 10D$ and a pile diameter $D = 5$ cm is shown in Figure 6 for the area ranging from $L = -5D$ to $+5D$. In the analysis, whole soil-pile system was initially consolidated with a confining pressure of 0.28 kPa for simulating the confining condition at the mid-depth of the model sand deposit (i.e. 2 cm from the surface). The cylindrical pile section was idealized using linear solid elements. This pile section was replaced by the soil elements in the initial phase of analysis for consolidation in order to avoid artificial stress concentration. Following this initial phase, the pile was loaded with a monotonically increasing load. Soil deformation around the cylindrical cross section of the pile was computed in drained and undrained conditions. Parameters for sand used for the analysis were determined referring to the results of laboratory tests on Silica sand No.7 as shown in Table 1.

Computed displacement field for the dry and saturated condition are shown in Figures 7 and 8. In the dry condition, the displacement vectors are directed away from the front of the pile in a pattern of a fan. The displacement vectors at the pile side rapidly decreases with an increasing distance from the soil-pile interface. For the saturated condition, displacement vectors beside the pile shows vortices as shown in Figure 8. These displacement fields are basically consistent with those measured in the laboratory and shown in Figures 2 and 3. Only difference is noted with respect to the formation of voids behind the pile in the model tests. No void was formed in the analysis

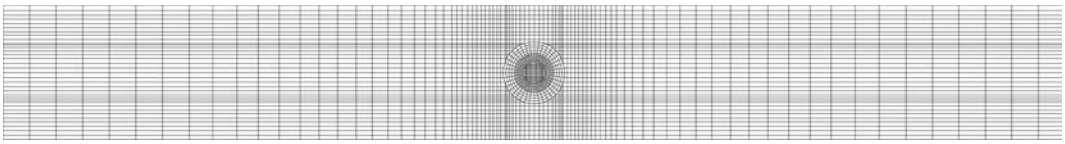

Figure 6. Finite element mesh used for the analysis.

Table 1. Parameters for silica sand No.7.

ρ_t (g/cm^3)	G_{ma} (kPa)	ν	σ'_{ma} (kPa)	ϕ_f (deg)	H_{max}
2.0	3760	0.33	0.28	35	0.24

ρ_t: density; G_{ma}: initial shear modulus at a confining pressure of σ'_{ma}; σ'_{ma}: reference confining pressure; ϕ_f: internal friction angle; ν: Poisson's ratio; H_{max}; limiting value of hysteretic damping factor (ϕ_p: phase transformation angle and w_1, p_1, p_2, c_1, s_1: parameters for dilatancy were not used.)

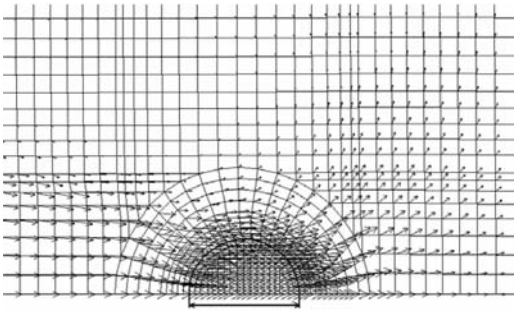

Figure 7. Computed displacement field around pile (drained) (Case-2).

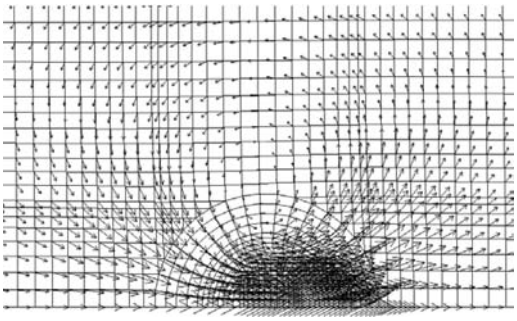

Figure 8. Computed displacement field around pile (undrained) (Case-4).

probably because the confining stress in the analysis was more uniform than the one in the model tests where the stress field became 3-*D* when the void began to form.

In order to clearly show the displacement distribution between the piles, horizontal components of the displacements are plotted in Figure 9. These results are basically consistent with those measured and shown in Figure 4. Only difference noted is with respect to the manner in which the displacements are decaying from the center of the pile: the model tests with large friction (not shown in this paper) shows much slower rate of decay at the soil-pile interface than the analysis. A further study may be needed to follow up this issue.

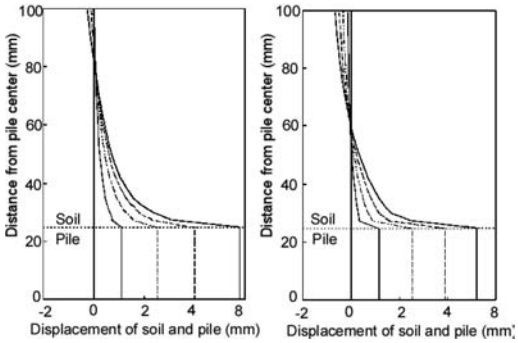

Figure 9. Computed displacement distributions between the piles: (left) dry (Case-2), (right) saturated (Case-4).

In Figures 4 and 9, the soil farthest from the pile moves in the opposite direction of pile movement. This phenomenon may be due to the fact that displacement of the total mass of soil is fixed so that soil has to move in order to maintain the overall mass balance.

Primary findings from this study are as follows:

(1) In dry condition, displacement vectors are directed away from pile front, and displacement at pile side rapidly decreases with an increasing distance from soil-pile interface. In saturated condition, displacement field shows vortices at pile side associated with push-out/pull-in pattern of displacements in front of and behind the pile.
(2) Distribution of local soil displacement between piles deployed perpendicular to direction of global displacement of soil shows high strain concentration (i.e. discontinuity in displacement) at soil-pile interface.

Generalization of the results of this experiment is obviously affected by various conditions such as pile-spacing, stress levels, sand grain size, soil angularities, relative densities and strain-softening/hardening soils. This aspect of the study remains as a homework in future.

3 SOIL-PILE INTERACTION SPRING

By using the same mesh and parameters, the load-displacement relationship of a pile under cyclic loading is computed for the horizontal cross section shown in Figure 6 for dry and saturated conditions. The displacement is defined as that of the pile relative to that at the periodic side boundary that is located at the pile to pile center. As a comparison, simple shear tests of a single element of soil were simulated using the same parameters for dry and saturated condition. In saturated condition, liquefaction front parameter S_0 was set equal to 0.05, which is equivalent to the states of excess pore water pressure ratio of 0.95. The initial confining pressure used for the computation was 24 kPa for dry sand and 98 kPa for saturated sand. The finite element mesh used for the simulation was assigned for the diameter of pile equal to $D = 1$ m. The analyses were performed for the pile spacing of 2.5D, 5D and 10D.

Examples of the computed results for spacing of 5D for dry and saturated conditions are shown in Figure 10. As shown in this figure, load-displacement curve for dry condition follows a typical shape of the *p-y* curve specified in the design recommendations whereas the curve for saturated condition follows a hardening-spring type shape similar to the stress strain curve during cyclic mobility of saturated sands. As a comparison, the simple shear test results of a single soil element of a multiple shear mechanism model are shown in Figure 11.

Although the mechanisms involved in the load-displacement curve are the results of complicated soil-pile interaction as exemplified by the local displacement field shown in Figures 3 through 9, the load-displacement curves shown in Figure 10 have practically the same shapes as those of the single soil element shown in Figure 11.

There might be a several reasons for the similarity between the results of load-displacement relationship of pile-soil system and the shear stress-shear strain relationship of a single soil element. In this review paper, however, it may be sufficient to say that the similarity is confirmed for a wide range of pile spacing and geotechnical conditions. Based on the similarity between the results of load-displacement relationship of pile-soil system and the shear stress-shear strain relationship of a single soil element, the following relationships are derived (Ozutsumi 2003) as follows:

$$\gamma_{xy} = u / (D\beta_p) \tag{1}$$

$$F = (LD\alpha_p)\tau_{xy} \tag{2}$$

$$\tau_{xy} = f(\gamma_{xy}) \tag{3}$$

where u denotes relative displacement, D denotes pile diameter, L denotes pile length, $\alpha_p = 11.5$ to 12.6, and $\beta_p = 0.5$ (dry) to 2.5 (saturated) depending on the pile spacing and dry/saturated conditions. The path dependent function f in Equation (3) is given by using

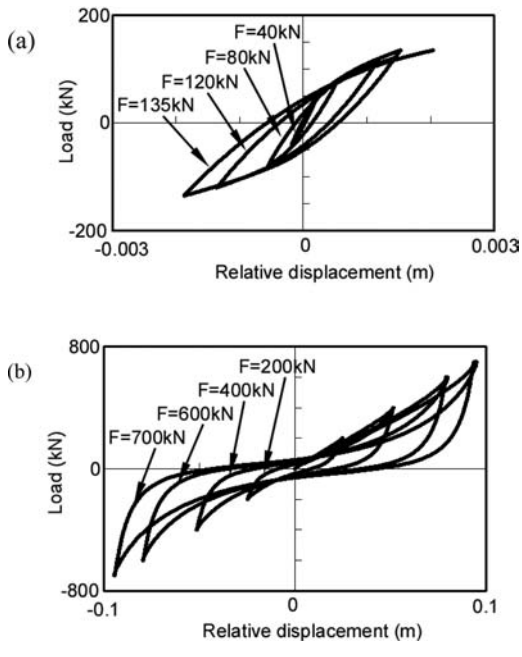

Figure 10. Load-displacement relationship of pile-soil system in horizontal plane under cyclic loading; (a) dry ($\sigma'_{m0} = 24.5$ kPa), (b) saturated ($S_0 = 0.05$) ($\sigma'_{m0} = 98$ kPa).

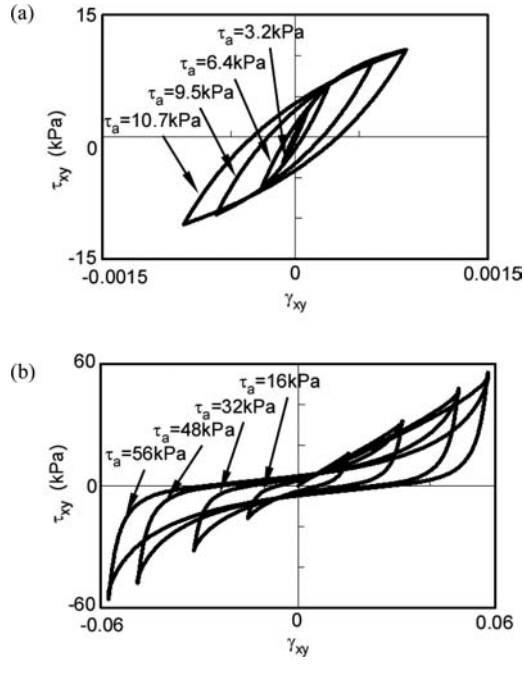

Figure 11. Shear stress-shear strain relationship of a single soil element under cyclic simple shear; (a) dry ($\sigma'_{m0} = 24.5$ kPa), (b) saturated ($S_0 = 0.05$) ($\sigma'_{m0} = 98$ kPa).

a fictitious single soil element of a multiple shear mechanism model.

For the analysis of pile-soil interaction during earthquakes, two dimensional analysis domain is set for a vertical cross section of soil-pile system. In this analysis, the soil–pile interaction in horizontal plane formulated through Equations (1) through (3) is idealized as a soil-pile interaction spring element as shown in Figure 12. While the conventional spring elements used in the analysis of soil-pile interaction is embedded in the same plane of the two dimensional finite element analysis domain, the soil-pile interaction spring defined in this study is used as a spring that connects a free pile to a two dimensional cross section of soil between the piles. If looked in a plan view, the soil idealized through the finite element analysis is in a plane that goes along the periodic boundary line shown in figure 5(b) while the pile analyzed is located a part at a distance of a half pile spacing.

In addition to the soil-pile interaction spring, soil-pile interface effect, including sliding and separation, should be appropriately taken into account in the analysis. In this study, this effect is idealized by inserting a joint element between the corresponding nodes on the pile-soil spring and the pile element. A schematic figure for representing soil-pile separation effect is shown in Figure 13.

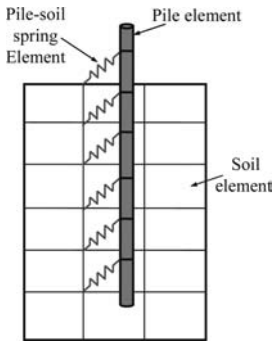

Figure 12. Schematic figure of pile-soil interaction spring.

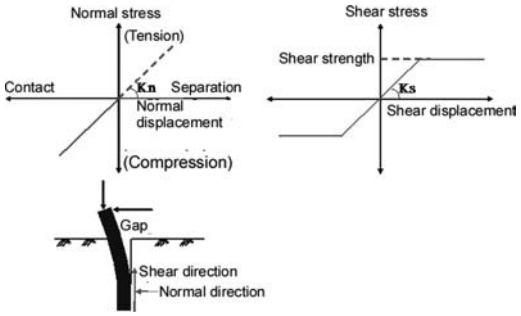

Figure 13. Schematic figure of joint element for representing soil-pile interface effect.

4 FULL SCALE MODEL TESTS & ANALYSIS OF PILE GROUP UNDER LATERAL LOAD

The applicability of the multiple shear mechanism model incorporating the soil-pile interaction spring and a joint element for allowing soil-pile separation effect is studied through a two dimensional analysis of a full scale lateral loading tests of a 3×5 pile group performed at the Salt Lake City Airport, USA (Rollins et al, 1998, Snyder, 2004). The idealized soil profile at the test site is shown in Figure 14. The evaluated shear strength of clay in the upper three clay layers from the unconsolicated undrained (UU) triaxial tests and cone penetration test ranged from 30 to 40 kPa, whereas those for the clay layers at 5 to 6 meters below the ground surface ranged from 30 to 60 kPa. Internal friction angle of sand layer at a depth of 3 to 5 m was evaluated from the standard penetration test as 38 degrees, whereas that below 6 m as 33 degrees.

For the full scale model tests, steel pipe piles were driven closed end to an embedment depth of 11.6 m. The test pile has a 0.324 m outside diameter with a 9.5 mm wall thickness. The piles in the group were driven in a 3×5 pattern with a nominal spacing of 3.92 pile diameters center to center in the loading direction and of 3.29 pile diameter perpendicular to it. The lateral load was applied 495 mm above the ground surface. A photograph of the overall layout of the 15-pile group, with a reference single pile in front, is shown in Figure 15. The piles and the load frame are pin-connected so that the rotation is free at the pile head. For static loading, the piles were pushed against reaction wall with two 1.34 MN hydraulic jacks powered by a hydraulic pump of a maximum pressure of 69,000 kPa.

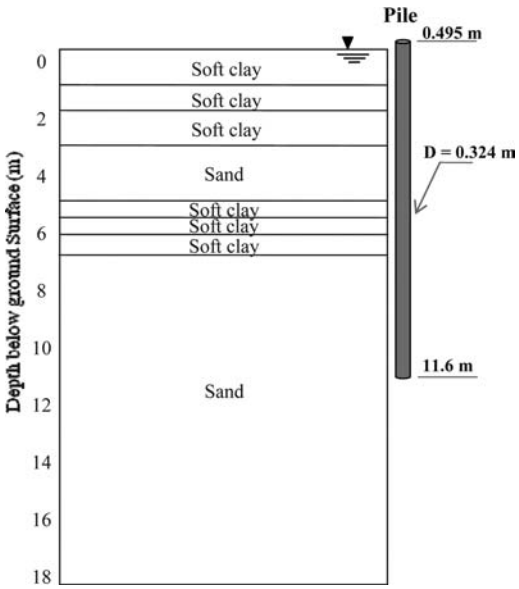

Figure 14. Idealized soil profile at the Salt Lake City International Airport Site, USA.

In the analysis of the full scale group pile test, the finite element mesh shown in Figure 16 was used for the computation. The lateral load is statically applied at pile heads (0.495 m above the ground surface) until the displacement of 90 mm is achieved at the loading point.

Figure 17 shows computed and measured response of a single pile with and without soil-pile separation. The analysis without separation highly overestimates the lateral load-carrying capacity of the pile. In fact, the soil-pile gap was observed in-situ at the full scale test sites as shown in Figure 18. In the analysis, when soil-pile separation is considered, the

Figure 15. Full-scale lateral load test layout; a reference single pile in front of 3×5 group pile.

Figure 18. Photograph of a gap formation behind the pile (the pile is deflected laterally to the right and the gap is formed on the left of the pile in the photo).

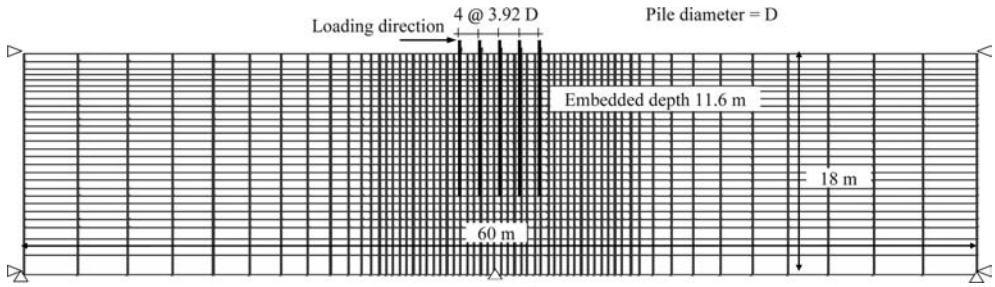

Figure 16. Finite element mesh for the group pile under lateral load test.

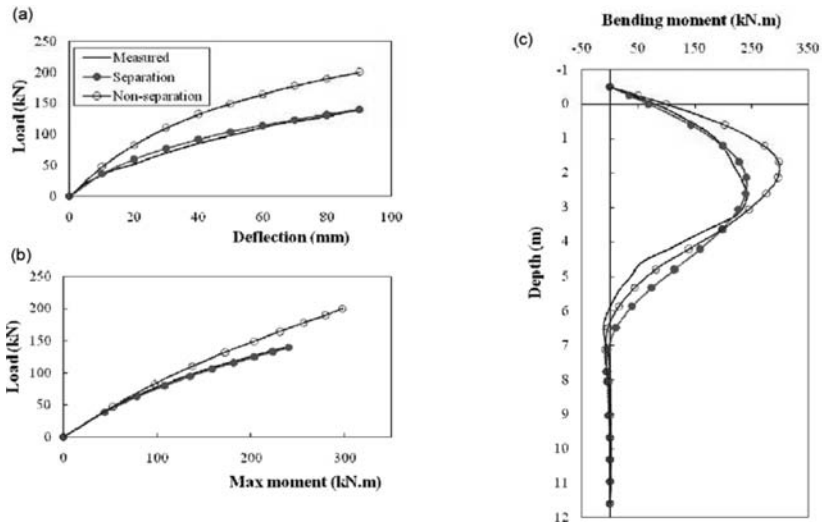

Figure 17. Single pile response under static load: load-deflection curve (a), load-maximum bending moment curve (b), and bending moment distribution (c).

load-deflection curve agrees well with those measured. The separation between soil and pile occurs in the analysis when the normal stress at the interface goes into tension regime as stated previously. The computed load-maximum bending moment curve and the bending moment distribution with soil-pile separation also agree well with the measured values. At the same load level, the analysis without soil-pile separation underestimates both deflection and maximum bending moment. At target deflection of 90 mm, ignoring soil-pile separation leads to 43% overestimation of the ultimate lateral load-carrying capacity of the pile.

Computed and measured load as an average per pile are shown in Figure 19. In the figure, the leading pile is designated as pile no (1), while the trailing pile as pile no (5). In comparison to the results for a single pile, the effect of the pile-soil separation is not significant for most of the piles in pile group except for the trailing pile, where the computed result with the effect of pile-soil separation effect agrees well with those measured. The computed results without this effect resulted in 73% overestimation of load-carrying capacity at the target deflection of 84 mm.

In order study further the mechanism that causes the difference in the effect of pile-soil separation among the piles within the pile group, lateral earth pressures computed in front of and at the back of a pile at a depth of 0.3 m from the ground surface are shown in Figure 20. The trailing pile shows that the potential tensile force that would be acting if the pile-soil separation is not allowed as shown on the right side of Figure 20(b) is released to zero when the pile-soil separation is allowed as shown in Figure 20(a). the positive earth pressure in front of the pile is not very sensitive to the effect of pile-soil separation. The leading pile and middle pile show little effects of soil-pile separation not only in front of the piles but also at the back of the piles. In the analysis, soils in active side (extension side) of each pile move in the direction of pile deflection due to the deformation of the next column of pile behind the pile in question, and therefore a gap cannot be formed behind the pile in a relatively closely spaced pile group as analyzed in this study. The soil-pile gap that could have been formed for these piles appeared to be closed by the soil mass that were actually pushed forward by the column of pile trailing behind.

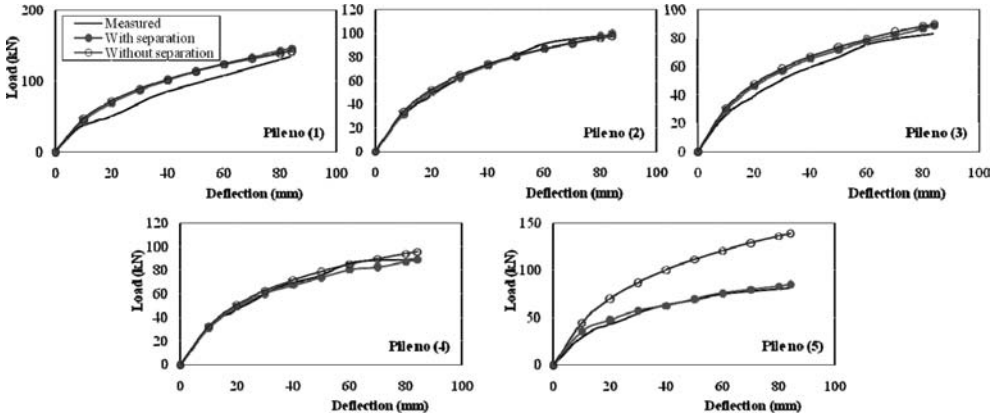

Figure 19. Group pile response under static load: load-deflection curves for piles no (1) through (5).

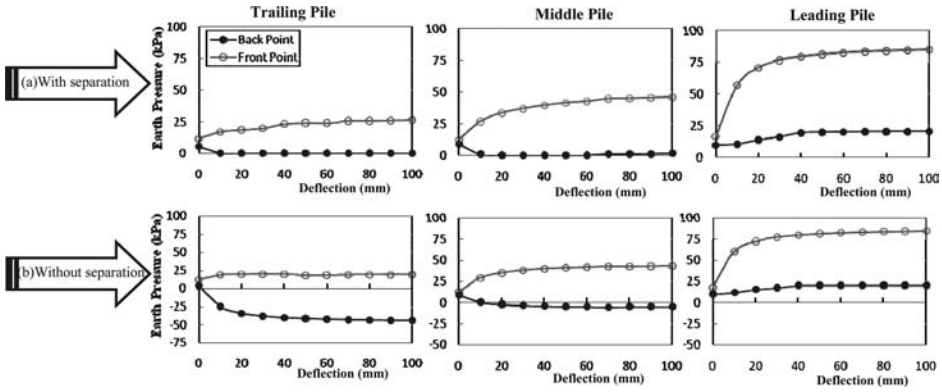

Figure 20. Earth pressures in front of and at the back of piles at depth 0.3 m below the ground surface; (a) with soil-pile separation, (b) without a separation.

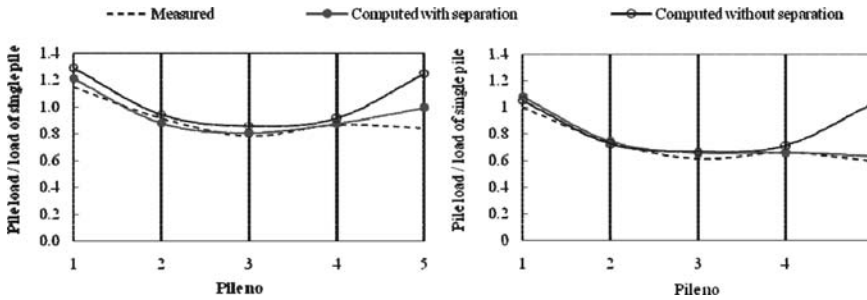

Figure 21. Load distribution among piles in group pile; (left) at a pile deflection of 10 mm, (right) at 84 mm.

Figure 21 shows the load distribution among the piles in pile group relative to the load of single pile at the same deflection levels. The distribution computed without the soil-pile separation effect shows minimum load at the middle pile, whereas that with soil-pile separation effect shows gradual decrease from the leading pile towards the trailing pile. The computed results with the soil-pile separation effect agrees well with those measured. The analysis without the soil-pile separation effect tends to exaggerate the load carried by the trailing pile.

5 CONCLUSIONS

The paper reviews recent developments on the soil-pile interaction in horizontal plane and effect of soil-pile separation for laterally loaded group pile. The primary conclusions can be summarized as follows:

(1) Local displacement field of soil in the vicinity of a pile associated with global displacement of soil around pile foundation shows vortices at the pile side. Displacement at the pile side shows strain localization at the soil-pile interface, indicating a mechanism similar to sliding. This fact implies that the finite element mesh size should be sufficiently small in the vicinity of the pile in order to represent these essential features of the local displacement field.

(2) Computed local displacement field of soil through a multiple shear mechanism model in a horizontal plane are basically consistent with those measured. The computed load-displacement curves indicates that, for dry sand, the curves have similar shapes to those currently used in design practice in terms of *p-y* curve, whereas, for saturated sand, the curve shows hard-spring type shape when the displacement becomes large.

(3) Although the mechanisms involved in the load-displacement curve are the results of complicated soil-pile interaction as exemplified by the local displacement field described above, the load-displacement curves have practically the same shapes as those of the shear stress-shear strain of a single soil element under cyclic simple shear. Based on this finding, the soil–pile interaction in horizontal plane is idealized as a soil-pile interaction spring element using a fictitious single soil element. While the conventional spring element is embedded in the same plane of the two dimensional finite element analysis domain, the soil-pile interaction spring proposed in this study is used as a spring that connects a free pile to a two dimensional cross section of soil between the piles.

(4) In addition to the soil-pile interaction spring, a joint element is used to idealize the pile-soil interface effect, including soil-pile separation effect. The analysis of a full scale model test of group pile indicate that the effect of soil-pile separation can be significant.

REFERENCES

Iai, S., Matsunaga, Y. & Kameoka, T. 1992. Strain space plasticity model for cyclic mobility, *Soils and Foundations*, 32(2), 1–15

Iai, S., Tobita, T., Donahue, M., Nakamichi, M. & Kaneko, H. 2006. Soil-pile interaction in horizontal plane, *Geotechnical Special Publication* 145, ASCE, 38–49

Ozutsumi, O. 2003. *Numerical studies on soil-structure systems on liquefiable deposit during earthquakes*, Doctors Dissertation, Kyoto University

Rollins, K.M., Peterson, K.T., & Weaver, T.J. 1998. Lateral load behavior of full-scale pile group in clay, *Journal of Geotechnical and Geoenvironmental Engineering*, 124(6), 468–478

Snyder, J.L. 2004. *Full-scale lateral-load tests of a 3x5 pile group in soft clays and silts*, M. Sc. thesis, Brigham Young University

Soil-Foundation-Structure Interaction – Orense, Chouw & Pender (eds)
© 2010 Taylor & Francis Group, London, ISBN 978-0-415-60040-8

Investigation of seismic design of drilled shafts in cohesive soils

A. Shelman & S. Sritharan
Iowa State University, Ames, Iowa

ABSTRACT: Characterizing lateral load behavior of cast-in-drilled-hole (CIDH) shafts (or drilled shafts), although commonly used in seismic regions, is challenging due to their complex interaction with foundation soil. A recent study conducted at Iowa State University (ISU) identified deficiencies in the current practice of accounting for soil-foundation-structure interaction (SFSI) in the design of drilled shafts in cohesive soils. The main concern was that none of the existing simplified models were able to capture the response of the soil-shaft-column system behavior in both the elastic and inelastic regions. This paper investigates the current state of practice for modeling drilled shafts in high seismic regions and identifies the deficiencies. In addition, a new approach that more accurately simulates the lateral load response of bridge columns supported on CIDH shafts in cohesive soils is presented.

1 INTRODUCTION

All across the world, seismic design is an ever changing field based on the continuously gained knowledge in the field of seismology as well as structural and geotechnical engineering. Currently, a significant amount of research is being performed in the area known as soil-foundation-structure-interaction (SFSI) in order to better understand the lateral response of structures in different soil types. As part of an ongoing research effort in the field of SFSI, a recent project at Iowa State University (ISU), funded jointly by the Alaska University Transportation Center (AUTC) and Alaska Department of Transportation and Public Facilities (ADOT&PF), has examined the lateral load behavior of continuous column-foundation systems in cohesive soils. The type of system examined was the bridge column that extended into the ground as a cast-in-drilled-hole (CIDH) shaft. This system is commonly used in bridge design today due to the simplicity of construction, elimination of column-foundation connection and reduced construction costs.

Although CIDH shafts are commonly used in seismic regions because of the aforementioned benefits, the project identified a deficiency in the current practice of accounting for SFSI in the design of drilled shafts in cohesive soils. Currently, several different models exist for simplifying the Winkler soil spring concept that accounts for SFSI in cohesive soils; however, none of the models are able to capture the response of the system in both the elastic and inelastic ranges. This paper presents an investigation into the existing models in order to demonstrate some of these deficiencies. In addition to the investigation, a new approach is discussed that is able to capture the lateral response of the system in both the elastic and inelastic ranges and has the potential to provide information on both local and global design parameters.

2 CURRENT DESIGN MODELS

In order to reduce the number of iterative steps needed for analysis and design when using the Winkler soil spring concept, many models have been developed in order to simplify the process of accounting for SFSI in the design of drilled shafts. Although multiple models have been created [e.g., Chai (2002), Priestley, et al. (1996), Priestley, et al. (2007)], none of the models are able to capture the SFSI effects on the lateral load response throughout the entire loading range expected during design-level or greater seismic events. Furthermore, these models have not given consideration in quantifying all local design parameters. This section of the paper provides a summary of an in-depth investigation into some of the more common codes and models used in practice today.

2.1 *AASHTO LRFD bridge design specifications (2007)*

The state of bridge design practice within the United States is generally dictated by the current specifications and interim revisions published by the American Association of State and Highway Transportation Officials (AASHTO). The currently used code was published in 2007 with interim revisions updated yearly in order to maintain changes while the next version of the code is being produced. In the current code, two

methods are deemed appropriate for ensuring adequate displacement capacities for foundation shafts when designing them for lateral loads. These two methods require extensive knowledge on the subsurface surroundings as well as a long iterative process that is hard to complete by hand.

The first method uses the Winkler spring method in which p-y curves are created and placed along the shaft length in order to determine the structural equilibrium through a numerical iteration process. The second method is to use the strain wedge model and an iterative process in which an envisioned three-dimensional passive wedge of soil developed in front of a pile is related to the one-dimensional beam on elastic foundation theory (Ashour, et al. 1998). Although both models have been shown to accurately represent the behavior of the laterally loaded system, these models require a great deal of information on the pile and surrounding soil and take a significant number of iterations to complete especially in the inelastic displacement range of the system.

2.2 *Guide specifications for LRFD seismic bridge design (AASHTO, 2009)*

Recently, AASHTO published guidelines for the LRFD seismic design of bridges in order to better update the specifications when dealing with seismic conditions. In the seismic design guidelines, multiple methods are presented for determining the lateral response of pile foundations based on site location, bridge design and importance. Methods, from simple to complex, are discussed within the main guideline sections and additional simple methods are identified within the commentary. The complex method presented within the guidelines will not be presented within this section as the method uses the same procedures that were previously discussed within Section 2.1. The simplified method presented within the main text, although very simple, is very inaccurate.

The simple method models the bridge column with a shaft extended to an equivalent point of fixity within the soil using empirical means. The empirical equation determines the point within the soil that allows for the column/foundation system to be represented as an equivalent cantilever where the extended shaft is modeled without any surrounding soil and is fully constrained at the base from experiencing any deformation. The top end of the column/shaft unit is modeled using the constraints imposed by the bridge superstructure. The equivalent point of fixity within the system is located by determining the extended length of the shaft from an equation that is a function of the ratio between the flexural rigidity of the pile and a soil modulus using empirical means. The main deficiency of this approach is that it does not accurately capture the maximum moment location in the shaft as this point does not generally occur at the point of fixity, but rather above this point in most cases. The maximum moment location is critical in design as this will determine where the confinement reinforcement

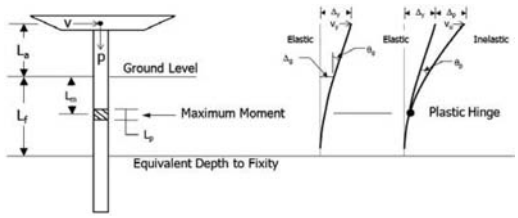

Figure 1. Equivalent fixed-base cantilever (reproduced from Chai 2002).

should be provided as this is where the plastic hinge will develop. When plastic hinges are not designed correctly, a brittle failure of the foundation shaft will most likely ensue. Other deficiencies of these code-based methods may be summarized as follows:

1. No validation for the estimated fixity point is given;
2. No clear information is provided on how plastic action in the shaft will be included when estimating the lateral column displacement;
3. Shear demand in the column and foundation shaft are assumed to be constant; and
4. The more detailed method is not straight forward and requires a significant amount of time and knowledge on the surrounding soil parameters.

Within the commentary, additional simple approaches are suggested in lieu of the point of fixity method if the systems are believed to not behave in a linear elastic manner [i.e., soil and structure are behaving elastically]. In most seismic design situations, this assumption is not valid and the other suggested approaches would be more applicable. Some of the models that are suggested include Chai (2002) and Priestley (2007). These models are discussed in Sections 2.3 and 2.4, respectively.

2.3 *Chai (2002)*

Chai proposed a model to determine the lateral response of extended pile shafts while accounting for the effects of soil. The model relies on the use of two points, fixity and maximum moment, along the length of the system in order to determine the systems flexural strength and ductility. A visual representation of the model and the two points defining the fixity and the maximum moment locations used to determine the lateral loading and displacements of the column/foundation system are shown in Figure 1.

The first critical part of Chai (2002) was to present the derivation of the point of fixity. The point of fixity was determined by relating the stiffness of the soil-shaft system to that of an equivalent cantilever system. In order to relate the two systems, the closed form solution to ground movement of a long pile subjected to lateral loading produced by Poulos and Davis (1980) was used. Using this information in conjunction with standard cantilever displacements, a fixity coefficient location was determined based off of the aboveground height coefficient, defined as the height

of the column divided by the characteristic length of the soil-shaft system, and an assumption about the modulus of horizontal subgrade reaction.

Once the point of fixity is located, the maximum moment location is also needed in order to determine the ductility capacity of the system. Using a modified version of Broms (1964) soil pressure distribution acting on the pile, shear and moment equations are suggested by Chai that allow for the depth to maximum moment to be located as well as the maximum shear force in the system to be determined. Using this information, the amount of plastic deformation in the system could be found using an idealized elasto-plastic moment-curvature response for the foundation shaft, which does not accurately represent the elastic and plastic curvatures that occur at the maximum moment location, and an analytical plastic hinge length suggested in Chai and Hutchinson (2002). Chai and Hutchinson (2002) demonstrated that the analytical plastic hinge length in the foundation shaft was related to the above ground column height only and would vary between 1.0D and 1.6D.

Although Chai's analytical plastic hinge length was verified experimentally, the verification did not include shaft response in cohesive soil even though this method was recommended by Chai (2002) for both cohesive and cohesionless soil. By using experimental data from Suleiman, et al. (2006) and current data from the ISU project, the research at ISU has found that the analytical plastic hinge length typically exceeds the upper limit of 1.6D in cohesive soils.

In addition, another deficiency arises within the bilinear force-displacement curve produced by Chai's model for the column-foundation system. The deficiency stems from the fact that the column-foundation system response is modeled to have a perfectly plastic response between the yield and ultimate conditions. This does not accurately represent the strength gained and changes in displacement between the yield and ultimate limit states due to the effects of soil nonlinearity and strain hardening of reinforcement in the plastic hinge region of the shaft.

2.4 *Priestley, et al. (2007)*

In 2007, Priestley, et al. published a book dealing with displacement-based seismic design. In the book, multiple topics are covered including the topic of bridge columns that extend into the ground as CIDH shafts. During the discussion of this topic, a model was introduced that would determine the design displacement values for pile/column systems based off of modifications made by Suarez and Kowalsky (2007) to the equations presented by Priestley, et al. (2007).

To determine the design displacement in this method, the following steps are taken:

1. Locate the in-ground plastic hinge using nomographs or equations;
2. Determine the yield and ultimate limit state curvatures using a moment-curvature analysis and the damage-control limit strains of steel and concrete;
3. Find the length of the plastic hinge based off of Chai's model (2002);
4. Determine a coefficient to account for the effects of soil type and boundary conditions using nomographs or equations; and
5. Find the yield and design displacements using the equations presented in the text.

This model is able to produce the displacements needed for design, but does not provide the lateral shear demands that the system must resist during the seismic event to ensure an adequate response.

Also, the cohesive model was created through a parametric study using OpenSees on medium to soft cohesive soils (Suarez and Kowalsky, 2007), with undrained shear strengths, s_u, between 20 kPa and 40 kPa (420 psf and 840 psf). The ability of the model to characterize columns supported by drilled shafts in stiff soils has not been studied. Undrained cohesive strengths of stiff soils will noticeably exceed the above mentioned range and could be as high as 400 kPa (8350 psf). The final deficiency with this model is that the plastic hinge length is determined using Chai's method (2002), which has been reported in Section 2.3 to generally underpredict the analytical plastic hinge length in cohesive soils.

3 PROPOSED NEW APPROACH

The previous section has demonstrated that the current design models are unable to capture both the local and global responses of a continuous column/foundation system during a seismic event. In response to the deficiencies noted within current practices, a new design model was created that would be able to account for local and global effects by performing a parametric study in LPILE (Reese, et al. 2004) using soil models based on the work done by Reese (1975). Given the impact of seasonally frozen clay on seismic response of column/shaft systems as detailed by Sritharan, et al. (2007), this issue is also given consideration when developing the design model so that it can be used in all seasonal conditions. More information on model development is provided in Shelman (2009).

The new model consists of a series of three springs, two translational and one rotational, located at critical points in the system using minimal input parameters. A depiction of the proposed new model is presented in Figure 2.

3.1 *Input parameters*

The new model was created on the basis of obtaining an accurate representation of SFSI while using the least amount of input parameters as possible. In order to achieve the desired results, the following parameters were deemed necessary:

- Soil parameters
  - Moist unit weight, γ_m;
  - Average undrained shear strength, s_u or c_u, taken over the first six pile diameters below ground; and

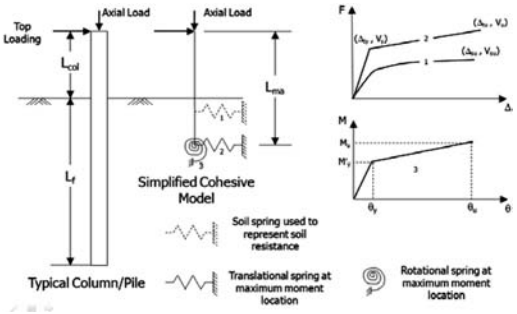

Figure 2. Proposed new model.

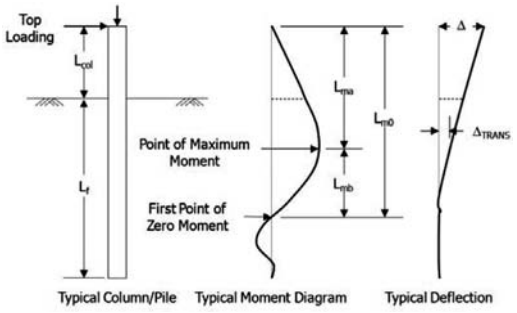

Figure 3. Critical locations terminology for proposed new model.

- Strain at fifty percent of maximum principal stress difference, ε_{50}.

- Pile parameters
  - Height of column above ground, Lcol;
  - Column axial load, P; and
  - Details necessary to perform a moment-curvature analysis.

3.2 *Output parameters*

Using the aforementioned parameters, the remaining development of the model uses a series of equations to determine the critical locations, depicted in Figure 3, as well as the three spring properties needed for the model as detailed below.

3.2.1 *Maximum moment location*

The maximum moment location is the most critical point to locate as this is the point used for defining the effective height of the model but with a flexible base. This point is the most critical to the proposed model as two of the aforementioned springs, the rotational and a translational, are located at this point. The maximum moment location was given significant consideration as the most damage to the system will occur due to a seismic event at this point and all plastic action is assumed to act solely in the vicinity of this point when determining the final displacements. The maximum moment location is found using Equation 1, where α_{ma}, β_{ma} and χ_{ma} are coefficients calculated based off of the soils undrained shear strength.

$$L_{ma} = D\left[\alpha_{ma}\left(\frac{L_{col}}{D}\right)^2 + \beta_{ma}\left(\frac{L_{col}}{D}\right) + \chi_{ma}\right]$$

where,

$$\alpha_{ma} = -0.000005c_u{}^2 + 0.0003c_u + 0.028 \quad (1)$$
$$\beta_{ma} = 0.0038c_u + 0.3247$$
$$\chi_{ma} = -1.28\ln[c_u\,(psi)] + 7.1307$$

3.2.2 *Zero moment location*

The next point to be determined is the point at which the moment profile first crosses back over the zero point below the maximum moment location. This point is needed in order to determine the properties of the rotational spring located at the maximum moment location. The zero moment location is found using Equation 2 where α_{m0} and β_{m0} are coefficients based on the above ground height of the column.

$$L_{m0} = D\alpha_{m0}(c_u)^{\beta_{m0}}$$

where,

$$\alpha_{m0} = 0.11\left(\frac{L_{col}}{D}\right) + 22.3 \quad (2)$$
$$\beta_{m0} = 0.021\left(\frac{L_{col}}{D}\right) - 0.33$$

3.2.3 *Maximum moment translational spring*

Once L_{ma} and L_{m0} are computed, the spring properties can be readily determined. The first set of bilinear spring properties to be determined is the properties of the translational spring located at the maximum moment location. This spring is used to model the translation that occurs at this point due to the movement of the pile below this point. The translation at the ultimate condition is found using Equation 3 while the translation at the yield condition is found using Equation 4.

$$\Delta_{tu} = D\left[0.0255\psi\left(\frac{L_{mb}}{D}\right) - 0.0652\right]$$

where, (3)

$$\psi = 0.0157\left(\frac{L_{col}}{D}\right) + 0.9342$$

$$\Delta_{ty} = \frac{\Delta_{tu}}{4.37} \quad (4)$$

In Equation 3, ψ is a correction factor used only if c_u is less than ~70 kPa (10 psi); otherwise the value is input as 1. The lateral forces needed to activate the aforementioned displacements are computed by ensuring static equilibrium of the simplified model representing the system shown in Figure 2. In determining the lateral force, the yield and ultimate limit states are examined thus providing specific conditions to ensure equilibrium in the system.

3.2.4 *Rotational spring properties*

The rotational spring placed at the maximum moment location is used to account for all of the plastic action that occurs within the system as well as the elastic rotation that occurs below the maximum moment location. In order to determine this bilinear moment-rotation spring, Equations 5 to 8 are used for the ultimate condition, where L_p is the analytical plastic hinge length used for the plastic rotation, θ_p, calculation. Equation 9 is used to determine the elastic rotation below the maximum moment location at the yielding condition, θ_{eby}. The moment value for each point shall be taken as the ultimate moment and the first yield moment of the system, respectively.

$$\theta_{ebu} = 0.0031\frac{L_{mb}}{D} + 0.0006 \tag{5}$$

$$L_p = 2(0.16L_{mb}) \tag{6}$$

$$\theta_p = \varphi_p L_p = (\varphi_u - \varphi_e)L_p \tag{7}$$

$$\theta_u = \theta_{ebu} + \theta_p \tag{8}$$

$$\theta_y = \theta_{eby} = 0.002\frac{L_{mb}}{D} + 0.00001 \tag{9}$$

where θ_{ebu} = elastic rotation below the maximum moment location at ultimate condition; ϕ_p = plastic curvature of the section which is defined as the ultimate curvature, ϕ_u, minus the elastic curvature, ϕ_e, at ultimate condition; θ_u = rotation at the maximum moment at maximum moment; θ_y = rotation at the maximum moment location when first yielding occurs.

3.2.5 *Soil spring*

The final translational spring used within the system is a soil spring. This spring, which may be replaced by multiple springs, is placed halfway between the maximum moment location and the ground surface in order to account for the resistance provided by the soil in this region. By locating a soil spring within the system, the influence of seasonal freezing on the soil properties and thus the system behavior may also be accounted for. The seasonal temperatures also affect the behavior of construction materials. Although their influence on the response of column-foundation systems is relatively small (Sritharan, et al., 2007), this issue can also be addressed in the proposed model by revising the moment-curvature response to account for the temperature effects on the material properties.

The properties of the translational spring can be found using the procedure used for establishing the p-y curve as outlined by Reese and Welch (1975) with the inclusion of γ_m and ε_{50}. If a hand calculation is performed to determine the tip lateral load and displacement, first determine the ultimate soil pressure, p_u, using γ_m and c_u in the equations presented in Reese and Welch (1975). Multiply this ultimate soil pressure by the height of the soil column to determine the resistance of the soil, V_{su}. When dealing with the yield condition, multiply this value by a coefficient, η, to adjust the soil resistance value to the limit state being analyzed. The coefficient, η, is presented in Equation 10 and was found experimentally using data obtained from the analytical models produced at ISU.

$$\eta = -0.03\ln[c_u\,(\text{psi})] + 0.7536 \tag{10}$$

3.2.6 *Force-displacement response*

A hand calculation may be used to determine the global response of the system using the summation of the individual parts presented above. The summation consists of adding the total elastic displacement of the system with the total plastic displacement and initial translation, Δ_t, at the maximum moment location. The total elastic displacement is a summation of the displacement due to elastic rotation below the maximum moment location, Δ_{eb}, and the elastic displacement above the maximum moment location, Δ_{ea}, due to the cantilever action produced from a loading applied at level of the bridge superstructure. The initial translation at the maximum moment location is computed using either Equation 3 or Equation 4 depending on the limit state being analyzed. The total plastic displacement, Δ_p, is due to the plastic rotation, θ_p, located at the maximum moment location. The final equation, Equation 11, is an iterative process as the final top elastic displacement must be computed using the cantilever equation with a modification for P-Δ effects.

$$\Delta_{final} = (\Delta_{eb} + \Delta_{et}) + \Delta_p + \Delta_t$$

where,

$$\Delta_{eb} = \theta_{eb} L_{ma}$$

$$\Delta_{et} = \frac{V_{top} L_{ma}^{\ 3}}{3EI_e} \tag{11}$$

$$\Delta_p = \theta_p L_{ma}$$

$$\Delta_t = \Delta_{tu} \text{ or } \Delta_{ty}$$

3.3 *Model verification*

As part of the model creation, a verification of the system was performed against an outdoor testing program that was performed at ISU. The experimental testing program performed by Suleiman et al. (2006) consisted of lateral load testing of three column foundation systems, two of which were identical in nature with the only difference being the temperature at which they were tested. These two specimens, SS1 and SS2, were tested at 23°C and −10°C (~73°F and 14°F), respectively. Each specimen was tested in a quasi-static cyclic manner to examine the differences between warm and cold weather conditions. Using the reinforcement properties of these test units, the proposed new model was verified against the experimental results and found to well simulate the lateral load response of both systems. The warm weather comparison, SS1, is provided in Figure 4 and the cold weather comparison, SS2, is provided in Figure 5.

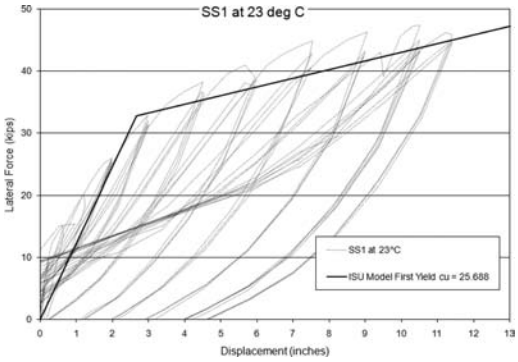

Figure 4. ISU warm weather model verification.

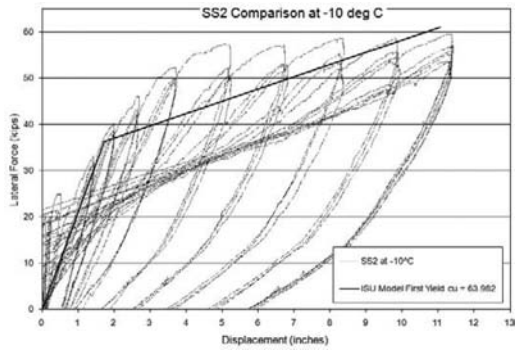

Figure 5. ISU cold weather model verification.

In addition to the experimental verification used for comparison purposes, the model was developed and verified for a range of structural parameters against nonlinear analysis of several column-foundation systems using a computer program that was based on the Winkler soil spring method. The computer program produced a basis for comparing the global and local responses of the model. The local responses were verified by examining the translation at the maximum moment location, the elastic and plastic rotations at the maximum moment location, the location of the maximum moment, and the location of the zero moment. The results were found to well simulate the analytical models presented in Sritharan, et al. (2007). Multiple points of comparison, including displacements and curvatures, were made in addition to the analytical models produced by Sritharan, et al. (2007) and have demonstrated that the model has the ability to handle a wide range of soil shear strengths and column axial loads. A final sensitivity analysis of the model needs to be completed that takes into account differing longitudinal reinforcement ratios, such as one and three percent, and differing transverse reinforcement ratios.

4 CONCLUSIONS

This investigation examined the current state of practice in regards to the seismic design of drilled shafts in cohesive soils. The investigation found that although several simplified models currently exist in order to determine the design displacements of drilled shafts, the models are not able to accurately capture both the local and global response of the system. In addition, an alternative model for predicting the seismic response envelope of a column supported on a drilled shaft in cohesive soils was explored. Based on the investigation summarized in this paper, the following conclusions are drawn:

1. Previous models specified to be used for cohesive soils [e.g., Chai (2002) and Priestley, et al. (2007)] have only been verified against experimentation on drilled shafts in cohesionless soils leading to inaccuracies in modeling drilled shafts in cohesive soil;
2. The models developed specifically for cohesive soils are typically for soft soils only;
3. Plastic action is typically underestimated due to the assumption that the analytical plastic hinge length will vary between 1.0D and 1.6D depending on the above ground height of the column. Although this is conservative for design, the system may be overly reinforced leading to higher costs;
4. The maximum moment location is not accurately identified within many of the models. This is a crucial point in the design to ensure that enough confinement is provided in the required region of the shaft to create a dependable response for the column-foundation system;
5. The proposed new model uses a series of three springs and has been shown to well simulate the response of continuous column/foundation systems in a global sense while enabling accurate estimates of the local design parameters at the critical locations; and
6. The new model has also been shown to handle the effects of seasonal freezing on the response of column/shaft system due to the presence of a soil spring above the maximum moment location and the modification of construction material properties with the temperature. The effects of seasonal temperature variation are not addressed in any of the others methods discussed in this paper.

ACKNOWLEDGEMENTS

The investigation presented within this paper was made possible through a project jointly funded by the Alaska University Transportation Center (AUTC) and the Alaska Department of Transportation and Public Facilities (ADOT&PF). Special thanks are due to Billy Connor, the Director of AUTC and Elmer Marx and Clint Adler of ADOT&PF for their support and assistance. Any opinions, conclusions, or recommendations made expressed in this article are those of the authors and do not necessarily reflect the views of the sponsors.

REFERENCES

American Association of State Highway and Transportation Officials (AASHTO). 2009. *Guide specifications for LRFD seismic bridge design.* Washington D.C.: AASHTO

AASHTO. 2007. *LRFD bridge design specifications with 2008 interim revisions, customary U.S. units, 4th edition.* Washington D.C.: AASHTO

Ashour, M., Norris, G. & Pilling, P. 1998. Lateral loading of a pile in layered soil using the strain wedge theory. *Journal of geotechnical and geoenvironmental engineering* 124(4): 303–315.

Broms, B. B. 1964. Lateral resistance of piles in cohesive soils. *Journal of soil mechanics foundation division* 90(SM2): 27–63

Chai, Y. H. 2002. Flexural strength and ductility of extended pile-shafts. I: Analytical model. *Journal of structural engineering* 128(5): 586–594.

Chai, Y. H. & Hutchinson, T. C. 2002. Flexural strength and ductility of extended pile-shafts. II: Experimental study. *Journal of structural engineering* 128(5): 595–602.

Poulos, H.G. & Davis, E. H. 1980. *Pile foundation analysis and design.* New York: Wiley.

Priestley, M. J. N., Seible, F. & Calvi, G. M. 1996. *Seismic design and retrofit of bridges.* New York: John Wiley & Sons, Inc.

Priestley, M. J. N., Calvi, G. M. & Kowalsky, M. J. 2007. *Displacement-based seismic design of Structures.* Pavia, Italy: IUSS Press

Reese, L. C. & Welch, R. C. 1975. Lateral loading of deep foundations in stiff clay. *Journal of geotechnical engineering division* 101(GT7): 633–649.

Reese, L. C., Wang, S. T., Isenhower, W. M., Arrellaga, J. A. & Hendrx, J. 2004. *LPILE plus 5.0, user's manual.* Austin: Ensoft, Inc.

Shelman, A. T. 2009. *Seismic design of drilled shafts in clay (master's thesis).* Ames: Iowa State University.

Sritharan, S., Suleiman, M. T. & White, D. J. 2007. Effects of seasonal freezing on bridge column-foumn-soil interaction and their implications. *Earthquake spectra* 23(1): 199–222.

Suarez, V. & Kowalsky, M. J. 2007. Displacement-based seismic design of drilled shaft bents with soil-structure interaction. *Journal of earthquake engineering* 11: 1010–1030.

Suleiman, M. T., Sritharan, S. & White, D. J. 2006. Cyclic lateral load response of bridge-column-foundation-soil systems in freezing conditions. *Journal of structural engineering* 132(11): 1745–1754.

Soil-Foundation-Structure Interaction – Orense, Chouw & Pender (eds)
© 2010 Taylor & Francis Group, London, ISBN 978-0-415-60040-8

Effect of shallow foundation modeling on seismic response of moment frame structures

L.M. Wotherspoon & M.J. Pender
University of Auckland, Auckland, New Zealand

ABSTRACT: This paper presents the development of numerical models that represent the seismic response of an integrated structure-foundation system, with similar levels of sophistication used to represent the response of the structure and shallow foundations. By adopting this approach, variations in response across the structure and the foundation in three dimensions can be identified. A range of footing models and design methods were used to indicate the impact of the foundation model inclusion on the structural demands. Uplift or compressive non-linearity of one footing dissipates energy and reduces demands on the structure directly above, but in the context of a full structure-foundation system, it can also shift actions to other footings and increase demands in other parts of the structure. Uplift reduces overall foundation system stiffness, creating shifts of moment and shear in single footings and causing residual actions to develop in the structure at the end of excitation.

1 INTRODUCTION

Current seismic design practice for low and medium rise structures highlights poor communication between structural and geotechnical engineering specialists. Buildings are commonly designed by ignoring the foundation structure and analyzed as a fixed base system, while foundations are designed using peak demands from the overlying superstructure. This approach treats the two as discrete units, whereas in reality they are intrinsically linked. In an environment where performance based design is the norm, soil-foundation-structure interaction (SFSI) effects must be incorporated into the evaluation of the seismic performance of such systems. By considering the structure and foundation as an integrated system, new opportunities may arise for achieving superior performance.

1.1 *Previous research*

Simple models were developed by Veletsos and Meek (1974), Bielak (1975) and Wolf (1985), representing a two dimensional structure-foundation system, with three degrees of freedom, by an equivalent single degree of freedom (SDOF) system. These were extended to multiple degree of freedom structures, with one degree of freedom representing each floor (Jennings and Bielak 1972, Parmalee et al. 1969, Tajimi 1967).

The Winkler bed of springs and the Beam on Nonlinear Winkler Foundation (BNWF) model has wide use in SSI applications due to its simplicity and the ease at which non-linear aspects can be incorporated into the model with minimal computational effort. Bartlett (1976) and Weissing (1979) developed Winkler based models using elastic plastic springs with uplift capabilities that provided good comparisons with experimental results. Nakaki and Hart (1987) used elastic springs and viscous dampers in their Winkler model at the base of a shear wall. Psycharis (1982), Chaallal and Ghlamallah (1996) and Filiatrault et al. (1992) modeled the nonlinear behavior of both the structural and foundation systems during seismic excitation. The foundation was represented by a Winkler spring bed with compressive yield and uplift. In each of these cases the above ground structure was represented as single column. Previous study in this area has been summarized by Kutter et al. (2003).

When structure and foundation have been modeled in an integrated scheme in previous research, one or both of the systems are usually significantly simplified. Even though sophisticated modeling techniques have been developed for the representation of foundations and structures, they have rarely been used in an integrated model (Wotherspoon et al. 2004a, 2004b, Wotherspoon 2009, El Ganainy and El Naggar 2009).

1.2 *Objectives of this study*

The goal of this paper is to determine the seismic response of a three dimensional frame structure with shallow foundations using Ruaumoko (Carr 2005), software capable of three-dimensional inelastic dynamic structural analysis. Details of the design and development of structural and shallow foundation models are presented. The integrated system consists of a three dimensional moment resisting frame building supported by discrete footings. Multiple shallow foundation models are presented based on the BNWF

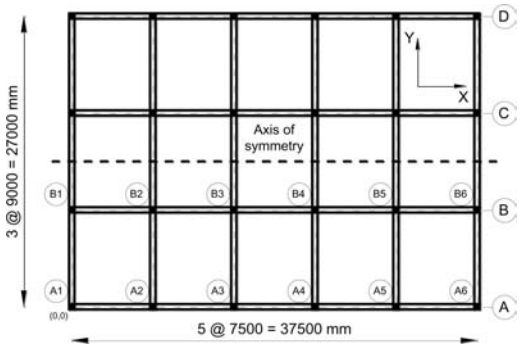

Figure 1. Structural plan indicating column/footing numbering scheme.

approach representing uplift, foundation compliance, radiation damping and coupling of degrees of freedom. The effect of foundation design is also investigated using two methodologies to size the footings.

Each integrated model is analyzed using a suite of earthquake records and the structural and foundation response identified. Results are compared against the response of a fixed base structure to provide a measure of the effect of integrated modeling on performance.

2 STRUCTURAL CHARACTERISTICS

2.1 *Structural details*

The structure used in this analysis was a three storey moment-resisting frame reinforced concrete commercial building. Figure 1 shows the plan of the building, which was five bays long and three bays wide, with bay dimensions of 7.5 m and 9.0 m respectively. Upper storey heights were 3.65 m and the first storey height was 4.50 m. The structure was designed for a 500 year return period event in the Wellington region using current New Zealand design standards ASNZS1170.5 (SNZ 2004) and NZS 3101:2006 (SNZ 2006). It was designed as nominally ductile with a ductility of 1.25 in order for the structure to remain elastic under seismic loading. To simplify the analysis, design focused on excitation in the x direction in Figure 1, and all members parallel to this direction contributed to the seismic resistance of the structure.

2.2 *Structural model*

In order to minimize the simplification of the structural model a structural component approach was used, with individual elements used to represent each beam and column of the actual structure. Even though seismic excitation was directed parallel to one axis, a three-dimensional model was created to represent the variation in response at each point in the structure. To reduce computation time, and as characteristics were identical for each half of the structure, the model was halved along the line of symmetry indicated in Figure 1. Only x displacement, z displacement and y rotation was allowable. All nodes at the column bases were fully fixed to represent the fixed base situation and the ground acceleration time-history was applied at these points. Nodal constraints were used at each floor level to create a rigid diaphragm.

The beams in the structural design were represented using the Giberson One Component Beam Model (Giberson 1969), and column members were represented using beam column elements. To account for the effect of cracking on member stiffness, effective moments of inertia (I_e) of the member sections were calculated using modifications to the gross moment of inertia (I_g) defined by NZS 3101:2006. Beam-column joint flexibility was represented with the same stiffness characteristics as the beam and column elements.

Using the permanent and imposed loads at each floor level, mass was concentrated at the nodes. The vertical and horizontal mass at each floor level was applied at the column nodes based on the tributary area of floor space of each node. In reality mass was distributed evenly across the surface of each floor, developing bending moments in the beams. These were represented in Ruaumoko by applying fixed end moments to each beam at the intersection of the column face, calculated using the distributed loads carried by the tributary area of each beam.

Elastic structural viscous damping was modeled by defining appropriate Rayleigh damping coefficients to the structure to provide 5% viscous damping to the fundamental mode, and at least 3% to every other mode (Carr 2005). Ruaumoko material specific Rayleigh damping coefficients were used to apply damping to the structure. Soil damping characteristics were modeled using dashpots as explained in the following section. Stiffness proportional damping parameters were applied to the structural elements, while mass proportional damping parameters were applied to the nodes due to the use of lumped masses. Stiffness proportional damping parameters of zero were used for the soil spring elements, as if Rayleigh damping had been applied to the whole model it would have resulted in an over-representation of the damping of the soil.

3 SHALLOW FOUNDATION CHARACTERISTICS

The foundation system used in this study consisted of independent shallow foundations beneath each of the structural columns. Each square footing was 1.0 m deep and constructed of reinforced concrete, providing a consistent connection between the column and the footing. All integrated models were founded on a 20 m deep homogeneous stiff clay deposit with a shear wave velocity (V_s) of 200 m/s, undrained shear strength (s_u) of 75 kPa, and a unit weight (γ) of 18 kN/m^3. The clay was assumed to remain undrained during seismic loading, with a poisson's ratio (υ) of 0.5. This material would be defined as Subsoil Class C (Shallow Soil) according to AS/NZS1170.5.

Table 1. Details of footing dimensions.

Footing Group		Footing length & width (m)	
		FOS3 design	CONS design
One	(A1, A6)	1.85	3.8
Two	(A2–A5)	2.65	3.8
Three	(B1, B6)	2.65	3.8
Four	(B2–B5)	3.8	3.8

Two design methodologies were used to size the footings using the static vertical factored loads from the overlying structure. First the shallow foundation bearing capacity equations were used design each individual footing to a static bearing capacity factor of safety of three (FOS3). This resulted in smallest footings at the corners of the building and largest in the centre. The second method used the same sized footings beneath each of the columns (CONS). The central footings, with the largest static vertical loading, were first designed to a static bearing capacity factor of safety of three. Footings of this size were used beneath all other columns so that the resulting factor of safety was three or above.

The footing sizes defined using the above methodologies are summarized in Table 1. Properties are presented in groups of footings with the same static vertical loads and positioning characteristics within the plan of the building. The labeling of each footing is presented in Figure 1.

3.1 *Foundation properties*

To define the stiffness characteristics of the shallow foundations, the small strain shear modulus of the soil (G0) was calculated using the shear wave velocity and the density. Guidelines for the effective shear modulus ratio (G/G0) in ASCE-41 (2006) were used to reduce the small strain shear modulus to an effective modulus (G) for use in the definition of foundation properties. The elastic stiffness characteristics of the foundations were defined using the solutions developed by Gazetas and his colleagues (Gazetas et al. 1985; Gazetas and Tassoulas 1987; Hatzikonstantinou et al. 1989), and summarized in Gazetas (1991).

Vertical and horizontal radiation damping characteristics were calculated using the methods presented in Mylonakis et al. (2006). The rotational damping of the foundation was defined by the vertical damping and the footing dimensions. As the radiation damping is dependant on frequency and the analysis undertaken in the time domain, a characteristic frequency equal to the fundamental period of the integrated structure foundation system was used.

Vertical compressive non-linearity of the soil beneath the foundation was defined assuming an elastic-plastic relationship. The ultimate vertical capacity of a footing was set to $6s_u$ multiplied by the base area of the footing. Horizontal non-linearity was not directly incorporated into the model.

3.2 *Foundation models*

A range of approaches using spring and dashpot elements were used to model the response of shallow foundations. Foundations were assumed to be rigid, with identical rotation at each point along its length. As excitation was applied parallel to one axis of the structure, these models provided a two-dimensional representation of the foundation response. Vertical, horizontal and rotational characteristics were modeled within the plane of excitation.

3.2.1 *Three spring model*

This simple model (3Spr) uses a spring and dashpot element to represent the stiffness and radiation damping characteristics of the three degrees of freedom of the foundation. Properties of each are defined using the approaches detailed in the previous section, and no non-linearity is incorporated into the model.

3.2.2 *Spring bed model*

This model (SBed) uses a bed of vertical, horizontal and rotational springs and dashpots to represent the characteristics of the footing. The same methods used for the 3Spr model define the footing properties. As a uniform vertical spring bed is unable to represent the rotational stiffness from these solutions (Wotherspoon 2009), this model uses rotational springs to increase the rotational stiffness of the foundation to the value defined by the Gazetas solutions. Each overall foundation property is split between the individual elements of the spring bed according to the fraction of total base area it represents. The rotational stiffness is also spread across the elements according to tributary area rather than tributary moment of inertia because of the cyclic nature of the loading.

3.2.3 *ASCE 41 model*

The ASCE 41-06 (2007) model (AS41) represents shallow foundation stiffness and damping using a bed of vertical and horizontal springs and dashpots. This model is the same as that presented by FEMA 273 (1997). The shallow foundation is divided into zones of different vertical stiffness, with the ends of the footing represented by zones of relatively high stiffness over a length of one-sixth of the footing width (B). Gazetas solutions were used to define the end zones as a B x B/6 footing, while the middle zone was based on a strip foundation. Total vertical stiffness is larger than the SBed model, while total rotational stiffness is less than that defined by the Gazetas solutions.

The original ASCE-41 model represented the horizontal stiffness of the foundation using a single horizontal spring. For this work, the ASCE-41 model is altered by spreading the horizontal stiffness across the foundation using multiple horizontal springs. The same scheme detailed for the SBed model is used, with horizontal stiffness defined by the Gazetas equations. The distribution and characteristics of the dashpot elements are the same as those detailed for the SBed model.

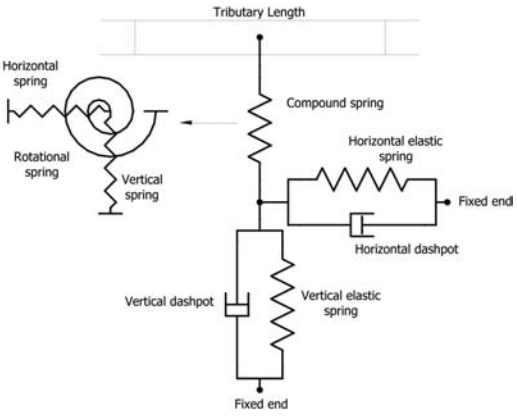

Figure 2. Series radiation damping configuration (elastic rotational spring for SBed model not shown for clarity).

3.3 *Element distribution*

Both the SBed and the AS41 models were divided into 20 regions to represent the characteristics across the foundation. Spring and dashpot elements for each region were arranged using a *series radiation damping configuration* indicated in Figure 2. This term was coined by Wang et al. (1998) to describe a non-linear hysteretic element in series with a linear visco-elastic element. The soil is separated into a plastic zone close to the foundation where non-linear soil-foundation interaction occurs, and an elastic zone further from the foundation where the behavior is linear elastic. This configuration means that forces radiating from the foundation must first travel through the hysteretic zone before being radiated away.

The Ruaumoko compound spring was used for the inner spring element, representing the non-linear response when uplift occurs and the vertical compressive non-linearity. Each compound spring consisted of a single vertical, horizontal and rotational spring. The uplift response and the use of the compound spring element is explained in the following section. Outside the plastic zone, Figure 2 shows that elastic stiffness was represented by spring elements and the radiation damping by dashpot elements.

3.4 *Uplift modelling*

Individual spring elements have no interaction between each loading direction, meaning when a vertical spring detaches in uplift, load will still be carried by the horizontal and rotational springs. To model the uplift of the foundation, springs in all directions should detach during uplift events, requiring the vertical force to control the detachment and attachment of the other spring elements.

To achieve this, modifications were made to the original compound spring element in Ruaumoko to allow the vertical stiffness to control the other stiffnesses within the compound spring. By defining interaction between the internal elements, all detach when the vertical force in the element reduces to zero. When the vertical force becomes compressive again the stiffnesses in all degrees of freedom are restored (Wotherspoon 2009). At the onset of uplift, the forces in the elastic spring and dashpot elements also reduced to zero as they were in series with the compound spring element.

4 INTEGRATED SEISMIC ANALYSIS

4.1 *Integrated model*

To develop the integrated structure-foundation model, column base nodes were released to allow movement in the same plane as the other structural nodes. Shallow foundation models were attached between these nodes and fixed nodes to represent the point of application of seismic loads. At ground level tie-beams were used to connect each footing both parallel and perpendicular to loading. Connection to each footing was pinned so that no moment was transferred by the tie-beams, only shear and axial force.

The ground floor was constructed of a 125 mm deep concrete slab poured onto the ground surface and over the shallow foundations. As the stiffness of the slab was comparatively small it was not included in the analysis. Horizontal masses at ground nodes were calculated from a combination of the structural loads below the first storey mid-height, tributary ground floor live and dead loads, and the footing mass itself. Vertical loads at these points were a combination of structural loads below the first storey and the effective weight of the footing. As the ground floor slab was poured directly onto the ground surface, it was assumed that the loads from the ground floor would not contribute any additional vertical load to the individual footings.

4.2 *Analysis details*

Integrated structure-foundation systems were analyzed using a set of four earthquake records appropriate for events in the Wellington region of New Zealand. Using the methodology detailed in NZS1170.5 (SNZ 2004), these records were scaled using the fundamental period of the integrated model and assuming a 500 year return period event in the Wellington region.

Ruaumoko non-linear time history analysis used the Newmark constant average acceleration method and was solved using a Newton Raphson iteration scheme. P-delta effects were also accounted for in the analysis. Prior to time history analysis, static analysis of the structure was carried out to impose the static loads on the structure, which were carried through to the non-linear time history analysis. The earthquake record applied to the structure was directed parallel to the longest dimension of the structure (the x direction).

5 ANALYSIS RESULTS

Fundamental period and elastic damping values for each model are summarized in Table 2. The 3Spr and

Table 2. Fundamental period and elastic damping characteristics.

Foundation	Period (secs)	Damping (%)
Fixed base	0.770	5.0
FOS3	0.809	5.3
CONS	0.792	5.3
CONS (AS41)	0.800	5.3

the SBed model had the same stiffness characteristics, whereas the increased vertical stiffness and reduced rotational stiffness of the AS41 model slightly altered the fundamental period. All foundation models provided the very similar increases in elastic damping for the integrated system.

Integrated models were compared with the fixed base structure without any foundation representation by plotting peak actions against each other. Using this comparison method, points above a 1:1 (45°) line represent increases in integrated model actions, and decreases below this line. Also shown on these figures are lines representing percentage changes in the fixed base values. Data is presented in terms of the footing groups detailed in Table 1.

5.1 *Elastic response*

Without foundation non-linearity, this model provides a simple representation of foundation response and the effect on the integrated system. Peak base shear characteristics for each column for the FOS3 foundation design are presented in Figure 3. FOS3 design has large variations in stiffness characteristics across the foundation system, resulting in the spread in peak shear in the figure. The smallest stiffness group 1 footings attracted less force and therefore developed reductions in action for all earthquake records. Groups 2 and 3 developed both increased and decreased shear, while the stiffest group 4 footings all attracted increased actions. Data points for each individual group showed a fairly linear relationship between peak integrated model and fixed base peak shear.

In contrast to the FOS3 design, the CONS design has identical stiffness properties across the foundation system. As a consequence, the peak shear properties in Figure 4 were very similar for each footing group, as indicated by the linear nature of all the data points. Shear for the CONS design varied by ±10% of the fixed base values, compared to values of approximately ±25% for the FOS3 design. Similar characteristics were also apparent for the maximum bending moment characteristics for each model, and have therefore not been shown here.

5.2 *FOS3 foundation design*

The effect of the inclusion of foundation compliance and uplift into the foundation model is shown by the difference in peak shear characteristics in Figure 3 and

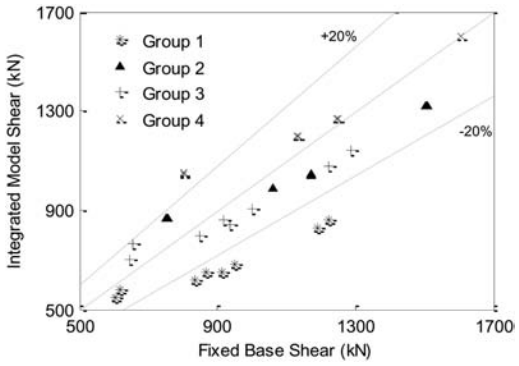

Figure 3. Peak column base shear for the FOS3 foundation design with elastic 3Spr model.

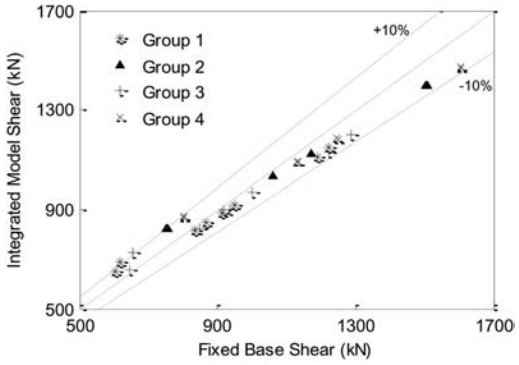

Figure 4. Peak column base shear for the CONS foundation design with the elastic 3Spr model.

5, with maximum variation in peak shear increasing to ±35%. During excitation, group 1 and 2 footings at the ends of the structure developed uplift and non-linear compressive deformation, with other footings remaining elastic. Because of this, the slope of a line drawn through the group 1 points for the FOS3 model is less than the 3Spr. The slope for the group 2 footings reduces to a smaller extent as they experience less non-linearity.

When a footing uplifts or the soil beneath yields, the demand on the rest of the foundation system will increase to balance the loads. The peak shear in group 3 and 4 footings increases as load shifts inward due to the reduction in the stiffness of the outer footings. The slopes of the line through these points are similar for both the FOS3 and the 3Spr model as these footings remain elastic during the excitation. Even though soil non-linearity in the horizontal direction is not directly modeled, the vertical compliance and reduction in soil contact area beneath the foundation reduces the stiffness horizontally with the use of the compound spring element.

To provide an indication of the bending moment characteristics, Figure 6 presents the peak bending moment for the integrated model with FOS3 foundation. Spread in the peak bending moment data points

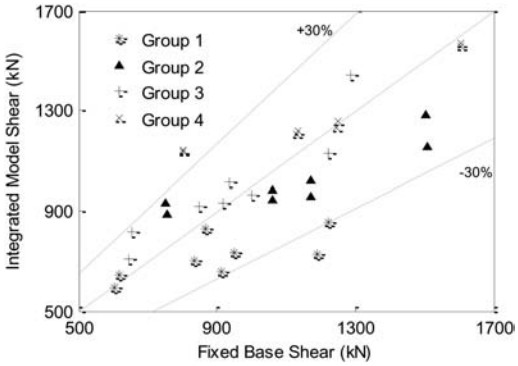

Figure 5. Peak column base shear for the FOS3 foundation design with the SBed model.

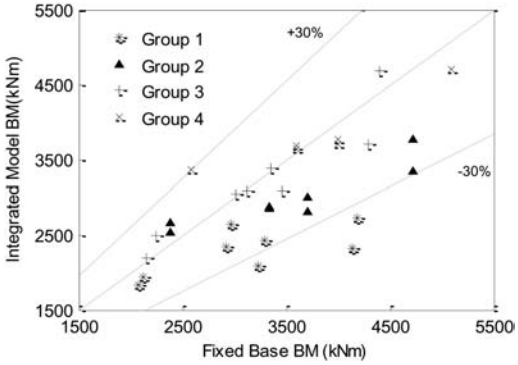

Figure 6. Peak column base bending moment for the FOS3 foundation design with the SBed model.

for each footing group is similar to the peak shear in Figure 5. Bending moment data is shifted down, moving data points closer to and below the 1:1 line. This shows that soil non-linearity and uplift have a similar effect on both shear and bending moment.

The AS41 footing model could not be used to represent this foundation design because of the combination of increased stiffness end zones and the small static factor of safety of the corner footings. For this footing the static vertical forces carried by the end zones were larger than the yield forces defined in Section 3.1, significantly reducing the stiffness prior to excitation. As this does provide a satisfactory representation of the properties of this footing, this analysis was not included.

5.3 *CONS foundation design*

5.3.1 *SBed foundation model*

The increased footing dimensions of the CONS foundation design reduced the vertical settlement and the compressive non-linearity of the SBed foundation model. The peak shear characteristics in Figure 7 show that this design is more likely to experience an increase in peak shear compared to the FOS3 design. The group 1 footings all experienced increases in peak shear of up

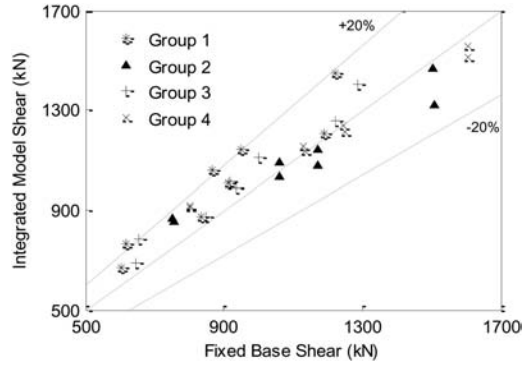

Figure 7. Peak column base shear for the CONS foundation design with the SBed model

to 20%, a considerable shift from the group 1 footing response for the FOS design in Figure 5. As all footings were identical, data points were grouped in a more linear trend than the FOS design, similar to the comparison of the characteristics of these designs for the elastic 3Spr footing model. While not shown here, the peak bending moment characteristics for the CONS design were analogous to the peak shear characteristics, again indicating the link between these responses for the shallow foundation model.

5.3.2 *Time history response*

To provide insight into the effect of uplift on the response of the SBed model with the CONS foundation design, the shear time history response for column A6 of the elastic 3Spr and Sbed model are compared in Figure 8. When a footing uplifts, the stiffness of the foundation system decreases, allowing increased displacements while the detached footing moves with the rest of the integrated system. Actions that were carried by the footing prior to uplift are transferred to other footings. When it reattaches, it may not at the same point in horizontal space as when it detached, resulting in the shift in the axes of oscillation of shear in Figure 8. This may also be accompanied by a residual displacement at the end of excitation (Wotherspoon 2009). Because of this shift, the maximum shear in this footing was larger than that developed by the 3Spr footing model.

For equilibrium, the total shear and bending moment in the columns should be equal to zero at the end of excitation. Therefore, if there is a shift in these actions in a footing due to uplift, this must be equilibrated by a shift in the actions in the other footings. Although not shown here, bending moment also developed these shifts in actions. These characteristics were also apparent for the AS41 footing model detailed in the next section.

5.3.3 *AS41 foundation model*

To determine the influence of the choice of foundation model on response, the integrated model with CONS footing design was analyzed using the AS41 foundation model. The resulting peak shear characteristics are

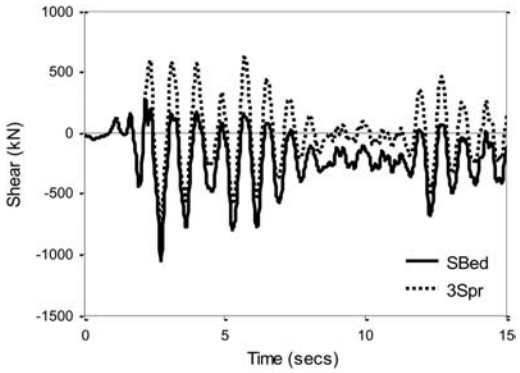

Figure 8. Shear force in column A6 for the CONS foundation design during the El Centro event.

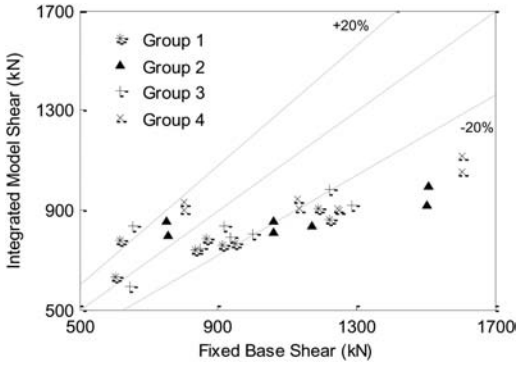

Figure 9. Peak column base shear for the CONS foundation design with the AS41 model.

presented in Figure 9, indicating response characteristics very different to the SBed foundation model in Figure 7. Although the responses of all footing groups are again quite similar, the trend is more towards a reduction in the peak shear compared to the fixed base response. At peak fixed base shear values less than 900 kN, the excitation is not large enough to develop extensive uplift and compressive non-linearity, allowing larger shear to develop in the integrated model. But as the peak shear values get larger in the fixed base model, the shear in the integrated model rises at a reduced rate due to foundation non-linearity. So while the SBed model develops reduction up to 15%, the AS41 model develops over 40% reduction in some footings. These are quite significant differences in peak actions due to choice of foundation model.

5.3.4 *Discussion*

The AS41 model has larger vertical stiffness due to the increased stiffness zones at the end of the footing. These larger stiffness zones require less load for vertical non-linearity to initiate than the SBed model, therefore are more likely to experience hysteretic energy dissipation in the soil. This reduces demands on the structure, the effects of which increase with increased excitation levels. The integrated model with the AS41 foundation had a larger fundamental period than the SBed model, with rotational stiffness of the AS41 foundations approximately 60% of the SBed values. Once yield occurs, the rotational and vertical stiffness of the overall system reduces even further, which in a general sense will reduce the demands on the system.

The SBed represents vertical foundation compressive non-linearity, but as uncoupled rotational springs were used to make up the difference in the rotational stiffness of the footing, when vertical yield occurs the reduction in rotational stiffness is not adequate. This reduces the level of hysteretic energy dissipation, preventing large reductions in column base actions.

As majority of rotational stiffness for the AS41 model is from the outer edges, when uplift occurs there is a significant reduction in the stiffness of the footing. Comparison of the moment-rotation response for a single footing with uplift and elastic soil (Wotherspoon et al. 2009) showed that AS41 model has only 10% of the total rotational stiffness when 15% of footing detached, while SBed model still has approx 60% of stiffness when half the footing detached. This rapid stiffness decrease will reduce demands on the foundation, and as uplift occurs during peak acceleration will have a significant effect on the peak demands.

Although these foundation models provide a far better representation that the elastic 3Spr model, both have weaknesses. The SBed model does not provide a good representation of hysteretic energy dissipation and coupling of degrees of freedom during compressive yield, while the AS41 model does not represent the uplift mechanism well. Depending on the dominant foundation response mechanism, these two models could provide bounds on the overall characteristics of the integrated model.

6 CONCLUSIONS

Using a range of foundation models and design approaches, the effect of modeling a structure and foundation as integrated system on the overall seismic response was presented in this paper. The effect of the inclusion of the foundation on peak structural demands and the difference in response across the three dimensional integrated model were presented.

When a single footing is part of a larger foundation system, it can no longer be thought of as a discrete element. As it is connected to the structure above, any change in the properties of one footing will have an impact on the demands of others in the system. The reduced stiffness and non-linearity experienced by the smaller footings of the FOS3 design reduced the actions in the structure above and shifted them to other parts of the structure. When the footing dimensions were increased for the CONS design, foundation non-linearity reduced and the actions in the structure increased. The variation in response resulting from integrated modeling emphasizes the importance of including foundation effects in the determination of structural performance.

Comparison of different foundation models shows the effect that different approaches can have on response. Variation in characteristics of SBed and AS41 models have shown that the characteristics of the transition during uplift and soil compressive non-linearity will have a significant effect on the response of the integrated structure-foundation system. The dominant response mechanism of each footing will determine the most appropriate approach to modeling. An accurate representation of uplift, soil non-linearity, and the interaction between degrees of freedom is required in order to characterize response.

REFERENCES

American Society of Civil Engineers ASCE. 2007. *Seismic rehabilitation of existing buildings. ASCE/SEI 41-06*. Reston, VA.

Bartlett, P.E. 1976. *Foundation rocking on a clay soil*. ME Thesis, University of Auckland, New Zealand.

Bielak, J. 1975. Dynamic behaviour of structures with embedded foundations, *Earthquake Engineering and Structural Dynamics* 3: 259–274.

Carr, A. 2005. *3D RUAUMOKO: inelastic three-dimensional dynamic analysis program*. University of Canterbury – Dept. of Civil Engineering, Christchurch, New Zealand.

Chaallal, O. & Ghlamallah, N. 1996. Seismic response of flexibly supported coupled shear walls. *ASCE Jnl of. Structural Engineering* 122(10): 1187–1197.

Federal Emergency Management Agency FEMA. 1997. *NEHRP guidelines for the seismic rehabilitation of buildings. FEMA Publication No. 273*. Washington, DC.

Filiatrault, A., Anderson, D.L. & De Vall, R.H. 1992. Effect of weak foundation on the seismic response of core wall type buildings. *Canadian Jnl of Civil Engineering* 19: 530–539.

Gazetas, G., Dobry, R. & Tassoulas, J.L. 1985. Vertical response of arbitrarily shaped foundations. *ASCE Jnl of. Geotechnical Engineering* 111(6): 750–771.

Gazetas, G. & Tassoulas, J.L. 1987. Horizontal stiffness of arbitrarily shaped foundations. *ASCE Jnl of Geotechnical Engineering* 113(5): 440–457.

Giberson M.F. 1969. Two nonlinear beams with definitions of ductility. *ASCE Jnl of Structural Divn.* 95(ST2): 137–57.

El Ganainy, H. and El Naggar, M.H. (2009) Seismic performance of three-dimensional frame structures with underground stories. *Soil Dynamics and Earthquake Engineering*, 29: 1249–1261.

Hatzikonstantinou, E., Tassoulas, J.L., Gazetas, G., Kotsanopoulos, P. & Fotopoulou, M. 1989. Rocking stiffness of arbitrarily shaped embedded foundations. *ASCE Jnl of. Geotechnical Engineering* 115(4): 457–472.

Jennings, P.C. & Bielak, J. 1972. Dynamics of building-soil interaction, EERL 72-01, EERL, Pasadena, USA.

Kutter, B.L., Martin, G.R., Hutchinson, T.C., Harden, C., Sivapalan, G. &Phalen, J. D. 2003. *Status report on a study of modelling of nonlinear cyclic load-deformation behaviour of shallow foundations*, PEER Workshop Report.

Mylonakis, G., Nikolaou, S. & Gazetas, G. 2006. Footings under seismic loading: Analysis and design issues with emphasis on bridge foundations. *Soil Dynamics and Earthquake Engineering* 26(9): 824–853.

Nakaki, D.K. & Hart, G.C. 1987. Uplifting response of structures subjected to earthquake motions. *US-Japan coordinated program for masonry building research*. Los Angeles, USA.

Parmelee, R.A., Perelman, D.S. & Lee, S.L. 1969. Seismic response of multiple-story structure on flexible foundations, *Bull. Seismic Society of America* 59: 1061–1070.

Psycharis, I.N. 1982. Dynamic behaviour of rocking structures allowed to uplift. EERL-81-02. *Earthquake Engineering Research Laboratory*. Pasadena, USA.

Standards New Zealand. 2004. *NZS1170.5 Earthquake actions*. Wellington, NZ.

Standards New Zealand. 2006. *NZS3101 Concrete Structures Standard*. Wellington, NZ.

Tajimi, H. 1967. Discussion: Building-foundation interaction effects, ASCE *Jnl. Engineering Mech. Div* 93: 294–298.

Veletsos, A.S. & Meek, J.W. 1974. Dynamic behaviour of building-foundation systems, *Earthquake Engineering and Structural Dynamics* 3(2):121–138.

Wang, S., Kutter, B.L., Chacko, M.J., Wilson, D.W., Boulanger, R.W. & Abghari, A. 1998. Nonlinear seismic soil-pile structure interaction. *Earthquake Spectra* 14(2): 377–396.

Wiessing, P.R. 1979. *Foundation rocking on sand*. ME Thesis, University of Auckland, New Zealand.

Wolf, J.P. 1985. *Dynamic soil-structure interaction*. Prentice-Hall: New Jersey.

Wotherspoon, L.M., Pender, M.J. & Ingham, J.M. 2004a. Effects of foundation model on the earthquake response of building systems. *3rd ICEGE and 11th ICSDEE*. Berkeley, USA: 766–773.

Wotherspoon, L.M., Pender, M.J. & Ingham, J.M. 2004b. Combined modeling of structural and foundation systems. *13th World Conference on Earthquake Engineering*. Vancouver.

Wotherspoon, L.M. 2009. *Integrated modelling of structure-foundation systems*. PhD Thesis, University of Auckland, New Zealand.

Soil-Foundation-Structure Interaction – Orense, Chouw & Pender (eds)
© 2010 Taylor & Francis Group, London, ISBN 978-0-415-60040-8

High fidelity modeling and simulation of SFS interaction: Energy dissipation by design

Boris Jeremić
University of California, Davis, CA, 95616, U.S.A.

ABSTRACT: It is hypothesized that interplay of earthquake, soil, foundation and structure (SFS) dynamic characteristic, and their interaction in time domain, control the behavior of SFS system during earthquakes. Moreover, (passive and active) control of spatial and temporal location of seismic energy dissipation (preferably in soil) can improve safety and economy of SFS systems. Such energy dissipation by design requires high fidelity modeling and simulations. This paper briefly describes modeling and simulation aspects of energy flow in SFS system. In addition to that, examples of directed energy dissipation are presented that show how soil can be used for the benefit of overall SFS system response to seismic excitation.

1 INTRODUCTION

Seismic behavior of soil-foundation-structure (SFS) systems has recently gained increased attentions. Improvements in modeling and simulation technology currently allow modeling and simulations of a complete SFS interaction with high fidelity. These models and simulations allow us, in turn, to gain better understanding of seismic response of the SFS system. Moreover, such high fidelity models and simulations allow us to design the SFS system(s). Of particular interest is the notion that a designer can/should be able to direct/design the location, in time and space, where dissipation of seismic energy takes place. This notion is based on understanding that incoming seismic energy affects both soils and structures. While focus is usually on structural performance, interaction of soil with foundation/structure plays a very important (crucial) role in seismic response. The idea is that while energy dissipation in structure (and its components) leads to damage, and potentially failure, soil medium offers significant energy dissipation capacity and benefits.

In this paper we briefly discuss seismic energy dissipation mechanisms in soils and their potential use in improving seismic soil-foundation-structure system performance.

While SFS interaction has been modeled and simulated for a number of years. We mention a number of references related to SFS interaction importance and modeling, starting with the very first mention of SFS interaction beneficial and detrimental effects by Late Prof. Suyehiro (Suyehiro 1932). A number of researchers have developed and analyzed SFS systems in last 3 decades, and we mention some of them: (Chi Chen and Penzien 1977), (Makris et al. 1994), (McCallen and Romstadt 1994), (Gazetas and Mylonakis 1998), (Mylonakis and Nikolaou 1997), (Fenves and Ellery 1998), (Elgamal et al. 2008), (Jeremić et al. 2004), (Jeremić and Jie 2007), (Jeremić and Jie 2008).

In this paper we briefly describe energy dissipation mechanisms for SFS system. In addition to that, it is claimed that only high fidelity models can be used for such model based simulation (design) of energy dissipation.

Our main hypothesis is that the interplay of earthquake (nonlinear seismic wave propagating from source to the structure of interest) with soil and the structure plays major role in potentially catastrophic failures, but also in success. Timing and spatial location of energy dissipation within the SFS system, determines amount of damages and in general controls survivability of structure during earthquake. If timing and spatial location of energy dissipation can be controlled, one could optimize the SFS system for safety and economy. This is particularly true if energy dissipation can be directed to soil instead of foundation and structure.

Directing (by design) energy dissipation for SFS systems requires development and simulations on high fidelity numerical models. There are a number of cases where interaction of SFS and dissipation of seismic energy in soil can be deduced by observing structural damage. The very notion that soil SFS has significant role in dynamic response of structures comes from Professor Kyoji Suyehiro, (a Naval Engineer turned Earthquake Engineer, following his personal experience of Great Kantō earthquake (11:58am(7.5), 12:01pm(7.3), 12.03pm(7.2) (shaking until 12:08pm), 1st. Sept. 1923, in Tokyo) who reported $4\times$ (four) more damage to soft wooden buildings on soft ground than same building on stiff ground (Suyehiro 1932). This was probably due to the close to resonance of building (soft) with foundation soil (soft) with a long lasting (soft, long period) earthquake. Many years later, (Trifunac and Todorovska 1998), show how during

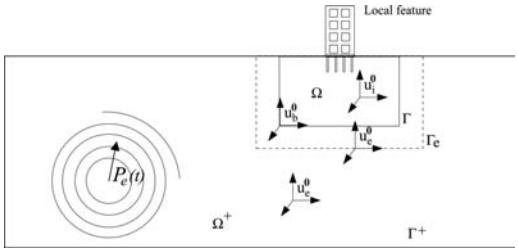

Figure 1. Geometry of the SFS system.

Northridge earthquake, areas with damage to buildings (signifying structural damage) was quite nicely separated from areas of water pipe breaks (signifying much plasticity and energy dissipation in soil). In this case, much energy is dissipated in the (soft) soil, never making it to the building, while for stiff soil do not have such energy dissipation capacity, transmitting such energy to the building for dissipation (damage).

There are many other cases where such phenomena is observed. Our primary goal here is to emphasize how high fidelity modeling and simulations of SFS systems can help understand mechanics of such interactions. In addition to that, we use high fidelity models to present examples of interplay of earthquake, soil and structure dynamic characteristics, together with the location and timing of energy dissipation.

2 SEISMIC ENERGY INPUT AND DISSIPATION

2.1 *Seismic energy input into SFS system*

Earthquakes release large amounts energy at the source[1] Part of released energy is radiated as mechanical waves ($\approx 1.6 \times 10^{-5}$) and part of that energy makes it to the surface where SFS system is located.

Mechanical seismic wave energy enters the SFS system through a closed surface Γ that encompasses (significant) soil volume as well as foundation system and the structure (Fig. 1). Kinetic energy flux through closed surface Γ includes both incoming and outgoing waves and can be calculated using Domain Reduction Method (Bielak et al. 2003) as:

$$E_{flux} =$$

$$\left[0; -M_{be}^{\Omega+}\ddot{u}_e^0 - K_{be}^{\Omega+}u_e^0; M_{eb}^{\Omega+}\ddot{u}_b^0 + K_{eb}^{\Omega+}u_b^0\right]_i \times u_i$$

where $M_{be}^{\Omega+}$, $M_{eb}^{\Omega+}$, $K_{be}^{\Omega+}$, $K_{eb}^{\Omega+}$ are mass and stiffness matrices, respectively for a single layer of elements just outside of the boundary Γ, while $\ddot{u}_e^0$ and u_e^0 are accelerations and displacements from a free field model for nodes belonging to that layer of elements. Alternatively, energy flux can be calculated using (Aki and Richards 2002):

$$E_{flux} = \rho A c \int_0^t \dot{u}_i^2 dt$$

Outgoing kinetic energy can be obtained from outgoing wave field w_i, (from DRM, (Bielak et al. 2003)), while the difference then represents the incoming kinetic energy that needs to be dissipated with SFS region.

2.2 *Seismic energy dissipation in SFS system*

Seismic energy that enters the SFS system will be dissipated in a number of ways. part of the energy that enters SFS system can be reflected back into domain outside Γ by

- wave reflection from impedance boundaries (free surface, soil/rock layers…).
- SFS system oscillation radiation.

While the rest of seismic energy is dissipated through one of the following mechanisms within SFS domain:

- Elasto-plasticity of soil
- Viscous coupling of porous solid with pore fluid (air, water)
- Elasto-plasticity/damage of the foundation system
- Elasto-plasticity/damage of the structure
- viscous coupling of structure with surrounding fluids (air, water)

It is also important to note that in numerical simulations (advocated and used in this work), part of the energy can be dissipated or produced by purely numerical means. That is, numerical energy dissipation (damping) or production (negative damping) has to be carefully controlled (Argyris and Mlejnek 1991), (Hughes 1987).

Energy Dissipation by Plasticity. Elastic-plastic deformation of soil, foundation and structure is probably responsible for major part of the energy dissipation for large earthquakes. This, displacement proportional dissipation is a result of dissipation of plastic work $\left(W = \int \sigma_{ij} d\epsilon_{ij}^{pl}\right)$ and is present in all three components of the system (soil, foundation and the structure). Ideally, majority of the incoming energy would be dissipated in soil, before reaching foundation and structures. The possibility to direct energy dissipation to soil can be used in design by recognizing energy dissipation capacity for different soils. For example, simple elastic-plastic models of stiff and soft clay as well as dense and loose send predict different energy dissipation capacities, as shown in Figure 2, for single loading-unloading-reloading cycle. While Figure 2 shows that stiff clay and dense sand have much higher dissipation capacity, it is important to note that soft/loose soils can undergo much larger deformation/strain, thus offering increased energy dissipation capacity through flexibility.

[1] for example, some of the recent large earthquake energy releases are listed: Northridge, 1994, $M_{Richter} = 6.7$, $E_r = 6.8 \times 10^{16} J$; Loma Prieta, 1989, $M_{Richter} = 6.9$, $E_r = 1.1 \times 10^{17} J$; Sumatra-Andaman, 2004, $M_{Richter} = 9.3$, $E_r = 4.8 \times 10^{20} J$; Valdivia, Chile, 1960, $M_{Richter} = 9.5$, $E_r = 7.5 \times 10^{20} J$;

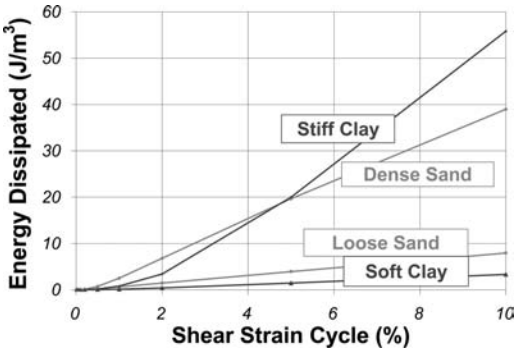

Figure 2. Energy dissipation capacity for one cycle at various strains for four generic soils.

Energy Dissipation by Viscous Coupling. Viscous coupling of pore fluid (air, water…) and soil particles and/or foundation or structural components is responsible for velocity proportional energy dissipation. In particular, viscous coupling of porous solid and fluid results in $E_{vc} = n^2 k^{-1} (\dot{U}_i - \dot{u}_i)^2$ energy loss per unit volume. It is noted that this type of dissipation is realistically modeled using $u - p - U$ formulation (Jeremić et al. 2008).

Numerical Energy Dissipation and Production. As noted above, numerical integration of nonlinear equations of motions affects calculated energy in various ways. Most common effect for nonlinear (elastic-plastic) systems is the positive (energy dissipation) and negative (energy production) damping. For example Newmark (N) (Newmark 1959) and Hilber–Hughes–Taylor (HHT) (Hilber et al. 1977) are energy preserving for linear elastic system with proper choice of constants ($\alpha = 0.0$; $\beta = 0.25$, $\gamma = 0.5$). Both methods can also be used to dissipate higher frequency modes for linear elastic models by changing constants so that for N: $\gamma \geq 0.5$, $\beta = 0.25(\gamma + 0.5)^2$, while for HHT: $-0.3\dot{3} \leq \alpha \leq 0$, $\gamma = 0.5(1 - 2\alpha)$, $\beta = 0.25(1 - \alpha)^2$. However, for nonlinear problems it is impossible to maintain energy of the system throughout computations (Argyris and Mlejnek 1991).

2.3 *Uncertainty aspects*

Uncertainty of soil material parameters and forcing represents a significant source of uncertainty of a final computed (simulated) response of SFS system. Recent development of Probabilistic Elasto-Plasticity (PEP) and Spectral Stochastic Elastic-Plastic Finite Element Method (SSEPFEM) ((Jeremić et al. 2007), (Sett et al. 2007a), (Sett et al. 2007b), (Jeremić and Sett 2009), (Sett and Jeremić 2009b), (Sett and Jeremić 2009a)) allows accurate analysis of influence of uncertain soil properties and forcing on seismic response. Calculation of seismic energy (propagation and dissipation) is affected by such, ever present uncertainties and such uncertainties should be taken into account as best as possible, Above cite (already) published papers and a number of near future papers (under review) present development of methodology for forward and backward propagation of uncertainties in dynamic (and static) simulation of elastic-plastic solids made of (geo-)materials. Such newly developed, highly accurate, numerical methdology for treatment of material (left hand side) and forcing (right hand side) uncertainty allows for full quantification of stochastic (probabilistic) aspects of SFS interaction.

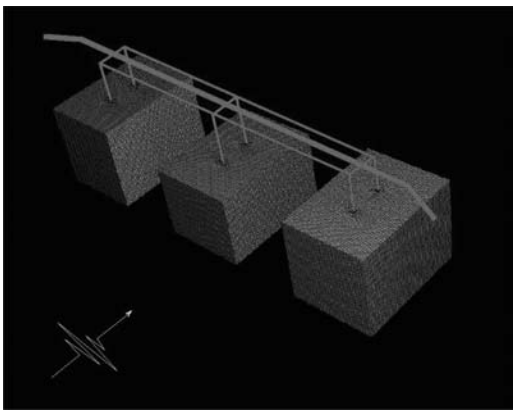

Figure 3. Detailed finite element model of a SFS system.

3 SELECT EXAMPLES OF ENERGY DISSIPATION

This section briefly describes two examples of SFS system modeling, simulation and energy dissipation.

Use of Soft Soil. Simulations on high fidelity model for bridge SFS system (Jeremić et al. 2009) were used to investigate energy flow and dissipation. Proper modeling of nonlinear wave propagation required large number of elements and DOFs (1.6×10^6 for largest model). Such large models required development of efficient parallel finite element methodology (Plastic Domain Decomposition, PDD) that could handle elastic-plastic computations on multiple generation distributed memory parallel computers including DataStar at SDSC, Longhorn at TACC and our own GeoWulf at UCD (Jeremić and Jie 2007), (Jeremić and Jie 2008). Great care was taken to develop high fidelity model for both soil, foundation and the structure. Seismic waves were input into the model using DRM (Bielak et al. 2003), and no numerical damping was used, leaving energy dissipation to elasto-plasticity and radiation damping. Figure 3 shows a detailed FEM model.

It is important to note that a full (numerical) construction process was performed, with soil self weight applied first, followed by excavation and pile installation, pile self weight application, with structure construction (self wight) application preceding application of seismic input via DRM.

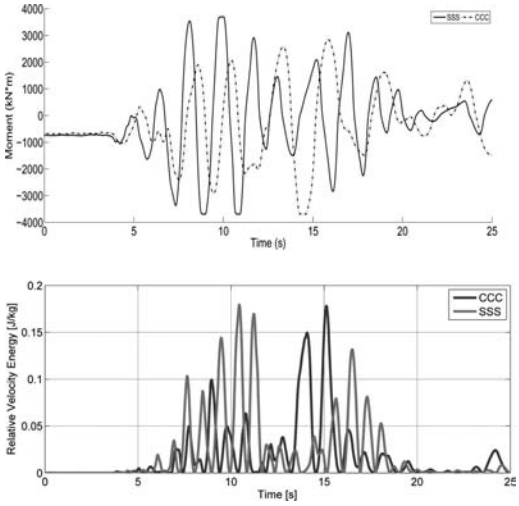

Figure 4. Bending moment response for bent # 1 (left column) (top) and relative velocity energy (lower).

Figure 4 shows moment response (upper) of the top of bent # 1, contrasted with relative velocity energy (lower) for the same bent. Two cases are analyzed, CCC is a case with all foundations (piles) in a soft clay (Bay mud) while SSS is for all foundations (piles) resting in dense send soil. Input motion is from Northridge earthquake, characterized with fairly high energy input in higher frequencies (stiff earthquake). It is obvious that soft soil dissipates seismic energy by plasticity and that SFS system in soft clay does not sustain much damage (possibly one case of plastic yielding on top of bent, at t between 14 and 15 seconds. On the other hand, in stiff sand, soil does not dissipate much seismic energy, hence bent # 1 suffers much plastic yielding (plastic hinge development between t 8 until 12 seconds. It is noted also that the dynamic characteristics of stiff earthquake, with stiff soil and stiff structure contribute to early close to resonance response and increase damage. Relative velocity energy plot (Fig. 4, lower) presents similar information, this time in terms of kinetic energy, that is dissipated through plastic work. Note early peaks for SSS SFS system, that get dissipated by plastic hinging, while sole peak for CCC SFS system contributes to one sided plastic hinge development at $t \approx 14s$.

Use of Liquefaction. Liquefaction has been consistently put in negative connotation in geotechnical earthquake engineering. There are many cases where liquefaction is to be blamed for unacceptable SFS system performance ((Youd and Bartlett 1989), (Yokoyama et al. 1997), (Berril et al. 1997), (Kawakami and Asada 1966), (Hamada 1992a), (Hamada 1992b), (Japanese Society of Civil Engineers 1966)), However, there is not much evidence (it was not searched for) that liquefaction actually provided benefit by decreasing (damping out) ground motions.

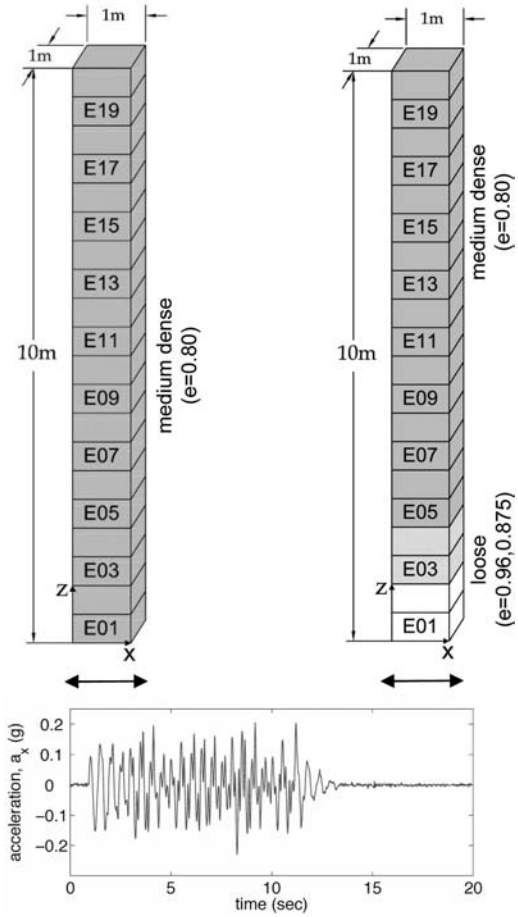

Figure 5. Two soil column models, left is all dense sand, right is dense sand on top of loose sand layers. Seismic motions applied to the bottom are also shown.

A simple example is used to illustrate this idea (Taiebat et al. 2009). Figure 5 presents two models for 1D seismic wave propagation, namely one (left) with all dense sand, while the other one (right) is dense sand on top of loose sand layers.

Seismic wave is propagated through the soil (input is also shown in Fig. 5) with resulting acceleration records at different soil depths shown in Figure 6. Since bottom loose soil layers do liquefy (from effective stress results), seismic energy does not propagate much above bottom layers. Main dissipation mechanisms are related to soil plasticity and coupling of solid skeleton with pore fluid.

Figure 7 shows measured (simulated) kinetic energy at the top of both soil models. Layered model (with loose, liquefiable layer at the bottom) has reduction of top of model kinetic energy of at least three times, which might significantly contribute to damage reduction of any foundation and structure placed on top of such soil system.

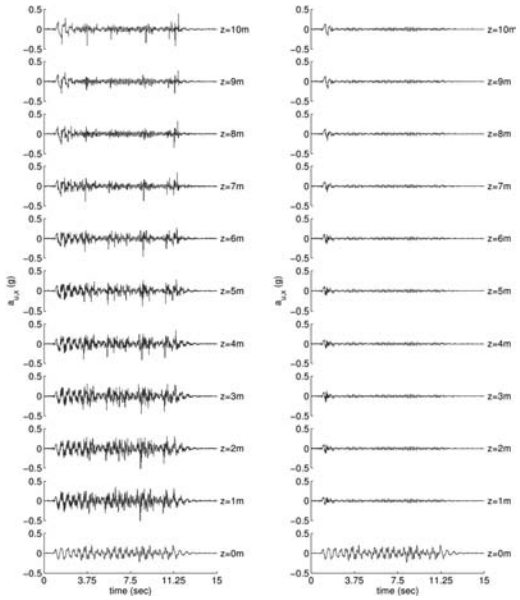

Figure 6. Acceleration time history, at different soil levels. Left is all dense sand model, right is dense with loose bottom sand layer.

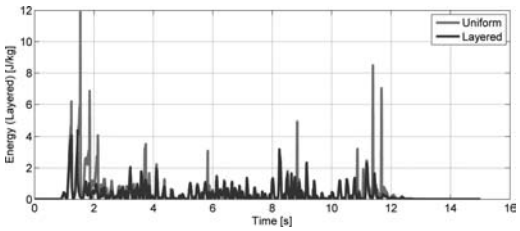

Figure 7. Kinetic energy at the top of soil layers.

4 SIMULATION PLATFORM

Numerical simulations described in this paper were done using sequential and parallel application programs developed at UCD, with use of a number of publicly available numerical libraries. Parallel simulation were based on recently developed Plastic Domain Decomposition (PDD) method (Jeremić and Jie 2007; Jeremić and Jie 2008). Graph partitioning used in PDD is based on ParMETIS libraries (Karypis et al. 1998)). Small part of OpenSees framework (McKenna 1997) was used to connect the finite element domain. In particular, Finite Element Model Classes from OpenSees (namely, class abstractions Node, Element, Constraint, Load, Domain and set of Analysis classes) where used to describe finite element model and to store results of analysis performed on a model. The domain and analysis classes were significantly modified to improve parallel performance and were organized as Modified OpenSees Services (MOSS) library. In addition to that, build process and organization of libraries was completely redone in order to remove known limitations of OpenSees program. On a lower level, a set of Template3Dep numerical libraries (Jeremić and Yang 2002) were used for constitutive level integrations, nDarray numerical libraries (Jeremić and Sture 1998) were used to handle vector, matrix and tensor manipulations, while FEMtools element libraries from UCD CompGeoMech toolset (Jeremić 2009) were used to supply other necessary libraries and components. Parallel solution of system of equations has been provided by PETSc set of numerical libraries (Balay et al. 2001; Balay et al. 2004; Balay et al. 2004; Balay et al. 1997)).

Application programs used for simulation were created by linking above mentioned libraries in the Finite Element Interpreter (FEI). Large part of simulation was carried out on our local sequential computers and and our parallel computer GeoWulf. Only the largest models (too big to fit on GeoWulf system) were simulated on TeraGrid machine at SDSC and TACC.

5 CONCLUSIONS

Interplay of Earthquake, Soil, Foundation and Structure dynamics in time domain plays a major role in catastrophic failures and great successes. High fidelity modeling and simulation offers an unprecedented opportunity to improve design. The ability to model and simulate flow of seismic energy in the SFS system with high fidelity, makes it possible to design energy dissipation in most economical way, in soil, Directing, in space and time, seismic energy flow in the SFS system will lead to increase in safety and economy. The main purpose of this brief paper was to overview modeling and simulations issues and show illustrative examples of directing energy flow for SFS systems.

It is hoped that public domain modeling and simulations tools, such as FEI and recently developed www.OpenHazards.com will be used more in future to increase safety and reduce cost of infrastructure objects in earthquake prone areas.

ACKNOWLEDGMENT

I would like to thank Professors Zhaohui Yang (University of Alaska), Mahdi Taiebat (University of British Columbia), Kallol Sett (University of Akron) and Drs. Zhao Cheng (EarthMechanics Inc.), Guanzhou Jie (Wells Fargo Securities), Matthias Preisig (Ecole Polytechnique Fédérale de Lausanne) and graduate student researcher Mr. Nima Tafazzoli (UCD) for their contributions to this paper.

REFERENCES

Aki, K. and P. G. Richards (2002). *Quantitative Seismology* (2nd ed.). University Science Books.

Argyris, J. and H.-P. Mlejnek (1991). *Dynamics of Structures*. North Holland in USA Elsevier.

Balay, S., K. Buschelman, V. Eijkhout, W. D. Gropp, D. Kaushik, M. G. Knepley, L. C. McInnes, B. F. Smith,

and H. Zhang (2004). PETSc users manual. Technical Report ANL-95/11 – Revision 2.1.5, Argonne National Laboratory.

Balay, S., K. Buschelman, W. D. Gropp, D. Kaushik, M. G. Knepley, L. C. McInnes, B. F. Smith, and H. Zhang (2001). PETSc Web page. http://www.mcs.anl.gov/ petsc.

Balay, S., W. D. Gropp, L. C. McInnes, and B. F. Smith (1997). Efficient management of parallelism in object oriented numerical software libraries. In E. Arge, A. M. Bruaset, and H. P. Langtangen (Eds.), *Modern Software Tools in Scientific Computing*, pp. 163–202. Birkhäuser Press.

Berril, J. B., S. A. Christensen, R. J. Keenan, W. Okada, and J. K. Pettinga (1997). Lateral–spreading loads on a piled bridge foundations. In S. E. Pinto (Ed.), *Seismic Behavior of Ground and Geotechnical Structures*, pp. 173–183.

Bielak, J., K. Loukakis, Y. Hisada, and C. Yoshimura (2003). Domain reduction method for three–dimensional earthquake modeling in localized regions. part I: Theory. *Bulletin of the Seismological Society of America 93*(2), 817–824.

Chi Chen, M. and J. Penzien (1977, August). Nonlinear soil–structure interaction of skew highway bridges. Technical Report UCB/EERC-77/24, Earthquake Engineering Research Center, University of California, Berkeley.

Elgamal, A., L. Yan, Z. Yang, and J. P. Conte (2008, July). Three-dimensional seismic response of humboldt bay bridge-foundation-ground system. *ASCE Journal of Structural Engineering 134*(7), 1165–1176.

Fenves, G. and M. Ellery (1998, December). Behavior and failure analysis of a multiple-frame highway bridge in the 1994 northridge earthquake. Technical Report 98/08, PEER Center.

Gazetas, G. and G. Mylonakis (1998, August 1998.). Seismic soil–structure interaction: New evidence and emerging issues. In P. Dakoulas, M. Yegian, and R. D. Holtz (Eds.), *Proceedings of a Specialty Conference: Geotechnical Earthwuake Engineering and Soil Dynamics III*, Geotechnical Special Publication No. 75, pp. 1119–1174. ASCE.

Hamada, M. (1992a). Large ground deformations and their effects on lifelines: 1964 niigata earthquake. In *Case studies of liquefaction and lifeline performance during past earthquakes*, Volume 1, Japanese case studies, pp. 3.1–3.123. State Univ. of New York, Buffalo, N.Y.: Natl. Center for Earthquake Engineering Research.

Hamada, M. (1992b). Large ground deformations and their effects on lifelines: 1983 nihonkai–chubu earthquake. In *Case studies of liquefaction and lifeline performance during past earthquakes*, Volume 1, Japanese case studies, pp. 4.1–4.85. State Univ. of New York, Buffalo, N.Y.: Natl. Center for Earthquake Engineering Research.

Hilber, H. M., T. J. R. Hughes, and R. L. Taylor (1977). Improved numerical dissipation for time integration algorithms in structural dynamics. *Earthquake Engineering and Structure Dynamics 5*(3), 283–292.

Hughes, T. (1987). *The Finite Element Method; Linear Static and Dynamic Finite Element Analysis*. Prentice Hall Inc.

Japanese Society of Civil Engineers (1966). *The report of damage investigation in the 1964 Niigata Earthquake*. Tokyo: Japanese Soc. of Civil Engineers. in Japanese.

Jeremić, B. (2004–2009). Lecture notes on computational geomechanics: Inelastic finite elements for pressure sensitive materials. Technical Report UCD-CompGeoMech–01–2004, University of California, Davis. available online: http://sokocalo.engr.ucdavis.edu/∼jeremic/CG/LN.pdf.

Jeremić, B., Z. Cheng, M. Taiebat, and Y. F. Dafalias (2008). Numerical simulation of fully saturated porous materials. *International Journal for Numerical and Analytical Methods in Geomechanics 32*(13), 1635–1660.

Jeremić, B. and G. Jie (2007). Plastic domain decomposition method for parallel elastic–plastic finite element computations in gomechanics. Technical Report UCD–CompGeoMech–03–07, University of California, Davis. available online: http://sokocalo.engr. ucdavis.edu/∼jeremic/wwwpublications/CV-R24.pdf.

Jeremić, B. and G. Jie (2008). Parallel soil–foundation–structure computations. In N. L. M. Papadrakakis, D.C. Charmpis and Y. Tsompanakis (Eds.), *Progress in Computational Dynamics and Earthquake Engineering*. Taylor and Francis Publishers.

Jeremić, B., G. Jie, M. Preisig, and N. Tafazzoli (2009). Time domain simulation of soil–foundation–structure interaction in non–uniform soils. *Earthquake Engineering and Structural Dynamics 38*(5), 699–718.

Jeremić, B., S. Kunnath, and F. Xiong (2004, February). Influence of soil–structure interaction on seismic response of bridges. *International Journal for Engineering Structures 26*(3), 391–402.

Jeremić, B. and K. Sett (2009). On probabilistic yielding of materials. *Communications in Numerical Methods in Engineering 25*(3), 291–300.

Jeremić, B., K. Sett, and M. L. Kavvas (2007, October). Probabilistic elasto-plasticity: formulation in 1D. *Acta Geotechnica 2*(3), 197–210.

Jeremić, B. and S. Sture (1998). Tensor data objects in finite element programming. *International Journal for Numerical Methods in Engineering 41*, 113–126.

Jeremić, B. and Z. Yang (2002). Template elastic–plastic computations in geomechanics. *International Journal for Numerical and Analytical Methods in Geomechanics 26*(14), 1407–1427.

Karypis, G., K. Schloegel, and V. Kumar (1998). *ParMETIS: Parallel Graph Partitioning and Sparse Matrix Ordering Library*. University of Minnesota.

Kawakami, F. and A. Asada (1966). Damage to the ground and earth structures by the niigata earthquake of june 16, 1964. *Soils and Foundations 6*(1), 14–30.

Makris, N., D. Badoni, E. Delis, and G. Gazetas (1994, October). Prediction of observed bridge response with soil–pile–structure interaction. *ASCE Journal of Structural Engineering 120*(10), 2992–3011.

McCallen, D. B. and K. M. Romstadt (1994). Analysis of a skewed short span, box girder overpass. *Earthquake Spectra 10*(4), 729–755.

McKenna, F. T. (1997). *Object Oriented Finite Element Programming: Framework for Analysis, Algorithms and Parallel Computing*. Ph. D. thesis, University of California, Berkeley.

Mylonakis, G. and A. Nikolaou (1997). Soil-plie-bridge seismic interaction: Kinematic and inertial effects. part i: Soft soil. *Earthquake Engineering & Structural Dynamics 26*, 337–359.

Newmark, N. M. (1959, July). A method of computation for structural dynamics. *ASCE Journal of the Engineering Mechanics Division 85*, 67–94.

Sett, K. and B. Jeremić (2009a). Forward and backward probabilistic simulations in geotechnical engineering. In M. Iskander, D. F. Laefer, and M. H. Hussein (Eds.), *Contemporary Topics in Insitu Testing, Analysis, and Reliability of Foundations (Selected Papers from the 2009 International Foundation Congress and Equipment Expo, held in Orlando, FL, from March 15–19,*

2009), Volume 186 of *Geotechnical Special Publications No. 186*, pp. 1–11. American Society for Civil Engineers.

Sett, K. and B. Jeremić (2009b). Probabilistic yielding and cyclic behavior of geomaterials. *International Journal for Numerical and Analytical Methods in Geomechanics*. in Print.

Sett, K., B. Jeremić, and M. L. Kavvas (2007a, October). Probabilistic elasto-plasticity: Solution and verification in 1D. *Acta Geotechnica 2*(3), 211–220.

Sett, K., B. Jeremić, and M. L. Kavvas (2007b, June). The role of nonlinear hardening in probabilistic elasto-plasticity. *International Journal for Numerical and Analytical Methods in Geomechanics 31*(7), 953–975. In Print (published online in the Early View section).

Suyehiro, K. (1932, May). Engineering seismology notes on American lectures. In *Proceedings of the American Society of Civil Engineers*, Volume 58, 4, pp. 2–110. American Society of Civil Engineers.

Taiebat, M., B. Jeremić, and A. M. Kaynia (2009, March). Propagation of seismic waves through liquefied soils. In *In proceedings of the GeoOrlando, Geo Institute Annual Conference*, Orlando, Florida.

Trifunac, M. and M. Todorovska (1998, January). Nonlinear soil response as a natural passive isolation mechanism – the 1994 Northridge, California, earthquake. *Soil Dynamics and Earthquake Engineering 17*(1), 41–51.

Yokoyama, K., K. Tamura, and O. Matsuo (1997, 27–28 Feb.). Design methods of bridge foundations against soil liquefaction and liquefaction induced ground flow. In *2nd Italy–Japan Workshop on Seismic Design and Retrofit of Bridges*, Rome, Italy, pp. 23 pages.

Youd, T. L. and S. F. Bartlett (1989, Feb 1.). Case histories of lateral spreads from the 1964 Alaskan earthquake. In *Proceedings of the Third Japan–U.S. Workshop on Earth Resistant Design of Lifeline Facilities and Countermeasures for Soils Liquefaction*, Number 91-0001 in NCEER.

Soil-Foundation-Structure Interaction – Orense, Chouw & Pender (eds)
© 2010 Taylor & Francis Group, London, ISBN 978-0-415-60040-8

Seismic response of bridge structures under non-uniform ground excitations

N. Chouw
University of Auckland, New Zealand

H. Hao
University of Western Australia, Australia

ABSTRACT: The work describes the significance of the interrelation between dynamic properties of adjacent bridge structures, soil and bridge structures interaction and spatially non-uniform ground excitation in causing damages to bridge deck and a possible mitigation measure. The spatially varying ground excitations are simulated stochastically based on New Zealand design spectrum for soft soil. A three span bridge structure, footing and subsoil are described using finite elements and boundary elements. The investigation shows that not only spatially non-uniform ground motions but also unequal soil-structure interaction can contribute significantly to the relative movement and increase the damage potential of the bridge girders.

1 INTRODUCTION

Damages to bridge structures occur not only at bridge pier and supports. Damages to bridge decks and even deck unseating have also been observed in almost all major earthquakes, e.g. Chi-Chi earthquake in 1999 (JSCE 1999), Kobe earthquake in 1995 (Kawashima and Unjoh 1996) and Wenchuan earthquake in 2008 (Lin et al. 2008). While bridge pier damage depends strongly on the overall seismic behaviour of bridge structures in transversal direction, damages to bridge girders are determined by relative responses of adjacent bridge structures in the longitudinal direction. When opening relative girder movements are larger than the seat length collapse of bridge decks occurs due to seat loss. When closing girder movements are larger than the gap of expansion joints, damages to girder ends due to pounding occur.

The cause of damages related to relative girder movements has been studied by many researchers in the past three decades, e.g. Ruangrassamee and Kawashima (2001), and their outcomes are implemented in design specifications, e.g. CALTRANS (2006). However, most investigations were performed based on the assumption that participating structures experienced the same ground excitations, although it is well known that the development of ground motions along a long bridge depends strongly on seismic wave properties and conditions and profile of local sites (Hao 1989, Hao et al. 1989, Zerva 2009).

Recent investigations confirmed the significance of spatially non-uniform ground motions among other identified influence factors, i.e. ratio of fundamental frequencies of adjacent structures and soil-structure interaction (SSI) and their consequence for structural responses (Chouw and Hao 2008a and b and Bi et al. 2010). The implementation of these research results can significantly contribute to safer bridge design in the future. So far the Japanese design specification (JRA 2004) is probably one of the very few design regulations that considered the effect of spatial variation of ground motions, even only empirically. However, although they are currently the most advanced design specification, it may still underestimate the required seat length to avoid collapse of bridge decks, especially when the ground is soft (Chouw and Hao 2005).

In this study the spatial ground motion variation and SSI effect on responses of bridges with New Zealand seismic conditions are investigated. Three bridge segments are considered. The spatially non-uniform ground motions are simulated stochastically based on New Zealand design spectrum for soft soil (NZS1170.5 2005).

2 BRIDGE STRUCTURES WITH SUBSOIL AND GROUND EXCITATIONS

Figure 1 shows the considered bridge structures. For simplicity in the numerical analysis the multiple bridge piers of each bridge segment will be modeled by a collective bridge pier indicated by the dotted lines with a distance of 50 m. The left and right bridge piers have the same height of 12.2 m and the one of the middle bridge segment is 18.3 m. They are adopted from the work performed by DesRoches and Muthumar (2002).

It is assumed that the length of surface footing of each collective pier is 9 m. It is also assumed that all bridge structures including footings and soil should remain elastic. The material data is given in Table 1.

The material damping of the bridge structures is described by a complex Young's modulus. The chosen

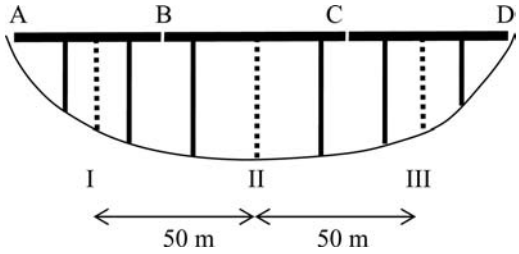

Figure 1. Multiple bridge frames with subsoil

Table 1. Bridge material data.

	Bridge member		
Left and right segments	Girder	Pier	Footing
Mass (10^3 kg/m)	151	5.26	91.5
EA (10^8 kN)	63.42	1.407	768.6
EI (10^8 kN m^2)	50.49	1.546	1024.8
Middle segment	Girder	Pier	Footing
Mass (10^3 kg/m)	217.5	7.89	91.5
EA (10^8 kN)	63.42	2.111	768.6
EI (10^8 kN m^2)	50.49	2.32	1024.8

damping model consists of a chain of Kelvin elements with the parameters $E_1 = 0.1$ and $E_n = 10^{28}$ for defining the real and imaginary parts of the modulus of elasticity (Hashimoto and Chouw 2003). The equivalent damping ratio is about 1.4%. The fundamental frequency of the left and right bridge segments with an assumed fixed base is 2.14 Hz, and the one of the middle structure is 0.9 Hz. The ground is assumed to be a half space with the soil density of 2 t/m^3, the Poisson's ratio of 0.33 and the shear wave velocity of 200 m/s which correspond to the subsoil class D according to New Zealand standard (NZS1170.5 2005). The considered return period and zone are 2500 years and 0.4, respectively. The average PGAs are normalized to 0.24 g. To limit the number of considered parameters it is assumed that the soil has no material damping. Hence, only the radiation damping owing to waves propagating from the vibrating footings are taken into account in the analysis.

In the numerical analysis the bridge segments with their footings and the subsoil are described by finite elements and boundary elements, respectively. Using the substructure technique the governing equations for the whole soil-structure system can be determined.

The structures and footings are modeled using continuous-mass model (Kodama and Chouw 2002). The dynamic stiffness $\tilde{\mathbf{K}}^b$ of each bridge segment is obtained by adding the stiffness of each structural member. The dynamic stiffness $\tilde{\mathbf{K}}^s$ of the subsoil is obtained by transforming the wave equation

$$\left(c_p^2 - c_s^2\right) u_{j,ji} + c_s^2\, u_{i,jj} + P_i = \ddot{u}_i \tag{1}$$

into the Laplace domain

$$\left(c_p^2 - c_s^2\right) \tilde{u}_{j,ji} + c_s^2\, \tilde{u}_{i,jj} + s^2 \tilde{u}_i = -\tilde{P}_i \tag{2}$$

where c_p and c_s are the compressive and shear wave velocities, respectively. P_i is the component of the body force per unit mass. i and $j = 1, 2, 3$. Tilde indicates a vector or matrix in the Laplace domain. By applying the full-space fundamental solution and by assuming a distribution of displacement and traction along the boundaries the relationship between displacement and traction at the footing-soil interface can be obtained. A consideration of the area of the elements leads to the dynamic stiffness $\tilde{\mathbf{K}}^s$ of the subsoil (Chouw 2002).

The obtained governing equations of a bridge segment with subsoil in the Laplace domain are

$$\begin{bmatrix} \tilde{\mathbf{K}}_{bb}^{bn} & \tilde{\mathbf{K}}_{bc}^{bn} \\ \tilde{\mathbf{K}}_{cb}^{bn} & \tilde{\mathbf{K}}_{cc}^{bn} + \tilde{\mathbf{K}}_{cc}^{sn} \end{bmatrix} \begin{bmatrix} \tilde{\mathbf{u}}_b^{bn} \\ \tilde{\mathbf{u}}_c^{bn} \end{bmatrix} = \begin{bmatrix} \mathbf{0} \\ \tilde{\mathbf{P}}_c^n \end{bmatrix} \tag{3}$$

where $\tilde{\mathbf{P}}_c^n = \tilde{\mathbf{K}}_{cc}^{sn}\, \tilde{\mathbf{u}}_g^n$. $\tilde{\mathbf{u}}_g^n$ are the ground motions at the interface between footing and subsoil. n, b, s, c stand for the left, middle or right bridge segment, bridge, soil and contact degree-of-freedom, respectively.

To incorporate the unilateral contact condition, i.e. pounding and girder separation, of the adjacent soil-structure systems, the calculation is performed in the Laplace and time domain.

While the unbalanced forces, required to correct the change from one contact condition to the other, are determined in the time domain, the system response is calculated in the Laplace domain. A transformation of the results from the Laplace to the time domain provides then the time history of the response of the bridge structures. To incorporate the influence of poundings and loss contact the non-linear analysis of the soil-structure system is performed subsequently in the Laplace and time domain. Details about the non-linear algorithm are given in (Chouw 2002 and Chouw and Hao 2008a). The spatially varying ground motions are simulated stochastically based on the New Zealand design spectrum for soft soil sites (class D according to NZS1170.5 2005) using the following coherency loss function (Hao 1989).

$$\gamma_{ij} = \exp\left(-\beta d_{ij}\right) \exp\left(-\alpha d_{ij}^{0.5} f^2\right) \exp\left(-i\, 2\pi f\, d_{ij} / c_a\right) \tag{4}$$

where β is a constant, d_{ij} is the distance between two observed locations i and j in the wave propagating direction, f is the frequency in Hz, and c_a is the apparent wave velocity. α has the following form

$$\alpha(f) = \frac{a}{f} + b f + c, \qquad f \le 10\,\text{Hz} \tag{5}$$

When f > 10 Hz, the α function is constant and equals to the value at 10 Hz. a, b, c and β are 3.582 10^{-3}, $-1.811\ 10^{-5}$, 1.177 10^{-4} and 1.109 10^{-4}, respectively. These coefficients are obtained using SMART-1 data. They are the best-fitting values for the empirical coherency loss function to the recorded ground motions spatial variations. It is assumed that c_a is 500 m/s and the ground motions are highly correlated. Details about the ground motion simulation procedure are given in (Hao 1989 and Hao et al. 1989).

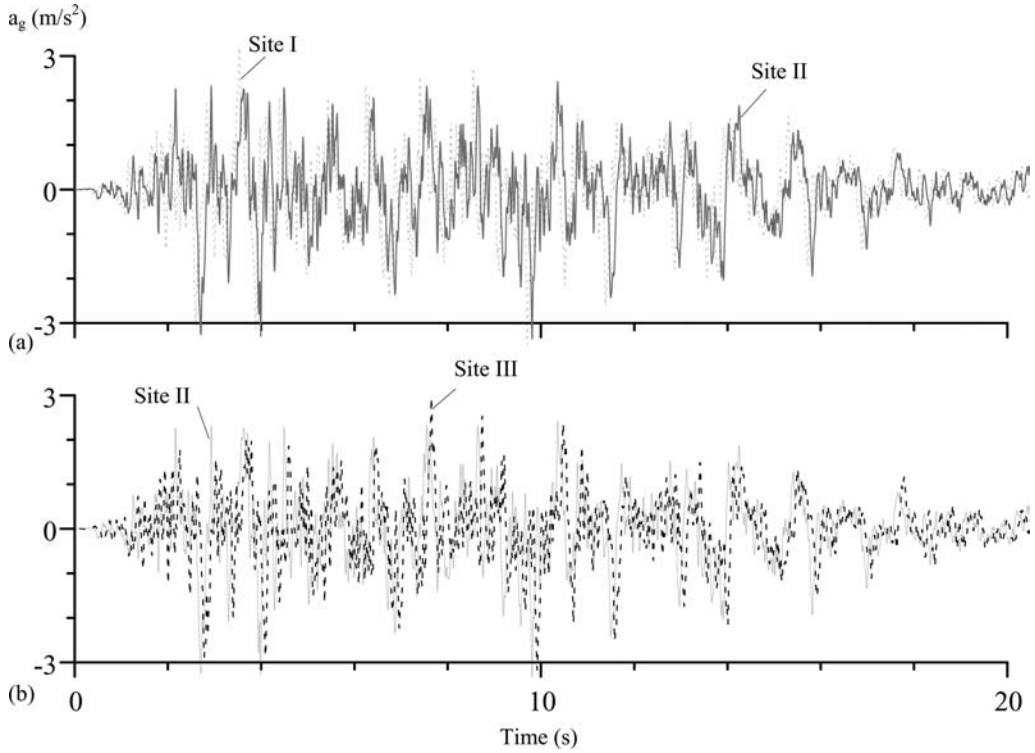

Figure 2. Non-uniform ground acceleration at (a) sites I and II and (b) sites II and III.

Figures 2 and 3 show the non-uniform ground accelerations and displacements at the considered sites I, II and III, respectively. The time delay due to wave propagation from one site to the adjacent one and the alteration due to coherency loss can be clearly seen. The peak ground accelerations at the corresponding sites are 3.49 m/s^2, 3.35 m/s^2 and 2.93 m/s^2, respectively. The peak ground displacements are 15.03 cm, 15.44 cm and 13.67 cm, respectively.

3 CONSEQUENCE OF RELATIVE BRIDGE GIRDER MOVEMENTS

To reveal the consequence of relative girder movements, the left and middle bridge segments are considered. The gap between the girders is 3 cm. For simplicity it is assumed that the influence of the left abutment and the right bridge segment can be neglected. Figures 4(a) and (b) show the pounding forces due to uniform and non-uniform ground excitations, respectively. The solid and dotted lines are the results with and without SSI effect, respectively.

In the case of uniform excitation it is assumed that the middle bridge segment experiences the same ground motions as the left bridge segment. While the maximum pounding force of 79.7 MN occurs at 18.26 s when fixed base structures are assumed, SSI clearly reduces the pounding force to 19.1 MN which occurs at 14.02 s.

If spatially non-uniform ground excitations are considered, the maximum pounding force of 80.76 MN takes place at 6.18 s when fixed base structures are assumed. When SSI effect is considered, the maximum pounding force occurs at 5.42 s and has the value of 26.6 MN.

The results show that spatially non-uniform ground excitations increase the maximum pounding forces irrespective of the support condition of the bridge structures. In contrast, SSI reduces the activated pounding forces.

In the considered cases the relative girder movements are caused by the different dynamic properties of the adjacent bridge structures characterized by the ratio of their fixed base fundamental frequencies ($f_{II}/f_I = 0.42$) and SSI effect.

To have a closer look at SSI effect, the pier of the middle bridge segment is strengthened so that it has almost the same fixed base fundamental frequency and $f_{II}/f_I = 0.99$. Figure 5(a) shows the girder movement of the left and middle bridge structures due to uniform ground excitation. SSI is not considered. The bridge response is determined solely by the properties of the ground motions and bridge structures. As expected even the small gap of 3 cm is sufficient to prevent bridge girder pounding, since both bridge

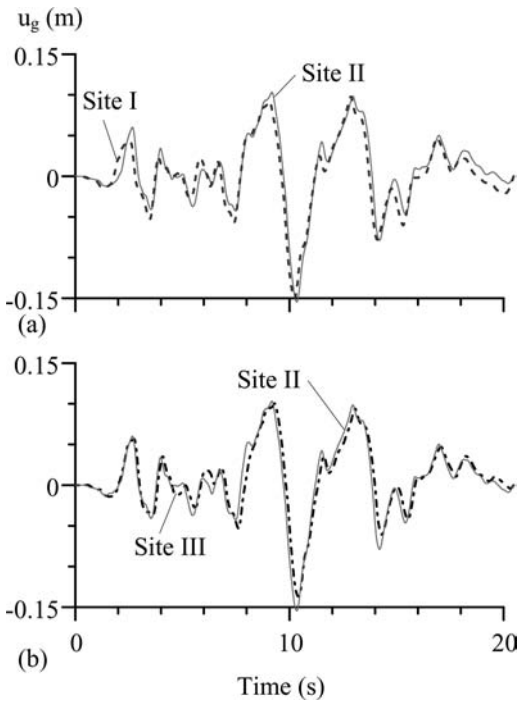

Figure 3. Non-uniform ground displacements at (a) sites I and II and (b) sites II and III.

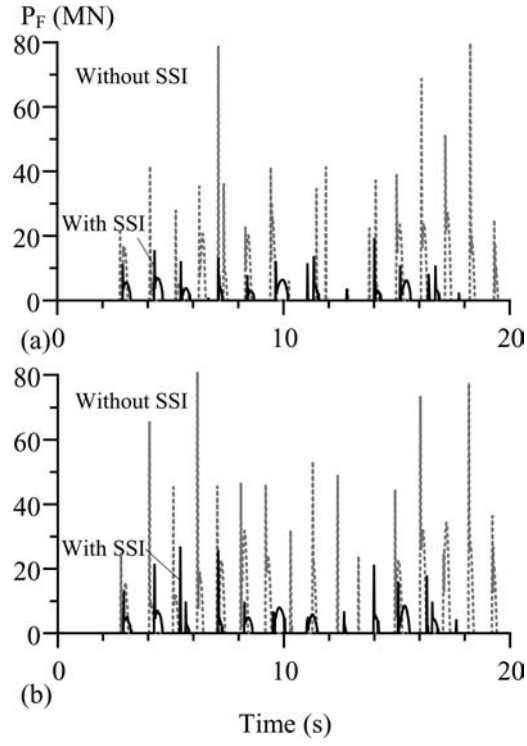

Figure 4. Pounding forces due to (a) uniform and (b) non-uniform ground excitations at site I and II.

structures respond to the uniform excitation in phase. Even though both structures vibrate very close to each other, pounding does not take place.

Figure 5(b) shows the girder responses without pounding effect when SSI is considered. The subsoil not only reduces natural frequencies of the soil-structure system, it also increases the intensity of structural responses. The existing gap of 3 cm is clearly insufficient to prevent the bridge girders from pounding as it can be seen from the response at around 4 s. The reason is that although both adjacent structures have the same ground excitation and almost the same fixed base fundamental frequencies ($f_{II}/f_I = 0.99$), because of their unequal slenderness both bridge structures interact with the subsoil differently. In contrast to the response of the structures with an assumed fixed base this unequal SSI causes different increase of the structural responses which lead then to relative responses and pounding between the girders. Figure 6 shows the development of the pounding forces with the maximum value of 22.3 MN at 7.08 s which cannot be observed if SSI effect is neglected.

The consequence of loading and support conditions for the structural responses can be clearly seen also in the development of bending moments at the pier support of the middle bridge segment (Figure 7). The thin solid line is the result when uniform ground excitation and fixed base structures are assumed.

The thick solid and dotted lines are the results due to uniform ground excitation with SSI effect when pounding effect is not and is taken into account, respectively. Their corresponding maximum values are 1260.7 MNm, 1157.5 MNm and 843.4 MNm, respectively. In this considered case SSI reduces the bending moment and impediment of the girder movement due to pounding causes further reduction.

4 MITIGATION MEASURE USING MODULAR EXPANSION JOINTS

To avoid pounding between bridge girders current design specifications, e.g. CALTRANS (2006), recommend that bridge structures should have the same or at least similar fixed base fundamental frequencies. The adjacent structures will then respond mainly in phase and the gap will be able to cope with small relative movements of the adjacent girders as confirmed in Figure 5(a). When conventional expansion joint is used, the gap is small to ensure serviceability of the bridge. This recommendation works, when the expected ground motions at adjacent bridge supports are indeed uniform. Owing to the properties of seismic waves and soil along the bridge, the ground motions vary along the path of the propagating waves. As a consequence the recommendation of the current design specifications will just cause relative response between adjacent bridge structures and hence increase the pounding potential as indicated in the discussion of the results in Figure 5(b).

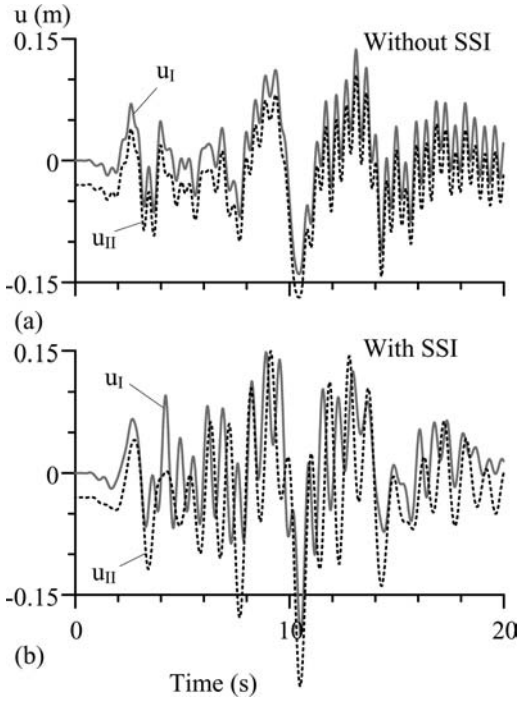

Figure 5. Girder displacements due to uniform ground excitation (a) without and (b) with SSI effect ($f_{II}/f_I = 0.99$).

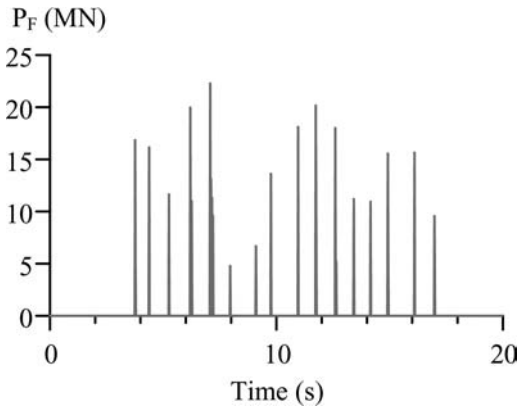

Figure 6. Pounding forces due to unequal SSI effect.

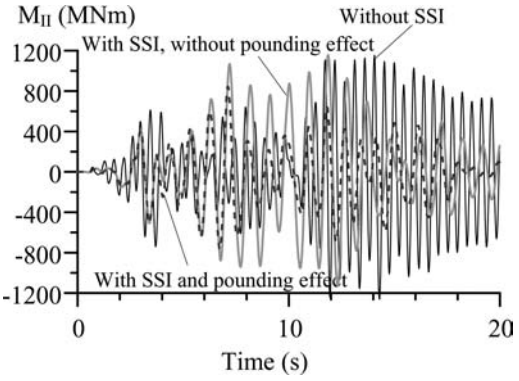

Figure 7. Bending moment due to unequal SSI effect.

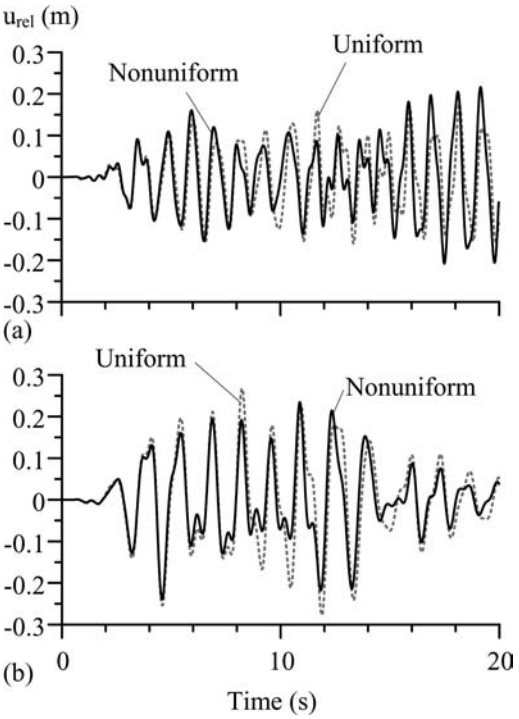

Figure 8. Relative girder movement at B (see Figure 1) due to uniform and nonuniform ground motions (a) without and (b) with SSI effect.

To overcome this difficulty, the authors have proposed the usage of modular expansion joints (MEJs) (Chouw and Hao 2008b and Bi et al. 2010). A MEJ consists of a number of center beams and edge beam at each girder end. Seals cover the gaps between these beams to ensure watertightness of the joint. Traffic loading of these beams will be transferred to both adjacent bridge girders by yokes, support bar and a number of springs and bearings. These sliding springs, bearings and yokes ensure that the beams can move uniformly and enable the adjacent bridge girders to accommodate expected relative movement at the joint. The number of the beams determines the maximum capability of the joint to move without causing any pounding between the adjacent bridge girders. Detailed description of MEJs is given, e.g. in (Dexter et al. 2002).

Figures 8(a) and (b) show the relative girder movements at the location B (see Figure 1) without and with SSI effect, respectively. Figures 9(a) and (b) are the corresponding relative girder displacements at the location C (see Figure 1). The dotted and solid lines are the responses due to uniform and spatially non-uniform ground excitations.

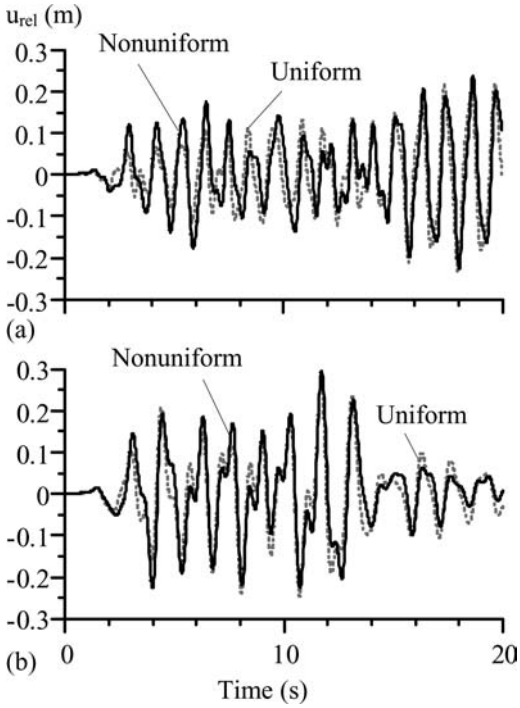

Figure 9. Relative girder movements at C (see Figure 1) due to uniform and non-uniform ground motions (a) without and (b) with SSI effect.

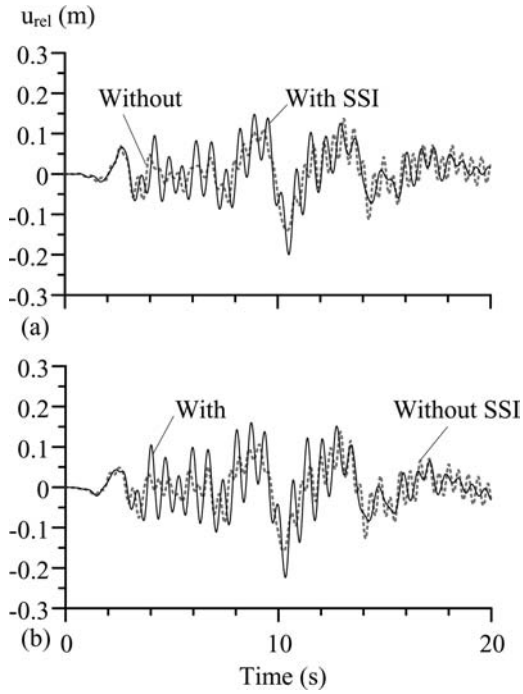

Figure 10. Relative girder movements with and without SSI effect at (a) location A and (b) location D (see Figure 1).

Figures 10(a) and (b) display the relative girder movements at the locations A and D (see Figure 1) due to uniform site I and site III ground motions, respectively. The solid and dotted lines are the results with and without SSI effect.

Table 2 displays the minimum total gap that a MEJ at the particular locations must have to avoid any pounding between adjacent bridge girders and between girder and adjacent abutment. The number in parentheses indicates the time when the maximum relative girder movements occur. Two uniform ground motions are considered, and all structure experience the ground motions of site I or those of site III. It is assumed that the abutments are fixed.

A comparison of the results clearly shows that at all locations, SSI effect always causes larger required total MEJ gap. This is independent of the ground motions.

Spatially non-uniform ground motions can cause larger total MEJ gap irrespective of the support conditions of the bridge structures (with or without SSI).

Table 2. Minimum required total gap of MEJ.

Excitation	Location	A	B	C	D
Uniform	Without	0.14 m (10.5 s)	0.176m (18.2s)	0.236m (18s)	0.14 m (10.5 s)
	With SSI	0.2 m (10.56s)	0.278m (11.92s)	0.273m (11.78s)	0.2 m (10.56s)
Non-uniform	Without	0.159m (10.3s)	0.216m (19.1s)	0.238m (18.68s)	0.159m (10.3s)
	With SSI	0.224m (10.36s)	0.239m (4.62s)	0.297m (11.74s)	0.224m (10.36s)

5 CONCLUSIONS

Three bridge segments are considered to study the influence of SSI, spatially non-uniform ground motions and dynamic properties of structures. The ground motions are simulated based on New Zealand design spectrum for soft soil.

In the considered cases it can be observed that unequal SSI increases significantly the bridge girder damage potential.

The total gap that a MEJ must have to prevent pounding at girder end is determined by the effect of SSI and spatially non-uniform ground motions. Both of them can amplify the necessary total gap.

ACKNOWLEDGEMENTS

This research was supported by FRDF under the Grant No. 3622738/9572. The authors would like to thank the reviewers for their constructive comments.

REFERENCES

Bi, K., H. Hao, Chouw, N. 2010. Required separation distance between decks and at abutments of a bridge crossing

canyon site to avoid seismic pounding, *Earthquake Engineering and Structural Dynamics* 39: 303–323.

CALTRANS. 2006. Seismic design criteria: Version 1.4, Sacramento, California.

Chouw, N. 2002. Influence of soil-structure interaction on pounding response of adjacent buildings due to near-source earthquakes, *JSCE J Applied Mechanics* 5, 545–553.

Chouw, N., Hao, H. 2005. Discussion on required seat length of bridge girders under current Japanese design specification, Proceedings of the annual Australian earthquake engineering conference, Albury, 1–7.

Chouw, N., Hao, H. 2008a. Significance of SSI and nonuniform near-fault ground motions in bridge response I: Effect on response with conventional expansion joint, *Engineering Structures* 30(1): 141–153.

Chouw, N., Hao, H. 2008b. Significance of SSI and nonuniform near-fault ground motions in bridge response II: Effect on response with modular expansion joint, *Engineering Structures* 30(1): 154–162.

DesRoches R., Muthumar S. 2002. Effect of pounding and restrainers on seismic response of multiple-frame bridge. *ASCE J. Structural Engineering* 128: 860–869.

Dexter, R.J., Mutziger, M.J., Osberg, C.B. 2002. Design, specification, installation and maintenance of modular bridge expansion joint system, *ASCE J Bridge Eng.* 6: 529–538.

Hashimoto, K., Chouw, N. 2003. Investigation of the effect of Kobe earthquake on a three-dimensional soil-structure system, *JSCE J Earthquake Engineering* 27: 1–8.

Hao, H. 1989. *Effects of spatial variation of ground motions on large multiple-supported structures*, Report No. UCB-EERC 89/06, UC Berkeley.

Hao, H., Oliveira, C.S., Penzien, J. 1989. Multiple-station ground motion processing and simulation based on SMART-1 array data. *J. Nuclear Engineering Design* 111: 293–310.

Japan Road Association (JRA) 2004. *Specifications for highway bridges –Part V: Seismic design*. 5th edition, Tokyo (in Japanese).

Japan Society of Civil Engineers (JSCE). In: Hamada, M., Nakamura, S., Ohsumi, T., Megro, K., Wang, E., editors. *The 1999 Ji-Ji earthquake, Taiwan – Investigation into damage to civil engineering structure*. Tokyo, 160pp.

Kawashima, K., Unjoh, S. 1996. Impact of Hanshin/Awaji earthquake on seismic design and seismic strengthening of highway bridges. *JSCE Structural Engineering/Earthquake Engineering* 13(2): 211–240.

Kodama, T., Chouw, N. 2002. Soil-structure interaction with uplift due to near-source earthquakes. In : *Proc. of the 4th int. conf. on structural dynamics*, Lisse, A. A. Balkema Publishers, 1375–1380.

Lin, G.J., Hung, H., Liu, Y., Chai, J. 2008. Reconnaissance report of 0512 China Wenchuan earthquake on bridges, *Proc. of the 14th world conference on earthquake engineering*, Beijing, S31-006.

New Zealand Standard (NZS) 2005. 1170, *Part 5: Earthquake Actions*.

Ruangrassamee, A., Kawashima, K. 2001. Relative displacement response spectra with pounding effect, *Earthquake Engineering and Structural Dynamics* 30: 1511–1538.

Zerva, A. 2009. *Spatial variation of seismic ground motions – Modeling and engineering application*, CRC Press, 468pp.

Soil-Foundation-Structure Interaction – Orense, Chouw & Pender (eds)
© 2010 Taylor & Francis Group, London, ISBN 978-0-415-60040-8

Seismic response of gravity walls using Newmark-type modelling with double-support excitation

M. Corigliano & C.G. Lai
European Centre for Training and Research in Earthquake Engineering (EUCENTRE), Pavia, Italy

R. Pasquali
Province of Macerata – Civil Engineering Service, Macerata, Italy

ABSTRACT: The design of gravity earth-retaining structures is one of the first applications of the modern engineering approach based on calculations rather than experience on physical models (Coulomb, 1776). Also the problem of accounting for earthquake loading on such structures dates back to the early days of modern earthquake engineering (Mononobe and Matsuo, 1929). Despite this promising early history, this topic has then received comparatively minor attention especially in recent decades, and the last major theoretical innovation in seismic design of these structures dates back to Newmark (1965). Whereas in recent years the capabilities of numerical analysis have improved considerably, dynamic time-history analysis of gravity earth-retaining walls remains a complex problem to deal with and it is far from being included in the toolbox of practicing engineers. In the framework of performance-based design, the need is felt for a simplified, yet accurate, method of analysis enabling designers to overcome the deficiencies of currently available methods without embarking in complex numerical analyses. A proposal on this regard is proposed in this paper.

1 INTRODUCTION

Performance-based design is the new trend in the earthquake engineering community and also code writers are quickly moving toward such direction. Compared to other kinds of structures, performance-based design of gravity earth-retaining walls can be relatively straightforward: in fact for this typology of structures it is often easy to drive the seismic response until failure through the most ductile failure mechanism which is sliding. If both overturning and excessive residual tilting are avoided, then the only parameter to be checked against performance criteria is the residual horizontal displacement of the wall (Pasquali et al., 2010).

Seismic design of gravity earth-retaining walls is most commonly performed by using the pseudo-static approach which has all the limitations of force-based design methods applied to earthquake engineering (Priestley et al., 2007). Its "*safety factor*" is purely conventional while performance-based design focuses on the expected wall displacement thus providing a measure of the expected damage (Pasquali et al., 2010).

Therefore it is clear that the power and usefulness of performance-based design entirely depends on the possibility of estimating the wall displacement. Actually for a given seismic input, performance-based design of gravity walls coincides with an estimate of the expected wall displacement.

Non-linear, numerical time-history analyses represent the most rigorous method for the computation of co-seismic and post-seismic displacement of an earth-retaining structure. It potentially allows modeling all the relevant aspects of the hydro-mechanical response but at the price of a great modeling and computational effort. Indeed, great attention and expertise are required for performing such kind of analyses. The risk of obtaining meaningless results is high and these type of analyses will probably continue to remain a too sophisticate tool for routine design, at least in the near future.

Thus for everyday design there is a strong demand for simplified methods allowing a quick and sufficiently accurate estimate of the wall displacement. Available methods of this kind are based on the sliding block equivalence proposed by Newmark (1965). Such approach, known as the "*Newmark method*", has been originally developed for the seismic analysis of dams and embankments, but it has been used also for earth-retaining walls. However, several differences exist between a sliding block and an earth-retaining wall which, differently to the former, is also subjected to a lateral seismic excitation induced by the backfill soil.

In this paper, a method is proposed to improve the applicability of the Newmark method to gravity earth-retaining structures. The first part of the paper summarizes the available methods for the seismic design of gravity walls highlighting their advantages and limitations. The second part describes the proposed method to estimate the final displacement of an earth-retaining structure subjected to earthquake loading based on the modified Newmark approach.

2 STATE OF THE ART IN THE SEISMIC DESIGN OF GRAVITY RETAINING WALLS

2.1 *Force-based methods*

The most traditional approach to account for seismic loading in designing gravity earth-retaining structures is the inclusion of a set of (pseudo-static) forces in the equilibrium check. The safety factor is directly calculated as the minimum value among the ratios of stabilizing versus destabilizing actions. Different methods have been established in order to calculate the actions and the resistant forces, but in the end a static equilibrium check is the core of the procedure first proposed by Mononobe and Matsuo (1929).

Such method is still considered as the standard approach to seismic analysis of earth-retaining structures and embankments by most seismic codes worldwide. The weak point is, evidently, the definition of a static force capable of reproducing the effects of a real acceleration time history. As a matter of facts, this correspondence is entirely empirical and also difficult to corroborate, short of real-scale experiments (Pasquali, 2008).

The pseudo-static approach takes into account, in an oversimplified fashion, the following dynamic phenomena: the inertia of the wall itself, the increment of soil thrust due to seismic shaking and the hydrodynamic effect in case of fluid-saturated soils. A delicate point of the procedure lies in the choice of the "*seismic coefficient*". Such parameter is defined as the ratio between the design acceleration (horizontal or vertical component) and the acceleration of gravity.

In principle, as the pseudo-static method is based on the free-body diagram of a rigid body, it seems reasonable to assume the wall subjected to the design Peak Ground Acceleration (PGA). However, experience has shown that, in high seismicity regions, such approach would lead to an overconservative design, predicting the collapse of most existing gravity walls, which actually behaved well in strong earthquakes.

Starting from this empirical observation, engineers have realized that for most gravity earth-retaining structures, and especially for the squatter ones, sliding is the governing failure mechanism (Pasquali et al., 2010). Thus exceedance of the sliding resistance of the wall will result in a permanent displacement of the wall, which may turn to be acceptable or even unnoticeable after the earthquake.

For such reason, in most seismic codes, the seismic coefficient is calculated by applying to the design PGA a so called "*reduction factor*", whose specific value depends on the amount of displacement tolerable by the structure; this is defined empirically (see for instance Hynes Griffin and Franklin, 1984; DM, 2008; EN 1998-5:2005; Arulmoli et al., 2008; Pasquali, 2008).

The direct consequence of this reasoning is that checking equilibrium under seismic loading is not really necessary because the key point lies in calculating the permanent displacement of the wall and judging if this is acceptable (Pasquali et al., 2010). Sliding at the wall base can be a stable and safe ductile behaviour because, in most cases, the sliding resistance of the wall is not affected by previous movement, and after an earthquake the static factor of safety regain the same value assumed prior to the seismic event, even though the wall did slid meanwhile. Thus, temporary loss of equilibrium of an earth-retaining wall that fails by sliding during an earthquake may be acceptable as long as it leads to a tolerable amount of displacement.

2.2 *Displacement-based methods*

Arguments in favor of a displacement-based design approach, as opposed to a force-based approach, are well known especially referring to seismic structural design (Priestley et al., 2007). However the same arguments apply also to geotechnical engineering. Specifically the following statement: damage *is* displacement. In fact, for a massive and rigid structure such as a gravity earth-retaining wall, the permanent displacement at the end of the earthquake is the only measurable form of damage.

As it is well known, a gravity earth-retaining wall can fail through three different mechanisms: by excessive sliding, by overturning, and by failure of the foundation soil. The first of these three mechanisms is inherently ductile, with a ductility factor being virtually infinite: as a matter of fact a friction slider is often used to idealize a perfectly plastic behavior. Therefore, it is desirable that, through an appropriate *capacity design*, sliding be the governing failure mechanism of the wall. If this is ensured, then the concept of "failure" becomes strictly connected to the concept of "*allowable displacement*". Very similarly to what happens to a reinforced concrete member undergoing flexural yielding, different limit states may be associated to different amounts of unrecoverable strain or displacement. The capacity design philosophy consists in this case in favoring a flexural failure over a shear failure being the former far more ductile than the latter.

A simplified method for analyzing the seismic stability of embankments and slopes in terms of displacements was outlined by Newmark in his 1965 *Rankine* Lecture. The method is based on the analogy with a rigid block sliding on a plane (Newmark, 1965), and despite of being initially developed for evaluating the seismic behavior of dams and embankments, it has been extended without conceptual changes also to the seismic analysis of earth-retaining walls (Kramer, 1996).

The method requires the definition of a threshold ("yield") acceleration that would induce incipient movement (i.e. factor of safety of one) of the rigid block under study. Integrating twice the part of acceleration time history exceeding the yield acceleration, one can calculate the permanent displacement undergone by the block.

When calculating the yield acceleration, the most critical failure mechanism needs to be considered. As mentioned above, for gravity retaining walls, the governing failure mechanism should desirably be

base sliding. Only if such condition is met, a meaningful application of the Newmark method can be made. Luckily, this situation is fairly common, but an explicit check is always needed, e.g. by performing a preliminary pushover analysis.

3 PROS AND CONS OF AVAILABLE METHODS

3.1 *Force-based methods*

The major advantage of this approach is its simplicity. Seismic design can be carried out by hand following the very same procedure which is employed for static design, simply by including additional forces in the free body diagram. The pseudo-static forces are usually determined according to the Mononobe-Okabe theory (Okabe, 1926; Mononobe and Matsuo, 1929).

The major drawback of force-based methods is logical inconsistence. As equilibrium of the wall is checked, movement should not occur and the Peak Ground Acceleration (PGA) could be used for calculating the pseudo-static seismic forces. However, if the value of PGA is large, this approach would lead to overconservative design. Therefore the method, is usually applied with a modification: the design PGA is reduced by a certain factor depending on the amount of displacement that can be tolerated by the structure at the end of the earthquake. The reduction factor to be used is usually specified by seismic codes; see for instance Eurocode 8-Part 5.

The relationship between force reduction factor and expected displacement is established on a completely empirical basis. Indeed, it is an implicit admission that displacement is the real key parameter. The designer knows that, if the factor of safety were equal to one, the wall would then be subjected to a certain displacement (given by the seismic code). However, as the safety factor must be larger than one, nobody knows if and how much the wall will displace. This makes the implementation of performance-based design practically impossible.

A substantiation of the main drawbacks of the pseudo-static approach is provided by the results of numerical modeling (e.g. Whitman and Liao, 1985; Pasquali et al., 2010) and laboratory experiments (e.g. Nakamura, 2006; Sitar and Al Atik, 2009). Whitman and Liao (1985) showed the results of analyses conducted on a finite element model of an earth-retaining wall excited by 3 cycles of sinusoidal motion. Figure 1 from this work shows that the slip at the base occurs when the thrust between backfill and wall is relatively low. On the other hand, the maximum thrust from the backfill occur at times when no slip is occurring and when the base shear is relatively low (Whitman and Liao, 1985).

Sitar and Al Atik (2009) used data from centrifuge experiments to study the seismic behavior of wall-backfill systems and to assess the validity of the Mononobe-Okabe theory. The physical models consisted of two U-shaped, stiff and flexible

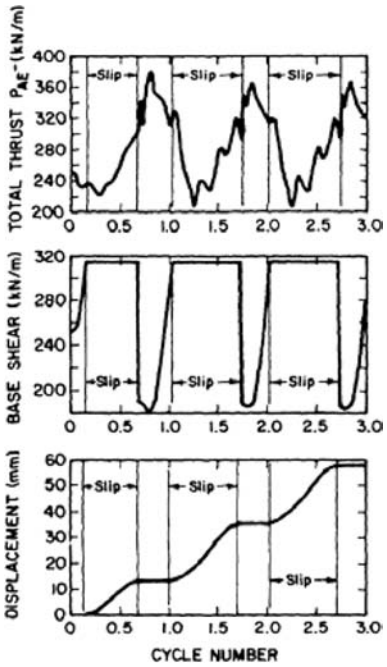

Figure 1. Results from finite element analysis of an earth-retaining wall subjected to 3 cycles of sinusoidal ground motion (from Whitman and Liao, 1985).

earth-retaining structures. Both structures supported a backfill constituted by medium dense sand. The experimental results obtained by Sitar and Al Atik (2009) showed that dynamic earth pressures and inertia forces do not take their maximum values simultaneously. The authors also compared the dynamic wall bending moments, earth pressures and inertia forces acting on the walls. Figure 2 shows the out-of-phase relation between dynamic earth pressures and dynamic wall bending moments (due to dynamic earth pressures and wall inertia) acting on the wall. When the inertial force is at its local maximum, the dynamic wall bending moment is also at its local maximum, but the dynamic earth pressure increment is at its local minimum or around zero (Sitar and Al Atik, 2009).

In designing gravity earth-retaining structures, two are the main issues that should be considered: the definition of the permanent displacement of the wall and, for cantilever walls, the calculation of the maximum bending moment (for the design of steel reinforcement bars). Numerical and physical modeling (as illustrated by Whitman and Liao, 1985 and Sitar and Al Atik, 2009) show that there is no direct correlation between the maximum dynamic earth pressure and the permanent displacement or alternatively, between the maximum earth pressure and the dynamic bending moment acting on the wall.

Another aspect which strongly influences the seismic response of an earth-retaining structure is represented by the characteristics of seismic input (e.g. amplitude, frequency content, duration, polarity, etc).

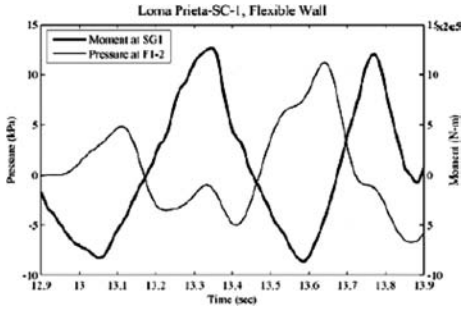

Figure 2. Comparison in centrifuge testing of dynamic wall bending moments and earth pressures on an earth-retaining structure during Loma Prieta shaking (Sitar and Al Atik, 2009).

Pasquali et al. (2010) showed through advanced numerical modeling the large variability of calculated permanent displacement of blockwork wharves depending on the specific seismic input adopted for the analyses. The latter was constituted by a set of 7 spectrum-compatible accelerograms. Since each record was scaled to the same PGA, a conclusion from the work by Pasquali et al. (2010) is that PGA is not the major controlling parameter in the response of gravity walls (represented by the permanent displacement) and other ground motion parameters play a more important role. The strong influence of the characteristics of seismic input on the response of gravity walls can possibly be associated with a resonance-like phenomenon taking place during the excitation of the structure by ground shaking and that causes the top displacement of the wall to increase as the frequency content of the input gets closer to the main frequency of the wall-backfill system (Pasquali et al., 2010). Also the number and duration of the peaks of ground motion are very important in determining the amount of final displacement.

3.2 *Displacement-based methods*

The Newmark method is simple and robust. It requires the use of a computer, but it has been implemented in freeware software (e.g. Jibson and Jibson, 2003). However, the method was not directly developed to study the response of earth- retaining walls, therefore it has some drawbacks which are listed below:

- even though the wall is considered excited at its base by the foundation soil, in reality it is subjected to a double seismic excitation: one from the foundation soil and the other from the backfill. In general, due to a different stiffness of the backfill compared with the one of the foundation soil, the two seismic inputs are potentially different and out-of-phase: a soft backfill may undergo significant amplification and induce "*whiplash effect*" on the wall. This is completely overlooked by the Newmark method, which assumes that the wall is subjected to only a base excitation;
- the Newmark method requires preliminary definition of the yield acceleration. The user is free to choose the most suitable method for calculating such parameter, but in practice the threshold acceleration is usually calculated according to the pseudo-static method, by looking at the value of the seismic coefficient that makes the safety factor to sliding equal to unity. Using the pseudo-static approach for the definition of the yield acceleration implies that the inconsistencies and uncertainties of the force-based approach are somehow carried over also to the displacement-based method;
- the effect of vertical shaking can be taken into account only if considering that the vertical accelerogram is a scaled copy of the horizontal record. Otherwise, the threshold acceleration should be re-calculated at each time step, which is still possible in theory, but it is not standard practice;
- if in front of the wall there is a water pool (such as it happens for instance to a wharf structure), hydrodynamics effect arises. This is usually simulated by an added mass applied to the wall, to be considered only for horizontal inertia and not for gravity action (Westergaard, 1933). The Newmark method does not allow this effect to be considered.

4 SIMPLIFIED MODEL: RIGID BLOCK WITH DOUBLE SUPPORT EXCITATION

The seismic response of a gravity earth-retaining wall is a complex problem to be studied. For instance, the permanent displacement undergone by the structure depends on several variables including the frequency content of the input motion, the duration of the accelerogram, the fundamental natural frequency of the backfill compared with the predominant frequency of the input signal, the inertial characteristics of the wall, and several others. In this regard, neither the pseudo-static method nor the Newmark approach is completely satisfactory for the seismic design of gravity walls. For instance the former uses only the PGA to characterize the seismic input, which is therefore poorly modelled, whereas the latter does not account for the presence of the lateral seismic excitation due to the presence of the backfill (see Figure 3), which strongly influences the permanent displacement of the wall.

A novel approach is proposed in the following aiming at overcoming the limitations of the standard Newmark method while retaining most of its simplicity. The wall is idealized as a single degree of freedom system (SDOF) having only the horizontal degree of freedom.

In absence of water (i.e. assuming dry conditions), the wall is subjected to the static earth pressure, the inertia of the wall itself and the dynamic increment of earth pressure due to the shaking of the backfill. Therefore, the wall, modelled as a rigid body, is excited by a double support excitation: from the foundation base (as in the standard Newmark approach) and laterally from the backfill.

The wall slides when the sum of the horizontal forces acting on the wall is greater than the friction

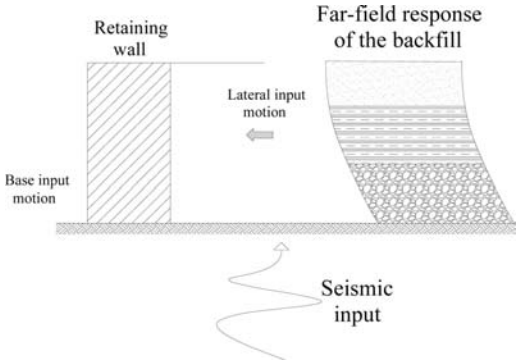

Figure 3. Simplified sketch of a gravity earth-retaining wall excited by both base motion and lateral backfill excitation.

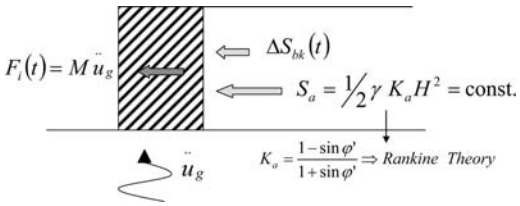

Figure 4. Forces acting on a gravity earth-retaining wall during a seismic excitation.

resistance between the wall and the soil. The dynamic equilibrium equation which governs the sliding is therefore:

$$\sum F_H(t) > W \cdot tg\,\delta = M \cdot g \cdot tg\,\delta \tag{1}$$

where W and M are the weight and the mass of the wall respectively, δ is the friction angle between the soil and the wall and g is the acceleration of gravity. The term "$g \cdot tg\delta$" *then*, represents the *critical acceleration* that is a threshold acceleration above which the wall slides. Figure 4 shows the forces acting on the retaining wall reported in Eq. (1).

The resultant horizontal force is the sum of three contributions:

$$\sum F_H(t) = S_a + F_i(t) + \Delta S_{bk}(t) \tag{2}$$

where:

- $S_a = 0.5 K_a \cdot \gamma \cdot H^2 =$ is the static earth pressure, which in this work was computed according to the Rankine classical theory (i.e. $K_a = (1 - \sin\varphi')/(1 + \sin\varphi')$), H is the height of the wall and γ is the soil unit weight;
- $F_i(t) = K_h \cdot W = M \cdot \ddot{u}_g =$ is the inertia force of the wall, K_h is the seismic coefficient and $\ddot{u}_g$ is the base acceleration of the ground;
- $\Delta S_{bk}(t) =$ is the dynamic thrust increment induced by the backfill, which will be defined below.

Differently than with the classical Newmark method, the proposed method does not require the definition of the critical ("yield") acceleration, therefore it does not require the use of the pseudo-static approach. For such purpose the dynamic thrust increment induced by the backfill (ΔS_{bk}) is obtained as the product of the backfill acceleration ($\ddot{u}_{bk}$) and the dynamic mass increment (Δm_{bk}).

Figure 5 shows the inclination of the failure surface under both static and dynamic loading. For simplicity, the static thrust has been calculated according to the Rankine theory (i.e. $\alpha_R = 45 + \varphi'/2$). This obviously does not imply any loss of generality as a more refined approach to compute the static thrust could be used. The dynamic thrust was calculated using the Mononobe-Okabe theory (Okabe, 1926; Mononobe and Matsuo, 1929).

The inclination of the failure surface affects the value of the lateral force acting on the wall. Steedman and Zeng (1990) introduced the effects of phase change in the calculation of the dynamic thrust. The inclination of the failure surface obtained by these authors depends on the frequency content of the signal and the shear wave velocity of the backfill. Steedman and Zeng (1990) showed that the dynamic wedge obtained with their model is smaller in size than the active wedge obtained using the Mononobe-Okabe theory. Unfortunately there is no closed-form solution for the computation of inclination of failure surface proposed by Steedman and Zeng (1990).

In the method proposed in this work, the inclination derived by the Mononobe-Okabe theory was used, because it was easier to handle (a closed-form solution actually exists), and also because it represents an upper bound solution of the inclination. This implies an higher value of the computed horizontal forces induced by the backfill, therefore the approach is conservative. The closed-form solution of the inclination of failure surface of Mononobe-Okabe theory (α_{MO}) was obtained by Zarrabi-Kashani (1979):

$$\alpha_{MO} = \varphi' - \psi + tg^{-1}\left[\frac{-tg(\varphi'-\psi) + C_1}{C_2}\right]$$
$$C_1 = \sqrt{tg(\varphi'-\psi)\left[tg(\varphi'-\psi) + \text{cotg}(\varphi'-\psi)\right]\ldots \ldots\left[1 + tg(\delta+\psi)\,\text{cotg}(\varphi'-\psi)\right]} \tag{3}$$
$$C_2 = 1 + \left\{tg(\delta+\psi)\left[tg(\varphi'-\psi) + \text{cotg}(\varphi'-\psi)\right]\right\}$$
$$\psi = tg^{-1}(k_h)$$

$$k_h = \ddot{u}_g / g \Rightarrow k_h(t) \Rightarrow \alpha_{MO}(t) \tag{4}$$

Equations (3) and (4) show that the inclination of the failure surface depends on the acceleration time history, therefore it varies with time.

The dynamic mass increment (Δm_{bk}) is obtained as the difference between the inertia of the dynamic wedge (m_{dyn}) (i.e. triangle ACD of Figure 5) and the static active wedge (m_{stat}) (i.e. triangle ABC):

$$m_{stat} = \frac{1}{2}\rho \frac{H^2}{\tan\alpha_R} \tag{5}$$

$$m_{dyn} = \frac{1}{2}\rho \frac{H^2}{\tan\alpha_{MO}} \tag{6}$$

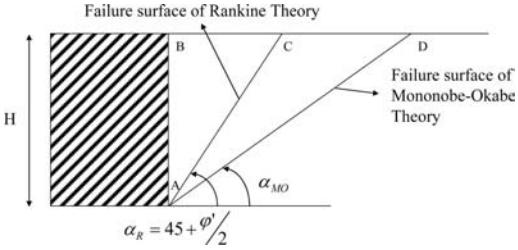

Figure 5. Failure surfaces in the backfill under both static and dynamic loading conditions.

where ρ is the mass density of the soil, and the dynamic mass increment is:

$$\Delta m_{bk} = m_{dyn} - m_{stat} \tag{7}$$

Finally, the dynamic thrust increment (ΔS_{bk}) induced by the backfill has been computed as:

$$\Delta S_{bk}(t) = \Delta m_{bk} \cdot \ddot{u}_{bk} \tag{8}$$

where $\ddot{u}_{bk}$ is the backfill acceleration. Figure 6 shows the soil mass included between the static and dynamic active wedges, which induces dynamic thrust increment to the wall due to backfill shaking.

The proposed method requires the definition of two different shaking time-histories. The first from the foundations soil ($\ddot{u}_g$), the second from the backfill ($\ddot{u}_{bk}$). Vertical excitation could be taken into account directly in the calculation of the normal force at the base of the wall, but for simplicity in the presented work it was neglected.

As the wall is modeled as a SDOF system, only sliding can be taken into account, and safety against overturning and foundation failure mechanisms should be assessed independently using a force-based approach. For such a purpose, a pushover analysis could be carried out. If sliding results to be the controlling failure mechanism, then the analysis does not need to consider the other two possible failure modes.

As underlined above, the wall slides when:

$$\sum F_H(t) > M \cdot g \cdot tg\,\delta \tag{9}$$

During the time lapse in which the horizontal forces acting on the wall are greater than the friction resistance at the wall base, a permanent displacement occurs and it is accumulated. The relative acceleration of the wall can be obtained by dividing the fraction of the total horizontal force exceeding the friction resistance by the mass of the wall as follows:

$$a_{rel} = \frac{\left[\sum F_H(t) - M \cdot g \cdot tg\,\delta\right] > 0}{M} \tag{10}$$

According to the classic Newmark theory, double integration of the relative acceleration obtained from Eq. (10) provides an estimate of the permanent displacement undergone by the wall.

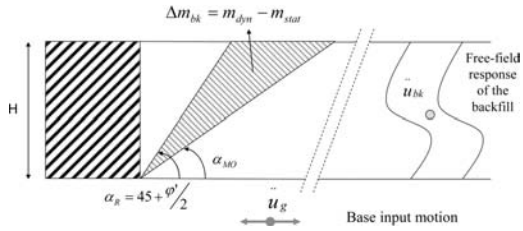

Figure 6. Soil mass which induces dynamic thrust increment in the wall due to backfill shaking.

5 COMPARISON BETWEEN NUMERICAL AND SIMPLIFIED MODEL

In order to validate the model proposed in Section 4, numerical time-history analyses have been performed using the finite difference code FLAC v5 (Itasca, 2005). A two-dimensional model of the earth-retaining wall under plane strain conditions was adopted. The reference soil profile was constituted by two layers. The bottom layer, from the base of the model to the foundation of the wall, was idealized using a linear viscoelastic constitutive model.

The backfill behind the wall was modeled using a linear visco-elastic perfectly-plastic constitutive law with a Mohr-Coulomb failure criterion and a non-associated flow rule (i.e. the soil dilatancy angle was assumed to be equal to zero) with cohesion equal to zero and angle of shearing resistance equal to 30°.

Viscous damping was modeled through the standard Rayleigh formulation using a value of 0.01% centered at 1 Hz. Due to the nature of the problem the value of the assumed soil damping ratio does not have a great influence on the estimate of permanent displacement. The retaining wall was assumed 4 m height and 3 m thickness, and it was modeled using linear elastic, isotropic plane strain elements. The elastic material parameters used for the numerical time-history analysis are listed in Table 1.

Figure 7 shows the numerical model of the wall. Since the objective of the numerical simulation was the validation of the proposed model, the seismic input to be used in the simplified model for the base excitation ($\ddot{u}_g$) and for backfill acceleration ($\ddot{u}_{bk}$) were directly taken from the numerical model. The base acceleration was recorded at a control point of the model in free-field conditions at the foundation level, while the backfill acceleration was recorded at a control point of the numerical model located in the backfill at mid-height of the wall. Both the accelerograms used in the simplified model are shown in Figure 7.

Interface elements between the wall and the soil were adopted. Interfaces were characterized by normal and shear stiffness, as well as friction resistance. The parameters of the interfaces used in the analysis are summarized in Table 2. In order to simulate the initial geostatic stress within the soil under static conditions before the earthquake excitation, the stages of excavation and wall construction were explicitly simulated. Seismic input was constituted by an accelerogram

Table 1. Elastic properties assumed for the soil and wall.

Soil properties	Bottom layer	Backfill	Wall
Bulk modulus (MPa)	875	66.7	16700
Shear modulus (MPa)	404	40	12500
Mass density (kg/m^3)	2000	1700	2400

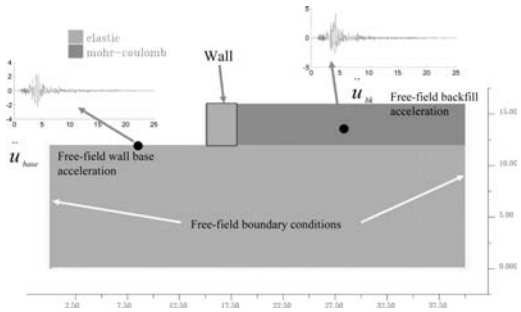

Figure 7. Numerical model obtained using FLAC of the gravity earth-retaining wall (acceleration time histories are in m/s^2).

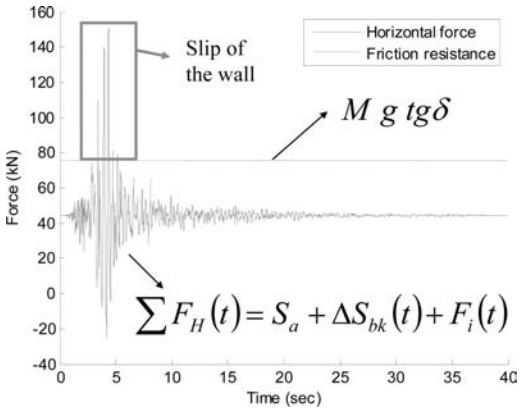

Figure 8. Resultant of the horizontal forces acting on the gravity wall and friction resistance at the soil wall interface.

recorded during the 1989 Loma Prieta earthquake (M_W=6.93 - R_{epi} = 28.6 km). The input motion was applied at the base of the model as a stress wave.

Figure 8 shows the time-histories of the resultant of horizontal forces acting on the retaining wall, computed using the simplified model (black line) and compared to the friction resistance at the base of the wall (grey line). Figure 8 allows to estimate the interval of time during which the total horizontal force is greater than the friction resistance (window in Figure 8), with the consequent sliding of the wall.

Double integration of the relative acceleration obtained according to Eq. (10) provides an estimate of the permanent displacement undergone by the wall.

Table 2. Interface properties adopted in the numerical model.

Interfaces properties	Wall/base interface	Wall/backfill Interface
Normal stiffness (Pa)	1E8	1E7
Normal stiffness (Pa)	1E8	1E7
Friction angle (°)	15	15
Cohesion (kPa)	0	0

Figure 9a) shows the comparison between the acceleration measured at the center of gravity of the earth-retaining wall using the numerical model (grey line) and the acceleration obtained by dividing the resultant of the horizontal forces with the mass of the wall (black line).

Double integration of the relative acceleration obtained according to Eq. (10) provides an estimate of the permanent displacement undergone by the wall. Figure 9a) shows the comparison between the acceleration measured at the center of gravity of the earth-retaining wall using the numerical model (grey line) and the acceleration obtained by dividing the resultant of the horizontal forces with the mass of the wall (black line).

Figure 9b) shows a close-up view of the two acceleration time histories, in the interval between 1 and 7 sec. The figure shows a quite good agreement, in amplitudes and phases, between the accelerogram obtained using the numerical model and that calculated using the simplified, Newmark-type approach.

The negative values of acceleration obtained from the simplified model occur when the horizontal forces applied at the wall are smaller than the friction resistance of the wall, namely:

$$\sum F_H(t) < M \cdot g \cdot tg\,\delta \qquad (11)$$

Figure 9a) shows also the relative velocity of the wall computed by integrating the relative acceleration obtained using the simplified model. The comparison between the permanent displacement obtained from the numerical model (grey line) and the proposed model (black line) is shown in Figure 9a). The agreement between the results obtained with two models is excellent.

6 CONCLUDING REMARKS

A novel method is proposed to overcome the main drawbacks of the Newmark method applied to the seismic analysis of gravity walls. Compared to the conventional Newmark approach, the proposed model allows introducing the effects of the double-support seismic excitation with a modeling effort extremely reduced with respect to that required by advanced numerical time-history analyses (THA).

This method would not require the designer to own one of the few, expensive commercial programs

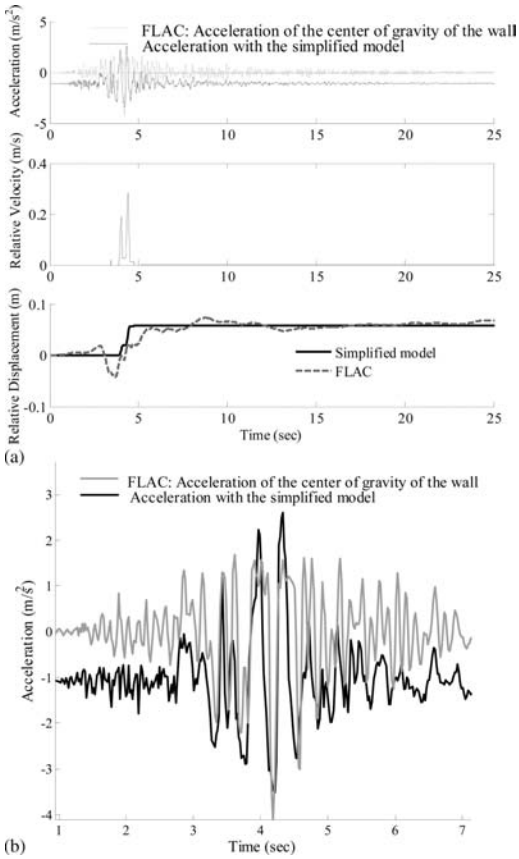

Figure 9. Comparison between numerical (FLAC) and simplified model: a) acceleration, relative velocity and relative displacement of the wall; b) close-up view of the acceleration of the wall between 1 and 7 sec.

capable of performing reliable non-linear, dynamic THA of geotechnical systems. However, as for the Newmark method, also the proposed model would be applicable only to sliding systems. Therefore, safety against overturning and foundation failure must be independently assessed.

The modified Newmark model proposed in this article aimed to verify and validate the capabilities of the method to predict the permanent displacement undergone by gravity earth-retaining structures. Therefore, the seismic input was directly taken from the results of the numerical model used for comparison. For real design applications, the numerical model is not required and the two input accelerograms could be obtained by simplified 1D wave propagation analyses such as those carried out using SHAKE (Schnabel et al., 1972) or similar programs.

REFERENCES

Arulmoli, A. K., Gayle, S. J., Yin, P., Jaradat, O. A., and Mays, T.W. 2008. "Geotechnical considerations and soil-structure interaction: proposed ASCE standards for seismic design of piers and wharves". *GEESD IV*.

Coulomb, C.A. 1776. Essai sur une application des regles des maximis et minimis à quelques problemes de statique relatifs à l'architecture. *Memoires de l'Academie Royale des Divers Savantes* 7.

DM 2008. Italian Building Code. Ministerial Decree January 14, 2008. "*Norme Tecniche per le Costruzioni*", Ministry of Infrastructures, Italian Government. G.U. 29 (in Italian).

EN 1998-5:2005 2005. *Eurocode 8 - Design of Structures for Earthquake Resistance - Part 5: Foundations, Retaining structures and Geotechnical aspects*, CEN, Bruxelles.

Hynes-Griffin, M. E. and Franklin, A. G. 1984. "Rationalising the seismic coefficient method". *Paper GL-84-13*, USACE Waterways Experiment Station, Vickburg, MS.

Itasca Consulting Group Inc. 2005. *FLAC (Fast Lagrangian Analysis of Continua)*, ICG, Minneapolis, MN.

Jibson, R.W. and Jibson, M.W. 2003. Java programs for using Newmark's method and simplified decoupled analysis to model slope performance during earthquakes, *USGS*.

Kramer, S. L. 1996. *Geotechnical Earthquake Engineering*, Prentice-Hall, Englewood Cliffs, NJ.

Mononobe, N. and Matsuo, H. 1929. On the determination of the earth pressures during earthquakes. *Proc. World Engineering Congress.*

Nakamura, S. 2006. Re-examination of Mononobe-Okabe theory of gravity retaining walls using centrifuge model tests. *Soils and Foundations* 46(2): 135–146.

Newmark, N.M. 1965. Effects of earthquakes on dams and embankments, *Geotechnique*, 15-2: 139–160.

Okabe, S. 1926. "General theory of earth pressures," *Journal of the Japan Society of Civil Engineering* 12(1).

Pasquali, R. 2008. Some issues in seismic analysis and design of wharves. *Msc Dissertaion*, ROSE School, Pavia, Italy.

Pasquali, R., Lai, C. G., Corigliano, M. 2010. "Some Issues in Seismic Analysis and Design of Blockwork Wharves". *Journal of Earthquake Engineering*, 14–1, 102–130.

Priestley, M.J.N., Calvi, G.M., Kowalsky, M.J. 2007. *Displacement-based Seismic Design of Structures*, IUSS Press.

Schnabel, P. B., Lysmer, J., and Bolton Seed, H. 1972. "SHAKE: a computer program for earthquake response analysis of horizontally layered sites," *UCB/EERC-71/12*.

Sitar N., Al Atik L. 2009. "On seismic response of retaining structures". Performance-Based Design in Earthquake Geotechnical Engineering – Taylor and Francis.

Steedman, R.S. and Zeng, X. 1990. "The Influence of Phase on the Calculation of Pseudo-Static Earth Pressure on a Retaining Wall". *Geotechnique*, Vol. 40, No.1, 103–112.

Westergaard, H.M. 1933. "Water pressure on dams during earthquakes", *Transactions of ASCE*, 98: 418–472.

Whitman, R.V. and Liao, S. 1985. Seismic design of gravity walls. *Paper GL-85-1*, U.S. Army Engineer Waterways.

Zarrabi-Kashani, K. 1979. *Sliding of gravity retaining wall during earthquakes considering vertical accelerations and changing inclination of failure surface*. MIT, Cambridge.

Soil-Foundation-Structure Interaction – Orense, Chouw & Pender (eds)
© 2010 Taylor & Francis Group, London, ISBN 978-0-415-60040-8

Backbone curves for passive lateral response of walls with homogeneous backfills

P. Khalili-Tehrani & E. Taciroglu
University of California, Los Angeles, CA, USA

A. Shamsabadi
California Department of Transportation, Sacramento, CA, USA

ABSTRACT: Recent advances in performance-based seismic assessment and design of bridges call for the development of computationally efficient high-fidelity models for nonlinear transient dynamic analyses. A significant component of such models is that of the nonlinear lateral force-deflection of bridge abutment-embankment systems. In this study, we perform extensive parametric studies using a previously validated limit-equilibrium model, and aim to obtain a simple closed-form relationship for lateral response of abutment backwalls with uniform backfill. The resulting hyperbolic force-deformation (HFD) backbone curve has explicit dependency on the physical properties of the abutment system, including the backwall height. All input parameters to the HFD equation are measurable via standard geotechnical laboratory tests; and we demonstrate that the HFD formulas are valid for a broad variety of backfill materials. As opposed to limit-equilibrium models that produce only discrete data points on the backbone curve, the HFD equation can easily be implemented in a structural analysis package as a nonlinear spring that accounts for the bridge abutment-backfill interaction.

1 INRODUCTION

The interaction between the abutment and the embankment plays an important role in the overall response of the bridge in the event of an earthquake. The passive earth pressure against the structure counters the lateral inertial forces due to earthquakes or thermal expansion of the bridge deck. Passive forces computed through the standard earth-pressure theories (e.g., Rankine, or Coulomb) vary broadly. So new attempts have been made in recent years to obtain more reliable methods for modeling the nonlinear lateral force-displacement behavior of bridge abutments. Among those, the Log-Spiral-Hyperbolic (LSH) model and the resulting Hyperbolic-Force-Displacement (HFD) is particularly attractive, because the lateral abutment response can be computed from first principles and physical parameters of the abutment system (see, for example, Shamsabadi et al., 2005, 2007, and 2009). Several small-scale and full-scale experiments have been performed on bridge abutments and pile caps to quantify the passive pressure and the development of the passive failure plane. The results of these experiments has been documented and reported by numerous researchers including Rollins & Cole (2006), Gadre & Dobry (1998), Gadre (1997), Romstad et al. (1995), Fang et al. (1994), and Lemnitzer et al. (2009). In turn, the LSH model has been validated against a number of these experiments by Shamsabadi et al. (2007, 2009).

Performance-based design approach calls for nonlinear analyses of the bridge system, which, in turn, requires a passive abutment backbone curve for a range of applicable deformations. Although the LSH model with suitably selected input parameters can provide an accurate lateral response, it cannot be used directly in a nonlinear pushover (or transient dynamic) analysis because it does not provide a closed-form backbone curve. Consequently, Shamsabadi et al. (2007) proposed the use of a simple Hyperbolic Force-Displacement relationship between the lateral load per unit width of the abutment backwall (F) and the lateral displacement (y), which is given by

$$F(y) = Cy/(1 + Dy) \quad (1)$$

C and D in this equation are related to the parameters that define the shape of the curve as follows

$$C = \left(2K_{50} - F_{ult}/y_{\max}\right), \quad D = \left(K_{50}/F_{ult} - 1/y_{\max}\right) \quad (2)$$

where F_{ult} is the maximum abutment force per unit length, which is developed at displacement $y_{\max}$. $K_{50} = F_{ult}/(2y_{50})$ is the average abutment stiffness, and y_{50} is the displacement at half of the maximum abutment force. The shape parameters are shown in Figure 1 schematically.

Both C and D values in the above equation depend on the backwall height. In order to account for backbone curve's height dependence explicitly, we had

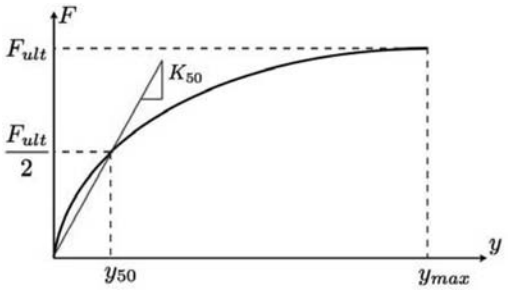

Figure 1. Hyperbolic force-displacement relationship (Shamsabadi et al., 2007).

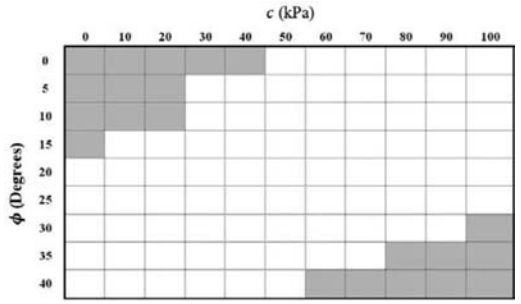

Figure 2. Matrix of possible combinations of friction angle and cohesion values used in parametric studies with grey cells showing unrealistic backfills.

suggested (see, Shamsabadi et al., 2009) the use of a *Enhanced* HFD equation (EHFD) given by

$$F(y) = \frac{a_r y}{\hat{H} + b_r y}\hat{H}^n, \quad \hat{H} = H / H_r \tag{3}$$

where F and y denote the lateral force per unit width of the backwall (kN/m) and the lateral deflection (cm), respectively. The parameters a_r and b_r are height-independent parameters that depend only on backfill properties. H is the backwall height (meter) and H_r in Equation 3 is a reference height equal to 1 meter. In Shamsabadi et al. (2009), we provided experimentally calibrated values of a_r and b_r for two specific types of backfills—namely purely cohesive and silty sand. In what follows, we generalize the HFD backbone curve, and provide closed-form equations for a_r and b_r that are parameterized with fundamental soil properties so that Equation 3 can be applied for *all* types of backfills. We then compare the results of these generalized equations with the LSH model for a broad variety of input parameters. Finally, we propose a set of equations amenable for routine bridge analysis and design tasks.

2 ENHANCED HYPERBOLIC FORCE-DISPLACEMENT (EHFD) EQUATIONS

If we substitute the values of C and D from Equation 2 into Equation 1 and compare that with Equation 3, with some algebraic manipulation, we can state a_r and b_r in the following form,

$$a_r = (\eta - 1)\alpha/\beta, \quad b_r = (\eta - 2)/\beta \tag{4}$$

where parameters α, β, and η are related to the HFD curve's shape parameters as follows

$$\alpha = F_{ult}/\hat{H}^n, \quad \beta = y_{\max}/\hat{H}, \quad \eta = y_{\max}/y_{50} \tag{5}$$

We investigated the "height-independence" of these parameters by back-calculating their values from the LSH model's results for different backfills and wall-heights. We found that the coefficients of variation with height for all three parameters were negligible. As such, it was possible for us to back-calculate the value of each individual parameter for a specific backfill, and subsequently develop approximation formulae for a general backfill. This effort is summarized in the following subsections.

2.1 *Parametric studies on α, β, η, and n*

First, we implemented the LSH model in Matlab; and employed this tool to relate the EHFD equation parameters to fundamental soil properties. The goal was to obtain a set of closed-form equations for EHFD parameters (α, β, η, and n) that can approximate the LSH backbone curve for a broad range of soil properties. We carried out a parametric study by varying the LSH input parameters that affect the results significantly, and by assuming suitable constant values for those that do not.

The parameters varied were chosen to be the backfill soil internal friction angle (ϕ), cohesion (c), the unit weight (γ), and the soil strain at 50% of the ultimate stress (ε_{50}), because these parameters are physical and can be measured in the laboratory. The ranges of these parameters envelop all possible backfill soils, and the increments chosen were reasonably small. To wit, the internal friction angle varied in the range 0 to 40 degrees with increments of 5 degrees; the cohesion ranged from 0 to 100 kPa with increments of 10 kPa; the unit weight varied from 14 to 24 kN/m^3 with increments of 2 kN/m^3, and finally, ε_{50} ranged from 0.0015 for very stiff backfills to 0.0075 for very loose backfills with increments of 0.001. Some combinations of the soil internal friction angle and cohesion are not either realistic, such as $\phi = 0$ and $c = 0$ kPa, or practical, such as $\phi = 10°$ and $c = 20$ kPa. Therefore, only reasonable combinations of these two parameters (shown in Figure 2) were used for the parametric study. All of the above mentioned values of γ and ε_{50} were considered whenever applicable.

The remaining LSH input parameters were either assumed to be constant, or were related to the varying parameters considered before. In particular, the LSH soil failure ratio was assumed to be constant throughout the analysis with the value of $R_f = 0.96$;

Backfill Poisson's ratio was set to the constant value of $\nu = 0.35$. With the exception of the component α in the definition of a_r, the remaining components do not depend on the soil unit weight, and thus, a constant value of $\gamma = 19\ \text{kN/m}^3$ was assumed in their parameterization. All components except β are independent of ε_{50}. Therefore, for those components, a constant value of $\varepsilon_{50} = 0.004$ was used when $\phi \geq 10°$, and $\varepsilon_{50} = 0.006$ otherwise. The interface friction angle (δ) between the backfill soil and the backwall was constrained to the internal friction angle via the relationship $\delta = 2/3\ \phi$. Similarly, the adhesion between the soil and the wall (c_a) was always assumed to be a constant fraction of the soil cohesion, defined as $c_a = 0.\ 0.65c$. Thus, for a general c-ϕ soil, the interfacial backfill-backwall interaction is controlled by a combination of adhesion and interface friction.

2.2 *Calibration of parameters*

We employed a nonlinear least-squares procedure to obtain closed-form formulas for expressing the different components of a_r and b_r in terms of the introduced independent variables namely the backfill ϕ, c, γ, and ε_{50}. The specific procedure that we employed for back-calculating the values of a_r and b_r is the so-called general *Robust Nonlinear Least-Squares Method* (RNLSM) (Matlab, 1997). The procedure starts with an initial estimate for the fitting coefficients, which are updated such that the fit improves through successive iterations. For the present study, we adopted the well-known *Trust Region* algorithm (see, for example, Moré & Sorensen, 1983, and Branch et al., 1999) to determine the direction and magnitude of the updating vector. *Trust Region* algorithm has been employed several times in the process of calibrating the components α, β, n, and η. The following subsections describe the procedure for each parameter, in detail.

2.2.1 The β-equation

The value of the backwall ultimate lateral deflection ($y_{\max}$) when normalized with the wall height ($\hat{H}$) is constant. Thus, the fitting parameter β is height-independent. Parametric studies with the LSH model for different values of the independent fitting parameters introduced previously reveals that $\beta = y_{\max}/\hat{H}$ is not a function of γ, and its variation with the backfill cohesion (c) is negligible. The values of β were calculated using the LSH model for different values of the rest of the fitting parameters (i.e., ε_{50} and ϕ). This calculation revealed that, for very stiff backfills, the ultimate failure surface is mobilized at smaller ultimate lateral deflection values, and as the stiffness decreases (i.e., for larger values of ε_{50}) the ultimate deflection increases significantly—meaning that the wall should slide more, in order to fail the backfill soil completely. Moreover, failure occurs at smaller deflections as the backfill material becomes more frictional.

In order to obtain a closed form equation for β, we had to define a surface that fits the values of β in terms of ε_{50} and ϕ. We employed Matlab's curve-fitting toolbox and ultimately, RNLSM yielded the following relationship for β

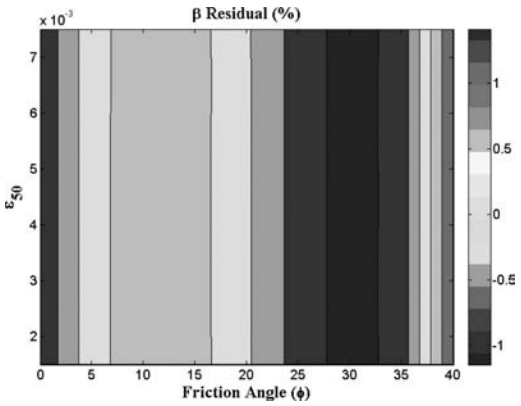

Figure 3. The β-residual contours, showing the discrepancy between LSH and Eq. 6 plotted for c = 50 kPa and $\gamma = 19\ \text{kN/m}^3$.

$$\beta = \left[1703 - 683.4(\tan\phi)^{1.23}\right]\varepsilon_{50}. \quad (6)$$

In order to assess the accuracy of Equation 6, the residual (percentage error) values can be computed for all combinations of the values of ε_{50} and ϕ. The said residual values, as well as all others presented throughout this paper, are based on the following equation

$$\text{Resid.} = 100 \times \left(\text{value}_{LSH} - \text{value}_{Approx}\right) / \text{value}_{LSH}. \quad (7)$$

The residual contours for β are shown in Figure 3, which indicates that the maximum relative error in approximating its value through Equation 6 is 1.5%.

2.2.2 *The α-equation*

The parameter α controls the capacity of the abutment load-deflection backbone curve. The LSH model indicates that the variation of $\alpha = F_{ult}/\hat{H}^n$ for different wall heights is negligible. On the other hand, the parameter α is dependent on the soil friction angle (ϕ), cohesion (c), and the unit weight (γ).

Results obtained from the LSH model for different values of γ reveals that α is linearly dependent on the soil unit weight. This is in agreement with the classical theories such as Rankine (1857), by which the passive capacity of the wall is stated as

$$F_{ult} = \frac{1}{2}\gamma K_p H^2 + 2c\sqrt{K_p}H. \quad (8)$$

We computed the value of α for the different values of c, ϕ presented in Figure 2, and for various values of γ. Using linear regression, we then fitted the linear relationship "α = slope $\times\ \gamma$ + intercept" to the γ-α pairs. By carrying successive curve and surface fittings

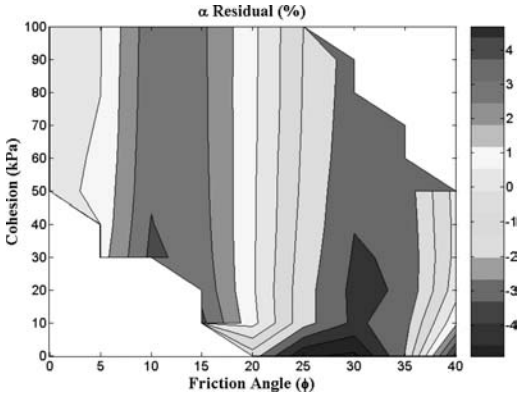

Figure 4. The α-residual contours, showing the discrepancy between LSH and Equations 9 and 10 for $\gamma = 19$ kN/m^3.

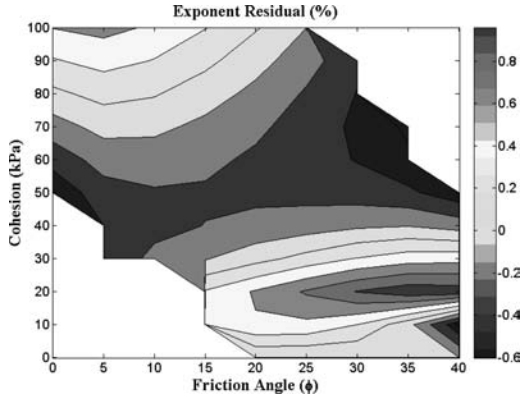

Figure 5. Residual contours for the height-exponent (n), showing the relative error between the LSH model and Equation 11 for $\gamma = 19$ kN/m^3.

via RNLSM, finally the following composite equation was obtained for α

$$\alpha = [5.62(\tan\phi)^2 + 0.53]\gamma + [10.58(\tan\phi)^{1.79} + 2.86]c \quad (9)$$

As it turns out, Equation 9 overestimates the capacity of the abutment backwall for purely cohesive backfills, and underestimates it for purely frictional (clean sand) backfills. Therefore we recommend increasing the α value calculated from Equation 9 by 6% for clean sands, and use

$$\alpha = 0.50\gamma + 2.63c \quad \text{when } \phi = 0 \qquad (10)$$

instead of Equation 9, for purely cohesive backfills.

The accuracy of these approximation formulae for parameter α can be assessed from Figure 4, which displays the %-difference between values computed from LSH model and the closed-form approximations for the mid-range value of $\gamma = 19$ kN/m^3. The quality of the results should not be affected if any other values of γ were chosen since the dependence of component α on the backfill unit weight γ is perfectly linear; and Equations 9 and 10 reflect this linearity. It is worth noting that, whereas a positive residual value indicates a conservative approximation, a negative residual means that the closed-form equations may over-predict the backfill capacity but the discrepancy is always less than 5% (Figure 4).

2.2.3 *The n-equation*

The height exponent (n) in Equation 3 is a function of c, ϕ, and γ as indicated by both the LSH model, and standard Rankine theory (cf., Eq. 8). Parametric studies with the LSH model reveals that the exponent is sensitive to the cohesion (c) the most, and varies only moderately with the internal friction angle and soil unit weight. We carried out parametric and calibration studies on the height exponent using all three of the said parameters, but the resulting closed-form equation turned out to be too complex. Thus, we opted to find an equation for the exponent by considering the cohesion and the internal friction angle only. Our logical basis for omitting the soil unit-weight rather than the friction angle was that the latter varies in a much wider range for different backfills encountered in construction practice, while the range of variation for γ is generally narrower than what we assumed in the parametric studies.

In order to derive the exponent equation, we fixed the unit weight to $\gamma = 19$ kN/m^3, and varied the values of c and ϕ according to Figure 2, with the exception of the limiting value of $c = 0$, for which we know that $n = 2$. For the rest of the backfill soils, the exponent range is $1 < n < 2$, noting that more cohesion in the backfill soil implies a smaller exponent value. We computed results from the LSH model for different heights ranging from 1 to 2.5 meters, and obtained the exponent value for the parameter matrix of different c-ϕ values, by finding the slope of the backwall lateral capacity versus height in the *log-log* plane.

By implementing the successive fitting processes and RNLSM, the details of which are omitted here for brevity, the following equations were obtained for approximating n:

$$n = \begin{cases} 2 & \text{if } c = 0, \\ \left(0.91(\tan\phi)^{1.2} + 1.49\right)/\sqrt{c} + 0.90 & \text{otherwise.} \end{cases} \qquad (11)$$

Again, the goodness-of-fit can be assessed through the error residual, the contour plot of which for $\gamma = 19$ kN/m^3 is shown in Figure 5, which indicates that the maximum relative error is less than 1%. Similar to the residual in α, positive residuals in the exponent approximation represent conservatism, whereas a negative residual means that Equation 11 yields a larger exponent than the LSH model.

2.2.4 *The η-equation*

The parameter η is dimensionless, and measures the quotient of the ultimate backwall deflection at failure (y_{max}) over deflection at 50% of the ultimate capacity of the wall (y_{50}). The LSH model results imply that η is independent of the backwall height, and the soil unit

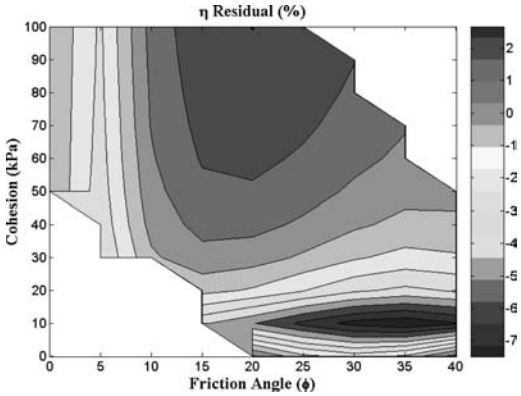

Figure 6. The η-residual contours, showing the discrepancy between LSH and Equation 12 for $\gamma = 19\,\text{kN/m}^3$.

weight does not affect its value. We back-calculated the value of this parameter for all input values of the c-ϕ matrix (cf., Figure 2) for soil unit weight of $\gamma = 19\,\text{kN/m}^3$. These results reveal that the variation of η with respect to the soil cohesion is not significant. Thus, this parameter can be expressed in terms of the internal friction angle alone. The final results of the fitting process is condensed in the following equations

$$\eta = \begin{cases} 15.47 & \text{for } \phi < 5^\circ \text{ and } c \neq 0, \\ 18.10 - 9.38\sqrt{\tan\phi} & \text{for } \phi \geq 5^\circ \text{ and } c \neq 0, \\ 14.36 - 7.49\sqrt{\tan\phi} & \text{for all } \phi, \text{ and } c = 0. \end{cases} \quad (12)$$

Again, we examined the accuracy of Equation 12 through the residual contours of η in the c-ϕ plane. The residual contours for $\gamma = 19\,\text{kN/m}^3$ are shown in Figure 6, which indicates that, the maximum relative error between LSH results and those obtained via Equation 12 is less than 4% for all backfills (with the exception of backfills with $c = 10\,\text{kPa}$, for no apparent reason). In case of $c = 10\,\text{kPa}$, the relative error reaches up to nearly 8%. Because the direct effect of parameter η on the final backbone curve is not trivially and directly expressible, we opted not to devise more complex approximation formulae, merely because of the aforementioned exception.

2.3 *A correction factor for the backbone curve*

The preceding tasks yield the formulae for all components (α, β, γ, and n) of Equations 3 and 4, so that the values of a_r and b_r can be computed for any backfill soil based on its readily measurable (physical) properties. Substitution of a_r and b_r in Equation 3 yields the closed-form abutment backbone equation that can be used in routine bridge superstructure analysis and design.

Throughout the fitting process of the components in Equation 4, we assumed that $\delta = 2/3\phi$. In order to broaden the use of Equation 3 for backfills where $\delta \neq 2/3\phi$—and it should be noted that the difference can become significant—we recommend to apply the following correction factor to the whole backbone equation,

$$f = 0.64\,\delta/\phi + 0.56\,. \quad (13)$$

We obtained the factor f by a similar back-calculation procedure described in previous sections; we omit the details here for brevity.

Table 1. Representative backwall systems for verification of calibrated parameters in Equation 3.

#	c (kPa)	ϕ (°)	γ (kN/m^3)	ε_{50} (10^{-3})	H (m)	F_{ult}^{LSH} (kN/m)	$y_{\max}^{LSH}$ (cm)
(1)	0	38	22.0	3	1.5	212	5.7
(2)	85	0	16.5	6.5	1.8	432	19.7
(3)	55	25	18.0	4.5	2.0	727	12.8
(4)	20	40	20.0	3.5	1.1	344	4.5

2.4 *Ultimate deflection of the abutment backwall*

The ultimate lateral deflection of the wall ($y_{\max}$) must also be known in order to completely define the lateral force-displacement backbone curve. It is recommended to use the values of $y_{\max}$ that are tabulated as a fraction of the backwall height for different types of backfill soils in open literature (see, for example, Cole & Rollins, 2006; and Shamsabadi et al., 2007). These $y_{\max}$ values are based on (full-scale and laboratory) experiments, as well as detailed numerical simulations. This method is preferable over using Equation 5 and the value of parameter β, as the value of β is highly sensitive to the choice of failure ratio (R_f) in the LSH model. The value of $R_f = 0.96$ was not varied in the calibration of β, because this is not a physical parameter that can be measured in the laboratory.

3 A VERIFICATION OF EHFD FORMULAS

In order to verify the closed-form equations we devised and calibrated earlier, we compare the resulting parametric EHFD backbone curves with those obtained from the LSH model. We consider four representative backwall systems, as shown in Table 1. These systems represent a broad range of backfill properties (cf., the matrix of c-ϕ values in Figure 2), along with wide ranges of values for γ, ε_{50} and wall height (1.1 to 2.0 m). The remaining LSH input parameters are assumed to be identical to those used in the back-calculation process.

The normalized backbone curves obtained from the LSH model, and from the combination of Equations 3 and 4 are plotted for all four backwall systems in Figure 7, which reveals that the parametric EHFD formulas are quite accurate in reproducing the LSH model's results, and that the overall RNLSM fitting process had been successful. Figure 7 also indicates that the height-dependency incorporated into

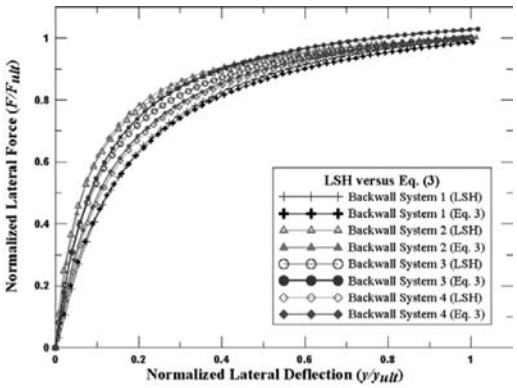

Figure 7. Lateral behavior of representative backwall systems introduced in Table 1 by LSH model and Equation 3.

Equation 3 (Shamsabadi et al., 2009) is quite accurate, because a constant $\hat{H}^n = 1$ m had been assumed during the subsequent parameterization and calibration of the EHFD components α, β, and η.

4 CONCLUSIONS AND RECOMMENDATIONS

In this study, we utilized the extensively validated LSH model (Shamsabadi et al., 2007, 2009) to devise and calibrate a closed-form Enhanced Hyperbolic Force-Displacement (EHFD) equation that is parameterized with physical properties of backwall-backfill system. Verification of these closed-form equations was performed through comparisons with the LSH model. We made use of a robust nonlinear leastsquares procedure for calibrating the various components of the proposed equation.

The EHFD model ideally makes use of a few physically measurable backfill soil input parameters—namely, the soil internal friction angle, cohesion, unit weight, and strain at 50% of the ultimate stress—in addition to the wall height. Additionally, we introduced a backbone curve *correction factor* to extend the application of the introduced equation, beyond the limiting assumptions made during the derivation process. In closing, we note here that the backbone equations introduced in this article are only applicable to walls with a uniform backfill.

The proposed model *can be validated* with data from full- and laboratory-scale tests. These include, for example, tests by Gadre & Dobry (1998) on dry dense sand, and by Rollins & Cole (2006) on clean and silty sands. This validation study is deferred to a subsequent publication.

ACKNOWLEDGEMENTS

The authors would like to thank Jonathan Stewart (UCLA) for providing his insights, and the discussions that led to this work. Funding was provided in part by Transportation Research Program of the Pacific Earthquake Engineering Research Center (PEER), and the California Department of Transportation (Caltrans Grant #59A0247). Their financial support is gratefully acknowledged. Any opinions, findings, conclusions, or recommendations expressed in this manuscript belong to the authors, and do not necessarily reflect those of PEER or Caltrans.

REFERENCES

Branch, M.A., Coleman, T.F. & Li, Y. 1999. A Subspace, interior, and conjugate gradient method for large-scale bound-constrained minimization problems. *J. Scientific Computing, SIAM* 21(1): 1–23.

Cole, R.T. & Rollins, K.M. 2006. Passive earth pressure mobilization during cyclic loading. *J. Geotech. & Geoenviron. Eng., ASCE* 132(9): 1154–1164.

Fang, Y.-S., Chen, T.-J. & Wu, B.-F. 1994. Passive earth pressures with various wall movements. *J. Geotech. Eng., ASCE* 120(8): 1307–1323.

Gadre, A.D. 1997. Lateral response of pile-cap foundation system and seat-type abutment in dry sand. *Ph.D. thesis*, Rensselaer Institute, Civil Engineering Dept., Troy, N.Y.

Gadre, A.D. & Dobry, R. 1998. Centrifuge modeling of cyclic lateral response of pile-cap systems and seat-type abutments in dry sand. *Rep. MCEER-98-0010*, Rensselaer Institute, Civil Engineering Dept., Troy, N.Y.

Lemnitzer, A., Ahlberg, E.R., Nigbor, R.L., Shamsabadi, A., Wallace, J.W. & Stewart, J.P. 2009. Lateral performance of full-scale bridge abutment wall with granular backfill. *J. Geotech. & Geoenviron. Eng., ASCE* 135(4): 506–514.

Matlab 1997. *The Users' Manual, Version 5.1: Curve Fitting and optimization* Toolboxes, Mathworks Inc.

Moré, J.J. & Sorensen, D.C. 1983. Computing a trust region step. *J. Scientific and Statistical Computing*, SIAM 3: 553–572.

Rankine, W. 1857. On the stability of loose earth. *Philosophical Transactions of the Royal Society of London*, Vol. 147.

Rollins, K.M. & Cole, R.T. 2006. Cyclic lateral load behavior of a pile cap and backfill. *J. Geotech. & Geoenviron. Eng., ASCE* 132(9): 1143–1153.

Romstad, K., Kutter, B., Maroney, B., Vanderbilt, E., Griggs, M. & Chai, Y.H. 1995. Experimental measurements of bridge abutment behavior. *Report No. UCD-STR-95-1*, Dept. of Civil and Environmental Eng., Univ. of California, Davis, Calif.

Shamsabadi, A., Ashour, M. & Norris, G. 2005. Bridge abutment nonlinear force-displacement-capacity prediction for seismic design. *J. Geotech. & Geoenviron. Eng.*, ASCE 131(2): 151–161.

Shamsabadi, A., Rollins, K.M. & Kapuskar, M. 2007. Nonlinear soil-abutment-bridge structure interaction for seismic performance-based design. *J. Geotech. & Geoenviron. Eng.*, ASCE, 133(6): 707–720.

Shamsabadi, A., Khalili-Tehrani, P., Stewart, J.P. & Taciroglu, E. 2010. Validated simulation models for lateral response of bridge abutments with typical backfills. *J. Bridge Eng., ASCE* (in press, doi:10.1061/(ASCE) BE.1943-5592.0000058).

Soil-Foundation-Structure Interaction – Orense, Chouw & Pender (eds)
© 2010 Taylor & Francis Group, London, ISBN 978-0-415-60040-8

Earthquake response of liquid storage tanks on layered sites

T. Larkin
Department of Civil and Environmental Engineering, University of Auckland

ABSTRACT: The earthquake response of a liquid storage tank on a layered site, incorporating soil-foundation-structure interaction, is evaluated by using a equivalent linear strain compatible solution. The dynamic impedance functions from Wolf and Deeks (2004) for layered media are used to formulate the combined solution in the frequency domain to the horizontal impulsive mode and the vertical (breathing) mode of tank response. The solution space is partitioned into a near field high strain domain and a far field linear elastic low strain domain. Nonlinearity is captured through the use of strain compatible dynamic impedance functions based on a representative strain in the near field foundation soil. Examples are given of the dynamic stiffnesses of a circular foundation to enable some insight into the tank foundation response. Conclusions are drawn on the degree of soil structure interaction involved. The focus of the work is on the tank foundation rather than the tank structure itself.

1 INTRODUCTION

This paper considers the seismic response of liquid storage tanks on relatively soft heterogeneous sites. This is the situation at many sites particularly in countries of relatively young complex geology such as New Zealand. Tanks are commonly placed in the vicinity of harbours, lakes and rivers for ease of access. The geology at sites in these areas is often composed of soft or medium stiff soils with strength and stiffness at the low end of the scale.

The work incorporates the effect of foundation compliance by performing analyses in the frequency domain. The soil-foundation-structure interaction effects are thus incorporated. In this method computation of soil structure interaction requires the use of dynamic impedance functions to quantify the stiffness and damping of the foundation supported by the underlying soils. These functions have been available for irregular foundation shapes for homogeneous sites for some time, largely through the work of Gazetas (1991). The situation for layered sites is more difficult and few closed form solutions exist. Wong and Luco (1985) have published tables of impedance functions for square foundations on layered media.

Relatively recent work by Wolf and Deeks (2004) has made available a means of computing dynamic impedance functions for circular foundations on layered sites. The work presented here uses these functions to compute the dynamic response of tanks on layered sites to strong ground motion. Wolf and Deeks (2004) use one dimensional wave dynamics, with refracted and reflected waves moving in conical zones of influence to calculate the impedance functions. Previous work, Larkin (2008), considered the impulsive earthquake response of liquid storage tanks on homogeneous sites. This work extends that of Larkin (2008) by considering layered sites and the flexible vertical (breathing) mode of tank response. The general concept behind the work is shown in Figure 1. A liquid storage tank is represented by a single degree of freedom oscillator, with a horizontal, rotational and vertical degree of freedom. A near field domain exists immediately beneath the tank foundation to a depth of one quarter of the foundation radius. Beyond that zone there exists a far field. The near field is a zone of high strain soil response with a shear modulus and material damping computed to be consistent with a representative shear strain in the zone. The far field is a zone

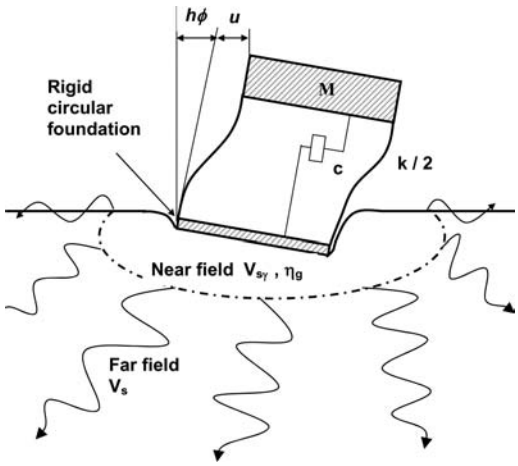

Figure 1. General concept of solution.

of linear response with a low strain shear modulus and zero material damping.

The seismic response of a liquid storage tank is a complex problem in soil-foundation-structure-liquid interaction. Early work by Haroun and Housner (1981) and Veletsos (1984) established that there are fundamentally two modes of horizontal response and one mode of vertical response of the tank system. The horizontal modes are the impulsive mode which entails a part of the liquid moving as if rigidly fixed to the tank structure and the convective (sloshing) mode which represents the motion of the near surface liquid within the tank. The vertical (breathing) mode entails the whole mass of the liquid moving as one mass within the tank. All three modes of reaction result in foundation loading and produce soil-foundation-structure interaction by way of horizontal shear, overturning moment and vertical loading.

The magnitude of the convective loading is generally significantly lower than the impulsive loading and is sometimes ignored in tank design other than for determining the height of the waves at the free surface in the tank. In the case of large diameter tanks the convective loading may need closer attention. This work focuses on the impulsive mode and the vertical mode of oscillation since these modes produce the bulk of the loading on the foundation.

These two modes may be represented as two structurally independent single mass systems. These systems are coupled through the foundation since the foundation loads result from the sum of the motion of the two modes and the properties of the foundation soil are calculated to be compatible with a representative strain in the foundation soil. The two modes are similar in frequency content. Typical fixed base periods are 0.05 to 0.25 seconds.

Research from Haroun and Housner (1981), Veletsos (1984) or Malhotra (2000) may be used to establish the dynamic properties of the oscillator representing each mode. Closed form solutions for the period and mass of the impulsive mode are available from Malhotra (2000), amongst others, and these are used to evaluate the stiffness of the single degree of freedom oscillator for this mode. The properties of the vertical mode are taken from the work of Veletsos (1984).

2 METHOD OF DYNAMIC ANALYSIS

Analysis is implemented in the frequency domain and is described in detail in Larkin (2008). A near field and far field are established in the solution domain. The near field (high strain domain) occupies a region immediately below the foundation to a depth of D/4, where D is the diameter of the foundation, and represents the region of the foundation soil undergoing high shear strain nonlinear response. The strain compatible dynamic properties in this region are considered to be the shear wave velocity, $V_{s\gamma}$, and the material damping η_g.

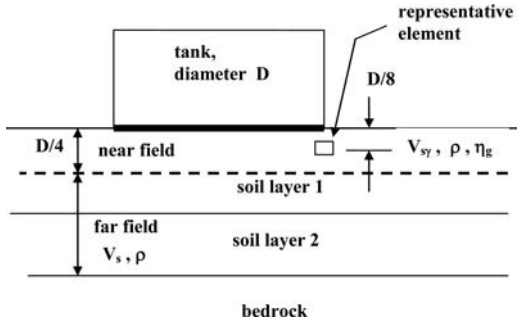

Figure 2. Representative element.

A representative soil element located below the edge of the foundation, at a depth of D/8, is used and the shear strain history of this element is computed. The representative strain is taken as one quarter of the maximum shear strain. This value is intended to reflect the variation of shear strain with position and time in the near field. Linear elastic theory is used to calculate the shear strain from horizontal shear, moment and vertical loading on the foundation. Equation 1 is used for this purpose. The first term is the result of horizontal force, the second term is the result of moment loading and the last term is the result of vertical loading.

$$\gamma_{rp} = \frac{P}{4}\left(\frac{2}{\pi}\right)^{0.5}\left(\frac{3}{4r^2 6V_{s\gamma}{}^2\rho}\right)\left(0.061+\left(\frac{0.18r}{8}\right)+0.3026\right) + \frac{M}{4}\left(\frac{2}{\pi}\right)^{0.5}\left(\frac{13.84r}{32r^2 6V_{s\gamma}{}^2\rho}\right)+\frac{V}{4}\left(\frac{2}{\pi}\right)^{0.5}\left(\frac{2.35r}{16r^2V_{s\gamma}^2\rho}\right) \quad (1)$$

where P is the horizontal load
M is the moment load
V is the vertical load
r is the radius of the tank
ρ is the mass density of the soil
$V_{s\gamma}$ is the strain compatible shear wave velocity in the near field region

The far field is that region beyond the near field and is considered to have a shear wave velocity equal to the maximum (low strain) wave velocity. Figure 3 shows the situation.

An outline is given below of the formulation of the solution for the impulsive mode. The detail of the method of analysis for horizontal motion only is given more fully in Larkin (2008). Using a complex shear modulus the stiffness of the foundation, in terms of horizontal displacement (S_h) and rotation (S_r) , sited at the surface of the soil profile is

$$S_x(a_0) = K_x[k_x(a_0)+c_x(a_0)ia_0] \quad (2)$$

$$S_r(a_0) = K_r[k_r(a_0)+c_r(a_0)ia_0] \quad (3)$$

where a_0 is the dimensionless frequency,

$$a_0 = \frac{\omega r}{V_{s\gamma}} \quad (4)$$

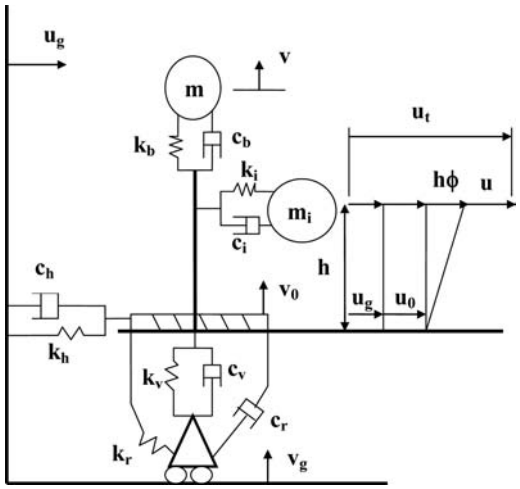

Figure 3. Impulsive and breathing modes.

k_h, k_r, c_h, c_r are the dynamic impedance factors that are a function of frequency and the foundation geometry.

K_h *and* K_r are the static stiffnesses in the horizontal and rotational direction respectively.

Wolf and Deeks (2004) present work to evaluate the dynamic stiffness coefficients k_h and k_r and the viscous damping coefficients c_h and c_r. They use a strength of materials approach employing wave propagation in cones to arrive at the dynamic impedance functions that employ k_h, k_r, c_h, c_r as functions of a_0 and the foundation geometry. These dynamic impedance functions represent the reaction of the complete soil profile on the foundation. The method is suitable for a layered profile with an elastic half space at the base. Figure 3 shows the mechanical analogue of the system with the two modes (impulsive and breathing) and the definitions of the displacement components.

The equations of equilibrium of the foundation are used to establish the response of each system to a harmonic wave of frequency ω and a set of the following equations result for the impulsive mode.

$$[A(\omega)]\langle b(\omega)\rangle = \langle c(\omega)\rangle \tag{5}$$

where

$$[A] = \begin{bmatrix} k(1+2\eta i) & -m\omega^2 & -m\omega^2 \\ -m\omega^2 & S_h - m\omega^2 & -m\omega^2 \\ -m\omega^2 & -m\omega^2 & \frac{1}{h^2}[S_r] - m\omega^2 \end{bmatrix} \tag{6}$$

$$\langle b\rangle = \begin{Bmatrix} u \\ u_0 \\ h\phi \end{Bmatrix} \tag{7}$$

$$\langle c\rangle = -m \begin{Bmatrix} \ddot{u}_g^f(\omega) \\ \ddot{u}_g^f(\omega) \\ \ddot{u}_g^f(\omega) \end{Bmatrix} \tag{8}$$

where $\ddot{u}_g^f(\omega) =$ frequency domain representation of the individual harmonics of the ground acceleration.

The dependent variables, u, u_0 and $h\phi$ are realized through the equation

$$\langle b\rangle = [A]^{-1}\langle c\rangle \tag{9}$$

Alternatively the transfer function associated with each of the 3 dependent variables may be found by replacing each the elements of the $\langle c\rangle$ vector with unity. A parallel companion set of equations exists for the vertical mode of response. The only differences are that the dynamic stiffnesses and damping coefficients are for vertical motion, there is no rotational motion, and the vertical earthquake motion is the forcing function.

3 EXAMPLES OF THE DYNAMIC STIFFNESS OF A FOUNDATION ON LAYERED MEDIA

Equations 2 and 3 are expressions of the stiffness of the foundation in horizontal displacement and rotation. These stiffnesses are complex and the magnitude (absolute value) of the horizontal stiffness, $\tilde{S}_r$, may be found from

$$\tilde{S}_r(a_0) = K_r\sqrt{k_r{}^2(a_0) + a_0{}^2 c_r{}^2(a_0)} \tag{10}$$

There is a companion equation for the horizontal mode and the vertical mode. The shape of the stiffness magnitude in the frequency domain gives some insight into the response of the foundation to harmonic waves and hence earthquake loading. As a simple example consider a 10 m diameter foundation resting on a 5 m layer of soil with a shear wave velocity of 120 m/sec and damping of 15% of critical. Beneath the soil is weathered rock with a shear wave velocity of 900 m/sec. Figures 4 to 6 show the magnitude of the stiffnesses as a function of frequency. Also for comparison is shown the case of the same foundation seated on a 5 m layer of soil with a wave velocity of 300 m/sec and 2% material damping.

In the case of the horizontal stiffness the softer material shows an impedance function that is sensitive to frequency, the a maximum stiffness is double that of the static value and the minimum is one half of the static value. In the case of the stiffer material for frequencies up to about 10 Hz the stiffness is not a strong function of frequency. In the cases of rotation and vertical motion the stiffnesses are a strong function of frequency for the weaker material.

Figures 4, 5 and 6 show collectively that the variation in stiffness with frequency is considerably more pronounced in the case of the softer material. This is due to the dynamic stiffness factors and viscous damping coefficients being strong functions of frequency. For the stiffer material a larger part of the stiffness is due to the dynamic stiffnesses k_r, k_h and k_v rather than the frequency dependent viscous damping coefficients.

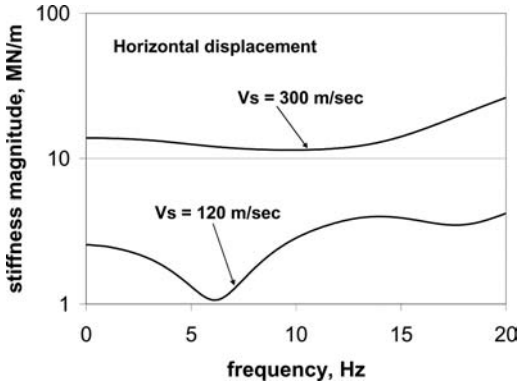

Figure 4. Stiffness magnitude for horizontal displacement.

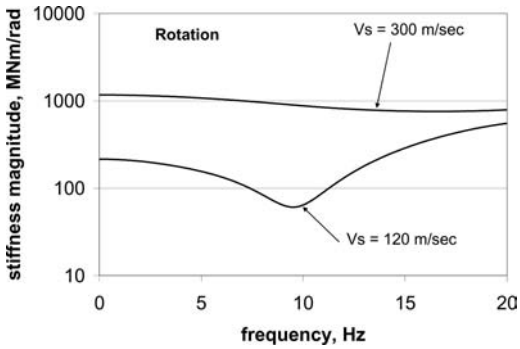

Figure 5. Stiffness magnitude for rotational displacement.

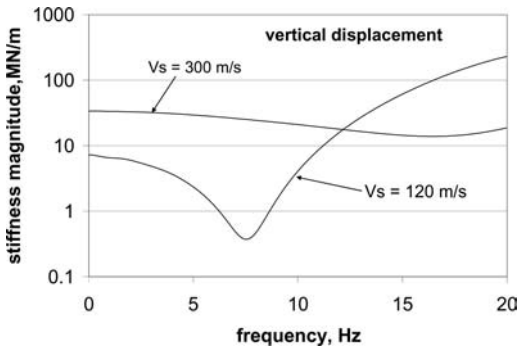

Figure 6. Stiffness magnitude for vertical displacement.

Consider the case of the same foundation sited on a more complex soil profile, that shown in Figure 7. The whole profile down to and including the rock is involved in the interaction of the soil and foundation, although the influence of the soil and rock diminishes rapidly with depth below, and lateral offset from, the footing. The uppermost layer is sand with a wave velocity of 120 m/sec. Since soil is a highly nonlinear material (and thus the wave velocity is a function of shear strain) this value of wave velocity needs to be compatible with the shear strain in the sand that results from interaction.

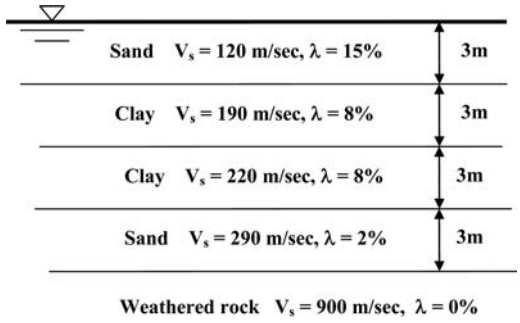

Figure 7. Soil profile, λ is the percentage of critical viscous damping.

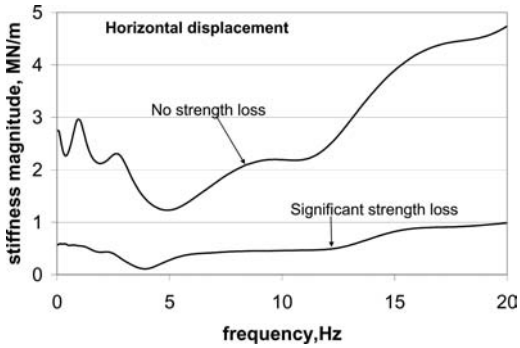

Figure 8. Stiffness magnitude.

The upper layer of soil is saturated sand and has the potential for loss of strength due to the generation of excess pore water pressure from seismic motion. Ignoring this possibility for the moment then the upper curve in Figure 8 shows the horizontal stiffness magnitude for the foundation on this profile. Note the stiffness is a more complex function of frequency than previously was the case and the static stiffness is not a good approximation to the stiffness of the foundation over the earthquake range of frequencies.

The more complex shape of the stiffness function is a result of wave scattering in the media surrounding the footing. The layer interfaces create wave reflections and refractions that partition the energy of the stress waves and destructive and constructive wave patterns emerge that are a function of frequency.

The generation of excess pore water pressure during earthquake response will lower the state of effective stress in the sand. This will lead to strength and stiffness reduction in the sand and a reduction in the dynamic stiffness of the foundation. For example should the wave velocity reduce to 65 m/s and the damping increase to 22% then the dynamic stiffness takes the form shown on Figure 8. The reduction in dynamic stiffness magnitude of the foundation results in the foundation becoming semi-isolated from the soil media beneath the sand.

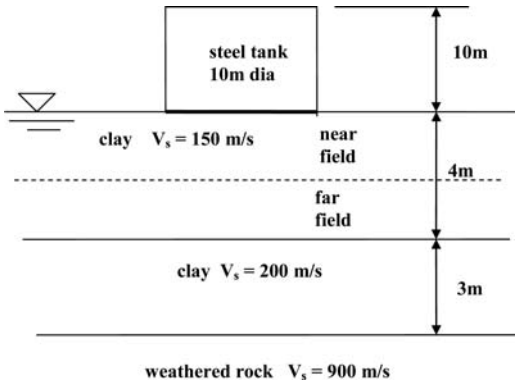

Figure 9. Soil profile for response analysis.

Table 1. Response quantities.

Representative strain	7.8×10^{-4}
Near field V_s	125 m/s^2
Near field damping	10%
Fixed base period, impulsive	0.10 s
Fixed base period, vertical	0.104 s
Maximum accn. impulsive	7.44 m/s^2
Maximum accn. vertical	8.7 m/s^2
Maximum base shear	4.3×10^3 kN
Maximum vertical force	6.8×10^3 kN
Flexible base period, impulsive	0.19 s
Flexible base period, vertical	0.15 s

4 EARTHQUAKE RESPONSE OF A TANK

The seismic response of a 10 m diameter steel tank on a layered profile is considered. The tank is 10 m in height, giving an aspect ratio of 1, and sits on the soil profile shown in Figure 9.

The tank was subjected to the North component and the vertical component of the Takarazuka motion from the 1995 Kobe earthquake. These records have a maximum acceleration for the horizontal component of 6 m/s^2 and 4.24 m/s^2 for the vertical component. The magnitudes of the accelerations reflect the close proximity (0.3 km) of the strong motion station to the fault. Table 1 gives details of the parameters of the analysis once strain compatibility was reached using the data on the dynamic properties of cohesive soils published by Sun et al (1988).

The computed loadings on the foundation are shown in Figures 10, 11 and 12. The loadings are substantial, in particular the vertical loading is approximately 85% of the static gravitational loading. Dynamic loading of this magnitude sometimes results in the "elephant foot" failures of tanks producing the characteristic rippling of the tank wall adjacent to the foundation. The horizontal loading produces a maximum shear stress on the foundation of 54 kPa.

The period elongation was substantial for both the breathing mode and impulsive mode, being approximately 90% for the impulsive mode and 50% for the

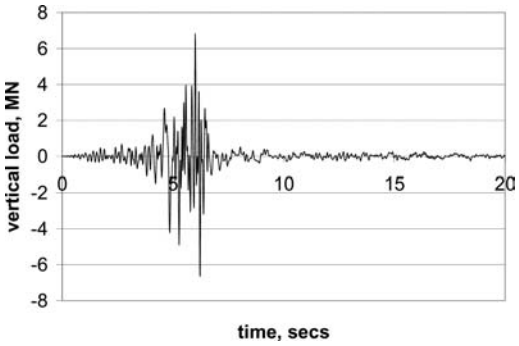

Figure 10. Vertical load on foundation.

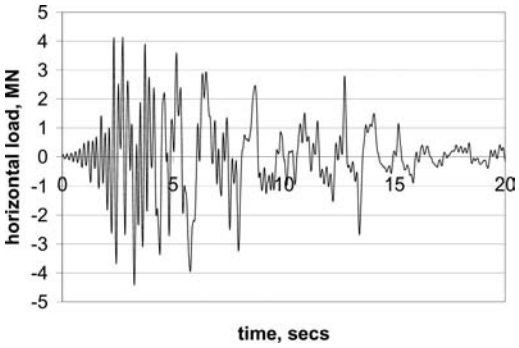

Figure 11. Horizontal shear loading on the foundation.

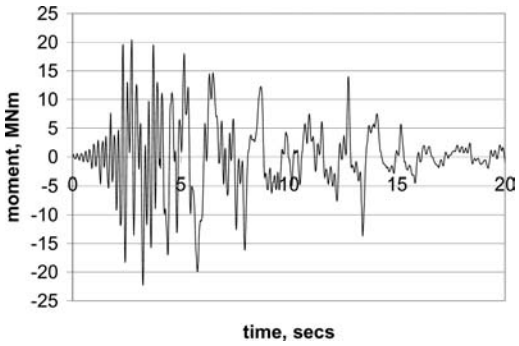

Figure 12. Moment loading on foundation.

vertical mode. The period elongation was assessed from the transfer functions, an example of which is shown in Figure 13 for the structural distortion (the u displacement component). The major peak in the transfer function is seen to be at a period of 0.19 seconds. Similar transfer functions are applicable to the other displacement components. Figure 14 shows the shear strain history of the representative element. The maximum shear strain is substantial being 0.3%.

The response spectra of the forcing motions are shown in Figure 15. There is proportionally more high frequency motion in the vertical component as might be expected. In the high frequency section of the horizontal motion it is seen that the acceleration increases

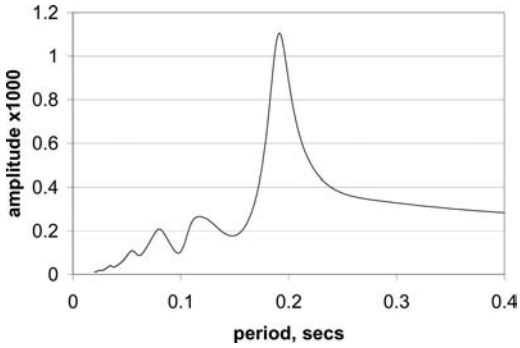

Figure 13. Amplitude transfer function for displacement *u*.

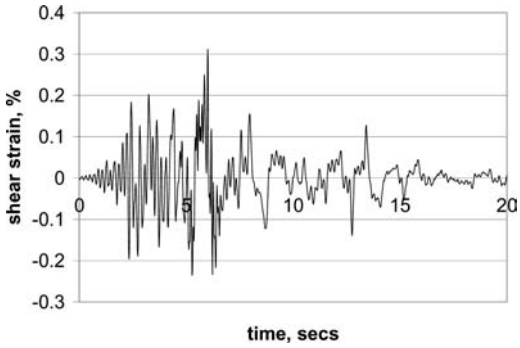

Figure 14. Shear strain of representative element.

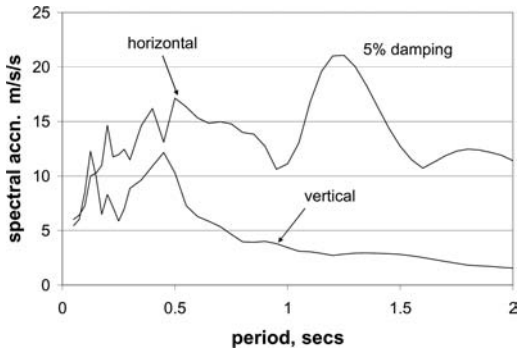

Figure 15. Response spectra of earthquake motion.

up to a period of approximately 0.4 seconds while for the vertical motion the acceleration increases up to a period of approximately 0.13 seconds.

Using these response spectra, and thus ignoring interaction of the foundation with the supporting soil, results in a maximum horizontal load on the foundation of 4.37 MN and a maximum vertical load of 6.68 MN. Comparing these loads with those found from Table 1 that incorporate compliance there is seen to be no real difference. The reason for this is that the fixed base periods are very short and lie on the ascending part of the response spectrum, thus period elongation leads to an increase in acceleration. This is offset by the radiation and material damping leading to energy loss and the net effect being no increase in loading from interaction.

This illustrates that each situation is unique and period lengthening may lead to load increase, decrease or no change in comparison to the fixed base case.

5 CONCLUSIONS

The method of Wolf and Deeks (2004) has been implemented to calculate the dynamic impedance functions of layered sites. The results show increasing frequency dependence and complexity with site layering. A dynamic model, incorporating soil-foundation-structure interaction, has been presented of the impulsive and vertical seismic response of liquid storage tanks. The intent of the work is to capture the main features of soil-foundation-structure interaction in a manner that allows ready incorporation in design. These main features are period elongation from foundation compliance and energy dissipation from hysteretic soil response and radiation damping. The work has focused on calculating the foundation shear and moment under conditions of foundation compliance to allow improved estimations of the footing loads. The structural loads on the tank could be assessed in a similar manner.

The method is built around a postulated near field and far field domain and utilizes a representative soil element as a means of assessing the level of strain in the near field. The method could be described as equivalent linear and is iterative since the properties of the near field need to be strain compatible. This is a point of weakness in the method since the strain is assessed on the basis of closed form linear elastic response of a foundation under moment and shear loading.

An example of the seismic response of a tank to an earthquake from the 1995 Kobe event is presented. This example illustrates that for very short period structures such as liquid storage tanks there is a balance between the effects of period lengthening and energy absorption. The energy absorption will decrease the magnitude of the tank foundation response. The period lengthening will in many cases have the reverse effect since tanks, being very short period structures, have a period that lies on the ascending arm of the response spectrum of the earthquake motion. Period lengthening will thus produce higher response. In the example presented both these effects were of approximately equal amplitude but opposite in sign. The net effect of compliance on the loads on the foundation was minimal. For specific design a number of earthquake records would need to be considered. Incorporation of the vertical component introduces additional complexity since the magnitude and frequency content of the vertical component is usually significantly different from the horizontal component. Most structural codes ignore the vertical component when discussing

interaction. However in the case of tanks this is not a satisfactory assumption since the breathing mode of tank response can be very significant.

REFERENCES

Gazetas, G. (1991). Foundation vibrations, *Chapter 15 of Foundation Engineering Handbook*, 2nd edition,Van Nostrand Reinhold, New York.

Haroun, M.A. & Housner, G.W. Dynamic interaction of liquid storage tanks and foundation soil, *Proc. 2nd ASCE Eng. Mech. Spec. Conf. on the Dynamic response of Structures*, Atlanta, pp. 346–360.

Larkin, T.J. (2008). Seismic response of liquid storage tanks incorporating soil structure interaction. Proc. ASCE, *Journal of Geotechnical and Geoenvironmental Engineering*, 134(12): 1804–1814.

Malhotra, L. (2000). Practical nonlinear seismic analysis of tanks,*Earthquake spectra*, 16(2): 473–492.

Sun, J.I., Golesorkhi, R. & Seed, H.B. (1988). Dynamic moduli and damping ratios for cohesive soil, *Report No. UCB/EERC-88/15*, College of Engineering, University of California, Berkeley.

Veletsos,A.S. & Tang, Y. (1984). Soil-structure interaction effects for laterally excited liquid storage tanks, *Earthquake Engineering and Structural Dynamics*, 19, 473–496.

Wolf, J.P. & Deeks, A.J. (2004). *Foundation Vibration Analysis: A Strength of materials Approach*, Elsevier, Oxford.

Wong, H.L. and Luco, J.E. (1985). Tables of Impedance functions for square foundations on layered media, *Soil Dynamics and Earthquake Engineering*, 4: 64–81.

Soil-Foundation-Structure Interaction – Orense, Chouw & Pender (eds)
© 2010 Taylor & Francis Group, London, ISBN 978-0-415-60040-8

Settlement analysis of wind turbines

G. Buscarnera, R. Nova & M. Vecchiotti
Politecnico di Milano, Milan, Italy

C. Tamagnini & D. Salciarini
University of Perugia, Perugia, Italy

ABSTRACT: In this paper, the soil-foundation-structure interaction processes due to wind loading of a wind turbine founded on a circular raft are modelled by means of the FE method. The cyclic/dynamic response of the soil-foundation system is assumed to be fully described by a set of uncoupled viscous dampers and a nonlinear, inelastic macroelement which links the external loads and moment acting on the foundation with its displacements and rotation. The constitutive equations of the macroelement is formulated within the framework of the theory of strain hardening elastoplasticity. To account for cyclic loading effects, it is assumed that irreversible displacement increments may occur even for loading paths contained within a conveniently defined state boundary surface. The corresponding flow rule and hardening law can be formulated by means of a suitable mapping rule, establishing a correspondence between the current loading state and a uniquely defined image state on the state boundary surface. By means of the macroelement approach, it is possible to couple in a simple and efficient way the dynamic behaviour of the structure to the foundation movements. Settlement and rotation of the structure can then be predicted for any convenient number of cycles.

1 INTRODUCTION

The analysis of the behaviour of structures subject to cyclic or transient loading requires the modelling of the interaction between the foundation and the soil underneath. This can be done in various ways. For instance, the soil volume which undergoes significant deformations under the applied loads can be described as an inelastic continuum and the resulting continuum model can be analyzed by means of the finite element method. Due to the strong nonlinearity of soil behaviour, the use of such an approach in connection with any realistic inelastic soil model would be extremely time-consuming.

A possible alternative approach consists of lumping the soil-foundation system compliance into a finite (small) number of discrete deformable elements – typically elastic springs and viscous dashpots – which act on the superstructure as uncoupled deformable constraints placed at the foundation level. The springs are typically used to reproduce the soil stiffness under applied loads and moments, while the viscous dashpots are responsible for modelling the damping effects (geometrical dissipation and mechanical damping) which occurs in the subsoil.

This latter method is clearly much more cost-effective, but has several important limitations. The assumed linear behaviour of the springs implies fully reversible response under closed cyclic loading paths. Moreover, the uncoupled character of the equations describing the load-displacement response of the deformable constraints makes it impossible to reproduce a number of important features of the observed response of shallow foundations. In particular, no vertical displacement is predicted under the cyclic action of a rocking moment and a horizontal force, in sharp contrast with the available experimental observations, see e.g., di Prisco et al. (2002).

The goal of this paper is to show that it is possible to overcome this difficulty by adopting a third, different approach which, while retaining the simplicity and efficiency of the deformable constraints, can effectively reproduce the nonlinear, irreversible and hysteretic response of shallow foundations subject to non-proportional, cyclic/dynamic loading conditions. In this case, a set of suitable inelastic constitutive equations – a so-called "macroelement" as originally defined by Nova & Montrasio (1991) – linking the load increments applied to the foundation to the corresponding work-conjugated displacement increments, are derived within the framework of the theory of strain-hardening elastoplasticity. The macroelement which reproduces the soil/foundation system at the global level can then be easily coupled to any FE structural model to analyze quite complex soil-structure interaction (SSI) problems.

It is worth noting that other approaches can be used to define the inelastic constitutive equations of the macroelement. For example, Salciarini & Tamagnini (2009) have developed an inelastic macroelement within the framework of the theory of hypoplasticity, which is characterized by a very small (pseudo)elastic

domain and a continuous dependence of the tangent stiffness from the loading direction (incremental non-linearity).

In order to demonstrate the effectiveness of the macroelement approach in the analysis of complex SSI problems, the elastoplastic macroelement developed by Nova & Montrasio (1991) has been used to simulate the cyclic/dynamic response of a wind turbine founded on a circular raft foundation, subject to time-dependent wind forces. This particular type of structure – characterized by relatively low vertical loads, and high horizontal loads and moments – represents an interesting benchmark to investigate the influence of possible coupling effects between the different degrees of freedom of the system.

The outline of the paper is as follows. In Sect. 2, the details of the macroelement developed by Nova & Montrasio (1991) are given. The modification of the basic isotropic-hardening model to account for cyclic/dynamic loading effects is discussed in Sect. 3. The characteristics of the wind turbine considered in this study and the results of preliminary quasi-static, monotonic simulations are presented in Sect. 4, while the results of a series of dynamic simulations are discussed in Sect. 5. Finally, Sect. 6 summarizes the main conclusions.

2 THE ELASTOPLASTIC MACROELEMENT MODEL OF NOVA & MONTRASIO

2.1 *Constitutive equations*

In the macroelement model developed by Nova & Montrasio (1991), the mechanical response of a circular foundation of diameter D resting on a homogeneous soil layer is described globally by means of the following constitutive equation in rate-form:

$$d\boldsymbol{Q} = \boldsymbol{K}(\boldsymbol{Q}, V_c, \boldsymbol{\eta})\, d\boldsymbol{q} \qquad \boldsymbol{\eta} := \frac{d\boldsymbol{q}}{\|d\boldsymbol{q}\|} \tag{1}$$

relating the increment of the generalized load vector:

$$\boldsymbol{Q} = \{V,\ H,\ M/D\}^T \tag{2}$$

and the increment of the generalized displacement vector:

$$\boldsymbol{q} = \{u,\ v,\ \theta D\}^T \tag{3}$$

In the above equations, V, H and M are the vertical load, the horizontal load and the rocking moment, respectively, while u, v and θ are the vertical displacement, the horizontal displacement and the rotation of the foundation (see Fig. 1).

The (3×3) matrix $\boldsymbol{K}$ in eq. (1) is the generalized tangent stiffness matrix of the foundation-soil system. In order to reproduce the non-linear and irreversible response of the foundation, $\boldsymbol{K}$ is assumed to depend on the current generalised load $\boldsymbol{Q}$, on the loading direction

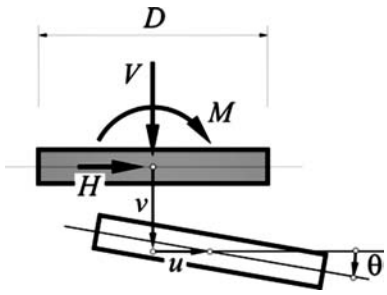

Figure 1. Components of generalized load and displacement.

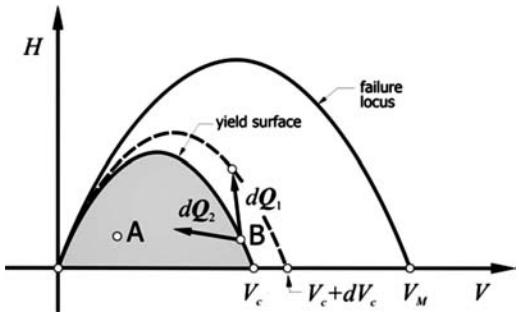

Figure 2. Representation of the elastic domain, of the yield surface and of the bounding surface in the H:V space.

(in displacement space) $\boldsymbol{\eta}$, and on the previous loading history of the system, globally accounted for by a set of suitable internal variables. In the simplest case considered by Nova & Montrasio (1991), the internal variables reduce to a single scalar quantity V_c, which controls the size of the elastic domain, i.e., the convex locus in load space within which the response of the macroelement is assumed to be linear elastic.

Within the framework of the theory of plasticity, the elastic domain is defined as follows:

$$\mathbb{E} = \{\boldsymbol{Q} \in \mathbb{R}^3 \mid f(\boldsymbol{Q}, V_c) \le 0\} \tag{4}$$

where f is the yield function and the curve $f = 0$ is the yield surface (see Fig. 2). In the Nova & Montrasio (1991) model, the yield surface is given by the following expression:

$$f = \left(\frac{M}{\psi D}\right)^2 + \left(\frac{H}{\mu}\right)^2 - V^2\left(1 - \frac{V}{V_c}\right)^{2\beta} = 0 \tag{5}$$

where ψ, μ and β are model constants.

If a certain load state such as point A in Fig. 2 lies within the elastic domain, any (infinitesimal) loading path will produce recoverable displacements. The same will occur if the current state lies on the yield surface (point B in Fig. 2) and the load increment points towards the interior of the elastic domain (load increment $d\boldsymbol{Q}_2$ in Fig. 2).

On the contrary, when the load increment points outwards, as for $d\boldsymbol{Q}_1$ in Fig. 2, the loading process is

plastic and the generalised displacement increment is partly irreversible.

Given the plastic potential function:

$$g = \left(\frac{M}{\psi_g D}\right)^2 + \left(\frac{H}{\mu_g}\right)^2 - V^2\left(1-\frac{V}{V_g}\right)^{2\beta} = 0 \tag{6}$$

the plastic displacement increment is given by the flow rule:

$$d\boldsymbol{q}^p = \Lambda \frac{\partial g}{\partial \boldsymbol{Q}} \tag{7}$$

where $\Lambda \geq 0$ is the plastic multiplier. In eq. (6):

$$\psi_g = \frac{\psi}{\lambda_M}; \qquad \mu_g = \frac{\mu}{\lambda_H};$$

λ_M and λ_H are material constants, and V_g is a dummy variable. When $\lambda_M = \lambda_H = 1$ the plastic flow is associative.

In the Nova & Montrasio (1991) model, the evolution equation for the internal variable is provided by the following hardening law:

$$\begin{aligned} dV_c &= \left(1-\frac{V_c}{V_M}\right)\frac{R_0}{V_M}\left(dv^p + \alpha\left|du^p\right| + \gamma D\left|d\theta^p\right|\right) \\ &= \Lambda h_c(\boldsymbol{Q}, V_c) \end{aligned} \tag{8}$$

where α, γ, R_0 and V_M are model constants, and:

$$h_c = \left(1-\frac{V_c}{V_M}\right)\frac{R_0}{V_M}\left(\frac{\partial g}{\partial V} + \alpha\left|\frac{\partial g}{\partial H}\right| + \gamma D\left|\frac{\partial g}{\partial (M/D)}\right|\right)$$

is the hardening function for V_c.

From eq. (8) it is clear that V_M represents the maximum size of the yield surface, i.e., the size of the failure locus (Fig. 2).

From the consistency condition, $df = 0$, the following expression is obtained for the plastic multiplier:

$$\Lambda = \frac{1}{K_p}\left(\frac{\partial f}{\partial \boldsymbol{Q}}\right)^T \boldsymbol{K}^e d\boldsymbol{q} \geq 0 \tag{9}$$

in which:

$$K_p = \left(\frac{\partial f}{\partial \boldsymbol{Q}}\right)^T \mathbf{C}^e\left(\frac{\partial g}{\partial \boldsymbol{Q}}\right) - \frac{\partial f}{\partial V_c}h_c > 0; \tag{10}$$

is a strictly positive scalar quantity and $(-\partial f/\partial V_c)h_c$ is the so-called plastic modulus. Substituting the expression (9) in the flow rule and taking into account the elastic constitutive equation, the following expressions are obtained for the elastoplastic tangent stiffness matrix of eq. (1):

$$\begin{aligned} &\boldsymbol{K} = \boldsymbol{K}^e - \frac{1}{K_p}\boldsymbol{K}^e\left(\frac{\partial g}{\partial \boldsymbol{Q}}\right)\left(\frac{\partial f}{\partial \boldsymbol{Q}}\right)^T \boldsymbol{K}^e \quad (\text{if } \Lambda > 0) \\ &\boldsymbol{K} = \boldsymbol{K}^e \qquad\qquad\qquad\qquad\qquad\qquad (\text{otherwise}) \end{aligned} \tag{11}$$

where $\boldsymbol{K}^e$ is the elastic stiffness matrix.

2.2 *Calibration of model constants*

The model is fully characterized by the elastic stiffness matrix $\boldsymbol{K}^e$ and 9 material constants controlling the shape of the yield locus, of the plastic potential, and the amount of hardening. It is shown in Montrasio and Nova (1997) that many of them vary in a relatively narrow range and their actual values play only a secondary role on the overall response of the foundation. In fact, only the variables R_0, V_M, μ, ψ are relevant in this respect. Furthermore these constants can be easily related to traditional soil constants, such as the elastic modulus of the soil or the friction angle at the soil-foundation interface.

For instance, consider a rigid circular foundation resting on a deep, uniform sand layer modeled as a linear elastic material. The settlement increment Δs induced by a centered vertical load increment ΔV can be derived from the theory of elasticity as follows:

$$\Delta s = \frac{2(1-\nu)}{GD}\Delta V \equiv \frac{\Delta V}{R_0} \tag{12}$$

The parameter R_0 can be easily determined from eq. (12), given the elastic properties of the soil and the foundation geometry.

The value of V_M – representing the bearing capacity of the foundation under a perfectly centered vertical load – can be determined from the classic bearing capacity formulas. If the soil is cohesionless and the depth of the foundation is small with respect to its diameter the contribution of the cohesion and the lateral surcharge vanish, and:

$$V_M = \frac{\pi D^2}{4}\left(\frac{1}{2}\gamma D N_\gamma s_\gamma\right) \tag{13}$$

where, according to Poulos et al. (2001), the bearing capacity factor N_γ is given by:

$$N_\gamma = 0.0663\exp(9.3\phi) \tag{14}$$

and the shape factor s_γ can be assumed equal to:

$$s_\gamma = 1 + 0.1K_p \qquad K_p = \frac{1+\sin\phi}{1-\sin\phi} \tag{15}$$

The constant μ is identified with the tangent of the friction angle $\hat{\phi}$ at the foundation-soil interface. Typically, $\hat{\phi} = \phi_{cv} = 3\phi/4$.

According to Montrasio & Nova (1997), the constant ψ can be deduced from the following empirical relation:

$$\psi = 0.35 + 0.3\frac{d}{D} \tag{16}$$

where d is the depth of the foundation base.

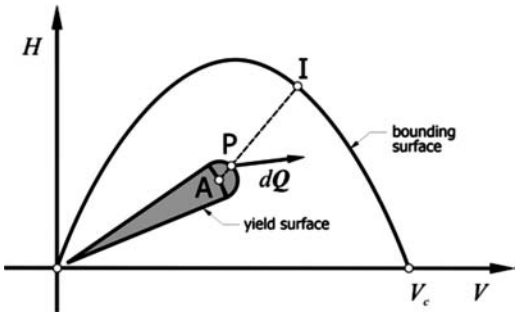

Figure 3. Bounding surface and cone-shaped elastic domain. Point I is the image point of the current loading state P.

3 MODIFICATION FOR CYCLIC LOADING CONDITIONS

Macroelement models developed within the framework of strain-hardening elastoplasticity exhibit important limitations when the cyclic/dynamic response of shallow foundations is of concern. In fact, in isotropic hardening macroelement models, the irreversible displacements accumulated during the first loading cycle determine an expansion of the elastic domain, so that the subsequent loading cycles are fully contained within the elastic domain. As a result, the foundation response is fully reversible, and the model is unable to capture such relevant phenomena as hysteresis or ratcheting.

Various strategies can be pursued to improve the model performance for cyclic loading conditions. Here, the so-called Bounding Surface (BS) approach is adopted (di Prisco et al. 2002), following the strategy proposed by Dafalias & Herrmann (1982) for continuum plasticity.

In this approach, plastic deformations can occur even for loading states within the BS. The plastic modulus controlling the magnitude of the plastic displacement rates is assumed to be a function of the distance of the current state from the BS, determined by suitably defining an image point on the BS by means of a non-invertible mapping rule. A small elastic region is maintained in the vicinity of the current load state, similar to the concept of elastic 'bubble' introduced by Al Tabbaa and Wood (1989).

In particular, it is postulated that the elastic domain is delimited by a small cone closed at the end by a spherical cap, as shown in Fig. 3. The cone is entirely contained within the BS, whose size V_c is determined by the plastic deformations accumulated during the monotonic loading stage.

In fact, the BS coincides with the yield locus of the standard Nova & Montrasio (1991) model, so that when the current state is on the BS (e.g., during virgin monotonic loading) the response of the two models are identical.

The elastic cone is defined by the position of the centre of the spherical 'cap' (point A in Fig. 3) and by its radius, which is set to a small fixed quantity. The angle at the cone apex, at the origin of the load space, is determined by enforcing a C_1 continuity condition at the transition between the cone and the spherical cap.

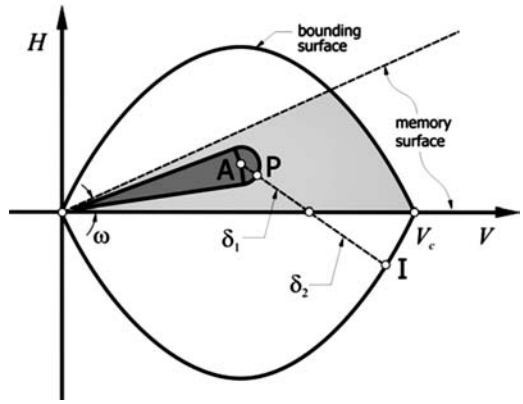

Figure 4. Definition of memory surface and of the distances δ_1 and δ_2.

Assume now that a point P on the yield surface represents the current loading state and that the stress increment $d\boldsymbol{Q}$ is such that plastic loading occurs. Then, the plastic deformation increment is determined by the following modified flow rule:

$$d\boldsymbol{q}^p = \bar{\Lambda}\,\boldsymbol{\Phi}\frac{\partial g}{\partial \bar{\boldsymbol{Q}}} \qquad \boldsymbol{\Phi} = \mathrm{diag}\left\{\Phi_V, \Phi_H, \Phi_M\right\} \tag{17}$$

In Eq. (17), the plastic multiplier $\bar{\Lambda}$ as well as the gradient to the plastic potential $\partial g/\partial \bar{\boldsymbol{Q}}$ are calculated at the image point I, enforcing the consistency condition at $\boldsymbol{Q} = \bar{\boldsymbol{Q}}$ on the bounding surface. As shown in Fig. 4, the image point I is determined by the intersection of the bounding surface with the straight line AP. The matrix $\boldsymbol{\Phi}$ is a diagonal matrix which operates on the plastic flow vector as a weighting function: the smaller the components of $\boldsymbol{\Phi}$, the smaller the magnitude of plastic displacement increment. In particular, each component of $\boldsymbol{\Phi}$ is evaluated as:

$$\Phi_\alpha = \exp\left\{-\zeta_\alpha\sqrt{\frac{\delta V_c}{V V_M}}\right\}\exp\left\{-\xi_\alpha \rho_k\right\} \tag{18}$$

where $\alpha = V, H$ or M. In eq. (18), ζ_α and ξ_α are material constants; the variable δ is a scalar measure of the distance of the current state to the BS, and ρ_k is a scalar memory variable.

The distance δ is evaluated by introducing the concept of memory surface, as shown in Fig. 4. The domain within the bounding surface is divided into two regions by a cone with vertex at the origin and opening angle ω equal to the maximum load obliquity reached upon reloading:

$$\tan\omega = \frac{\sqrt{H^2 + \left(M/D\right)^2}}{V} \tag{19}$$

Figure 5. A typical medium size wind turbine.

The distance δ is then computed as:

$$\delta = \delta_1 + \chi\delta_2 \tag{20}$$

where the quantities δ_1 and δ_2 are defined in Fig. 4, and χ is a model constant. According to eq. (17), the magnitude of the components Φ_α decrease with increasing distance of the current state from the BS. Therefore, the plastic flow magnitude decreases as δ increases.

The memory variable ρ_k appearing in eq. (18) is a function of the loading history and is updated formally as V_c/V_M in eq. (8). For the details of the evolution equations of the yield locus and the memory surface, the reader is referred to di Prisco et al. (2002).

Finally, the elastic stiffness matrix is defined as follows:

$$\boldsymbol{K}^e = \text{diag}\left\{K_V^e, K_H^e, K_M^e\right\} \tag{21}$$

where the coefficients K_V^e, K_H^e and K_M^e are computed as:

$$K_V^e \equiv R_{ur}; \quad K_H^e = 2R_{ur}\frac{1-\nu}{2-\nu}; \quad K_M^e = \frac{1}{6}R_{ur}D^2 \tag{22}$$

according to Gazetas (1991).

4 SSI ANALYSIS OF A WIND TURBINE: QUASISTATIC CONDITIONS

In this section, the macroelement model illustrated in the previous sections is used to analyze the quasi-static behaviour of a medium size (850 kW) wind turbine similar to the one shown in Fig. 5.

The weight of the turbine and the rotor is 320 kN, and these are mounted on a 30 m high conical steel tower. The external tower diameter varies from a maximum of 3.5 m at the base to a minimum of 2.0 m at the top. The moment of inertia of its section varies from about 0.56 m^4 at the base to about 0.13 m^4 at the top.

Table 1. Model constants adopted in the simulations.

ψ	μ	λ_M	λ_H	β
0.30	0.60	0.286	0.80	0.95
R_{ur} (GPa)	α	γ	ζ_V	$\zeta_H = \zeta_M$
1.26	2.83	1.71	4.00	20.00
ξ_V	$\xi_H = \xi_M$	χ		
50.00	100.00	0.01		

The weight of the tower is 406 kN. The foundation is a circular concrete raft, with diameter D ranging from 12 to 14 m, and a thickness equal to $0.1D$. It is worth noting that the weight of the foundation is larger than the entire weight of the structure (rotor+turbine+tower).

The foundation rests on a coarse-grained soil layer, with a friction angle of 40°, shear modulus of 40 MPa and Poisson's ratio equal to 0.30. The unit weight of the soil is assumed equal to 20 kN/m^3.

Starting from the given soil properties and foundation sizes, the macroelements have been calibrated following the guidelines provided by Nova & Montrasio (1991), Montrasio & Nova (1997) and di Prisco et al. (2002). Table 1 shows the values of the model constants adopted in the simulations.

4.1 *Monotonic loading conditions*

To demonstrate the capability of the macroelement to reproduce the wind turbine behavior under monotonic loading conditions, a 3D FE model of the 12 m circular foundation raft has been developed, using the FE code Abaqus (Simulia, 2010). The foundation soil has been modeled as an elastic-perfectly plastic material, with Mohr-Coulomb yield condition. The soil-foundation contact has been modeled as a unilateral frictional contact, to simulate the possible opening of the contact at high load eccentricities.

The foundation has been subjected to the following loading program: 1) application of the vertical load corresponding to the weight of the structure and the foundation; 2) application of a horizontal load of 400 kN at the turbine hub, simulating the wind action on the rotor. For the chosen soil properties and foundation diameter, this value of the horizontal load is relatively close to the horizontal collapse load.

The macroelement predictions for loading stage (2), in terms of horizontal load-displacement curve, are compared to the 3D FE simulation in Fig. 6. The results show that, at least for load values within the range of working load levels (i.e., H $\leq$ 200 kN), the macroelement prediction matches reasonably well the FE results. However, the macroelement approach allows for a dramatic increase in computational efficiency, as the 3D FE analysis required several hours of CPU time to complete, while only fractions of seconds are needed for the macroelement simulation.

This means that the macroelement approach can be effectively used in the simulation of soil-structure interaction problems characterized by complex loading conditions with large number of cycles, whereas the FE approach would be practically inapplicable.

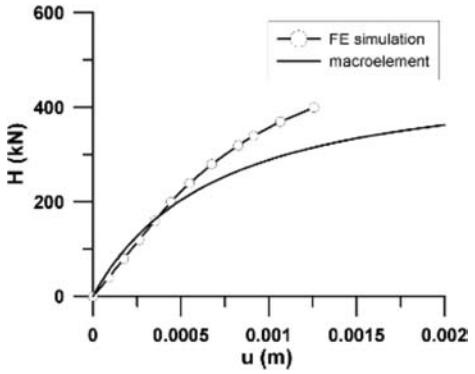

Figure 6. Horizontal load-displacement curves for wind loading under monotonic, quasi-static conditions: comparison between macroelement and 3D FE predictions.

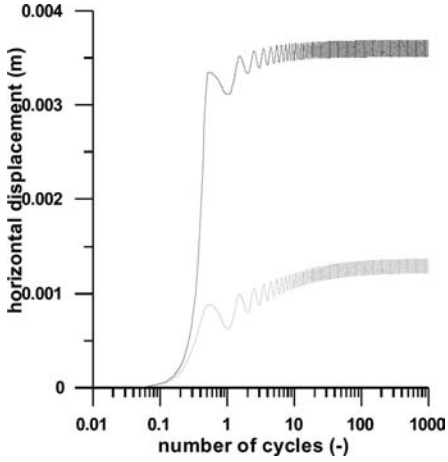

Figure 7. Horizontal displacement *vs*. number of wind load cycles. Black curve: $D = 12$ m; grey curve: $D = 14$ m.

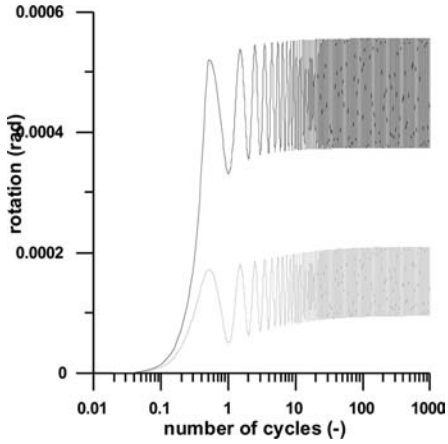

Figure 8. Foundation rotation *vs*. number of wind load cycles. Black curve: $D = 12$ m; grey curve: $D = 14$ m.

4.2 *Cyclic loading conditions*

To assess the effects of cyclic wind loading, a second series of simulations has been performed under quasi-static conditions, considering two different foundations with a diameter of 12 m and 14 m, respectively.

In this case, the wind load – a horizontal force applied at the turbine hub – is assumed to vary with time according to the following relation:

$$H = H_0 \frac{1 - \cos \Omega t}{2} \tag{23}$$

with $H_0 = 400$ kN.

The results of the simulations are shown in Figs. 7 and 8 in terms of horizontal displacements and rotations, respectively, as a function of the number of cycles.

It is interesting to note that, in both cases, both horizontal displacements and rotations reach a stationary condition characterized by constant maximum and minimum values very rapidly, in just a few cycles. As expected, the stationary values of displacements and rotations depend on the foundation size, the larger movements being associated with the smaller foundation.

As far as vertical displacements are concerned, the results in Fig. 9 (computed for foundation diameters ranging from 13 to 16 m) show that foundation settlements increase steadily with the number of cycles, reaching values which, after 1000 cycles, are about one order of magnitude larger than observed horizontal movements. This effect is only slightly influenced by the foundation diameter.

After about 50 cycles, the settlements increase almost linearly with the logarithm of the number of cycles. This observation allows us to establish a simple relation which could be used to predict the expected settlement of the structure when subject to very large numbers of cycles, a condition which is typical for wind turbines during their operating life.

5 SSI ANALYSIS OF A WIND TURBINE: DYNAMIC CONDITIONS

The third and final series of simulations has been carried out considering the cyclic wind action under fully dynamic conditions. This requires the set up of a simplified FE model of the structure (shown in Fig. 10), in which the tower is discretized into 4 linear elastic 2-noded beam elements with lumped mass at the nodes. The turbine and the rotor are schematized as a concentrated mass at the top of the tower, and the soil-foundation system is modeled with a single macroelement. The foundation diameter has been set equal to 14 m.

To model the inertial effects of the foundation and the energy dissipation due to radiation damping, the macroelement has been enriched with a mass matrix and a viscous damping matrix. The damping matrix

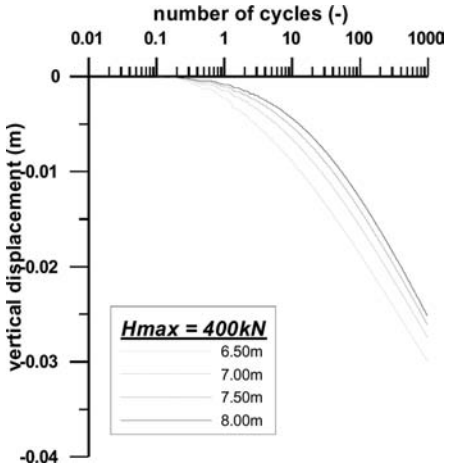

Figure 9. Accumulated vertical displacement *vs*. number of wind load cycles for different foundation radii.

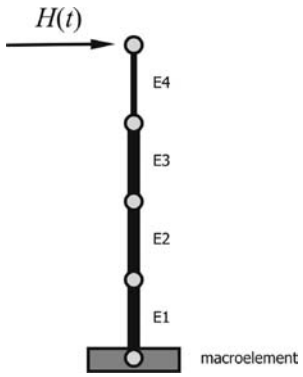

Figure 10. Simplified FE model of the wind turbine.

has been assumed as suggested by Sieffert & Cevaer (1991):

$$\boldsymbol{C} = \mathrm{diag}\left\{C_V, C_H, C_M\right\} \tag{24}$$

where:

$$C_\alpha = K_\alpha^e \frac{D}{2V_S}\tilde{\eta}_\alpha \qquad (\alpha = V, H \text{ or } M) \tag{25}$$

V_S is the shear wave velocity of the foundation soil and $\tilde{\eta}_\alpha$ the viscosity parameter associated with each degree of freedom. In the simulations, the two translational viscosity parameters have been set to $\tilde{\eta}_V = 0.85$ and $\tilde{\eta}_H = 0.58$, while the rotational viscosity parameter has been computed from the following relation (Sieffert & Cevaer, 1991):

$$\tilde{\eta}_M = 0.30\left\{1 + \frac{4J_F G}{\rho K_M^e D^2}\right\}^{-1} \tag{26}$$

in which J_F is the rotational moment of inertia of the foundation.

Table 2. Geometric and material properties of beam elements.

Element no.	L (m)	A (m^2)	J (m^4)	ρ (t/m^3)
1	9.33	0.350	0.4657	1.60
2	9.33	0.306	0.3131	7.85
3	9.33	0.263	0.1981	7.85
4	9.33	10.000	20.833	7.85

Note: L = element length; A = cross section area; J = cross section moment of inertia; ρ = apparent density.

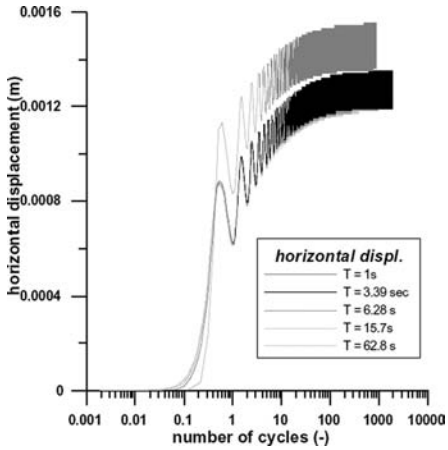

Figure 11. Horizontal displacements *vs*. number of wind load cycles for different excitation periods.

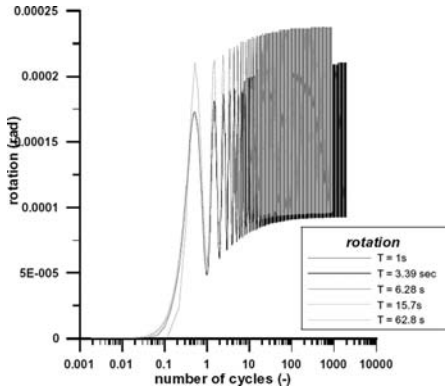

Figure 12. Foundation rotation *vs*. number of wind load cycles for different excitation periods.

The geometry and the mechanical properties of the structural elements are summarized in Table 2.

The evolution of horizontal displacements and rotations with the number of cycles, for periods $T = 2\pi/\Omega$ of the wind load excitation ranging from 1 s to 62.8 s, are shown in Figs. 11 and 12, respectively. The accumulated vertical displacement of the foundation is plotted in Fig. 13 as a function of the number of cycles and excitation period.

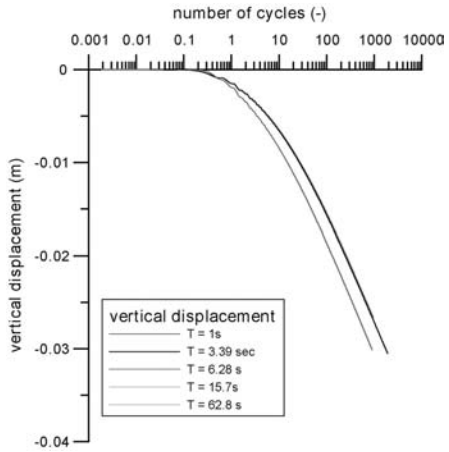

Figure 13. Accumulated vertical displacement vs. number of wind load cycles for different excitation periods.

The results of all the dynamic simulations are very close to each other and to the quasi-static solution presented in Sect. 4.2. The only significant differences occur for the lowest period considered ($T = 1$ s), where a slight dynamic amplification of the computed displacements and rotations can be observed. This is due to the fact that the range of frequencies considered – typical of wind load excitations – are relatively far from the characteristic frequencies of the system and therefore the computed response of the structure is almost frequency-independent.

6 CONCLUSIONS

The analysis of soil-structure interaction problems under cyclic/dynamic conditions poses significant problems when the cumulative effect of the application of a very large number of load cycles is of concern. In this case, the macroelement approach can represent a valuable alternative to more traditional approaches, as it couples effectively the advantage of computational efficiency – typical of the deformable constraints approach – to the ability of reproducing such aspects of foundation response as hysteresis, ratcheting, and coupling between translational and rotational degrees of freedom.

The macroelement of Nova & Montrasio (1991), suitably modified to allow the modelling of cyclic/dynamic response of foundations, has been used to analyze the static and dynamic behavior of a wind turbine founded on a circular raft foundation subject to time-dependent wind forces. This particular type of structure – characterized by relatively low vertical loads, and high horizontal loads and moments – has been chosen as a benchmark to investigate the influence of coupling between the different degrees of freedom of the system.

Although the simulations refer to an ideal structure, and are therefore to be considered more from a qualitative than a quantitative point of view, the predicted response of the wind turbine under both cyclic and dynamic condition appears to be quite realistic. In particular, as far as horizontal displacements and rotations are concerned, the results clearly indicate the occurrence of shake-down, as the foundation experiences only recoverable displacements after a finite, and relatively small number of cycles.

On the contrary, after a few initial cycles the vertical displacements increase linearly with the logarithm of the number of cycles. This effect is only slightly influenced by the foundation diameter. This observation allows us to establish a simple relation which could be used to predict the expected settlement of the structure when subject to a very large number of cycles, a condition which is typical for this type of structure during their operating life. It is worth noting that this result could not have been achieved by means of a conventional FE analysis, due to the very large number of cycles considered.

Finally, the results of the dynamic analyses indicate that for the range of frequencies which are typical of wind load excitations, dynamic amplification effects can be disregarded, and only the cyclic nature of the wind action appears to be relevant for engineering purposes.

REFERENCES

Al Tabbaa A., Wood D.M. 1989. An experimental based 'bubble' model for clay. *Proc. NUMOG 3*, Niagara Falls, 91–99.

Dafalias Y.F., Herrmann L.R. (1982). Bounding surface formulation of soil plasticity. In: *Soil Mechanics – Transient and Cyclic Loads*. Pande G.N., Zienkiewicz eds., Wiley, 253–282.

di Prisco C., Nova R., Sibilia A. 2002. Analysis of soil-structure interaction of towers under cyclic loading. Invited lecture. *Proc. NUMOG 8*, Rome, G.N.Pande & S. Pietruszczak editors, Swets & Zeitlinger, Lisse, 637–642.

Gazetas G. 1991. Foundations vibrations. *Foundation Engineering Handbook*, 2nd ed., Van Nostran Reinhold.

Montrasio L., Nova R. 1997. Settlements of shallow foundations on sand: geometrical effects. *Géotechnique*, 47,1,49–60.

Nova R., Montrasio L. 1991. Settlements of shallow foundations on sand. *Géotechnique*, 41, 2, 243–256

Poulos H.G., Carter J. P., Small J. C. (2001). Foundations and Retaining Structures – Research and Practice. *Proc. XV ICSMGE*, Instanbul, Balkema.

Salciarini D., Tamagnini C. 2009. A hypoplastic macroelement model for shallow foundations under monotonic and cyclic loads. *Acta Geotechnica*, 4(3), 163–176.

Sieffert, J.-G. & Cevaer F. 1991. Handbook of impedance functions-surface foundations. *Ouest Editions*, Nantes.

Simulia 2010. Abaqus FEA; http://www.simulia.com.

Towards improved SFSI design procedures

Soil-Foundation-Structure Interaction – Orense, Chouw & Pender (eds)
© 2010 Taylor & Francis Group, London, ISBN 978-0-415-60040-8

Design approaches and criteria for earthquake-resistant shallow foundation systems

J.C.W. Toh
Pells Sullivan Meynink, Sydney, Australia

M.J. Pender
University of Auckland, New Zealand

ABSTRACT: Current practice for earthquake-resistant shallow foundation design does not allow the foundation to fail in bearing, and does not consider the interaction of non-linear responses of the soil, foundation, and superstructure. Design tools exist that allow this interaction to be considered, and with the use of these tools, an alternative design approach that allows shallow foundations to yield during an earthquake becomes available. This paper uses examples to demonstrate the benefits of this alternative design approach. The approach enables the performance of the foundation to be balanced against that of the superstructure. Foundation and superstructure actions may be reduced significantly, whilst incurring only modest permanent foundation displacements. Broad suggestions of the type of criteria that might be required for the yielding foundation design approach are made. It is concluded that it may be preferable to develop criteria that describe performance aspects and system responses that should be considered, rather than prescribe firm quantitative criteria.

1 INTRODUCTION

The current practice for earthquake-resistant design of shallow foundations on non-liquefiable soil is to ensure that a generous reserve of bearing strength is available throughout the design earthquake. This practice is typically used with design processes where the structural and geotechnical components of design are separated. Such design processes do not properly account for the effect of non-linear foundation behaviour on the superstructure response, and can lead to overly conservative foundation designs or have undesirable effects on the performance of the superstructure.

In recent years, understanding of the earthquake performance of shallow foundation systems has progressed rapidly, through both experimental studies and development of numerical modelling techniques. Using such numerical modelling techniques, the soil, foundation, and structure can be realistically incorporated in a single model, allowing the effect of each component of the system on the other components to be assessed.

With the ability to model the entire soil-foundation-structure system as a whole, the question is raised as to whether alternative approaches to the earthquake-resistant design of shallow foundation systems could be adopted. When considering such systems, sizing shallow foundations to prevent them from yielding during the design earthquake may not always be the most robust design approach.

This paper examines design approaches and performance criteria for the earthquake-resistant design of shallow foundations and the superstructures that they support. The paper is in two parts. Firstly, alternative design approaches and methodology are discussed, with reference to an example design scenario (Sections 2, 3 and 4). Secondly, possible design criteria for yielding foundations are considered (Sections 5 and 6).

2 ALTERNATIVE DESIGN APPROACHES

Three different approaches to the earthquake-resistant design of shallow foundations on non-liquefiable soil and the superstructures that they support are considered herein.

2.1 *Traditional design approach*

The current practice for earthquake-resistant design of shallow foundations (referred to herein as the 'traditional' design approach) prevents yielding of the foundation by providing a generous reserve of bearing strength during the design earthquake. Under a Load and Resistance Factor Design (LRFD) framework, the earthquake loading demands on the foundation are unfactored, but a strength reduction factor of 0.5 is applied to the available vertical bearing strength. This is approximately equivalent to a seismic factor of safety of two.

The traditional design approach can result in foundations being significantly larger than would be required under static loading only, especially for tall

slender structures that can impose large eccentric loadings on foundations. Larger foundations are stiffer than smaller ones, and have a shorter natural period. This affects the dynamic response of the soil-foundation-structure system.

2.2 *No reserve of bearing strength during design earthquake (seismic factor of safety of unity)*

One alternative to the traditional design approach is to size the foundation so that bearing failure is only just prevented from occurring during the design earthquake. Under a LRFD framework, this would correspond to both the earthquake loading demands on the foundation and the available vertical bearing strength being unfactored (a seismic factor of safety of one).

Possible advantages to this design approach are a smaller, presumably cheaper foundation, and a less stiff soil-foundation-structure system (which may have benefits for structural performance). A disadvantage to this design approach is that although in theory no yielding will occur during the design earthquake, there is no margin for error. Thus the approach may not be acceptable if it is critical to prevent bearing failure occurring, given the uncertainty that is usually present in assessing soil strength. However, as will be demonstrated, minor instances of bearing failure during an earthquake may not have significant consequences.

2.3 *Design based on static LRFD requirements only (seismic yielding allowed)*

A second alternative to the traditional design approach, and the one that is the focus of this paper, is to size the foundation based only on static considerations (bearing capacity and settlement). Under this approach, brief instances of foundation yielding (bearing failure) might occur during an earthquake, resulting in the accumulation of permanent displacements. This is referred to herein as the 'yielding foundation' approach.

A major advantage to this approach would be the ability to consider and balance the performance of the foundation and the superstructure, without having the prerequisite requirement that the foundation is not permitted to yield. In many cases, allowing the foundation to yield may have beneficial effects for the superstructure performance or for the system as a whole, and under this approach, these benefits could be obtained.

3 DESIGN METHODOLOGY

In order to use and compare each of the three design approaches discussed in Section 2, appropriate design tools (numerical models) are required. The linear bed of springs model that is the basis of 'classical' soil-structure interaction is not able to model yielding of the foundation. There are however several tools available now that can capture non-linear behaviour and foundation yielding under dynamic loading: finite element and finite difference models, variations of non-linear yielding spring models (for example, Gajan & Kutter, 2007, Pender et al, 2008), and shallow foundation macro-element models (for example, Cremer et al, 2001, Paolucci, 1997, and Chatzigogos et al, 2007). This paper uses a macro-element to model dynamic soil-foundation-structure interaction.

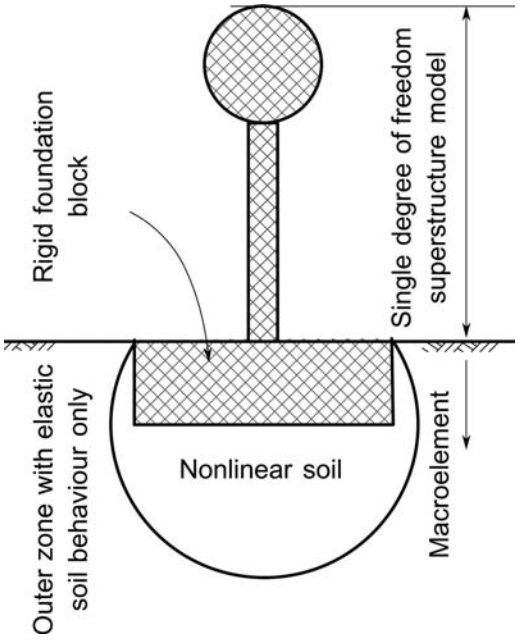

Figure 1. Macro-element concept (after Cremer et al, 2001).

3.1 *The macro-element model*

A macro-element is a single computational entity that represents the behaviour of a shallow foundation and the adjacent soil (Figure 1). The approach is the antithesis of the finite element technique which requires discretisation of a substantial volume of soil beneath the foundation and is therefore not a practical design tool. From the macro-element, only the response at a representative point (the foundation centre) is obtained, but this gives a useful approximation to the foundation response. In this way the macro-element is a practical option for modelling soil-foundation-structure interaction.

The model used herein was developed by Toh (2008). It is a version of the macro-element model developed by Paolucci (1997). Although the model is simple compared to other shallow foundation macro-elements (for example, Cremer et al, 2001, and Chatzigogos et al, 2007), it provides results that compare well to those from experimental results and yielding spring models (Pender et al, 2009).

3.2 *Bearing strength surfaces*

Bearing strength surfaces define the combinations of vertical load, horizontal shear, and moment that cause bearing failure beneath a shallow foundation.

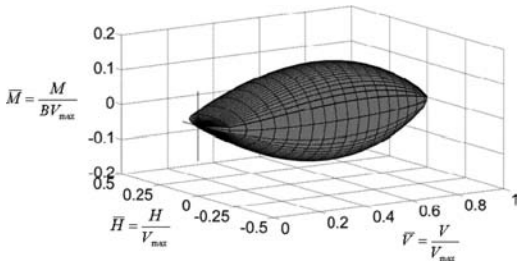

Figure 2. Eurocode 8 undrained clay bearing strength surface.

They are a convenient and elegant way of representing the bearing capacity of a shallow foundation, as they show how the amount of moment and shear that can be applied to a shallow foundation depends on the vertical load carried. Examination of the path followed by the actions locus in relation to the bearing strength surface can also give an enhanced understanding of the foundation response to different types of loading.

The macro-element model used in this paper is based on the Eurocode 8 bearing strength surface for cohesive soils (Figure 2). The surface acts as a yield surface in that when the actions locus lies inside the surface, behaviour is considered to be elastic, while when the actions locus reaches the surface, bearing failure occurs and behaviour is considered to be perfectly plastic. In this manner, the macro-element is able to capture nonlinear foundation response.

4 EXAMPLE DESIGN SCENARIO

To demonstrate the relative performance of the three alternative design approaches considered, the macro-element was used in an example design scenario to model a bridge pier founded on clay with an undrained shear strength of 100 kPa. The static factor of safety was varied by changing the size of the square, surface foundation.

4.1 *Model parameters and dynamic input*

The macro-element used requires minimal input parameters which are all easily obtained. Table 1 presents the structural parameters used in the model. The structural parameters were selected to represent a hypothetical bridge pier that behaves as a single-degree-of-freedom oscillator in the transverse direction. The foundation stiffness and damping values varied depending on the size of the foundation, and were calculated using formulae presented by Gazetas (1991).

An earthquake acceleration time history from the 1940 El Centro earthquake (scaled up marginally) was used as the dynamic input to the model. The response spectrum of this time history (Figure 3) closely represents the design response spectrum at a shallow soil site for an Importance Level 4 structure

Table 1. Structural parameters for example design scenario.

Height of superstructure centre of gravity above centre of foundation	15 m
Effective mass of superstructure	2×10^6 kg
Mass of foundation	5×10^5 kg
Rotational inertia of superstructure and foundation	5.15×10^6 kg · m^2
Horizontal stiffness of superstructure	4.94×10^5 kN/m
Horizontal damping of superstructure	6280 kN · s/m

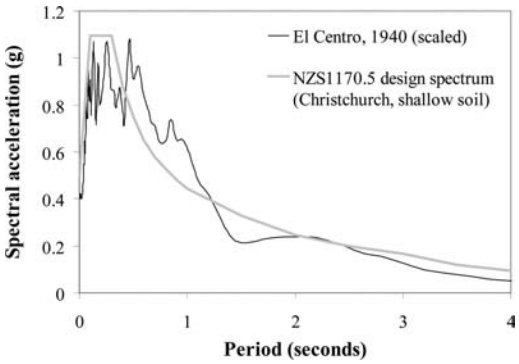

Figure 3. Response spectrum of earthquake record overlaid on NZS1170.5:2004 design spectrum.

(an essential facility or one with post-disaster function) in Christchurch, New Zealand, as specified by NZS1170.5:2004.

In a real design scenario, more than one earthquake record would usually be adopted (for example, under NZS1170.5:2004, three or more records must be used). For clarity, only one record was used in this example scenario.

4.2 *Behaviour under alternative design approaches*

Figure 4 shows the path followed by the actions locus in $[M, H]$ space (i.e. within a section of the bearing strength surface at a constant vertical load V) for all three design approaches considered. Overlaid are the outlines of the different sized bearing strength surfaces of each design approach.

For this particular example scenario, a static factor of safety of three was adopted for the yielding foundation design approach, although it is noted that any foundation with a seismic factor of safety less than one will experience some yielding. Figure 4 shows how, for the yielding foundation design approach, occasional instances of bearing failure occur during the earthquake, as the actions locus momentarily reaches the bearing strength surface.

It was found that a static factor of safety of eight was required to only just prevent seismic bearing failure from occurring (seismic factor of safety of unity). Figure 4 shows the path of the actions locus almost reaching, but not touching, the bearing strength surface for a static factor of safety of eight.

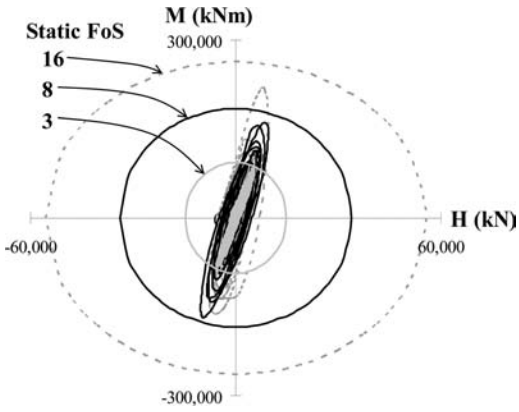

Figure 4. Bearing strength surface and path followed by foundation actions locus under various design approaches.

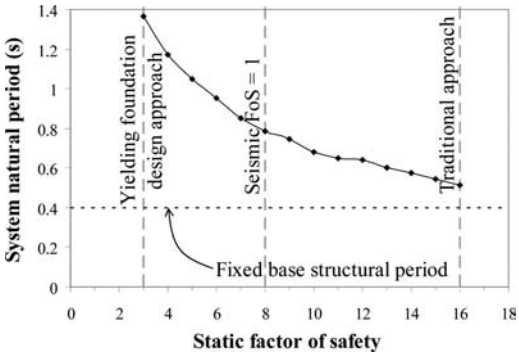

Figure 5. Natural period of soil-foundation-structure system under various design approaches.

Based on this, the static factor of safety required to satisfy traditional design approach requirements is 16. Note that the factor of safety is defined in terms of vertical action, not moment or shear, so the dimensions of the bearing strength surface in the $[M, H]$ plane do not double when the static factor of safety is doubled. This is demonstrated in Figure 4, which shows that for a static factor of safety of 16, the actions locus passes further than half of the distance from the origin of the $[M, H]$ plane to the bearing strength surface.

The definition of factor of safety in terms of vertical loads only can therefore give a misleading impression of the reserve of bearing strength available under lateral loading (when the actions locus moves mainly within the $[M, H]$ plane).

4.3 *Dynamic soil-foundation-structure system characteristics*

Figure 5 shows how the natural period of the soil-foundation-structure system varies with static factor of safety. The natural periods were obtained by analysing response spectra. Overlaid on the plot is the fixed-base period of the single-degree-of-freedom superstructure.

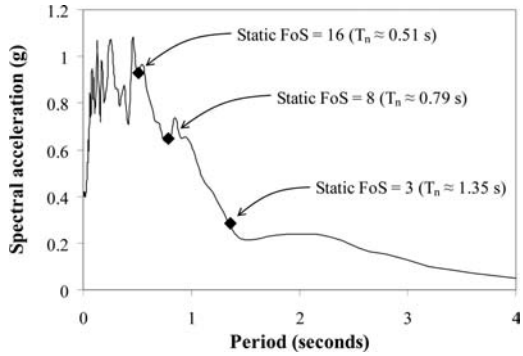

Figure 6. Natural period of soil-foundation-structure system compared with El Centro earthquake response spectrum.

As the static factor of safety increases, the soil-foundation-structure system becomes stiffer, and the system period decreases towards the fixed-base period of the structure. Under the traditional design approach, the foundation is so stiff that the system period is very close to the fixed-base period of the structure and the effect of soil-foundation-structure interaction is minimized.

The consequences of the different system natural periods obtained under the three alternative design approaches depend on the characteristics of the design earthquake spectrum. The system natural periods for the three design approaches overlaid on the earthquake response spectrum for this design example are shown in Figure 6.

For the particular earthquake acceleration time history used, the spectral acceleration at the system natural period increases as the system natural period decreases. Consequently, the foundation designed according to the traditional approach experiences the highest spectral acceleration, whereas the yielding foundation experiences the lowest spectral acceleration. This has important implications for the foundation and structural actions, as discussed in the following section.

4.4 *Foundation and structural actions*

Figure 7 presents plots of the structural action and foundation moment for a range of static factors of safety. The factors of safety corresponding to the three alternative design approaches are marked. Similar behaviour is observed for foundation shear.

As discussed above, under the traditional design approach the system is subjected to high spectral acceleration. This causes both the foundation and the superstructure to attract more load than under the other two design approaches.

The reason why such a high static factor of safety is required to prevent any yielding during this particular earthquake is that as the foundation size is increased, it becomes stiffer and attracts more load. This in turn requires the foundation to be sized even larger

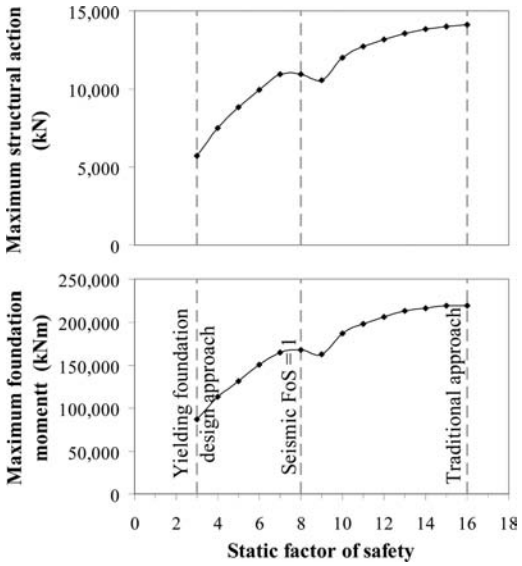

Figure 7. Foundation and superstructure actions under various design approaches.

to prevent bearing failure from occurring under the higher attracted load. Significant inefficiencies can result from this process of "chasing one's tail".

Under the design approach where the foundation is permitted to yield during an earthquake, the system is comparatively much less stiff, with a longer natural period. It is subjected to lower spectral acceleration, and as a result, the foundation and superstructure both attract less than half the loads of those in the traditional design approach.

Note that behaviour opposite to that discussed may occur for earthquakes with different shaped response spectra.

4.5 *Permanent foundation displacements*

Although the yielding foundation design approach may have the benefit of lower foundation and structural loading when compared with the traditional design approach, there is of course the consequence of accumulated permanent foundation displacement as a result of the instances of bearing failure.

Table 2 presents the range of elastic displacements and the residual plastic (permanent) displacements for each of the three design approaches.

The permanent displacements under the yielding foundation design approach are quite modest, especially when compared with the elastic displacements. Therefore, the question must be asked: is it time to reassess the traditional design approach for earthquake resistant shallow foundations? It is proposed that a yielding foundation that experiences some permanent displacement may be acceptable if the displacements are modest, and if significant benefits can be obtained in terms of reduced foundation and superstructure actions.

Table 2. Foundation displacements under various design approaches.

Design approach	Traditional	Seismic FoS = 1	Yielding foundation
Static factor of safety	16	8	3
Elastic sliding (mm)	−10 to 12	−19 to 18	−17 to 17
Elastic rotation (mrad)	−1 to 1	−3 to 3	−7 to 7
Residual sliding (mm)	0	0	2
Residual rotation (mrad)	0	0	0.5
Settlement (mm)	0	0	0.5

If this yielding foundation design approach is to be adopted in practice, a set of criteria are required as a framework within which to assess the performance of the foundation. The remainder of this paper explores possible bases for the development of such design criteria.

5 BASIS OF DESIGN CRITERIA FOR YIELDING FOUNDATIONS

This section examines two existing documents that deal with earthquake-resistant design of shallow foundations, and attempts to garner elements that may provide a basis for appropriate criteria for a yielding foundation design approach. It then goes on to discuss aspects of foundation performance that might require criteria under this approach.

5.1 *Eurocode 8, Part 5*

Eurocode 8 (BSI, 2005) sets out requirements for the design of structures for earthquake resistance: Part 5 deals with foundations and geotechnical aspects. The code specifies that the occurrence of bearing failure must be prevented during an earthquake.

However, Section 5 of Part 5, dealing with foundation systems, states that:

– The foundation of a structure in a seismic area shall transfer the relevant forces from the superstructure to the ground without substantial permanent deformations; and
– The seismically-induced ground deformations are required to be compatible with the essential functional requirements of the structure.

These requirements could be compatible with criteria for yielding foundations. The first requirement would leave some flexibility for the designer to judge what 'substantial' permanent deformations are, which would be important when balancing the performance of the foundation with that of the superstructure. The second requirement would seem to be more suited to quantitative criteria, where permissible displacements depend on the type of structure.

5.2 *FEMA 356*

FEMA 356 (FEMA, 2000) is different from Eurocode 8 in that it is a prestandard and commentary that deals

with the seismic rehabilitation of existing buildings. In accord with the theme of this paper, Section C.4.1 (a commentary) states that "*the acceptability of the behaviour of the foundation system and foundation soils for a given performance level cannot be determined apart from in the context of the behaviour of the superstructure*".

This infers that it would be difficult and/or limiting to set inflexible blanket criteria for the yielding foundation design approach, and that the performance of the superstructure is an equally important, or more important consideration than that of the foundation.

5.3 *Displacement during an earthquake*

One aspect of seismic foundation performance that would require criteria under a yielding foundation design approach are the dynamic displacements that occur during an earthquake. The dynamic displacements predominantly comprise elastic rotation and sliding.

The criteria would need to consider the effect of elastic foundation displacements (and associated superstructure displacements) on adjacent buildings, service connections, and building fittings.

Is it noted that elastic displacements during an earthquake should also be a design consideration under other design approaches.

5.4 *Residual displacement following an earthquake*

A second aspect that would require design criteria are the residual foundation displacements that remain following an earthquake. The residual displacements would comprise rotation and sliding. The criteria would need to consider the damage to the foundation compared with the damage to the building, and ease of repair of the deformation. The residual displacements could be compared to the elastic displacements during the earthquake to help assess their significance (e.g. see Table 2).

5.5 *Earthquake-induced settlement*

A third aspect to be considered would be earthquake-induced settlement. Considerations would be similar to those for residual rotation and sliding. It would also be valuable to compare the earthquake-induced settlement to the static elastic settlement, to get an idea of the relative significance of the earthquake-induced settlement.

6 DESIGN CRITERIA FOR ASPECTS OF FOUNDATION PERFORMANCE

This section uses modelling to demonstrate the type of foundation behaviour that may be expected in relation to each of the performance aspects discussed in the previous section. The results of the modelling are used to discuss how criteria may be developed for each aspect.

Table 3. Foundation stiffness and damping parameters for static factor of safety of three.

Foundation horizontal stiffness	3.3×10^5 kN/m
Foundation rotational stiffness	1.2×10^7 kNm/rad
Foundation vertical stiffness	5.0×10^5 kN/m
Foundation horizontal damping	1.6×10^4 kN · s/m
Foundation rotational damping	3.5×10^4 kN · m · s/rad
Foundation vertical damping	3.5×10^4 kN · s/m

This paper does not go so far as to propose specific criteria.

For the modelling, the foundation from the example in Section 4 with a static factor of safety of three was used. Table 3 presents the soil stiffness and damping values that were calculated for the foundation using formulae presented by Gazetas (1991). The dynamic inputs for the modelling were 20 different earthquake records. For the purposes of illustration, and to capture a wide range of foundation responses, the earthquake records were selected indiscriminately, and do not represent a single type of site condition.

6.1 *Foundation rotation and sliding*

Figure 8 presents scatter plots of the maximum absolute total (elastic plus plastic) rotation experienced by the foundation at any time during each of the earthquakes. The top plot presents the data against the horizontal peak ground acceleration of the earthquake, while the bottom plot presents the data against the spectral acceleration of the earthquake at the system natural period (approximately 1.35 seconds, Figure 5). Similar results were obtained for sliding.

The rotation exhibits no correlation with horizontal peak ground acceleration, but very good correlation with the earthquake spectral acceleration at the system natural period. This reinforces the idea that the entire soil-foundation-structure system should be considered in design, as each component of the system has an effect on its dynamic characteristics and natural period. It may be possible to develop guidelines that require the system natural period to be sufficiently different to that of the design earthquake.

Figure 9 elaborates on Figure 8 by separating out the different components of foundation rotation. The components considered are the maximum absolute elastic, plastic, and total rotation experienced by the foundation at any time during the earthquakes, and the residual plastic rotation that remained at the end of the earthquakes. Similar results were obtained for sliding, and the points noted below are equally applicable to sliding:

- In this example, foundation bearing failure and associated plastic rotation do not occur below a spectral acceleration of approximately 0.2 g;
- During the earthquake, maximum elastic rotation is higher than maximum plastic rotation for spectral accelerations up to approximately 0.4 g to 0.5 g. At such levels of spectral acceleration, performance

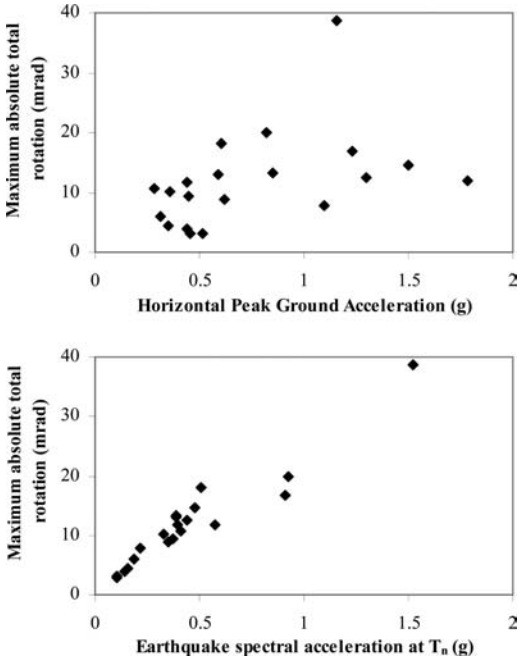

Figure 8. Residual foundation rotation versus PGA and spectral acceleration at system natural period.

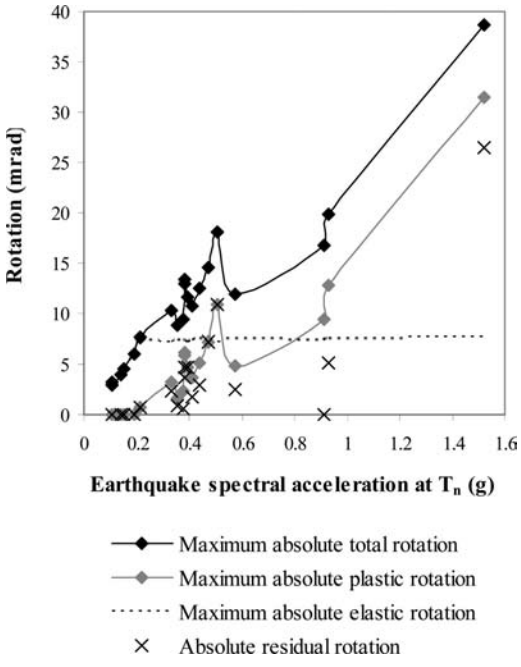

Figure 9. Elastic and plastic foundation rotation versus spectral acceleration at system natural period.

during an earthquake may be a more critical criterion than post earthquake residual displacements, and therefore allowing a foundation to yield may not result in performance worse than that of a non-yielding foundation;

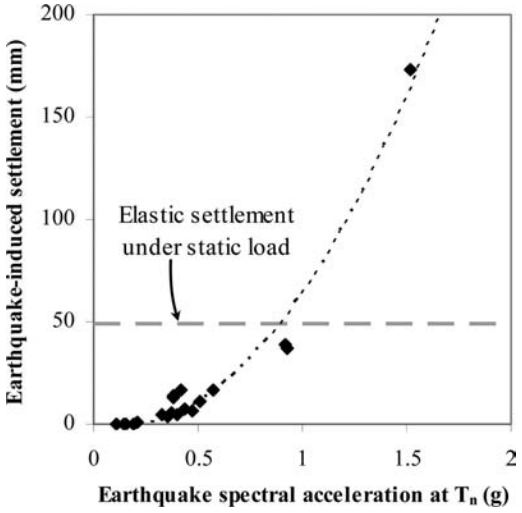

Figure 10. Earthquake-induced foundation settlement versus spectral acceleration at system natural period.

- If bearing failure occurs, the maximum elastic rotation is virtually constant regardless of the spectral acceleration. This is because the maximum foundation actions (shear and moment) are limited by the bearing strength of the soil;
- Conversely, if bearing failure occurs, maximum plastic rotation during an earthquake increases roughly linearly with spectral acceleration, which is a good indicator of foundation performance;
- The maximum plastic rotation does not always equal the residual rotation, as plastic rotation can occur in both directions during an earthquake;
- Therefore, the residual rotation obtained from the numerical model does not reliably represent the maximum possible residual rotation of the foundation. In many cases, the calculated residual rotation following the earthquake is less than the maximum plastic rotation that occurs during the earthquake, due to the characteristics of the particular earthquake records used;
- In reality, the actual residual rotation could lie anywhere within the range of plastic rotations that are experienced, so the calculated maximum plastic rotation during the earthquake may be a better indicator of residual rotation for design purposes.

6.2 *Foundation settlement*

Figure 10 presents the calculated earthquake-induced foundation settlement versus spectral acceleration at the system natural period, for all of the 20 earthquake records used.

There is a non-linear (approximately parabolic) relationship between settlement and spectral acceleration. As a result, earthquake-induced settlements are zero or negligible at low spectral accelerations.

The static elastic foundation settlement of approximately 50 mm is higher than earthquake-induced settlements for spectral accelerations below approximately 0.9 g, which would usually correlate to a very strong earthquake. In fact, of the 20 earthquakes records used, only one caused settlement greater than the static elastic settlement.

Design criteria could compare static and earthquake-induced settlement to assess the significance of the earthquake-induced settlement.

The results suggest that earthquake-induced settlements are only significant under very unfavourable conditions where strong spectral accelerations coincide with the natural period of a soil-foundation-structure system.

7 CONCLUSIONS

The main conclusions drawn from the work presented in this paper are as follows:

- The current practice of providing a generous reserve of foundation bearing capacity during the design earthquake may no longer be the best approach available, given the availability of tools that can capture soil-foundation interaction;
- When undertaking earthquake-resistant design, soil-foundation-structure systems should be considered as a whole. The performance of the foundation should be considered alongside, not separate from, the performance of the superstructure;
- A design approach that allows shallow foundations to yield during an earthquake is suggested as a way to optimise system efficiency and performance, by minimising foundation size and potentially reducing foundation and superstructure actions;
- Results obtained using this design approach suggest that foundation displacements that occur due to yielding are often very modest. This indicates that some yielding should be acceptable in most cases, and that in such cases, the performance of the superstructure is likely to be of greater concern than that of the foundation;
- There are no existing criteria for the yielding foundation design approach. Given the need to consider whole-of-system behaviour, it seems limiting to set quantitative criteria for foundation performance. It may be preferable to provide criteria that describe key performance indicators and system responses that should be considered.

Clearly, there is further work required in this area: firstly, to explore and promote the design approach of allowing foundations to yield during an earthquake, and secondly, to develop a set of robust criteria that can be used with such an approach.

REFERENCES

BSI British Standards, 2005. *BS EN 1998-5 Eurocode 8: Design of structures for earthquake resistance – Part 5: Foundations, retaining structures and geotechnical aspects.*

Chatzigogos, C. T., Pecker, A. & Salençon, J. 2007. A macro-element for dynamic soil-structure interaction analyses of shallow foundations. *4th Int. Conf. on Earthquake Geotechnical Engineering, Thessaloniki, Greece, June 25–28.*

Cremer, C., Pecker, A. & Davenne, L. 2001. Cyclic macro-element for soil-structure interaction: material and geometrical non-linearities. *International Journal for Numerical and Analytical Methods in Geomechanics*, 25: 1257–1284.

Federal Emergency Management Agency 2000. *FEMA 356: Prestandard and Commentary for the Seismic Rehabilitation of Buildings*. Washington, D.C.

Gajan, S. & Kutter, B. L. 2007. A contact interface model for nonlinear cyclic moment-rotation behaviour of shallow foundations. *4th Int. Conf. on Earthquake Geotechnical Engineering, Thessaloniki, Greece, June 25–28.*

Gazetas, G. 1991. Foundation vibrations, in *Foundation Engineering Handbook*, edited by Fang, H. Y. 2nd edition. New York: Van Nostrand Reinhold: Chapter 11.

Paolucci, R. 1997. Simplified evaluation of earthquake-induced permanent displacements of shallow foundations. *Journal of Earthquake Engineering* 1(3): 563–579.

Pender, M. J., Wotherspoon, L. M. & Toh, J. C. W. 2008. Foundation stiffness estimates and earthquake resistant structural design. *The 14th World Conference on Earthquake Engineering, Beijing, China, October 12–17.*

Pender, M. J., Toh, J. C. W., Wotherspoon, L. M. & Algie, T. B. 2009. Earthquake induced permanent displacements of shallow foundations – performance based design. *Int. Conf. of Performance-Based Design in Earthquake Geotechnical Engineering, Tsukuba, Japan, June 15–17.*

Standards New Zealand 2004. *NZS1170.5:2004. Structural design actions Part 5: Earthquake actions – New Zealand*. Wellington.

Toh, J. C. W. 2008. *Performance based aseismic design of shallow foundations*. ME thesis, University of Auckland.

Soil-Foundation-Structure Interaction – Orense, Chouw & Pender (eds)
© 2010 Taylor & Francis Group, London, ISBN 978-0-415-60040-8

Soil-pile interaction under kinematic lateral spread loading

I. Lam
Earth Mechanics Inc., Fountain Valley, CA, USA

P. Arduino & P. Mackenzie-Helnwein
University of Washington, USA

ABSTRACT: This paper presents some numerical solutions for the generic three-layered liquefaction lateral spread problem when an upper block of unliquefied soil crust is moving laterally due to lateral soil flow at a middle liquefied soil layer above a stable foundation soil mass. From the numerical solutions, simplified equation are developed for estimating the location, the amplitude for maximum pile moment, curvature and shear as a function of the amplitude of relative displacement between the upper and the lower soil layers or ground slippage at the middle liquefied soil layer. The paper presents some comparisons between the proposed method (referred as the coupled SSI approach) with corresponding conventional methods and point out some inherent problems in some of the commonly used approaches.

1 BACKGROUND INFORMATION

Pacific Earthquake Engineering Research Center (PEER) funded a project to study the classical generic 3-layered kinematic loading pile design problem (see Figure 1). The study involves numerical pile loading solutions and parametric 3-dimensional (3-D) finite-element (FE) soil-pile interaction analyses (see Figure 2) using the OPENSEES numerical platform. The project is documented in an unpublished report (Lam, et al. 2007), and later published in the Lam et al. (2009) paper.

The Lam et al. 2009 study (as well as this paper) are limited to modeling linear soil and pile properties and therefore be valid only for initial loading prior to yielding. Also the boundary conditions and the finite element meshes were to model the basic single solitary pile problem (i.e. without pile group effect) sufficiently far away from the top free field ground surface boundary conditions. These were intentional to keep the problem sufficiently simple to enhance the chance for better understanding of the basics mechanics of the kinematic pile loading problem. However the procedure is easily expandable and there are ongoing efforts by PEER to extend to nonlinear pile solutions and other boundary conditions. However, the Lam et al. (2009) method and solutions presented in his paper will still provide valuable insights to the problem and believed useful for preliminary design and screening.

2 PARAMETRIC SOLUTIONS

The basic FE mesh used for the study (referred as coupled soil-pile interaction model) is presented in Figure 2. The configuration is more meaningful for designing smaller piles (say 0.61 m diameter) embedded in relatively thin liquefied layers. Some of the implied configurations can become unreasonable. For example, the 10 D upper crust thickness case corresponds to the liquefied layer at a 24.4-m depth for a 2.5-m pile which may be too deep for design concern. Nevertheless, the configuration was maintained for simplicity.

The Lam et al. paper (2009) outlined a parametric analyses encompassing a large range of pile types and diameters, including three pile diameters (D): (1) 2.5-m (8-ft) steel pipe, (2) 1.37-m (54-inch) hollow cylinder concrete piles for major bridges, and (3) 0.61-m (24-in) solid concrete piles for onland bridges and wharf structures. The study also included various liquefied layer thicknesses: (1) 1D, (2) 2D and (3) 4D. Scaling factors were applied to the basic reference benchark bending stiffness (EI): (1) 0.125, (2) 0.25, (3) 0.5, (4) 1.0, (5) 2.0, (6) 4.0 and (7) 8.0, resulting in 56 basic sensitivity cases in the parametric study. Additionally, variations in soil modulus E_s expanded the parametric solutions to over 84 cases for developing the presented coupled SSI procedure for the generic 3-layered liquefaction lateral spread pile loading problem (see Figure 1).

3 COUPLED SOIL-PILE INTERACTION CONTINUUM MODEL

As shown in Figure 2, loading condition on the coupled soil-pile interaction model was introduced by prescribing a shear-beam mode ground displacement profile on the vertical outside boundaries of the FE mesh,

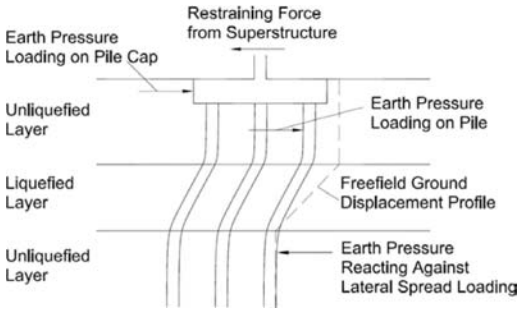

Figure 1. Three layer SSI liquefaction pile problem.

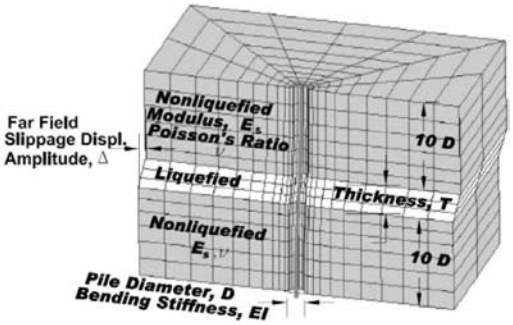

Figure 2. Parameters for coupled SSI FE model.

while the soil nodes inside the boundary nodes, especially nearfield to the pile are free to respond to the kinematic constraints of the pile. The amplitude of the ground slippage displacement, Δ boundary condition in Figure 2 is monotonically increased in analyses until a steady state solution is reached (i.e. when pile moment, curvature and pile shear become proportional to the amplitude of slippage displacement, Δ).

It should be pointed out that whereas a shear-beam formulation (spatial displacement only continuous for the first order) is valid for free field response of soil columns (i.e. without piles). Including the pile to a soil mass introduces kinematic effects of the pile, especially for nearfield soil nodes adjacent to the pile. A continuum SSI model such as the coupled model presented in this paper will implicitly account for the kinematic effect of the pile and its influence on the near field soils (i.e. pile deflections is continuous to the 4th derivative as oppose to at free field which is continuous to only the first order).

4 UNCOUPLED SOIL-PILE INTERACTION BEAM ON WINKLER SPRING MODEL

Latter part of this paper (Section 7) presents some comparisons between coupled soil-pile interaction model (proposed in this paper) with an uncoupled soil-pile interaction approach referred as beam on nonlinear

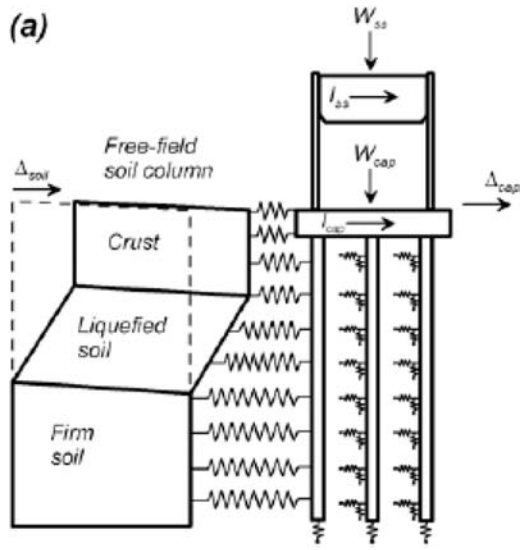

Figure 3. Uncoupled BNWS model.

Winkler spring Foundation (BNWF) as shown in Figure 3. In the uncoupled BNWF approach, separate analyses are conducted. Usually free field site response analyses are used to define the amplitude and the mode shape of ground displacements which are then prescribed at the ground nodes of a beam on Winkler spring model to solve for the pile response. Solutions for displacements are conducted ignoring the pile (resulting in the shear beam displacement mode shape). Also, most often, the Winkler springs are based on simplified approaches (e.g. Reese 1974 or Matlock 1970). There are inherent problems as discussed in Section 7 and the errors are quantified by comparing solutions between the two approaches.

5 SIMPLIFIED ANALYSIS PROCEDURE

Results from the 84 parametric solutions were compiled for developing the simplified procedure (Lam et al., 2009). The following outlines the procedure.

Step-1. Estimation of the relative slippage displacement amplitude, Δ, between the upper and the lower unliquefied layers is needed. This subject can become complex, but in this current context, any of the commonly used approaches (including empirical equations such as Youd et. al. 2002), or more refined approaches involving Newmark sliding block analyses in conjunction with the refinement of reducing the displacement amplitude reflecting pile pinning effects in a pile group (Martin et al., 2002) are all valid approaches and when properly used would be valid for design.

Step-2. Characteristic β Parameter. Lam et al (2009) compiled all the numerical solutions and found that there is a rational non-dimensional parameter useful

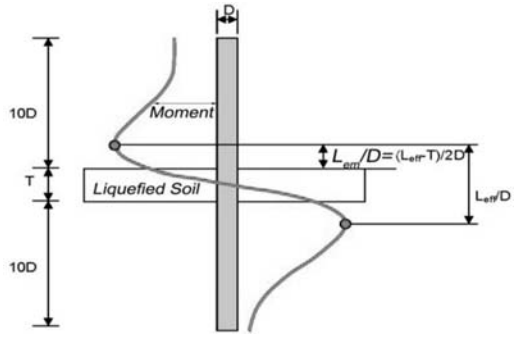

Figure 4. L_{em} *and* L_{eff} for maximum moment location.

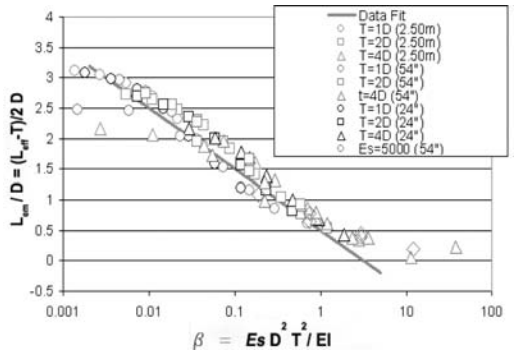

Figure 5. Solution for embedment depth, L_{em}.

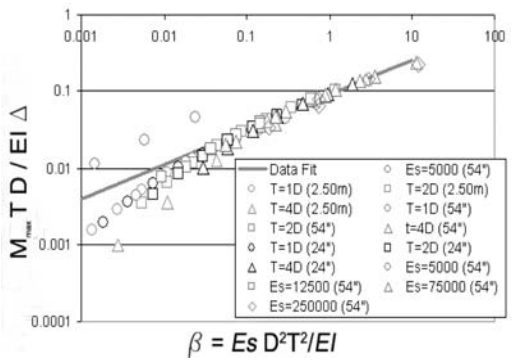

Figure 6. Maximum moment or curvature solutions.

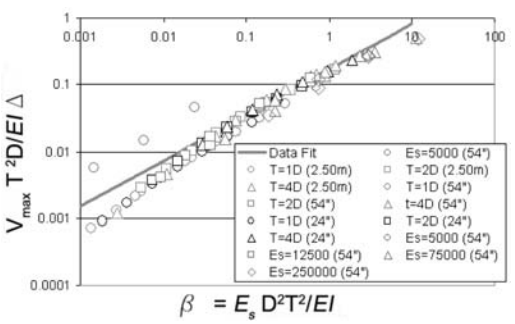

Figure 7. Maximum shear solutions.

for solving the generic 3-layer kinematic pile loading problem. This dimensionless parameter is defined as the characteristic soil-pile-liquefaction interaction parameter β by the following equation.

$$\beta = \frac{E_s T^2 D^2}{EI} \quad \text{.....(1)}$$

Step-3. Pile Solutions. After determining the characteristic β parameter, the next step involves estimating the location of the maximum pile moment above and below the boundaries of liquefaction, or to define the embedment depth L_{em} to the maximum pile moment locations shown in Figure 4.

Figure 5 can be used to develop the location of the maximum pile moment. Figure 6 can be used to develop the maximum moment or curvature and Figure 7 can be used to develop the maximum pile shear as a function of the estimated slippage displacement amplitude, Δ. As shown in Figures 5 through 7, when the solutions are plotted against the non-dimensional liquefaction soil-pile interaction parameter β, the solutions collapse to a rather narrow band of scatter which allowed the development of simplified equations for design. Simplified non-dimensional equations for location of maximum moment, and amplitudes of moment and shear, developed from best fit regression equations from the 84 sensitivity solutions shown in Figures 5, 6 and 7 are presented in Equations 2 through 4.

$$\frac{L_{em}}{D} = \frac{L_{eff} - T}{2D} = 0.5 - \log_{10}(\beta) \quad \text{.....(2)}$$

$$Moment\ Moment = M_{max} = 0.09\,\beta^{0.45}\,\frac{EI \cdot \Delta}{T \cdot D} \quad \text{.....(3)}$$

$$Moment\ Shear = V_{max} = 0.17\,\beta^{0.68}\,\frac{EI \cdot \Delta}{T^2 \cdot D} \quad \text{.....(4)}$$

6 COMPARISON TO FIXED-FIXED BEAM

Figure 8 presents the comparison between the coupled SSI solutions with the fixed-fixed beam model (still sometimes favored by structural engineers). For each of the case shown in Figure 8, the coupled FE solution is used to define the equivalent length L_{eff}. The ratio of moment from the coupled SSI solution versus the fixed-fixed beam equation is plotted against the β parameter in Figure 8. The fixed-fixed-beam equation over predicts pile moments by about ten times due to the fact that there is a significant degree of rotational compliance inherent in the coupled SSI solutions (see typical F.E. pile deflection solutions shown in the Figure 8 insert). One should recognize that a

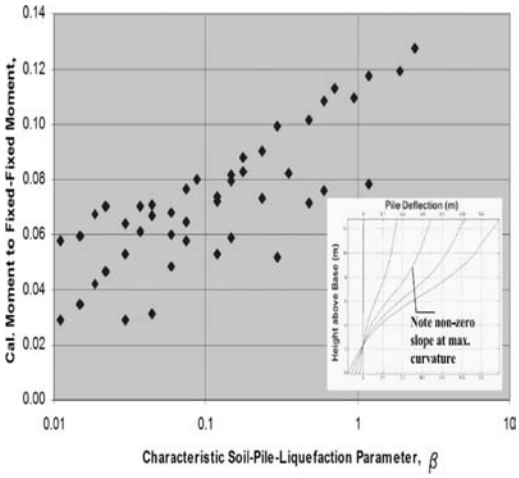

Figure 8. Moment solution vs. fixed-fixed beam.

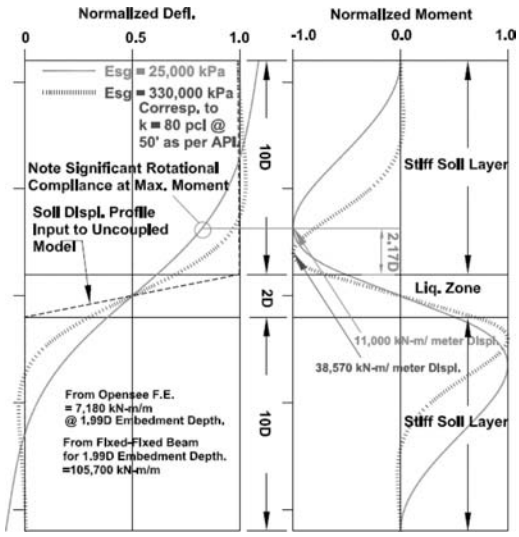

Figure 9. Coupled SSI vs. BNWS solutions.

fixed pile head implies an infinite rotational constrain, which requires the soil adjacent to the pile to have an infinite soil modulus (which is physically impossible). Recent pile to pile-cap structural details test data presented by Blandon (2007) revealed that even for the more rigid concrete pile-concrete deck connection details adopted for wharf facilities, there is a considerable degree of rotational compliance and the fixed head equation over predicts the pile head moment by sometimes a factor of 2. Considering that soils are much softer than concrete, it is easy to appreciate the gross error inherent in a fixed-fixed beam model.

7 COMPARISON TO UNCOUPLED BNWF

The inherent problem in the overly simplified fixed-fixed beam equation is easily recognized and nowadays, engineers (especially geotechnical engineers) favor the use of the more sophisticated approach for the kinematic pile loading problem such as the uncoupled beam on nonlinear Winkler spring (BNWF) approach schematically shown in Figure 4 (Boulanger, 1997 and Martin et al., 2002). As discussed earlier, the uncoupled SSI approach generally initiates from an independent free field displacement profile solution which is input to a nonlinear Winkler spring foundation (p-y) model.

Figure 9 presents comparisons between the couple SSI model with the corresponding BNWF model for a 24-inch diameter concrete pile. The dashed line on the left figure shows the displacement profile (with an assumed shear beam mode shape) prescribed at the ground nodes of the Winkler springs. The other ends of the Winkler springs are attached to the pile modeled as an elastic beam. The Winkler springs are assigned a zero stiffness value at the liquefied soil layer, but a constant subgrade modulus E_{sg} at the upper and the lower unliquefied soil layers for direct comparison to the linear elastic soil model in the coupled SSI approach. Two E_{sg} cases were analyzed for comparison to the OPENSEESS coupled SSI solution. The dotted lines represent solutions for an E_{sg} of 330,000 kPa (48,000 psi $= 50 \times 12 \times 80$) based on a typical coefficient of variation of subgrade modulus with depth, k of 21.7 MN/m^3, or 80 pci typical from conventional practice. The solid lines present solutions for an E_{sg} of 25,000 kPa (3,636 psi) which is identical to the soil modulus, E_s used for the FE solution based on Vesic's study that E_{sg} would be approximately equal to the elastic Young's modulus E_s. Maximum pile moment from the FE solution was estimated at 7,180 as compared to 38,570 and 11,000 kN-m per meter of slippage displacement for the stiff and soft E_{sg} cases, respectively.

The comparison showed that the uncoupled BNWF approach overestimated pile moments depending on the basis for the subgrade modulus, E_{sg}. The conventional empirical API p-y curve approach, especially the Reese's sand p-y curve criterion (1974) can potentially lead to grossly conservative kinematic pile moment solutions (38,570 kN-m as compared to 7,180 kN-m, or a variation of 5.37 times). It should be recognized that Reese (1974) and Matlock's p-y curve (1970) criteria relied on pile load test data at the upper 3 to 5 pile diameters from the ground surface and were originally developed for wave loading, placing more emphasis on the ultimate capacity portion of the p-y curves close to the mudline. The formulations on the initial moduli of p-y curves are most often deficient for extrapolation to larger depths relevant for the liquefaction kinematic pile loading problem. The softer E_{sg}, solid lines in Figure 9 provided the solution for an E_{sg} equal to the soil modulus E_s based on Vesic's (1961) theoretical study and would be a more valid basis for E_{sg} than conventional p-y curve procedures.

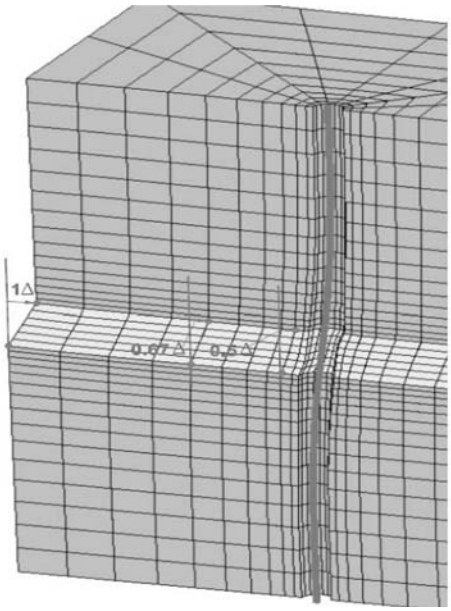

Figure 10. Changes in displacement profiles.

However, the solution still showed a significant error that it over-predicted the pile moment by over 50%. By observing that the solid line BNWF solution led to the location of maximum pile moment or a L_{em} at 2.17 D from the liquefaction interface as compared to the 1.99 D from the coupled FE solutions, one can argue that the E_{sg} of 25,000 kPa is already too stiff for a direct comparison to the coupled FE problem. It can be argue that the E_{sg} in the BNWF should be increased so that L_{em} matches the 1.99 D from the FE solution (implying the same characteristic length implicit in both solutions). This will imply an even larger error inherent in the BNWF model than 50%.

The reason for the inherent error in the BNWF model can be explained by examining the deformed mesh plot from the coupled FE solution as shown in Figure 10. One should realize that there is an important difference between how the displacement profile is used to load the pile between the coupled FE SSI and the BNWF model. The shear beam displacement profile is used as the prescribed displacement only at the side boundaries of the finite element mesh referred as far field soil nodes where a shear beam displacement function should be valid. However, as observed in the figure, the ground displacement profile changes progressively especially near the pile. For those soil nodes near the pile, there are progressive reductions in the relative displacement amplitude implying smoothening of the nearfield ground curvature. Such changes are due to the reinforcing (kinematic) effect of the pile as pile deflections would be continuous to the fourth derivative as compared to the free field shear beam formation where there is an implicit infinite curvature at the liquefaction interfaces. Such a reinforcing effect of the pile has been ignored by the BNWF model because of inherent complexities to account for the kinematics of the pile on the ground displacement function. The resultant effect is an overly conservative displacement function in the BNWF model regarding the implied ground curvature. The error in affecting pile moment increases for stiffer E_s associated with the deep seated liquefaction lateral-spread kinematic pile loading problem as compared to usually smaller E_s for softer soils for the shallower inertial pile loading problem.

It should be noted that conceptually one might be able to use a softer soil spring model in the BNWF solution to compensate for the overly conservative far-field free field ground curvature so as to result in a smaller pile moment. However, as can be observed in the coupled solutions (see Figures 5 through 7), the Winkler spring model needs to be adjusted depending on the pile bending stiffness, EI, diameter D, and liquefaction layer thickness T in order to achieve the correct L_{em} (shown in Figure 5) and the moment amplitude (shown in Figure 6). The comparison presented in Figure 9 illustrates that without rationalizing these factors for a proper Winkler spring model to compensate for shear beam displacement function (which does not account for the kinematic effect of the pile), the resultant pile moments are usually overly conservative and tend to penalize the use of large diameter piles.

The following lists some of the inherent problems in prescribing the shear beam displacement mode shape for the BNWF model for the liquefaction lateral spread problem:

- The approach usually results in an erroneous or ill-defined ground displacement (infinite) curva-ture nearfield to the pile inducing gross error to the pile moment solution.
- Current uncoupled BNWF models in arbitrarily prescribing the maximum moment location say at 2 D from the liquefaction interface without regards to pile diameter and other factors tend to penalize larger piles. Solutions from Figure 5 indicate that the location of maximum moment depends on many factors. A larger L_{em}/D is inherent for larger piles, smaller liquefied soil thickness T and softer soil modulus E_s.

8 MERITS IN THE PROPOSED PROCEDURE

The proposed method is simple and superior to most commonly used procedures. The shortcomings of some of the common methods have been discussed earlier and most of them over-predict the pile moment by a large extent especially penalizing the use of large diameter piles for liquefiable sites.

The soil-pile-liquefaction non-dimensional parameter β provides for a mechanistically sound way to account for the kinematic effects of the soil-pile interaction problem for the three layered soil-pile liquefaction interaction problem. By way of the characteristic SSI liquefaction parameter β, interaction among key

design parameters can be factored into design, including: pile diameter D, pile bending stiffness EI, soil modulus, E_s and liquefied layer thickness, T based on rational mechanistic principals. Through the use of this non-dimensional parameter β, designers can make more rational judgment in pile selection.

The OPENSEESS solutions presented in this paper were intended for developing an initial framework to improve current liquefaction design practice. Additional research will lead to further refinements, including:

- Extension to nonlinear moment-curvature relations of the pile should lead to increases in the displacement capacity of the pile as a function of inelastic structural strain following performance based engineering principals.
- Extending to a wider class of boundary conditions (e.g. pile group and pile spacing effects and closer free field ground surface to the liquefaction zone) is expected to reduce the pile moment, especially for larger diameter piles etc.
- Refinement in the soil model, especially softening of the soils in the unliquefied soil adjacent to the high pore pressure zone of the liquefied soil mass can reduce the pile moment or curvature.
- The above refinements should result in lower pile moments and should lead to more cost effective foundations for liquefied sites.

ACKNOWLEDGEMENT

This work was supported primarily by the Earthquake Engineering Research Centers Program of the National Science Foundation under award number EEC-9701568 through the Pacific Earthquake Engineering Research Center (PEER). Their financial support is gratefully acknowledged.

REFERENCES

Blandon, C.A. (2007) Seismic Analysis and Design of Pile Supported Wharfs, *Ph.D. Thesis*, Rose School of Engineering, Pavia, Italy, October, 2007.

Lam, I.P., Arduino, P. and Mackenzie-Helnwein, P., (2007) "OPENSEES Soil-Pile Interaction Study under Lateral Spread Loading", *Final Report to PEER, November 30, 2007, U.C. Berkeley Agreement No. SA5628-23584*, Purchase Order No. 1291149.

Lam, I.P., Arduino, P. and Mackenzie-Helnwein, P., (2009) "OPENSEES Soil-Pile Interaction Study under Lateral Spread Loading", *ASCE Geotechnical Special Publication No. 186*, pp. 206–213.

Martin, G.R., Marsh, M.L., Anderson, D.G., Mayes, R.L. and Power, M.S. (2002). "Recommended design approach for liquefaction induced lateral spreads." *Proc. 3rd National Seismic Conf. And Workshop on Bridges and Highways*, MCEER-02-SP04, Buffalo, NY.

Matlock, Hudson, 1970, "Correlations for Design of Laterally Loaded Piles in Soft Clay," *Proceedings, Second Annual Offshore Technology Conference*, Paper No. 1204, Houston, Texas, April 22–24.

Reese, L.C., Cox, W.R., and Koop, F.D., 1974. "Analysis of Laterally Loaded Piles in Sand," *Proceedings, Sixth Annual Offshore Technology Conference*, Vol. 2, Paper No. 2080, Houston, Texas.

Vesic, A. (1961) "Beam on Elastic Foundations", *Proceedings, 5th ICSMFE*, Paris, Vol. 2:1, pp. 24–28.

Youd, T.L., Hansen, C.M. and Barlett, S.F. (2002). "Revised MLR equations for prediction of lateral spread displacement", *J. Geotechnical Geoenviron. Eng*. 129(12).

Soil-Foundation-Structure Interaction – Orense, Chouw & Pender (eds)
© 2010 Taylor & Francis Group, London, ISBN 978-0-415-60040-8

Significance of interaction and non-linearity in piled raft foundation design

H.G. Poulos
Coffey Geotechnics, Sydney, Australia

ABSTRACT: This paper sets out a procedure for the analysis of piled raft foundation systems. It is based on an elastic formulation initially, but makes approximate allowances for non-linear raft behaviour by imposing an upper limit on the contact pressure between the raft and the underlying soil, and for nonlinear pile behaviour by assuming that the pile behaviour can be characterized by a hyperbolic load-settlement curve. It also makes approximate allowances for the various components of interaction within the foundation system. Examples are given to demonstrate the importance of taking non-linearity and pile-raft interaction into account with respect to settlement, differential settlement, pile load distribution and raft bending moments.

1 INTRODUCTION

The benefits of using piled raft foundations have become more widely recognised in recent years, since both the raft and the piles can provide bearing support as well as contributing towards settlement reduction. The most suitable ground conditions for the use of piled rafts are those where the soil is reasonably stiff at the surface.

Various methods of analysis of piled rafts have been developed, including the finite layer methods of Small and Zhang (2002), and Chow and Small (2005), the approximate boundary element methods employed by Poulos (1994), and the method of Clancy and Randolph (1993) that combines finite element analysis for the raft and analytic solutions for the piles. The approach of Kitiyodom and Matsumoto (2003) considers both axial and lateral loads.

Finite element analyses have been presented by Katzenbach and Reul (1997) who incorporated non-linear behaviour for the soil into the analysis. Prakoso and Kulhawy (2001) used a two-dimensional finite element model to predict piled raft performance. Reul and Randolph (2003) have also presented a three-dimensional analysis of piled rafts in the over-consolidated Frankfurt clays, and made comparisons with measured behaviour. While finite element analyses allow complex geometries and soil behaviour to be modelled, there is a significant amount of effort required to set up meshes, especially when there are large numbers of piles and they are not suitable for practical design purposes, where the number of piles and their location may have to be altered several times.

Combinations of finite element analysis of the raft and analytical or semi-analytical methods for the piles and soil are attractive because of the speed of solution. Small and Poulos (2007) describe such a method which is implemented via the computer program GARP (Geotechnical Analysis of Rafts with Piles) and combines finite element analysis for the raft, with a boundary element analysis for the piles. This program is used in this paper to explore the significance of two aspects of piled raft analysis:

1. The non-linearity of pile and raft behaviour;
2. The importance of including the various components of interaction within the analysis.

The program GARP will be used to analyse a case which is deliberately simplified so that behavioural trends are not masked by practical complications. Examples of comparison between GARP and measured foundation behaviour are given by Poulos et al (1997) and Poulos (2001).

2 FEATURES OF THE GARP PROGRAM

In the GARP analysis, the contact pressure between the raft and the soil is assumed to be made up of uniform blocks of pressure that correspond to the elements of the raft. These are divided into eight-noded isoparametric thin shell elements which are rectangular in shape, and so the uniform blocks of pressure are also rectangular.

The piles are located at the nodes of the finite element mesh for the raft and are assumed to provide a point load acting upward at the node. In order to solve the interaction problem, the unknown loads acting on each of the piles, and the unknown contact pressures acting on each raft element, need to be obtained.

Non-linear behaviour of the piles is modelled by reducing the stiffness of the pile in an incremental fashion as load is increased. This is done approximately by using a hyperbolic function to fit the pile load-deflection behaviour up to failure. The tangent stiffness, K, of the pile head is expressed as follows:

$$K = K_i[1 - R_f (P/P_u)]^2 \quad (1)$$

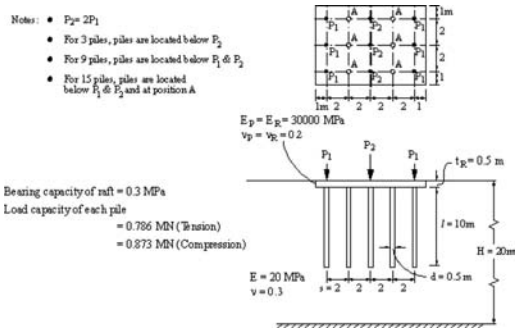

Figure 1. Example analyzed.

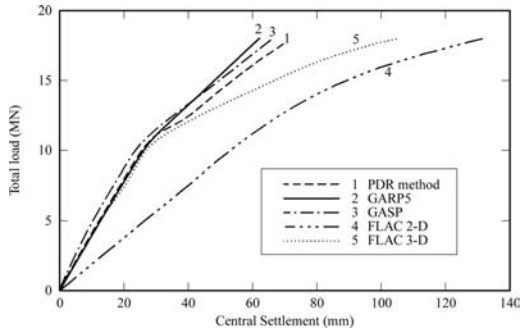

Figure 2. Computed load-settlement curves from various analyses.

where K_i = initial tangent stiffness, R_f = hyperbolic factor, P = load on pile head, P_u = ultimate load capacity of pile.

The stiffness of an individual pile in the group is therefore decreased as the load level increases towards the ultimate load. For the raft, a limiting contact pressure is specified in both compression and tension. When the elastic analysis gives a contact pressure at a raft element that exceeds these limiting values, the pressure on that element is set to the limiting value. This is a simplistic approach but at least provides some indication of non-linear behaviour of the raft.

There are four components of interaction that are considered in the analysis:

1. Raft elements interaction with other raft elements;
2. Piles interacting with piles;
3. Raft elements interacting with piles;
4. Piles interacting with raft elements;

GARP considers all four components of interaction, albeit approximately. Raft-raft interaction is computed via elastic theory for uniformly loaded areas on a layered elastic medium, while pile-pile interaction employs superposition of two-pile interaction factors. Raft-pile interaction is approximated by considering the displacements due to raft elements at a representative depth along each pile (typically one-third of the pile length). Finally, pile-raft interaction is approximated by again using two-pile interaction factors. When simulating the effect of this pile on the settlement of other piles within the system and on the raft, interaction is only assumed to be applied to the elastic component of the settlement, as per the approach described by Mandolini and Viggiani (1997).

As will be shown later in this paper, consideration of all four interactions is necessary to avoid obtaining misleading, and unconservative, results.

3 APPLICATION TO SIMPLIFIED PROBLEM

3.1 *The problem considered*

In order to compare the predicted behaviour of a piled raft from a number of different methods, the hypothetical example in Figure 1 has been analyzed (Poulos et al, 1997). While the problem is rather simplistic, it is useful in that the inevitable differences which are involved in the assessment of parameters in real cases are avoided, and the problem involves column loading rather than merely uniformly distributed loading. The comparisons focus on the predicted behaviour of the piled raft for a given set of soil, pile and raft parameters. However, some consideration is also given to the influence on the foundation behaviour of some of the pile and raft parameters.

A variety of methods has been used to analyze this problem, as follows:

1. The simplified Poulos-Davis-Randolph (PDR) method, described by Poulos (2002);
2. The program GASP, for a strip on ground supported by piles;
3. The program GARP, as described in the previous section;
4. The FLAC2D analysis, a finite difference analysis in which plane strain conditions are assumed and the piles and loads are "smeared" over a 6 m width. The soil was modeled as a Mohr Coulomb material;
5. The FLAC3D analysis, a full three dimensional finite difference analysis in which solid elements are used to model the piles, the raft and the soil with the latter again being modeled as a Mohr Coulomb material.

3.2 *Load-settlement behaviour*

Figure 2 compares the computed load-settlement relationships (up to a total load of 18 MN) computed from a variety of methods for the centre of the raft with 9 identical piles, one under each column. There is reasonably good agreement between the computed load-settlement curves from all methods, other than the FLAC2-D analysis. Even the simple Poulos-Davis-Randolph method gives results which agree reasonably with the FLAC3-D and GARP analyses. The FLAC3-D analysis gives a softer response than the other methods for loads in excess of about 12 MN, presumably because of the progressive development of plastic zones beneath the raft, and the consequent increasing importance of plastic deformations.

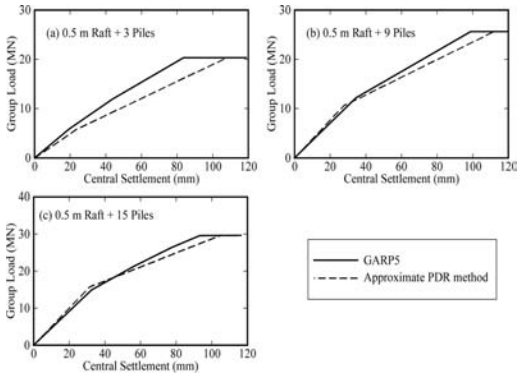

Figure 3. Comparison between GARP and approximate analyses.

However, the FLAC2-D analysis seriously over-predicts the settlements because of the implicit assumption of plane strain in the analysis. The comparisons in Figure 2 therefore suggest that plane strain analyses of piled rafts must be approached with extreme caution because the results may be misleading if the raft is essentially square or rectangular.

The importance of non-linearity can be seen from Figure 2, in that, when the load capacity of the piles is fully utilized, the load-settlement behavior reflects that of the raft, which is much less stiff than the combined pile-raft system. Assumption of linear behaviour beyond a load of about 10 MN could lead to significant under-estimation of the settlements.

Figure 3 compares load-settlement curves obtained from GARP and from the simplified PDR method, for a raft with 3, 9 and 15 piles. The agreement is relatively good in all cases, and Figure 3 again emphasizes the importance of considering the "softer" behavior after full mobilization of the pile capacity.

Figures 2 and 3 demonstrate that an analysis which accounts for non-linearity, despite that fact that it may be approximate, is preferable to a complex analysis in which linear behavior is assumed and inappropriate assumptions such as plane strain behaviour, are made.

3.3 *The importance of interaction effects*

The above analyses have indicated the importance of incorporating nonlinear behavior of the piles and the raft on the computed load-settlement behavior. Another critical factor that influences the computed behavior is the interaction among the various components of the piled raft system. The significance of interaction effects has been examined by considering the case of a piled raft with 9 piles, and obtaining solutions from GARP for the following cases:

1. A linear analysis taking account of all four components of interaction (raft-raft, raft-pile, pile-raft and pile-pile) – Case 1;
2. A non-linear analysis taking account of all four components of interaction – Case 2;

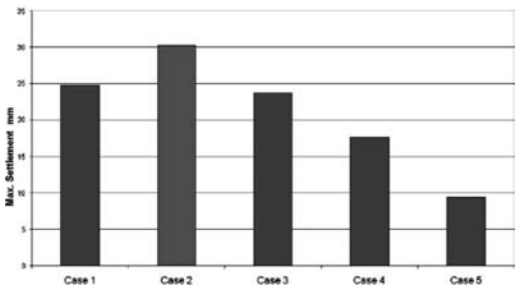

Figure 4. Effect of analysis type on computed maximum settlement – raft with 9 piles.

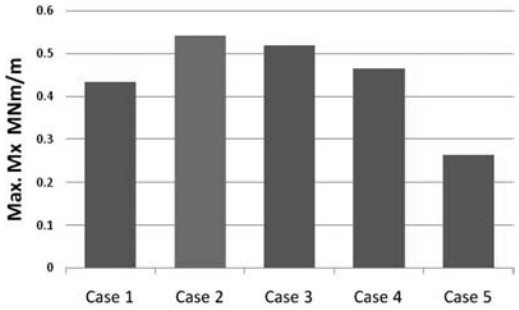

Figure 5. Effect of analysis assumptions on maximum raft moment in x-direction.

3. A non-linear analysis taking account of only pile-pile interaction – Case 3;
4. A non-linear analysis taking no account of any of the components of interaction – Case 4;
5. A linear analysis taking no account of any of the components of interaction – Case 5.

For a factor of safety of 2.5 against vertical bearing failure, Figure 4 compares the maximum computed settlements for the above five cases. Case 2 is the most complete and correct analysis. The computed settlement from the linear analyses is smaller than that from the non-linear analyses, and if the four components of interaction are ignored (Case 5), the computed settlement is less than one-third of that from a non-linear analysis in which the interactions are properly accounted for. Such an under-estimation of settlement could clearly have serious consequences.

Figure 5 compares computed values of the maximum moment in the raft in the x-direction, using various assumptions about linearity and interaction (Cases 1 to 5 above). Ignoring non-linearity and interaction leads again to an under-estimate of the bending moment and is therefore unconservative.

This is particularly so if both non-linear and interaction effects are not taken into account.

The computed maximum pile loads for the various analysis assumptions are shown in Figure 6. Ignoring non-linearity and interaction effects leads to a considerable over-estimation of the maximum pile load. It also leads to an over-estimation of the proportion of load carried by the piles, as shown in Figure 7.

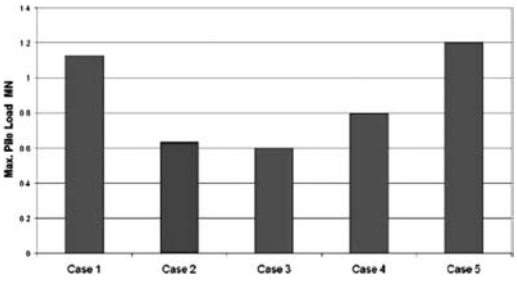

Figure 6. Effect of analysis assumptions on maximum pile load.

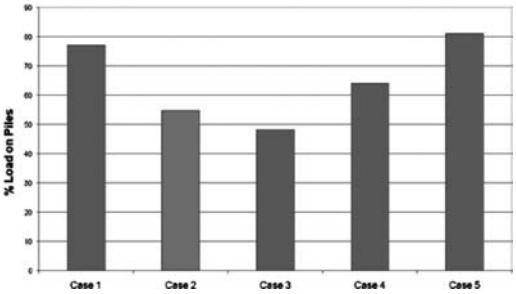

Figure 7. Effect of analysis assumptions on proportion of pile load.

4 APPLICATION TO HIGH-RISE TOWER IN QATAR

4.1 *Introduction*

A 510 m tall tower in Doha Qatar is to be constructed on a piled raft foundation, and analyses were undertaken to estimate the long-term foundation settlement behaviour. The foundation system consisted of a total of 525 piles, with diameters ranging between 1.0 and 1.5 m, and lengths ranging from 8 to 42 m. The piles were located beneath a raft 4 m thick over most of the building footprint, with thickened areas below the lift over-run and core wall areas, up to 12.7 m thick. The raft for the podium area outside the tower footprint was 0.8 m thick.

4.2 *Geotechnical profile and model*

The soil profile consisted of three key strata:

- A relatively strong limestone layer extending about 3.5 m below the base of the raft;
- A relatively strong shale layer about 3 m thick;
- A relatively weak chalk layer about 75 m thick, becoming stronger at a depth of about 80 m below the base of the raft.

Table 1 summarises the soil profile and the geotechnical design parameters selected for the site. These parameters were from previous experience with similar projects in Doha, and were checked against the results of Osterberg cell pile load tests carried out on 3 test piles.

Table 1. Geotechnical profile and parameters.

Stratum	Thickness m	Long-Term Young's Modulus MPa	Skin Friction kPa	End Bearing MPa
Limestone	3.5	2500	600	–
Shale	3.0	700	525	–
Chalk	75.5	500	425	5.9
Chalk	>50	1000	–	–

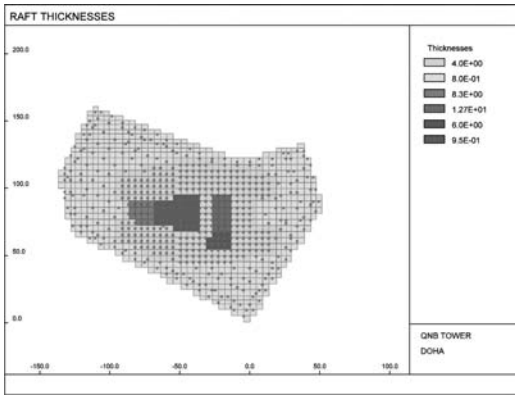

Figure 8. Mesh employed for GARP analysis.

4.3 *Analysis procedure*

The program GARP was employed for the settlement analysis. The foundation model employed consisted of 945 elements for the raft and 3006 nodes, and is shown in Figure 8 which sets out the various raft thicknesses and pile locations. The original design analyses were undertaken using a non-linear analysis and taking into account all four components of interaction within the foundation system (raft-raft, pile-pile, raft-pile, pile-raft). Subsequently, additional analyses were undertaken to examine the influence that the analysis assumptions had on the computed settlements and the foundation behaviour.

In all, four different assumptions were used:

1. A full non-linear analysis considering all interactions (Case A);
2. A linear analysis considering all interactions (Case B);
3. A linear analysis considering only pile-pile interactions but no pile-raft or raft-pile interactions (Case C);
4. A linear analysis considering no interactions (Case D).

The applied loading was that for full dead plus live loading. The loading pattern was complex and consisted of 240 point loads, 11 sets of moments and 11 areas of uniformly distributed load. The total load applied was about 8006 MN, which represented a load level of about 13% of the estimated ultimate static vertical load capacity of approximately 61000 MN. This

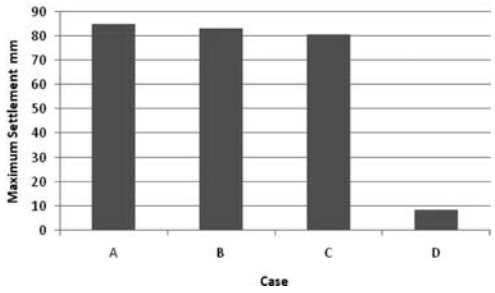

Figure 9. Maximum settlement for various cases.

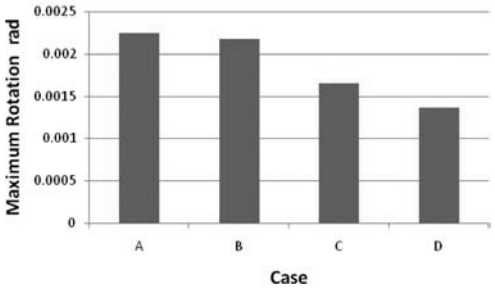

Figure 10. Maximum rotation for various cases.

Table 2. Summary of Computed Foundation Behaviour.

Case	Max. Moment M_x MNm/m	Max. Moment M_y MNm/m	Max. Pile Load MN
A	124.8	295.9	46.5
B	125.8	293.6	59.9
C	125.7	294.7	63.7
D	107.3	203.0	63.9

is clearly a much lower load level than in the simple example described in Section 3 above.

For the piles, a hyperbolic factor Rf of 0.74 was used.

Figures 9 and 10 summarise the computed maximum settlements and rotations from these four analyses, while Table 2 summarises various aspects of the raft and pile behaviour.

From these figures and Table 2, the following observations can be made:

1. The computed behaviour from the linear analysis with all interactions considered (Case B) is very similar to the corresponding non-linear analysis (Case A), i.e. in this case, non-linearity does not play a major role in the foundation performance under serviceability conditions.
2. In this case, ignoring raft-pile and pile-raft interactions (Case 3) gives similar results to Cases A and B.
3. Ignoring all interactions (Case D) leads to a very serious under-estimate of the settlement, by a factor of about 10.
4. The maximum rotation for Case D is also less than in the other cases.

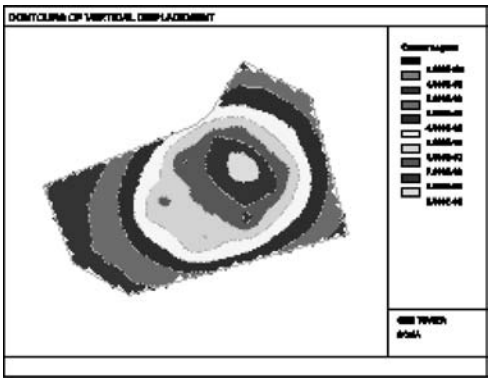

Figure 11. Settlement contours for Case A (all interactions considered).

5. The maximum pile loads from the linear analyses (Cases B, C and D) are all significantly higher than from the full non-linear analysis (Case A). In this case, ignoring non-linearity would result in the piles having to be designed structurally to resist a load that is more than 38% greater than in the non-linear analysis.
6. If interaction effects are ignored, as in Case D, then the computed bending moments are significantly less than those from analyses in which interactions are taken into account.

A further consequence of ignoring interaction in the analysis is that the pattern of settlement across the foundation becomes very localized. This is illustrated by comparing the settlement contours for Cases A and D in Figures 11 and 12 respectively. For Case A in Figure 11, the interaction effects result in an overall "dishing" of the foundation and in relatively large settlements. In contrast, for Case D (Figure 12) in which interaction is ignored, the settlements are highly localized around the areas of largest load, and the magnitude of the settlements is much smaller than for Case A.

Figure 13 shows computed settlement profiles across a longitudinal section of the foundation for Cases A and D. The characteristics noted from the settlement contours in Figures 11 and 12 are even more starkly evident in these figures.

In summary, for the tall building analysed here, non-linear effects are not of major importance because the factor of safety against overall failure is relatively large (approximately 7.6). However, the effects of interaction are of major importance, and ignoring these effects leads to serious under-estimates of settlement and raft moments, and such under-estimates are unconservative. In contrast, ignoring interaction leads to over-estimates of the pile loads and thus to over-design of the requirements for structural strength of the piles.

5 CONCLUSIONS

This paper has examined the importance of considering the various interactions within a piled raft system and taking account of the non-linearity of foundation

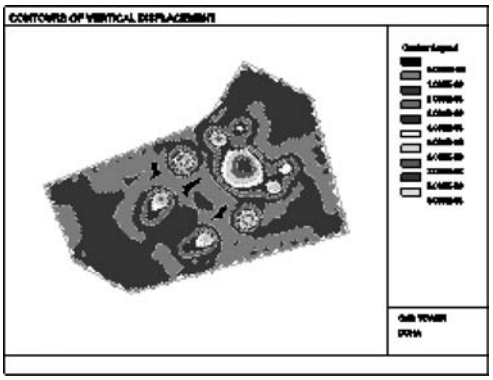

Figure 12. Settlement contours for Case D (no interactions considered).

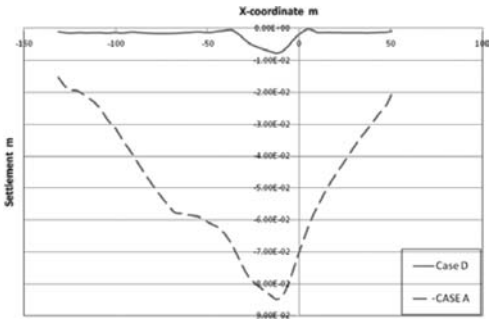

Figure 13. Settlement profiles across the foundation for Cases A and D.

behaviour. Ignoring either of these factors can lead to inaccurate predictions of foundation settlement and structural actions within the system.

The most critical aspect of interaction that must be considered is pile-pile interaction, and ignoring this aspect can lead to serious under-predictions of settlement and raft bending moments.

Non-linearity becomes increasingly important as the applied load level increases. For piled rafts designed with the "creep piling" philosophy in which the piles operate at a relatively low factor of safety (Randolph, 1994), non-linear behaviour of the piles must be taken into account. For more conventional foundation design, such as for the Qatar tall building analysed herein, the serviceability load level is relatively low in relation to the ultimate load capacity, and hence non-linearity is less important. However, for such buildings which are founded on large numbers of piles, consideration of interaction among the raft and piles is critical if meaningful estimates of settlement and structural actions (raft moments and shears, and pile loads) are to be obtained.

It is clear that structural analyses which model the piles as springs may be in serious error if the effects of interaction are not taken into account. Thus, simply adopting the stiffness from a test pile, without considering interaction effects, is a dangerous practice that must be avoided. The most satisfactory approach is for the spring stiffness values to be obtained from a geotechnical analysis such as GARP, and then provided to the structural analyst to be incorporated into the overall structural model. Close cooperation between structural and geotechnical specialists assists greatly in avoiding the embarrassment of seriously under-predicting settlements and structural actions in the raft.

ACKNOWLEDGEMENTS

The author is indebted to his colleagues at Coffey Geotechnics for their efforts in analysing the building described herein, in particular, Frances Badelow, Tristan McWilliam, Helen Chow and John Small.

REFERENCES

Chow, H.S.W. and Small, J.C. 2005. Finite layer analysis of combined pile-raft foundations with piles of different lengths. *Proceedings of the 11th IACMAG (International Conference on Computer Methods and Advances in Geomechanics)*, June 19–24, Turin, Italy, 2005, Editors Giovanni Barla and Marco Barla, Patron Editore (pub.). 2, 429–436.

Clancy, P. and Randolph, M.F. 1993. An approximate analysis procedure for piled raft foundations. *Int. Jl. For Numerical and Analytical Methods in Geomechanics.* 17(12), 849–869.

Katzenbach, R. and Reul, O. 1997. Design and performance of piled rafts. *Proc. of XIVth ICSMFE 97*, Hamburg. 4, 2253–2256.

Kitiyodom, P. and Matsumoto, T. 2003. A simplified analysis method for piled raft foundations in non-homogeneous soils. *Int. Jl. Numerical and Analytical Methods in Geomechanics*. 27, 85–109.

Mandolini, A. & Viggiani, C. 1997. Settlement of piled foundations. *Géotechnique*, 47(4): 791–816.

Prakoso, W.A. and Kulhawy, F.H. 2001. Contribution to piled raft foundation design. *Jl. Geotechnical and GeoEnvironmental Engng., ASCE.* 127(1), 17–24.

Poulos, H.G., 1994. An approximate numerical analysis of pile-raft interaction. *Int. Jl. Num. Anal. Methods in Geomechs.*, 18: 73–92.

Poulos, H.G. 2001. Piled raft foundations: design and applications. *Geotechnique* 51(2): 95–113.

Poulos, H.G. and Davis, E.H. 1980. *Pile foundation analysis and design.* Wiley, New York.

Poulos, H.G., Small, J.C., Ta, L.D., Sinha, J. and Chen, L.T. 1997. Comparison of some methods for analysis of piled rafts. *Proc. 14th Int. Conf. Soil Mechs. Found. Eng., Hamburg, Balkema, Rotterdam*, 2: 1119–1124.

Randolph, M.F. 1994. Design methods for pile groups and piled rafts. *Proc. 13th Int. Conf. S.M. & Found. Eng.*, 5: 61–82.

Reul, O. and Randolph, M.F. 2003. Piled rafts in overconsolidated clay: comparison of in situ measurements and numerical analyses. *Géotechnique.* 53(3), 301–315.

Small, J.C. and Poulos, H.G. 2007. A method of analysis of piled rafts. *Proc. 10th Australia-New Zealand Conf. Geomechanics*, Brisbane, 1: 55–555.

Small, J.C. and Zhang, H.H. 2002. Behaviour of piled raft foundations under lateral and vertical loading. *International Journal of Geomechanics.* 2(1), 29–45.

Soil-Foundation-Structure Interaction – Orense, Chouw & Pender (eds)
© 2010 Taylor & Francis Group, London, ISBN 978-0-415-60040-8

Soil-foundation-structure interaction considerations for performance-based design of RC wall structures on shallow foundations

T.J. Sullivan
University of Pavia, Pavia, Italy

S. Salawdeh
MEEES Graduate, Pavia, Italy

A. Pecker
Géodynamique et Structure, Bagneux, France

M. Corigliano & G.M. Calvi
EUCENTRE, Pavia, Italy

ABSTRACT: Modern earthquake engineering appears to be embracing the concepts of performance-based seismic design. This is becoming possible because the past decade has seen the development of a range of tools for performance-based seismic design, including the direct displacement-based design method. Much of the developments made to date, however, have focused on the performance-based design of structures without consideration of soil-foundation structure interaction. In this work a number of SFSI considerations are made for performance-based design of reinforced concrete wall structures on shallow foundations. In particular, possible performance criteria for foundation systems are discussed, existing methods of accounting for SFSI in seismic design are reviewed and a new Direct DBD procedure to account for SFSI in RC wall structures is proposed. The design procedure is applied to a number of case study structures to highlight the impact of SFSI on design requirements, and trends are compared with force-based design solutions.

1 INTRODUCTION

1.1 *Performance-based seismic design*

Modern earthquake engineering appears to be embracing the concepts of performance-based seismic design. The aim of performance based seismic design (PBD) procedures is essentially to offer engineers an effective means of controlling the risk posed by earthquakes. As part of a PBD process, engineers ensure that certain performance levels (or damage states) are satisfied for different design ground motion intensities, such as those proposed in the PBD matrix of Table 1. With knowledge of the probability of exceedence of a given ground motion, the engineer can control the risk posed by an earthquake, provided that they can successfully limit the structural response under a given ground motion to the prescribed performance limits.

Values of strain and storey drift are commonly used as structural performance limits for different performance levels such as the Serviceability limit state or the Damage-control limit state (eg. see SEAOC 1997, Priestley et al. 2007). This trend reflects the fact that deformations, rather than forces, are most closely correlated to structural damage. However, other parameters (such as floor accelerations in museums or galleries) can also be specified within a PBD approach if such parameters could impact on the building performance.

Table 1. Performance-based design matrix (adapted from Priestley et al. 2007) specifying the design intensity or probability of exceedence of different levels of damage for different categories of structure.

	Earthquake Design Level		
Importance Class*	Level 1	Level 2	Level 3
I	Not Required	50% in 50 years	10% in 50 years
II	50% in 50 years	10% in 50 years	2% in 50 years
III	20% in 50 years	4% in 50 years	1% in 50 years
IV	10% in 50 years	2% in 50 years	1% in 50 years

* Structures are categorized from Class I (low importance to public) through to Class IV (very high importance to public).

Table 2. Preliminary performance criteria proposed for foundation and retaining structures in Draft Model Code for DBD (Calvi & Sullivan, 2009).

	Performance Level		
Soil System	Level 1	Level 2	Level 3
Foundation Structures	γ such that $G/G_{max} \geq 0.80$	γ such that $G/G_{max} \geq 0.20$	γ such that $G/G_{max} > 0.20$
Retaining Structures Distant from Buildings	γ such that $G/G_{max} \geq 0.40$	γ such that $G/G_{max} \geq 0.20$	γ such that $G/G_{max} > 0.20$

1.2 *How should foundations perform?*

The notion of setting performance limit states for foundation systems raises some interesting questions; *What defines a Serviceability limit state and a Damage-Control limit state for soil structures?* and *What should constitute "acceptable performance" of foundation systems?* As part of a recent research project undertaken in Italy, referred to as the RELUIS project (www.reluis.it), the preliminary deformation limits presented in Table 2 have been proposed (Calvi & Sullivan, 2009) as performance criteria for soils in foundation and retaining systems.

The strain limits proposed in Table 2 are defined as a function of a G/G_{max} ratio. This ratio refers to the soil-foundation interface, and does not suppose that engineers can control the soil strains imposed by the passage of seismic waves. The G/G_{max} limits should be considered equivalent to limits in the allowable reduction in foundation stiffness, although the relation between G and K is not linear and the direct specification of foundation stiffness reduction limits may be more appropriate. Note that the elastic dynamic rotational stiffness, $K_{f,0}$, of shallow rectangular foundations about their lateral axis can be approximated as (Gazetas, 1991):

$$K_{f,0} = \frac{G}{1-\nu} I_y^{0.75} \left[3 \left(\frac{L}{B} \right)^{0.15} \right] \quad (1)$$

where ν is Poisson's ratio for the soil, I_y is the area moment of inertia of the foundation-soil contact surface around the lateral axis, L is the footing length and B is the footing width. During intense seismic response the rotational stiffness of a foundation will reduce and Paolucci et al. (2009) have developed curves, such as that shown in Figure 1, to relate the rotation of shallow foundations on dense sand or medium dense sand to an equivalent reduction in foundation stiffness.

Using a stiffness reduction limit (such as those in Table 2), designers can therefore identify maximum allowable foundation rotations for certain performance limit states.

One could question the logic of using the foundation stiffness reduction limits for different performance states. The motivation for the limits set in Table 2 was principally to ensure similar levels of non-linear

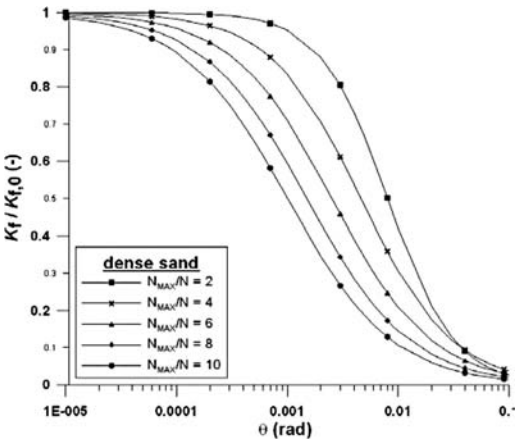

Figure 1. Curves of rotational stiffness as a function of foundation rotation and axial load ratio for shallow foundations on dense sand, as developed by Paolucci et al. (2009).

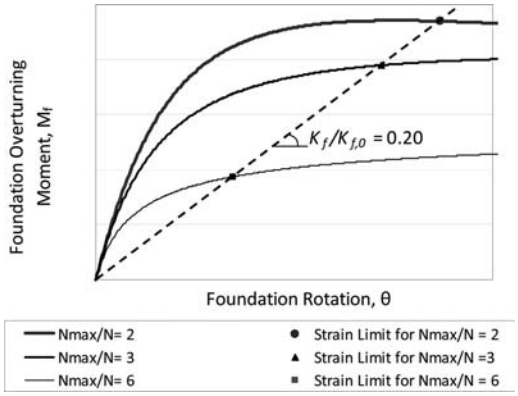

Figure 2. Moment-rotation response of three different shallow foundations on dense sand, characterized by the same initial stiffness, K_{f0}, but subject to different axial load ratios, N_{max}/N.

behavior for systems with different axial load ratio. Figure 2 shows the moment-rotation response developed using the curves of Figure 1 for three different foundation systems possessing the same initial stiffness ($K_{f,0}$) but subject to different axial load ratios (N_{max}/N). Included in the plots are the points on the moment-rotation curve associated with the damage control strain limit (Performance Level 2 of Table 2). Note that the use of a limiting stiffness reduction ratio implies different allowable foundation rotation for the three axial load ratios examined.

However, if one were to consider the residual foundation rotation as a performance requirement, the performance of the three different foundations shown in Figure 2 could be very different, even though the stiffness reduction is constant.

There are still some doubts therefore as to *what defines acceptable foundation behavior?* This question should be a point for discussion and agreement

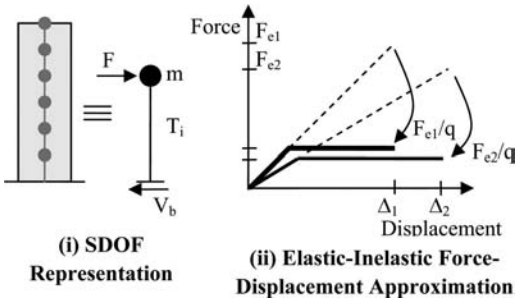

Figure 3. Two important force-based design steps: (i) Equivalent SDOF representation and (ii) Use of a force-reduction or behaviour factor to correlate elastic and inelastic force levels.

in the engineering community. Two important criteria should be that foundations are designed to avoid collapse due to overturning in extreme events and that residual deformations are limited for serviceability and damage-control performance levels. Collapse prevention could be considered a capacity design issue and limits could be set on foundation moment ratio for the collapse prevention state. Research into residual deformations is on-going, but there are still a number of questions as to appropriate residual deformation limits, particularly for vertical settlements that can be significant for shallow foundation systems.

1.3 *Considering SFSI in traditional force-based seismic design methods*

Despite increasing awareness that structural and non-structural damage under seismic attack can be directly related to the deformations imposed by the earthquake, the design approach in current codes is still largely based on force (and hence acceleration) rather than displacement. As demonstrated by Priestley (1993) and Priestley et al. (2007), there are several conceptual drawbacks associated with the use of force-based methods in seismic design, even when concepts of ductility capacity are included.

The main steps of the equivalent-lateral force method can be described with reference to Figures 3 and 4. The first step is to estimate the fundamental period of vibration for the building (left side Fig. 3), which is then used to read off an elastic design acceleration from a code-defined design spectrum (Fig. 4). The design base shear is then found by multiplying the design acceleration by the participating mass of the structure and dividing by a force-reduction factor that considers the ductility capacity of the structure (right side Fig. 3).

The simplest form of the FBD approach uses height-dependent period expressions for the structure, independent of foundation characteristics. If the building period is estimated with account for foundation flexibility, design forces will typically be lower, since lower spectral accelerations are obtained (Fig. 4) which are reduced by a constant behaviour factor to obtain

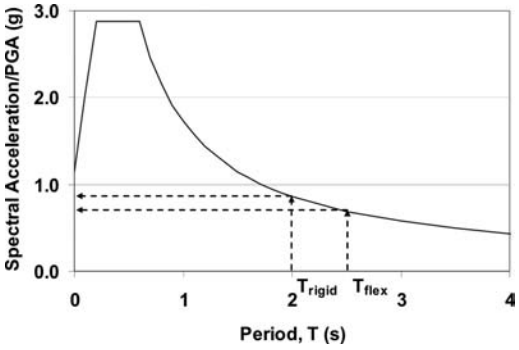

Figure 4. Design acceleration response spectrum, with indication of effect of foundation flexibility on elastic spectral acceleration highlighted considering period of rigid-base (T_{rigid}) versus flexible base (T_{flex}) structure.

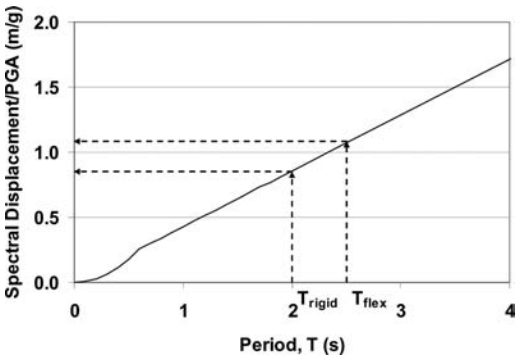

Figure 5. Design displacement response spectrum, with indication of elastic spectral displacements for rigid-base (T_{rigid}) versus flexible base (T_{flex}) structure.

design forces (see right side of Fig. 3). This observation has lead to the idea that SFSI can be conservatively ignored. Figure 5 shows that, in fact, period lengthening causes larger deformations of the structure, imposing greater levels of damage on non-structural elements (typically critical for wall structures, as reported by Priestley & Kowalsky 2000), or alternatively necessitating greater levels of structural stiffness in order to limit deformations to acceptable values.

In addition to increasing flexibility, foundations will dissipate energy and such energy dissipation is typically represented by system damping values. It could therefore be argued that while a period shift is expected, this will be offset by an increase in system damping. However, as will be demonstrated in this work, values of foundation damping may not be large enough to counter the effects of reduced energy dissipated by the RC walls because of lower ductility demands for a given design drift limit.

1.4 *Direct displacement-based seismic design*

Recognising the issues associated with force-based design methods, Priestley et al. (2007) and their

co-researchers developed the direct displacement-based design (DDBD) methodology. The basic process of the Direct DBD procedure, is illustrated in Figure 6. The first two steps in the procedure, shown as Figure 6(a) and Figure 6(b), aim to establish the effective mass, (m_e), height (h_e) and design displacement (Δ_d) of an equivalent SDOF system representation of the MDOF building, responding to a selected deformation limit (associated with either material strain or non-structural storey drift limits). This is based on the Substitute Structure approach pioneered by Gulkan & Sozen (1974) and Shibata & Sozen (1976).

For MDOF systems, the displacement profile at peak response is used to establish the equivalent SDOF design displacement, Δ_d, effective mass, m_e, and effective height, h_e, as per Equations 2–4 respectively.

$$\Delta_d = \sum_{i=1}^{n}\left(m_i\Delta_i^2\right) \Big/ \sum_{i=1}^{n}\left(m_i\Delta_i\right) \tag{2}$$

$$m_e = \frac{\sum_{i=1}^{n}\left(m_i\Delta_i\right)}{\Delta_d} \tag{3}$$

$$h_e = \frac{\sum_{i=1}^{n}\left(m_i\Delta_i h_i\right)}{\sum_{i=1}^{n}\left(m_i\Delta_i\right)} \tag{4}$$

As indicated in Figure 6(c), the ductility demand expected at the design deformation limit is then used to set an equivalent viscous damping value for the equivalent SDOF system. The equivalent viscous damping value obtained from Figure 6(c) represents the energy dissipated by the structure and therefore damping values vary depending on the hysteretic properties of the structure being designed. For RC wall structures the damping can be evaluated as:

$$\xi_S = 0.05 + 0.444\,\frac{\mu - 1}{\mu\pi} \tag{5}$$

The ductility demand to be used in Equation 5 can be evaluated by dividing the design displacement from Equation 2 by the yield displacement, which, for regular RC wall structures on rigid foundations, is given by Equation 6.

$$\Delta_{y,Wall} = \frac{\phi_{yWall} h_e^2}{2} - \frac{\phi_{yWall} h_e^3}{6H} \tag{6}$$

where ϕ_{yWall} is the yield curvature of the wall and H is the total height of the wall.

To account for the impact that energy dissipation has on the dynamic response, the design displacement-spectrum is developed at the expected equivalent viscous damping level. As shown in Figure 6(d), the design displacement is then used to enter the highly-damped spectrum and read off the effective period that will ensure the design displacement is not exceeded.

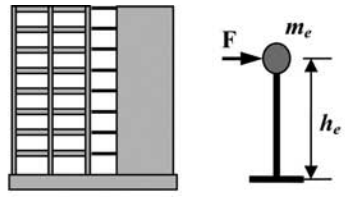

(a) SDOF representation

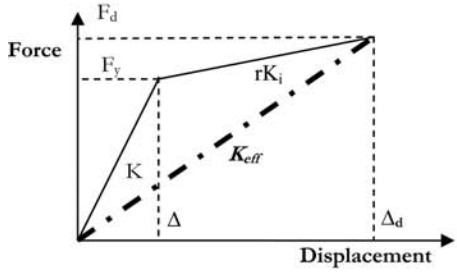

(b) Effective Stiffness

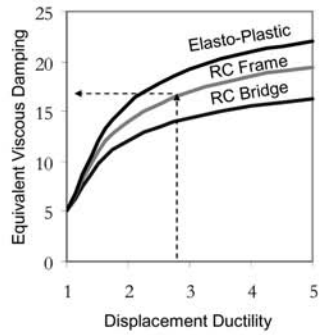

(c) Equivalent Viscous Damping

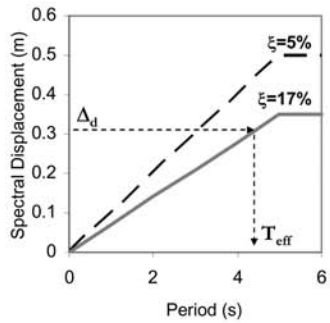

(d) Highly-damped Displacement Spectrum

Figure 6. Fundamentals of Direct Displacement-Based Design adapted from (Priestley et al. 2007).

The effective period, T_e, can be related to an equivalent SDOF effective stiffness, K_{eff}, using Equation 7.

$$K_{eff} = 4\pi^2\,\frac{m_e}{T_e^2} \tag{7}$$

where m_e is the effective mass of the equivalent SDOF system (Eq. 3). The design base-shear, V_b, is then obtained by multiplying the required effective stiffness by the design displacement, as shown in Equation 8.

$$V_b = K_{eff} \Delta_d \tag{8}$$

As such, the design procedure is relatively simple and the main challenge for different structural typologies is to identify the design displacement profile and the equivalent viscous damping, with account for effects such as SFSI.

2 ACCOUNTING FOR SFSI WITHIN A DIRECT DBD APPROACH

2.1 *Existing recommendations in the literature*

The first considerations of SFSI within a DDBD procedure appear to have been made by Priestley and Kowalsky (2000). In their work the system yield displacement was increased in recognition of foundation flexibility (as per Figure 1) which lead to a decreased system ductility and therefore reduced equivalent viscous damping with respect to a rigid-base scenario. In order to know the foundation deformation component at yield, the moment demand on the system was required. As such, an iterative procedure was necessary to ensure that an initially assumed foundation rotation matched that associated with the final design forces.

A means of accounting for the influence of foundation damping within the DDBD procedure is also outlined by Priestley et al. (2007). If the foundation damping, ξ_f, is known, it can be combined with a structural component of damping, ξ_s, (Eq.5) to give the system damping value, ξ_{sys}, as per Equation 9.

$$\xi_{sys} = \frac{\xi_f \Delta_f + \xi_s \Delta_s}{\Delta_f + \Delta_s} \tag{9}$$

where Δ_f and Δ_s are the displacements of the equivalent SDOF system due to foundation and structural deformations respectively.

Recently, Paolucci et al. (2009) found that the equivalent viscous damping of shallow foundations can be related to the imposed rotation. This enabled the development of damping curves, such as those of Figure 7, for dense and medium dense sands.

Paolucci et al. (2009) have also developed a more detailed means of accounting for SFSI for shallow foundation systems within a Direct DBD procedure. The principle developments with respect to the procedure of Priestley et al. (2007) have been to define damping curves, such as those shown in Figure 7, stiffness reduction curves, such as those shown in Figure 1, and to separate the stiffness representation of the foundation from that of the overlying structure utilizing the recommendations of Wolf (1985). In addition to iterating on the displacement component due to foundation rotations, Paolucci et al. (2009) check the ultimate resistance of the foundation once the displacement components have been identified, and if required, the foundation dimensions are increased to provide sufficient resistance and the design process is repeated.

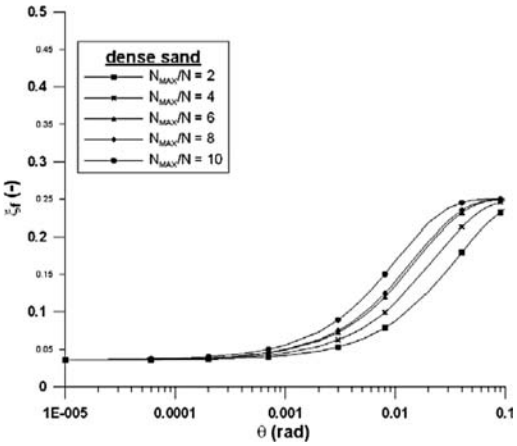

Figure 7. Equivalent viscous damping curves proposed by Paolucci et al. (2009) for shallow foundations on dense sand.

2.2 *Direct DBD of RC wall structures with account for soil-structure interaction*

In this paper the Direct DBD procedure that accounts for SFSI, developed by Priestley & Kowalsky (2000) and Paolucci et al.(2009), is extended to RC wall structures on shallow foundations and refinements are made to improve the design process.

An overview of the proposed performance-based design procedure is presented in Figure 8. A number of design inputs are required, including performance criteria which may be defined using non-structural drift limits, material strain limits (ε_c and ε_s) for the reinforced concrete and stiffness reduction limits for the foundations. Most of the design inputs are standard engineering parameters, but it is assumed that engineers would have access to stiffness reduction curves, such as those shown in Figure 1, and damping curves, such as those shown in Figure 7.

In contrast to the methods of Priestley et al. (2007) and Paolucci et al. (2009), the designer is in direct control of the amount of rotation that will develop at foundation level. The foundation rotation and factor of safety are set at the start of the design process, and the foundation is sized at the end of the procedure to give the required foundation stiffness. Furthermore, the procedure does away with the Wolf (1985) approach in which the foundation and superstructure stiffness and displacement components were separated (see Paolucci et al. 2009), as it can be shown that identical results are obtained with the equivalent SDOF representation.

The new framework gives the designer freedom to dictate the role that the foundations will play. If foundation response must be limited then a small foundation rotation should be imposed. Alternatively, if the foundation size must be minimised, a larger foundation and smaller N_{max}/N ratio can be selected. More than one

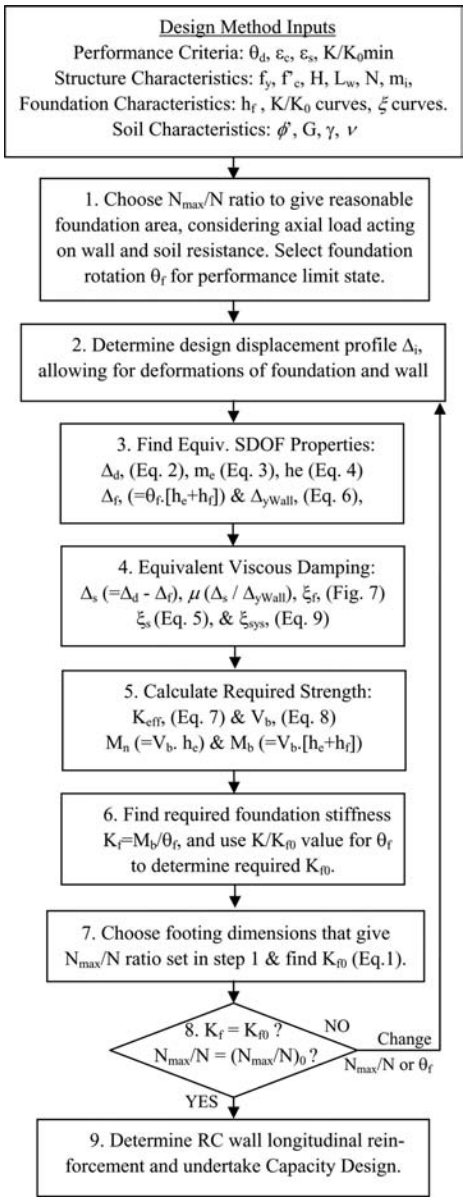

Figure 8. Overview of Direct DBD procedure proposed for RC wall structures with shallow foundations.

foundation solution can satisfy the design objectives and the minimum foundation size will be achieved by increasing the allowable foundation rotation and minimizing the foundation N_{max}/N ratio. For smaller foundation rotations a multitude of larger foundation solutions are possible as one approaches a rigid-base design solution.

2.3 *Uncertainties and areas for future research*

While significant developments have been made for the Direct DBD of systems with shallow foundations, there are a number of aspects that require further research. Firstly, the design procedure shown in Figure 8 considers only one direction of seismic excitation and the manner in which bi-directional excitation can be addressed in design requires further research.

In addition, the equivalent viscous damping developed by Paolucci et al. (2009) are area-based formulations, in line with the work of Jacobsen (1960). However, as discussed by Priestley et al. (2007) and others, area-based equivalent viscous damping expressions should be calibrated to the non-linear analysis results obtained using real earthquake records, in order to improve the accuracy of the equivalent-viscous damping approach.

Another aspect of the design approach that requires further consideration is the interaction between axial load, moment resistance and shear demand. The curves of stiffness reduction, shown in Figure 1, are dependent only on the axial load ratio. This implies that the moment-rotation response of the foundation, such as that shown in Figure 2, has an ultimate moment resistance that does not account for shear-moment interaction. Paolucci et al. (2009) account for this by checking that the design shear does not exceed a limiting shear value, obtained using the axial-moment-shear interaction using the expression of Nova & Montrasio (1991) shown in Equation 10, although one could use other interaction expressions such as that provided in the EC8 (CEN 1998).

$$\left(\frac{V_b}{\mu N_{max}}\right)^2 + \left(\frac{M_f}{\psi B N_{max}}\right)^2 - \left(\frac{N}{N_{max}}\right)^2 \left(1 - \frac{N}{N_{max}}\right)^{2\beta} = 0 \quad (10)$$

where V_b, M_f and N are the shear, moment and axial load respectively. For definition of other parameters refer to Nova & Montrasio (1991).

The design procedure presented in Figure 8 assumes that future research will develop stiffness-reduction curves similar to those shown in Figure 1, proposed by Paolucci et al. (2009), that directly incorporate the axial-shear-moment interaction effects of shallow foundations. Furthermore, higher mode effects on the interaction and response of RC wall systems with shallow foundations should be investigated.

3 IMPACT OF SOIL-FOUNDATION-STRUCTURE INTERACTION ON DESIGN

In order to gauge the impact of SFSI on the seismic response according to a displacement-based seismic design philosophy, the design procedure outlined in the previous section is applied to a number of different case study wall structures and the results are compared with DDBD results for rigid-base systems and force-based design results obtained using the equivalent-lateral force method.

3.1 *Case study structures*

The trial design methodology has been applied to two sets of 2, 4, 6 and 8-storey RC wall structures

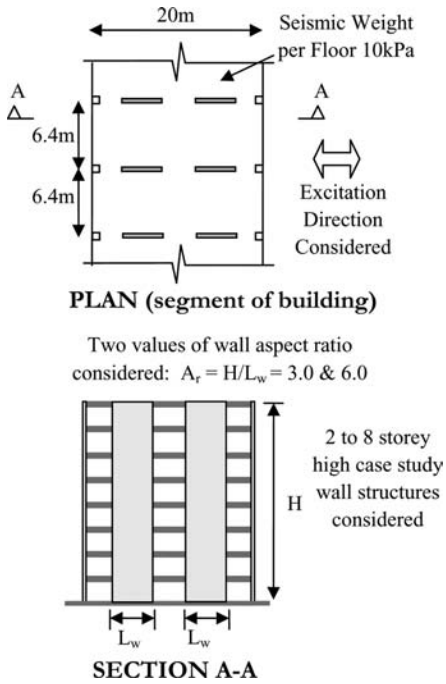

Figure 9. Plan and elevation of case study wall structures.

Table 3. Case study characteristics and performance limits.

	Number of Storeys			
	2	4	6	8
Building Height, H (m)	6.6	13.2	19.8	26.4
Wall Axial Load, N (kN)	1280	2560	3840	5120
Footing height, h_f (m)	1.60	1.60	1.60	1.60
RC Wall Curvature Limit	0.066	0.033	0.022	0.016
Foundation K_f/K_{f0} Limit	0.20	0.20	0.20	0.20

illustrated in Figure 9. The first set possess walls with an aspect ratio of 3 and the second possess walls with and aspect ratio of 6.

3.2 *Design approach*

The case-study wall structures have been designed to a damage control-limit state with a non-structural drift limit 2.5%. The Eurocode 8 design spectrum (shown in Figs. 4–5) for type 1 earthquakes on soil type C, has been used with a design PGA of 0.30 g. Design solutions have been developed using the equivalent lateral force method, and the Direct DBD method with and without account for SFSI.

Only a single excitation direction (indicated in Fig. 9) has been considered and the design solutions have been developed considering a rectangular RC shallow foundation. The footing is assumed to be resting on dense sand with $\phi = 35°$, $\gamma = 20\,\text{kN/m}^3$, $G = 80{,}000\,\text{kPa}$, and $\nu = 0.30$. Material properties for the reinforced concrete are typical of values found in practice with concrete compressive strength $f'_c = 30\,\text{MPa}$ and an expected reinforcement strength of $f_y = 500\,\text{MPa}$. The mass of the foundation has been neglected in the seismic design. In order to highlight differences between design procedures, minimum reinforcement quantities have not been imposed for the RC walls, and as such, capacity design (step 9 of Figure 8) might lead to larger footing sizes.

The EC8 requirements of the equivalent-lateral force method have been adopted, with a structural behaviour factor of 4.0. Height-dependent expressions for the period of vibration of the buildings were used, and consequently the design strengths are independent of foundation characteristics.

Table 4. Intermediate design results for case study buildings with wall aspect ratio of $A_r = 6.0$.

	Number of Storeys			
	2	4	6	8
FBD				
Building Period, T (s)	0.21	0.35	0.47	0.58
Elastic Spectral Acc. (g)	0.86	0.86	0.86	0.86
DDBD – Rigid Base				
Design Disp. Δ_d (m)	0.110	0.196	0.280	0.367
Wall Ductility Demand	2.03	2.18	2.24	2.27
E.V. Damping, ξ_{sys}	12.2%	12.6%	12.8%	12.9%
Effective Period, T_e (s)	1.12	2.03	2.92	3.82
DDBD – with SFSI				
Axial Load FOS N_{max}/N	30	15	10	9
Foundation Rotation (rad.)	0.0009	0.0011	0.0007	0.0009
Design Disp. Δ_d (m)	0.113	0.199	0.284	0.368
Wall Ductility Demand	1.94	2.05	2.15	2.16
Wall Damping, ξ_s	11.8%	12.2%	12.6%	12.6%
Foundation Damping, ξ_f	9.8%	7.1%	5.0%	5.2%
System Damping, ξ_{sys}	11.7%	11.9%	12.3%	12.2%
Effective Period, T_e (s)	1.11	1.99	2.88	3.75
Foundation K_f/K_{f0}	20%	33%	59%	58%

3.3 *Required design strengths*

Intermediate design results are shown in Table 4 for the set of cast study walls with aspect ratio, $A_r = 6.0$. Similar trends were observed for $A_r = 3.0$, but these are not included due to space limitations. For the Direct DBD with SFSI, it was noted that the optimum solution may not always be to maximise the foundation rotation, as this can increase the strength requirements for the walls. It was also found that the system damping of the DDBD solution with Rigid Base was always greater than the system damping obtained for the DDBD solution with SFSI, despite foundation damping values of up to 10%.

The design base shear strengths obtained for the different procedures are shown in Figure 10. The base shear required by the DDBD procedure is relatively constant for the different height structures whereas the FBD base shear increases significantly with building height. This suggests that shallow foundations may be more feasible for medium rise buildings when DDBD

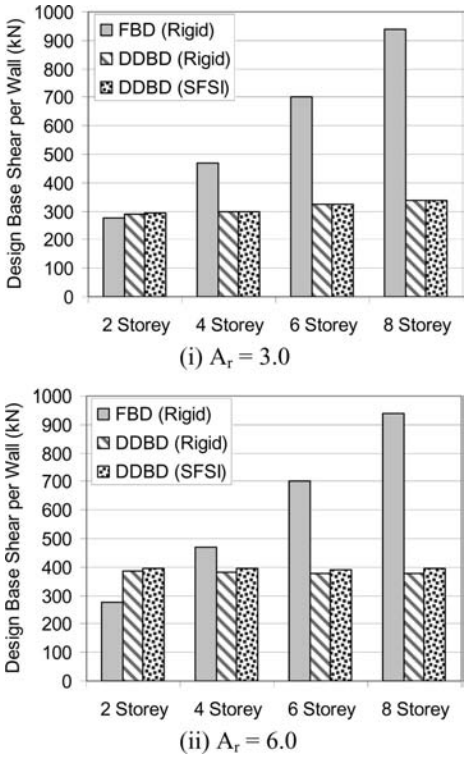

Figure 10. Design Base Shear for Case Study Buildings with (i) Wall Aspect Ratio $A_r = 3$, and (ii) Wall Aspect Ratio $A_r = 6$.

considerations are made. In fact, for the 2-storey structure with $A_r = 6$ the base shear limits of Equation 10 indicated that a shallow foundation solution was not feasible. This also highlights the need to consider axial-shear-moment interaction directly within the design procedure.

4 CONCLUSIONS

Significant progress is being made towards the formation of performance-based seismic design procedures that consider soil-foundation-structure interaction. Several questions still remain, however, as to how different performance states should be defined for foundation systems. In this work a refined formulation of the Direct DBD procedure is presented for RC wall buildings on Shallow foundations. The new design procedure gives the designer direct control of the peak rotation that will develop at foundation level (assuming maximum rotations are caused by the response of the overlying structure and not the soil deformations caused by the passage of seismic waves). Application of the design procedure to a number of different case study structures illustrates that the required design strengths tend to be greater when account for SFSI is made. In addition, the Direct DBD method required considerably lower design strengths than the FBD procedure for the 6 & 8 storey case study buildings, suggesting that shallow foundation solutions may be more feasible for medium rise buildings when a DDBD approach is used.

A number of areas for future research have been identified. In particular, alternative means of considering axial-shear-moment interaction should be explored and calibrated equivalent viscous damping curves for shallow foundation systems should be developed. Finally, the performance of the new method of accounting for SFSI using DDBD should be thoroughly investigated.

ACKNOWLEDGEMENTS

The authors would like to thank Prof. Michael Pender, Dr. Liam Wotherspoon, and Dr. Carlo Lai for fruitful discussions and clarifications during the preparation of this work. The authors also thank the anonymous reviewers for their useful suggestions. The assistance of FAR2009 in funding parts of this research is also gratefully acknowledged.

REFERENCES

Calvi G.M., Sullivan T.J. (editors) 2009. *A Model Code for the Displacement-Based Seismic Design of Structures*, IUSS press, Pavia, Italy.

CEN 1998. *Eurocode EC8 - Design of structures for earthquake resistance - Part 1: General rules, seismic actions and rules for buildings, prEN-1998-1*, Comite Europeen de Normalization, Brussels, Belgium.

Gazetas G., 1991. Foundation vibrations, Chapter 15 (2nd edition). In *Foundation Engineering Handbook*, Fang H-Y (ed.). Van Nostrand, Reinhold: New York, 553–593.

Gulkan, P., Sozen, M. 1974. Inelastic response of reinforced concrete structures to earthquake motions, *ACI Journal*, 71(12), pp.604–610.

Jacobsen, L.S. 1960. Damping in composite structures *Proceedings, Second World Conference on Earthquake Engineering*, Tokyo, pp.1029–1044.

Nova, R. and Montrasio, L. 1991. Settlement of shallow foundations on sand, *Geotechnique*,41(2):243–256.

Paolucci R., di Prisco C., Figini R., Petrini L., Vecchiotti M. 2009. Interazione dinamica non-lineare terreno-struttura nell'ambito della progettazione sismica agli spostamenti *Progettazione Sismica* 1(2), Italy.

Priestley, M.J.N. 1993. Myths and Fallacies in Earthquake Engineering – Conflicts Between Design and Reality, *Bulletin of NZ National Society for Earthquake Engineering*, NZSEE, 26(3), 329–341.

Priestley, M.J.N., Calvi, G.M., Kowalsky, M.J., 2007. *Displacement Based Seismic Design of Structures*, IUSS Press, Pavia, Italy, 721pages.

Priestley M.J.N and Kowalsky M.J. 2000. Direct Displacement-Based Design of Concrete Buildings *Bulletin of the New Zealand National Society for Earthquake Engineering*, NZSEE, Silverstream. 33(4).

SEAOC, 1997. *Seismic Design Manual*. Vol. III.

Shibata, A., Sozen, M.A., 1976. Substitute Structure Method for Seismic Design in Reinforced Concrete, *Journal of the Structural Division, ASCE*, 102(ST1).

Wolf, J. P. 1985. *Dynamic Soil-Structure Interaction*, Prentice Hall, Englewood Cliffs, N. J., U.S.

Soil-Foundation-Structure Interaction – Orense, Chouw & Pender (eds)
© 2010 Taylor & Francis Group, London, ISBN 978-0-415-60040-8

Procedures for seismic design of below ground structures

J.W. Pappin & R. Koo
Ove Arup and Partners, Hong Kong, Ltd., Kowloon, Hong Kong

ABSTRACT: There are various methods of designing deep foundations, retaining walls, basement walls, tunnels and other below ground structures to resist earthquake ground motion. They range from relatively simple pseudo static methods to full non-linear dynamic time history analyses. This paper presents the range of methods that the authors have used to design below ground structures and discusses the relative merits of these methods. Comparison is made between ground motions appropriate to regions of high seismicity as opposed to regions of low to moderate seismicity and the effects of the differences between these ground motions is explored for retaining wall design. Preliminary results show that conventional simplified methods may be over conservative for regions of low to moderate seismicity and possibly optimistic for regions of high seismicity.

1 INTRODUCTION

There are various methods of designing deep foundations, retaining walls, basement walls, tunnels and other below ground structures to resist earthquake ground motion. They range from relatively simple pseudo static methods to full non-linear dynamic time history analyses. This paper presents the range of methods that the authors have used to design below ground structures and discusses the relative merits of these methods.

2 DESIGN REQUIREMENTS

It is recommended that Performance Based Design techniques should be used as the basis for establishing methods of analysis and design. Performance based earthquake design relies on explicitly considering the requirements of the structure when subjected to future earthquake events. For example, the performance design code FEMA 356 requires that an ordinary building achieves the following objectives:

- Life safety must be ensured for occupants of the building if it is subjected to an earthquake ground motion with a likelihood of a 10% chance of being exceeded in a 50 year design life (equivalent to a return period of 475 years).
- The building should not collapse upon experiencing an earthquake ground motion with a likelihood of a 2% chance of being exceeded in a 50 year design period (equivalent to a return period of 2475 years).

Special buildings, that are essential for earthquake recovery, may require more stringent requirements. FEMA 356 also includes enhanced objectives for the Operational Performance Level where the building should have *no damage* and be suitable for *immediate occupancy* after experiencing an earthquake ground motion with a likelihood of a 50% and 20% chance of being exceeded in a 50 year design period respectively (equivalent to return periods of 72 and 225 years).

The life safety requirement for a return period motion of 475 years is similar to that required in the Eurocode 8 and the 1997 Uniform Building Code in California. In areas of high seismicity, if the rules in these codes are followed, then the no collapse objective is also likely to be satisfied. This is because these codes demand a certain level of ductile detailing which will ensure that in the event of an extreme ground motion (taken as the 2475 year return period or Maximum Considered motion), the structure will be able to withstand the additional forces without experiencing brittle failure. In areas of low to moderate seismicity however, buildings are not usually designed with the same ductility requirements and the no collapse requirement under the extreme seismic loading arising from a 2475 year return period ground motion may well dominate the design. The United States Code (International Building Code 2006) explicitly considers this aspect and requires that the 2475 year return period ground motion is used as the basis for the design of the building. Depending on the level of this ground motion different detailing requirements and associated reduction factors are recommended. Many other codes also have multiple performance objectives.

3 SITE RESPONSE EFFECTS

Before discussing the design methods for various types of below ground structures the influence of site response effects needs to be considered. It is well known that the site specific soil profile has a significant effect on the ground motion. Both the frequency content and the amplitude of the ground motion is affected. Figure 1 shows the effects of a deep, medium dense sand site and a deep soft clay site on the calculated

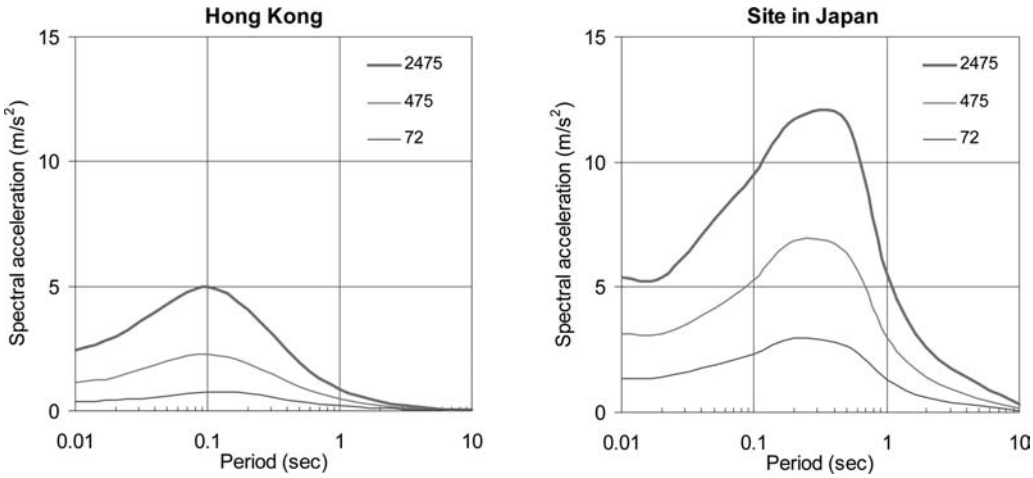

Figure 1a. Predicted response spectra for a rock site in Hong Kong and Japan.

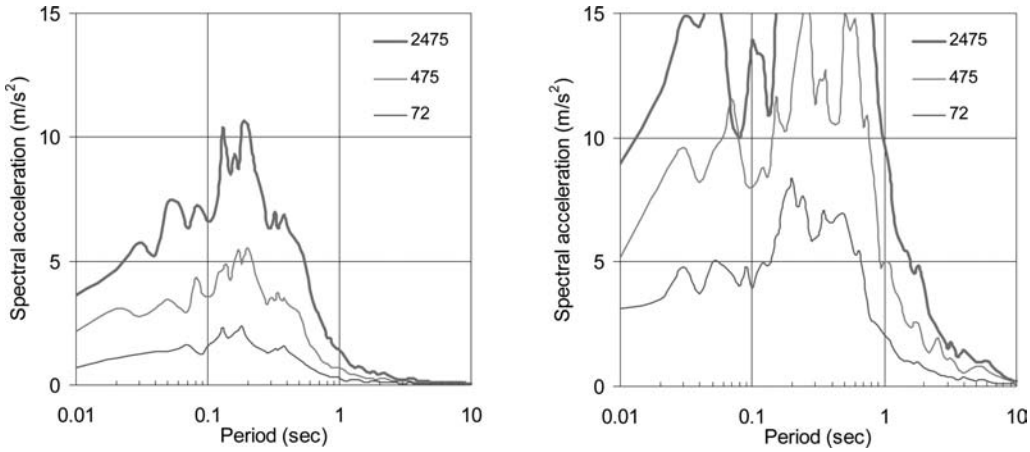

Figure 1b. Predicted response spectra for a deep sand site in Hong Kong and Japan.

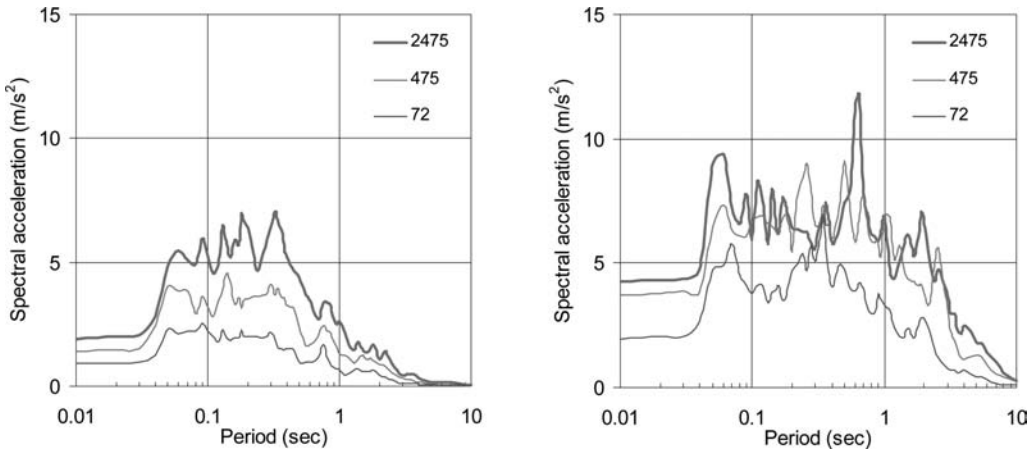

Figure 1c. Predicted response spectra for a deep soft clay site in Hong Kong and Japan.

ground surface motions appropriate to an area of low to moderate seismicity, Hong Kong, and in an area of high seismicity, a site in Japan. Full details are included in Pappin et al. (2000).

It can be seen that on a rock site (Figure 1a) the 72, 475 and 2475 year ground motions vary between each other by about a factor of 2 and that the seismicity at Hong Kong is about 3 times less than that the site in Japan. For the deep sand site (Figure 1b), in Hong Kong the ground motion is up to 3 times greater than the rock motion and in Japan up to 2 times greater. For the deep soft clay site however a different trend is observed as shown in Figure 1c. In Hong Kong the site amplifies the motion by up to a factor of 4 at periods between 1 and 2 seconds. The response of the Japan site is very dependent on the level of input motion. For the 72 year return period the amplification is similar to that predicted for Hong Kong but for the extreme 2475 year return period motion the site only amplifies the ground motion at longer periods and reduces the ground motion at periods less than 1 second.

Figure 2 shows the same set of spectra plotted as demand spectra. The corresponding buildings periods are also shown by the dashed grey lines at 45 degrees. These curves show a clearer representation of the predicted seismic ground motions at structural periods greater than 0.5 seconds. Figure 2a shows that for rock sites the ground motion in Japan is over 10 times that of Hong Kong at periods greater than 2 seconds. For the deep sand site (Figure 2b) this difference is reduced somewhat and for the deep soft clay site the Japan site is about 5 times greater than that in Hong Kong. Figure 2c shows that the Japan deep soft clay site has similar ground motion for the 475 and 2475 year return periods.

The implication to the design of foundations is that different performance objectives will be controlling the foundation design as the ground conditions and level of seismicity changes.

In areas of low to moderate seismicity the extreme loading will generally control with the performance objective being that the structure does not collapse. It would be acceptable for the foundation to yield and move significantly provided that this movement is not sufficient to lead to instability and collapse of the structure. Figures 1 and 2 also show that site response effects can be significant for the design of low to mid-rise structures up to 10 storeys. The amplification and consequent ground motion for the 2475 year return period motion is significantly higher than that for the rock site.

In regions of high seismicity, rock or stiff soil sites will be governed by the life safety requirement but for soft (and possibly loose) soil sites the requirement for immediate occupancy under the expected maximum earthquake having a return period of 225 years will probably control. In other words, the requirement for no damage to the foundation under expected loading will be more difficult to achieve than the no collapse or life safety requirement. The foundation structures must essentially remain elastic and there should not be noticeable yield of the soil supporting the foundation.

4 PILE FOUNDATIONS

Determining the effect of seismic motion on piles involves considering the lateral soil load on the piles in addition to the lateral seismic load from the superstructure. For piles that are flexible relative to the soil, the effects of soil movement will be minimal. For stiff large diameter piles or caissons however the loading from the soil may be significant and allowance must be made for this when checking the pile design. A way of analysing this problem is to set up a full three-dimensional model and carry out non-linear dynamic analysis. Figure 3 shows an example of this for an ethylene tank. This analysis will not only calculate the response of the piles but also predict any effects the foundation system may have on the dynamic response of the superstructure because of dynamic soil structure interaction effects. The analysis often shows that the piles experience significant bending moments where they pass through a soil boundary between a hard and soft soil and also near the head of the pile (see the lower right hand part of Figure 3 where the red sections are indicating yielding in bending of the piles).

A robust procedure for doing general design analysis is described in Pappin et al., 1998, and comprises setting up a model of the pile as a beam on elastic/plastic springs and applying a pseudo static free field soil displacement to the ends of the springs as illustrated in Figure 4. The soil displacement can be obtained directly from a site response analysis such as *Oasys* SIREN (Heidebrecht et al., 1990). As the soil displacements from the site response and the building response are not likely to be in phase, a load combination rule using SRSS (Square Root of the Sum of the Squares) or the 100%:40% rule needs to be used to combine the soil and structural loading.

For pile groups the method is not very reliable and it may be necessary to model several piles simultaneously to allow for the stiffening effect of the mass of piles or revert to the full three-dimensional analysis shown in Figure 3. For moderate size pile groups the seismic effects can be estimated using pseudo static two dimensional finite element analysis. An example was used for the design of the recently completed Stonecutters Bridge in Hong Kong (see Pappin & Kite, 2008). A section through the East Tower and Back Spans showing the ground conditions and the pile foundations is shown in Figure 5. There are 29 piles, each 2.8 m diameter in the group under the tower and 6 piles in the group under each of the piers, typically 2.5 m diameter.

The effect of the imposed distortion from the seismic ground motion was determined using a pseudo static finite element analysis program with two-dimensional slices being taken through each of the two major axes of each foundation group. The piles and pile cap were represented in the model as a series

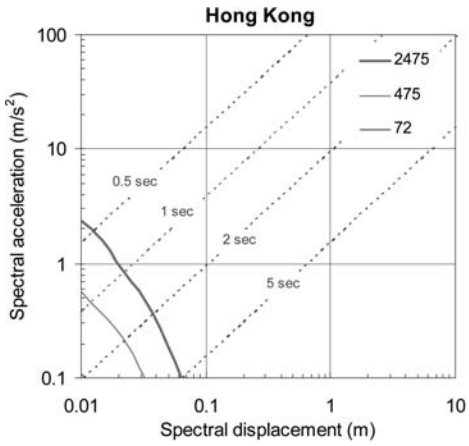

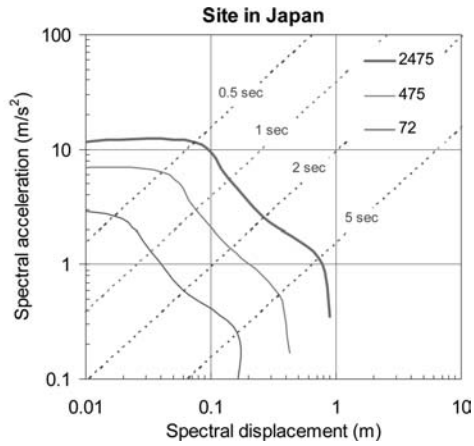

Figure 2a. Predicted demand spectra for a rock site in Hong Kong and Japan.

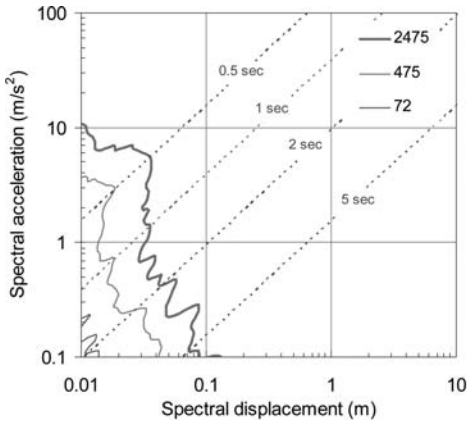

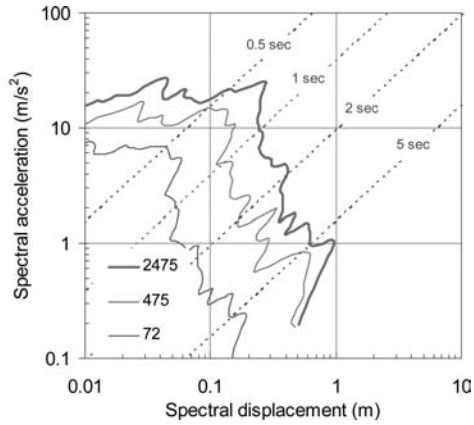

Figure 2b. Predicted demand spectra for a deep sand site in Hong Kong and Japan.

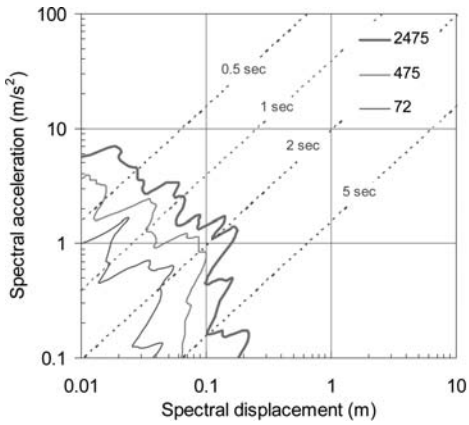

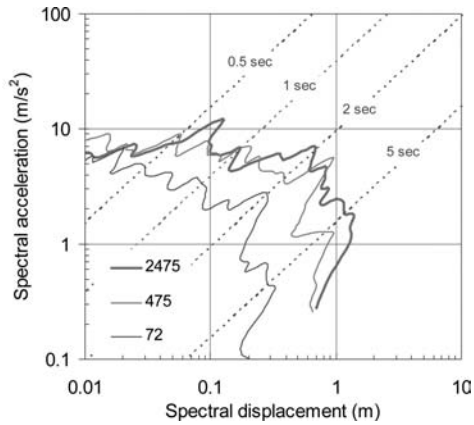

Figure 2c. Predicted demand spectra for a deep soft clay site in Hong Kong and Japan.

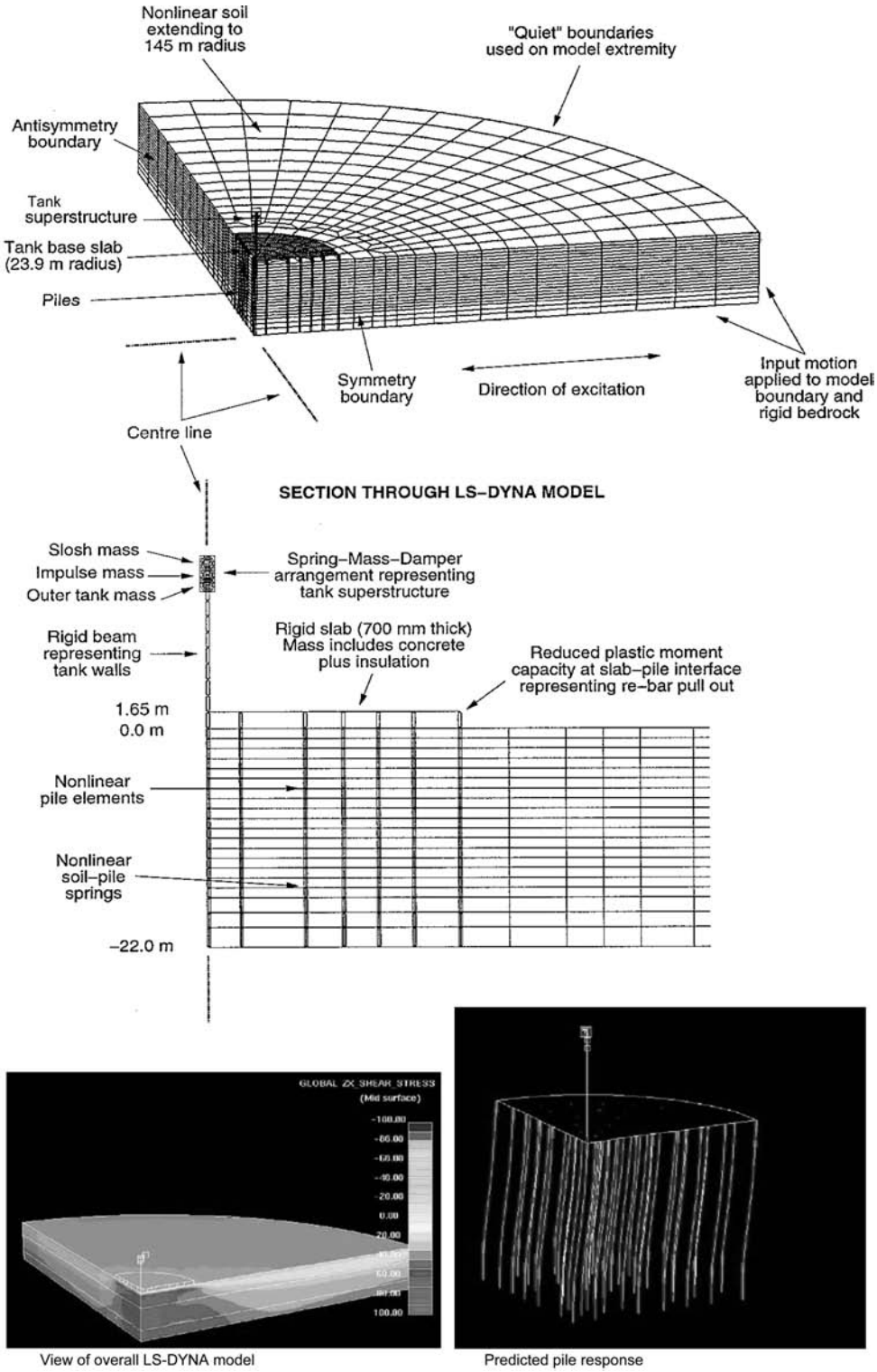

Figure 3. Use of LS-DYNA to model piles and soil structure interaction (Lubkowski et al., 2000).

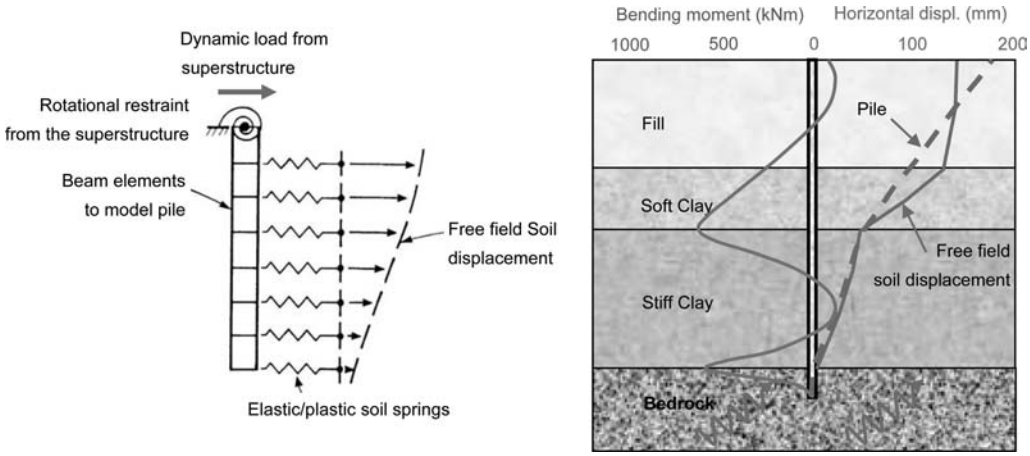

Figure 4. Diagrammatic model of pile soil system and typical results.

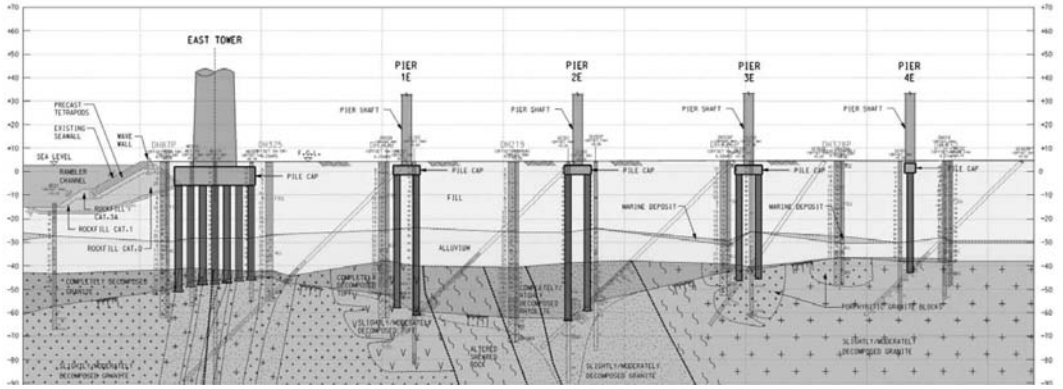

Figure 5. Section through the East Tower and Back Spans of Stonecutters Bridge, Hong Kong.

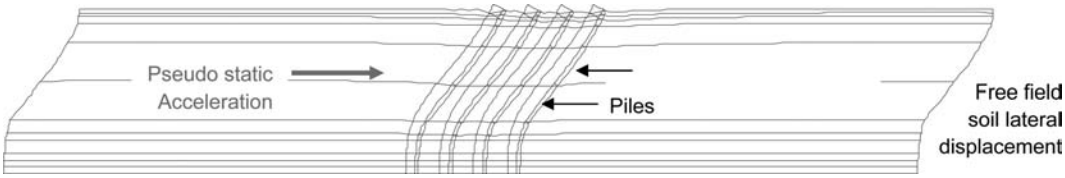

Figure 6. Diagrammatic model of pile soil system and typical results.

of elements with the appropriate concrete material properties. The piles were connected to the soil mesh using interface elements that allowed relative movement between the piles and the surrounding soil. The effect of the ground movement on the piles was modelled by inducing the soil displacement profiles derived from the site response analysis as a pseudo static load case. Figure 6 schematically shows the resulting pile movement for a typical seismic load case. A combination rule which took the maximum effect of the soil displacement or structural loading in one direction, and 40% of the maximum effects in all other directions was adopted.

For very large pile groups it is possible to represent the pile group as a single pile with its own piece of soil attached to it. This was used for the analysis of the foundations of an LNG tank illustrated in Figure 7 (see Lubkowski et al., 2004). The foundation consisted of about 1200, 0.6 m diameter steel tubular piles.

The keys aspects of the LSDYNA model were:

- Non-linear soil elements where their stiffness is formulated using the Iwan (1967) multi linear type model and the model exhibits hysteretic damping in accordance with the Masing principles.

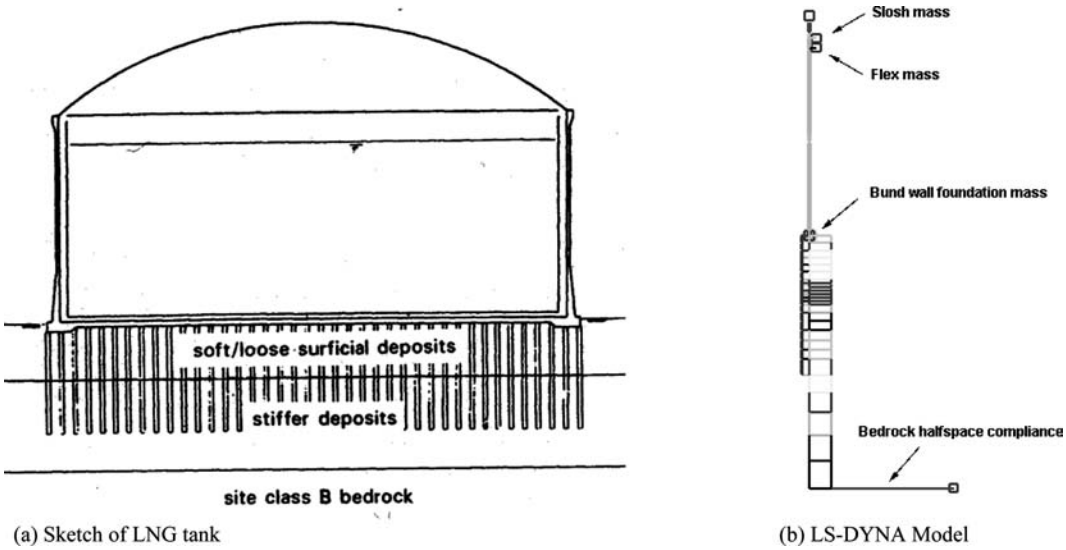

(a) Sketch of LNG tank (b) LS-DYNA Model

Figure 7. LNG Tank.

- The piles were lumped together as a single vertical beam element. For the purpose of these analyses the piles were modelled assuming non-linear stiffness parameters to model their ductile behaviour. A pinned pile to slab connection was modelled.
- The interaction between the soil and piles was modelled by using transverse kinematic springs, with appropriate stiffness and limiting strength. More details of can be found in Lubkowski et al. (2000).
- The inner tank and product was modelled as a two mass-spring-damper system using the standard mechanical analogues based on the New Zealand Guidelines (1986). The height of the masses was set such that the overall moment (pressure on the base plus shell moment) is simulated. The outer tank and roof was represented as a single mode mass/spring/damper system.

5 BASEMENT STRUCTURES

Underground structures such as cut and cover tunnels, station boxes and building basements are similar to piles in that they must be able to withstand the seismic forces imposed on them by the superstructure and by the lateral soil movements that result from the free field site response. An additional requirement is that the walls are able to withstand the earth pressures that occur during the seismic event.

As for a pile group foundation a three-dimensional non-linear dynamic analysis can be carried out, using *Oasys* LS-DYNA for example, following the principles shown in Figure 4. A particular advantage of this approach is that the point of fixity between the retaining structure and the soil body is established and the correct allowance for soil structure interaction effects is made. Generally this will lead to lower responses of the structure as a whole leading to reduced requirements within the superstructure.

For long retaining structures a two dimensional finite element analysis can be used to approximate the force and displacement requirements imposed on the basement structure. Figure 8 shows a two-dimensional section drawn through a station box in Hong Kong. This station is about 700 metres long and about 35 metres wide. To assess the ability of this station box to resist seismic loading the maximum free field displacement profile was assessed using *Oasys* SIREN. This displacement profile was then imposed on a two-dimensional finite element computer program. This was achieved by applying the maximum free field displacement profile to the side boundaries and applying a pseudo-static horizontal acceleration to the soil profile such that the desired maximum free field lateral displacement profile was observed throughout the soil mass. This same boundary condition and applied horizontal acceleration was then applied to a combined model of the soil profile and the station structure. Figure 8b shows the resulting displacement shape and Figure 9 the changes in the horizontal soil stresses acting on the sides of the station box. Bending moments and shear forces arising within the structure were also predicted by the analysis. The procedure presented here is based on the recommendations by the Earthquake Engineering Committee of the Japan Society of Civil Engineers and is described in detail in Free et al. 2001.

While the above procedure is valid for most of the length of the station box it is not sufficient where the station box and tunnels join. The high shear stiffness of the end wall of the station will induce significant stresses into both the tunnels and station box at this location. For design purposes either a movement or sacrificial joint is required or the three dimensional analysis carried out.

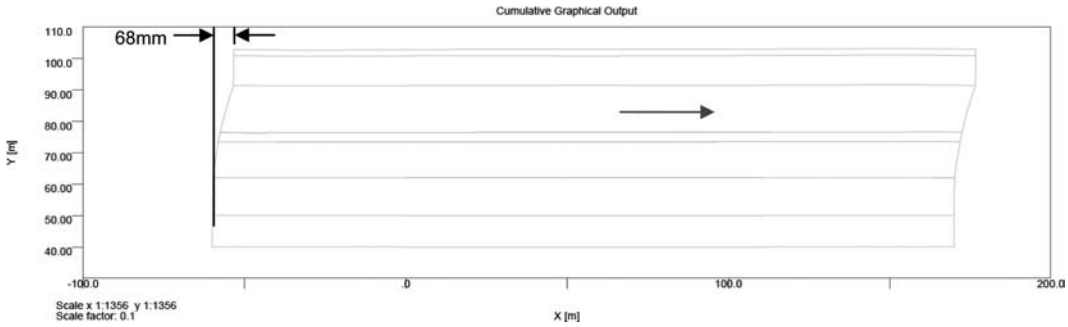

Figure 8a. Analysis Step 1 – Soil only

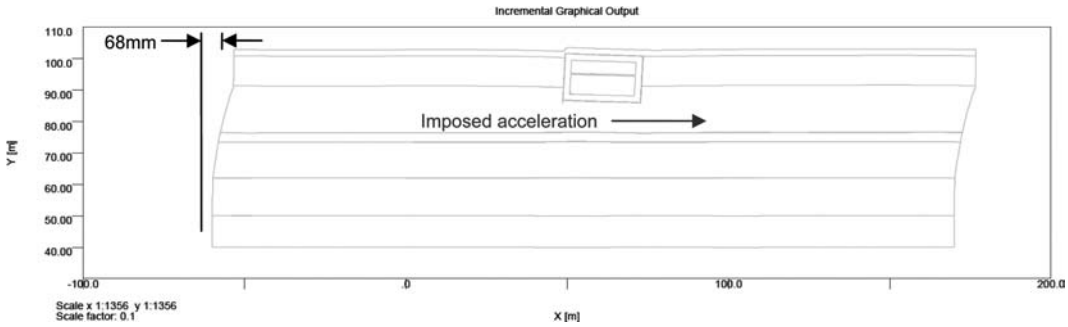

Figure 8b. Analysis Step 2 – Soil and structure

Figure 8. Two step finite element analysis.

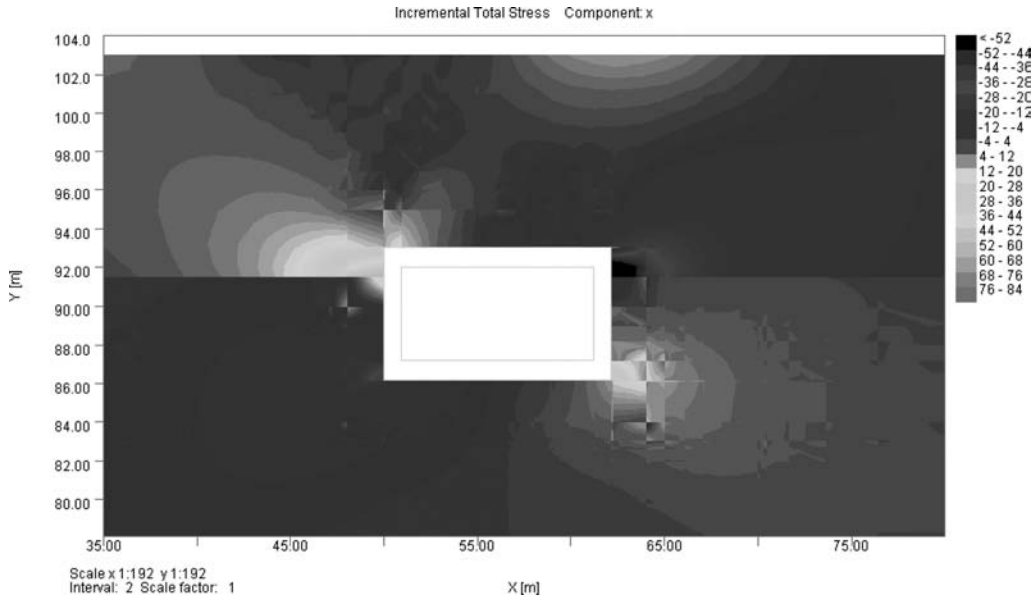

Figure 9. Calculated incremental horizontal soil stresses.

6 RETAINING WALLS

Eurocode 8 Part 5 gives a very useful summary of how to calculate seismic earth pressures acting onto retaining walls. For walls that are very flexible or able to move forwards during the earthquake event they propose the conventional method of calculating the seismic active earth pressure using the Mononobe

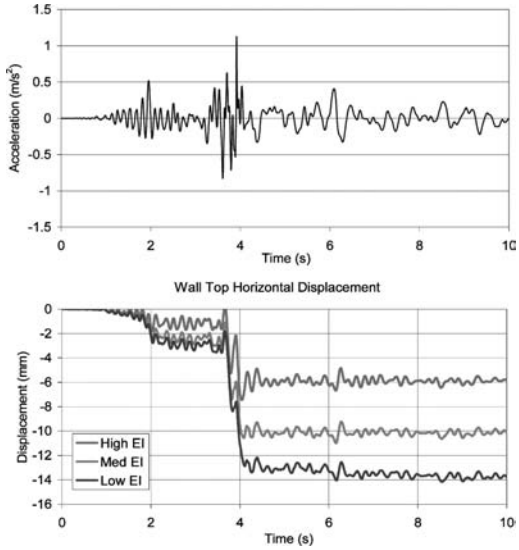

Figure 10a. Hong Kong 475 year ground motion

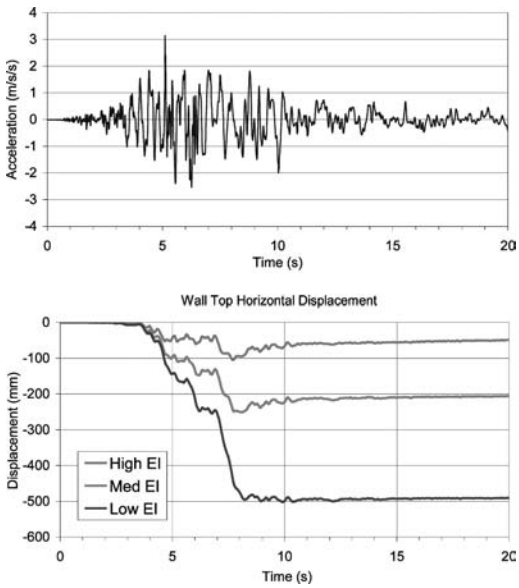

Figure 10b. Japan 475 year ground motion

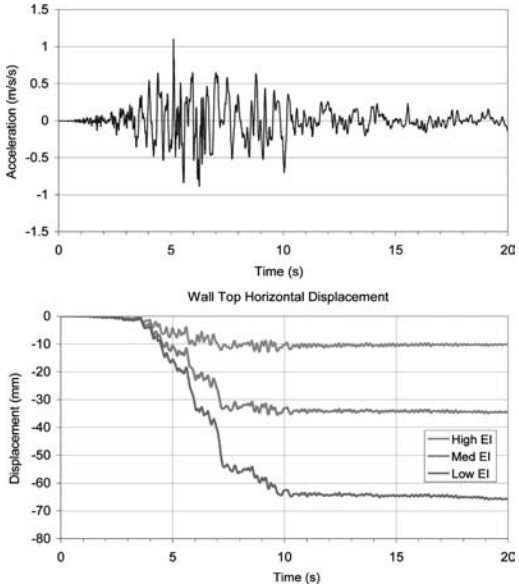

Figure 10c. Japan ground motion scaled to Hong Kong 475 year peak ground acceleration

Figure 10. Input time histories and retaining wall top deflections.

Okabe methodology and for fixed walls the simplified Wood's method (1973) where the soil force increase $\Delta P = \gamma H^2 k_h$ and γ is the soil unit weight, H the height of the wall and k_h the peak horizontal acceleration as a fraction of gravity. To determine this additional earth pressure profile, the recommendation of Matthewson et al. (1980) is often adopted, where the dynamic earth pressure decreases linearly from the top of the wall with the top pressure being three times that at the base.

A frequent difficulty is how to assess whether the retaining wall is effectively flexible or rigid whereas it is often somewhere in between. To explore this question a series of "FLAC Dynamic" analyses have been carried out. The model comprises a single 9 m deep dry soil layer acting against an elastic cantilever beam with both the soil and cantilever beam being rigidly restrained at their base. Three wall stiffnesses (EI) of 167 MNm^2/m, 525 MNm^2/m and 1670 MNm^2/m have been assumed to represent walls ranging from relatively flexible to relatively stiff. A 9 m high by 100 m wide mesh was used with 1m square elements throughout. A non-reflecting 'quiet' boundary was used at the far end from the retaining wall. The soil is assumed to have a density of 1900 kg/m^3, a shear wave velocity of 200 m/s and a standard G/Go degradation curve for sand. 0.5% Rayleigh damping at 3 Hz was also assumed.

Three time histories have been used corresponding to the 475 year ground motion for Hong Kong, the 475 year ground motion for Japan and the Japan ground motion scaled to same peak ground acceleration as that for Hong Kong (0.11 g). These were generated using RSPMatch such that they matched the bedrock response spectra shown in Figure 1a using the April 1984 Morgan Hill event (M6.2 @ 38 km) and the January 1994 Northridge event (M6.7 @ 19 km) as the seed events for the Hong Kong and Japan ground motions respectively as the seed ground motions.

Figure 10 shows the acceleration time histories and the relative wall top displacement time history plots for the high, medium and low wall stiffness walls. For comparison the deflection of the top of the walls under static loading was 2 mm, 8 mm and 23 mm for the high, medium and low EI values respectively. It can be seen from Figure 10a that the Hong Kong 475 year ground motion increases the wall displacements

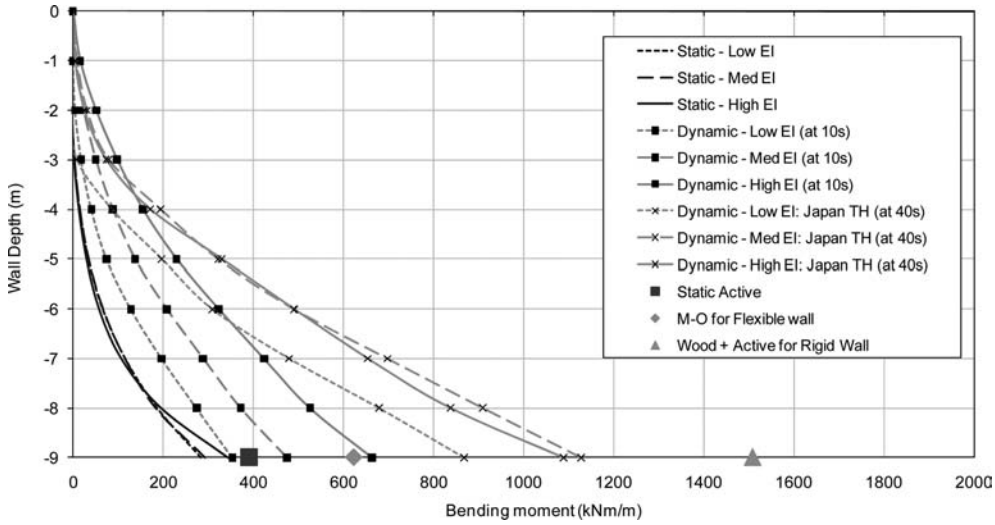

Figure 11a. Hong Kong 475 year ground motion

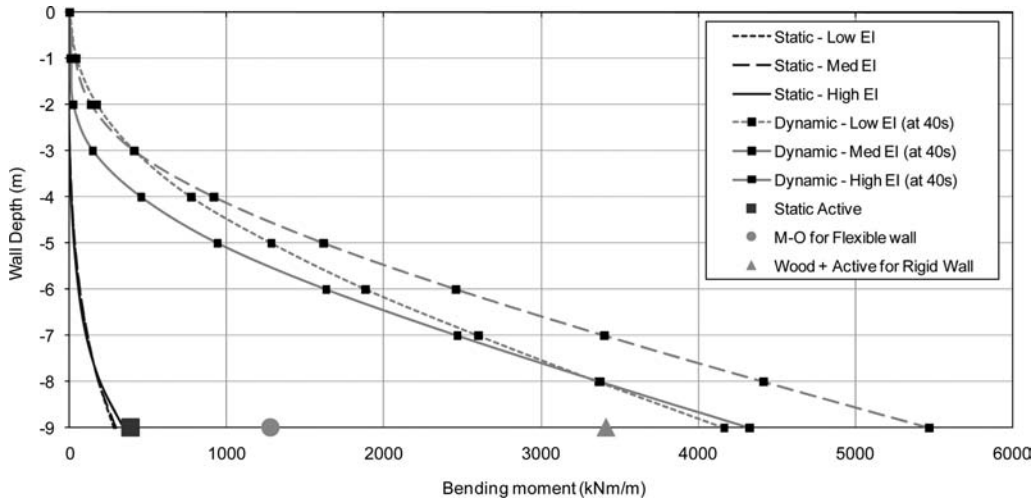

Figure 11b. Japan 475 year ground motion

Figure 11. Predicted cantilever wall bending moments.

to be 4, 2.3 and 1.6 times these original values. As expected for the Japan 475 year ground motion, Figure 10b, shows at least a 25 times increase for all wall stiffnesses. Figure 10c shows the predictions for the Japan ground motion scaled to the same PGA as that for the Hong Kong 475 year ground motion (0.11 g) and indicates displacement increases of between 6 to 4 times. This is somewhat surprising as conventional design approaches imply that the effect on the wall should be similar for ground motion having similar peak ground accelerations.

Figure 11 shows the predicted wall base bending moments for the various ground motions. The bending moments at the base of the wall predicted by the Mononobe Okabe method for flexible walls and by the Wood's method for rigid walls are also shown. Figure 11a shows the values for the Hong Kong 475 year ground motion and for the Japan ground motion scaled to the Hong Kong 475 year peak ground acceleration. The Japan type ground motion is seen to agree well with the Wood's method for the medium and high stiffness wall. Interestingly the Mononobe Okabe method agrees well with that predicted for the stiff wall when the Hong Kong 475 year ground motion is used. Figure 11b shows the bending moments predicted for the Japan 475 year ground motion. The values are very much higher than the Mononobe Okabe method and even somewhat higher than that predicted by the Wood's method even for the low stiffness (flexible) wall.

These preliminary calculations show that the conventional design methods are reasonable for ground motions corresponding to regions of high seismicity acting on stiff retaining walls. However for flexible walls that are fixed at their base, they may be optimistic. Conversely for areas of low to moderate seismicity they may well be very conservative.

It must be stressed that this is a very limited study and only presented to illustrate the effects of the ground motion frequency content in addition to variation in the size of the ground motion. Scaling of ground motions from one location to another purely by amplitude scaling is not recommended and only done here to explore the effects on the derived wall forces due to variations in frequency content and consequently spectral amplitudes. Other conclusions may also result if the soil is saturated.

7 SUMMARY

This paper presents the range of methods that the authors have used to design below ground structures to resist seismic ground motion and discusses the relative merits of these methods. The methods range from relatively simple pseudo static methods to full nonlinear dynamic time history analyses. Applications are considered for piles, retaining walls, basement walls and tunnels. Comparison is made between ground motions appropriate to regions of high seismicity as opposed to regions of low to moderate seismicity and the effects of the differences between these ground motions is explored for retaining wall design. Preliminary results show that conventional simplified methods may be over conservative for regions of low to moderate seismicity and possibly optimistic for regions of high seismicity.

REFERENCES

EN1998, Eurocode 8. 2004. *Design of structures for earthquake resistance.* Comite Europeen de Normalisation (CEN).

EN1998-5. 2004. Design of Structures for Earthquake Resistance – Part 5: *Foundations, Retaining Structures and Geotechnical Aspects*. Comite Europeen de Normalisation (CEN).

FEMA 356. 2000. Prestandard and commentary for the Seismic Rehabilitation of Buildings, *Federal Emergency Management Agency*, Washington, DC. (http://ww2.debenkolb.com/fema273/ps-fema356.html).

Free, M.W., Pappin, J.W., Sze, J.W.C. & McGowan, M.J. 2001. Seismic design methodology for buried structures. *14th South East Asian Geotechnical Conf. Hong Kong*, AA Balkema.

IBC. International Building Code. 2006. *International Code Counci*l, California, 2006.

Iwan, W.D. 1967. On class of models for the yielding behaviour of continuous and composite systems. *Journal of Applied Mechanics* 34(E3): 612–617.

Heidebrecht, A.C., Henderson, P., Naumoski, N. & Pappin, J.W. 1990. Seismic response and design for structures located on soft clay sites. *Canadian Geotechnical Journal* 27(3): 330–341.

JSCE. 1992. Earthquake resistant design features of submerged tunnels in Japan. In: *Earthquake resistant design for civil engineering structures in Japan. Compiled by Earthquake Engineering Committee, The Japan Society of Civil Engineers.*

Lubkowski, Z.A., Pappin, J.W. & Willford, M.R. 2000. The influence of dynamic soil structure interaction analysis on the seismic design and performance of an ethylene tank. *Proc. 12th World Conf. on Earthquake Engineering*, Auckland.

Lubkowski, Z.„ Willford, M., Duan, X., Thompson, A. & Kammerer, A. 2004. Providing value to clients through non-linear dynamic soil structure interaction. *13th World Conference on Earthquake Engineering*, Paper No. 1415. Vancouver, B.C., Canada.

Matthewson, M.B., Wood, J.H. & Berrill, J.B. 1980. Seismic Design of Bridges – Earth Retaining Structures, *Bulletin of the New Zealand Society of Earthquake Engineering* 13(3): 280–293.

New Zealand National Society for Earthquake Engineering. 1986. *Seismic Design of Storage Tanks.*

Pappin, J.W. & Kite, S. 2008. Seismic design of Stonecutters Bridge, Hong Kong. *14th World Conf. on Earthquake Engineering*, Beijing.

Pappin, J.W., Lubkowski, Z.A. & King, R.A.. 2000. The significance of site response effects on performance based design. *Proc. 12th World Conf. on Earthquake Engineering*, Auckland.

Pappin, J.W., Ramsey, J., Booth, E.D. & Lubkowski, Z.A. 1998. Seismic response of piles: some recent design studies. *Proc. of The Institution of Civil Engineers, Geotechnical Engineering* 131: 23–33.

Wood, J.H., Earthquake Induced Soil Pressures on Structures. Report No. EERL 73-05, *Earthquake Engineering Research Laboratory, Calif. Inst. Tech*., Pasadena. 1973.

UBC. Uniform Building Code. 1997. *International Conference of Building Officials*, Whittier, California USA.

Soil-Foundation-Structure Interaction – Orense, Chouw & Pender (eds)
© 2010 Taylor & Francis Group, London, ISBN 978-0-415-60040-8

Beyond conventional capacity design: Towards a new design philosophy

I. Anastasopoulos
National Technical University of Athens, Greece

ABSTRACT: The paper illuminates a new seismic design philosophy, which takes advantage of soil "failure" to protect the superstructure. A reversal of conventional "capacity design" is introduced, through intentional under-designing of the foundation. A simple but realistic bridge is used as an illustrative example of the effectiveness of the new philosophy. Two alternatives are compared: one in compliance with conventional capacity design, with over-designed foundation so that the plastic "hinge" develops in the superstructure ; and one with under-designed foundation, so that the plastic "hinge" may occur in the soil. The seismic performance of the two alternatives is investigated through numerical (finite element) and experimental (shaking table) simulation. It is shown that the performance of both alternatives is totally acceptable for moderate seismic motions. For large intensity seismic motions, the performance of the new scheme is shown to be advantageous, not only avoiding collapse but hardly suffering any inelastic structural deformation. Naturally, there is always a price to pay, which is none other than increased foundation settlement and residual rotation.

1 INTRODUCTION

Seismic design of structures recognises that highly inelastic material response is unavoidable under the strongest possible earthquake. "Ductility" levels of the order of 3 or more are usually allowed to develop under strong seismic shaking, implying that the strength of a number of critical elements is fully mobilized. In the prevailing structural terminology, "plastic hinging" is allowed as long as the overall stability is maintained.

In marked contrast, a crucial goal of current practice in seismic "foundation" design, particularly as entrenched in the respective codes [e.g. EC8], is to avoid the mobilization of "strength" in the foundation. In structural terminology: no "plastic hinging" is allowed in the foundation soil. In simple geotechnical terms, the designer has to ensure that the below-ground (difficult to inspect) support system will not even reach a number of "thresholds" that would statically imply failure. Thus, mobilization of the "bearing-capacity" failure mechanism, foundation sliding and uplifting, or any relevant combination is prohibited.

To make sure that such mechanisms will not develop, "overstrength" factors plus (explicit and implicit) factors of safety larger than 1 are introduced against each of those "failure" modes. This way, the engineer feels certain that foundation performance will be satisfactory and that there will be no need to inspect and/or repair after strong earthquake shaking.

However, a growing body of evidence suggests that soil–foundation plastic yielding under seismic excitation may be advantageous, and should be seriously considered in analysis and perhaps allowed in design [Pecker, 1998; Martin & Lam, 2000; FEMA-356, 2000; Kutter et al., 2003; Kawashima et al., 2007].

This paper investigates numerically and experimentally a new design philosophy, beyond conventional capacity design, in which superstructure plastic "hinging" is replaced by full mobilization of the bearing capacity of the foundation (Figure 1): i.e. soil yielding is used as a "shield" for the superstructure (exactly the opposite of conventional capacity design). A simple but realistic typical highway bridge is used as an illustrative example of the potential effectiveness of the new seismic design philosophy.

2 PROBLEM DEFINITION

We consider a typical highway bridge in the transverse direction (Figure 1). A deck of mass $m = 1200$ ton is monolithically connected to a reinforced concrete pier of diameter $d = 3$ m and height $H = 12$ m. The bridge chosen for analysis is similar to the Hanshin Expressway Fukae bridge, which dramatically collapsed in the 1995 Kobe earthquake [Seible et al., 1995; Iwasaki et al., 1995; Park, 1996]. The bridge is designed according to EC8 [2000] and the Greek Seismic Code [EAK 2000] for design acceleration $A = 0.24$ g, considering a behavior factor $q = 2$. With an elastic (fixed-base) vibration period $T = 0.48$ sec and design spectral acceleration $SA = 0.3$ g, to undertake the resulting design bending moment $MD \approx 43$ MNm, a longitudinal reinforcement of 100 $d_{bL} = 32$ mm bars (100Φ32) is required, combined with $d_{bw} = 13$ mm hoops spaced at 8 cm.

The pier is founded through a square foundation of width B on an idealized homogeneous 25 m deep (stiff clay for the numerical simulation; dense sand

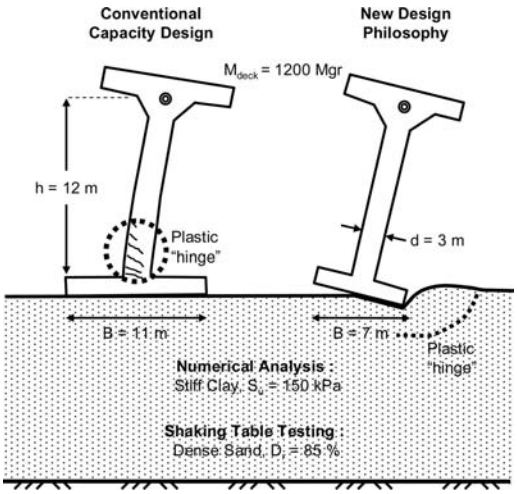

Figure 1. Problem outline: conventional capacity design (left) compared to the new design philosophy.

for shaking table testing). Two different foundation widths are considered to represent the two alternative design approaches. A larger foundation, $B = 11$ m, designed according to conventional capacity design, with overstrength factor $\gamma_{Rd} = 1.4$ to ensure that the plastic "hinge" will develop in the superstructure (base of pier). With the maximum allowable uplift criterion being critical, the resulting safety factors for static and seismic loading are $FSV = 5.6$ and $FSE = 2.0$, respectively (numerical analysis). A smaller, under-designed, $B = 7$ m foundation is considered in the spirit of the new design philosophy. Its static safety factor $FSV = 2.8$, but applying an "under-strength" factor $1/\gamma_{Rd} = 1/1.4 \approx 0.7$ for seismic loading. Thus, $FSE \approx 0.7$, i.e. lower than 1.0. In fact, as it will be shown, the under-designed foundation will not allow the design seismic action to develop. Hence, *FSE* does not bear a physical meaning in this case; it is just an apparent temporary factor of safety.

3 NUMERICAL SIMULATION

As schematically illustrated in Figure 2, the finite element analysis is conducted assuming plane-strain conditions, taking account of material (in the soil and the superstructure) and geometric (due to uplifting and P-Δ effects) nonlinearities. The pier is modeled with nonlinear beam elements, while the deck is represented by a mass element. Soil and foundation are modeled with quadrilateral continuum elements, nonlinear for the former and elastic for the latter. The foundation is connected to the soil with special contact elements, allowing for realistic simulation of possible detachment and sliding at the soil–foundation interface – representing with realism the tensionless interface. The mass of the footing and of the pier are also taken into account.

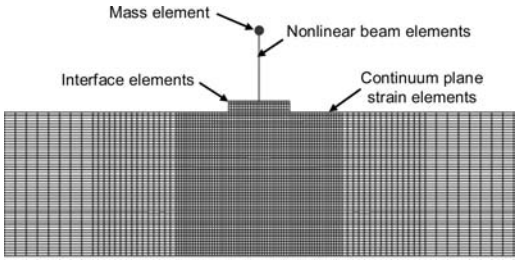

Figure 2. Numerical simulation: finite element model.

3.1 *Constitutive modeling of soil*

A nonlinear constitutive model with Von Mises failure criterion, nonlinear kinematic hardening and associative plastic flow rule is employed. The evolution of stresses is described by:

$$\sigma = \sigma_o + \alpha \tag{1}$$

where: σ_o is the value of stress at zero plastic strain, assumed constant, and α the backstress. The evolution of the kinematic component of the yield stress is given by:

$$\dot{\alpha} = C\frac{1}{\sigma_0}(\sigma - \alpha)\dot{\bar{\varepsilon}}^{pl} - \gamma\alpha\dot{\bar{\varepsilon}}^{pl} \tag{2}$$

where: $\dot{\bar{\varepsilon}}^{pl}$ is the plastic strain rate, C the initial kinematic hardening modulus and γ a parameter that determines the rate at which the kinematic hardening decreases with increasing plastic deformation.

Model parameters are calibrated to fit published G–γ curves of the literature, following the procedure described in Gerolymos et al. [2005]. More details on the constitutive model and its calibration can be found in Anastasopoulos et al. [2009].

3.2 *Constitutive modeling of reinforced concrete*

The same constitutive model is calibrated to match the response of the reinforced concrete pier in the macroscopic moment–curvature level. The calibration is conducted with respect to the moment-curvature response of the reinforced concrete section. The latter is computed through section analysis employing the *USC-RC* software, which uses the Mander model [Mander et al., 1984]. The softening behavior of the concrete section after ultimate capacity, is incorporated in the model through a user subroutine, encoded in the *ABAQUS* finite element code. More details on constitutive model calibration can be found in Anastasopoulos et al. [2009].

3.3 *Static pushover*

We first analyze the response of the two alternatives subjected to static "pushover". Figure 3 compares the F–δ (force-displacement) response of the two systems. For the conventional design ($B = 11$ m), we also plot

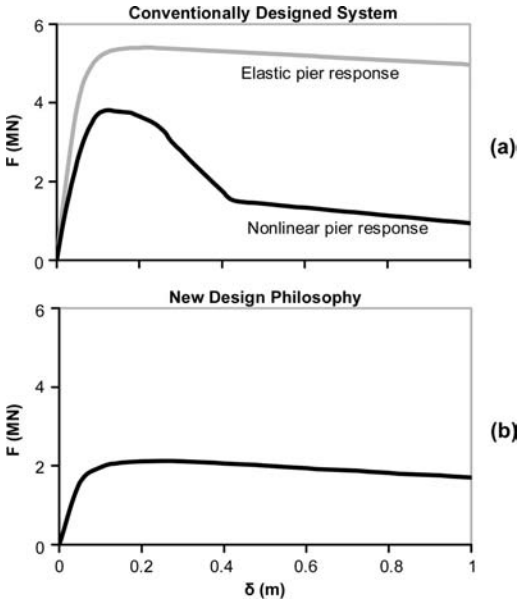

Figure 3. Static pushover F–δ (force-displacement) response for: (a) the conventionally designed system, and (b) the system designed according to the new philosophy.

the F–δ response assuming elastic pier behavior, to illustrate the difference in the capacity of the two foundations. Evidently, the $B = 11$ m foundation can sustain substantially larger load (5.5 MN instead of 2 MN for $B = 7$ m). In terms of system performance (black line, nonlinear pier response), the conventional system can sustain almost 2 times the inertial load of the new concept (4 MN instead of 2 MN). While the capacity of the conventional system is limited by the ultimate flexural strength of the pier, the capacity of the new concept is limited by the bearing capacity of the under-designed foundation (the pier remains elastic).

Figure 4 compares the M–θ (moment-rotation) response of the two systems. As for F–δ, we also plot the response assuming elastic pier behavior (grey line), to show the difference in the capacity of the two foundations. The $B = 11$ m foundation can sustain a moment of 76 MNm instead of 30 MNm of the $B = 7$ m foundation. The moment capacity of the conventionally designed bridge is limited by the strength of the pier to $M_{ult} = 54$ MNm. In contrast, the moment capacity of the new concept is limited by the bearing capacity of the under-designed foundation to $M_{ult} = 30$ MNm (black line, nonlinear pier response). In other words, the new design concept is almost 2 times "weaker" than the conventional.

But as it will be shown in the sequel, the key difference between the two alternatives lies in their ductility capacity. The curvature ductility capacity μ_ϕ is equal to 16.6, and its displacement ductility capacity can be computed as follows [Priestley et al., 1996]:

$$\mu_\Delta = \frac{\Delta_u}{\Delta_y} = \frac{M_u}{M_n} + 3(\mu_r - 1)\frac{L_p}{H}\left(1 - 0.5\frac{L_p}{H}\right) \qquad (3)$$

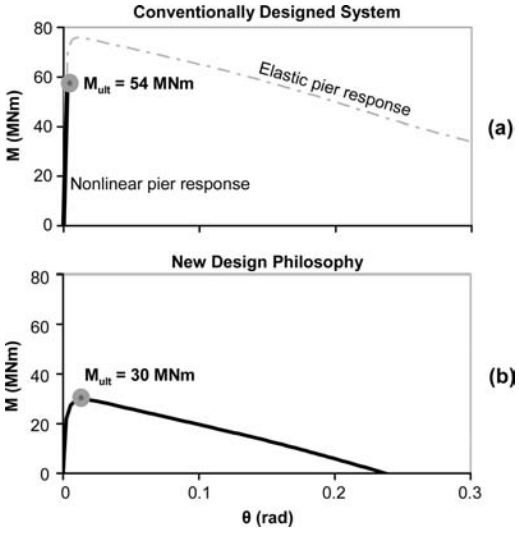

Figure 4. Static pushover M–θ (moment-rotation) response for: (a) the conventionally designed system, and (b) the system designed according to the new philosophy.

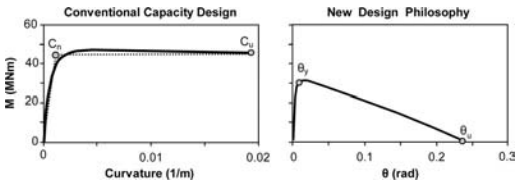

Figure 5. Moment-curvature response of the conventionally designed structure, and foundation moment-rotation response of the new design concept.

where: M_u the ultimate and M_n the "yield" bending moment of the reinforced concrete section (c_n in the *Moment-curvature* diagram of Figure 5), H the height of the pier, and L_p the length of the plastic hinge:

$$L_p = 0.08L + 0.022 f_{ye} d_{bl}{}^3 \quad 0.044 f_{ye} d_{bl} \qquad (4)$$

where: f_{ye} and d_{bl} the design yield strength (in MPa) and the diameter of the longitudinal reinforcement. This results in a displacement ductility capacity of the conventionally designed system $\mu_\Delta = 5.6$.

In the case of the new design concept, the behavior of the pier is elastic. Hence, the ductility capacity of the system is associated with foundation rotation due to bearing capacity failure, rendering the conventional definition of curvature ductility not applicable. Therefore, we define an equivalent displacement ductility capacity μ_Δ, relying on foundation rotation (see also Figure 5):

$$\mu_\Delta = \frac{\Delta_u}{\Delta_y} = \frac{H\theta_u}{H\theta_y} = \frac{\theta_u}{\theta_y} \qquad (5)$$

where: θ_u is the ultimate (critical for overturning) foundation rotation, and θ_y the "yield" rotation. This results

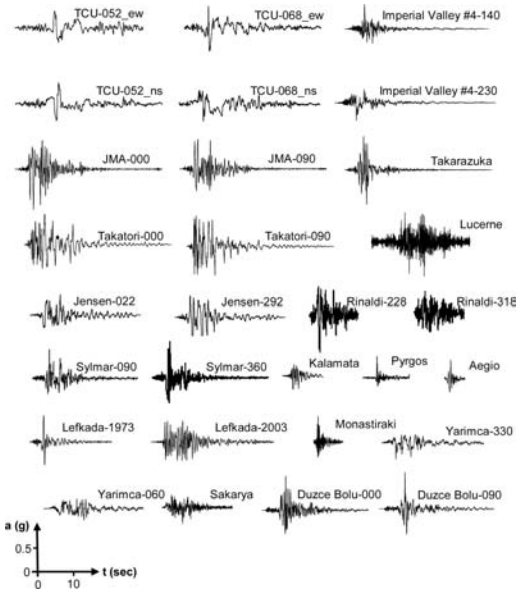

Figure 6. Real records used as seismic excitation at bedrock.

in a displacement ductility capacity of the new concept ($B = 7$ m) $\mu_\Delta = 42.2$, which is almost an order of magnitude larger than the capacity of the conventionally designed system.

3.4 *Dynamic analysis and seismic excitations*

The seismic performance of the two alternatives is now investigated through nonlinear dynamic time history analysis. A variety of articificial motions (Ricker and Tsang-type) and real records were used as seismic excitation at bedrock [Loli, 2008]. As shown in Figure 6, the selected records cover a wide range of seismic motions, ranging from motions characteristic of moderate intensity earthquakes, to very strong seismic events (e.g. Kobe 1995, Northridge 1994, Chi-Chi 1999). In terms of spectral acceleration, many of the considered accelerograms substantially exceed the PGA = 0.24 g design spectrum [Anastasopoulos et al., 2009].

3.5 *Performance in moderate seismic motions*

A comparison of the performance of the two design alternatives subjected to a moderate intensity earthquake is illustrated in Figures 7 and 8. We use as example the record of the 1973 M_w 5.9 Lefkada (Greece) earthquake.

Figure 7 depicts the comparison between the two alternatives in terms of foundation response: moment–rotation (M–θ) and settlement-rotation (w–θ). As it would be expected, while the response of the conventionally designed foundation is practically elastic, the under-designed foundation (new design philosophy) experiences some inelasticity.

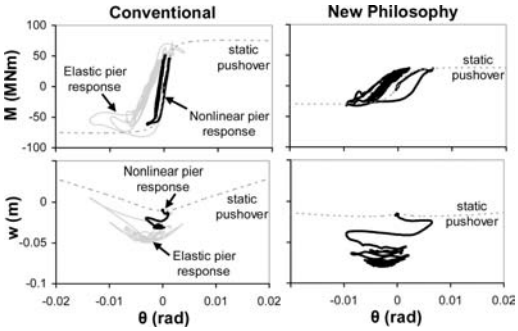

Figure 7. Comparison of the response of the two alternatives subjected to a moderate intensity seismic motion (Lefkada, 1973): overturning moment versus rotation (M–θ) and settlement–rotation (w–θ) response for the two foundations.

As a result, the conventionally designed system is subjected to limited settlement $w \approx 2$ cm. In stark contrast, the new concept experiences larger but tolerable *dynamic* settlement: $w \approx 5$ cm. The residual foundation rotation is also larger in the case of the under-designed foundation.

The results are also plotted for the idealized case of linear pier response (grey lines). It can be concluded that the seismic response of the larger foundation is not necessarily better. In fact, the maximum rotation θ of the $B = 11$ m foundation assuming liner pier response is larger than that of the under-designed $B = 7$ m foundation. The latter may experience larger θ due to soil yielding, but the larger foundation is subjected to larger quasi-elastic θ due to its increased swaying stiffness and strength. Observe also, that the residual θ is practically the same.

Figure 8 compares the time histories of deck drift Δ for the two alternatives. As schematically illustrated in the sketch notation, the drift has two components [see also Priestley et al., 1996]: (i) the "flexural drift" Δ_C, i.e. the structural displacement due to flexural distortion of the pier column, and (ii) the "rocking drift" $\Delta_r = \theta H$, i.e. the displacement due to rocking motion of the foundation. As might have been expected, while for the conventional design (over-designed foundation) Δ is mainly due to pier distortion Δ_C, exactly the opposite is observed for the under-designed foundation (new design philosophy). Despite the differences in the mechanism leading to the development of Δ (Δ_C versus Δ_r), the maximum Δ is similar. Interestingly, despite the aforementioned residual θ, the residual Δ of the new concept is much smaller than that of the conventionally designed system.

The reason is none other than the pier flexural failure of the conventionally designed system (Figure 8, bottom). This inelasticity would imply structural damage in the form of micro-cracking. But since the curvature ductility capacity of the reinforced concrete section is substantially larger (by a factor of 2), the damage would be tolerable. In the case of the new design philosophy, thanks to foundation yielding the response of

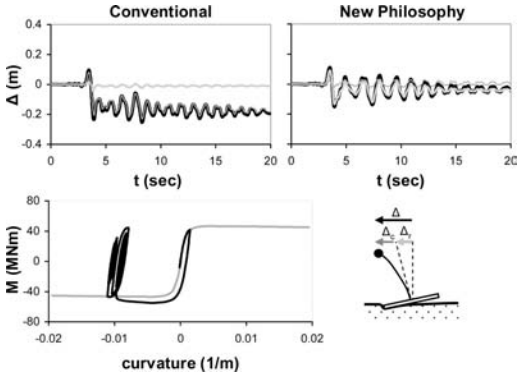

Figure 8. Comparison of the response of the two alternatives subjected to a moderate intensity seismic motion (Lefkada, 1973): time histories of deck drift Δ and bending moment–curvature response of the conventionally designed pier. The response of the pier designed according to the new philosophy is purely elastic, and is not shown here.

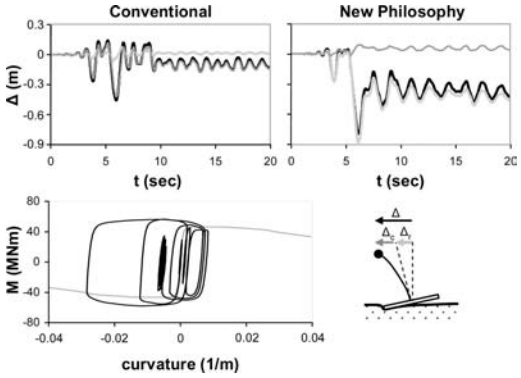

Figure 9. Comparison of the response of the two alternatives subjected to a large intensity seismic motion (Jensen, Northridge 1994): time histories of deck drift Δ and bending moment–curvature response of the conventionally designed pier. The response of the pier designed according to the new philosophy is purely elastic, and is not shown here.

the pier (not shown herein) is purely elastic (i.e. no structural damage).

3.6 *Performance in large seismic motions*

We now compare the response of the two alternatives for a large intensity seismic motion, substantially exceeding the design limits (Figures 9 and 10): the Jensen (292) record of the 1994 Ms 7.2 Northridge earthquake [Trifunac et al., 1998].

Figure 9 compares the response of the two alternatives, in terms of deck drift and moment-curvature response of the conventionally designed system. The pier of the conventional system suffers a curvature ductility exceeding the design limit by about 50% (0.03 instead of 0.02), implying very serious – non-repairable – damage at the limit of collapse. On the other hand, the system designed according to the new

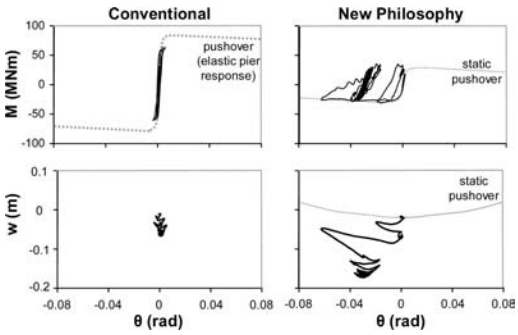

Figure 10. Comparison of the response of the two alternatives subjected to a large intensity seismic motion (Jensen, Northridge 1994): overturning moment versus rotation (M–θ) and settlement–rotation (w–θ) response for the two foundations.

philosophy survives structurally unscathed, at the cost of increased residual deck drift (about 40 cm), almost purely due to foundation rotation Δ_r.

Figure 10 focuses on the moment–rotation (M–θ) and settlement–rotation (w–θ) response of the two foundations. Evidently, the conventional $B = 11$ m foundation–soil system remains practically elastic. Exactly the opposite is observed for the under-designed ($B = 7$ m) foundation, the response of which is strongly inelastic, with the mobilization of bearing capacity failure acting as a "safety valve" for the superstructure.

The cost of this seismic "protection" is the increase of residual deck drift Δ (already discussed) and of foundation settlement w, which reaches in this particular case 17 cm. Although such settlement is certainly not negligible, it can be considered as a small price to pay to avoid collapse under such tremendous ground shaking.

3.7 *Synopsis*

The performance of the two design alternatives is summarized in Figure 11, in the form of displacement ductility demand over capacity $\mu_{demand}/\mu_{capacity}$. For the conventional design, the likely damage level according to *Response Limit States* of Priestley et al. [1996] are also shown.

The damage to the conventional system is within the serviceability limits only in moderate earthquake motions. In stronger motions, it falls within damage control or survival, and for very strong motions (such as Jensen, Takatori, TCU-068) failure is unavoidable. The "under-designed" new concept never even approached its displacement ductility capacity, with the ratio of $\mu_{demand}/\mu_{capacity}$ being systematically lower than 0.25. The new seismic design concept appears to provide increased safety margins for the superstructure.

In terms of residual deck drift Δ (not shown herein) the new concept can be advantageous for large intensity earthquakes [see Anastasopoulos et al., 2009]. On

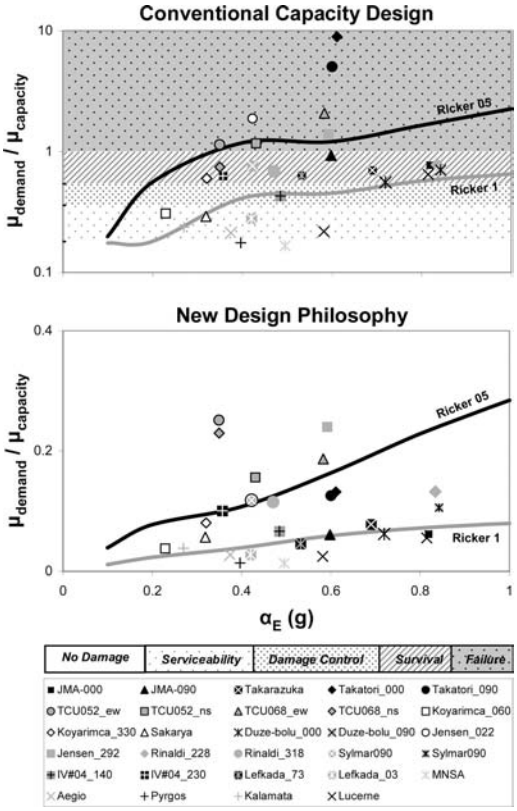

Figure 11. Summary comparison of the performance of the two alternatives: ratio of displacement ductility demand over ductility capacity with respect to the maximum acceleration a_E of the seismic excitation (Ricker 05 and Ricker 1, correspond to Ricker wavelets with 0.5 Hz and 1 Hz frequency, respectively).

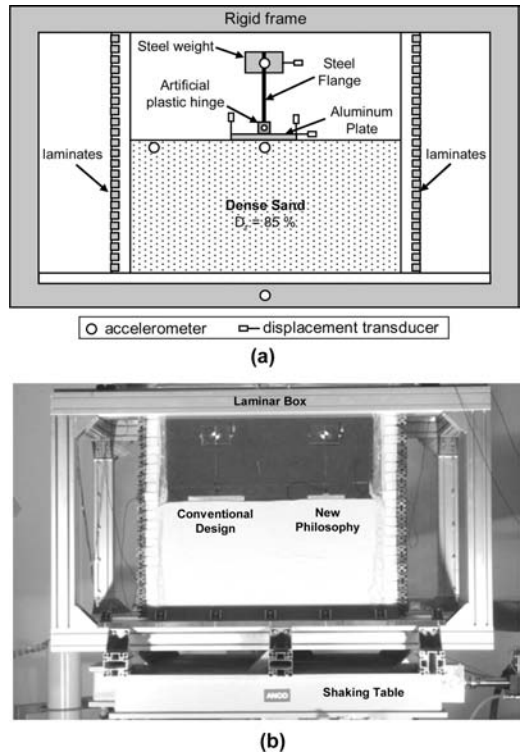

Figure 12. Shaking table testing: (a) basic physical model configuration, and (b) photo of the two bridge models inside the laminar box.

the other hand, the dynamic settlement w [not shown here, see Anastasopoulos et al., 2009] of the new concept is always substantially larger compared to conventional capacity design (by a factor of 3). However, even in the worst-case scenarios, w barely exceeds 0.2 m, a value which could be considered tolerable.

4 SHAKING TABLE SIMULATION

To further elucidate the potential advantages of the new seismic design philosophy, the same problem (but using dense sand instead of stiff clay) was simulated in a shaking table. Physical models of the two bridge alternatives were constructed and tested in a newly-established facility in the Lab. of Soil Mechanics of the Nat. Techn. Univ. of Athens (*NTUA*), utilizing a recently installed shaking table.

Taking account of the capacity of the shaking table, a scale factor $N = 50$ was selected for the experiments. The selection of model materials was conducted taking account of scaling laws, so that the simulation is as realistic as possible for the given prototype. The bridge piers were constructed using commercially available steel and aluminium plates (Figure 12a).

At small scale, it is practically impossible to model stiffness correctly (in consistency with the scaling laws) and achieve the desired (scaled) bending moment capacity of the pier at the same time. Hence, an artificial plastic hinge was custom designed and constructed, and placed at the base of the pier of the conventionally designed alternative. As schematically illustrated in Figure 4a, the ultimate bending moment M_{ult} of the plastic hinge can be calibrated through adjustment of the torque applied at the nut-bolt assembly. To achieve repeatability, Teflon washers were added between the bolts and the central steel plate. The calibration of the assembly was performed through static pushover testing.

The physical models were placed inside a transparent laminar box, custom designed and constructed (Figure 12b). The 15 m (in prototype scale) foundation soil consisted of dry "Longstone" sand, a very fine industrially produced uniform quartz sand with $D_{50} = 0.15$ mm, uniformity coefficient $D_{60}/D_{10} = 1.42$, $e_{max} = 0.995$, $e_{min} = 0.614$, and $G_s = 2.64$. The shaking table models were prepared by raining the sand from a specific height (0.7 m) with controllable mass flow rate (which controls the density of the sand), using a custom raining system, designed

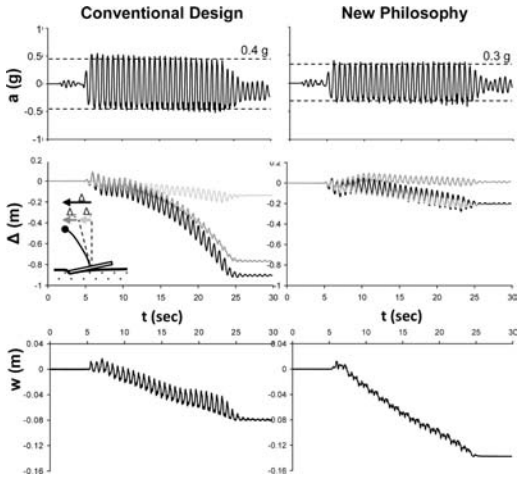

Figure 13. Comparison of the response of the two systems subjected to 30 cycle 2 Hz sinusoidal seismic excitation of PGA = 0.4 g: acceleration time histories at deck level, deck drift time histories (total, flexural, and rotational), and foundation settlement time histories.

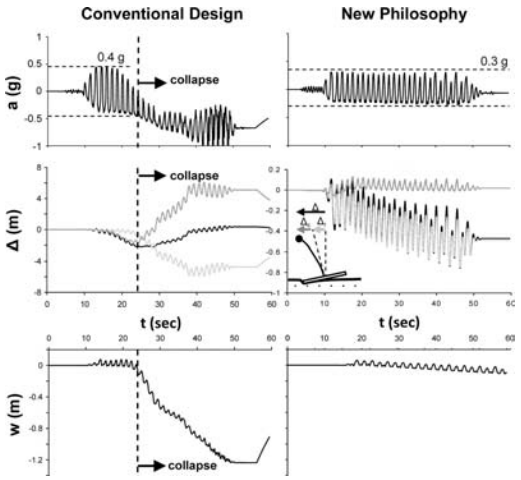

Figure 14. Comparison of the response of the two systems subjected to 30 cycle 1 Hz sinusoidal seismic excitation of PGA = 0.4 g: acceleration time histories at deck level, deck drift time histories, and foundation settlement time histories.

and constructed in our Lab. The tests were conducted at the maximum density (i.e. $D_r = 85\%$).

Tests were conducted with two different configurations: (i) each model was placed and tested separately (Figure 12a), and (ii) both bridge physical models were placed inside the laminar box (Figure 12b). The first configuration was used to measure horizontal and vertical displacements of the pier and its foundation. The purpose of the second configuration (Figure 12b) was to demonstrate the differences between the two design alternatives under practically identical conditions.

4.1 *Seismic motions*

The shaking table tests were conducted using four real records and two artificial accelerograms as seismic excitations. The latter (30-cycle sinusoidal motions) were used to investigate the performance of the two alternatives in extreme events. The results for real earthquakes are qualitatively identical with the already discussed numerical simulation. Hence, we focus on the performance of the two alternatives under extreme shaking conditions.

4.2 *30-cycle sinusoidal motion, f = 2 Hz*

We compare the response of the two systems subjected to an artificial 30-cycle sinusoidal motion at a frequency of 2 Hz and $PGA = 0.4$ g. Figure 13 compares the response of the two alternatives in terms of deck acceleration and drift, and foundation settlement (all results shown in prototype scale).

Observe the accumulation of deck drift for both alternatives. In the case of the conventional system Δ is mostly due to flexural pier drift Δ_C, but some rotational drift Δ_r is also accumulated. The conventionally designed bridge is subjected to a residual drift of about 90 cm (i.e. 7.5% of the pier height). Obviously, in reality such flexural distortion would imply collapse of the bridge, and the survival in the experiment is only due to the unrealistically large ductility capacity of the artificial plastic hinge.

Exactly the opposite is observed for the new design concept. The accumulation of drift is much smaller: it does not exceed 20 cm (i.e. less than 2% of the pier height). Exactly the opposite conclusion can be drawn for the settlement: $w \approx 14$ cm for the new concept versus $w \approx 8$ cm of the conventionally designed system.

4.3 *30-cycle sinusoidal motion, f = 1 Hz*

We now compare the response of the two schemes subjected to a small frequency ($f = 1$ Hz) seismic excitation.

As shown in Figure 14, while the conventional system actually collapses at $t = 23$ sec, the new concept survives this tremendous seismic motion at the price of residual deck drift $\Delta \approx 50$ cm and settlement $w \approx 18$ cm.

5 CONCLUSIONS

The purpose of this paper is to present numerical and experimental evidence on the potential effectiveness of a new seismic design philosophy, in which soil failure is "utilized" to protect the superstructure. The seismic performance of the new concept (involving an under-designed foundation) has been compared to a conventionally designed system.

For moderate intensity seismic motions, the performance of both alternatives is acceptable, and both would be utilizable right after such an earthquake.

The conventionally designed bridge pier would probably sustain limited structural damage (minor flexural cracking), and would be easily repairable. On the other hand, the new concept would be subjected to slightly increased – but tolerable – deck drift and settlement, but would remain structurally unscathed.

The advantage of the new seismic design philosophy becomes clear for large intensity seismic motions, clearly exceeding the limits of the design. In such cases, while the conventionally designed system is driven to collapse, the new concept may survive the seismic motion with the damage being "contained" in the form of deck drift and foundation settlement.

ACKNOWLEDGEMENT

This work forms part of an EU 7th Framework research project funded through the European Research Council's (ERC) Programme "Ideas", Support for Frontier Research – Advanced Grant, contract number ERC-2008-AdG 228254-DARE to Professor G. Gazetas.

REFERENCES

Anastasopoulos I., Gazetas G., Loli M., Apostolou M, Gerolymos N. (2009), Soil Failure can be used for Earthquake Protection of Structures, *Bulletin of Earthquake Engineering*, Vol. 7, No. 4 (available online).

Apostolou, M., Gazetas G. (2005), Rocking of Foundations under Strong Shaking: Mobilisation of Bearing Capacity and Displacement Demands, *Proc. 1st Greece–Japan Workshop, Seismic Design, Observation, Retrofit*, Athens 11–12 October, pp. 131–140.

EAK (2000), *Greek Seismic Code*, Organization of Seismic Planning and Protection, Athens (in Greek).

EC8 (2000), *Design Provisions for Earthquake Resistance of Structures, Part 5: Foundations, Ret. Str. and Geot. aspects*, prEN, 1998-5 Eur. Com. for Standard., Brussels.

ΕΚΩΣ (2000), *Greek Code for Reinforced Concrete*, Org. of Seismic Planning and Protection, Athens (in Greek).

FEMA 356 (2000), Prestandard and Commentary for the Seismic Rehabilitation of Buildings.

Gazetas, G., Dakoulas, P., and Papageorgiou, A. S. (1990), Local soil and source mechanism effects in the 1986 Kalamata (Greece) earthquake, *Earthquake Engineering & Structural Dynamics*, 19, pp. 431–456.

Gerolymos, N., Gazetas, G., Tazoh, T., (2005), Seismic Response of Yielding Pile in Non-Linear Soil, *Proceedings of the 1st Greece –Japan Workshop, Seismic Design, Observation, Retrofit*, pp. 25 36, Athens 11–12 October.

Iwasaki T., chm, et al. (1995), *Report on Highway bridge damage caused by the Hyogoken Nanbu Earthquake of 1995*, Committee on Highway Bridge Damage, Japan.

Kawashima K., Nagai T., Sakellaraki D. (2007), Rocking Seismic Isolation of Bridges Supported by Spread Foundations, *Proc. 2nd Japan-Greece Workshop on Seismic Design, Observation, and Retro-fit of Foundations*, April 3–4, Tokyo, Japan, pp. 254–265.

Kutter BL, Martin G, Hutchinson TC, Harden C, Gajan S, Phalen JD. (2003), *Status report on study of modeling of nonlinear cyclic load-deformation behavior of shallow foundations*, PEER Workshop, University of California, Davis, March 2003.

Loli M. (2008), *Bridge Pier – Foundation: Beyond Seismic Capacity Design*, Diploma Thesis, National Technical University of Athens, Greece.

Mander J.B., Priestley M.J.N., Park R., (1988), Theoretical Stress Strain Model for Confined Concrete, *ASCE Journal of Structural Journal*, Vol. 114, No. 8, pp. 1804–1825.

Martin, G., R., and Lam, I. P. (2000). Earthquake Resistant Design of Foundations: Retrofit of Existing Foundations, Proc. *GeoEng 2000 Conference*, Melbourne.

Park, R. (1996), An Analysis of the failure of the 630 m elevated expressway in Great Hanshin Earthquake, *Bulletin of the New Zealand National Society for Earthquake Engineering*, 29, 2

Pecker, A. (1998), Capacity Design Principles for Shallow Foundations in Seismic Areas, *Proc. 11th European Conference on Earthquake Engineering*, A.A. Balkema Publishing.

Priestley, M.J.N., Seible, F. and Calvi, G.M. (1996), *Seismic Design and Retrofit of Bridges*, John Wiley and Sons, New York.

Seible, F., Priestley, M.J.N. and MacRae, G. (1995), *The Kobe earthquake of January 17, 1995; initial impressions from a quick reconnaissance*, Structural Systems Research Report-95/03, University of California, San Diego, 1995.

Trifunac, M.D., Todorovska, M.I., and Lee V.W. (1998), The Rinaldi strong motion accelerogram of the Northridge, California, earthquake of 17 January, 1994, *Earthquake Spectra*, 14(1), pp. 225–239.

Soil-Foundation-Structure Interaction – Orense, Chouw & Pender (eds)
© 2010 Taylor & Francis Group, London, ISBN 978-0-415-60040-8

Probabilistic seismic performance and loss assessment of a bridge-foundation-soil system

B.A. Bradley
GNS Science, Lower Hutt, New Zealand

M. Cubrinovski, R.P. Dhakal & G.A. MacRae
Department of Civil and Natural Resources Engineering, University of Canterbury, New Zealand

ABSTRACT: This paper presents the probabilistic seismic performance assessment of an actual bridge-foundation-soil system, the Fitzgerald Avenue twin bridges. A two-dimensional plane strain finite element model of the longitudinal direction of the bridge-foundation-soil system is modeled using advanced soil and structural constitutive models. Ground motions are selected based on the seismic hazard deaggregation at the site, which is dominated by both fault and distributed seismicity. Based on rigorous examination of several deterministic analyses, engineering demand parameters (EDP's) are determined which capture the global and local demand and damage to the bridge and foundation, and multiple ground motions at various intensity levels are used to conduct seismic response analyses of the system. A probabilistic seismic loss assessment of the structure considering both direct repair and loss of functionality consequences was performed to holistically assess the seismic risk of the system. It was found that the non-horizontal layering of the sedimentary soils has a pronounced effect on the seismic demand distribution to the bridge components, of which the north abutment piles and central pier are critical in the systems seismic performance. The consequences due to loss of functionality of the bridge during repair were significantly larger than the direct repair costs, with over a 2% in 50 year probability of the total loss exceeding twice the book-value of the structure.

1 INTRODUCTION

Methods for assessment of the seismic performance of soil-structure systems have evolved significantly in the past two decades. This evolution has involved further improvement of simplified design-oriented approaches, and also development of more robust, and complex, analysis procedures. In addition to the development in methods of analysis, attention has shifted from the implicit assessment of seismic performance via seismic response analysis, to an explicit consideration of seismic performance based on the consequences of seismic response and associated damage.

Consideration of the seismic response of soil-structure systems is complicated by the complexity of the ground motion excitation and the non-linear dynamic response of soil-structure systems. In addition to this complexity, the seismic response of soil-structure systems is burdened by a significant amount of uncertainty. Such uncertainty arises due to the uncertain nature of future ground motions which will occur at the site, as well as the lack of knowledge of the properties governing the response of the soil-structure system. In addition to the ground motion and seismic response uncertainties there are also uncertainties associated with the levels of damage to the structure and the corresponding consequences in terms of direct repair costs and loss of functionality and human injuries.

Recent efforts (Bradley et al. 2009b), predominantly following the Pacific Earthquake Engineering Research (PEER) Centre framework formula have focused on performance-based methodologies which allows the computation of seismic performance measures encompassing direct and indirect consequences associated with the seismic response of engineered facilities as well as addressing the significant aforementioned uncertainties in the seismic assessment problem.

The focus of this paper is the probabilistic seismic performance assessment of a two-span bridge structure supported on pile foundations which are founded in liquefiable soils. Firstly, the structure, site conditions, and computational model of the soil-pile-bridge system are discussed. An overview of the seismic response of the system for a single ground motion is discussed to elucidate the predominant deformation mechanisms of the system and to identify the engineering demand parameters (EDP's) to use in the probabilistic seismic demand assessment. Ground motions are selected in accordance with the seismic hazard deaggregation for various intensity levels, and the results of the seismic response analyses are used to perform probabilistic seismic demand assessments of the system.

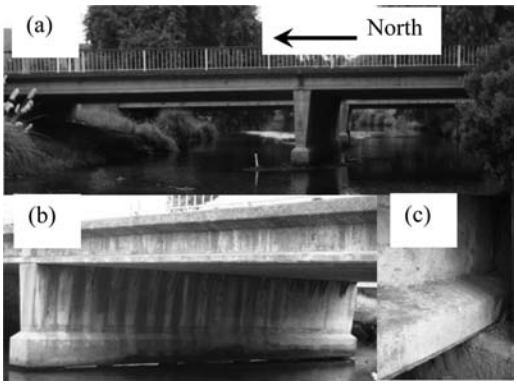

Figure 1. The Fitzgerald Avenue twin bridges: (a) elevation of the west bridge; (b) illustration of the central pier and pile cap; and (c) seating connection of bridge deck on abutments.

2 CASE STUDY: FITZGERALD AVENUE BRIDGES

2.1 *Details of the structure*

The Fitzgerald Avenue twin bridges are located near to the north-west of central Christchurch, New Zealand. Each of the two-span bridges is 30 m long, 12.1 m wide and 3.2 m high (Figure 1a). The 15 m bridge deck spans consist of 21 prestressed concrete I-girders and cast-in-place concrete slabs. The bridge superstructure is supported on two seat abutments and one central pier (Figure 1b). The abutments and pier which are 2.5 m and are the same width as the superstructure deck and are supported on pile group foundation consisting of eight – 0.3 m diameter piles. All piles have continuous moment connections at the pile cap. At both abutments the bridge deck is seated on a 10 mm bearing pad as illustrated in Figure 1c.

Because of their location in the transportation network, the Fitzgerald Avenue bridges have been designated by the Christchurch City Council as a key lifeline for post-earthquake transportation. A recent assessment of the bridge structure recommended the installation of two additional driven piles at each of the abutments and central pier to a depth of 25 m. The two piles on each side of the central pier are 1.5 m in diameter, while those at the abutments are 1.2 m in diameter.

2.2 *Site conditions*

Previous site investigations conducted to confirm ground conditions and assess material strengths and liquefaction potential include: boreholes with standard penetrometer tests (SPT's); cone penetrometer tests (CPT's) with direct push Dual Tubes (DT's); and installation of piezometers. Based on these site investigations, the generic soil profile for the longitudinal axis of the bridge given in Figure 2 was developed. The soil profile consists of four distinct layers. The shallowest two horizontal layers have thicknesses of 4.5 m and 6.5 m, and normalised SPT blowcounts of $N_1 = 10$ and $N_1 = 15$, respectively. Below these two layers, the profile deviates from a simple horizontal layering, with a weaker layer of 6.5 m depth and SPT blowcount of $N_1 = 10$ on the left hand side of the model. Below 17.5 m on the left hand side of the model, and up to 11 m depth on the right hand side of the model is a significantly stiffer layer of $N_1 = 30$. Both the $N_1 = 10$ and $N_1 = 15$ layers are highly susceptible to liquefaction, while the $N_1 = 30$ base layer was deemed to be of a significantly lower liquefaction potential. Behind the abutments, gravel backfills extend at an angle of 30 degrees above horizontal to the surface.

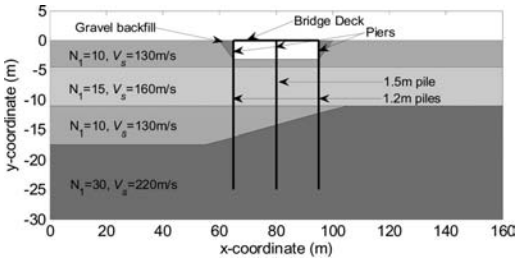

Figure 2. Schematic illustration of generic soil profile used in the computational model.

3 COMPUTATIONAL MODEL

A non-linear finite element plane-strain model of longitudinal direction of the bridge-foundation-soil system was constructed in the finite element program Diana-J (1987). While the seismic response of the bridge-pile-soil system is clearly a 3-dimensional problem, only the analyses of the longitudinal direction are discussed herein. Details of the effective stress analyses of the transverse direction of the bridge system are presented in Bowen and Cubrinovski (2008) and Cubrinovski and Bradley (2009).

Because of symmetry, the out-of-plane width of the longitudinal plane-strain model was taken to be half of the bridge width (6.05 m). That is, half of the bridge deck, abutments and piers were considered, as well as the same dimension for the soil thickness. Therefore, in the computational model, each abutment and pier is supported by a single 1.2 m and 1.5 m pile, respectively. The 0.3 m diameter piles (length 9.5m) which supported the structure before the installation of the 1.2 m and 1.5 m piles provide negligible contribution to the stiffness and strength of the pile group and were not considered in the computational model.

Because of the high liquefaction potential of the foundation soil, its dynamic response was considered to be a dominant feature affecting the response of the bridge-pile-soil system. The soil was modelled using the two-phase (soil-water) Stress-Density (S-D) constitutive model of Cubrinovski and Ishihara (1998). Further details on the computation of the constitutive model parameters used in the analysis is given in

Bowen and Cubrinovski (2008) and Cubrinovski and Ishihara (1998).

The bridge abutments, central pier and pile foundations were modelled using displacement-based beam elements with three gauss points. At each gauss point, the moment-curvature response was parameterized by a hyperbolic curve, with the initial stiffness, *EI*, and peak moment, M_F, chosen to match the moment curvature relationship of the pile (See Bowen and Cubrinovski (2008) for details). The unloading/reloading path for the moment-curvature relationship is based on the Masing rule, and no strength degradation was considered due to limitations of the constitutive model. The bridge superstructure was modelled as linear elastic because of its significantly higher axial stiffness compared to the lateral stiffness of the abutments/piers and its higher flexural and shear strength.

A static analysis was performed in order to determine the initial stress distribution in the model. In particular, a correct distribution of shear stresses near the abutments is critical for modelling the tendency for lateral spreading of soil toward the river channel.

In addition to hysteretic damping occurring as a result of the inelastic constitutive models, Rayleigh damping was used to provide enhanced numerical stability with parameters $\alpha = 0$ and $\beta = 0.005$.

4 SEISMIC HAZARD AND GROUND MOTIONS

The seismic hazard due to earthquake-induced ground motion is determined using probabilistic seismic hazard analysis (PSHA). In order to obtain the seismic hazard curve it is first necessary to specify which ground motion intensity measure (IM) is to be used. In this study, *PGA* is used as the IM, both for its historical use and because it and spectral accelerations at various periods are the only IM's for which seismic hazard curves are publicly available for this location. Recent studies (Bradley et al. 2009a) have shown however that velocity-based IM's (e.g. peak ground velocity, *PGV*, and spectrum intensity, *SI*) are better IM's for such analyses of structures in liquefiable soils.

Figure 3a illustrates the ground motion hazard at the site of the bridge structure, while Figure 3b illustrates the hazard deaggregation used for ground motion selection. Ground motion selection in accordance with the seismic hazard deaggregation has been shown important (Shome & Cornell 1999), particularly for inefficient and insufficient IM's such as *PGA*. As noted by Stirling et al. (2007) and evident in Figure 3b the seismic hazard is dominated by: (i) $M_W = 5.5$–6.5 earthquakes at short distances ($R = 15$–30 km), associated with background seismicity, and (ii) larger ($M_W = 7$–7.5) earthquakes on mapped faults ranging from $R = 25$–50 km.

Ground motions were selected for seismic response analyses at 9 different intensity levels as shown in Figure 3a. For each intensity level, ground motions were selected from the NGA database

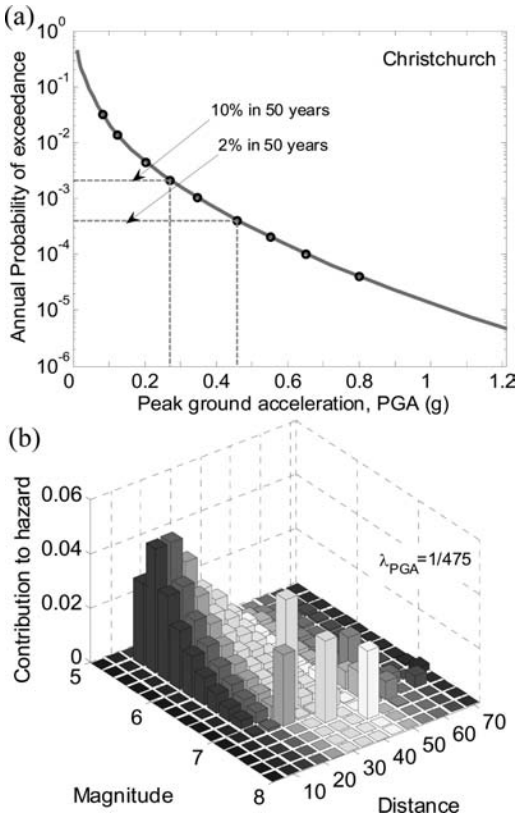

Figure 3. Details of the PGA seismic hazard for class C soil in Christchurch: (a) Seismic hazard curve; (b) Deaggregation of the hazard curve for an annual probability of exceedance of $\lambda_{PGA} = 1/475$.

(http://peer.berkley.edu/nga/) based on the hazard deaggregation . A further limitation of an amplitude scale factor in the range, $SF = 0.6$–1.6, was used to help ensure that ground motions with the correct frequency content (i.e. spectral shape) were selected.

5 DETERMINISTIC PERFORMANCE ASSESSMENT

Before conducting the probabilistic seismic response analyses with multiple ground motions and at multiple intensity levels, it is necessary to first rigorously examine the computational model and its response to various levels of ground motion excitation. This is important for: (i) verification of the analysis algorithms, (ii) validation of the computational model with engineering judgment and observations, and (iii) to understand the predominant deformation mechanisms which control the response. The latter point, in particular, is necessary before conducting probabilistic effective stress analyses since the number of analyses means it is not feasible to examine each analysis in detail, with various engineering demand parameter (EDP's) simply used to indicate the seismic

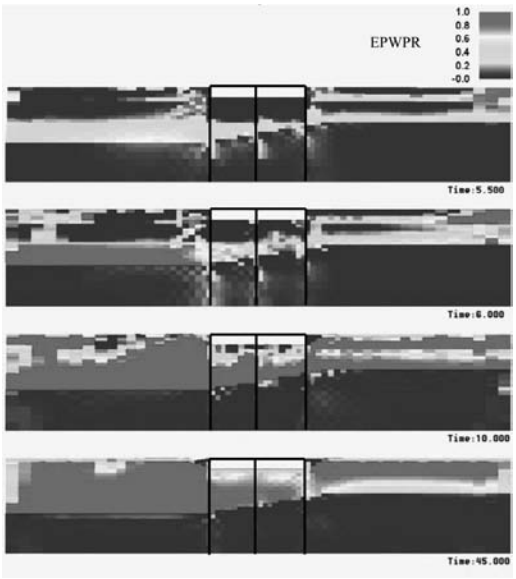

Figure 4. Development of excess pore water pressures and eventual liquefaction in the model during the deterministic analysis.

response. Thus an understanding of the deformational mechanism is critical in the selection of appropriate EDP's, and below the seismic response of the computational model is illustrated for a single ground motion scaled to an intensity level with a 2% probability of exceedance in 50 years (i.e. 0.463 g *PGA* from Figure 3a).

5.1 *Foundation soil response*

Figure 4 illustrates the development of excess pore pressures and eventual liquefaction in the soil surrounding the bridge. It can be seen that pore pressure ratios in the range $EPWPR = 0.2$–0.5 first develop in the bottom $N_1 = 10$ layer on the left hand side of the model, and at the base of the N_1 = 15 layer on the right hand side of the model. The bottom $N_1 = 10$ layer has almost entirely liquefied by 6.0 seconds. As time progresses, pore water pressures continue to increase in the $N_1 = 15$ layer on the right hand side of the model, and the re-distribution of excess pore pressures causes liquefaction to spread to shallower depths (predominantly on the left hand side of the model).

Figure 5a illustrates excess pore water pressure ratios 45 m to the left of the bridge. The three depths of $z = 6.15$, 14.75, and 19.75 m are located in the $N_1 = 15$, 10, and 30 layers, respectively. It can be seen that complete liquefaction of the $N_1 = 10$ (i.e. $z = -14.75$ m) layer by 7.0 s causes the removal of high frequency waves in the upper 10 m of the model. The liquefaction of the bottom $N_1 = 10$ layer also reduces the ground motion intensity in the above soil layers, which prevents full liquefaction from eventuating at

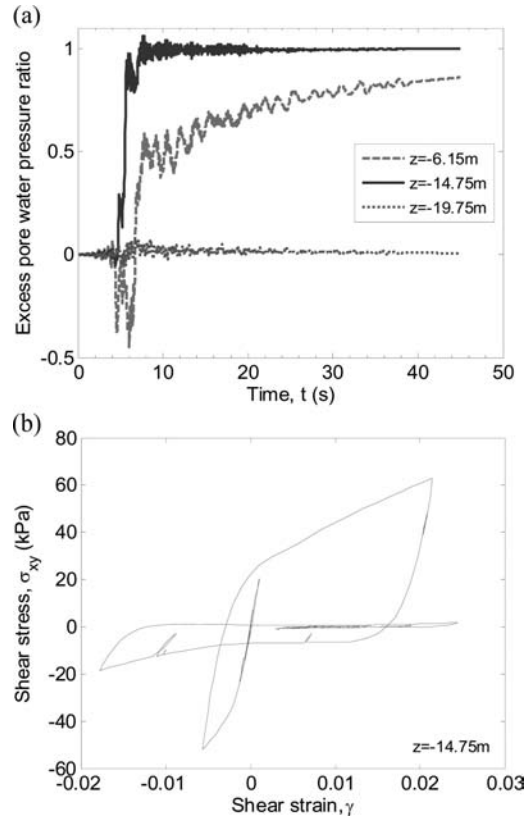

Figure 5. (a) Typical excess pore water pressure ratio development in the north free field ($x = 20$ m in Figure 2); and (b) shear stress-strain response.

$z = -6.15$ m. Figure 5b illustrates the shear stress-strain response of the soil at $z = -14.75$ m. It can be seen that following dilation to a shear stress of ~63 kPa, the soil liquefies and the response is characterised by very low shear stiffness and shear strains up to 2.5%.

5.2 *Bridge and pile response*

Figure 6a illustrates the displacement time histories at the three footings of the bridge, and the north and south free-field response (all at a depth of $z = -3.2$ m). In the first 7.0 s, it is apparent that the displacement in the north free-field is larger than the south free-field and footing displacements, which are essentially identical. After 7.0 s relative displacements between the three footings becomes apparent due to significant liquefaction occurring in the surrounding soils. It is also apparent in Figure 6a that the displacement histories of the footings appear to be not completely in-phase with the free-field responses (both north and south). Figure 6b provides a comparison of the acceleration histories at the north free-field ($z = 0$ m), central pile cap, and at 27.5 m depth, near the base of the model. It can be seen that the stiffening effect of the pile foundations allows waves of significantly higher amplitude

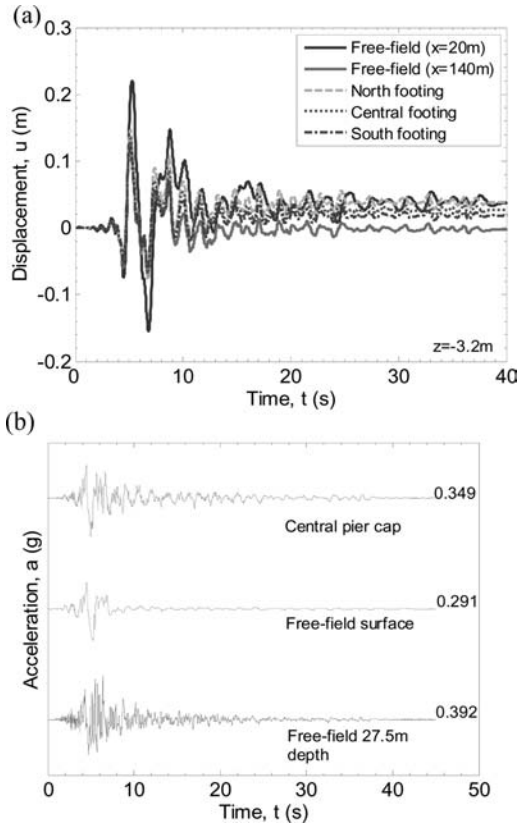

Figure 6. (a) displacement response history of the free field and at the pile footings; and (b) comparison of input, free-field, and pier cap acceleration histories (peak values given on the right hand side).

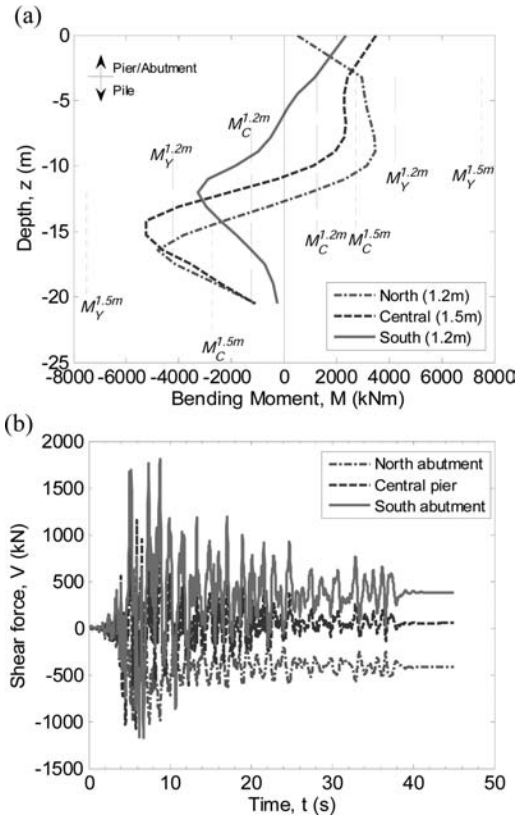

Figure 7. (a) bending moment profiles of the pile foundations at t = 5.15 s (M_C, M_Y are the cracking and yielding moments, respectively); and (b) shear force time histories in the abutments/pier.

and frequency to propagate to the central pier cap than to the free-field surface, thus the reason for the aforementioned out-of-phasing and smaller amplitude of the footing displacements in Figure 6a compared to that in the free-field.

Figure 7a illustrates the bending moment profiles in piles and abutments/pier at $t = 5.15$ s which corresponds to the peak footing displacements in Figure 6a. It can be seen that the seismic demand on the pile foundations is significant with both north and central piles exceeding their respective yield moments, and the south pile exceeding the cracking moment. The variation in the $N_1 = 10 - N_1 = 30$ boundary depth (e.g. Figure 2) is also observed to have a pronounced effect on the depth at which the peak negative bending moment is developed in the piles. The effect of this depth variation also causes larger soil displacements on the north side of the model relative to the south. As the large axial stiffness of the bridge superstructure effectively enforces equal displacements of the top of the abutments (with the exception of seating displacement discussed in the next paragraph), this variation in soil displacements in the horizontal direction also causes significantly different moments in the upper half of the piles and the abutments/pier. Figure 7b illustrates the shear force histories for the two abutments and central pier. It is immediately evident that forces in the north and south abutments are of opposite sign indicating that the bridge superstructure is predominately restraining the displacements of the north abutment/pile (where soil displacements are relatively large), and increasing the displacement of the south abutment/pile (where soil displacements are relatively smaller).

Figure 8 illustrates the relative displacement between the bridge superstructure and abutment (herein referred to as seating displacement) at the north and south abutments (the superstructure is fixed to the central pier). While for this particular ground motion the absolute value of the seating displacements are small (∼1 cm) compared with those necessary to cause unseating failure, this effect may be more important for higher levels of ground motion. In addition, correctly modelling the seating displacement also restricts the maximum shear force which can be transmitted between the bridge superstructure and abutments, which was observed to reduce the bending moments in the north and south abutments relative to those in the central pier.

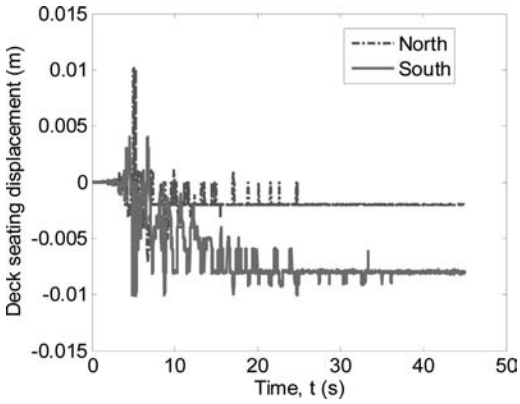

Figure 8. Deck seating displacement at the north and south abutments.

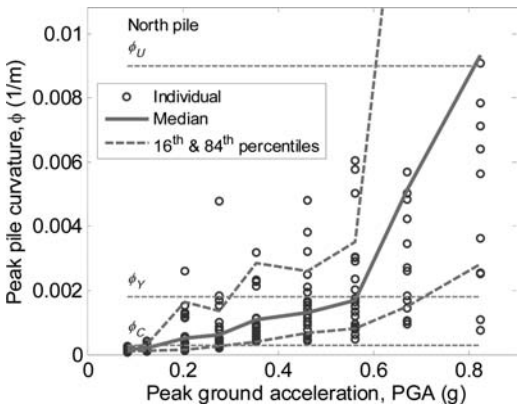

Figure 9. Example probabilistic seismic response analysis results for the north pile foundation.

6 PROBABILISTIC SEISMIC RESPONSE AND SEISMIC DEMAND HAZARD

6.1 *Probabilistic seismic response analyses*

Clearly a vast amount of information and insight into the seismic response of the entire bridge-pile-soil foundation is possible by rigorously examining such seismic effective stress analyses discussed in the previous section. Based on the observations of various deterministic analyses, a total of nine different engineering demand parameters (EDP's) were monitored in each of the probabilistic seismic response analyses discussed in this section. These EDP's were: the peak curvature throughout the length of each of the three piles; the peak curvature in the abutments and central pier; the maximum seating displacement at the two abutments; and the maximum value of the settlement of the gravel approaches to the bridge superstructure. Due to space limitations only the EDP|IM plot for a single EDP is discussed below.

Figure 9 illustrates the results of the seismic response analyses for twenty ground motions at nine intensity levels for peak curvature in the north pile.

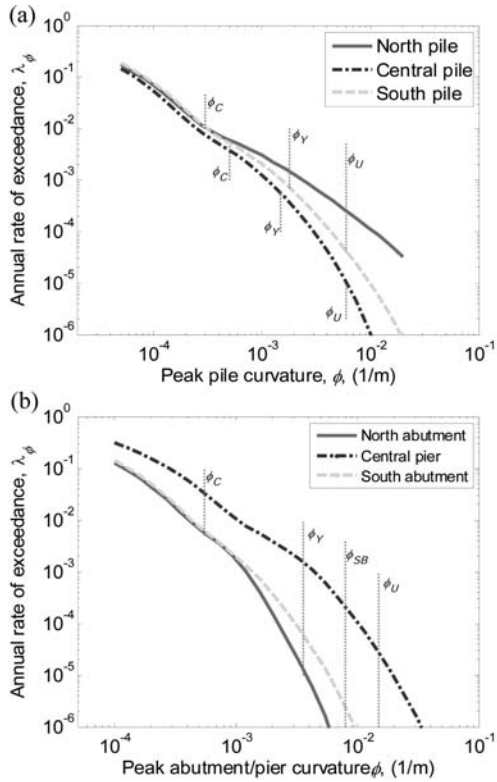

Figure 10. Demand hazard curves for: (a) peak pile curvature; and (b) peak abutment/pier curvature.

Several points are worthy of note in Figure 9. Firstly, as expected the demand increases with an increase in the input ground motion intensity. Secondly, there is a large amount of dispersion in the results (e.g. for $PGA = 0.46$ g the peak curvature in the north pile ranges from 0.0004–0.005). This large dispersion occurs because of the acknowledged inefficiency of *PGA* as a ground motion intensity measure for the seismic response of soft soil deposits.

6.2 *Seismic demand hazard*

By combining the seismic response analyses obtained in the previous section, which account for the variability in response due to the complexity of the ground motion excitation, with the seismic hazard curve in Figure 3a it is possible to compute the demand hazard curve for each of the different EDP's monitored. The demand hazard curve gives the annual frequency of exceeding a specified level of demand. Mathematical details can be found in Bradley et al. (2009b).

Figure 10a illustrates the demand hazard curves for peak pile curvature for each of the three piles in the computational model. The effect of the variation in demand for the piles observed in Figure 9 is also apparent in the demand hazard curves. Based on the monotonic moment-curvature relationship of the piles, cracking, yielding, and ultimate damage states

are also given in Figure 10a. It can be seen that the north and south piles are more vulnerable (i.e. have higher damage state exceedance frequencies) than the larger central pile, with the north pile significantly more vulnerable than the south pile, for higher levels of curvature. Figure 10b illustrates the demand hazard curves for the peak curvature of the abutments and central pier. It can be seen that the demand on the central pier is significantly greater than the north and south abutments, with the central pier having annual damage state exceedance frequencies typically an order of magnitude larger than the abutments.

Using relationships between demand, damage and loss for the nine demand measures used here it is possible to create loss hazard curves (loss vs. annual frequency of exceedance). Such loss hazard curves allow coupling of the likelihood of demand occurrence with the consequences of its occurrence, and are useful in communicating seismic risk to non-engineering stakeholders (Bradley et al. 2009b).

7 PROBABILISTIC SEISMIC LOSS ASSESSMENT

The seismic risk of the bridge-foundation-soil system in terms of the explicit loss consequences due to structural response may be viewed as ultimate measures of seismic performance for decision making. In order to conduct such a seismic loss assessment, the consequences, in the form of direct repair cost and repair duration, due to various states of damage for each of the components of the system are required. To this end, a professional cost estimator was engaged to develop cost estimates and repair durations due to various levels of damage in each of the components of the Fitzgerald bridge (Hopkins 2009). For brevity only a brief summary of the loss assessment results are given below, and further details can be found in Bradley et al. (2010).

Figure 11 illustrates the deaggregations of the expected direct loss and downtime for the 2% in 50 year exceedance probability. It can be seen that the direct repair loss is primarily attributed to damage to the north piles, central pier and liquefaction of the approach embankments. Conversely, the cost to repair damage to the north and south abutments comprise a significantly smaller proportion of the total repair costs. Similar trends are also observed regarding the downtime deaggregation, except it is worthy of note that the total repair time for repair group 2, RG_2 (in particular, the central pier), is small considering the significance of the central pier in the deaggregation of the direct repair costs. This is because the duration required to repair cracking (using epoxy injection) in the central pier does not require excavation of the gravel backfills as in the case of repairing cracking in the bridge abutments. As for the direct repair cost, the downtime to repair damage in the north piles is larger than that for the central and south piles. The time to re-establish adequate seating length of the bridge deck

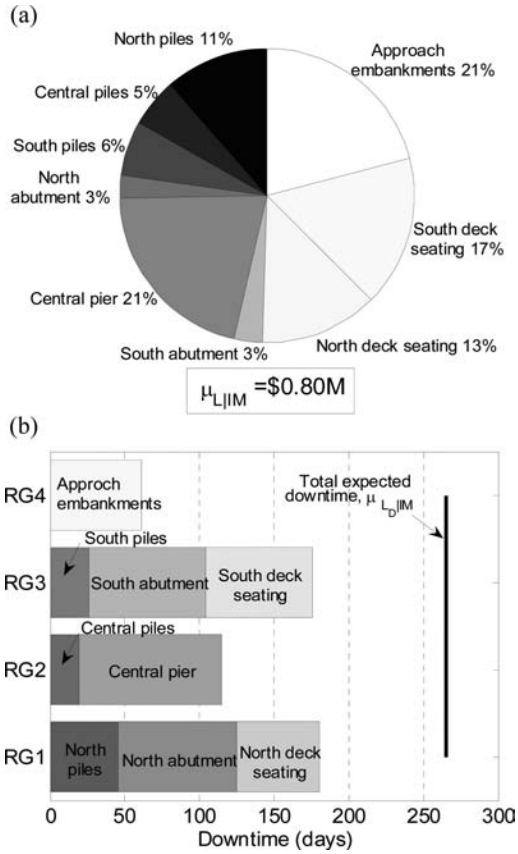

Figure 11. Deaggregation of the different components of the bridge-foundation-soil system for PGA = 0.46 g (2% in 50 years) (a) the expected direct repair cost; and (b) expected downtime.

at both the north and south abutments is also an important contributor to the total expected downtime of the bridge-foundation-soil system.

Knowing that travel delay and vehicle running costs due to inoperability of the bridge structure amount to $10,720/day (MWH 2008), the annual rate of exceeding a specified level of downtime (in days) can be converted to the annual rate of exceeding a specified level of economic loss. Figure 12 illustrates the annual rate of exceeding some level of economic loss due to inoperability of the bridge, as well as the annual rate of exceeding some level of direct repair cost of the system. It can be seen that over the full range of economic losses, the economic implications due to loss of functionality is significantly larger than that due to direct repair of damage. In particular, the 2% in 50 year exceedance probability ($\lambda_L = 4.0 \times 10^{-4}$) losses are $1.20 M and $3.95 M respectively. For comparative purposes it is again noted that the book-value of the Fitzgerald Avenue twin bridges is only $2.4M. Thus, there is a 2% in 50 year probability that the total loss will exceed almost $5.2 M, over two-times the book-value of the infrastructure itself.

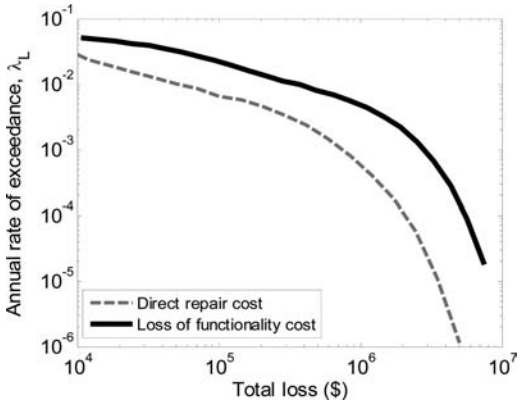

Figure 12. Comparison of the annual rate of exceedance of losses due to direct repair cost and loss of functionality.

8 CONCLUSIONS

This paper has presented the probabilistic seismic performance assessment of an actual bridge-foundation-soil system, the Fitzgerald Avenue twin bridges. The significant insight which can be gained regarding bridge-foundation-soil interaction and associated nonlinearities using effective stress analysis was illustrated for a particular ground motion. The significant uncertainty regarding the input ground motion was addressed by subjecting the model to twenty different ground motions at nine different intensity levels. By combining the probabilistic EDP|IM relationships with the ground motion hazard curve, it is possible to compute the demand hazard for the various EDP's and compare them to various damage states for each of the components.

It was observed that the non-horizontal soil profile layering and soil liquefaction were key factors in the response of the bridge-foundation-soil system. The critical components governing the seismic performance of the system were the north abutment piles and the central pier, which had the highest annual frequencies of exceeding various damage states.

Loss analysis was used to provide further insight into the key components affecting the direct repair cost and downtime.

ACKNOWLEDGEMENTS

Financial support from the New Zealand Tertiary Education Commission and the New Zealand Earthquake Commission is greatly appreciated.

REFERENCES

Bowen, H. & Cubrinovski, M. (2008). Effective stress analysis of piles in liquefiable soil: A case study of a bridge foundation. *Bulletin of the New Zealand Society for Earthquake Engineering* 41(4): 247–262.

Bradley, B. A., Cubrinovski, M., Dhakal, R. P. & MacRae, G. A. (2009a). Intensity measures for the seismic response of pile foundations. *Soil Dynamics and Earthquake Engineering* 29(6): 1046–1058.

Bradley, B. A., Dhakal, R. P., Cubrinovski, M., MacRae, G. A. & Lee, D. S. (2009b). Seismic loss estimation for efficient decision making. *Bulletin of the New Zealand Society for Earthquake Engineering* 42(2): 96–110.

Bradley, B. A., Cubrinovski, M., Dhakal, R. P. & MacRae, G. A. (2010). Probabilistic seismic performance and loss assessment of a bridge-foundation-soil system. *Soil Dynamics and Earthquake Engineering*: DOI: 10.1016/j.soildyn. 2009.12.012.

Cubrinovski, M. & Ishihara, K. (1998). Modelling of sand behaviour based on state concept. *Soils and foundations* 28(3): 115–127.

Cubrinovski, M. & Bradley, B. A. (2009). Evaluation of seismic performance of geotechnical structures. International Conference on Performance-Based Design in Earthquake Geotechnical Engineering — from case history to practice, Tokyo, Japan, 16.

Diana-J3. (1987). Finite-element program for effective stress analysis of two-phase soil medium. Software science.

Hopkins, W. (2009). Cost estimates for seismic damage to the Fitzgerald Avenue twin bridges. (personal communication).

MWH. (2008). Avonside/Fitzgerald/Kilmore Intersection: Economic Evaluation. Prepared for: Christchurch City Council, 42pp.

Shome, N. & Cornell, C. A. (1999). Probabilistic seismic demand analysis of nonlinear structures. *Report No. RMS-35, RMS Program*, Stanford University, Stanford, CA, 357pp.

Stirling, M. W., Gerstenberger, M., Litchfield, N., McVerry, G. H., Smith, W. D., Pettinga, J. R. & Barnes, P. (2007). Updated probabilistic seismic hazard assessment for the Canterbury region. *GNS Science Consultancy Report 2007/232, ECan Report Number U06/6*, 58pp.

Soil-Foundation-Structure Interaction – Orense, Chouw & Pender (eds)
© 2010 Taylor & Francis Group, London, ISBN 978-0-415-60040-8

Summary of discussion session 1

ABSTRACT: At the end of each day of the workshop, discussion sessions were conducted with the aim of eliciting important comments about the current state of understanding in soil-foundation-structure interaction and indicating which developments are likely to be most beneficial. The first discussion session dealt with issues related to shallow foundations, while the second session was concerned with pile foundations.

SPECIAL NOTE

The two discussion sessions were conducted under intense yet enjoyable exchange of opinions among the workshop participants. Because of the inherent difficulty in capturing everything what was said and perhaps losing the context when transforming them into a written form, readers are cautioned that what follows represents the best efforts of the editors to capture the flow and cut-and-thrust of the discussions.

1 SHALLOW FOUNDATIONS FOR BRIDGES

1.1 *Nonlinear soil behaviour*

Several papers submitted to the workshop extolled the virtues of nonlinear soil behaviour under shallow bridge foundations. Three participants summarized their findings to get the discussion session underway. The main point made was that brief instances in which the shallow foundation bearing strength was realized result in only modest permanent displacements of the foundations and the design actions were less than those on a foundation which maintained a reserve of strength right through the earthquake excitation. These conclusions have been reached mainly through numerical calculations, but they have been supplemented by shaking table and centrifuge tests.

During the course of the discussion, the term rocking was also used and a clarification was made that the phenomenon of rocking is associated with the yielding of the soil, not with the mechanism that dissipates the energy away from the structure.

A counter argument questioned the validity of this as a design approach because of the inherent uncertainty in the shear strength of natural soil and hence the uncertainty in the shallow foundation bearing strength. It was suggested that the capacity of a reinforced concrete column, for example, was, in principle, capable of more accurate specification than the bearing strength of a foundation on natural ground. The geotechnical team was thus challenged to demonstrate that nonlinear soil behaviour was indeed a reliable mechanism on which to base foundation design.

To further emphasize this point, it was explained that the earthquake resistant design of structures following the capacity design approach is based on adopting a mechanism and then ensuring that all plastic hinging is localized at these positions and no others. Thus, the challenge to the geotechnical team was further refined to require that unexpected foundation behaviour does not interfere with the expected behaviour of the structure-foundation system. Consequently many design teams might prefer to rely on a foundation design which has an ample reserve of strength and provide a yielding mechanism elsewhere in the structure-foundation system.

As a rejoinder, it was emphasized that the nonlinear foundation effect was controlled more by the geometry of the footing than the shear strength of the underlying soil. So the vexing question of uncertainty in soil property values might not be as critical as suggested. Furthermore, one contributor explained that centrifuge modeling of bridge structures on shallow foundations had shown that smaller footings resulted in smaller structural actions. In this case, structural yielding of columns might not be induced.

Another comment made was the nonlinear foundation behaviour might be satisfactory for an earthquake with a, say, 200 year return period, but would it also be satisfactory for a 2000 year event? The agreed approach is that the structure must not collapse in the 2000 year event and that for the 200 year event any damage should be easily repaired. The proposal is that nonlinear behaviour of the soil beneath the foundation in the 200 year event is likely to reduce the foundation actions. It was emphasized though that a column is readily apparent and, since it is above ground, comparatively easy to repair. What happens when the foundation has a large residual rotation, how easy is it to repair that?

Another query was related to the post-earthquake deformations of the structure-foundation system. For taller structures, permanent rotation is probably the most critical deformation and so the question of self -centering was raised. It was agreed that there is no formal self-centering mechanism associated with nonlinear behaviour of the soil beneath shallow foundations.

One situation in which it was agreed that the contribution from nonlinear behaviour of soil beneath a foundation might be of importance is when it comes to considering existing infrastructure and whether retrofit is necessary. In this case, a sophisticated assessment of the behaviour of the existing foundation might provide enough assurance that retrofit could be avoided.

1.2 *Code implementation*

There was a concern that allowing the ground forming the foundation to yield is more of a theoretical exercise than a practical one, since the codes would not allow such to be constructed. However, one participant noted that EC8 would probably allow it as long as it is agreed that it is a good solution.

The conclusion of this part of the discussion was that a challenge was placed before those wishing to promote nonlinear behaviour of soil beneath shallow foundations as a viable method of design. The challenge is simple enough: to convince potential users that the mechanism is a reliable mode of foundation behaviour. One of the participants made the comment that much of the discussion had reminded him of the discussions thirty or so years ago in New Zealand when base isolation was first considered, that is, base isolations did not satisfy the code but met the intent of the code.

Thus the conclusion is that this is an idea in need of "selling". It was emphasized that for such selling to be accepted, care was needed with terminology. "Design sophistication" was suggested as likely to be a more "sellable" concept than foundation failure.

2 SHALLOW FOUNDATIONS FOR BUILDINGS

2.1 *Rocking of buildings*

Another point that was raised with respect to the use of shallow foundations is that they may be adopted because the ground is good so that the bearing strength is greatly in excess of the static bearing pressure and that even during earthquake loading, there is an adequate reserve of bearing strength. In this instance, the foundation will rock and with little nonlinear soil deformation. Behaviour like this will be likely for office type buildings with a modest number of stories (apparently not uncommon in New Zealand).

It was pointed out that compared to bridges, buildings are more sensitive to torsional effect and when it starts to rock, not only one plane is involved and therefore, distortion of the building may occur. Moreover, rocking also poses a problem on how the forces are going to interact between structural members and the floors.

The discussion contribution made the point that there is little to be gained from preventing this rocking motion, and doing so will simply increase the actions induced by the earthquake motion in the building. An example was given of a structure in Tokyo with an external steel frame. In this case, the designers decided that allowing the frame to rock lead to a more efficient design. They used a new structural system that relieves seismic forces vertically through a lifting rear column at ground floor level, restrained by dampers. This 'stepping column' system was able to move with the earthquake, thereby reducing forces and foundation and steelwork costs. In this case, of course, there is no contribution from nonlinear soil behaviour. A similar mechanism has been used in New Zealand in the Rangatiki Rail Bridge.

2.2 *Rocking of pile foundations*

There was a query as to whether the concept of rocking foundation could be used for piles at the end of the frame, and whether one can get those to move up and down. The sentiment of the participants was that it can be adopted in the design philosophically, that is, if the structure wants to move, let it move. By doing so, one can achieve an economically satisfactory design.

3 SOIL PROPERTIES

3.1 *Stiffness for settlement calculation*

A paper presented during the workshop showed that in calculating the vertical settlement of a footing subjected to cyclic loading, the appropriate ground stiffness to be used seemed to be far removed from the small-strain stiffness of the ground. One participant commented that for foundations under gravity loading, the small-strain stiffness should be modified to account for the nonlinearity, say using Schmertmann's method. Based on experience, the small-strain modulus must be modified by a factor of 0.4–0.5 to predict the long-term settlement of shallow foundations.

Another participant commented that he used a variety of methods to assess the long-term settlement of tall buildings, such as geophysical methods, maximum stiffness, pressuremeter data derived in-situ, stress path testing, etc. He noted that the G_{max} values resulted in significantly higher values than the others. Therefore, a recommended approach would be to scale down the G_{max} by a factor between 0.3–0.4.

On the other hand, when dealing with short-term settlement, say induced by earthquake or wind as in rocking motion, a higher modification factor is suggested. A single soil stiffness should not be used for different loading conditions. Moreover, it was stressed that such simplification is not meant to take the place of more sophisticated types of analysis.

3.2 *Soil variability*

In analyzing a field test which was presented during the workshop, it was stressed that the appropriate stiffness must be obtained within one or two days of the test. One participant noted that the stiffness can increase

by a factor of ten simply with the passage of a water truck. Thus, miniaturized tests beneath footings are recommended and tarps be used as cover to minimize changes in moisture content of the ground, especially when the ground consists of fine particles.

Moreover, material characteristics can change, especially in the zone of seasonal moisture change. If the foundation is below this zone, then there is no problem; however, if it is within the zone, then the change must be considered. Thus, shallow foundations have different resistance during winter than in summer.

One participant commented that soil variability must be considered in determining soil properties. For example, plate loading reaction tests using small diameter plates may not be good for buildings; engineers must know how sampling from a small zone would compare to the real-size footing. The whole picture of the load-settlement curve is not necessary.

It was also stressed that small strain stiffness is not very frequency dependent; however, damping is. One participant mentioned that stiffness also depends on the direction of loading.

4 GEOTECHNICAL AND STRUCTURAL ENGINEERING COLLABORATION

One participant mentioned that in the past, there was much separation between geotechnical and structural engineers because the approach adopted was excessively too simplistic – for structural engineers, the foundation ground is composed of springs while geotechnical engineers consider the structure as a lumped mass. Recently, the role of geotechnical people in providing appropriate foundation stiffnesses to structural engineers has been recognized, and it is a big mistake to ignore the interactions going on in the soil when designing the superstructure.

Care must be taken when talking about conservatism (in adopting values) and that understanding what it involves is necessary. For geotechnical capacity, conservatism means taking the lower bound value of strength, while for structures, it may be taking a high value or low value; the dynamic issue in terms of stiffness is that one is not sure if a high modulus or low modulus is critical. Thus, interaction between geotechnical and structural engineers becomes very important – the taller the building is, the more critical this interaction becomes.

Another comment made was that structural engineers in Australia moved away from the conventional working stress design concepts to ultimate strength LRFD concepts, and yet they tend to give geotechnical engineers working loads rather than ultimate loads.

The context of one of the workshop papers emphasized the need for the geotechnical and structural teams to work together to achieve the best foundation-structure system design. This was agreed by all present. It was commented that when a large multi-disciplinary practice is responsible for a complete project then the collaboration was easily achieved. It seemed to be more difficult when the people dealing with the foundation work in a different organization than those entrusted with the design of the structure.

One participant commented that engineers also need the cooperation of engineering seismologist, especially since site-specific data are often neglected in the design spectra. Through this interaction, a better understanding of the motion required for the structure can be obtained.

Finally, as noted early on in the discussion, the number of geotechnical engineers present was greater than the number of structural engineers. The organizers responded by explaining that many structural engineers had been invited but declined the invitation. However, the general feeling of success at the end of the workshop indicated that if another SFSI workshop was to take place then the event would likely attract many more structural engineering participants.

MAJOR CONTRIBUTORS

M. Pender (session chairman), I. Anastasopoulos, A. Carr, C.Y. Chin, N. Chouw, B. Deam, S. Iai, G. Jamieson, B. Jeremic, B. Kutter, C. Lai, I. Lam, J. Pappin, A, Pecker, H. Poulos, S. Prakash, S. Sritharan, K. Stokoe, T. Sullivan, E. Taciroglu, C. Tamagnini

Soil-Foundation-Structure Interaction – Orense, Chouw & Pender (eds)
© 2010 Taylor & Francis Group, London, ISBN 978-0-415-60040-8

Summary of discussion session 2

ABSTRACT: The second discussion session was patterned on the earlier discussion session on shallow foundation for bridges, i.e., the benefits of nonlinear soil behaviour and short instances of bearing failure, but focusing on pile foundations. Several topics were considered during the session.

SPECIAL NOTE

The two discussion sessions were conducted under intense yet enjoyable exchange of opinions among the workshop participants. Because of the inherent difficulty in capturing everything what was said and perhaps losing the context when transforming them into a written form, readers are cautioned that what follows represents the best efforts of the editors to capture the flow and cut-and-thrust of the discussions.

1 PILE FOUNDATIONS FOR BRIDGES UNDER EARTHQUAKE LOADS

One issue raised was whether piles should be allowed to undergo inelastic deformation when subjected to seismic loads (i.e. moderate to large earthquakes).

1.1 *Yielding in piles*

In the earlier discussion session on shallow foundation, the possibility of yielding was discussed, i.e., yielding of the soil. For pile foundations, there are two different possibilities: plastic deformation in the soil without plastic deformation of pile or allowing plastic deformation of the pile without reaching the soil failure condition by allowing one or more points of yielding within the length of the pile.

Design codes have provisions on safety evaluation with respect to the ultimate failure load. If yielding is not allowed in piles, then in the calculation of ultimate failure load, it follows that long piles should be considered as short piles, resulting in enormously large failure load and consequently, large bending moments within the pile, which are not realistic. Thus it is necessary, following the code provision, to at least allow the pile to yield at ultimate limit state, say during large earthquakes.

During the drafting of Eurocode 8, there was a big discussion that ensued because geotechnical engineers were generally in favor of allowing plastic yielding within the piles, but structural engineers were against it. Yielding should be allowed only at the pile cap connection, not anywhere else within the ground, because engineering calculations typically result in very high bending moment in this region.

1.2 *Superstructure-foundation system*

In conventional design procedures for the superstructure, the foundation is considered elastic, i.e., no large or significant plastic deformation within the foundation is allowed. Thus, from the design point view, problems arise when piles are allowed to yield because the current procedure does not consider the whole system when designing piles. Should piles be designed as isolated members, or as part of the whole system? This becomes complicated because we now have the problems of having two systems (superstructure and foundation) instead of a single structure-foundation system.

To answer this question, one participant stressed that it is necessary to understand the whole design principle. If the author of the design philosophy says that there is a need for plastic hinges in the foundation, then geotechnical and structural engineers must make sure that there is sufficient strength in the foundation. If a plastic hinge is introduced in the foundation, one needs to understand the strategy. Allowing plastic hinges in the pile is a case-to-case basis, and it depends on the need to allow some inelastic action within the system. There is a need to rationalize the inelastic action within the pile cap before the superstructure can be designed.

Another participant suggested that the answer to the question is uncertain. We as engineers do not have a choice because the system decides how it wants to behave, unless, as designers we account for that. If the answer to the question is uncertain, then we are also uncertain about the expected seismic performance of the structure. In the current capacity design philosophy, engineers pre-locate and detail the plastic hinges (e.g., there is a prescribed limit on how much transverse or confining reinforcement is necessary) and then perform capacity-protected design for regions outside the plastic hinges. In effect, based on capacity design philosophy, the piles are designed to remain elastic. However, most codes today require confining reinforcement in designing piles, i.e., they work outside the capacity design philosophy. Moreover, the inelastic demand on the pile is unknown, with acceptable ductility ratio ranging from 1–20. Thus, although existing design codes allow formation of plastic hinges, each code has different level of prescribed limit for the hinge to develop full-plastic capacity. Thus, the likely response of the pile can

be either elastic, limited inelastic (moderate ductility range) or full inelastic action. The system performance is largely influenced by the pile response during seismic action, and not by the design philosophy used. Hence, engineers need to account for foundation design flexibility in the design of the system, and this requires a joint effort between geotechnical and structural engineers.

1.3 *Stand-alone analysis vs global approach*

In conventional design processes, structural engineers give some data to geotechnical engineers to design the foundation, and the geotechnical engineers give some parameters/quantities to structural engineers to design the superstructures. However, the whole thing is a coupled process, and the analysis should be done in a single uniform way.

This brings to mind two types of approaches in designing pile-supported structures: (1) the stand-alone process, which may be acceptable as long as each group gives adequate information to the other group; and (2) the integrated approach with the single model containing all the details required. One participant commented that based on his experience with designing bridges, it is possible to carry out stand-alone analysis first (e.g., piers alone, abutment alone, etc), and then build those models (stiffness, damping, etc) into a single global type of analysis.

Finally, it was the consensus of that when dealing with nonlinearities in the foundation and nonlinearities in the structure, the analysis needs to be done together. It is not possible to compartmentalize or substructure two nonlinear parts of a system.

A question was raised on the role of kinematic interaction in the structural response. Specifically, how the stiffness of deep foundations (like large-diameter shafts) influence the excitation of the superstructure. The effect of rotational excitation produced by the filtering effect of the large diameter shafts have contributed to increase of 15–20% in the seismic demand of the superstructure. Thus, it is important to quantify the contribution of kinematic interaction in modifying the structural response.

1.4 *Allowable maximum pile displacement*

One possible alternative to pile yielding is to specify a permissible displacement for the foundation, such as 50 mm for bridges (according to Caltrans, Japanese practice, etc.). Meaning, the pile should not be designed whether it would be elastic or inelastic, but such that the maximum displacement will not exceed 50 mm, and this should be incorporated in the design of the superstructure. Based on functionality requirements for bridges, 50 mm appears to be the upper limit at which the bridge would remain serviceable.

However, many participants believed that this is a very small displacement. It would be best to define the gradient rather than pile head displacement, i.e., 50 mm over a 2 m length or 20 m length of pile. When dealing with liquefaction and lateral spreading, this maximum displacement will certainly be exceeded. In addition, performance-based design must not be mixed with displacement-based design. From the practical point of view, downtime (or loss of function) is a significant consequence of allowing failure of part of a system and therefore, the ease to repair the damage of the structure is also an important consideration that needs to be accounted for in the design, in addition to the seismic performance of the structure. This is one reason why it is not practical to allow failure at deeper locations of the system because of repair difficulty.

1.5 *Damage to pile foundations during earthquakes*

Based on the previous discussion, there was a general consensus that the way we design piles today is that they will yield at the pile cap connection. However, previous earthquakes showed that piles can be damaged at deeper locations, say within the liquefiable ground. Such damage is caused by lateral spreading, pile group effects and, possibly, buckling. If that is the case, how do we prevent damage in piles from occurring at these deeper locations?

During the Kobe earthquake, piles in liquefiable ground underwent cyclic lateral deformation in the order of 200–300 mm; piles were damaged by this excessive lateral deformation, which did not even include the effect of lateral spreading. Thus, piles in liquefiable ground require special design considerations.

A code-based approach is simply not to allow pile installations in liquefiable soils. Instead, implementation of ground improvement techniques is recommended, as in Eurocode. Based on Japanese practice, this is the first option, but because of the expense involved, engineers try to limit the improvement area by running sophisticated analyses.

Another method is to reduce the lateral load by putting the pile cap above the ground, i.e., when the soil is undergoing lateral spreading, passive pressure is created on the pile cap, thereby reducing the load on the piles. In this way, the pile could possibly remain elastic.

2 SOIL AND PILE NONLINEARITY

2.1 *Nonlinear stress-strain relation*

The second issue is the importance of detailed representation of nonlinear stress-strain relation in the soil and in the pile when examining pile response during earthquakes.

Instead of nonlinearity, one participant mentioned that a better terminology would be soil or pile inelasticity. Inelasticity is as significant as non-linearity because of plastic effects, such as in problems where dynamic loading induces changes in pore pressure in soil. It is the dilatancy of the soil which is paramount to

getting a reasonable prediction of the pore water pressure; this can not be obtained if the model is nonlinear but does not account for dilatancy. Moreover, the coupling effects which are typical in inelastic models can not be predicted with nonlinear springs.

It was mentioned that nonlinearity becomes increasingly important as the applied load level increases. For seismic/dynamic loads, a greater level of non-linearity is assumed as compared to vertical (gravity loads).

2.2 *p-y curves*

2.2.1 *Non-liquefiable soils*

It has been accepted that p-y curve is not unique but a function of both soil and pile properties. For example, it is well-established that independent springs work well for flexible piles, but for stiff piles, the interaction becomes more significant and p-y curve can not represent this. Moreover, based on actual projects, the boundary condition of the pile (free head, fixed head) has important effect on the p-y curve, but this is not reflected in current design practice. It was also pointed out that the p-y curve is just a tool, and it is important to look at experimental data and all the various aspects to make the right calculations.

2.2.2 *Liquefiable soils*

In liquefiable ground undergoing lateral spreading, case studies have shown that if the pile is weak and it fails, it is difficult to predict the shear and moment distribution within the pile. However, that is not the desired outcome. To avoid failure, the use of bigger/stronger piles is recommended so that soil can flow around it. In this case, the p-y method is more forgiving and the analysis is not difficult, resulting in more reliable results.

However, this is difficult to achieve for piles in liquefiable soils and therefore the alternative is to reduce the demand on the pile through implementation of ground improvement methods or to use a pneumatic caisson or similar type of foundation.

2.2.3 *Undrained behavior vs. Residual state*

One inconsistency in the present methodology of analyzing pile response in liquefiable soils is the appropriate soil behaviour to be used. In performing sophisticated ground response analysis like seismic effective stress approach, the very strong effect of the undrained response of the soil can be seen around the pile. However, when using a simplified approach based on say the residual strength concept, undrained behaviour is not assumed. Thus the ultimate strength levels used are very different between the two approaches. Although both approaches are valid, they are discontinuous in terms of philosophy and in the use of different soil properties, and this is a problem.

Laboratory tests indicate that the steady state strength is achieved at strains beyond 20% or 50%, or often beyond the limitation of the testing apparatus. Cyclic mobility type of behaviour, on the other hand, occurs much earlier, i.e., within a significant range used in design, such as at 1% or 5% strain level. For a comprehensive analysis of the whole system, there is a need for a good constitutive equations to idealize this range of behaviour. A wrong approach is simply adopting the hyperbolic stress-strain relation with the steady state strength value as peak value.

3 ROLE OF UNCERTAINTIES IN SEISMIC RESPONSE

3.1 *Ground motion characteristics*

In conventional practice, 3 or 7 ground motions with similar seismological signatures, i.e. magnitude, source properties and hypocentral distance, are adopted when performing time history analyses of the seismic response. These result in different outcomes, which are interpreted in terms of mean response, envelopes, etc. There are issues on how this philosophy fits the geotechnical program – is this acceptable?

One alternative is to use one stochastically simulated ground motion which can represent the ground motion. However, the use of such synthetic ground motion is not recommended, but is possible in the Eurocode. In designing bridges in the U.S., 7 structural-compatible ground motions are required to give reasonable answer. In France, when nonlinear analysis is performed, the result at the end is taken as the mean plus some fraction of the standard deviation, where the fraction is a function of the number of time histories used, which reflects 95% level of confidence.

Based on Swiss experience, one participant noted that the larger variability comes, not from seismic sources nor from geotechnical soil profiles, but from attenuation laws used to predict ground motion.

3.2 *Soil profiles and model parameters*

Uncertainties in soil profiles and soil parameters can be incorporated through probabilistic analysis. Using even a simplified approach, one can take the mean plus one standard deviation to represent the final result. Based on the results, one can go to the owner and confirm if he/she is willing to invest more money into site investigation. If not, the engineer must explain the expected displacement based on predicted profile. With more money, one can reduce the risk, and offer better solution through improved prediction.

There are two important aspects of the probabilistic approach: spatial variability and localized measurement vs. global measurement done using various sampling techniques. In performing site investigation, for example, surface wave techniques are averaged over much larger volume, PS suspension loggers average over short distance, while in cone penetration testing, the tip covers a much smaller area again. Note that the earthquake does not do this, and earthquakes typically have wavelengths of the order of a hundred meters, and this is not incorporated correctly into the whole scheme.

In most cases, engineers take the coefficient of variation (COV), layer locations, shear wave velocities, etc. In cases of high COV, taking the mean output means muting the site behavior, and all peak responses disappear. Thus, in a probabilistic approach, key aspects in site response analyses are more often that not muted when they should not be.

In areas where localized discontinuities occur in a large area under consideration, it is better to subdivide the generalized area, and each smaller section should reflect different outcomes and therefore different designs. Thus, how one handles the data at the start will have huge impact on the outcome of the analysis.

3.3 *Modeling/Prediction vs Design*

Geotechnical engineers are faced with analyzing the superstructure-foundation system behavior considering linear/non-linear aspects etc., but for practical purposes, adopt say 3 or 7 strong motions. These two approaches seem to be incompatible. One participant commented that there is a distinction between modeling/prediction and design. When a problem is analyzed, one tends to construct a theoretical/numerical model, with loads and properties modeled adequately, which is not what the designer will adopt in common practice. The goal of the designer is to design the structure to be safe and in accord with code regulations. Codes, therefore, must incorporate all these practical recipes to help the designers. Thus researchers must provide further insights so that code writers will improve the current practice.

Designers are concerned with the most economical solution which is compatible with building code requirements. This may not necessarily be the solution the researcher wants. If one is designing, it is necessary to know which parameters are controlling the design. However, this will cost money to the owners. Therefore, owners should be educated on the use of confidence level, or of parameters which can quantify losses, such as return of investment (ROI). Unfortunately, building owners can not make all decisions and in some cases, they do not understand that they are taking risks.

MAJOR CONTRIBUTORS

M. Cubrinovski (session chairman), A. Carr, N. Chouw, B. Deam, S. Iai, B. Jeremic, B. Kutter, C. Lai, I. Lam, S. Prakash, A, Pecker, M. Pender, S. Sritharan, K. Stokoe, E. Taciroglu, C. Tamagnini

Soil-Foundation-Structure Interaction – Orense, Chouw & Pender (eds)
© 2010 Taylor & Francis Group, London, ISBN 978-0-415-60040-8

Photos

Welcome reception.

Technical session.

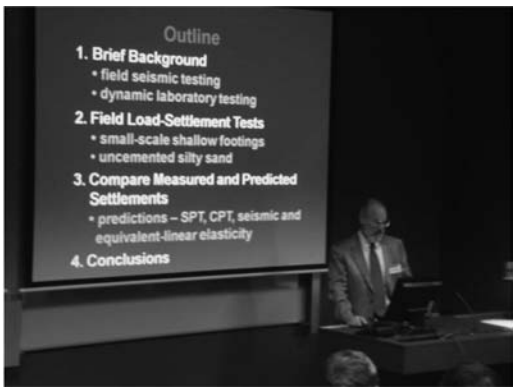

Ken Stokoe delivering his paper.

Discussion session.

Harry Poulos delivering his paper.

Dean Michael Davies giving his welcome remarks.

Workshop banquet.

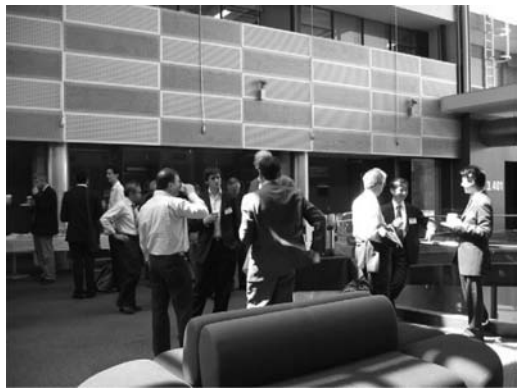

Scene during coffee break.

Workshop banquet.

Pre-workshop tour to Auckland Museum.

Workshop banquet.

Pre-workshop tour to Auckland Museum.

Soil-Foundation-Structure Interaction – Orense, Chouw & Pender (eds)
© 2010 Taylor & Francis Group, London, ISBN 978-0-415-60040-8

List of participants

International workshop on soil-foundation-structure interaction 2009

Name	Affiliation	Email
Algie, Tom	University of Auckland	talg001@aucklanduni.ac.nz
Anastasopoulos, Ioannis	National Technical University of Athens	ianast@civil.ntua.gr
Bradley, Brendon	GNS Science	b.bradley@gns.cri.nz
Carr, Athol	University of Canterbury	a.carr@civil.canterbury.ac.nz
Chin, C.Y.	AECOM	cy.chin@aecom.com
Chouw, Nawawi	University of Auckland	n.chouw@auckland.ac.nz
Cubrinovski, Misko	University of Canterbury	misko.cubrinovski@canterbury.ac.nz
Davies, Michael	University of Auckland	michael.davies@auckland.ac.nz
Deam, Bruce	University of Canterbury	bruce.deam@canterbury.ac.nz
Finn, Liam	University of British Columbia	finn@civil.ubc.ca
Gebreyohaness, Adane	University of Auckland	ageb004@aucklanduni.ac.nz
Harwood, Nick	Coffey Geotechnics	nick_harwood@coffey.com
Ho, Kah-Weng	CPG New Zealand Ltd	kah-weng.ho@nz.cpg-global.com
Iai, Susumu	Kyoto University	iai@geotech.dpri.kyoto-u.ac.jp
Iguchi, Michio	Tokyo University of Science	iguchi@rs.noda.tus.ac.jp
Itoh, Kazuya	University of Auckland / J-NIOSH	k-ito@s.jniosh.go.jp
Jamieson, Graeme	Bloxam Burnett & Olliver Ltd	gjamieson@bbo.co.nz
Jeremic, Boris	University of California, Davis	jeremic@ucdavis.edu
Keeran, Moss	Moss Engineering Ltd.	moss@mossengineering.co.nz
Khwaounjoo, Yadav	GHD Ltd.	Yadav.Khwaounjoo@ghd.co.nz
Kikuchi, Yoshiake	Port & Airport Research Institute	kikuchi@pari.go.jp
Kutter, Bruce	University of California, Davis	blkutter@ucdavis.edu
Lai, Carlo	EUCENTRE	carlo.lai@eucentre.it
Lam, Ignatius	Earth Mechanics Inc	P.Lam@earthmech.com
Larkin, Tam	University of Auckland	t.larkin@auckland.ac.nz
M.Sa'don, Norazzlina	University of Auckland	nmsa001@aucklanduni.ac.nz
Moghaddasi, Masoud	University of Canterbury	masoud.moghaddasi@pg.canterbury.ac.nz
Nagano, Masayuki	Tokyo University of Science	nagano-m@rs.noda.tus.ac.jp
Orense, Rolando	University of Auckland	r.orense@auckland.ac.nz
Pappin, Jack	Ove Arup and Partners Hong Kong	jack.pappin@arup.com
Pecker, Alain	Geodynamique & Structure	alain.pecker@geodynamique.com
Pender, Michael	University of Auckland	m.pender@auckland.ac.nz
Poulos, Harry	Coffey Geotechnics	harry_poulos@coffey.com
Prakash, Shamsher	Missouri S&T	Prakash@mst.edu
Singh, J.P.	JP Singh & Associates	jpsassoc@aol.com
Sritharan, Sri	Iowa State University	sri@iastate.edu
Stokoe II, Kenneth	University of Texas at Austin	k.stokoe@mail.utexas.edu
Sullivan, Tim	University of Pavia	timothy.sullivan@unipv.it
Taciroglu, Ertugrul	UCLA	etacir@ucla.edu
Tamagnini, Claudio	Università degli Studi di Perugia	tamag@unipg.it
Toh, Jeremy	Pells Sullivan Meynink	jcwtoh@hotmail.com
Wotherspoon, Liam	University of Auckland	l.wotherspoon@auckland.ac.nz